

Coarse Aggregate Deterioration in Granular Surfaces and Shoulders

**Final Report
April 2025**

About the Institute for Transportation

The mission of the Institute for Transportation (InTrans) at Iowa State University is to save lives and improve economic vitality through discovery, research innovation, outreach, and the implementation of bold ideas.

Iowa State University Nondiscrimination Statement

Iowa State University does not discriminate on the basis of race, color, age, ethnicity, religion, national origin, pregnancy, sexual orientation, gender identity, genetic information, sex, marital status, disability, or status as a U.S. Veteran. Inquiries regarding non-discrimination policies may be directed to Office of Equal Opportunity, 2680 Beardshear Hall, 515 Morrill Road, Ames, Iowa 50011, telephone: 515-294-7612, email: eooffice@iastate.edu.

Disclaimer Notice

The contents of this report reflect the views of the authors, who are responsible for the facts and the accuracy of the information presented herein. The opinions, findings and conclusions expressed in this publication are those of the authors and not necessarily those of the sponsors.

The sponsors assume no liability for the contents or use of the information contained in this document. This report does not constitute a standard, specification, or regulation.

The sponsors do not endorse products or manufacturers. Trademarks or manufacturers' names appear in this report only because they are considered essential to the objective of the document.

Iowa DOT Statements

Iowa DOT ensures non-discrimination in all programs and activities in accordance with Title VI of the Civil Rights Act of 1964. Any person who believes that they are being denied participation in a project, being denied benefits of a program, or otherwise being discriminated against because of race, color, national origin, gender, age, or disability, low income and limited English proficiency, or if needs more information or special assistance for persons with disabilities or limited English proficiency, please contact Iowa DOT Civil Rights at 515-239-7970 or by email at civil.rights@iowadot.us.

The preparation of this report was financed in part through funds provided by the Iowa Department of Transportation through its "Second Revised Agreement for the Management of Research Conducted by Iowa State University for the Iowa Department of Transportation" and its amendments.

The opinions, findings, and conclusions expressed in this publication are those of the authors and not necessarily those of the Iowa Department of Transportation.

Technical Report Documentation Page

1. Report No. IHRB Project TR-769	2. Government Accession No.	3. Recipient's Catalog No.	
4. Title and Subtitle Coarse Aggregate Deterioration in Granular Surfaces and Shoulders		5. Report Date April 2025	
		6. Performing Organization Code	
7. Author(s) Kanika H. Lamba (orcid.org/0000-0003-4811-2717), Jeramy C. Ashlock (orcid.org/0000-0003-0677-9900), Franciszek Hasiuk (orcid.org/0000-0002-6531-1710), and Bora Cetin (orcid.org/0000-0003-0415-7139)		8. Performing Organization Report No. InTrans Project 18-683	
9. Performing Organization Name and Address Institute for Transportation Iowa State University 2711 South Loop Drive, Suite 4700 Ames, IA 50010-8664		10. Work Unit No. (TRAIS)	
		11. Contract or Grant No.	
12. Sponsoring Organization Name and Address Iowa Highway Research Board Iowa Department of Transportation 800 Lincoln Way Ames, IA 50010		13. Type of Report and Period Covered Final Report	
		14. Sponsoring Agency Code	
15. Supplementary Notes Visit https://intrans.iastate.edu for color pdfs of this and other research reports.			
16. Abstract <p>The goal of this project was to characterize the relative performance and changes in microstructural and engineering properties for various types of coarse aggregates subjected to weathering as well as real and simulated traffic loads typical of granular surfaces and shoulders of Iowa roads. Through an extensive program of geotechnical laboratory tests, image analysis, geological laboratory tests, and analysis of data from prior projects, the deterioration of both fresh quarry samples and field test section samples was analyzed and compared.</p> <p>Of the five main quarry materials tested, the Class A materials from the Pedersen, Crescent, and Moore Quarries produced the lowest values of total breakage during gyratory compaction testing, with the Pedersen aggregates exhibiting the smallest changes in morphology. Clean aggregates from the Alden and Gehrke Quarries had the highest breakage values and among the largest changes in morphology during gyratory compaction tests.</p> <p>Among the three materials tested and analyzed from the TR-704 project's field test sections, the Bethany Falls Limestone (BFL) had the highest total breakage while the Oneota Formation Dolomite (OFD) had the lowest breakage, and the Lime Creek Formation (LCF) materials had only slightly greater breakage than the OFD. Overall, the BFL materials yielded the greatest changes in morphological parameters over time, whereas LCF exhibited slight changes and OFD exhibited the smallest changes.</p> <p>For the materials tested from 12 different test sections of the TR-721 project, the materials from the Optimized Gradation with Clay Slurry (OGCS) test sections had the best overall performance in terms of the smallest relative decreases in gravel fraction, smallest increases in sand and fines fractions, smallest cumulative total breakage values, and lowest changes in particle morphological parameters. The performance of the OGCS materials were followed by the surfacing materials of the Aggregate Columns test sections, which had intermediate performance, and finally those of the Control sections, which had the poorest performance.</p>			
17. Key Words aggregates—breakage parameters—chemical degradation—deterioration—granular roadways—gravel roads—geological degradation—gyratory compaction—mechanical degradation—morphology—shape parameters—triaxial testing—2D image analysis		18. Distribution Statement No restrictions.	
19. Security Classification (of this report) Unclassified.	20. Security Classification (of this page) Unclassified.	21. No. of Pages 504	22. Price NA

COARSE AGGREGATE DETERIORATION IN GRANULAR SURFACES AND SHOULDERS

Final Report
April 2025

Principal Investigator

Jeramy C. Ashlock, Professor and James M. Hoover Chair in Geotechnical Engineering
Department of Civil, Construction, and Environmental Engineering, Iowa State University

Co-Principal Investigators

Franciszek Hasiuk, Geologist
Geotechnology & Engineering Department (8912), Sandia National Laboratories

Bora Cetin, Professor
Department of Civil and Environmental Engineering, Michigan State University

Research Assistant

Kanika H. Lamba

Authors

Kanika H. Lamba, Jeramy C. Ashlock, Franciszek Hasiuk, and Bora Cetin

Sponsored by
Iowa Highway Research Board and
Iowa Department of Transportation
(IHRB Project TR-769)

Preparation of this report was financed in part
through funds provided by the Iowa Department of Transportation
through its Research Management Agreement with the
Institute for Transportation
(InTrans Project 18-683)

A report from
Institute for Transportation
Iowa State University
2711 South Loop Drive, Suite 4700
Ames, IA 50010-8664
Phone: 515-294-8103 / Fax: 515-294-0467
<https://intrans.iastate.edu>

TABLE OF CONTENTS

ACKNOWLEDGMENTS	xxv
EXECUTIVE SUMMARY	xxvii
CHAPTER 1. INTRODUCTION.....	1
1.1 Problem Statement.....	1
1.2 Research Objectives	1
1.3 Significance of the Research	2
1.4 Organization of the Report	2
CHAPTER 2. BACKGROUND.....	3
2.1 Coarse Aggregate Deterioration in Iowa	3
2.2 Research Plan	4
2.3 Evaluation of Degradation of Coarse Aggregates	6
CHAPTER 3. LABORATORY TESTING AND METHODOLOGY	15
3.1 Introduction	15
3.2 Laboratory Testing and Methodology	15
CHAPTER 4. RESULTS AND DISCUSSION	30
4.1 Coarse Aggregate Samples Collected from Quarries	30
4.2 Coarse Aggregate Samples Collected from Test Sections of IHRB Project TR-704.....	108
4.3 Coarse Aggregate Samples Collected from Test Sections of IHRB Project TR-721.....	152
CHAPTER 5. CONCLUSIONS AND RECOMMENDATIONS.....	269
5.1 Comparison of Breakage and Morphological Parameters for Different Aggregate Sources.....	269
5.2 Conclusions from Geological Tests on Quarry and Field Samples.....	276
5.3 Recommendations for Implementation and Further Research	276
REFERENCES	278
APPENDIX A. THIN SECTION PHOTOMICROGRAPHS OF GRAVEL ROCK TYPES COLLECTED FROM QUARRIES.....	A-1
APPENDIX B. THIN SECTION PHOTOMICROGRAPHS OF GRAVEL ROCK TYPES COLLECTED FROM ROADWAY TEST SECTIONS.....	B-1

LIST OF FIGURES

Figure 1. Locations of the quarries used in this study superimposed over USGS Iowa geological map	5
Figure 2. Field test section locations for the TR-704 and TR-721 projects	5
Figure 3. Morphological characterization for particle in 3D space	7
Figure 4. Morphological characterization for particle in 2D space	7
Figure 5. (a) Visual estimation of roundness and sphericity and (b) examples of particle shape characterization.....	11
Figure 6. Definition of total breakage	13
Figure 7. Definition of breakage potential.....	14
Figure 8. (a) Brovold gyratory compactor, (b) PDA device, (c) PDA internal components and battery compartment, (d) schematic demonstrating eccentricity of the resultant force calculated from three load cells	17
Figure 9. (a) Canon 2D scanner used in this study, (b) original image of scanned gravel-sized particles, (c) processed image used to automatically count the number of particles.....	18
Figure 10. (a) Original high-quality scanned image of particles retained on No. 4 sieve, (b) processed binary image overlain with circles denoting MinR radius in red and MaxR radius in green, computed using Landini's sphericity algorithm (Landini et al. 2012).....	19
Figure 11. Base setup for triaxial testing.....	20
Figure 12. Membrane placement for triaxial specimen.....	20
Figure 13. Split vacuum mold and filling of triaxial specimen.....	21
Figure 14. Placing of top cap and O-rings around membrane.....	22
Figure 15. Placement of second membrane around the specimen.....	22
Figure 16. Triaxial testing – shearing in progress	24
Figure 17. Triaxial testing – sample failed at 30% strain.....	24
Figure 18. Real-time graph for monitoring of CD triaxial testing during shearing.....	25
Figure 19. Laboratory equipment for geological tests in this study: (a) helium porosimeter to measure grain density, (b) Camsizer to measure particle size distributions, (c) petrographic microscope to characterize internal structure of particles, (d) mercury porosimeter to measure pore throat size distributions in coarse aggregate pebbles, (e) thin section showing interior nature of pebbles.....	28
Figure 20. Particle size distributions from sieve and hydrometer analysis and evaluation of total breakage of coarse aggregate samples from Moore Quarry	31
Figure 21. Particle size distributions from 2D image analysis and evaluation of total breakage of coarse aggregate samples from Moore Quarry	31
Figure 22. Comparison of roundness for BGT and AGT specimens from Moore Quarry.....	33
Figure 23. Comparison of sphericity for BGT and AGT specimens from Moore Quarry	33
Figure 24. Comparison of form factor for BGT and AGT specimens from Moore Quarry.....	34
Figure 25. Comparison of shape factor for BGT and AGT specimens from Moore Quarry	34
Figure 26. Comparison of roundness index for BGT and AGT specimens from Moore Quarry	35
Figure 27. Comparison of angularity for BGT and AGT specimens from Moore Quarry.....	35

Figure 28. Roundness versus inverse of aspect ratio for BGT and AGT specimens from Moore Quarry	37
Figure 29. Relationships between dry unit weight, gyratory compaction energy, shear resistance, and number of gyrations for coarse aggregates from Moore Quarry	38
Figure 30. Changes in shear resistance and void ratio of coarse aggregate sample from Moore Quarry during gyratory compaction test	38
Figure 31. Triaxial test results for Moore Quarry specimens before gyratory testing	39
Figure 32. Triaxial test results for Moore Quarry specimens after gyratory testing	40
Figure 33. Camsizer data for three rock types from Moore Quarry BGT (red lines) and AGT (dashed green lines). Arrows indicate resulting changes in relative abundance AGT.	42
Figure 34. Particle size distributions from sieve and hydrometer analysis and evaluation of breakage of coarse fraction for samples from Alden Quarry	43
Figure 35. Particle size distributions from 2D image analysis and evaluation of breakage of gravel fraction for samples from Alden Quarry	44
Figure 36. Comparison of roundness for BGT and AGT specimens from Alden Quarry	45
Figure 37. Comparison of sphericity for BGT and AGT specimens from Alden Quarry	45
Figure 38. Comparison of form factor for BGT and AGT specimens from Alden Quarry	46
Figure 39. Comparison of shape factor for BGT and AGT specimens from Alden Quarry	46
Figure 40. Comparison of roundness index for BGT and AGT specimens from Alden Quarry	47
Figure 41. Comparison of angularity for BGT and AGT specimens from Alden Quarry	47
Figure 42. Roundness versus inverse of aspect ratio for BGT and AGT specimens from Alden Quarry	48
Figure 43. Relationships between dry unit weight, gyratory compaction energy, shear resistance, and number of gyrations for coarse aggregates from Alden Quarry	49
Figure 44. Changes in shear resistance and void ratio of coarse aggregates from Alden Quarry during gyratory compaction test	50
Figure 45. Mohr-Coulomb plot of samples from Alden Quarry – before gyratory testing	51
Figure 46. Mohr-Coulomb plot of samples from Alden Quarry – after gyratory testing	52
Figure 47. Camsizer data for Alden Quarry Rock Type 1 BGT (red lines) and AGT (dashed green lines).	54
Figure 48. Magnified view of Rock Type 2 for Alden Quarry: (a) BGT sample with observed abundance of 30%, (b) AGT sample with observed abundance of 3%	55
Figure 49. Magnified views of Rock Type 1 for Alden Quarry AGT sample	55
Figure 50. Magnified view of Rock Type 2 for Alden Quarry AGT sample	56
Figure 51. Particle size distribution from sieve and hydrometer analysis and evaluation of breakage of coarse fraction for samples from Gehrke Quarry	57
Figure 52. Particle size distributions from 2D image analysis and evaluation of breakage of gravel fraction for samples from Gehrke Quarry	58
Figure 53. Comparison of roundness for BGT and AGT specimens from Gehrke Quarry	59
Figure 54. Comparison of sphericity for BGT and AGT specimens from Gehrke Quarry	59
Figure 55. Comparison of form factor for BGT and AGT specimens from Gehrke Quarry	60
Figure 56. Comparison of shape factor for BGT and AGT specimens from Gehrke Quarry	60
Figure 57. Comparison of roundness index for BGT and AGT specimens from Gehrke Quarry	61

Figure 58. Comparison of angularity for BGT and AGT specimens from Gehrke Quarry	61
Figure 59. Roundness versus inverse of aspect ratio for BGT and AGT specimens from Gehrke Quarry	62
Figure 60. Relationships between dry unit weight, gyratory compaction energy, shear resistance, and number of gyrations for coarse aggregates from Gehrke Quarry.....	63
Figure 61. Changes in shear resistance and void ratio of coarse aggregates from Gehrke Quarry during gyratory compaction test.....	64
Figure 62. Mohr-Coulomb plot of samples from Gehrke Quarry – before gyratory testing.....	65
Figure 63. Mohr-Coulomb plot of samples from Alden Quarry – after gyratory testing.....	65
Figure 64. Particle size distributions from sieve and hydrometer analysis and evaluation of breakage of coarse fraction for samples from Crescent Quarry	67
Figure 65. Particle size distribution from 2D image analysis and evaluation of breakage of gravel fraction for samples from Crescent Quarry	68
Figure 66. Comparison of roundness for BGT and AGT specimens from Crescent Quarry	69
Figure 67. Comparison of sphericity for BGT and AGT specimens from Crescent Quarry.....	69
Figure 68. Comparison of form factor for BGT and AGT specimens from Crescent Quarry	70
Figure 69. Comparison of shape factor for BGT and AGT specimens from Crescent Quarry	70
Figure 70. Comparison of roundness index for BGT and AGT specimens from Crescent Quarry	71
Figure 71. Comparison of angularity for BGT and AGT specimens from Crescent Quarry	71
Figure 72. Roundness versus inverse of aspect ratio for BGT and AGT specimens from Crescent Quarry	72
Figure 73. Relationships between dry unit weight, gyratory compaction energy, shear resistance, and number of gyrations for coarse aggregates from Crescent Quarry	73
Figure 74. Changes in shear resistance and void ratio of coarse aggregate sample from Crescent Quarry during gyratory compaction test.....	74
Figure 75. Mohr-Coulomb plot of samples from Crescent Quarry – before gyratory testing.....	75
Figure 76. Mohr-Coulomb plot of samples from Crescent Quarry – after gyratory testing.....	75
Figure 77. Magnified view of Rock Type 1 for Crescent Quarry AGT specimen: (a) cracks parallel to edge, (b) cracks nonparallel to edge, (c) healed fracture.....	79
Figure 78. Grain-boundary hugging fractures visible in Crescent Rock Type 6 BGT and Rock Type 2 AGT	80
Figure 79. Magnified view of Rock Type 5 for Crescent Quarry AGT specimen showing porous rims	81
Figure 80. Camsizer data for four rock types from Crescent Quarry BGT (red lines) and AGT (green lines). Arrows indicate resulting changes in relative abundance AGT.	82
Figure 81. Particle size distributions from sieve and hydrometer analysis and evaluation of breakage of coarse fraction for samples from Pedersen Quarry	83
Figure 82. Particle size distributions from 2D image analysis and evaluation of breakage of coarse aggregate samples from Pedersen Quarry	84
Figure 83. Comparison of roundness for BGT and AGT specimens from Pedersen Quarry	85
Figure 84. Comparison of sphericity for BGT and AGT specimens from Pedersen Quarry	85
Figure 85. Comparison of form factor for BGT and AGT specimens from Pedersen Quarry	86
Figure 86. Comparison of shape factor for BGT and AGT specimens from Pedersen Quarry	86

Figure 87. Comparison of roundness index for BGT and AGT specimens from Pedersen Quarry	87
Figure 88. Comparison of angularity for BGT and AGT specimens from Pedersen Quarry	87
Figure 89. Roundness versus inverse of aspect ratio for BGT and AGT specimens from Pedersen Quarry	88
Figure 90. Relationships between dry unit weight, gyratory compaction energy, shear resistance, and number of gyrations for coarse aggregates from Pedersen Quarry	89
Figure 91. Changes in shear resistance and void ratio of coarse aggregates from Pedersen Quarry during gyratory compaction test	90
Figure 92. Mohr-Coulomb plot of samples from Pedersen Quarry – before gyratory testing	91
Figure 93. Mohr-Coulomb plot of samples from Pedersen Quarry – after gyratory testing	92
Figure 94. Camsizer data for two rock types from Pedersen Quarry BGT (red lines) and AGT (green lines). Arrows indicate resulting changes in relative abundance AGT.	95
Figure 95. Macroscopic and microscopic views of thin sections of Pedersen Rock Type 2 BGT and AGT. Pore space is barely visible in macroscopic views (A1 and B1) but is more apparent at microscopic level (A2 and B2).	96
Figure 96. Porous rim visible in (A) Crescent Rock Type 5 AGT, (B) Moore Rock Type 4 BGT, and (C) Moore Rock Type 4 AGT	98
Figure 97. Examples of intergranular pore space (highlighted by blue-dyed epoxy) manifesting as open, connected pore space between sedimentary grains for Alden BGT and AGT samples	99
Figure 98. Examples of microporosity (highlighted by blue-dyed epoxy) manifesting as a hazy matrix between grains	100
Figure 99. Examples of separate vuggy pore space (highlighted by blue-dyed epoxy) manifesting as pore spaces between sedimentary grains either completely disconnected from other pores or only connected through a microporous matrix	101
Figure 100. Examples of intercrystalline pore space	102
Figure 101. Hairline fractures parallel to particle edges visible in various rock types before and after compaction	103
Figure 102. Hairline fractures perpendicular to particle edges visible in numerous rock types before and after gyratory compaction	104
Figure 103. Hairline fractures parallel (A) and nonparallel (B) to particle edges in Crescent Rock Type 1 after gyratory compaction. Evidence of healed fractures from before quarrying (C) were also visible.	105
Figure 104. Multiple hairline fractures extending oblique from particle edge in Atlantic (BFL) RT4 and Booneville (CRG) RT3	106
Figure 105. Grain-boundary hugging fractures visible in Crescent RT6 (BGT) and Crescent RT2 (AGT)	107
Figure 106. Particle size distributions of coarse fraction from sieve analysis and evaluation of total breakage between September 2016 and April 2017 for BFL Class A test section	110
Figure 107. Particle size distributions of coarse fraction from sieve analysis and evaluation of total breakage between May 2017 and June 2017 for BFL Class A test section ...	111

Figure 108. Particle size distributions of coarse fraction from sieve analysis and evaluation of total breakage between May 2018 and April 2019 for BFL Class A test section	111
Figure 109. Particle size distributions of gravel fraction from 2D image analysis and evaluation of total breakage between May 2017 and June 2017 for BFL Class A test section	112
Figure 110. Particle size distributions of gravel fraction from 2D image analysis and evaluation of total breakage between May 2017 and February 2018 for BFL Class A test section	112
Figure 111. Particle size distributions of gravel fraction from 2D image analysis and evaluation of total breakage between May 2017 and April 2018 for BFL Class A test section	113
Figure 112. Particle size distributions of gravel fraction from 2D image analysis and evaluation of total breakage between May 2018 and April 2019 for BFL Class A test section	113
Figure 113. Percent gravel, sand, and fines for samples of BFL Class A collected over time ...	114
Figure 114. Total breakage of coarse fraction evaluated from sieve analyses of samples from BFL Class A section collected over time.....	115
Figure 115. Total breakage of gravel fraction evaluated from 2D image analyses of samples from BFL Class A section collected over time.....	115
Figure 116. Comparison of roundness for BFL Class A samples collected over time.....	116
Figure 117. Comparison of sphericity for BFL Class A samples collected over time	117
Figure 118. Comparison of form factor for BFL Class A samples collected over time.....	117
Figure 119. Comparison of shape factor for BFL Class A samples collected over time	118
Figure 120. Comparison of roundness index for BFL Class A samples collected over time.....	118
Figure 121. Comparison of angularity for BFL Class A samples collected over time.....	119
Figure 122. Percentages of rock types in BFL Class A samples collected over time	123
Figure 123. Rock types, grain densities, abundances, and thin section images for Clean versus Class A BFL quarry samples from TR-704 project.....	124
Figure 124. Particle size distributions of coarse fraction from sieve analysis and evaluation of total breakage between September 2016 and April 2017 for LCF Class A test section	126
Figure 125. Particle size distributions of coarse fraction from sieve analysis and evaluation of total breakage between May 2017 and June 2017 for LCF Class A test section ...	126
Figure 126. Particle size distributions of gravel fraction from 2D image analysis and evaluation of total breakage between May 2017 and June 2017 for LCF Class A test section	127
Figure 127. Particle size distributions of gravel fraction from 2D image analysis and evaluation of total breakage between May 2017 and February 2018 for LCF Class A test section	127
Figure 128. Particle size distributions of coarse fraction from sieve analysis and evaluation of total breakage between May 2017 and April 2018 for LCF Class A test section	128
Figure 129. Particle size distributions of gravel fraction from 2D image analysis and evaluation of total breakage between May 2017 and April 2018 for LCF Class A test section	128

Figure 130. Particle size distributions of coarse fraction from sieve analysis and evaluation of total breakage between May 2018 and April 2019 for LCF Class A test section	129
Figure 131. Particle size distributions of gravel fraction from 2D image analysis and evaluation of total breakage between May 2018 and April 2019 for LCF Class A test section	129
Figure 132. Percent gravel, sand, and fines for sieve analysis of samples from LCF Class A section collected over time	130
Figure 133. Hardin's total breakage evaluated from sieve analyses of samples from LCF Class A section collected over time.....	131
Figure 134. Hardin's total breakage evaluated from 2D image analyses of samples from LCF Class A section collected over time.....	131
Figure 135. Comparison of roundness for LCF Class A samples collected over time.....	132
Figure 136. Comparison of sphericity for LCF Class A samples collected over time.....	132
Figure 137. Comparison of form factor for LCF Class A samples collected over time.....	133
Figure 138. Comparison of shape factor for LCF Class A samples collected over time	133
Figure 139. Comparison of roundness index for LCF Class A samples collected over time.....	134
Figure 140. Comparison of angularity for LCF Class A samples collected over time.....	134
Figure 141. Percentages of rock types in LCF Class A samples collected over time	138
Figure 142. Rock types, grain densities, abundances, and thin section images for Clean versus Class A LCF quarry samples from TR-704 project.....	139
Figure 143. Particle size distributions of coarse fraction from sieve analysis and evaluation of total breakage between September 2016 and April 2017 for OFD Class A test section	141
Figure 144. Particle size distributions of coarse fraction from sieve analysis and evaluation of total breakage between May 2017 and June 2017 for OFD Class A test section	141
Figure 145. Particle size distributions of coarse fraction from sieve analysis and evaluation of total breakage between May 2017 and April 2018 for OFD Class A test section	142
Figure 146. Particle size distributions of gravel fraction from 2D image analysis and evaluation of total breakage between June 2017 and February 2018 for OFD Class A test section.....	142
Figure 147. Particle size distributions of gravel fraction from 2D image analysis and evaluation of total breakage between June 2017 and April 2018 for OFD Class A test section.....	143
Figure 148. Particle size distributions of coarse fraction from sieve analysis and evaluation of total breakage between May 2018 and April 2019 for OFD Class A test section	143
Figure 149. Percent gravel, sand, and fines for samples of OFD Class A collected over time	144
Figure 150. Hardin's total breakage evaluated from sieve analyses of samples from OFD Class A section collected over time.....	145
Figure 151. Hardin's total breakage evaluated from 2D image analyses of samples from OFD Class A section collected over time.....	145
Figure 152. Comparison of roundness for OFD Class A samples collected over time.....	146

Figure 153. Comparison of sphericity for OFD Class A samples collected over time	146
Figure 154. Comparison of form factor for OFD Class A samples collected over time	147
Figure 155. Comparison of shape factor for OFD Class A samples collected over time	147
Figure 156. Comparison of roundness index for OFD Class A samples collected over time	148
Figure 157. Comparison of angularity for OFD Class A samples collected over time	148
Figure 158. Percentages of rock types in OFD Class A samples collected over time	151
Figure 159. Rock types, grain densities, abundances, and thin section images for Clean versus Class A OFD quarry samples from TR-704 project	152
Figure 160. Locations of test sections for TR-721 project in Hamilton, Cherokee, Howard, and Washington Counties	153
Figure 161. Satellite image of Howard County mechanically stabilized test sections	155
Figure 162. Layouts of mechanically stabilized test sections in Howard County	155
Figure 163. Particle size distribution curves of Howard County Control Section for samples collected over time	156
Figure 164. Particle size distributions and total breakage of coarse fraction for Howard County Control section between fall 2018 and spring 2019	157
Figure 165. Particle size distributions and total breakage of coarse fraction for Howard County Control section between fall 2019 and spring 2020	157
Figure 166. Cumulative total breakage of samples from Howard County Control section collected over time	158
Figure 167. Gravel, sand and fines fractions of samples from Howard County Control section collected over time	158
Figure 168. Visual surveys of Howard County Control section over time: (a) fall 2018 (b) spring 2019, (c) fall 2019, (d) spring 2020	159
Figure 169. Particle size distribution of coarse fraction of Howard County OGCS test section over time	161
Figure 170. Particle size distributions of coarse fraction from sieve analyses and evaluation of total breakage between fall 2018 and spring 2019 for OGCS test section	162
Figure 171. Particle size distributions of coarse fraction from sieve analyses and evaluation of total breakage between fall 2018 and fall 2019 for OGCS test section	162
Figure 172. Particle size distributions of coarse fraction from sieve analyses and evaluation of total breakage between fall 2018 and spring 2020 for OGCS test section	163
Figure 173. Cumulative total breakage for Howard County OGCS samples collected over time	164
Figure 174. Percent gravel, sand, and fines for Howard County OGCS samples collected over time	164
Figure 175. Visual surveys of Howard County OGCS section over time: (a) fall 2018, (b) spring 2019, (c) fall 2019, (d) spring 2020	165
Figure 176. Column layout pattern for Howard County Aggregate Columns section, road width = 40 ft	166
Figure 177. Particle size distributions of Howard County Aggregate Columns surface materials for samples collected over time	167
Figure 178. Particle size distributions and evaluation of total breakage of coarse aggregate for Howard County Aggregate Columns section from fall 2018 to spring 2019	168
Figure 179. Particle size distributions and evaluation of total breakage of coarse aggregate for Howard County Aggregate Columns section from fall 2018 to fall 2019	168

Figure 180. Cumulative total breakage of surface course of Howard County Aggregate Columns section over time	169
Figure 181. Percent gravel, sand, and fines fraction of the samples from Howard County Aggregate Columns section collected over time	169
Figure 182. Visual surveys of Howard County Aggregate Columns section over time: (a) fall 2018, (b) spring 2019, (c) fall 2019, (d) spring 2020.....	170
Figure 183. Comparison of cumulative total breakage of samples from Howard County OGCS section, Aggregate Columns section, and Control section collected over time	171
Figure 184. Comparison of cumulative relative breakage of samples from Howard County OGCS section, Aggregate Columns section, and Control section collected over time	172
Figure 185. Comparison of gravel fraction for samples from Howard County OGCS section, Aggregate Columns section, and Control section collected over time.....	173
Figure 186. Comparison of percent decrease in gravel fraction of samples from Howard County OGCS section, Aggregate Columns section, and Control section collected over time.....	173
Figure 187. Comparison of sand fraction for samples from Howard County OGCS section, Aggregate Columns section, and Control section collected over time.....	174
Figure 188. Comparison of percent increase in sand fraction for samples from Howard County OGCS section, Aggregate Columns section, and Control section collected over time.....	174
Figure 189. Comparison of fines fraction for samples from Howard County OGCS section, Aggregate Columns section, and Control section collected over time.....	175
Figure 190. Comparison of percent increase in fines fraction for samples from Howard County OGCS section, Aggregate Columns section, and Control section collected over time.....	175
Figure 191. Satellite image of Hamilton County chemically and mechanically stabilized test sections.....	176
Figure 192. Layouts of chemically and mechanically stabilized test sections in Hamilton County.....	177
Figure 193. Particle size distribution curves of Hamilton County Control Section for samples collected over time.....	178
Figure 194. Particle size distributions and evaluation of total breakage of coarse fraction for Hamilton County Control section between fall 2018 and spring 2019.....	179
Figure 195. Particle size distributions and evaluation of total breakage of coarse fraction for Hamilton County Control section between fall 2018 and fall 2019.....	179
Figure 196. Particle size distributions and evaluation of total breakage of coarse fraction for Hamilton County Control section between fall 2018 and spring 2020.....	180
Figure 197. Cumulative total breakage of samples from Hamilton County Control section collected over time.....	181
Figure 198. Gravel, sand and fines fractions of samples from Hamilton County Control section collected over time	181
Figure 199. Comparison of roundness for Hamilton County Control section samples from spring 2019 and fall 2019	182

Figure 200. Comparison of sphericity for Hamilton County Control section samples from spring 2019 and fall 2019	182
Figure 201. Comparison of form factor for Hamilton County Control section samples from spring 2019 and fall 2019	183
Figure 202. Comparison of shape factor for Hamilton County Control section samples from spring 2019 and fall 2019	183
Figure 203. Comparison of angularity for Hamilton County Control section samples from spring 2019 and fall 2019	184
Figure 204. Comparison of roundness index for Hamilton County Control section samples from spring 2019 and fall 2019	184
Figure 205. Visual surveys of Hamilton County Control section over time: (a) fall 2018, (b) spring 2019, (c) fall 2019, (d) spring 2020	186
Figure 206. Particle size distribution curves of Hamilton County OGCS Section for samples collected over time County	188
Figure 207. Particle size distributions and evaluation of total breakage of coarse fraction for Hamilton County OGCS section between fall 2018 and spring 2019	188
Figure 208. Particle size distributions and evaluation of total breakage of coarse fraction for Hamilton County OGCS section between fall 2018 and fall 2019	189
Figure 209. Particle size distributions and evaluation of total breakage of coarse fraction for Hamilton County OGCS section between fall 2018 and spring 2020	189
Figure 210. Cumulative total breakage of coarse fraction for Hamilton County OGCS section samples collected over time.....	190
Figure 211. Gravel, sand and fines fractions of the samples from Hamilton County OGCS section collected over time	190
Figure 212. Particle size distributions by 2D image analysis and evaluation of total breakage of gravel fraction for Hamilton County OGCS section between fall 2018 and spring 2019.....	191
Figure 213. Particle size distributions by 2D image analysis and evaluation of total breakage of gravel fraction for Hamilton County OGCS section between fall 2018 and spring 2020.....	191
Figure 214. Comparison of roundness for Hamilton County OGCS section samples from fall 2018, spring 2019 and spring 2020	192
Figure 215. Comparison of sphericity for Hamilton County OGCS section samples from fall 2018, spring 2019 and spring 2020	193
Figure 216. Comparison of form factor for Hamilton County OGCS section samples from fall 2018, spring 2019 and spring 2020	193
Figure 217. Comparison of shape factor for Hamilton County OGCS section samples from fall 2018, spring 2019 and spring 2020	194
Figure 218. Comparison of angularity for Hamilton County OGCS section samples from fall 2018, spring 2019 and spring 2020	194
Figure 219. Comparison of roundness index for Hamilton County OGCS section samples from fall 2018, spring 2019 and spring 2020	195
Figure 220. Visual surveys of Hamilton County OGCS section over time: (a) fall 2018, (b) spring 2019, (c) fall 2019, (d) spring 2020	197
Figure 221. Column layout pattern for Hamilton County Aggregate Columns section, road width = 28 ft.....	198

Figure 222. Particle size distributions of Hamilton County Aggregate Columns surface materials for samples collected over time.....	199
Figure 223. Particle size distributions and evaluation of total breakage of coarse aggregate for Hamilton County Aggregate Columns section from fall 2018 to spring 2019	200
Figure 224. Particle size distributions and evaluation of total breakage of coarse aggregate for Hamilton County Aggregate Columns section from fall 2018 to fall 2019	200
Figure 225. Particle size distributions and evaluation of total breakage of coarse aggregate for Hamilton County Aggregate Columns section from fall 2018 to spring 2020	201
Figure 226. Cumulative total breakage of surface course of Hamilton County Aggregate Columns section over time	202
Figure 227. Gravel, sand and fines fractions of surface course of Hamilton County Aggregate Columns section over time.....	202
Figure 228. Comparison of roundness for Hamilton County Aggregate Columns section samples from spring 2019 and fall 2019.....	203
Figure 229. Comparison of sphericity for Hamilton County Aggregate Columns section samples from spring 2019 and fall 2019.....	203
Figure 230. Comparison of form factor for Hamilton County Aggregate Columns section samples from spring 2019 and fall 2019.....	204
Figure 231. Comparison of shape factor for Hamilton County Aggregate Columns section samples from spring 2019 and fall 2019.....	204
Figure 232. Comparison of angularity for Hamilton County Aggregate Columns section samples from spring 2019 and fall 2019.....	205
Figure 233. Comparison of roundness index for Hamilton County Aggregate Columns section samples from spring 2019 and fall 2019	205
Figure 234. Visual surveys of Hamilton County Aggregate Columns section over time: (a) fall 2018, (b) spring 2019, (c) fall 2019, (d) spring 2020.....	207
Figure 235. Comparison of cumulative total breakage of samples from Hamilton County OGCS section, Aggregate Columns section, and Control section collected over time	208
Figure 236. Comparison of cumulative relative breakage of samples from Hamilton County OGCS section, Aggregate Columns section, and Control section collected over time.....	208
Figure 237. Comparison of gravel fraction for samples from Hamilton County OGCS section, Aggregate Columns section, and Control section collected over time.....	209
Figure 238. Comparison of percent decrease in gravel fraction relative to 2018 for samples from Hamilton County OGCS section, Aggregate Columns section, and Control section collected over time	209
Figure 239. Comparison of sand fraction for samples from Hamilton County OGCS section, Aggregate Columns section, and Control section collected over time.....	210
Figure 240. Comparison of percent increase in sand fraction relative to 2018 for samples from Hamilton County OGCS section, Aggregate Columns section, and Control section collected over time	210
Figure 241. Comparison of fines fraction for samples from Hamilton County OGCS section, Aggregate Columns section, and Control section collected over time.....	211

Figure 242. Comparison of percent increase in fines fraction relative to 2018 for samples from Hamilton County OGCS section, Aggregate Columns section, and Control section collected over time	211
Figure 243. Satellite image of Washington County chemically and mechanically stabilized test sections	212
Figure 244. Layouts of chemically and mechanically stabilized test sections in Washington County.....	212
Figure 245. Particle size distribution curves of Washington County Control section for samples collected over time	214
Figure 246. Particle size distributions and evaluation of total breakage of coarse aggregate samples of Washington County Control section between fall 2018 and spring 2019	214
Figure 247. Particle size distributions and evaluation of total breakage of coarse aggregate samples of Washington County Control section between fall 2018 and fall 2019.....	215
Figure 248. Particle size distributions and evaluation of total breakage of coarse aggregate samples of Washington County Control section between fall 2018 and spring 2020	215
Figure 249. Cumulative total breakage of samples from Washington County Control section over time.....	216
Figure 250. Gravel, sand and fines fractions of samples from Washington County Control section over time.....	216
Figure 251. Visual surveys of Washington County Control section over time: (a) fall 2018, (b) spring 2019, (c) fall 2019, (d) spring 2020	217
Figure 252. Particle size distribution curves of Washington County OGCS section for samples collected over time	219
Figure 253. Particle size distributions and evaluation of total breakage of coarse aggregate samples of Washington County OGCS section between fall 2018 and spring 2019	219
Figure 254. Particle size distributions and evaluation of total breakage of coarse aggregate samples of Washington County OGCS section between fall 2018 and fall 2019	220
Figure 255. Particle size distributions and evaluation of total breakage of coarse aggregate samples of Washington County OGCS section between fall 2018 and spring 2020	220
Figure 256. Gravel, sand and fines fractions of samples from Washington County OGCS section collected over time	221
Figure 257. Cumulative total breakage of samples from Washington County OGCS section collected over time.....	221
Figure 258. Particle size distributions from 2D image analysis and evaluation of total breakage of gravel fraction for Washington County OGCS section between fall 2018 and fall 2019	222
Figure 259. Comparison of roundness for Washington County OGCS samples from fall 2018 and fall 2019	223
Figure 260. Comparison of sphericity for Washington County OGCS samples from fall 2018 and fall 2019	223
Figure 261. Comparison of form factor for Washington County OGCS samples from fall 2018 and fall 2019	224

Figure 262. Comparison of shape factor for Washington County OGCS samples from fall 2018 and fall 2019	224
Figure 263. Comparison of angularity for Washington County OGCS samples from fall 2018 and fall 2019	225
Figure 264. Comparison of roundness index for Washington County OGCS samples from fall 2018 and fall 2019	225
Figure 265. Visual surveys of Washington County OGCS section over time: (a) fall 2018, (b) spring 2019, (c) fall 2019, (d) spring 2020	227
Figure 266. Column layout pattern for Washington County Aggregate Columns section, road width = 31 ft	228
Figure 267. Particle size distributions of Washington County Aggregate Columns surface materials for samples collected over time.....	229
Figure 268. Particle size distributions and evaluation of total breakage of coarse aggregate for Washington County Aggregate Columns section from fall 2018 to spring 2019	229
Figure 269. Particle size distributions and evaluation of total breakage of coarse aggregate for Washington County Aggregate Columns section from fall 2018 to fall 2019.....	230
Figure 270. Particle size distributions and evaluation of total breakage of coarse aggregate for Washington County Aggregate Columns section from fall 2018 to spring 2020	230
Figure 271. Percent gravel, sand, and fines of surface course of Washington County Aggregate Columns section over time.....	231
Figure 272. Cumulative total breakage of surface course of Washington County Aggregate Columns section over time	231
Figure 273. Visual surveys of Washington County Aggregate Columns section over time: (a) fall 2018, (b) spring 2019, (c) fall 2019, (d) spring 2020.....	232
Figure 274. Comparison of Hardin's total breakage of samples from Washington County OGCS section, Aggregate Columns section, and Control section collected over time	233
Figure 275. Comparison of Hardin's relative breakage of samples from Washington County OGCS section, Aggregate Columns section, and Control section collected over time.....	233
Figure 276. Comparison of gravel fraction for samples from Washington County OGCS section, Aggregate Columns section, and Control section collected over time.....	234
Figure 277. Comparison of percent decrease in gravel fraction relative to 2018 for samples from Washington County OGCS section, Aggregate Columns section, and Control section collected over time	235
Figure 278. Comparison of sand fraction for samples from Washington County OGCS section, Aggregate Columns section, and Control section collected over time.....	235
Figure 279. Comparison of percent increase in sand fraction relative to 2018 for samples from Washington County OGCS section, Aggregate Columns section, and Control section collected over time	236
Figure 280. Comparison of fines fraction for samples from Washington County OGCS section, Aggregate Columns section, and Control section collected over time.....	236

Figure 281. Comparison of percent increase in fines fraction relative to 2018 for samples from Washington County OGCS section, Aggregate Columns section, and Control section collected over time	237
Figure 282. Satellite image of Cherokee County mechanically stabilized test sections	238
Figure 283. Layout of mechanically stabilized test sections in Cherokee County	238
Figure 284. Particle size distribution curves of Cherokee County Control Section for samples collected over time	240
Figure 285. Particle size distributions and evaluation of total breakage of coarse fraction for Cherokee County Control section between fall 2018 and spring 2019	241
Figure 286. Particle size distributions and evaluation of total breakage of coarse fraction for Cherokee County Control section between fall 2018 and fall 2019	241
Figure 287. Particle size distributions and evaluation of apparent total breakage of coarse fraction for Cherokee County Control section between fall 2018 and after new aggregate was spread in spring 2020	242
Figure 288. Cumulative total breakage of samples from Cherokee County Control section collected over time	243
Figure 289. Gravel, sand and fines fractions of samples from Cherokee County Control section collected over time	243
Figure 290. Comparison of roundness for Cherokee County Control section samples from spring 2019 and fall 2019	244
Figure 291. Comparison of sphericity for Cherokee County Control section samples from spring 2019 and fall 2019	244
Figure 292. Comparison of form factor for Cherokee County Control section samples from spring 2019 and fall 2019	245
Figure 293. Comparison of shape factor for Cherokee County Control section samples from spring 2019 and fall 2019	245
Figure 294. Comparison of roundness index for Cherokee County Control section samples from spring 2019 and fall 2019	246
Figure 295. Comparison of angularity for Cherokee County Control section samples from spring 2019 and fall 2019	246
Figure 296. Visual surveys of Cherokee County Control section over time: (a) fall 2018, (b) spring 2019, (c) fall 2019, (d) spring 2020	248
Figure 297. Particle size distribution curves of Cherokee County OGCS Section for samples collected over time	250
Figure 298. Particle size distributions and evaluation of total breakage of coarse fraction for Cherokee County OGCS section between fall 2018 and spring 2019	250
Figure 299. Particle size distributions and evaluation of total breakage of coarse fraction for Cherokee County OGCS section between fall 2018 and fall 2019	251
Figure 300. Particle size distributions and evaluation of total breakage of coarse fraction for Cherokee County OGCS section between fall 2018 and spring 2020	251
Figure 301. Gravel, sand and fines fractions of samples from Cherokee County OGCS section collected over time	252
Figure 302. Total breakage of coarse fraction for Cherokee County OGCS section samples collected over time	252
Figure 303. Visual surveys of Cherokee County OGCS section over time: (a) fall 2018, (b) spring 2019, (c) fall 2019, (d) spring 2020	253

Figure 304. Column layout pattern for Cherokee County Aggregate Columns section, road width = 26 ft.....	254
Figure 305. Particle size distributions of Cherokee County Aggregate Columns surface materials for samples collected over time.....	255
Figure 306. Particle size distributions and evaluation of total breakage of coarse aggregate for Cherokee County Aggregate Columns section from fall 2018 to spring 2019	256
Figure 307. Particle size distributions and evaluation of total breakage of coarse aggregate for Cherokee County Aggregate Columns section from fall 2018 to fall 2019.....	256
Figure 308. Particle size distributions and evaluation of total breakage of coarse aggregate for Cherokee County Aggregate Columns section from fall 2018 to spring 2020	257
Figure 309. Gravel, sand and fines fractions of surface course of Cherokee County Aggregate Columns section over time.....	258
Figure 310. Cumulative total breakage of surface course of Cherokee County Aggregate Columns section over time	258
Figure 311. Particle size distributions from 2D image analysis and evaluation of total breakage of gravel fraction for Cherokee County Aggregate Columns section between fall 2018 and fall 2019.....	259
Figure 312. Comparison of roundness for Cherokee County Aggregate Columns section samples from fall 2018 and fall 2019	259
Figure 313. Comparison of sphericity for Cherokee County Aggregate Columns section samples from fall 2018 and fall 2019	260
Figure 314. Comparison of form factor for Cherokee County Aggregate section samples from fall 2018 and fall 2019	260
Figure 315. Comparison of shape factor for Cherokee County Aggregate Columns samples from fall 2018 and fall 2019	261
Figure 316. Comparison of roundness index for Cherokee County Aggregate Columns samples from fall 2018 and fall 2019	261
Figure 317. Comparison of angularity for Cherokee County Aggregate Columns samples from fall 2018 and fall 2019	262
Figure 318. Visual surveys of Cherokee County Aggregate Columns section over time: (a) fall 2018, (b) spring 2019, (c) fall 2019, (d) spring 2020.....	263
Figure 319. Comparison of cumulative total breakage of samples from Cherokee County OGCS section, Aggregate Columns section, and Control section collected over time	264
Figure 320. Comparison of cumulative relative breakage of samples from Cherokee County OGCS section, Aggregate Columns section, and Control section collected over time.....	264
Figure 321. Comparison of gravel fraction for samples from Cherokee County OGCS section, Aggregate Columns section, and Control section collected over time.....	265
Figure 322. Comparison of percent decrease in gravel fraction relative to 2018 for samples from Cherokee County OGCS section, Aggregate Columns section, and Control section collected over time	266
Figure 323. Comparison of sand fraction for samples from Cherokee County OGCS section, Aggregate Columns section, and Control section collected over time.....	266

Figure 324. Comparison of percent increase in sand fraction relative to 2018 for samples from Cherokee County OGCS section, Aggregate Columns section, and Control section collected over time	267
Figure 325. Comparison of fines fraction for samples from Cherokee County OGCS section, Aggregate Columns section, and Control section collected over time.....	267
Figure 326. Comparison of percent increase in fines fraction relative to 2018 for samples from Cherokee County OGCS section, Aggregate Columns section, and Control section collected over time	268

LIST OF TABLES

Table 1. Descriptions of 3D sphericity parameters	7
Table 2. Descriptions of 2D sphericity parameters	9
Table 3. Operational parameters for gyratory compaction tests.....	18
Table 4. Triaxial testing procedure parameters	25
Table 5. Sources for quarry samples tested in this study.....	26
Table 6. Hardin's breakage parameters determined from laboratory sieve and 2D image analyses, and corresponding percentages of gravel, sand, and fines for Moore Quarry samples	32
Table 7. Statistical results of morphological parameters of Moore Quarry	36
Table 8. Gyratory compaction energy and dry unit weights for Stages I and II of gyratory compaction test for Moore Quarry.....	39
Table 9. Geological parameters of Moore Quarry samples before gyratory compaction	41
Table 10. Geological parameters of Moore Quarry samples after gyratory compaction	41
Table 11. Breakage parameters determined from laboratory sieve analyses and 2D image analyses, and corresponding percentages of gravel, sand, and fines for Alden Quarry samples	44
Table 12. Statistical results of morphological parameters of Alden Quarry specimens.....	48
Table 13. Gyratory compaction energy and dry unit weights for Stages I and II of gyratory compaction test for Alden Quarry	50
Table 14. Geological parameters of Alden Quarry sample before gyratory compaction.....	53
Table 15. Geological parameters of Alden Quarry sample after gyratory compaction.....	54
Table 16. Breakage parameters determined from laboratory sieve analyses and 2D image analyses, and corresponding percentages of gravel, sand, and fines for Gehrke Quarry samples	58
Table 17. Statistical results of morphological parameters of Gehrke Quarry specimens.....	62
Table 18. Gyratory compaction energy and dry unit weight for Stages I and II of gyratory compaction test for Gehrke Quarry	64
Table 19. Geological parameters of Gehrke Quarry samples before gyratory compaction	66
Table 20. Breakage parameters determined from laboratory sieve analyses and 2D image analyses, and corresponding percentages of gravel, sand, and fines for Crescent Quarry samples	68
Table 21. Statistical results of morphological parameters of Crescent Quarry specimens	72
Table 22. Gyratory compaction energy and dry unit weights for Stages I and II of gyratory compaction tests.....	74
Table 23. Geological parameters of Crescent Quarry samples before gyratory compaction	77
Table 24. Geological parameters of Crescent Quarry samples after gyratory compaction.....	78
Table 25. Breakage parameters determined from laboratory sieve and 2D image analyses, and corresponding percentages of gravel, sand, and fines for Pedersen Quarry samples	84
Table 26. Statistical results of morphological parameters of Pedersen Quarry samples.....	88
Table 27. Gyratory compaction energy and dry unit weights for Stages I and II of gyratory compaction test for Pedersen Quarry.....	90
Table 28. Geological parameters of Pedersen Quarry samples before gyratory test (BGT).....	93
Table 29. Geological parameters of Pedersen Quarry samples after gyratory test (AGT).....	94

Table 30. Breakage parameters from sieve analysis and percent gravel, sand, and fines for BFL Class A samples collected over time	114
Table 31. Breakage parameters from 2D image analyses for BFL Class A samples collected over time.....	114
Table 32. Statistical results of morphological parameters of BFL Class A	119
Table 33. Geological rock types and percent increase in rock types for the BFL Class A samples collected over time.....	123
Table 34. Breakage parameters from sieve analysis and percent gravel, sand, and fines for LCF Class A samples collected over time	130
Table 35. Breakage parameters from 2D-image analyses and percent gravel, sand, and fines for LCF Class A samples collected over time.....	130
Table 36. Statistical results of morphological parameters of LCF Class A	135
Table 37. Geological rock types and percent increase in rock types for the LCF Class A samples collected over time.....	138
Table 38. Breakage parameters from sieve analysis and percent gravel, sand, and fines for OFD Class A samples collected over time	144
Table 39. Breakage parameters from 2D-image analyses and percent gravel, sand, and fines for OFD Class A samples collected over time.....	144
Table 40. Statistical results of morphological parameters for OFD Class A samples collected over time.....	149
Table 41. Geological rock types and their percentages for OFD Class A samples collected over time	151
Table 42. Traffic counts and overall lengths of TR-721 test sites.....	154
Table 43. Breakage parameters from laboratory sieve analyses and percent gravel, sand, and fines for the samples of Howard County Control section.....	158
Table 44. Breakage parameters from sieve analyses and percent gravel, sand, and fines for Howard County OGCS samples collected over time.....	163
Table 45. Breakage parameters from laboratory sieve analyses and percent gravel, sand, and fines for samples of Howard County Aggregate Columns section.....	169
Table 46. Breakage parameters from laboratory sieve analyses and percent gravel, sand, and fines for samples of Hamilton County Control section.....	180
Table 47. Statistical results of morphological parameters of Hamilton County Control section for spring 2019 and fall 2019 samples	185
Table 48. Breakage parameters of coarse fraction by laboratory sieve analyses and percent gravel, sand, and fines for samples of Hamilton County OGCS section.....	190
Table 49. Breakage parameters from 2D image analyses for the samples from Hamilton County OGCS section.....	192
Table 50. Statistical results of morphological parameters for Hamilton County OGCS section samples from fall 2018, spring 2019 and spring 2020	196
Table 51. Breakage parameters from laboratory sieve analyses and percent gravel, sand, and fines for samples of Hamilton County Aggregate Columns section.....	201
Table 52. Statistical results of morphological parameters of Hamilton County Aggregate Columns section, spring 2019 and fall 2019 samples.....	206
Table 53. Breakage parameters from laboratory sieve analyses and percent gravel, sand, and fines for samples of Washington County Control section	216

Table 54. Breakage parameters for coarse fraction from laboratory sieve analyses and percent gravel, sand, and fines for samples of Washington County OGCS section	221
Table 55. Breakage parameters for gravel fraction from 2D image analyses for samples of Washington County OGCS section	222
Table 56. Statistical results of morphological parameters of Washington County OGCS section for fall 2018 and fall 2019 samples	226
Table 57. Breakage parameters from laboratory sieve analyses and percent gravel, sand, and fines for samples of Washington County Aggregate Columns section	231
Table 58. Breakage parameters from laboratory sieve analyses and percent gravel, sand, and fines for samples of Cherokee County Control section	242
Table 59. Statistical results of morphological parameters of Cherokee County Control section for spring 2019 and fall 2019 samples	247
Table 60. Breakage parameters of coarse fraction by laboratory sieve analyses and percent gravel, sand, and fines for samples of Cherokee County OGCS section.....	252
Table 61. Breakage parameters from laboratory sieve analyses and percent gravel, sand, and fines for samples of Cherokee County Aggregate Columns section	257
Table 62. Breakage parameters for gravel fraction from 2D image analyses for samples of Cherokee County Aggregate Columns section.....	257
Table 63. Statistical results of morphological parameters of Cherokee County Aggregate Columns section for fall 2018 and fall 2019 samples.....	262
Table 64. Comparative summary of total breakage and changes in median morphological parameters for all materials.....	271
Table 65. Summary of triaxial test results for the quarry samples	275

ACKNOWLEDGMENTS

The authors would like to thank the Iowa Department of Transportation (DOT) and the Iowa Research Highway Board (IHRB) for sponsoring this project.

The authors would also like to thank the project technical advisory committee (TAC) members: Vanessa Goetz (Iowa DOT), Malcom Dawson (Iowa DOT), Lee Bjerke (Iowa County Engineers Association Service Bureau [ICEASB]), Brian Gossman (Iowa DOT), Brian Moore (ICEASB), Adriana Schnoebelen (Iowa DOT), Neal Tieck (Iowa DOT), Jeff DeVries (Iowa DOT), Todd Hanson (Iowa DOT), Bob Younie (Iowa DOT), Dan Miner (Iowa DOT), Jacob Thorius (Washington County), Rafe Koopman (Clayton County), and Todde Folkerts (Lucas County).

The authors are grateful for the extensive help with laboratory testing from undergraduate student research assistants at Iowa State University (ISU), including Ashley Price, Simone King, Serena Codacco, and Patrick Mukwalemba, as well as Malcom Dawson and Tyler Helm for providing training for and access to the Iowa DOT's Camsizer.

EXECUTIVE SUMMARY

The goal of this project was to characterize the relative performance and changes in microstructural and engineering properties for various types of coarse aggregates subjected to weathering as well as real and simulated traffic loads typical of granular surfaces and shoulders of Iowa roads. Through an extensive program of geotechnical laboratory tests, image analysis, geological laboratory tests, and analysis of data from prior projects, the deterioration of both fresh quarry samples and field test section samples was analyzed and compared. Laboratory gyratory compaction tests were used to simulate the abrasion and morphological changes experienced by aggregates in granular-surfaced roads. Image analyses were performed before and after the gyratory tests as well as on available field samples collected over time, to track changes in the morphology of particles as they deteriorated during testing and field service. Triaxial tests were also performed to assess changes in aggregate shear strength parameters (cohesion and friction angle) before and after gyratory abrasion. Pre-existing and newly measured particle size distribution curves were used to quantify particle breakage for the various aggregate types undergoing degradation in both field test sections and laboratory gyratory compaction tests.

Of the five main quarry materials tested, the Class A materials from the Pedersen, Crescent, and Moore Quarries produced the lowest values of total breakage during gyratory compaction testing, with the Pedersen aggregates exhibiting the smallest changes in morphology. Clean aggregates from the Alden and Gehrke Quarries had the highest breakage values and among the largest changes in morphology during gyratory compaction tests.

Among the three materials tested and analyzed from the TR-704 project's field test sections, the Bethany Falls Limestone (BFL) had the highest total breakage while the Oneota Formation Dolomite (OFD) had the lowest breakage, and the Lime Creek Formation (LCF) materials had only slightly greater breakage than the OFD. Overall, the BFL materials yielded the greatest changes in morphological parameters over time, whereas LCF exhibited slight changes and OFD exhibited the smallest changes. These results are consistent with BFL being the weakest in terms of breakage values, and OFD (closely followed by LCF) being the strongest.

For the materials tested from 12 different test sections of the TR-721 project, the materials from the Optimized Gradation with Clay Slurry (OGCS) test sections had the best overall performance in terms of the smallest relative decreases in gravel fraction, smallest increases in sand and fines fractions, smallest cumulative total breakage values, and lowest changes in particle morphological parameters. The performance of the OGCS materials were followed by the surfacing materials of the Aggregate Columns test sections, which had intermediate performance, and finally those of the Control sections, which had the poorest performance.

To implement the results of this study, county engineers can select from the material types that produced the least breakage in quarry samples and field test sections, as evaluated by breakage determined from both gyratory compaction tests and field gradation curves over time. These new understandings and methods will better guide the decision-making process used by county

engineers and geologists for planning the construction and maintenance of roads with granular surfaces.

Recommendations for further research include analyzing more of the data and samples from field test sections from the previous TR-704 and TR-721 projects, analyzing a wider variety of quarry materials and field test section samples from around the state using the methods of this study, quantifying the deterioration and field performance of recycled or synthetic aggregates or those stabilized with various chemical or mechanical methods, or constructing and monitoring new field test sections using the materials that had the best performance and lowest deterioration in this study.

CHAPTER 1. INTRODUCTION

1.1 Problem Statement

Approximately 74% of Iowa's 89,000 mi secondary road network consists of granular-surfaced roads (Iowa County Engineers Association 2018). Commonly referred to as "gravel roads," they provide the fabric for rural life and livelihood in Iowa by linking agricultural producers with markets and rural residents with their communities. The granular surfaces of these roads must be renewed as often as every three years, which imposes significant financial demands on county highway departments. Coarse aggregates (CA), which are the primary constituent of the granular surfaces of such roads, undergo both physical and chemical degradation due to weather and traffic loads, which affects their engineering and geological properties and, ultimately, their longevity. Despite the importance of such roads to the economic fabric of Iowa and their requirements for regular maintenance and rehabilitation, we lack a robust understanding of not only the deterioration mechanisms most responsible for the breakdown of CA but also the geological factors that make one CA perform better than another.

The present study aimed to characterize the changes that occur in such coarse aggregates by quantifying changes in their geological fabric and engineering properties, from both in-service roadway samples and laboratory specimens. Using this information, highway engineers and geologists can act in the best fiduciary interest of taxpayers to minimize costs while providing a safe and reliable transportation network for rural communities and producers.

1.2 Research Objectives

The objective of the research was to characterize changes in the microstructural and engineering properties of CA as they are exposed to weathering and traffic loads typical of the granular surfaces and shoulders of Iowa roads. This was achieved through geotechnical laboratory testing, image analysis, and both petrophysical testing and petrographic inspection to identify the chemical (e.g., dissolution of primary minerals, precipitation of secondary minerals) and physical (e.g., abrasion, freeze-thaw cycles) weathering processes responsible for CA deterioration. Geotechnical tests included measurement of particle size distributions (PSDs) through traditional sieve and hydrometer tests, gyratory compaction tests to simulate the effects of traffic loading, and two-dimensional (2D)-image analyses to study changes in particle morphology during gyratory testing and field service. The ultimate outcome of the research is a better understanding of the performance of CA used in granular surfaces and shoulders of roadways

The research is expected to yield a clearer understanding of the deterioration mechanisms for carbonate CA used in granular-surfaced roads and shoulders. For example, by knowing whether dissolution or fracturing is the dominant method for CA breakdown, one can recommend construction with CA that is less soluble or more mechanically strong, respectively. By understanding how the CA deteriorates, one will be able to (1) better predict the service life of a granular road and (2) judge the effectiveness of current methods and recommend amendment or replacement of these methods where appropriate. These new understandings and methods will

better guide the decision-making process used by county engineers and geologists for planning the construction and maintenance of roads with granular surfaces.

1.3 Significance of the Research

Granular surface materials must typically be replenished every one to five years to ensure proper maintenance of rural roads. This project investigated how different granular surface materials sampled from quarries and roadways degraded over time, with the goal of identifying the critical material properties that lead to longer service lives and thus reduced life-cycle costs for granular-surfaced roads.

1.4 Organization of the Report

Chapter 1 of this report presents the problem statement and objectives guiding this research. Chapter 2 provides background information about CA deterioration in Iowa, details the research plan, and summarizes methods for evaluating CA deterioration. Chapter 3 describes the laboratory tests performed and their methodologies. Chapter 4 presents details on the aggregate materials analyzed, including their sample collection locations and times, and presents the results of the laboratory tests and associated analyses. Chapter 5 summarizes the observations and conclusions of the study and presents suggestions for further research.

CHAPTER 2. BACKGROUND

2.1 Coarse Aggregate Deterioration in Iowa

Granular-surfaced roads typically have a traffic-bearing surface of loose crushed rock or rounded river rock but can also contain aggregate alternatives such as slag or recycled asphalt pavement. In Iowa, this rock is most often a crushed carbonate rock (limestone or dolostone) obtained from local bedrock quarries or mines. However, the high solubility and low hardness of carbonate minerals result in carbonate rock being especially prone to chemical and physical breakdown at the surface of the Earth (Dubois et al. 2015). Breakdown of these materials in roadway surfaces results in significant expense to local and state-level transportation agencies and, therefore, the Iowa taxpayers that support them (e.g., Baumel et al. 1989, Berthelot and Carpentier 2003, Huntington and Ksaibati 2011, White and Vennapusa 2013).

Freezing and thawing of water within and between the road materials and also physical abrasion from traffic are thought to be the dominant mechanisms for CA deterioration in gravel roads (White and Vennapusa 2013). Because of their lack of an insulating cover of pavement, gravel roads freeze sooner and thaw later than asphalt roads (Baker and Johnson 2000), resulting in the need for different loading guidelines. Numerous previous studies have suggested methods for rating and maintaining gravel roads (e.g., Walker 1991, Smadi et al. 1999, Huntington and Ksaibati 2011), but most were focused on the engineering and design aspects of gravel roads rather than the geology of the CA.

Federal guidelines offer that “it pays to use the best quality material available” (FHWA 2015), yet they provide no further guidance on what properties constitute a “quality gravel.” Gravel (or CA) for surfacing must have enough cohesive fines in the form of clays (and not silts) to bind the CA together and form a continuous surface (Baker and Johnson 2000). Therefore, sieve analysis is essential to establish a proper gradation (FHWA 2015) and consistency tests are necessary to establish an appropriate range of plasticity index, but the quality of aggregates also plays an important role. For example, South Dakota found that using high quality gravel reduces the life-cycle cost of gravel roads (van Dam 2012). Specifically, one location in Brookings County, South Dakota, required 405 tons per mile (TPM) of low-quality CA per year versus only 71 TPM of high-quality CA (van Dam 2012).

Baker and Johnson (2000) is one of the few studies that attempted to identify the properties of “quality gravel.” To do so, they assessed the absorption, surface dielectric, and percentage of fines. They recommended against using the absorption test because it is influenced by the amount, duration, and frequency of precipitation in a given area. They also recommended against using the surface dielectric test because their results were inconclusive as they did not have high-quality CA in their study. They did note, though, that with the marginal CA they had access to, the CA with the highest percentage of fines performed the best.

Various researchers have developed so-called “gravel loss deterioration models” that seek to predict the deterioration of CA used in gravel roads (e.g., Paige-Green and Visser 1991, Patterson 1991, van Zyl et al. 2007, Uys 2011). These models typically incorporate variables

related to material (e.g., type, plasticity, grain size), traffic (e.g., car and truck flux), local climate (e.g., mean annual precipitation and temperature), alignment geometry (e.g., gradient and curvature) as well as empirical calibration factors. Only within the “material type” variable category is there sufficient information to describe all the geological factors that could contribute to a CA’s performance. Furthermore, material type is only included in one of the significant gravel loss deterioration models, that of the Australian Road Research Board (Uys 2011).

In contrast, the Iowa Department of Transportation (DOT) already has rigorous chemical and physical standards (e.g., Myers and Dubberke 1980, Iowa DOT IM 409) for accepting carbonate CA for use in portland cement concrete. These include low alumina content, end-member calcite or dolomite mineralogy, and low secondary load on the Iowa Pore Index (IPI) test (Reyes and Dawson 2010). Further work has shown, for example, that IPI test results can be correlated to the geology of the CA; limestone particles with muddier fabrics tend to have higher IPI secondary loads, whereas grainier limestones have lower secondary IPI loads. In dolostones, crystal size is inversely correlated with secondary IPI (i.e., coarser crystals have lower secondary IPI) (Ridzuan et al. 2017). These findings can help geologists more effectively manage production from existing deposits to provide the highest quality rock to transportation agencies and explore new sources. Unfortunately, we do not know if these same relationships hold for CA used as granular surfacing materials. The only geological specifications for granular surfacing CA provided by the Iowa DOT that relate to CA geology refer to the presence of shale, clay lumps, or friable particles (Article 4120 of the Iowa DOT Standard Specifications).

2.2 Research Plan

The research plan consisted of the following tasks carried out to achieve the research objectives:

2.2.1 Collection of Coarse Aggregate Samples from Quarries and In-Service Roads Over Time

Samples of CA materials were obtained from quarries and from the surfaces of in-service test sections having similar traffic volumes during two previous research projects. The physical appearance of the CA was described and related to control samples from the CA sources. Petrophysical testing (helium and mercury porosimetry) was performed, along with morphometry to determine the physical properties of the CA.

Specifically, the new quarry samples in this study were collected from the Gehrke, Alden, Pedersen, Moore, and Crescent Quarries, whose locations are shown in Figure 1. The in-service roadway surface materials were obtained from surplus samples of the previous long-term Iowa Highway Research Board (IHRB) Projects TR-704 and TR-721. Figure 2 shows the counties where the five field test sections were constructed for these two projects. In both projects, samples of the granular surface course materials were collected at the time of test section construction, then at several subsequent dates over the life of the projects. The TR-704 test sections in Decatur County were built from four aggregate sources: (1) high-quality limestone, (2) dolomite, (3) crushed gravel, and (4) lower-strength limestone. IHRB Project TR-721 involved test sections in Howard, Hamilton, Washington, and Cherokee Counties. Both virgin

and weathered/abraded samples were collected periodically throughout these projects, particularly for TR-704.

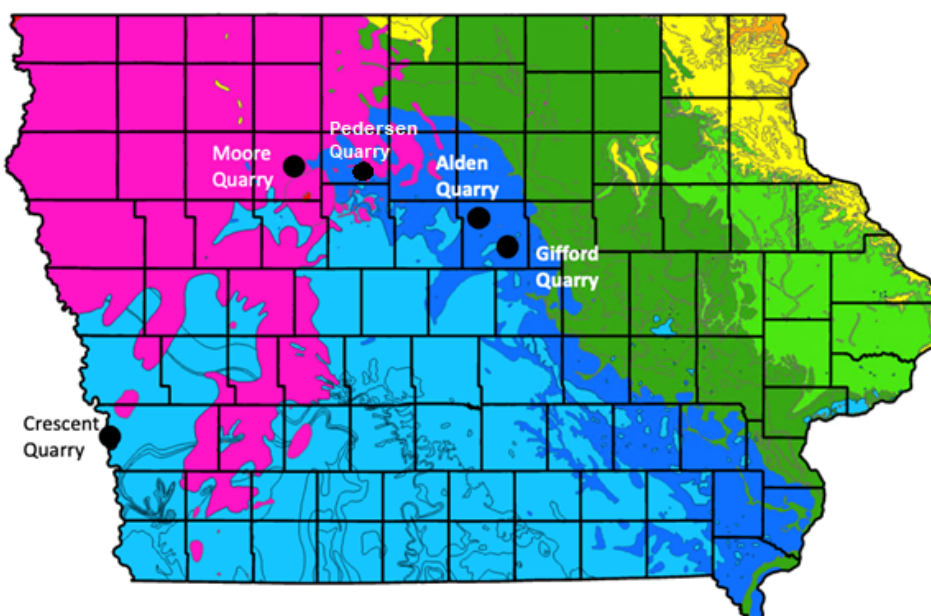


Figure 1. Locations of the quarries used in this study superimposed over USGS Iowa geological map

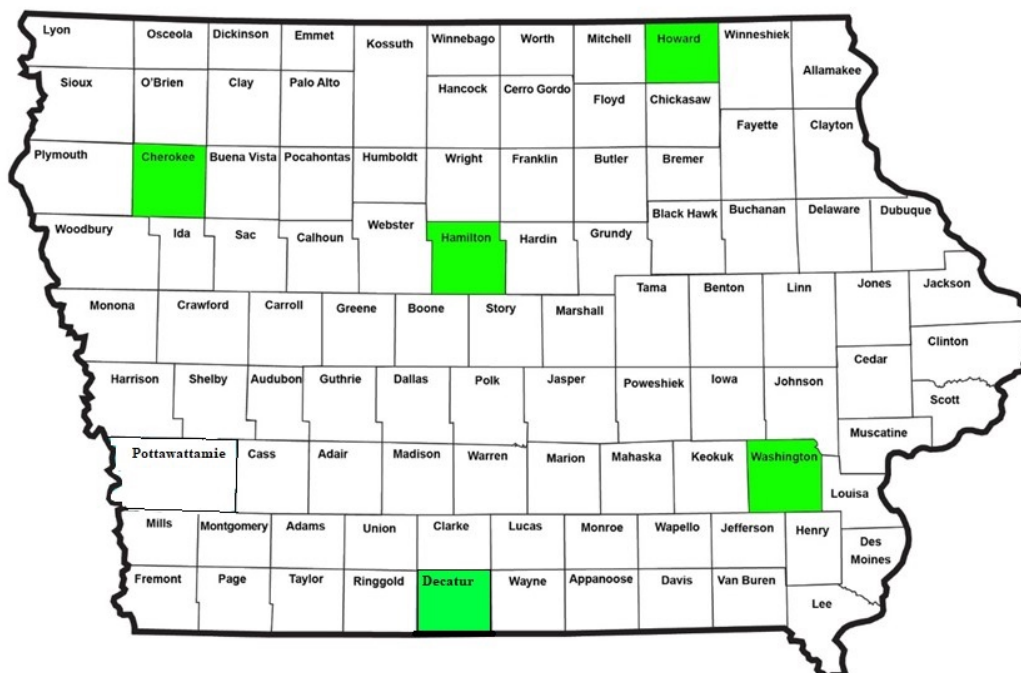


Figure 2. Field test section locations for the TR-704 and TR-721 projects

2.2.2 Geotechnical Laboratory Testing of Coarse Aggregate Samples

Geotechnical tests included sieve analysis, triaxial tests, and gyratory compaction tests. To quantify changes in CA particle morphology, 2D image analyses were also conducted on specimens before and after gyratory tests and on samples collected over time from the field test sections of the two previous projects. The triaxial tests were performed to investigate the impact of geological origins and aging on the shear strength parameters of the entire aggregate matrix.

2.2.3 Geological Testing of Coarse Aggregate Samples

Geological tests were performed, including helium pycnometry to obtain total porosity and grain density, mercury porosimetry to obtain pore throat size distribution, grain size and shape analysis via Camsizer (Dawson 2021), and thin section petrography to obtain images of deterioration textures, identify pore types and measure the relative abundance of components (e.g., CA and fine aggregates).

2.3 Evaluation of Degradation of Coarse Aggregates

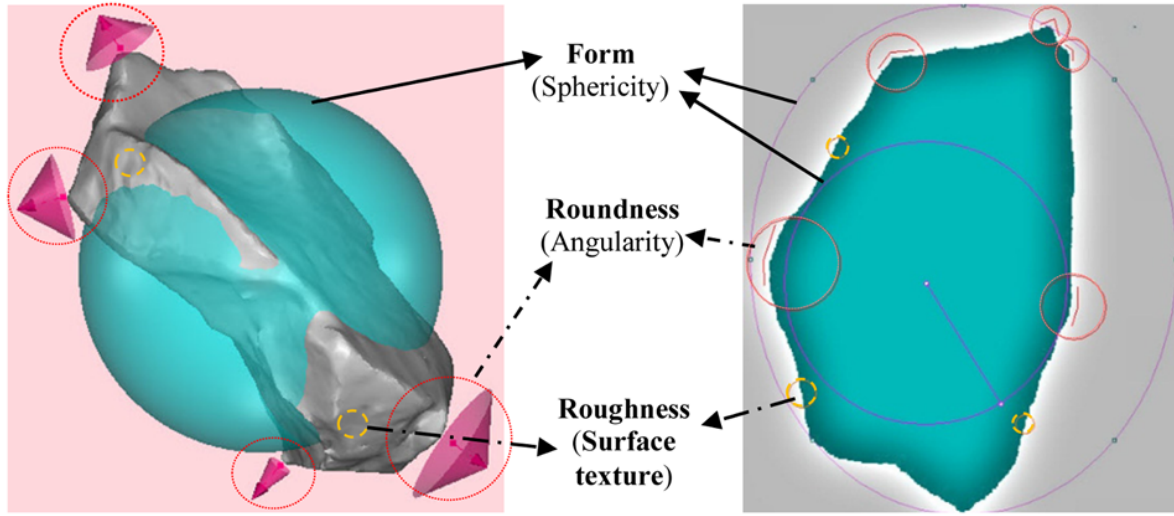
2.3.1 Morphological Characteristics of Coarse Aggregates

2.3.1.1 Sphericity

Sphericity is an important parameter for characterizing particle morphology and is integral to understanding the behavior of soils and aggregates in engineering applications. It significantly impacts various engineering properties, particularly particle packing, interlocking between particles, permeability, flow mechanisms, shear strength, and compaction behavior in both soils and aggregates.

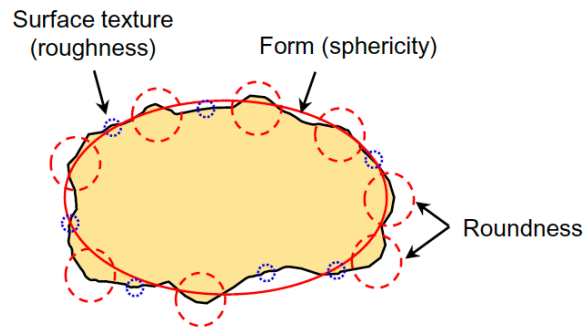
Since the earlier research studies, sphericity has been described in both three-dimensional (3D) and 2D contexts, given the practicality and simplicity of measuring 2D parameters. In 3D space, sphericity evaluates how close or divergent a particle is from the geometry of a perfect sphere, as shown in Figure 3. This assessment involves an analysis of the particle's overall resemblance to a sphere, considering its dimensions in terms of length, width, and height. In 2D space, sphericity is called circularity, serving as a metric to assess the degree to which a particle resembles a circle, as shown in Figure 4.

Sphericity values are typically expressed on a scale of 0 to 1, with 1 representing perfect sphericity. Particles with higher sphericity values are closer in shape to a sphere, while lower values indicate more irregular shapes. Numerous approaches have been proposed to quantify sphericity based on definitions related to ratios of volume, area, perimeter, and diameter, as well as chart-based methods. A summary of various 3D definitions of sphericity from several studies are presented in Table 1, while various 2D definitions for circularity are provided in Table 2.



Maroof et al. 2020

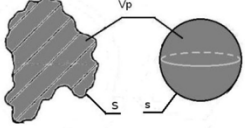
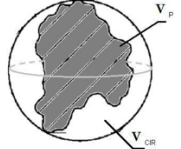
Figure 3. Morphological characterization for particle in 3D space

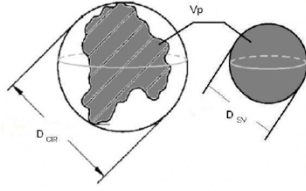
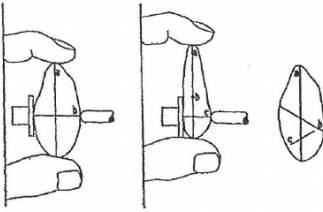


Zheng and Hryciw 2015, after Barrett 1980 and Mitchell and Soga 2005

Figure 4. Morphological characterization for particle in 2D space

Table 1. Descriptions of 3D sphericity parameters

#	Parameter	Definition	Figure	References
1	True Sphericity, Ψ (surface based)	$\frac{S}{\bar{S}}$		Wadell (1932) modified by Johansson and Vall (2011) and Zavala (2012)
2	Sphericity, Ψ (volume based)	$\sqrt[3]{\frac{V_P}{V_{CR}}}$		Wadell (1934) modified by Johansson and Vall (2011) and Zavala (2012)

#	Parameter	Definition	Figure	References
3	Sphericity, Ψ (diameter based)	$\frac{D_{SV}}{D_{CIR}}$		Wadell (1934) modified by Johansson and Vall (2011) and Zavala (2012)
4	Elongation ratio	$\frac{c}{b}$	(see footnote)	Zingg (1935)
5	Flatness ratio	$\frac{b}{a}$	(see footnote)	Zingg (1935)
6	Flatness and elongation ratio	$\frac{c}{a}$	(see footnote)	Blott and Pye (2008)
7	Wentworth flatness index	$\frac{a+b}{2c}$	(see footnote)	Wentworth (1922)
8	Intercept sphericity	$\sqrt{\frac{bc}{a^2}}$	 Measurement of the 3 axes perpendicular to each other	Krumbein (1941)
9	Corey's Shape Factor	$\frac{c}{\sqrt{ab}}$	(see footnote)	Corey et al. (1949)
10	Maximum Projection Sphericity	$\sqrt[3]{\frac{c^2}{a \cdot b}}$	(see footnote)	Sneed and Folk (1958)
11	Working Sphericity	$\frac{12.8 \sqrt[3]{(c/b)^2 \cdot (b/a)}}{1 + (c/b)(1 + (b/a)) + 6 \sqrt{1 + (c/b)^2 (1 + (b/a)^2)}}$		Aschenbrenner (1956)
12	Scalene ellipsoid equivalent sphericity	$\frac{c}{a} = \frac{(W/NG_s)(6/\pi ab)}{a}$	(see footnote)	Clayton et al. (2009)

a = Longest axis diameter of particle

N = Number of particles

b = Intermediate axis diameter of particle

s = Surface area of sphere having same volume as particle

c = Shortest axis diameter of particle

S = Particle surface area

D_{SV} = Diameter of sphere having same volume as particle

V_P = Volume of particle

D_{CIR} = Diameter of circumscribed sphere

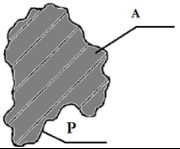
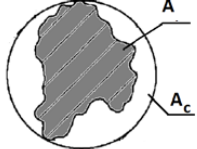
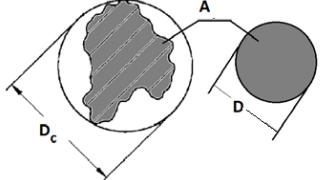
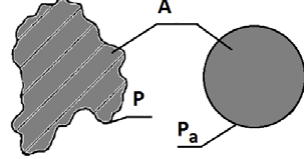
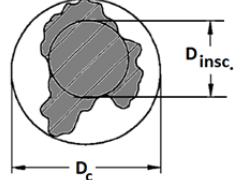
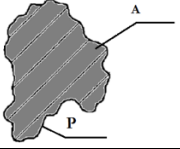
V_{CIR} = Volume of circumscribed sphere

G_s = Specific gravity

W = Sample weight

Source: After Rodriguez et al. 2012

Table 2. Descriptions of 2D sphericity parameters

#	Parameter	Equation	Figures	References
1	Circularity, ϕ_c	$\frac{4\pi A}{P^2}$		Cox (1927) modified after Johansson and Vall (2011)
2	Circularity, ϕ_p	$\frac{A}{A_d}$		Pentland (1927)
3	Circularity, ϕ_t	$\frac{A}{A_c}$		Tickell (1931) modified after Johansson and Vall (2011)
4	Degree of Sphericity, ϕ_w	$\frac{D}{D_c}$		Wadell (1933) modified after Johansson and Vall (2011)
5	Degree of Circularity	$\frac{P_a}{P}$		Wadell (1933) modified after Johansson and Vall (2011)
6	Inscribed circle sphericity, ϕ_o	$\sqrt{\frac{D_{inCs}}{D_c}}$		Riley (1941) modified after Johansson and Vall (2011)
7	Sphericity	$\frac{MinR}{MaxR}$		Landini (2006)
8	Circularity	$\frac{P^2}{A}$		Blott and Pye (2008) and Janoo (1998) modified after Johansson and Vall (2011)

A = 2D projected area of the particle

D_c = Diameter of smallest circle circumscribing particle

A_d = Area of circle having diameter equal to longest diameter of particle

P = Perimeter of 2D projected area of the particle

A_c = Area of smallest circumscribing circle

P_a = Perimeter of circle with area equal to A

D = Diameter of circle with area equal to A

MinR = Radius of inscribed circle centered at particle's center of mass

D_{inCs} = Diameter of largest circle inscribed in particle

MaxR = Radius of enclosing circle centered at particle's center of mass

Source: After Rodriguez et al. 2012

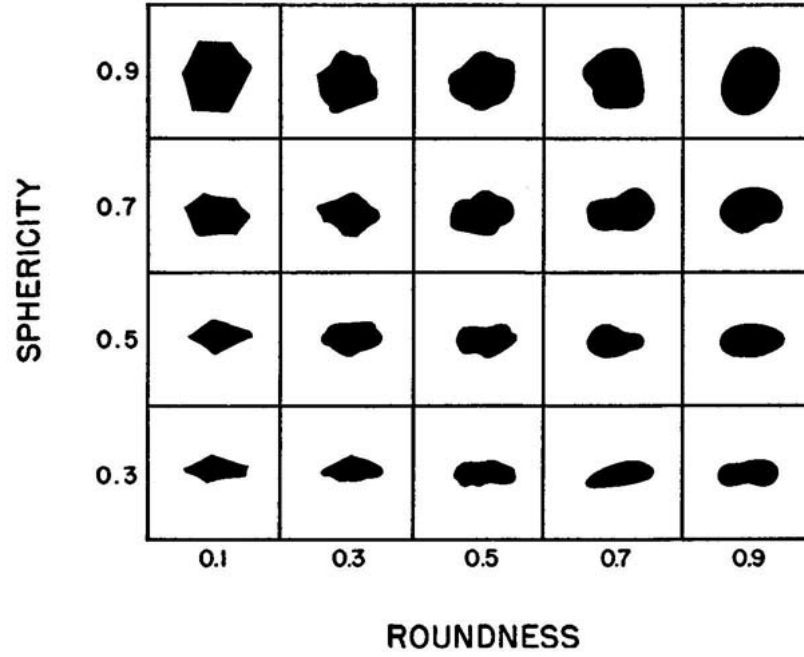
In the present study focusing on 2D image analysis of gravel-sized particles, the image processing program ImageJ was utilized in conjunction with Landini's algorithm (Landini et al. 2012) to calculate the 2D sphericity. The 2D sphericity is often referred to as circularity in 2D image analyses, and has also been referred to as roundness in earlier studies such as Cox (1927), Pentland (1927) and Tickell (1931). Landini's algorithm computes the ratio of the radius of an inscribed circle (*MinR*) to the radius of an enclosing (or circumscribed) circle (*MaxR*), with both circles centered at the particle's center of mass. The algorithm also includes adjustments based on the particle's center of mass to better represent the sphericity of irregularly shaped particles. This concept is parallel to that of inscribed circle sphericity as given by Riley (1941), which considers the ratio of diameter of the largest circle inscribing the particle to that of the smallest circle circumscribing the particle. However, Landini's sphericity algorithm incorporates the center of mass of the particle into the computation as explained previously.

2.3.1.2 Roundness

Roundness is a mesoscale property that measures the smoothness of a particle along its perimeter. It essentially quantifies the deviation of a particle from a perfect circle, from angular at the lower end of the scale to smoother and well-rounded at the upper end of the scale. Roundness is essentially the 2D analog of 3D sphericity. Figure 5 contains charts used to determine sphericity and roundness by visual estimation, along with examples of particles ranging from very angular to well rounded, and ranging from low to high sphericity. In the Sphericity section of this report, roundness in 3D space is illustrated in Figure 3 and roundness in 2D space is illustrated in Figure 4. In the present study, roundness was evaluated using equation (1) which defines roundness as the ratio of the particle area to its Feret length:

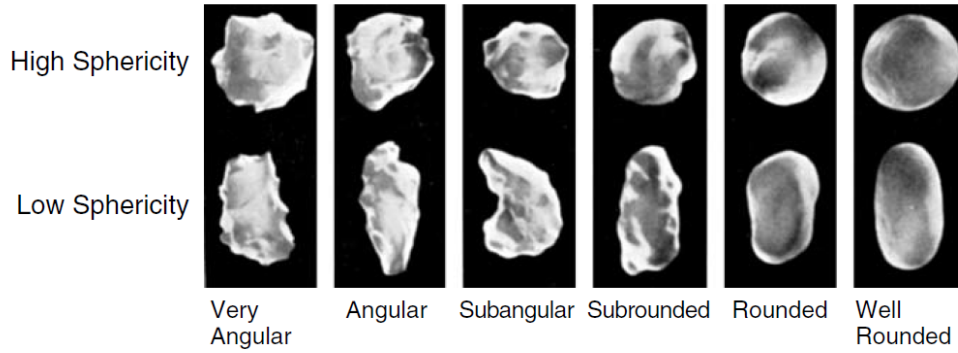
$$Roundness = \frac{4 \text{ Area}}{\pi \text{ Feret}^2} \quad (1)$$

where the Feret length is the largest axis length of the particle obtained by the Landini algorithm (Landini et al. 2012) previously discussed in the Sphericity section of this report.



Krumbein and Sloss 1963

(a)



Powers 1953

(b)

Figure 5. (a) Visual estimation of roundness and sphericity and (b) examples of particle shape characterization

2.3.1.3 Form Factor

Form Factor, alternately known as circularity or thinness ratio, is a dimensionless morphological parameter to describe how elongated or compact a particle is. The range of the Form Factor varies from 0 to 1, with a value of 1 indicating a perfect circle. For this study, the Form Factor was evaluated using equation (2) from the Landini algorithm (Landini et al. 2012), where Area is the area covered by the particle and perimeter is the length of the particle's outline:

$$Form\ Factor = \frac{4\pi\ Area}{Perimeter^2} \quad (2)$$

This equation for form factor can be thought of as the ratio of a particle's area to the square of its perimeter, normalized to the value for a perfect circle (i.e., $1/4\pi$).

2.3.1.4 Shape Factor

The shape factor is a dimensionless geometric descriptor used to characterize the morphology of a particle. It is calculated using equation (3) as the ratio of the particle's squared perimeter to its area, following the algorithm proposed by Landini et al. (2012):

$$\text{Shape Factor} = \frac{\text{Perimeter}^2}{\text{Area}} \quad (3)$$

This ratio is proportional to the inverse of the form factor defined in equation (2), but without the factor of 4π . A perfect circle will have a shape factor of 4π (approximately 12.6), while more elongated or bumpy particles will have a value higher value.

2.3.1.5 Roundness Index

The Roundness Index is another dimensionless geometric descriptor used to quantify the degree of roundness of a particle. In the present study, the following 2D roundness index introduced by Alshibli et al. (2015) was used:

$$I_{R-2D} = \frac{0.78 \text{ Perimeter}}{\pi \left(\frac{d_L + d_s}{2} \right)}, \quad (4)$$

where d_L and d_s are the maximum and minimum Feret diameters. This index is based on comparing the digitally calculated particle perimeter to a measure of πd . The factor 0.78 is a correction factor to compensate for the slight overestimation of a particle's actual perimeter caused by counting square pixels in a digital image. Conceptually, a perfect circle will give a roundness index of 1 using this definition, whereas a particle with a circular 2D projection and the same Feret diameters but a very bumpy surface will have a longer perimeter and therefore a higher roundness index. Other particle shapes can possess a roundness index less than 1 depending on their Feret diameters and accuracy of measurements.

2.3.1.6 Angularity

Angularity is a dimensionless morphological parameter, and an inverse measure of roundness. It evaluates the deviation of a particle from a smooth one, with higher angularity values indicating increased sharpness of the edges. In this study, angularity was evaluated using equation (5), from Arasan et al. (2011):

$$K = \frac{P}{P_{\text{ellipse}}}, \quad (5)$$

where P is the projected perimeter of the particle and $P_{ellipse}$ is the perimeter of the equivalent ellipse

2.3.2 Hardin's Breakage Parameters

In this study, Hardin's breakage parameters were used to quantify and compare the amount of breakage for particles larger than a selected threshold sieve size. For cases in which the full PSD curves were available from mechanical sieve analyses, breakage of the gravel and sand fractions were calculated by choosing the No. 200 sieve as the minimum threshold size. For 2D image analyses, only the gravel sized particles were typically scanned because it was not practical to scan all the sand-sized particles in a specimen. The breakage and particle morphology were therefore determined using the No. 4 sieve as the threshold size. Definitions of Hardin's three breakage parameters are given in the next three sections.

2.3.2.1 Total Breakage, B_t

Hardin (1985) defined total breakage (B_t) as the area enclosed between particle size curves measured before and after loading, bounded by a vertical line at a minimum threshold particle diameter of 0.074 mm which is essentially the No. 200 sieve (Figure 6). When this minimum threshold size is used, B_t quantifies the amount of total breakage of the gravel and sand-sized particles during loading.

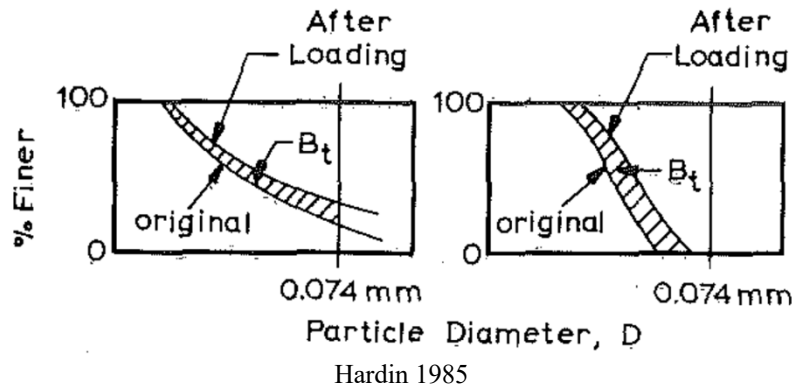


Figure 6. Definition of total breakage

2.3.2.2 Breakage Potential, B_p

The breakage potential (B_p) can be thought of as the maximum possible total breakage value that would result if all particles larger than the minimum threshold size (0.074 mm for Hardin's work) were to break down smaller than that threshold size. It is therefore represented graphically by the area bounded by the original PSD before loading, the vertical line at the minimum particle threshold size, and the horizontal line at 100% finer (Figure 7).

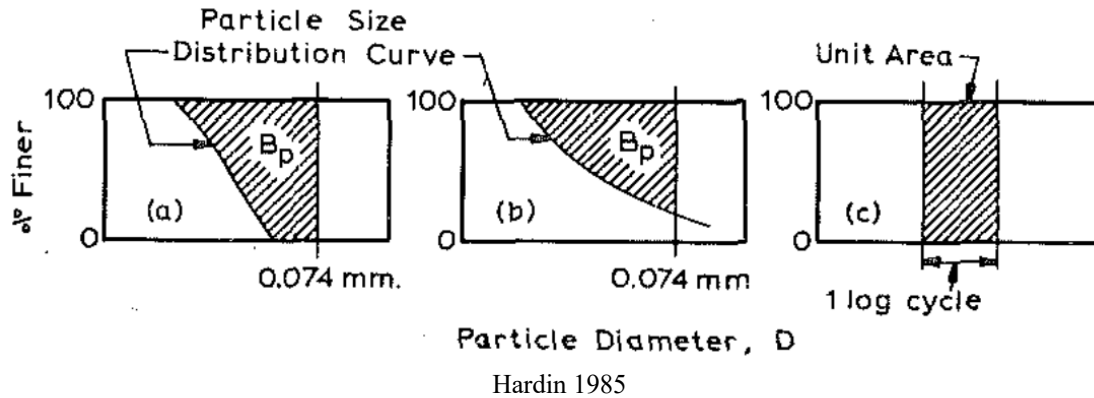


Figure 7. Definition of breakage potential

2.3.2.3 Relative Breakage, B_r

The relative breakage (B_r) is defined as the ratio of total breakage to breakage potential, and therefore varies between 0% and 100%. It represents the fraction of the breakage potential that was realized during loading. It is used in this study to compare the strength of different aggregate types subjected to loading from a gyratory compactor in the laboratory or from vehicle traffic in field test sections.

CHAPTER 3. LABORATORY TESTING AND METHODOLOGY

3.1 Introduction

The present project makes use of laboratory test data from two previous IHRB research projects on granular-surfaced roads (TR-704 and TR-721), in which field test sections were constructed and periodically sampled over multiple years. Additionally, new aggregate samples were collected from several quarries and tested in the present study. This chapter describes the procedures for the various geotechnical and geological laboratory tests performed in the present study.

3.2 Laboratory Testing and Methodology

3.2.1 Gyratory Compaction Tests

3.2.1.1 Background of Gyratory Compaction Tests

The Superpave Gyratory Compactor, as outlined in ASTM D6925-15, was developed for compacting hot mix asphalt (HMA) specimens while continually measuring their relative density during the process. The gyratory compaction test (GCT) is routinely used for laboratory mix design and field control of HMA pavements. The GCT device applies a constant vertical stress to a specimen confined in a mold, then imposes a gyratory shear stress by varying the angle of the vertical load. The gyratory compaction device has also proven useful for studying compaction of geomaterials in studies such as Ping et al. (2003), Lee et al. (2007), Mokwa et al. (2008), Cerni and Camilli (2011), Li et al. (2015), and Zhang et al. (2017). Some of these studies demonstrated that the device delivers greater compaction effort than Standard and Modified Proctor Compaction tests for geomaterials.

An additional rationale for performing the gyratory compaction test on granular surface materials is its ability to more accurately simulate the mechanical degradation of aggregates caused by traffic loads compared to Proctor compaction, Los Angeles (LA) Abrasion, and California Bearing Ratio (CBR) tests. Specifically, the LA Abrasion and CBR tests require that the sample be washed and altered to produce a different, standard gradation, which will not degrade in the same manner as the original full gradation subjected to vehicle loads in an actual gravel road. Furthermore, the LA Abrasion test involves steel spheres pulverizing the aggregates in a rotating drum, while the CBR test involves a metal piston penetrating an aggregate specimen at a constant rate, neither of which simulate the effects of vehicle tires on unbound aggregate surface courses.

In contrast, the GCT allows for testing of the actual full gradation, and its loading mechanism more closely simulates the effects of tire loads as it allows for shear distortions and particle rotations. Li et al. (2017) demonstrated that compared to the LA Abrasion test, the GCT can better determine differences in abrasion loss for specimens having different initial gradations.

Thus, both the initial gradation and the testing mechanism are important for assessing how a given aggregate gradation will perform in a gravel road surface course.

3.2.1.2 Gyratory Compaction Testing Procedure and Methodology

Li et al. (2017) developed the gyratory abrasion and image analysis (GAIA) method for assessing the mechanical degradation of compacted granular materials using the gyratory compaction device. The procedure involves compacting aggregate specimens in a gyratory compactor, while measuring the eccentricity of vertical force using a pressure distribution analyzer (PDA). The gravel-sized fractions of the test specimens are also scanned before and after the gyratory tests using a high resolution optical scanner. The resulting 2D images are then used to assess the degradation of particles caused by gyratory compaction, by determining the changes in gradation as well as morphological parameters such as particle sphericity and angularity.

In this study, GAIA tests were performed using a Brovold Gyratory Compactor with a TestQuip PDA placed on the loading platen on top of the specimen. The gyratory compactor also features a displacement transducer to continuously monitor changes in specimen height during the test. The PDA measures the vertical forces applied to the loading plate on top of the specimen through three 9-kN load cells arranged in a 120° pattern (Figure 8). As detailed in Li et al. (2017), for each gyration, the data from the three load cells and displacement transducer are used to calculate the specimen height, resultant applied force and its eccentricity, shear resistance between the specimen and top loading platen, and total compaction energy applied to the specimen. The dry unit weight can also be calculated for each gyration knowing the initial specimen mass and mold diameter along with the measured specimen height, from which void ratio can be determined for an assumed specific gravity.

For each GCT in this study, a mechanical splitter was used to obtain a representative sample weighing approximately 4,500 grams. The sample was sieved over the No. 4 (4.75 mm) sieve and the retained gravel-sized particles were then arranged on the scanner bed without touching each other. After scanning 2D images of all the gravel-sized particles, the sample was recombined, mixed, and placed in the gyratory compactor mold. The GCTs were then performed following the procedures given in Li et al. (2017), which generally follow ASTM D6925-15 but omit the steps related to HMA such as warming the chamber and recording the temperature. After the GCT, the plus No. 4 fraction of the specimen was again separated and scanned to enable image analyses from which the PSDs, breakage, and changes in morphological parameters during the test were determined.

The operational parameters used for the gyratory compaction tests are shown in Table 3. A vertical pressure of 600 ± 10 kPa was applied to the top of the specimen through the PDA and loading plate. To simulate the compaction process over a wide range of compaction energy, the number of gyrations was set to 500. This number was chosen based on Browne (2006) and Mokwa et al. (2008), who found that 90% of the total compaction of granular specimens was achieved in the first 100 gyrations, after which the rate of compaction decreased. Stopping at 500 gyrations also limits the amount of potential damage to the gyratory mold that can occur for large

numbers of gyrations. For reference, the quantity of 500 gyrations is five times the design number recommended by AASHTO (2001) to produce an HMA sample density corresponding to 20-year traffic loadings of 3 to 10 million Equivalent Single Axle Loads (ESALs). This traffic loading level represents that of medium-volume granular roads in Iowa. However, the Brovold device has a software limitation that enforces a maximum of 299 gyrations at a time. Therefore, the 500 gyrations were applied in two sets of 250, with each set preceded by two dwell gyrations. This procedure creates a slight discontinuity in the data plots at the 250th gyration as the specimen is unloaded and reloaded. The GCT specimens were tested in an air dry state, for which the moisture content was approximately 2%.



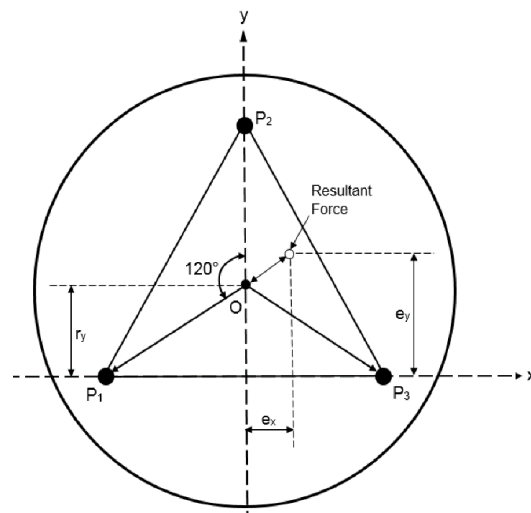
Li 2013
(a)



Li et al. 2017
(b)



(c)



Guler et al. 2000
(d)

Figure 8. (a) Brovold gyratory compactor, (b) PDA device, (c) PDA internal components and battery compartment, (d) schematic demonstrating eccentricity of the resultant force calculated from three load cells

Table 3. Operational parameters for gyratory compaction tests

Parameter	Value
Vertical applied pressure	600 \pm 10 kPa
Number of gyrations	500*
Angle of gyration	1.25° \pm 0.02°
Frequency of gyration	30 \pm 0.5 gyrations/min
Number of dwell gyrations	2

* Applied in two successive rounds of 250 gyrations each

3.2.2 2D Image Analyses of Coarse Aggregates

For the 2D image analyses in this study, the gravel-sized particles retained on the No. 4 (4.75 mm) sieve were manually arranged on the glass plate of a high resolution Canon CanoScan 9000F Mark II flatbed optical scanner, shown in Figure 9(a). To accurately capture the morphological features of each particle, adequate space was provided between the particles as shown in Figure 9(b), requiring several different scans per specimen. The resulting scanned images were saved as high-quality tagged image file format (TIFF) files for further 2D image analysis. The ImageJ program along with Landini's algorithm (Landini et al. 2012) was used to process the scanned images as binary images (Figure 9(c)) and compute the previously described MinR, MaxR, and sphericity values based on the center of mass of the particles. Figure 10(a) illustrates the original scanned image of the particles from the Gehrke Quarry and Figure 10(b) presents the corresponding processed binary image overlaid with the circles having the MinR (red) and MaxR (green) radii, providing a visual representation of the computational results of the Landini algorithm.

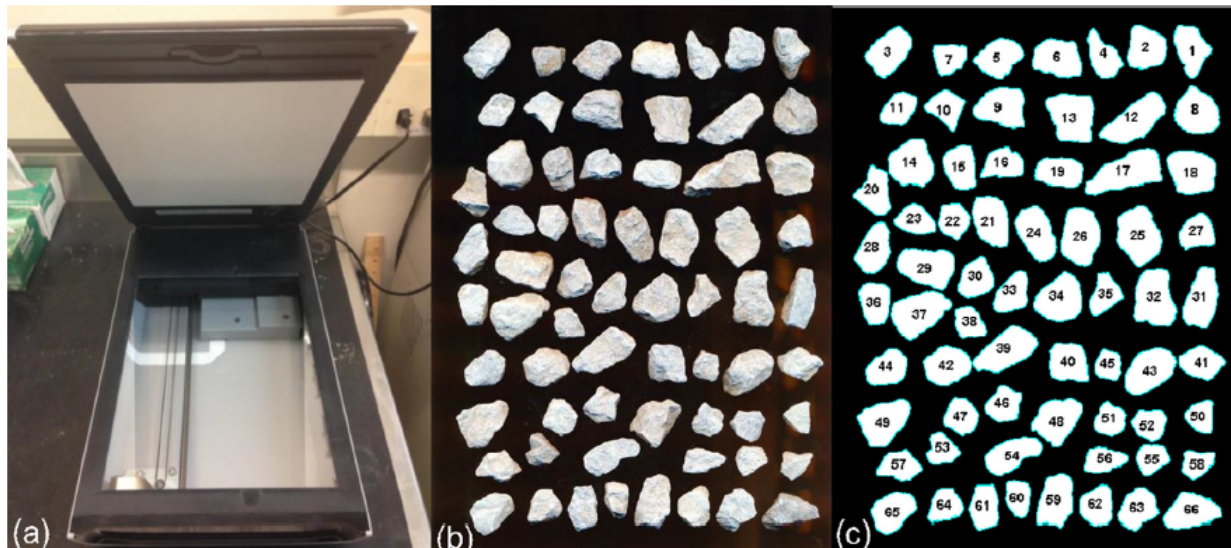


Figure 9. (a) Canon 2D scanner used in this study, (b) original image of scanned gravel-sized particles, (c) processed image used to automatically count the number of particles



Figure 10. (a) Original high-quality scanned image of particles retained on No. 4 sieve, (b) processed binary image overlain with circles denoting MinR radius in red and MaxR radius in green, computed using Landini's sphericity algorithm (Landini et al. 2012)

3.2.3 Triaxial Testing Procedure

Consolidated Drained (CD) triaxial tests were performed per ASTM D7181 on the quarry samples before and after gyratory tests. The purpose of the tests was to evaluate the shear strength of the materials under three different effective confining stresses (i.e., minor principal stresses) of 5, 10 and 15 psi, which are similar to the level of lateral stresses that surfacing aggregates may experience under traffic loading. The CD test procedure consisted of four different stages: (1) sample preparation, (2) saturation, (3) consolidation, and (4) shearing. These stages are described in the following sections.

3.2.3.1 Sample Preparation

This stage consisted of preparing a 4 in. diameter by 8 in. tall specimen for triaxial testing. The preparation involved the following steps:

3.2.3.2 Base Setup and Membrane Placement

As shown in Figure 11, the setup started by placing a porous stone and filter paper at the base of the triaxial cell. After spreading vacuum grease around the base pedestal, a membrane was

placed around the pedestal and an O-ring was applied around the membrane to help seal it, as shown in Figure 12.

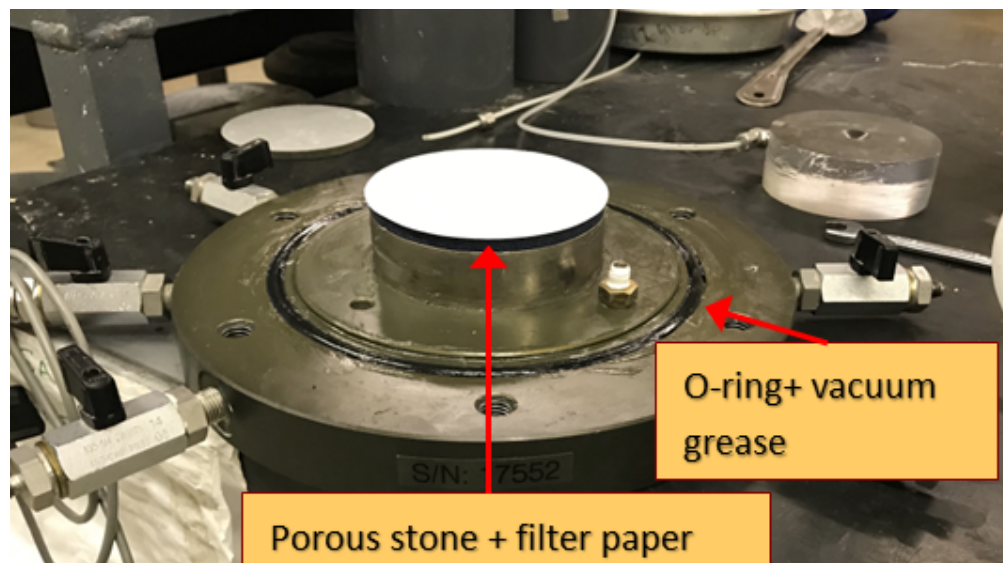


Figure 11. Base setup for triaxial testing

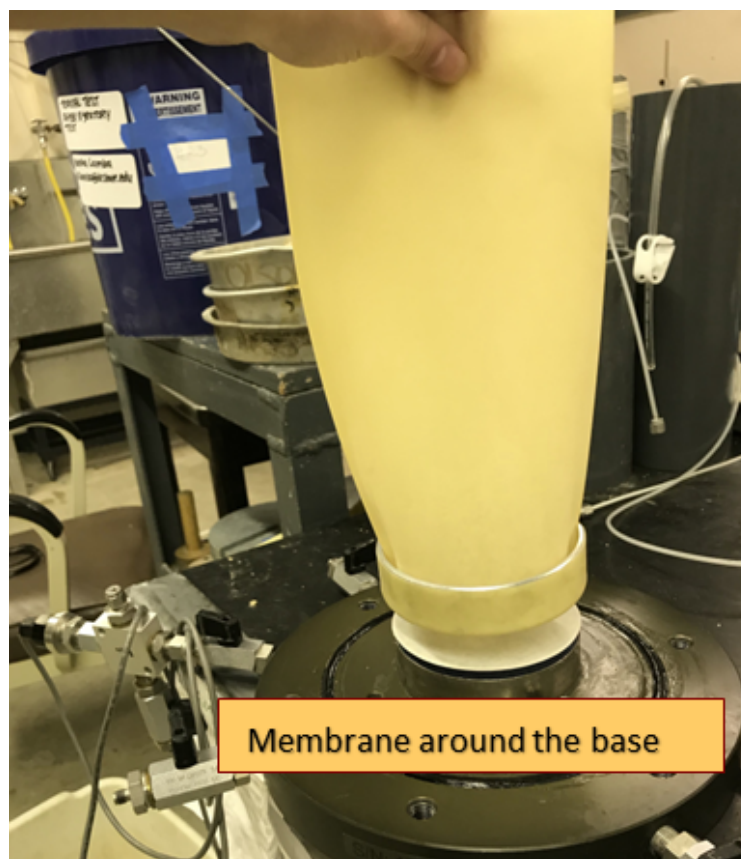


Figure 12. Membrane placement for triaxial specimen

3.2.3.3 Specimen Filling

The membrane was expanded and held in place by vacuum pressure applied to a split mold, as shown in Figure 13. The aggregate specimen was then poured loosely using a funnel to achieve a uniform distribution. The funnel was held as close to the sample as possible to avoid densifying the specimen. Wet paper towels were used on the base to keep the O-ring and vacuum grease free of soil to ensure good sealing at the base of the cell and prevent air leakage during tests.

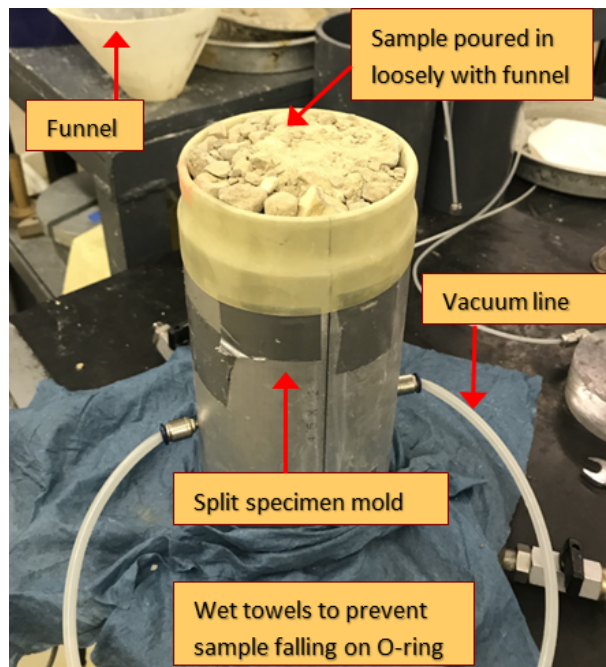


Figure 13. Split vacuum mold and filling of triaxial specimen

3.2.3.4 Final Assembly

The top cap was connected, and the membrane was secured with two O-rings as shown in Figure 14. A second membrane was carefully placed around the specimen as shown in Figure 15 to minimize puncturing of the membrane by the specimen during the shearing stage. The entire preparation procedure took approximately two to three hours per specimen.



Figure 14. Placing of top cap and O-rings around membrane



Figure 15. Placement of second membrane around the specimen

3.2.3.5 Saturation Procedure

After the specimens were prepared, they were saturated to ensure that the pore spaces within the soil were fully saturated with water. This process involved the following three steps:

1. The base assembly of the triaxial device was saturated by circulating water into one port of the base and out another port, until air bubbles were no longer detected in the outlet water line.
2. De-aired water from an overhead tank was supplied through the inlet port to completely saturate the specimen.
3. The de-aired water was slowly circulated through the specimen with the help of a back-pressure pump, while simultaneously increasing the chamber confining pressure around the specimen to keep it approximately 5 psi greater than the pore water pressure in the specimen. This kept the effective stress in the specimen approximately constant. This process was continued until Skempton's B value reached a value of at least 0.95.

This saturation procedure took approximately one to two hours per specimen and is critical to enable accurate pore water pressure measurements during the test.

3.2.3.6 Consolidation Stage

The saturation stage was followed by the consolidation stage, in which the specimens were subjected to controlled effective stresses of 5 psi, 10 psi, and 15 psi. This process took approximately 30 minutes to one hour per specimen and involved increasing the chamber confining pressure to the required level, while keeping the backpressure constant. This stage continued until the rate of change in the specimen volume became very small.

3.2.3.7 Shearing Stage

Once consolidated, the samples were sheared at a constant displacement rate of 0.0079 in./min (0.2 mm/min), corresponding to a strain rate of 0.098%/min (Figure 16). As shown in Figure 17, the specimens were tested to failure by large axial strains of approximately 20% to 30%. The slow shearing process allowed for the drained response to be captured, and required six to seven hours per test (Figure 18). A summary of the triaxial testing parameters obtained from the tests is presented in Table 4.



Figure 16. Triaxial testing – shearing in progress



Figure 17. Triaxial testing – sample failed at 30% strain

3.2.3.8 Test Monitoring and Completion

The shearing stage was carefully monitored and the data recorded in real-time, as depicted in Figure 18. The entire process, from sample preparation to the end of the shearing stage, was typically completed within one day per specimen.

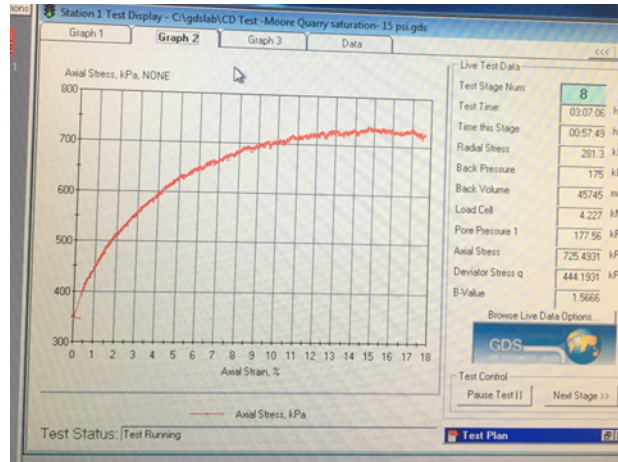


Figure 18. Real-time graph for monitoring of CD triaxial testing during shearing

Table 4. Triaxial testing procedure parameters

Parameter	Value
Sample Dimensions	4 in. x 8 in.
Sample Weight	4.5 – 5.5 lb
Shearing Rate	0.0079 in./min (0.2 mm/min)
Effective Confining Stress	5, 10, and 15 psi
Specimen Preparation Time	2–3 hours
Saturation Time	1–2 hours
Consolidation Time	0.5–1 hour
Shearing Time	6–7 hours

3.2.4 Geological Tests

3.2.4.1 Rock Typing and Relative Abundances

Analyses were performed at the Kansas Geological Survey (University of Kansas, Lawrence, Kansas) for samples collected from the quarries identified in Table 5. The laboratory equipment for geological tests performed in this study is shown in Figure 19. At KGS, samples were wet sieved over a 10 mm sieve to collect medium pebble and larger sized material. Retained material (wet pebbles) were sorted into different rock types visually with a bench mounted magnifier. After separation, the rock types were oven-dried at 100°C overnight. The oven-dried weight of each rock type was recorded for determining relative abundance in the original sample.

The rock types (RT) were labelled in decreasing order of abundance. The most abundant rock type in a sample was labeled “RT01,” the second most abundant was labeled “RT02” and so on. Note that RT01 from one source may not have the same geological characteristics or properties as RT01 from another source. No further testing was done on rock types that occurred in minimal quantity by weight (less than or equal to 5% of the oven-dried weight) However, it should be noted that these odd samples may affect the bulk properties of the aggregates and thus

may contribute to road performance. However, this effect would likely be localized rather than pervasive due to their low abundance. Further study is needed to assess the extent to which these low-abundance rock types affect road performance.

Table 5. Sources for quarry samples tested in this study

No.	Source	Collection Date	Geological Tests?	Geotechnical Tests?
1	Crescent Quarry	7/15/2019	Y	Y
2	Macedonia Quarry	7/15/2019	Y	N
3	Atlantic Quarry	7/15/2019	Y	N
4	Moore Quarry	7/29/2019	Y	Y
5	Pedersen Quarry	8/16/2019	Y	Y
6	Alden Quarry	8/16/2019	Y	Y
7	Gehrke Quarry	8/16/2019	Y	Y
8	Montour Quarry	8/16/2019	Y	N
9	Clayton Quarry	8/16/2019	Y	N

One pebble was selected from each rock type and subsequently analyzed quantitatively via helium porosimetry and qualitatively via thin section petrography. Since the color and the helium pycnometry results of both pebbles closely approximated each other, the subsequent analytical results from two pebbles can be considered with high confidence to be from the same precursor rock type.

Grain Density via Helium Pycnometry. Grain density (in g/cm³) is the true density of the solid phase of a specimen as opposed to bulk density which includes any void volume in the denominator. As such, grain density is useful in identifying the mineralogy of a specimen because it should reflect the mineralogies present in the sample according to their relative abundance.

Grain density was measured in this study using a helium pycnometer. The weight of each pebble was measured using a Mettler Toledo ME204E analytical balance to a precision of 0.0001 g. The calculation of grain density uses Boyle's Law ($P_1V_1 = P_2V_2$), where a known volume of helium gas at a fixed pressure is isothermally expanded into an unknown void volume. After expansion, the resultant stabilized pressure is measured and the grain volume calculated. Grain density (i.e., the density of the solid material excluding any open pores) was measured on each pebble using a Micromeritics AccuPyc II 1340 automatic pycnometer. Each pebble was purged (filled and vented) with helium gas for five cycles before grain density measurements were taken from the average of five cycles.

For the samples analyzed in this study, the most commonly observed minerals were quartz (in chert and sandstones) with a density of $\rho_g = 2.65$ g/cm³, calcite (in limestones) with a density of $\rho_g = 2.71$ g/cm³, and dolomite (in dolostones) with a density of $\rho_g = 2.84$ g/cm³.

Rock Type Abundance via Petrographic Thin Section Analysis. Slicing a rock thin enough makes it transparent and able to be investigated using transmitted light microscopy. In this study, thin sections of pebbles 30 μm (0.03 mm) in size were prepared from epoxy-impregnated coarse aggregate pebbles by TPS Enterprises of Houston, Texas. Epoxy was dyed blue to aid in the identification of pore space (air voids) and fractures (cracks). Thin sections were then dyed in Alizarin Red-S to discriminate between calcite (which dyes pink) and dolomite (which doesn't dye) and with potassium ferricyanide to identify iron-rich calcite (purple).

Pore Throat Size Distribution via Mercury Porosimetry. This method involves measuring the amount of mercury intruded into a sample's pore system at increasingly higher pressures (Washburn 1921). It is also referred to as "mercury intrusion porosimetry" or "mercury intrusion capillary pressure analysis." The pore throat size distribution can be calculated from the volumetric intrusion at each pressure step. It is important to note that this method measures the *pore throat* size distribution and not the *pore* size distribution, because volumetric intrusion at each pressure step is controlled by the connections between pores (i.e., pore throats), rather than the sizes of the pores themselves. This method is advantageous because it is quick (requiring approximately one hour per sample), it can evaluate pore-throat sizes across a wide size range from $\sim 500\ \mu\text{m}$ to $\sim 6\ \text{nm}$, and it can produce measurements for irregularly-shaped samples. This method is governed by the Washburn equation for the penetration of a nonwetting liquid into a porous solid (Washburn 1921):

$$D = \frac{4\gamma \cos \theta}{P} \quad (5)$$

where D is the pore-throat diameter, P is the applied pressure, γ is the surface tension of mercury, and θ is the contact angle between mercury and the sample. In this study, a Quantachrome PoreMaster 33 Pore Size Analyzer was used to measure the pore-throat size distributions by mercury intrusion. Each sample was oven-dried for 6 hours at 135°C and stored in a desiccator at room temperature for 24 hours before being analyzed. Mercury intrusion was conducted at room temperatures of 24°C to 28°C . The following parameters were used in the analysis: a mercury contact angle of 140° for both intrusion and extrusion, and a mercury surface tension of $480\ \text{erg/cm}^2$. The instrument had a maximum pressure of 33,000 psi ($\sim 230\ \text{MPa}$), corresponding to a minimum pore-throat diameter of 5.6 nm.

3.2.4.2 Research Hypotheses Investigated through Geological Tests

The following four specific geology related hypotheses were tested in this study using the petrography, pycnometry, mercury porosimetry, and grain size analysis tests:

1. The coarse aggregates are composed of multiple rock types.
2. The Clean and Class A coarse aggregates have different relative abundances of rock types.
3. Relative abundances of rock types change over time in granular-surfaced roads.
4. Relative abundances of rock types change during laboratory-performed gyratory compaction tests.

For the first hypothesis, previous studies have shown that the coarse aggregates used in concrete pavement construction are composed of multiple rock types and that the relative abundance of those rock types affects the bulk properties of the resulting pavement (e.g., Hasiuk et al. 2017, Hasiuk and Orso 2019, Hasiuk and Ishutov 2019). In the present study, different sources were sampled which typically produce materials for gravel roads, and they were each analyzed for the relative abundance of rock types.

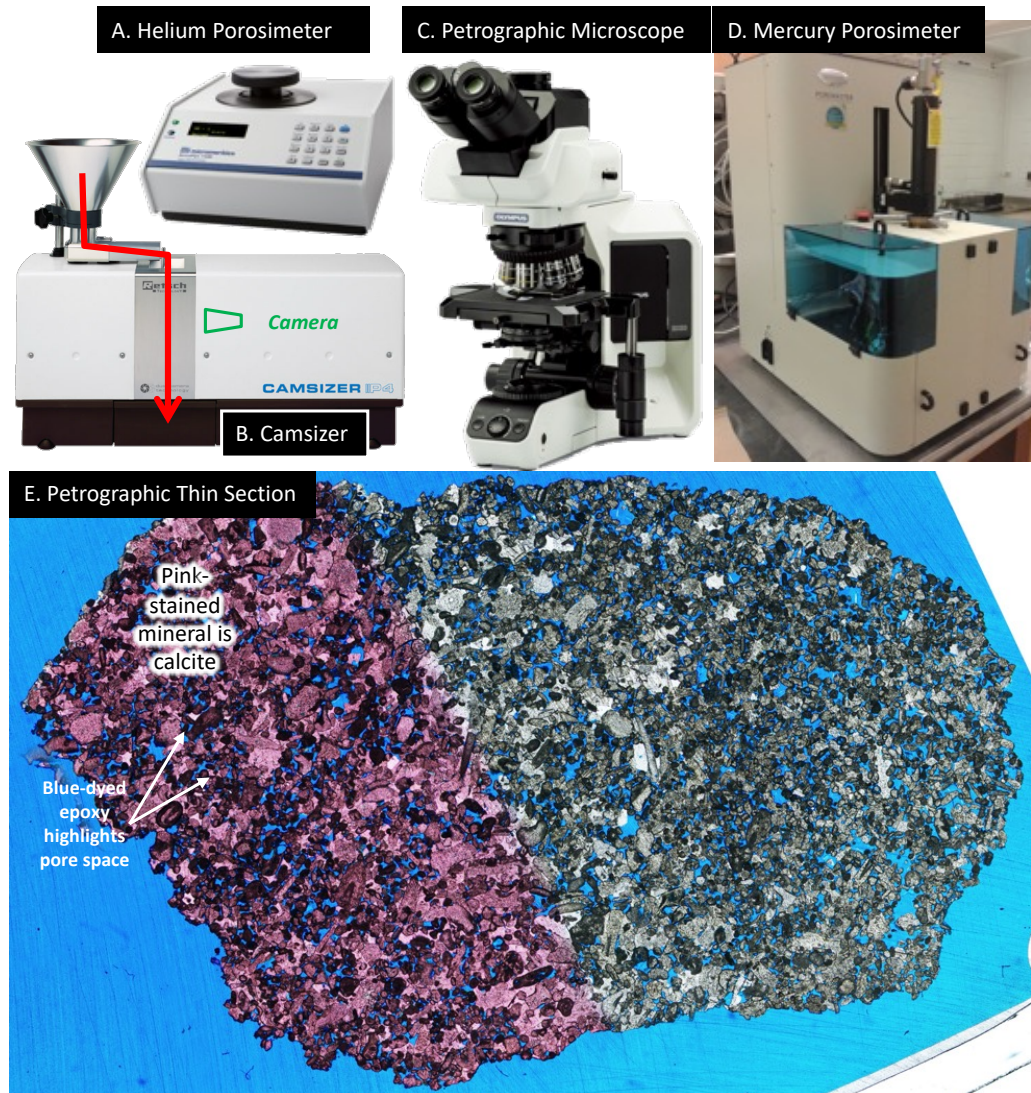


Figure 19. Laboratory equipment for geological tests in this study: (a) helium porosimeter to measure grain density, (b) Camsizer to measure particle size distributions, (c) petrographic microscope to characterize internal structure of particles, (d) mercury porosimeter to measure pore throat size distributions in coarse aggregate pebbles, (e) thin section showing interior nature of pebbles

For the second hypothesis, samples from three of the quarries in this study included both Clean and Class A types. The relative abundance of rock types was therefore compared for these samples.

For the third hypothesis, changes in the relative abundance of rock types as well as their pore systems might be expected as materials experience annual cycles of physical and chemical deterioration in service. It is hypothesized that less durable rock types such as those with higher clay contents or greater porosities will experience a greater reduction in abundance over time. To test this hypothesis, samples collected from in-service roads at multiple test sites over a 2-year period from April 2017 to April 2019 were evaluated and compared.

To test the fourth hypothesis, numerous gyratory compaction tests were performed to simulate and accelerate the mechanical compaction and crushing experienced by aggregate particles within a gravel road. Geological tests were performed on four aggregate types before and after the gyratory compaction tests. Results of the geological tests are discussed in Chapter 4.

CHAPTER 4. RESULTS AND DISCUSSION

4.1 Coarse Aggregate Samples Collected from Quarries

4.1.1 *Moore Quarry Aggregates*

Samples of Class A material were collected from the Moore Quarry located near Gilmore City, Iowa. Moore Quarry mainly produces crushed stone and gravel from the Mississippian Gilmore City Formation. This formation consists of both porous and nonporous varieties of limestone characterized as fossiliferous and exhibiting traits of skeletal lime grainstone or shaley lime mudstone.

4.1.1.1 PSD Comparison and Evaluation of Breakage Parameters for Moore Quarry

The mechanical degradation of Class A Moore Quarry samples during gyratory compaction testing, as represented by Hardin's total breakage from PSD curves, was determined to be 0.07 from laboratory sieve and hydrometer analysis of the entire gradation, and 0.10 via 2D image analyses of the plus #4 fraction. This degradation is shown by the shaded gray area enclosed between the two PSD curves determined by sieve analyses for grain sizes larger than 0.075 mm in Figure 20, and determined by 2D image analyses for grain sizes larger than 4.75 mm in Figure 21. In these figures and all similar ones that follow, the PSD curves measured before gyratory testing are labeled BGT, while those measured after gyratory testing are labeled AGT. Table 6 summarizes the corresponding Hardin breakage parameters (total breakage, breakage potential, and relative breakage) as well as the percentages of gravel, sand, and fines determined for the same specimens processed before and after gyratory tests. For the Moore Quarry aggregates, the gravel fraction decreased by 7.6% during the gyratory test, while the sand and fines fractions increased by 7.3% and 0.3%, respectively. Thus the gravel sized particles broke down under the simulated traffic loading provided by the gyratory compaction test as intended.

For a given gyratory test specimen, it is not theoretically possible for a point on the AGT curve to be below the BGT curve, because breakage of a particle can only cause either an increase or zero change in the percent finer for any given sieve size. However, a few points on the AGT curve in Figure 20 are slightly below the BGT curve, likely due to experimental error. Two possible sources of error that could cause such a decrease in the percent finer are as follows:

1. Any loss of material during retrieval or transfer of the specimen after the gyratory test would result in a smaller total sample mass for the AGT sieve analysis. By simulating this case for PSD calculations in a spreadsheet, it was found that the PSD curve's percent finer values can decrease for the sieves from which the material was lost.
2. If an elongated particle was shaken enough to rotate and pass through a sieve's openings during shaking before the gyratory test but it got stuck on the same sieve after the gyratory test, then the percent retained on that sieve would increase thereby decreasing its percent finer value.

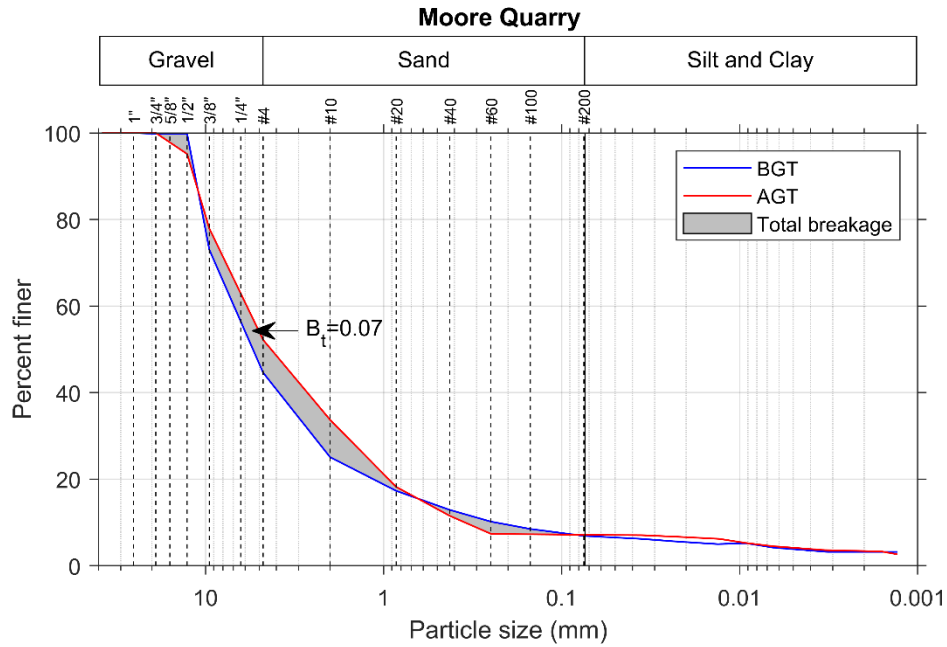


Figure 20. Particle size distributions from sieve and hydrometer analysis and evaluation of total breakage of coarse aggregate samples from Moore Quarry

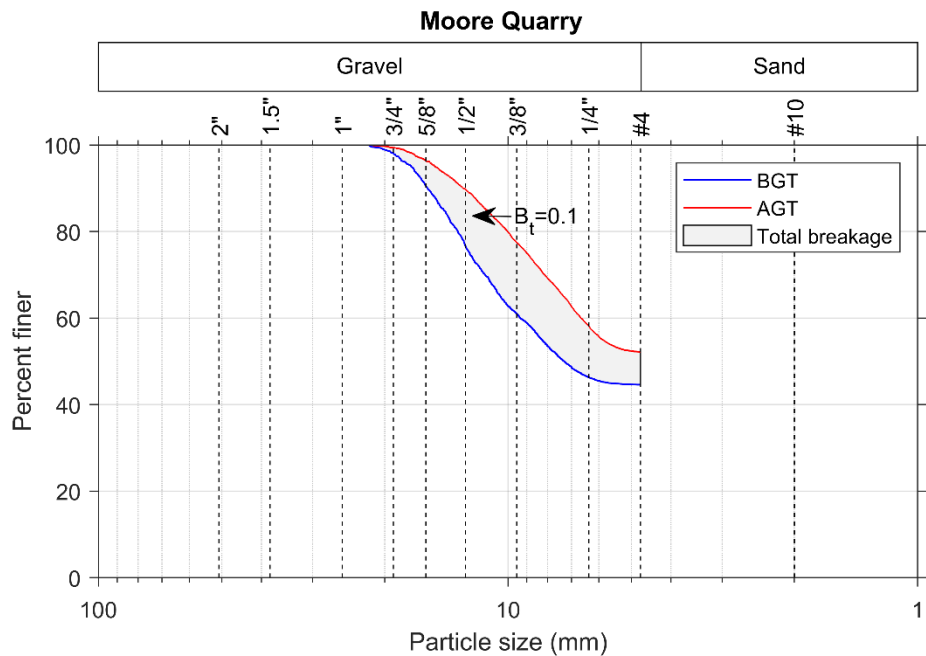


Figure 21. Particle size distributions from 2D image analysis and evaluation of total breakage of coarse aggregate samples from Moore Quarry

Table 6. Hardin’s breakage parameters determined from laboratory sieve and 2D image analyses, and corresponding percentages of gravel, sand, and fines for Moore Quarry samples

Analysis Type	Hardin’s Breakage Parameters			% Gravel		% Sand		%Fines	
	Total Breakage, B_t	Breakage Potential, B_p	Relative Breakage, B_r	BGT	AGT	BGT	AGT	BGT	AGT
Lab Sieve Analyses	0.0720	1.6252	0.0443	55.4	47.8	37.7	45.0	6.9	7.2
				% Reduction (red.) or % Increase (inc.)					
				7.6 % red.		7.3% inc.		0.3% inc.	
2D Image Analyses	0.0989	0.4335	0.2282	NA*		NA*		NA*	

* Not Available: Only gravel sized particles retained on #4 (4.75 mm) sieve were scanned.

4.1.1.2 2D Image Analyses and Comparison of Morphological Parameters for Moore Quarry

The calculated morphological parameters evaluated from 2D image analysis of manual scans of the Moore Quarry BGT and AGT specimens are presented in Figure 22 through Figure 27, and the statistical outputs of these morphological parameters along with their changes during gyratory testing are presented in Table 7. In all such statistical boxplots in this report, the top and bottom of the blue box denotes the extents of the 75th and 25th percentiles, the red line inside the box denotes the median, the diamond denotes the average, the whiskers extend to the 5th and 95th percentiles, and the plus marks denote the statistical outliers. The total number of gravel-sized particles scanned for each specimen are denoted as “ n ” in the figures, while the subset of points considered as outliers by the algorithm is denoted as “ o .”

As can be seen in in Figure 22 through Figure 27, the total number of gravel-sized particles (n) for Moore Quarry increased from 1,549 to 2,807 during gyratory compaction due to particle breakage, and the number of outliers was typically between 0.04% and 8.1% of n . The increase in number of gravel sized particles during gyratory compaction is opposite the trend observed for Pedersen Quarry (discussed in a later section), meaning that more of the Moore Quarry aggregates remained within the gravel size range above the No. 4 sieve after breaking, whereas more of the Pedersen Quarry aggregates broke into particles smaller than the No. 4 sieve. As shown in Table 7, the median values of roundness, sphericity, and form factor for Moore Quarry increased by 5.6%, 5.3%, and 20.1% respectively, indicating that the particles became more rounded and spherical during gyratory compaction. Conversely, corresponding decreases of 16.8%, 7.0%, and 22.0% in shape factor, roundness index, and angularity, respectively, were observed for the same specimens.

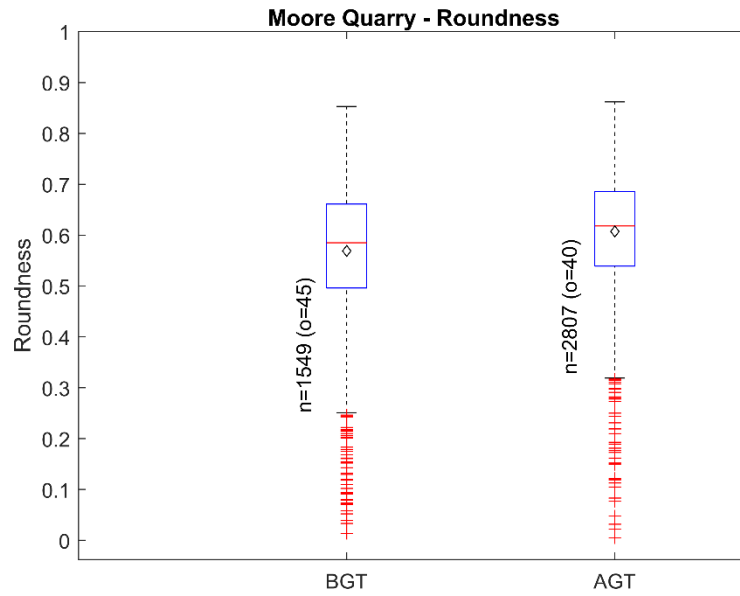


Figure 22. Comparison of roundness for BGT and AGT specimens from Moore Quarry

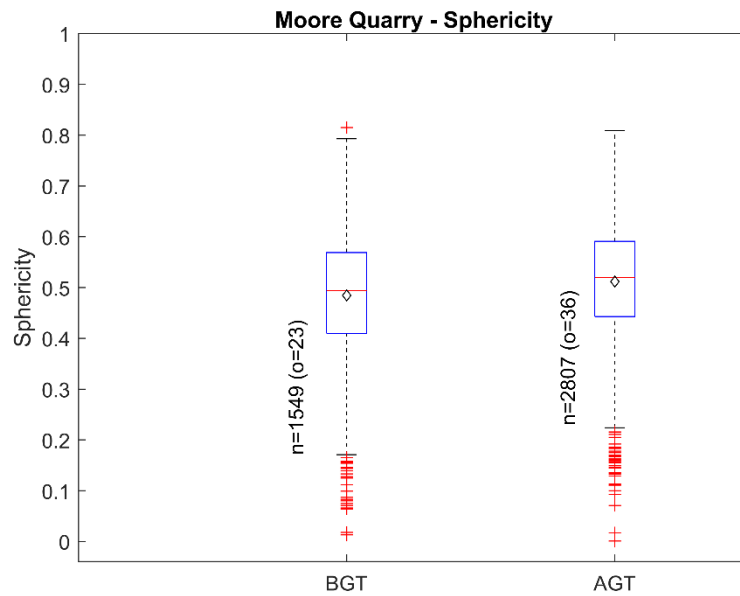


Figure 23. Comparison of sphericity for BGT and AGT specimens from Moore Quarry

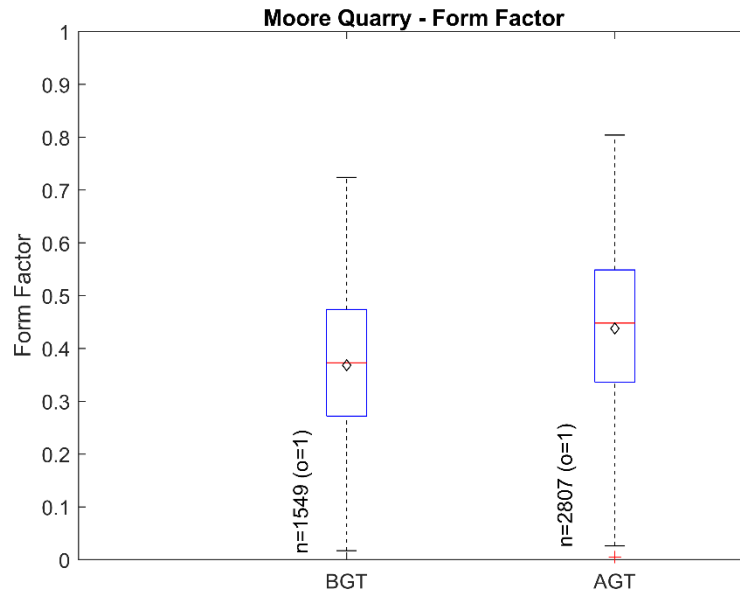


Figure 24. Comparison of form factor for BGT and AGT specimens from Moore Quarry

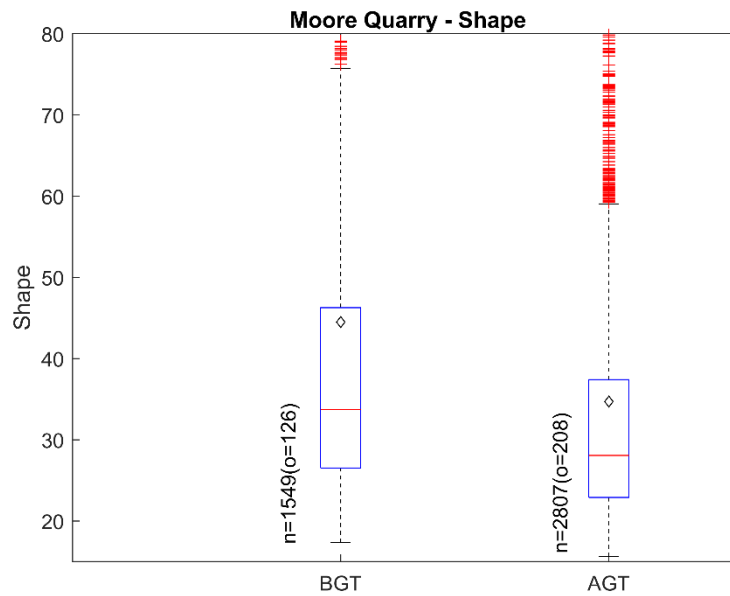


Figure 25. Comparison of shape factor for BGT and AGT specimens from Moore Quarry

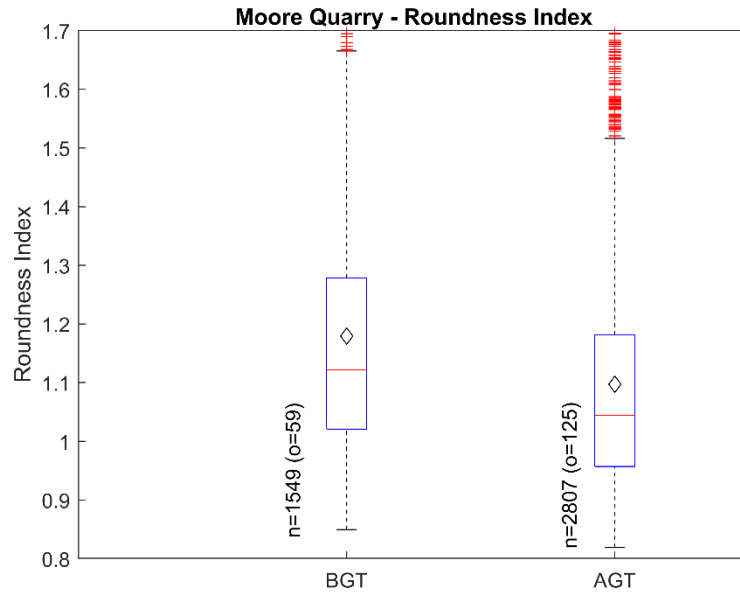


Figure 26. Comparison of roundness index for BGT and AGT specimens from Moore Quarry

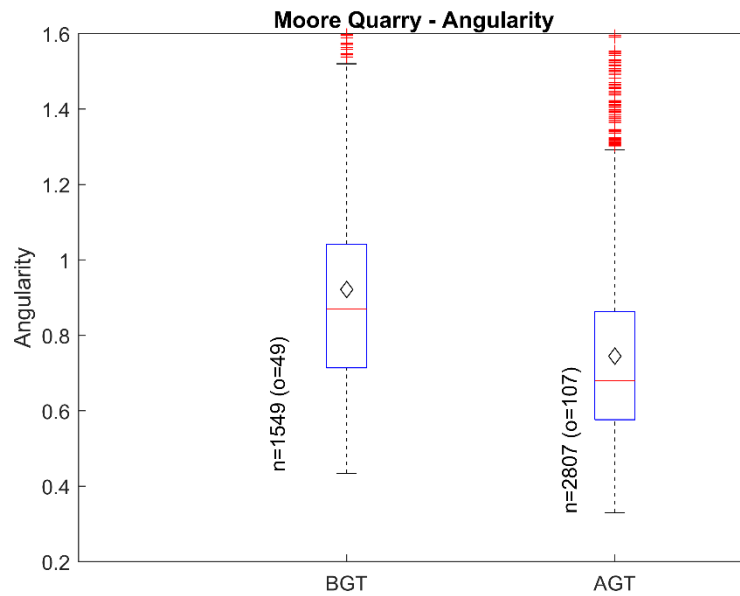


Figure 27. Comparison of angularity for BGT and AGT specimens from Moore Quarry

Table 7. Statistical results of morphological parameters of Moore Quarry

Parameter	Sample Type	Max.	Min.	Mean	Mode	Median	Std. Dev.	Skew-ness	Kurt-osis	Out-liers
Roundness	BGT	0.853	0.014	0.569	0.583	0.585	0.137	-0.914	4.471	45
	AGT	0.862	0.005	0.607	0.645	0.618	0.112	-0.91	5.231	40
	% increase			6.7%		5.6%				
Sphericity	BGT	0.815	0.013	0.484	0.487	0.494	0.124	-0.427	3.421	23
	AGT	0.809	0.001	0.512	0.446	0.520	0.113	-0.52	3.531	36
	% increase			5.8%		5.3%				
Form Factor (FF)	BGT	0.724	0.017	0.368	0.285	0.373	0.137	-0.154	2.448	1
	AGT	0.804	0.005	0.438	0.361	0.448	0.144	-0.231	2.407	1
	% increase			19.0%		20.1%				
Shape Factor (SF)	BGT	738.4	17.35	44.5	20.77	33.73	44.8	7.64	83.96	126
	AGT	2286	15.62	34.69	19.77	28.08	47.14	39.32	1857	208
	% increase			-22.0%		-16.8%				
Roundness Index (RI)	BGT	3.704	0.850	1.179	1.079	1.122	0.245	3.249	25.04	59
	AGT	2.457	0.819	1.097	0.993	1.044	0.2	1.767	7.778	125
	% increase			-7.0%		-7.0%				
Angularity	BGT	3.906	0.434	0.922	0.968	0.870	0.305	2.585	17.25	49
	AGT	2.265	0.330	0.745	0.637	0.679	0.235	1.582	6.914	107
	% increase			-19.2%		-22.0%				

The roundness is also plotted against the inverse of aspect ratio in Figure 28 similar to Dawson (2021), where aspect ratio is calculated as the particle's length (maximum Feret diameter) divided by its width (minimum Feret diameter). With this definition, the aspect ratio should always be greater than or equal to one. In the plot, however, the inverse of the aspect ratio is used because it varies between 0 (for infinitely elongated) and 1 (for perfectly square). The data show that as roundness decreases, the particles also generally become more elongated as evidenced by a smaller inverse aspect ratio. Additionally, most of the particles lie towards the rounded and square end of the scales, with a smaller percentage of particles being towards the origin (i.e., more angular and elongated). The increase in roundness from BGT to AGT can also be seen in the figure.

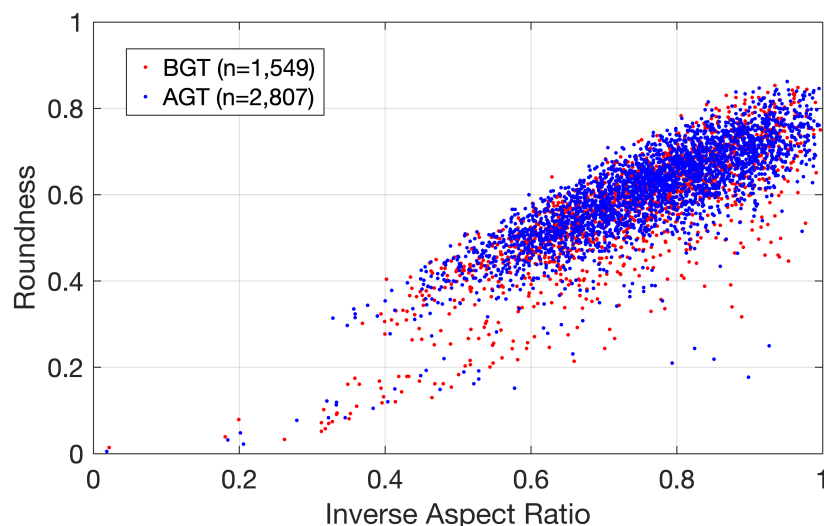


Figure 28. Roundness versus inverse of aspect ratio for BGT and AGT specimens from Moore Quarry

4.1.1.3 Gyratory Compaction Test Results for Moore Quarry

The continuously evolving dry unit weight and void ratio calculated from the specimen height recorded during the gyratory test of the Moore Quarry specimen are plotted in Figure 29 and Figure 30 with respect to the compaction energy and number of gyrations, respectively. As described in Section 3.2.1.2, reloading after the first 250 gyrations causes a discontinuity in the shear resistance data which can be seen in the figures. From the data in these two figures, a 57.4% decrease in void ratio and 27.4% increase in dry unit weight were observed during the gyratory compaction test on the Moore Quarry aggregates.

The shear resistance and gyratory compaction energy of the specimen were calculated from the force and eccentricity data recorded by the PDA during the test, and the shear resistance is also shown in Figure 29 and Figure 30. The point of maximum curvature for the resulting plot of dry unit weight versus gyratory compaction energy in Figure 29 occurs at a dry unit weight of 127.0 pcf, and the changes in compaction energy and dry unit weight before and after this point, defined herein as compaction Stages I and II, are tabulated in Table 8. Stage I is characterized by a rapid increase in dry unit weight and rapid decrease in void ratio, while State II is characterized by slower changes in these parameters. As illustrated by the figure and table, the point of maximum curvature in the dry unit weight curve used to define Stages I and II denotes the point after which continued compaction delivers diminishing returns, making it a good target for field compaction specifications. For the aggregates tested in this study, this point was typically found to occur above Standard compaction energy but below Modified Proctor compaction energy, as will be shown in subsequent sections.

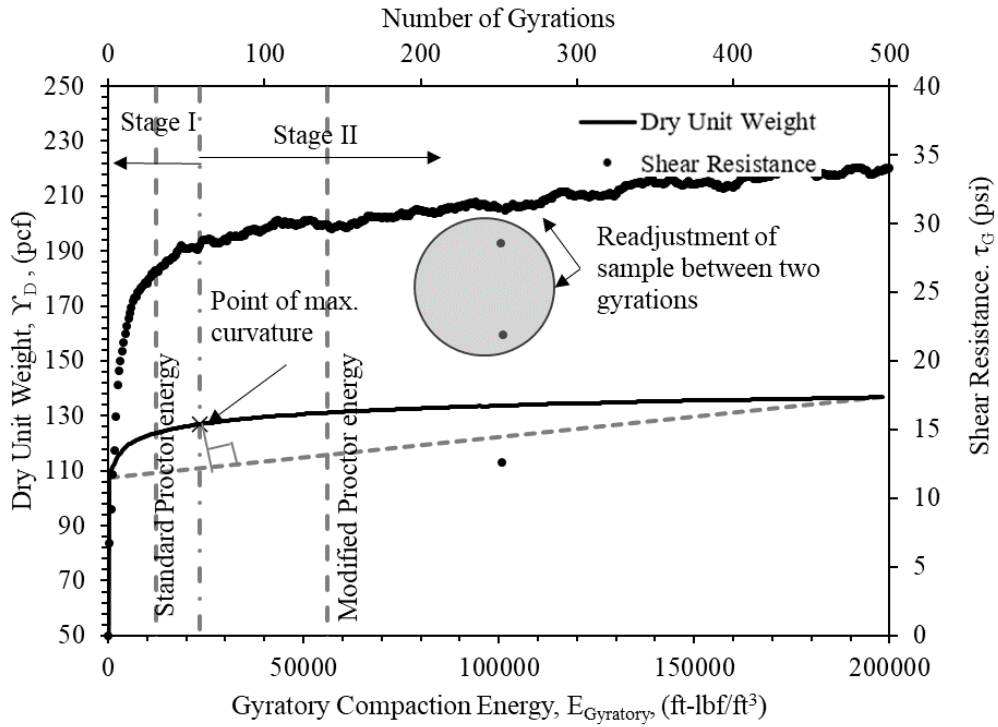


Figure 29. Relationships between dry unit weight, gyratory compaction energy, shear resistance, and number of gyrations for coarse aggregates from Moore Quarry

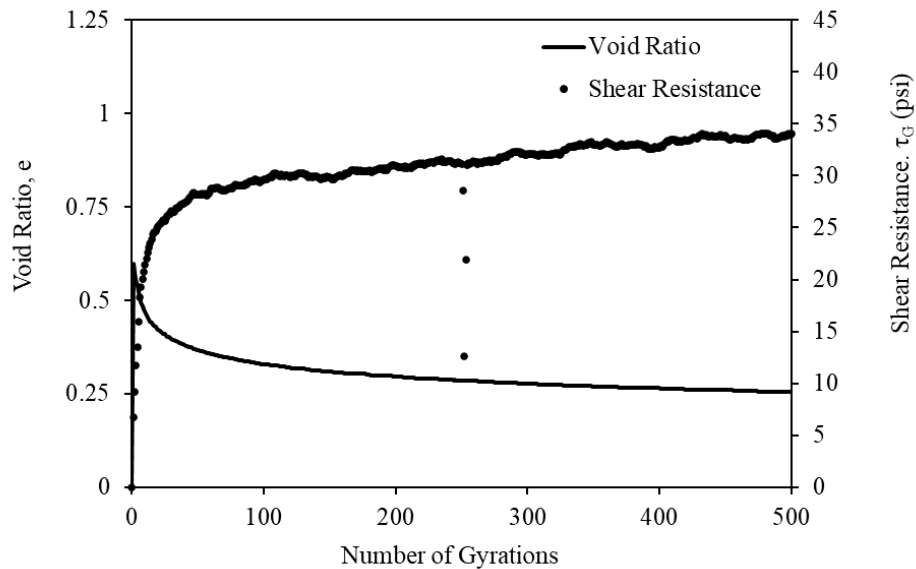


Figure 30. Changes in shear resistance and void ratio of coarse aggregate sample from Moore Quarry during gyratory compaction test

Table 8. Gyratory compaction energy and dry unit weights for Stages I and II of gyratory compaction test for Moore Quarry

Stage	Compaction Energy, E (ft-lbf/ft ³)			Dry Unit Weight, γ_d (pcf)		
	Initial E_i	Final E_f	Change ΔE	Initial γ_{di}	Final γ_{df}	Change Δ γ_d
I	286.6	23,393.8	23,107.2	107.3	127.0	19.7
II	23,393.8	198,224.8	174,831.0	127.0	136.7	9.7

4.1.1.4 Triaxial Test Results for Moore Quarry

The chamber confining pressures applied in the triaxial tests on the Moore Quarry aggregates were 5.8, 10.4 and 15.4 psi for the BGT specimens, and 5.2 and 12.7 psi for the AGT specimens. The Mohr-Coulomb failure envelopes resulting from the tests are shown in Figure 31 and Figure 32. The resulting drained cohesion (c') and friction angle (ϕ') values were 4.52 psi and 37.5° for the BGT specimens, and 6.14 psi and 32.5° for the AGT specimens. Therefore, the particle degradation caused by the gyratory compaction tests resulted in an increase of 35.8% in the cohesion but a 13.3% decrease in friction angle for this material.

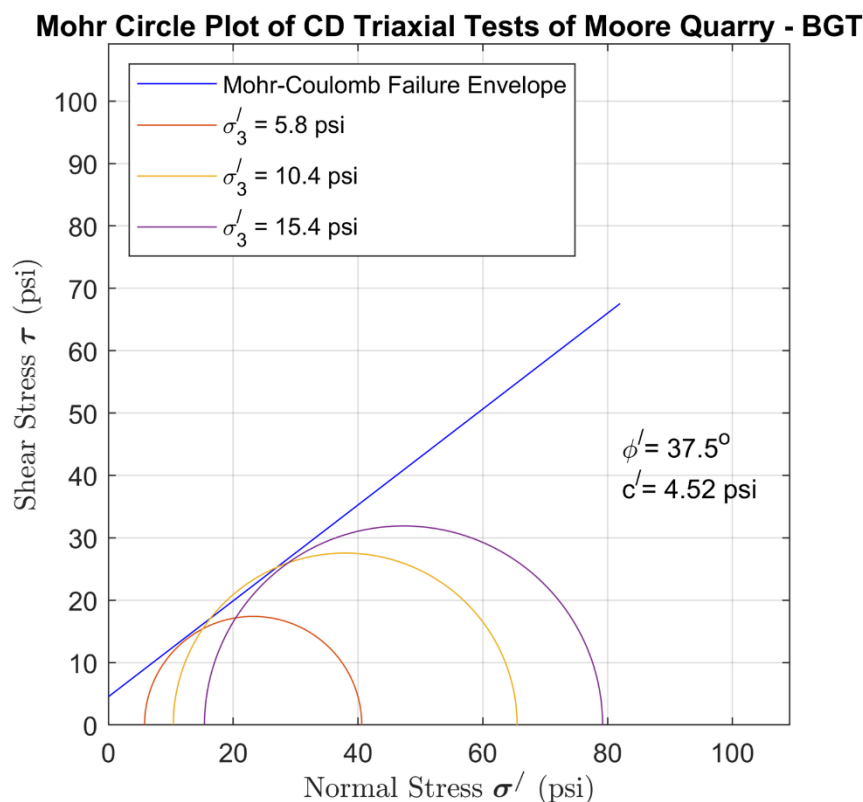


Figure 31. Triaxial test results for Moore Quarry specimens before gyratory testing

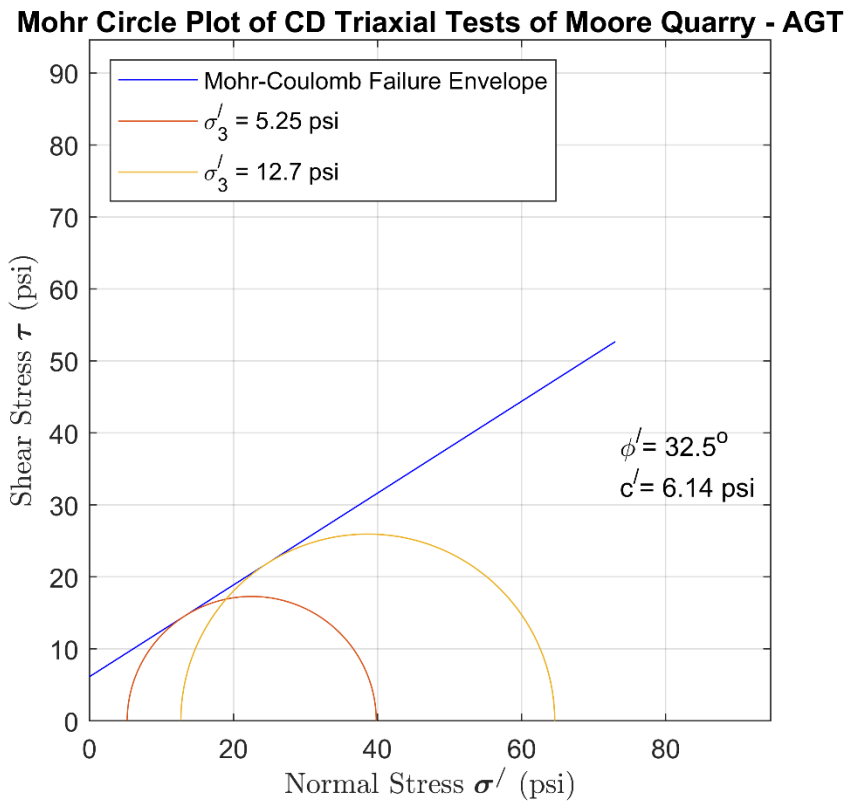


Figure 32. Triaxial test results for Moore Quarry specimens after gyratory testing

4.1.1.5 Geological Tests for Moore Quarry

The rock typing and thin section tests indicated that the Moore Quarry Class A sample consisted of four rock types. The three most abundant of these rock types were analyzed using thin sections, the results of which are presented in Table 9 and Table 10. The grain densities of the three rock types were within a small range, from 2.72 to 2.73 g/cm³ for both BGT and AGT specimens. However, the abundance of these rock types among the gravel-sized particles changed significantly during gyratory testing as noted in the tables. Specifically, Rock Type 1 (nonporous, stylolitized, medium grained, ooid lime grainstone) decreased from 53% to 31% during gyratory testing, while Rock Type 2 (nonporous, fine grained, skeletal ooid lime grainstone) increased from 32% to 38%, and Rock Type 3 (nonporous, lime wackestone; grain density) increased from 12% to 17%. Rock Type 4 (nonporous, stylolitized ooid lime grainstone, not imaged) went from 8% BGT to 4% AGT. These results indicate that Rock Types 2 and 3 were stronger than Rock Type 1, as they experienced fewer particles breaking down smaller than the #4 sieve size during the gyratory compaction test.

Additionally, Rock Types 1–3 all showed slight shifts to smaller particle sizes after gyratory testing as shown in the Camsizer data of Figure 33. The particles in Rock Type 1 went from having four peaks to three, with the peak at the largest particle size being eliminated completely

and contributing to increases in the other three peaks. Rock Types 2 and 3 exhibited only small decreases in particle sizes as evidenced by the slight shifts to smaller particle sizes.

Table 9. Geological parameters of Moore Quarry samples before gyratory compaction

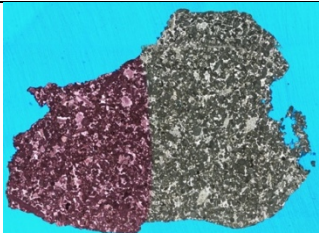
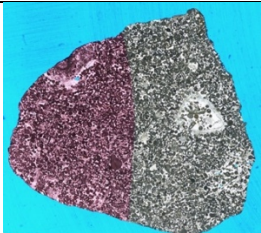
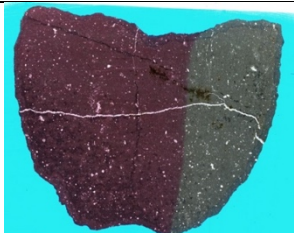
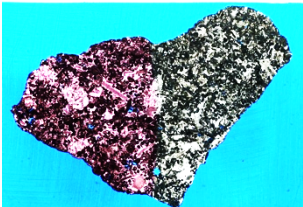
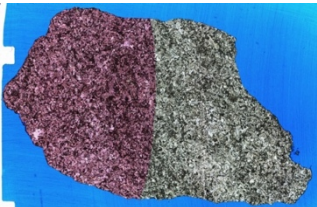
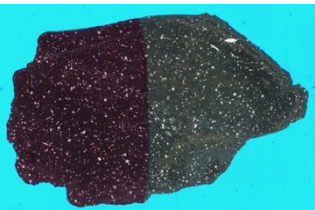
Geological Parameters	Rock Type 1	Rock Type 2	Rock Type 3
Grain Density (g/cm ³)	2.72	2.72	2.73
Abundance	53%	32%	12%
Images of the Thin Sections			

Table 10. Geological parameters of Moore Quarry samples after gyratory compaction

Geological Parameters	Rock Type 1	Rock Type 2	Rock Type 3
Grain Density (g/cm ³)	2.72	2.73	2.73
Abundance	31%	38%	17%
Images of the Thin Sections			

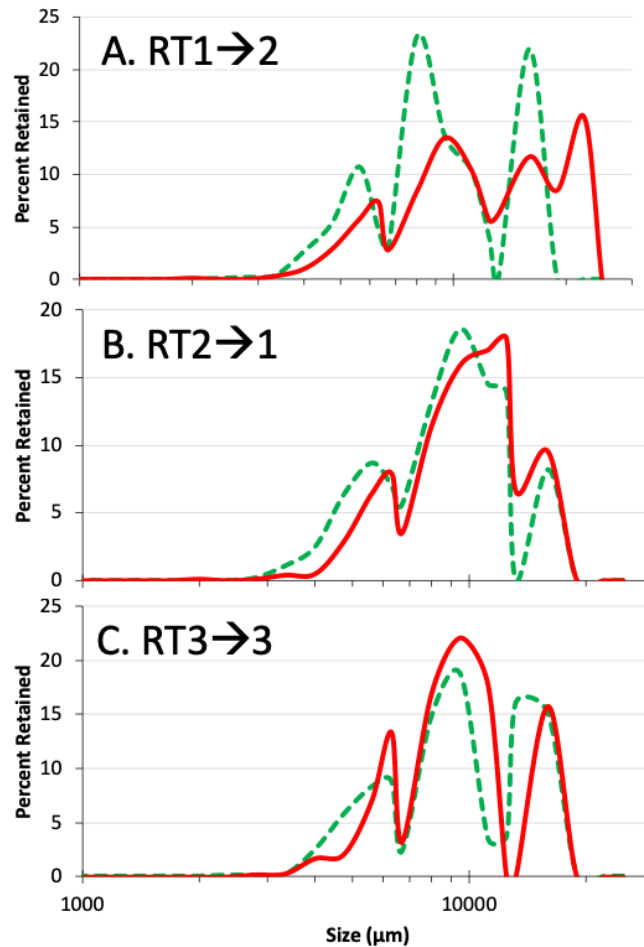


Figure 33. Camsizer data for three rock types from Moore Quarry BGT (red lines) and AGT (dashed green lines). Arrows indicate resulting changes in relative abundance AGT.

4.1.2 Alden Quarry Aggregates

Samples of 1 in.-minus clean aggregates were collected from the Alden Quarry situated near Alden, Iowa. This quarry extracts material from the Mississippian Gilmore City Formation, which consists of coarse- to medium-grained fossiliferous limestone (skeletal lime grainstone) that ranges from porous to nonporous.

4.1.2.1 PSD Comparison and Evaluation of Breakage Parameters for Alden Quarry

Particle size distribution curves were obtained for the Alden Quarry clean samples before and after gyratory compaction tests by sieve analyses and hydrometer tests. The PSD curves from sieve and hydrometer tests are presented in Figure 34. The gravel-sized particles retained on the No. 4 (4.75 mm) sieve for the BGT and AGT samples were also scanned using the Cannon scanner for 2D image analyses, the results of which are shown in Figure 35. As shown in these two figures, the mechanical degradation, represented by Hardin's total breakage, was determined to be 0.39 for the gravel and sand fractions using the laboratory PSD curves (Figure 34), and

0.28 for the gravel fraction from the 2D-image analyses (Figure 35). Table 11 details the corresponding breakage parameters—total breakage, breakage potential, and relative breakage—as well as the percentages of gravel, sand, and fines for the BGT and AGT specimens. Based on the sieve and hydrometer data, the gravel fraction decreased by 28.6% during gyratory compaction, while the sand and fines fractions increased by 23.2% and 5.4%, respectively. These values quantify the breakdown of the Alden Quarry materials during the gyratory tests which simulate the effects of traffic loading.

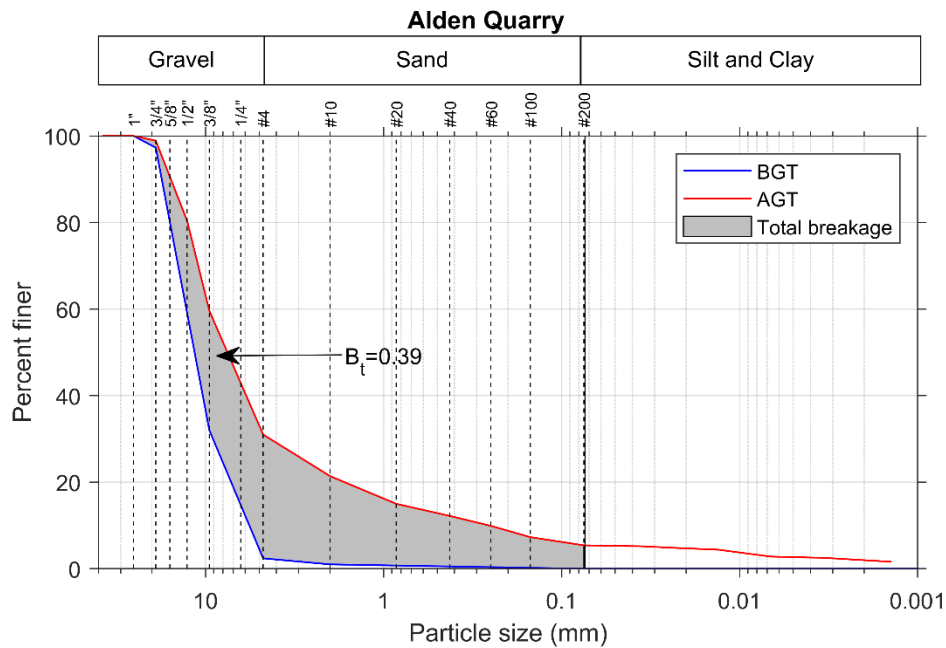


Figure 34. Particle size distributions from sieve and hydrometer analysis and evaluation of breakage of coarse fraction for samples from Alden Quarry

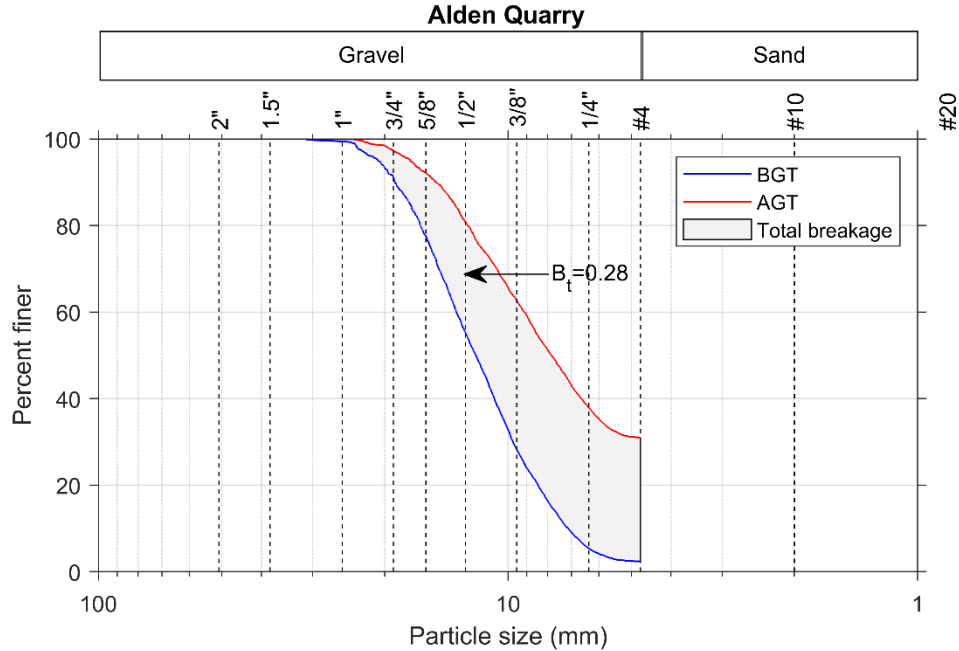


Figure 35. Particle size distributions from 2D image analysis and evaluation of breakage of gravel fraction for samples from Alden Quarry

Table 11. Breakage parameters determined from laboratory sieve analyses and 2D image analyses, and corresponding percentages of gravel, sand, and fines for Alden Quarry samples

Analysis Type	Hardin's Breakage Parameters			% Gravel		% Sand		% Silt and Clay	
	Total Breakage, B_t	Breakage Potential, B_p	Relative Breakage, B_r	BGT	AGT	BGT	AGT	BGT	AGT
Lab Sieve Analyses	0.3938	2.1464	0.1834	97.6	69.0	2.4	25.6	0.0	5.4
				% Reduction (red.) or % Increase (inc.)					
				28.6% red.		23.2% inc.		5.4% inc.	
2D Image Analyses	0.2829	0.7850	0.3604	NA*		NA*		NA*	

* Not Available: Only gravel sized particles retained on #4 (4.75 mm) sieve were scanned.

4.1.2.2 2D Image Analyses and Comparison of Morphological Parameters for Alden Quarry

The morphological parameters evaluated by 2D image analysis for the BGT and AGT Alden Quarry specimens are presented in Figure 36 through Figure 41, and the corresponding statistical measures of these morphological parameters are presented in Table 12. The relative changes in the morphological parameters during gyratory testing are also computed and presented in Table 12, quantifying the mechanical degradation experienced by the specimens as well as the changes in geometry of the gravel-sized particles. As detailed in Table 12, the median values of roundness, sphericity, and form factor increased by 8.4%, 7.9%, and 0.3% respectively. Accordingly, the specimen exhibited decreases of 28.7%, 13.3%, and 24.0% in shape factor, roundness index, and angularity, respectively, during the gyratory test.

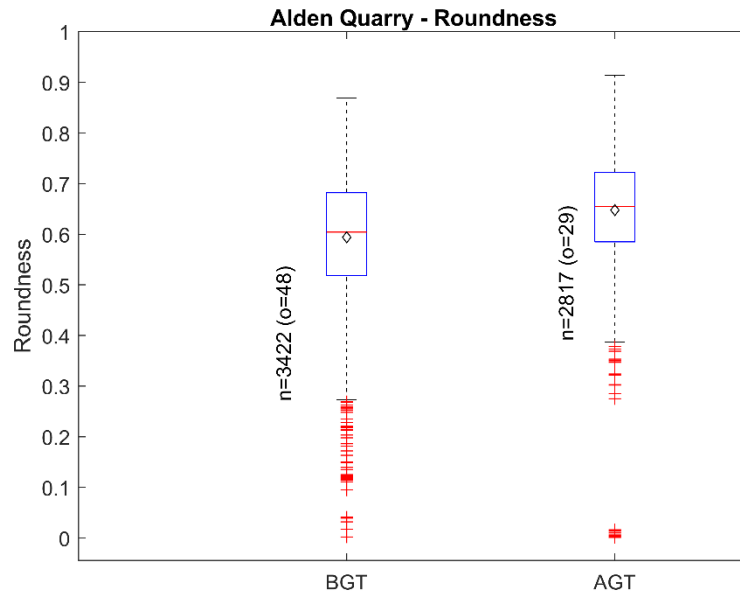


Figure 36. Comparison of roundness for BGT and AGT specimens from Alden Quarry

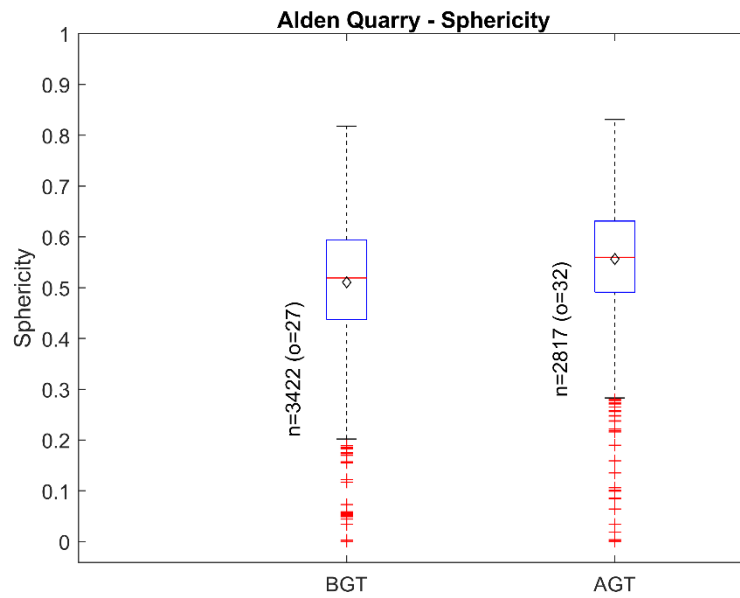


Figure 37. Comparison of sphericity for BGT and AGT specimens from Alden Quarry

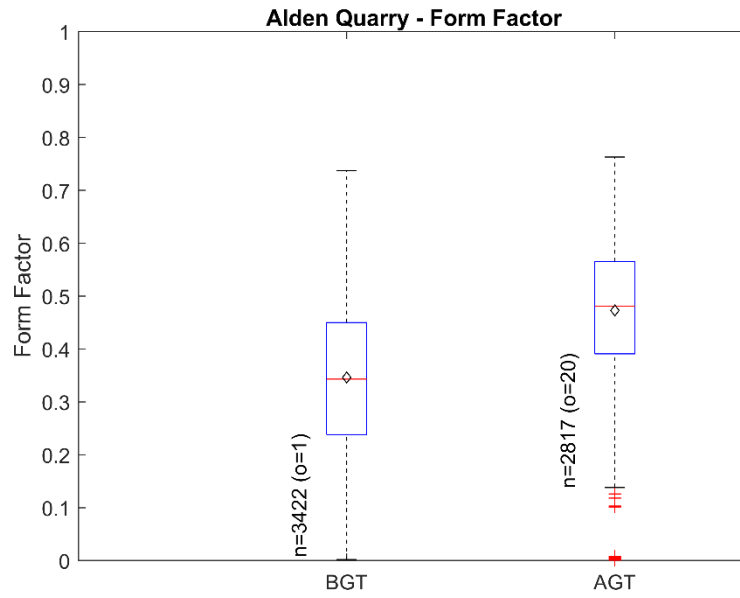


Figure 38. Comparison of form factor for BGT and AGT specimens from Alden Quarry

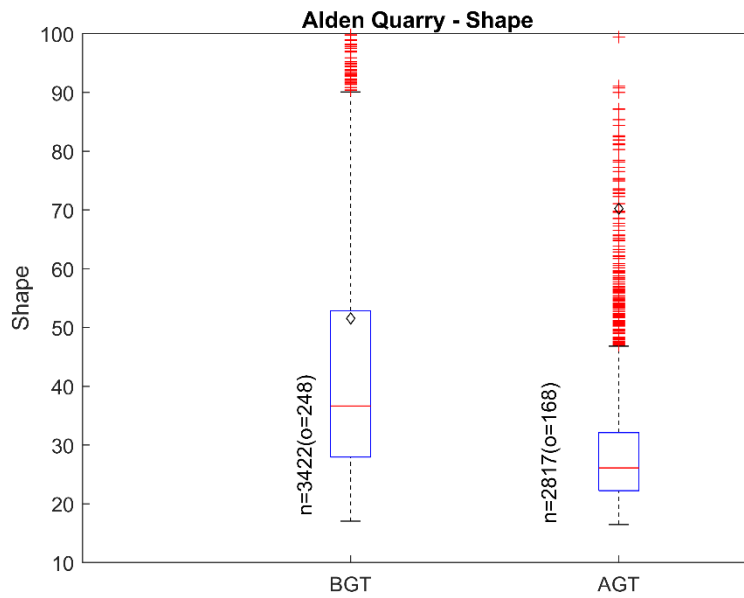


Figure 39. Comparison of shape factor for BGT and AGT specimens from Alden Quarry

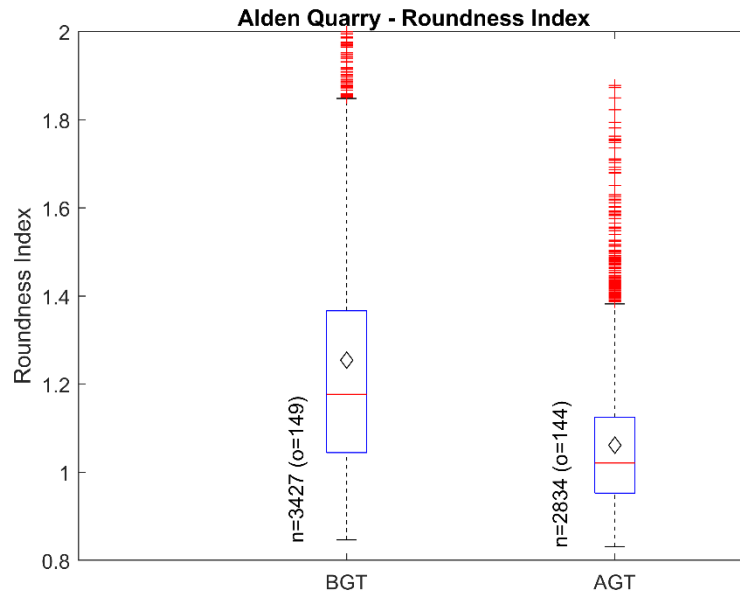


Figure 40. Comparison of roundness index for BGT and AGT specimens from Alden Quarry

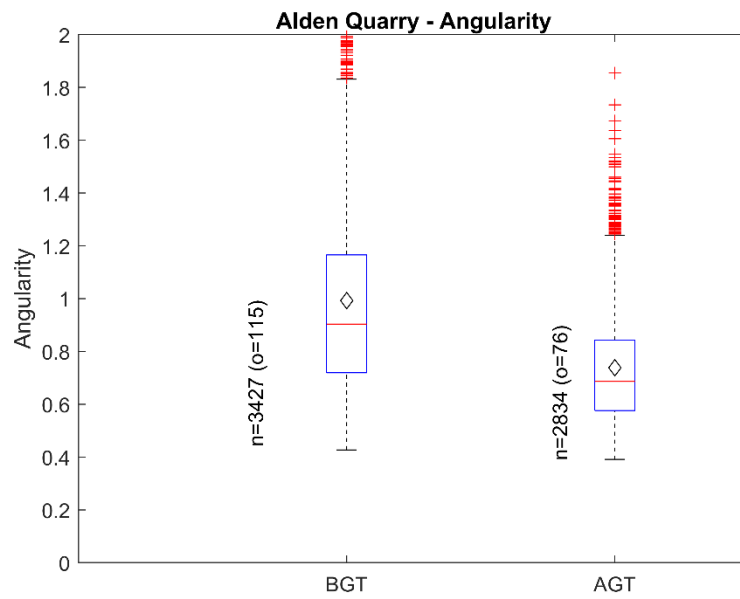


Figure 41. Comparison of angularity for BGT and AGT specimens from Alden Quarry

Table 12. Statistical results of morphological parameters of Alden Quarry specimens

Parameter	Sample Type (BGT/AGT)	Max. Value	Min. Value	Mean	Mode	Median	Std. Dev.	Skew-ness	Kurt-osis	Out-liers
Roundness	BGT	0.869	0.002	0.594	0.612	0.604	0.123	-0.726	4.266	48
	AGT	0.914	0.001	0.647	0.683	0.655	0.107	-1.348	9.239	29
	% increase			9.0%		8.4%				
Sphericity	BGT	0.818	0.000	0.511	0.471	0.519	0.117	-0.484	3.593	27
	AGT	0.831	0.000	0.556	0.528	0.560	0.106	-0.682	4.896	32
	% increase			8.9%		7.9%				
Form Factor (FF)	BGT	0.838	0.072	0.609	0.631	0.631	0.115	-1.092	4.619	66
	AGT	0.836	0.045	0.607	0.629	0.633	0.126	-1.17	4.587	75
	% increase			0.3%		0.3%				
Shape Factor (SF)	BGT	5,039	17.05	51.56	22.66	36.65	125.8	32.4	1210	248
	AGT	25,347	16.46	70.24	18.99	26.12	709.3	23.81	691.2	168
	% increase			36.2%		-28.7%				
Roundness Index (RI)	BGT	3.853	0.847	1.255	0.993	1.177	0.315	2.379	12.71	149
	AGT	3.121	0.832	1.062	0.993	1.021	0.161	2.379	16.63	144
	% increase			-15.4%		-13.3%				
Angularity	BGT	4.196	0.427	0.993	0.535	0.903	0.394	1.939	10.00	115
	AGT	4.107	0.391	0.738	0.477	0.686	0.238	3.073	26.52	76
	% increase			-25.7%		-24.0%				

The roundness is plotted versus the inverse of aspect ratio in Figure 42, exhibiting similar trends to those previously noted for Moore Quarry. The increase in roundness after gyratory compaction testing is also noticeable in this plot.

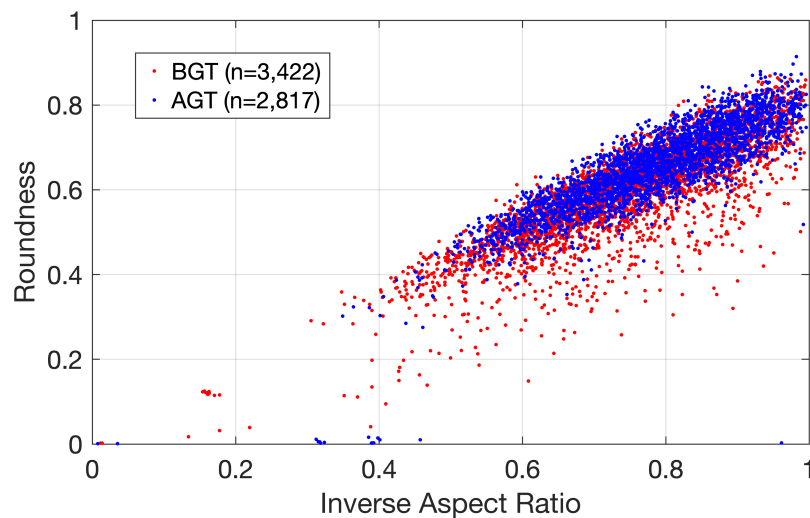


Figure 42. Roundness versus inverse of aspect ratio for BGT and AGT specimens from Alden Quarry

4.1.2.3 Gyrotory Compaction Test Results for Alden Quarry

The evolving void ratio and dry unit weight calculated from the specimen height during the gyrotory compaction test for the Alden Quarry material are plotted in Figure 43 and Figure 44 with respect to the number of gyrations and compaction energy. An overall decrease in void ratio of 70.5% and corresponding 52.2% increase in dry unit weight were observed through Stages I and II of the test. The shear resistance and gyrotory compaction energy of the materials were calculated using the data collected by the PDA during the test. The resulting point of maximum curvature for the plot of dry unit weight versus gyrotory compaction energy occurred at a dry unit weight of 118.66 pcf (Figure 43). The changes in compaction energy and dry unit weight for both stages of the test are shown in Table 13.

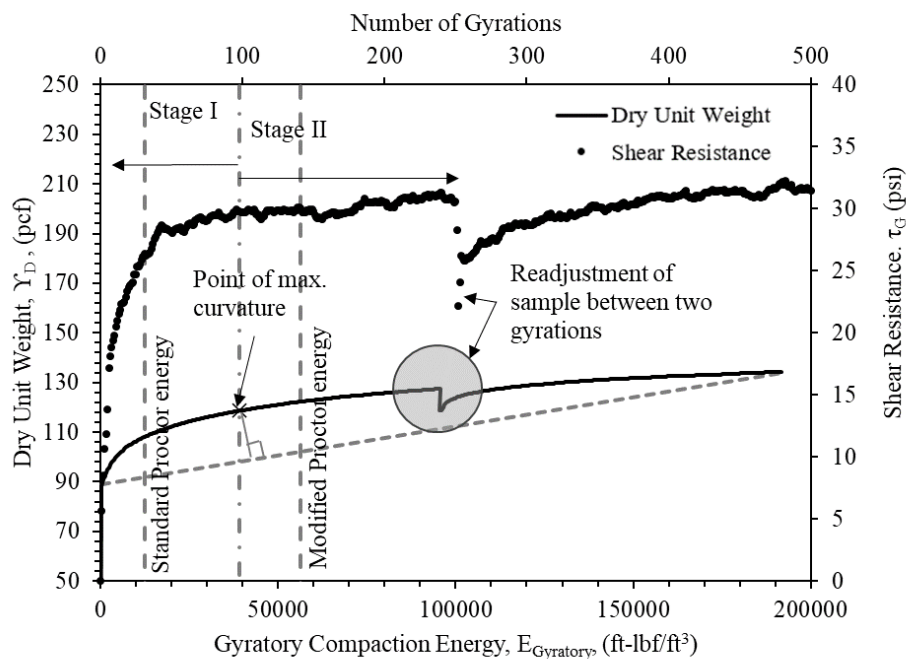


Figure 43. Relationships between dry unit weight, gyrotory compaction energy, shear resistance, and number of gyrations for coarse aggregates from Alden Quarry

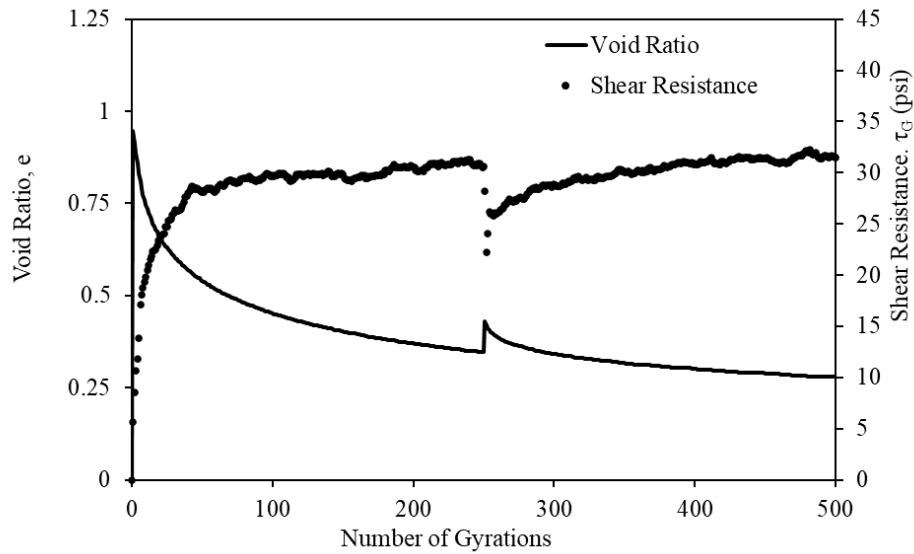


Figure 44. Changes in shear resistance and void ratio of coarse aggregates from Alden Quarry during gyratory compaction test

Table 13. Gyratory compaction energy and dry unit weights for Stages I and II of gyratory compaction test for Alden Quarry

Stage	Energy, E (ft-lbf/ft ³)			Dry Unit Weight, γ_d (pcf)		
	Initial E_i	Final E_f	Change ΔE	Initial γ_{di}	Final γ_{df}	Change $\Delta \gamma_d$
Stage I	285.7	39,079.5	38,793.8	88.17	118.66	30.49
Stage II	39,079.5	19,1736.7	152,657.2	118.66	134.19	15.53

4.1.2.4 Triaxial Test Results for Alden Quarry

Confining pressures of 5.2 and 10.3 psi were applied on the BGT triaxial test specimens, and pressures of 5.3, 10.4 and 15.2 psi were applied to the AGT specimens. The Mohr-Coulomb plots of the results are shown in Figure 45 and Figure 46. The resulting cohesion and friction angle values were 1.33 psi and 43.9° for the BGT specimens, decreasing to 0.181 psi and 43.4° for the AGT specimens. Therefore, the gyratory compaction caused a decrease of 86.4% in the cohesion and a decrease of 1.1% in the friction angle for this material.

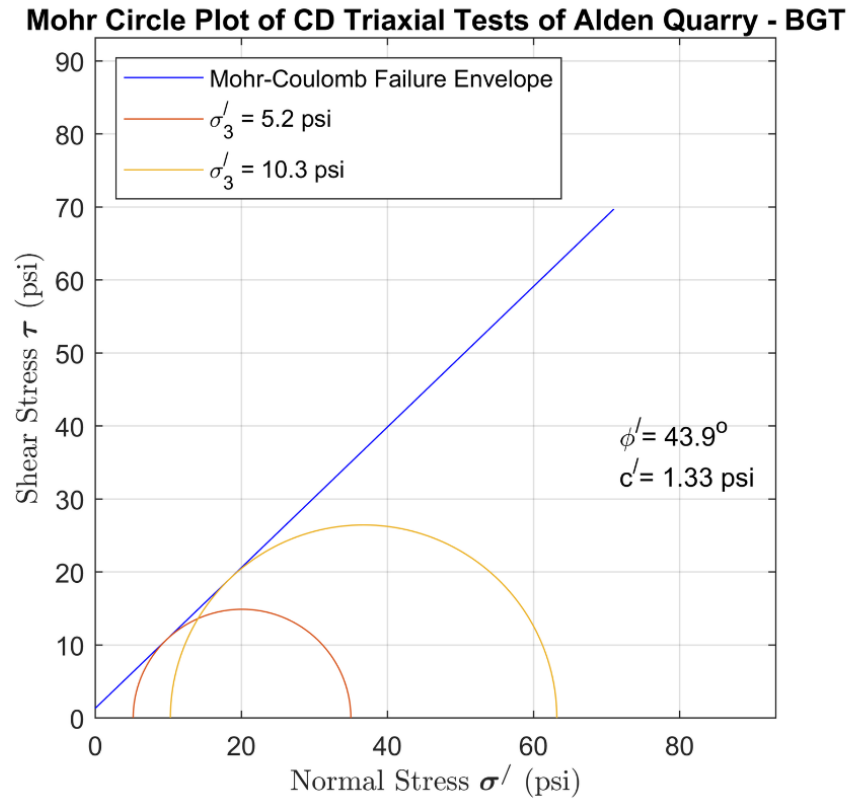


Figure 45. Mohr-Coulomb plot of samples from Alden Quarry – before gyratory testing

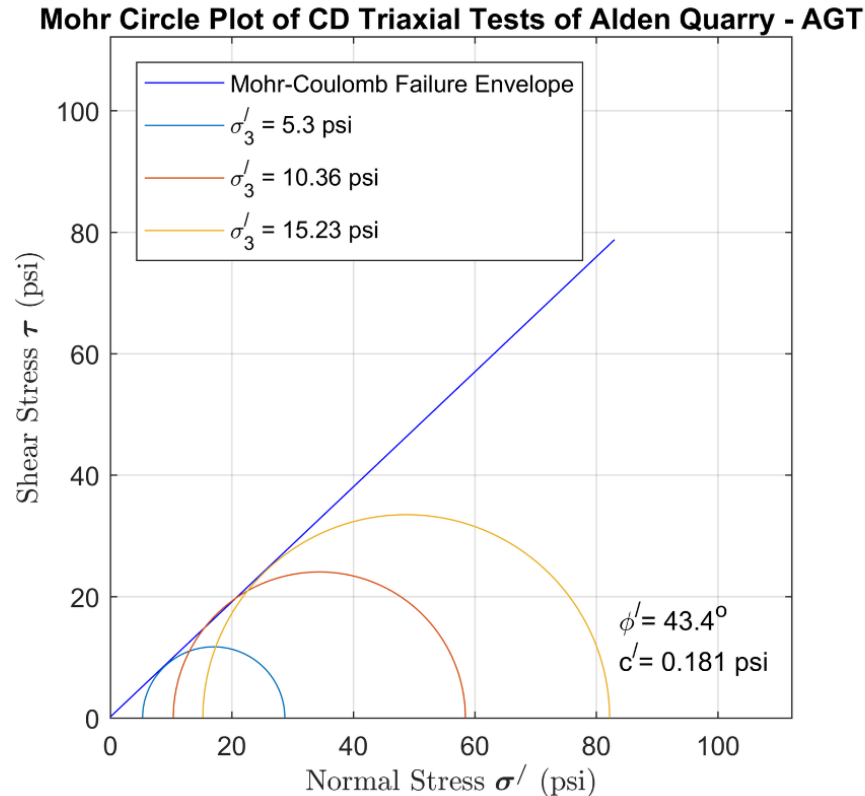


Figure 46. Mohr-Coulomb plot of samples from Alden Quarry – after gyratory testing

4.1.2.5 Geological Tests for Alden Quarry

The rock types for Alden Quarry were analyzed using thin sections, the results of which are presented in Table 14 and Table 15. Rock Type 1 (nonporous, fine grained skeletal grainstone) stayed relatively constant at 68% abundance before and 67% after gyratory testing, while its grain density remained unchanged at 2.71 g/cm³. Rock Type 2 (highly porous skeletal grainstone) decreased significantly from 30% BGT to 3% AGT, while its grain density increased slightly from 2.72 to 2.73 g/cm³. Conversely, Rock Type 3 (less porous skeletal grainstone) increased significantly from 2% BGT to 30% AGT while its grain density decreased noticeably from 2.83 to 2.72 g/cm³, suggestive of some dolomite content in that sample. These results suggest that nonporous lithologies (e.g., Rock Types 1 and 3) resist degradation from gyratory compaction. Rock Type 1 from Alden Quarry was analyzed using the Camsizer (Figure 47). The results showed a tri-modal particle size distribution that shifted to slightly smaller particle sizes after compaction.

Figure 48 provides magnified views of the BGT and AGT samples for Rock Type 2, indicating that the porous lithology degraded more significantly, with its abundance decreasing from 30% to 3% in the test. Figure 49 and Figure 50 show magnified views of the AGT samples for Rock Types 1 and 2, respectively. The magnified views show the development of hairline cracks perpendicular to the edges developed during gyratory compaction.

Table 14. Geological parameters of Alden Quarry sample before gyratory compaction

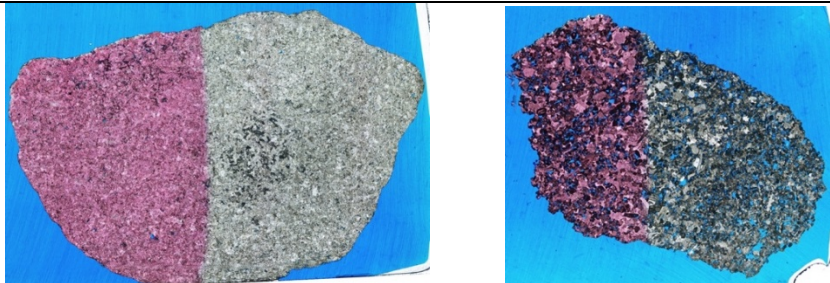
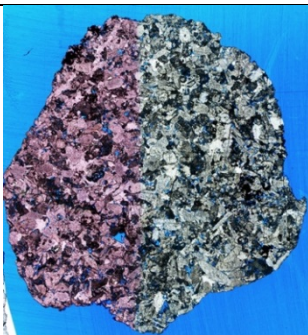
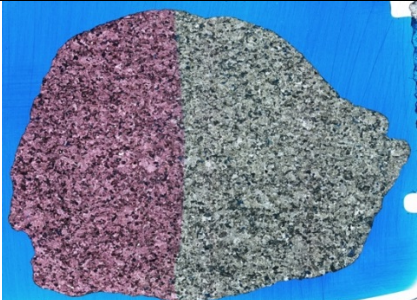
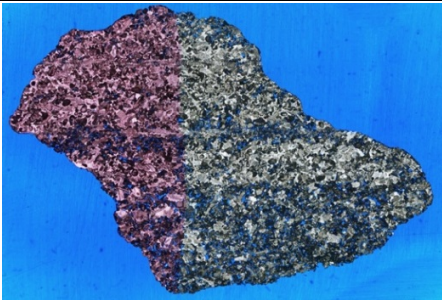

Geological Parameters	Rock Types	
	Rock Type 1	Rock Type 2
Grain Density (g/cm ³)	2.71	2.72
Abundance	68%	30%
Images of the Thin Sections		
	Rock Type 3	
Grain Density (g/cm ³)	2.83	
Abundance	2%	
Images of the Thin Sections		

Table 15. Geological parameters of Alden Quarry sample after gyratory compaction

Geological Parameters	Rock Types	
	Rock Type 1	Rock Type 2
Grain Density (g/cm ³)	2.71	2.73
Abundance	67%	3%
Images of the Thin Sections		
		
-	Rock Type 3	
Grain Density (g/cm ³)	2.72	
Abundance	30%	
Images of the Thin Sections		

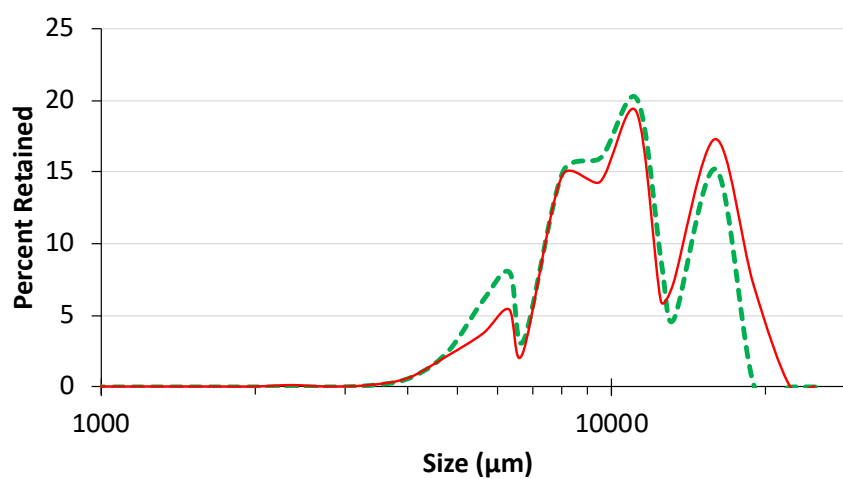


Figure 47. Camsizer data for Alden Quarry Rock Type 1 BGT (red lines) and AGT (dashed green lines).

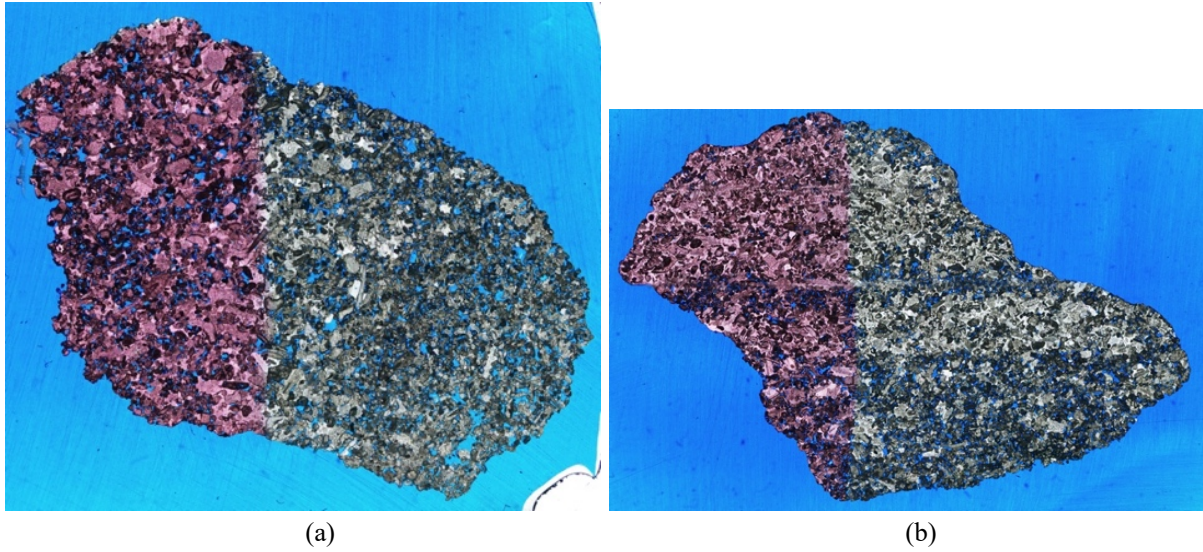


Figure 48. Magnified view of Rock Type 2 for Alden Quarry: (a) BGT sample with observed abundance of 30%, (b) AGT sample with observed abundance of 3%

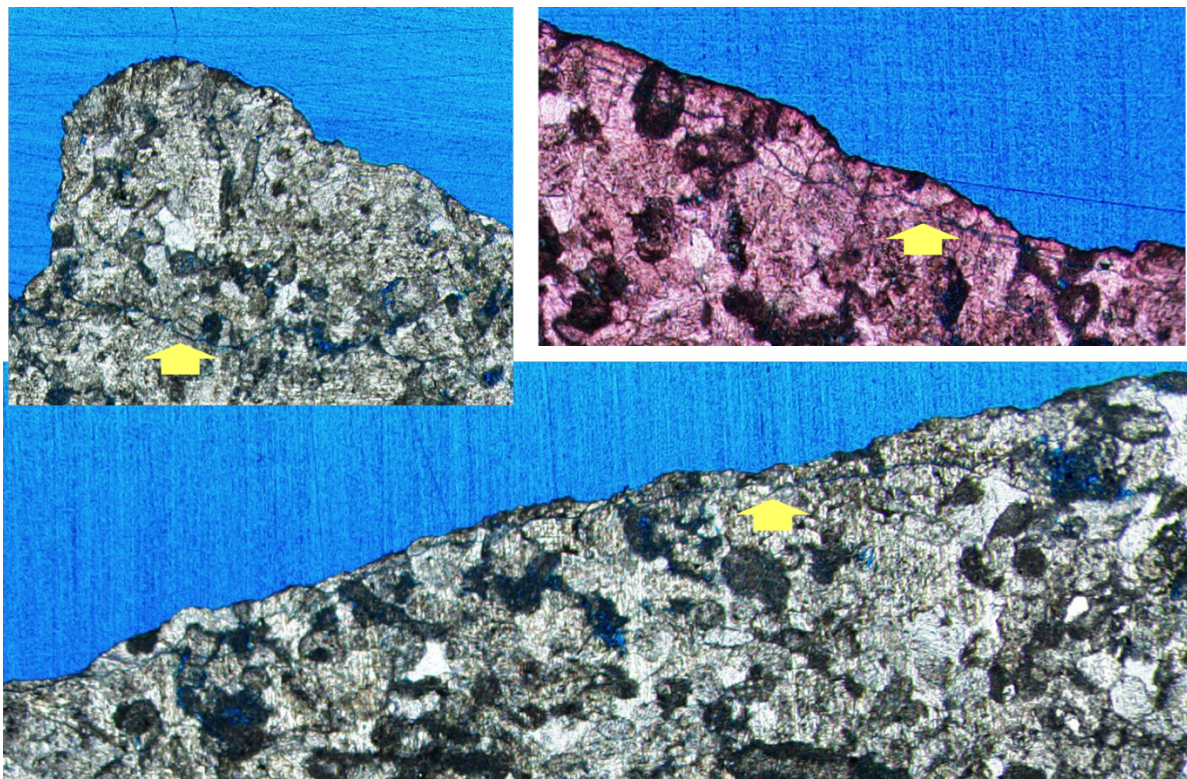


Figure 49. Magnified views of Rock Type 1 for Alden Quarry AGT sample

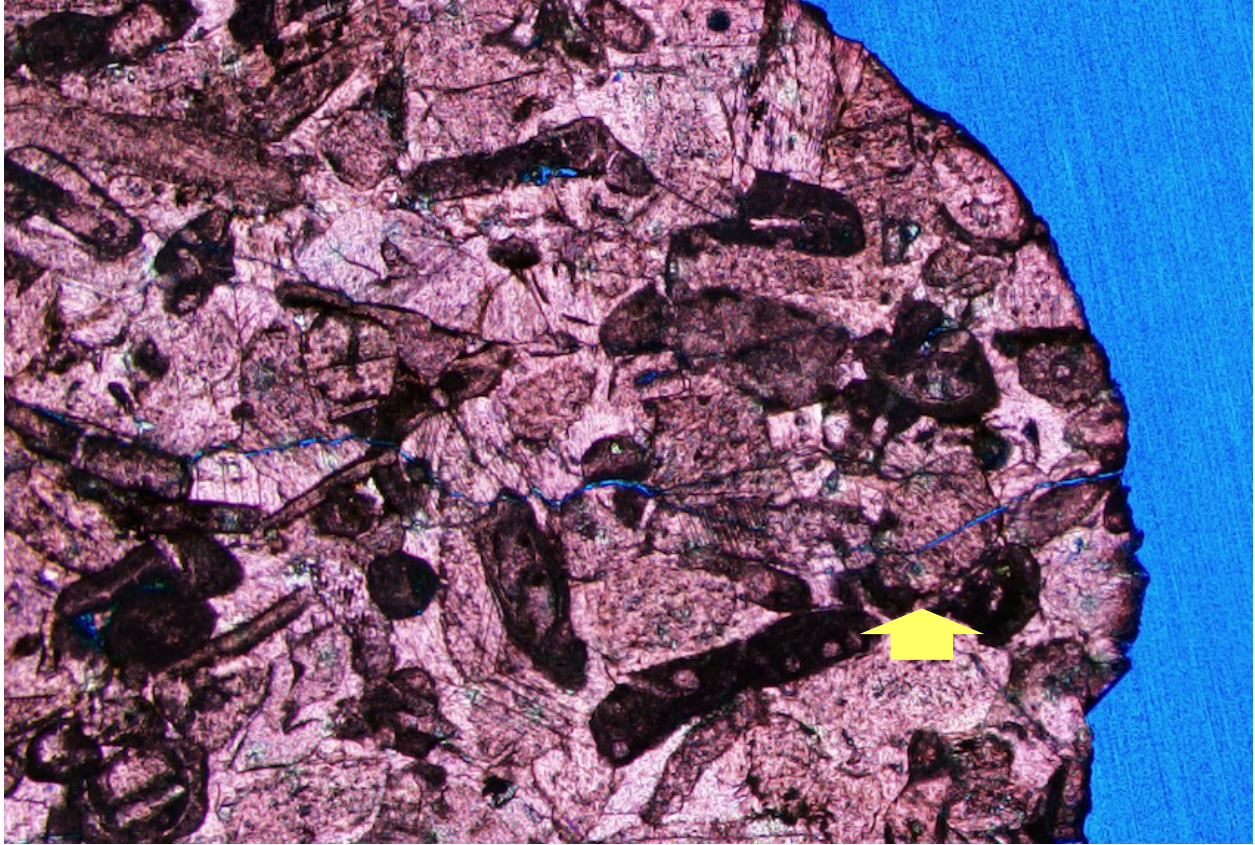


Figure 50. Magnified view of Rock Type 2 for Alden Quarry AGT sample

4.1.3 Gehrke Quarry Aggregates

Samples of 1.5 in.-minus clean aggregates were collected from the present day Gehrke Quarry located near Eldora, Iowa. When the samples for the present study were acquired, this quarry was named Gifford Quarry and was operated by Gehrke Quarries, Inc. However, Wendling Quarries acquired Gehrke Quarries in 2024 and subsequently renamed the quarry from Gifford to Gehrke to honor the legacy of the previous operator. Therefore, the material names Gifford and Gehrke should be considered interchangeable in this report. This quarry produces from the Mississippian Maynes Creek Formation, which has a complex lithology consisting of (1) highly porous, coarse-grained dolostone with calcite cement filling some pore space, and (2) porous chert.

4.1.3.1 PSD Comparison and Evaluation of Breakage Parameters for Gehrke Quarry

Particle size distribution analyses were carried out by laboratory sieve and hydrometer tests for the Gehrke Quarry clean samples before and after a gyratory compaction test. The resulting PSD curves are presented in Figure 51. The gravel-sized particles retained on the No. 4 (4.75 mm) sieve were also scanned using the Cannon scanner for 2D image analyses, which produced the PSD curves shown in Figure 52. As shown in these two figures, the mechanical degradation represented by Hardin's total breakage was determined to be 0.45 for the coarse fraction based

on the PSD curves from sieve and hydrometer analyses, and 0.43 for the gravel fraction according to the 2D image analyses. The corresponding breakage parameters are detailed in Table 16 along with the percentages of gravel, sand, and fines determined from the sieve analyses of the Gehrke Quarry clean samples before and after gyratory testing. As shown in the table, the gravel fraction decreased by 30.0% during the gyratory test, whereas the sand and fines fractions increased by 23.2% and 3.8%, respectively. These results quantify the breakdown of the Gehrke Quarry materials under gyratory compaction.

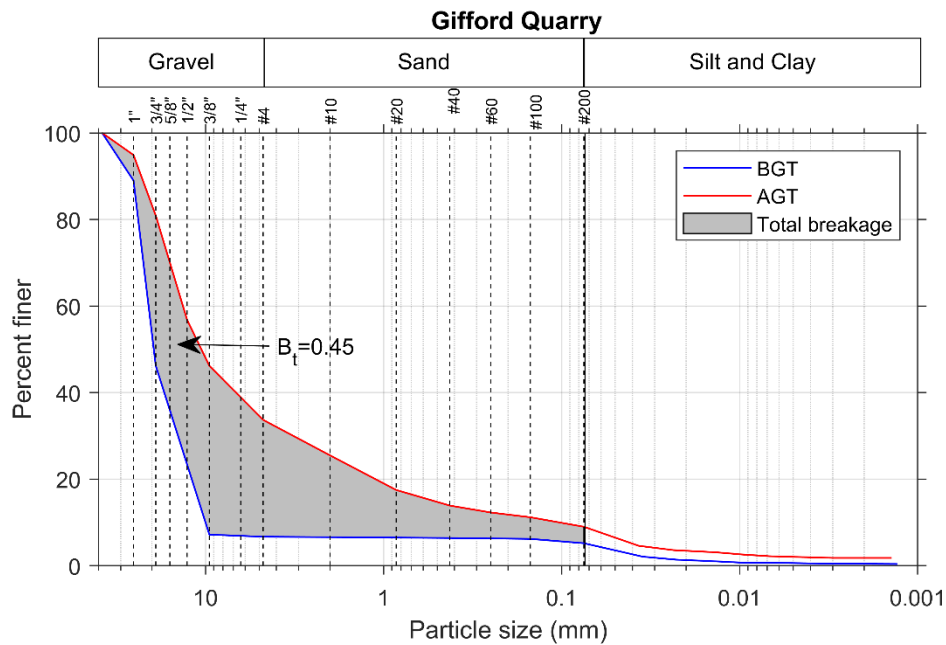


Figure 51. Particle size distribution from sieve and hydrometer analysis and evaluation of breakage of coarse fraction for samples from Gehrke Quarry

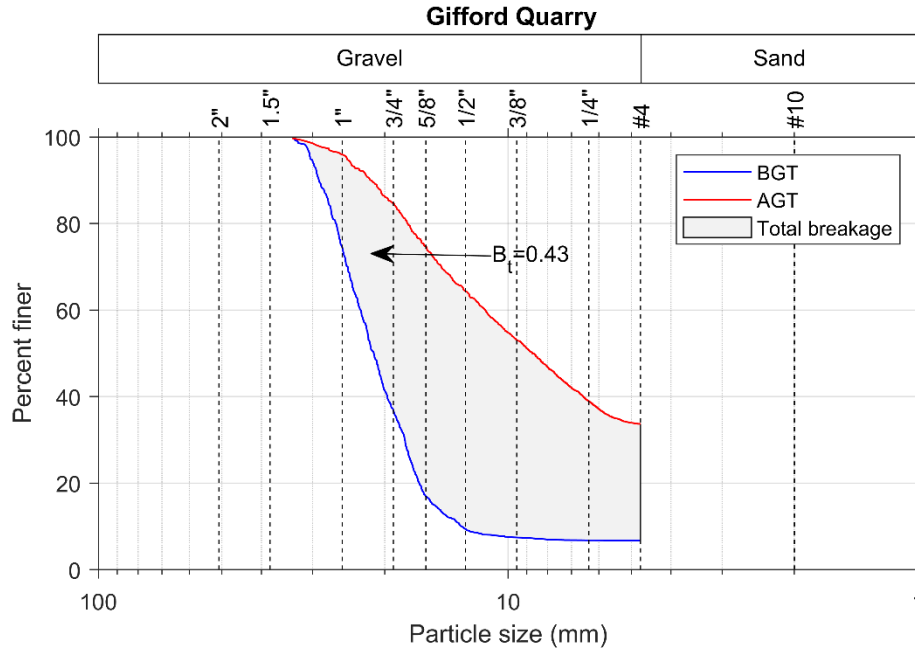


Figure 52. Particle size distributions from 2D image analysis and evaluation of breakage of gravel fraction for samples from Gehrke Quarry

Table 16. Breakage parameters determined from laboratory sieve analyses and 2D image analyses, and corresponding percentages of gravel, sand, and fines for Gehrke Quarry samples

Analysis Type	Hardin's Breakage Parameters			% Gravel		% Sand		% Silt and Clay	
	Total Breakage, B_t	Breakage Potential, B_p	Relative Breakage, B_r	BGT	AGT	BGT	AGT	BGT	AGT
Lab Sieve Analyses	0.4461	2.2392	0.1992	93.3	63.3	1.5	24.7	5.2	9.0
				% Reduction (red.) or % Increase (inc.)					
				30.0% red.		23.2% inc.		3.8% inc.	
2D Image Analyses	0.4263	0.9786	0.4357	NA*		NA*		NA*	

* Not Available: Only gravel sized particles retained on #4 (4.75 mm) sieve were scanned.

4.1.3.2 2D Image Analyses and Comparison of Morphological Parameters for Gehrke Quarry

The morphological parameters determined by 2D image analysis of the BGT and AGT Gehrke Quarry specimens are presented in Figure 53 through Figure 58. The statistical output of these morphological parameters is presented in Table 17, along with their relative changes which quantify the mechanical degradation and changes in shape experienced during gyratory compaction. As shown in Table 17, the median values of roundness, sphericity, and form factor increased by 1.1%, 3.7%, and 44.7%, respectively, while the shape factor and roundness index decreased by 30.9%, and 14.4%, respectively. However, the angularity increased by 42.3%.

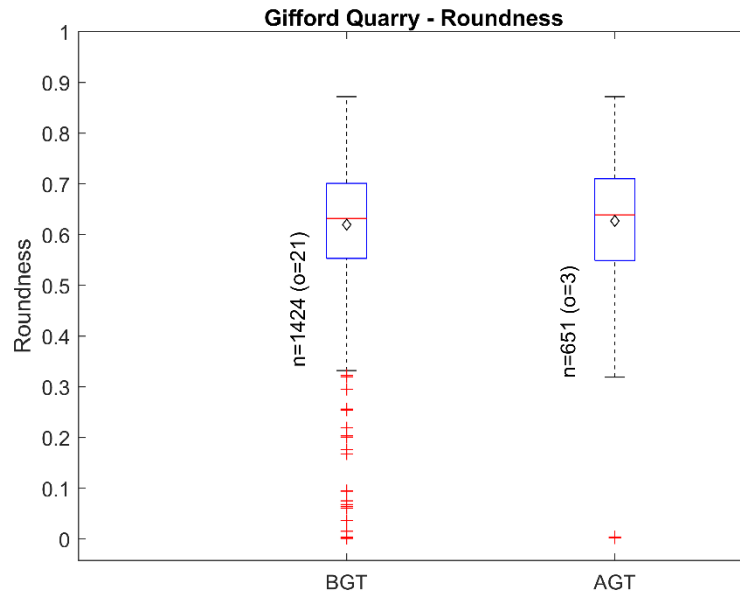


Figure 53. Comparison of roundness for BGT and AGT specimens from Gehrke Quarry

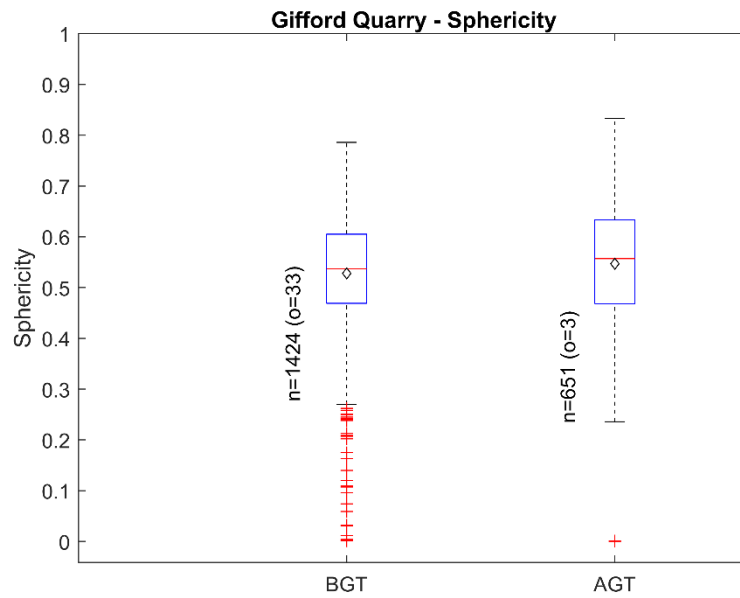


Figure 54. Comparison of sphericity for BGT and AGT specimens from Gehrke Quarry

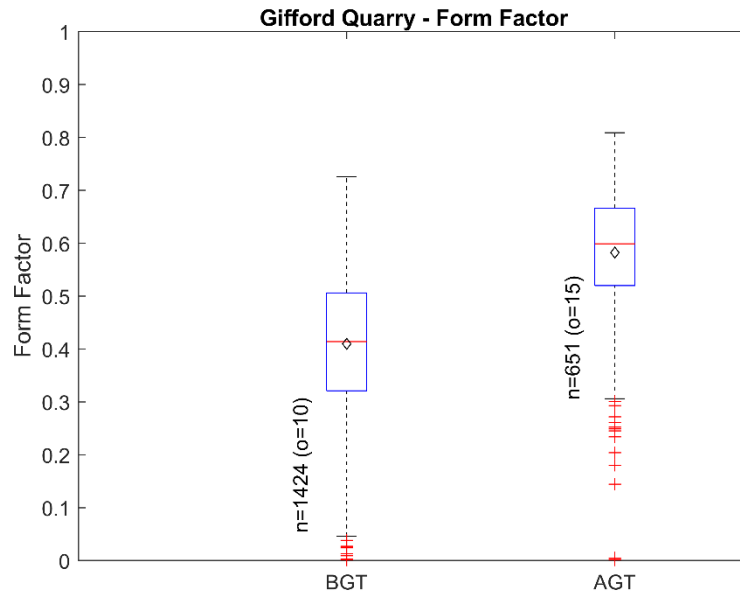


Figure 55. Comparison of form factor for BGT and AGT specimens from Gehrke Quarry

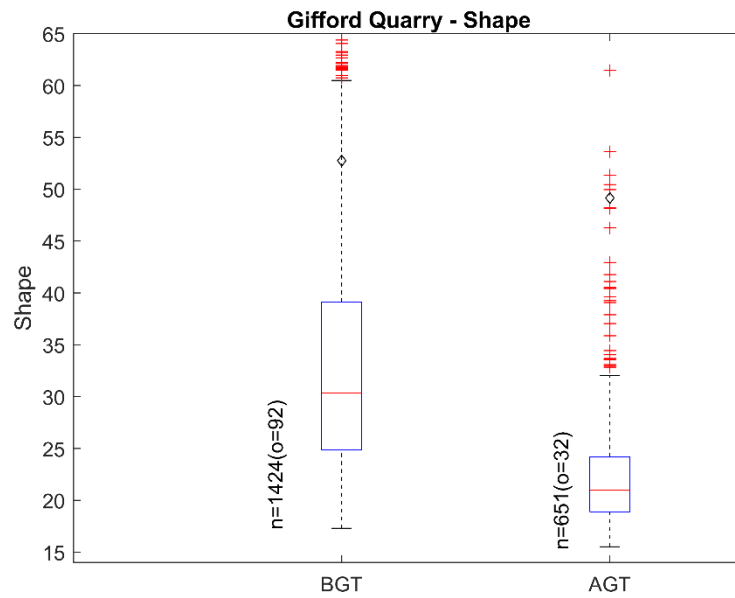


Figure 56. Comparison of shape factor for BGT and AGT specimens from Gehrke Quarry

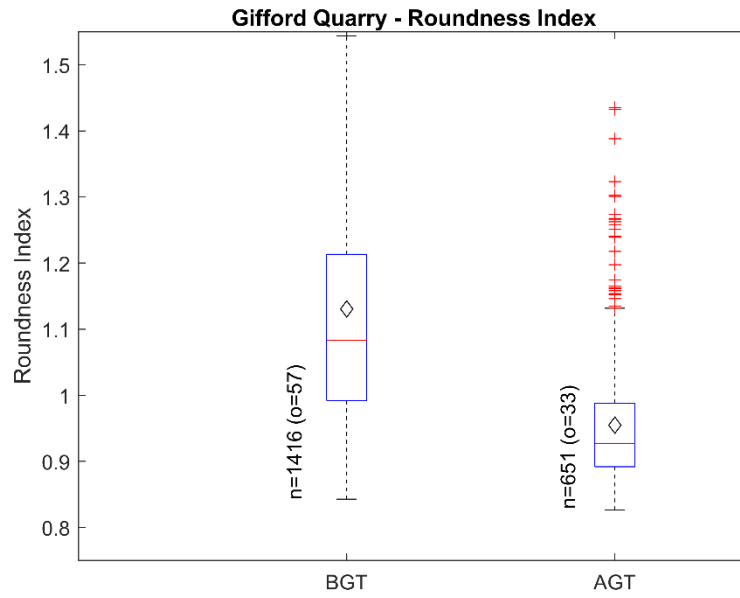


Figure 57. Comparison of roundness index for BGT and AGT specimens from Gehrke Quarry

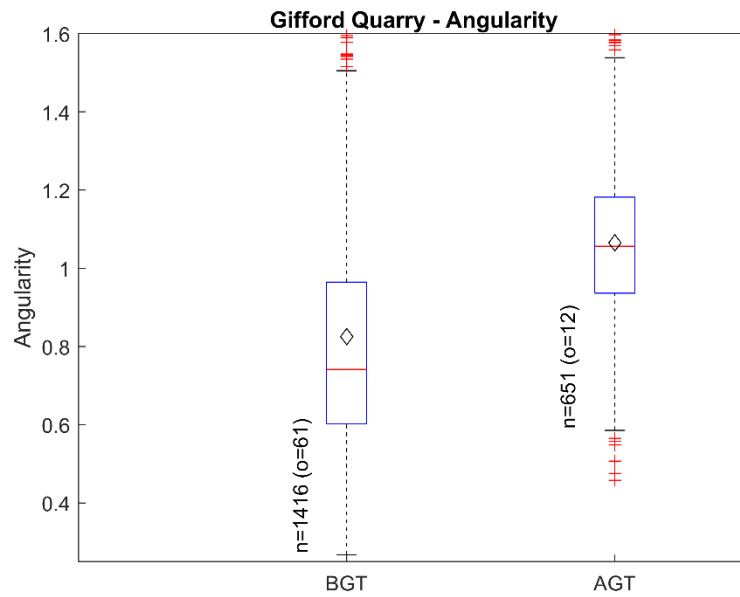
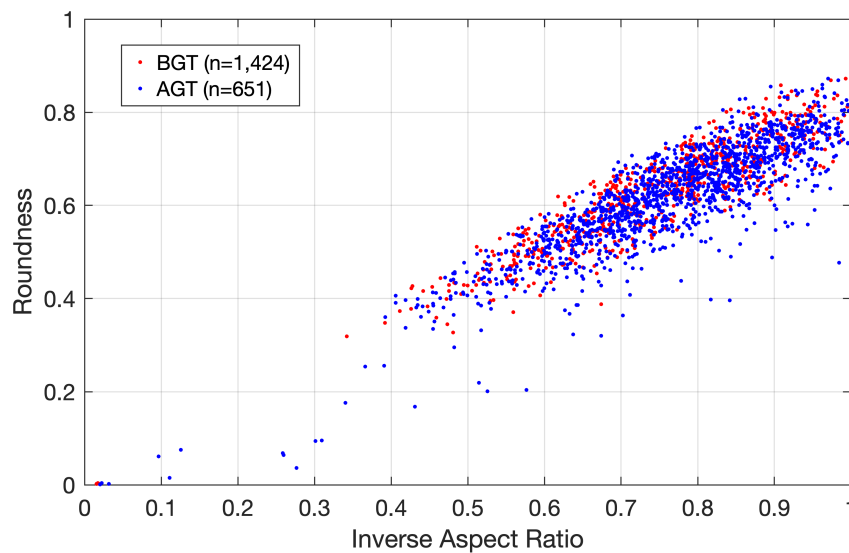


Figure 58. Comparison of angularity for BGT and AGT specimens from Gehrke Quarry

Table 17. Statistical results of morphological parameters of Gehrke Quarry specimens

Parameters	Sample Type (BGT/AGT)	Max. Value	Min. Value	Mean	Mode	Median	Std. Dev.	Skew-ness	Kurt-osis	Out-liers
Roundness	BGT	0.872	0.001	0.619	0.643	0.632	0.117	-1.229	6.768	21
	AGT	0.872	0.002	0.627	0.673	0.639	0.117	-0.845	5.64	3
	% increase			1.3%		1.1%				
Sphericity	BGT	0.786	0.001	0.528	0.56	0.537	0.114	-0.926	5.143	33
	AGT	0.833	0	0.547	0.473	0.557	0.115	-0.683	4.363	3
	% increase			3.6%		3.7%				
Form Factor (FF)	BGT	0.726	0.001	0.410	0.379	0.414	0.131	-0.279	2.839	10
	AGT	0.809	0.001	0.582	0.568	0.599	0.114	-1.201	6.007	15
	% increase			42.0%		44.7%				
Shape Factor (SF)	BGT	9968	17.3	52.74	24.47	30.36	342.6	24.16	628.6	92
	AGT	9700	15.53	49.17	16.8	20.99	440.9	18.9	384.4	32
	% increase			-6.8%		-30.9%				
Roundness Index (RI)	BGT	3.284	0.843	1.131	0.999	1.083	0.204	2.461	16.84	57
	AGT	1.777	0.826	0.955	0.826	0.927	0.105	2.988	17.36	33
	% increase			-15.6%		-14.4%				
Angularity	BGT	3.945	0.267	0.825	0.495	0.742	0.326	2.344	14.93	61
	AGT	2.105	0.458	1.065	0.458	1.056	0.206	0.494	5.009	12
	% increase			29.1%		42.3%				

The roundness is plotted against inverse aspect ratio in Figure 59, showing similar trends as described in the previous sections. Consistent with the very small increase in roundness of 1.1% for this material, the shift towards greater roundness is only slightly apparent in this plot.

**Figure 59. Roundness versus inverse of aspect ratio for BGT and AGT specimens from Gehrke Quarry**

4.1.3.3 Gyratory Compaction Test Results for Gehrke Quarry

The dry unit weight, shear resistance, and void ratio during the gyratory compaction test are plotted in Figure 60 and Figure 61 with respect to the compaction energy and number of gyrations. The corresponding changes in compaction energy and dry unit weight for Stages I and II of the test are shown in Table 18. Through both test stages, a total decrease in void ratio of 74.4% and increase in dry unit weight of 66.5% were observed. The point of maximum curvature for dry unit weight in Figure 60 occurred at a dry unit weight of 120.32 pcf, in between the Standard and Modified Proctor compaction energy levels.

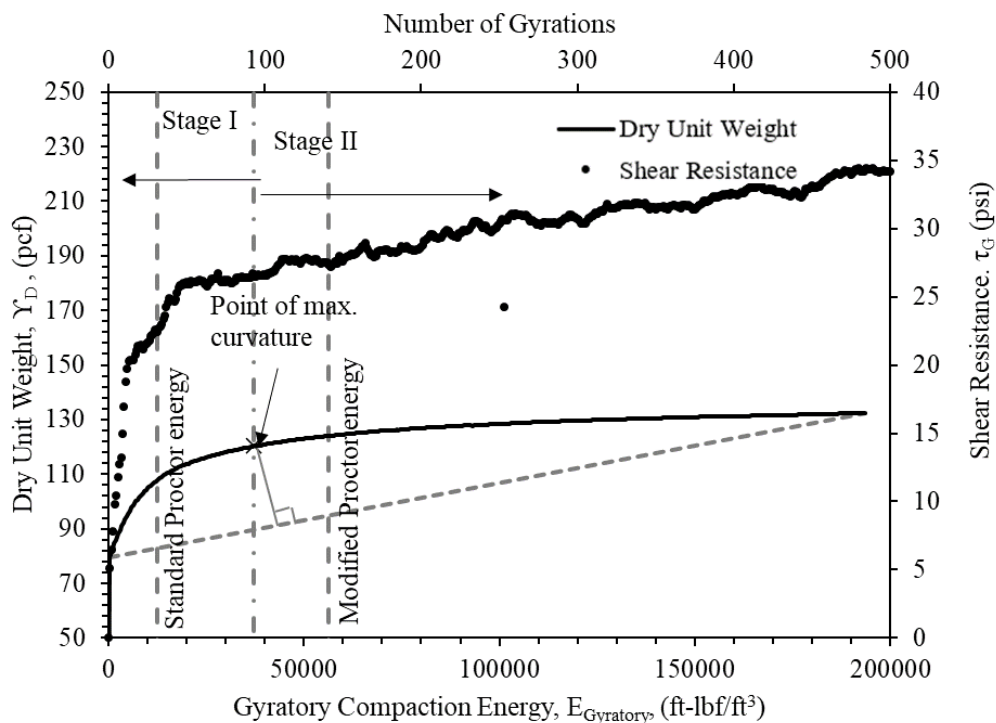


Figure 60. Relationships between dry unit weight, gyratory compaction energy, shear resistance, and number of gyrations for coarse aggregates from Gehrke Quarry

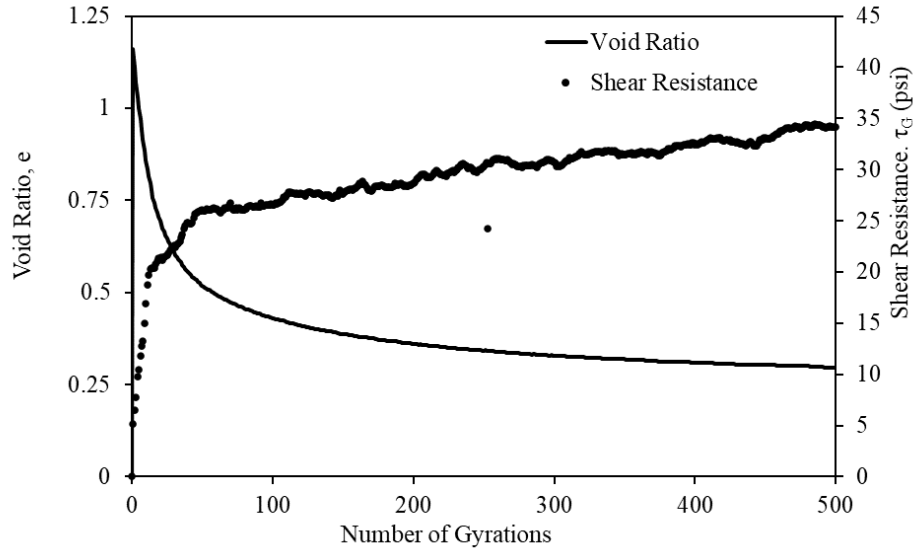


Figure 61. Changes in shear resistance and void ratio of coarse aggregates from Gehrke Quarry during gyratory compaction test

Table 18. Gyratory compaction energy and dry unit weight for Stages I and II of gyratory compaction test for Gehrke Quarry

Stage	Energy, E (ft-lbf/ft ³)			Dry Unit Weight, γ_d (pcf)		
	Initial E_i	Final E_f	Change ΔE	Initial γ_{di}	Final γ_{df}	Change $\Delta \gamma_d$
Stage I	388.47	37,292.97	3,6904.50	79.57	120.32	40.75
Stage II	37,292.97	193,724.62	156,431.65	120.32	132.41	12.09

4.1.3.4 Triaxial Test Results for Gehrke Quarry

Triaxial tests were performed on both BGT and AGT samples from the Gehrke Quarry. Confining pressures of 5.4, 10.5 and 15.5 psi were applied on the BGT samples and 5.3, 10.4 and 12.7 psi were applied on the AGT samples. The Mohr-Coulomb plots of the results are shown in Figure 62 and Figure 63. The resulting cohesion and friction angle values were 1.64 psi and 41.2° for the BGT specimens, which changed to 2.73 psi and 37.8° for the AGT specimens. Therefore, there was an increase of 66.5% in the c' value and a decrease of 8.3% in the ϕ' value due to gyratory compaction.

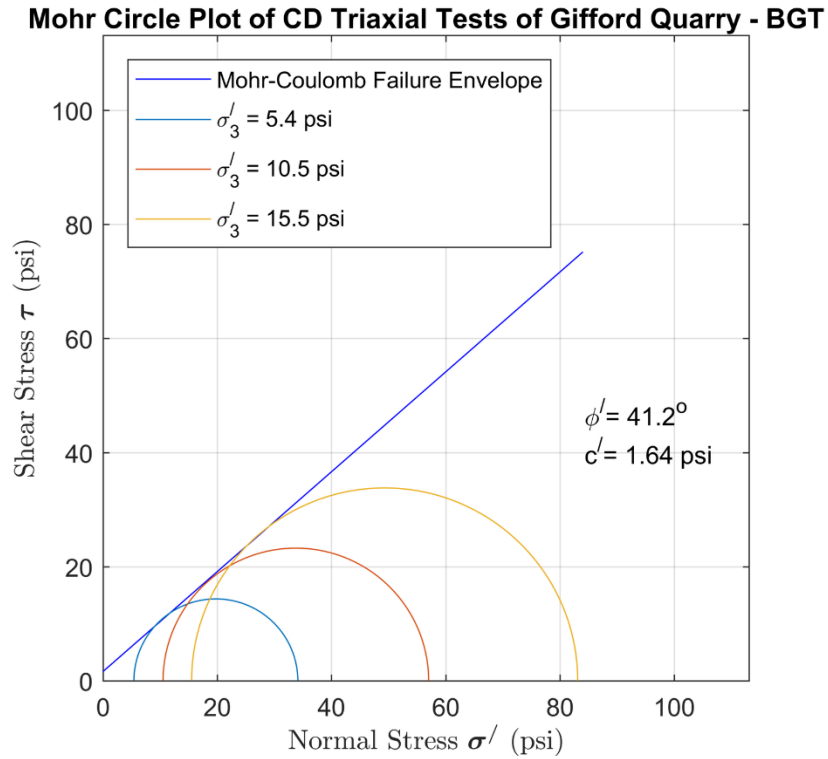


Figure 62. Mohr-Coulomb plot of samples from Gehrke Quarry – before gyratory testing

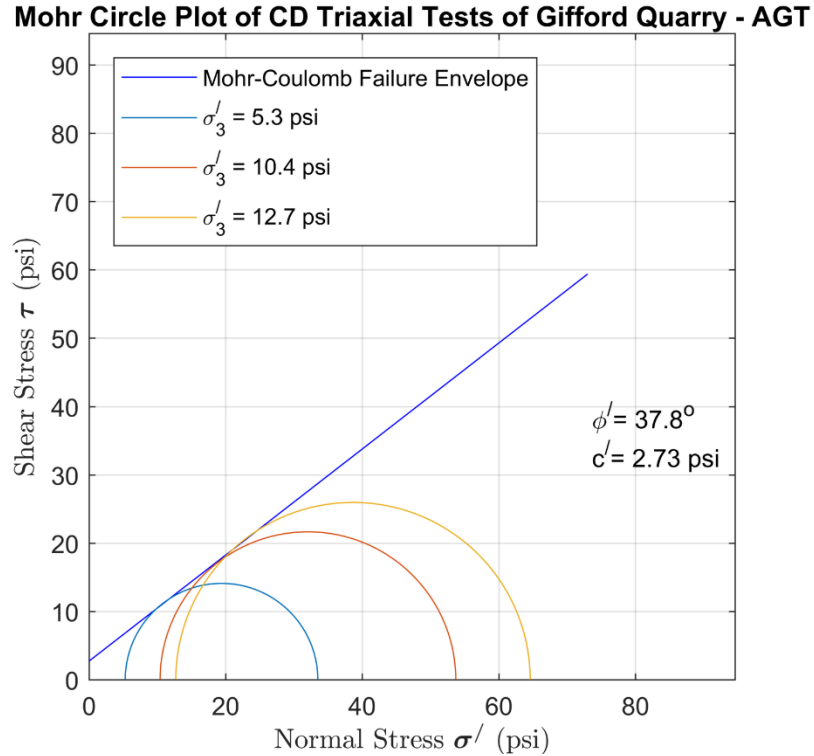


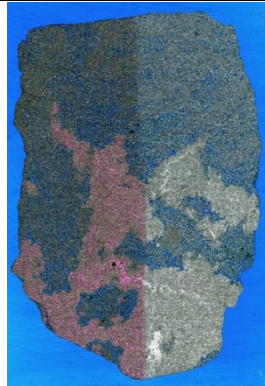




Figure 63. Mohr-Coulomb plot of samples from Alden Quarry – after gyratory testing

4.1.3.5 Geological Tests for Gehrke Quarry

The Gehrke Quarry BGT clean samples comprised five widely differing rock types. The most abundant (RT1) was a nonporous dolostone with 63% abundance and 2.91 g/cm³ grain density, while the second most abundant (RT2) was a microporous chert with 14% abundance and 2.68 g/cm³ grain density. The third most abundant (RT3) was a porous calcitic dolostone with 9.1% abundance and 2.89 g/cm³ grain density. The fourth most abundant (RT4) was a dolostone with calcite fracture fill having 8.6% abundance and 2.89 g/cm³ grain density. The lowest abundance (RT5) was a porous calcitic dolostone with 6% abundance and 2.89 g/cm³ grain density. These rock types were analyzed using thin sections of the BGT sample, the results of which are presented in Table 19. Due to time and material constraints, Camsizer tests and grain density and abundance tests on the AGT specimen could not be performed.

Table 19. Geological parameters of Gehrke Quarry samples before gyratory compaction

Geological Parameters	Rock Types		
	Rock Type 1	Rock Type 2	Rock Type 3
Grain Density (g/cm ³)	2.91	2.68	2.89
Abundance	63%	14%	9%
Porosity	Nonporous	Porous	Porous
Images of the Thin Sections			
	Rock Type 4	Rock Type 5	
	Grain Density (g/cm ³)	2.89	2.89
	Abundance	9%	6%
	Porosity	Minor-porosity	Porous
Images of the Thin Sections			

4.1.4 Crescent Quarry Aggregates

Samples of clean 1 in.-minus aggregates were collected from the Crescent Quarry situated just outside Crescent, Iowa near Omaha. This quarry extracts material from the Pennsylvanian Upper Hertha Formation, which consists of a nonporous, fossiliferous limestone, specifically skeletal lime packstone to grainstone.

4.1.4.1 PSD Comparison and Evaluation of Breakage Parameters for Crescent Quarry

Following the same procedures described in previous sections, particle size distribution analyses were carried out by laboratory sieve and hydrometer tests and 2D image analyses for the Crescent Quarry clean samples before and after a gyratory compaction test. The PSD curves from sieve and hydrometer analysis are presented in Figure 64, and the curves from 2D image analyses are presented in Figure 65. The mechanical degradation represented by Hardin's total breakage was determined to be 0.06 for the coarse fraction based on sieve and hydrometer data, and 0.05 for the gravel fraction based on the 2D image analyses. The corresponding breakage parameters, detailed in Table 20, show that the gravel fraction decreased by 4.1% during the gyratory test, while the sand and fines fractions increased by 3.8% and 0.3%, respectively.

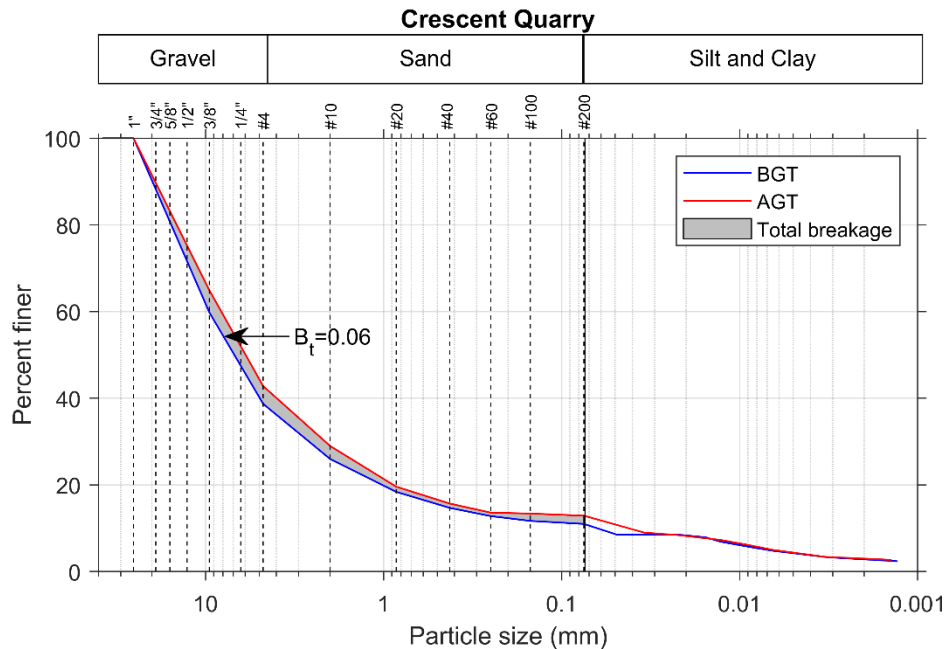


Figure 64. Particle size distributions from sieve and hydrometer analysis and evaluation of breakage of coarse fraction for samples from Crescent Quarry

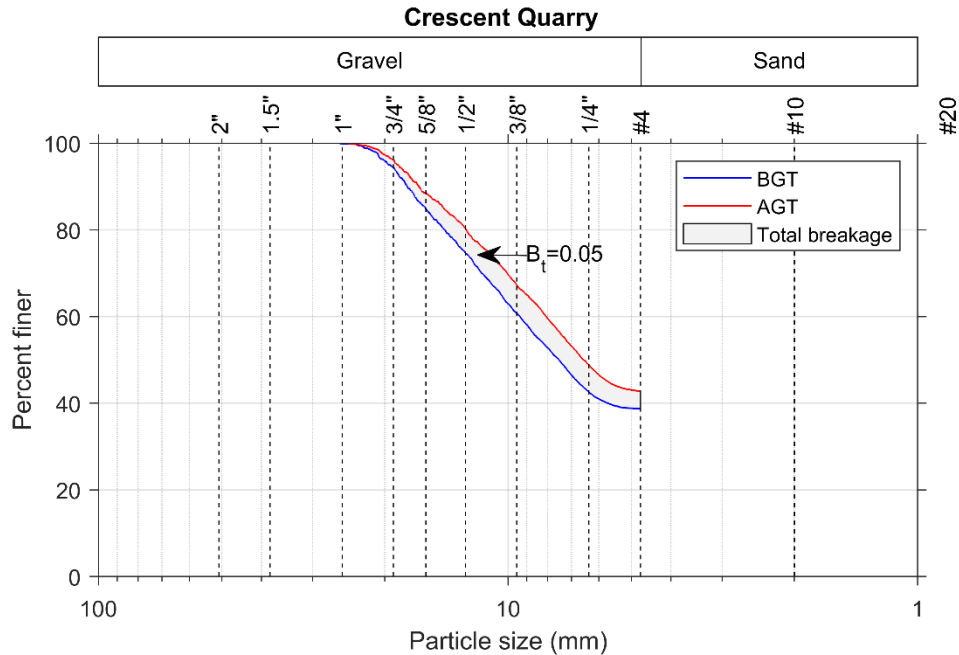


Figure 65. Particle size distribution from 2D image analysis and evaluation of breakage of gravel fraction for samples from Crescent Quarry

Table 20. Breakage parameters determined from laboratory sieve analyses and 2D image analyses, and corresponding percentages of gravel, sand, and fines for Crescent Quarry samples

Analysis Type	Hardin's Breakage Parameters			% Gravel		% Sand		% Silt and Clay	
	Total Breakage, B_t	Breakage Potential, B_p	Relative Breakage, B_r	BGT	AGT	BGT	AGT	BGT	AGT
Lab Sieve Analyses	0.0563	1.6705	0.0337	61.3	57.2	36.3	40.1	2.4	2.7
				% Reduction (red.) or % Increase (inc.)					
				4.1% red.		3.8% inc.		0.3% inc.	
2D Image Analyses	0.0508	0.4780	0.1063	NA*		NA*		NA*	

* Not Available: Only gravel sized particles retained on #4 (4.75 mm) sieve were scanned.

4.1.4.2 2D Image Analyses and Comparison of Morphological Parameters for Crescent Quarry

The morphological parameters evaluated for the BGT and AGT Crescent Quarry specimens are presented in Figure 66 through Figure 71. The statistical output of these morphological parameters is presented in Table 21 along with their relative changes during the gyratory compaction test. As shown in Table 21, gyratory compaction increased the median roundness, sphericity, and form factor by 4.9%, 5.0%, and 1.8%, respectively, while decreasing the shape factor, roundness index, and angularity by 1.8%, 0.3%, and 7.7%, respectively.

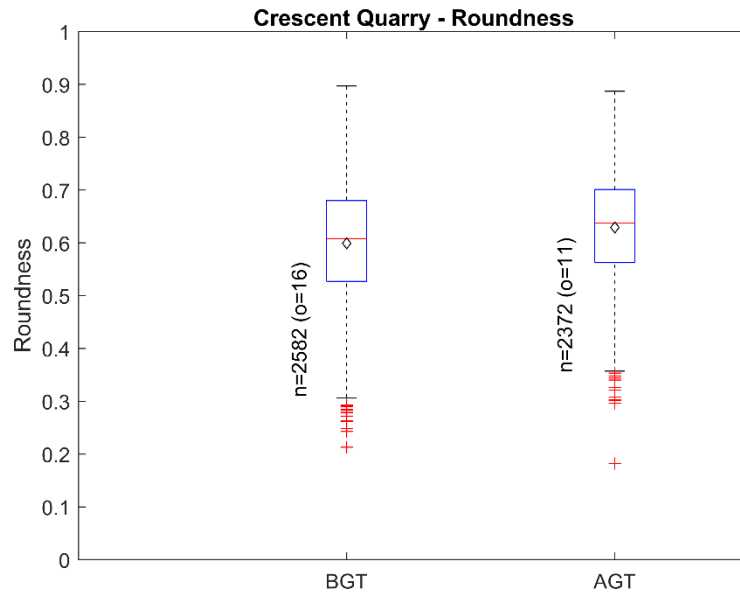


Figure 66. Comparison of roundness for BGT and AGT specimens from Crescent Quarry

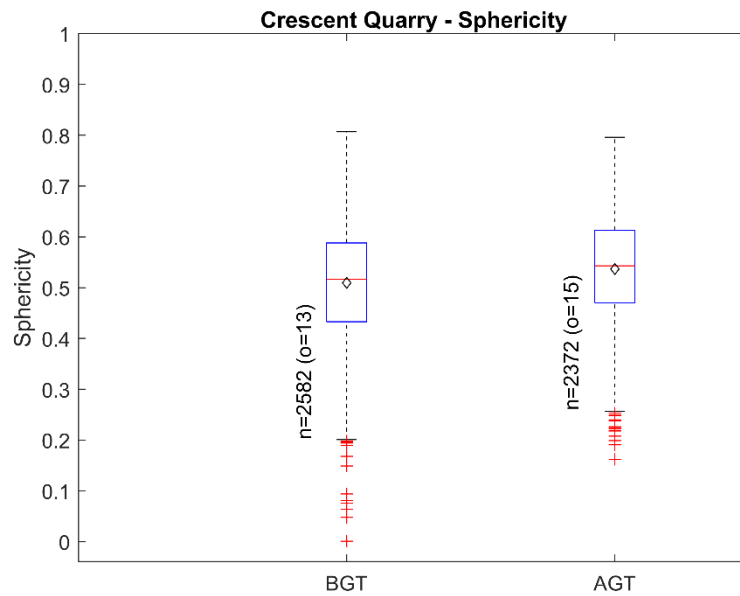


Figure 67. Comparison of sphericity for BGT and AGT specimens from Crescent Quarry

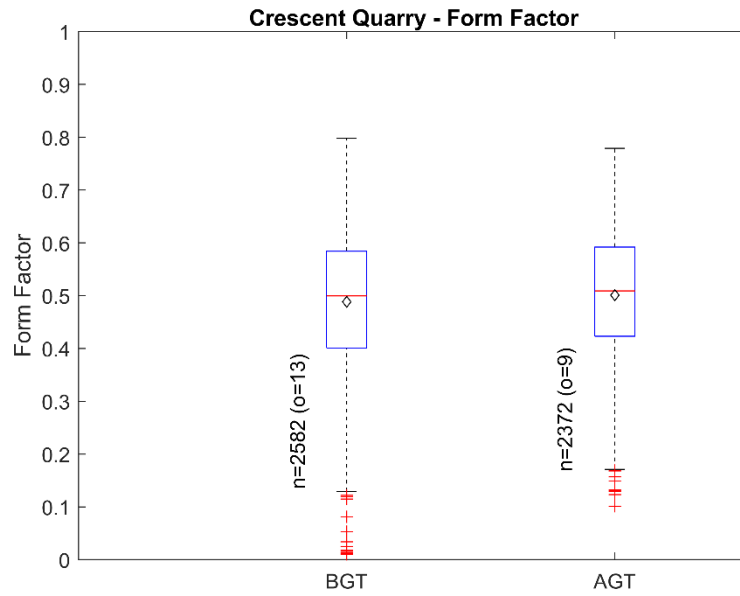


Figure 68. Comparison of form factor for BGT and AGT specimens from Crescent Quarry

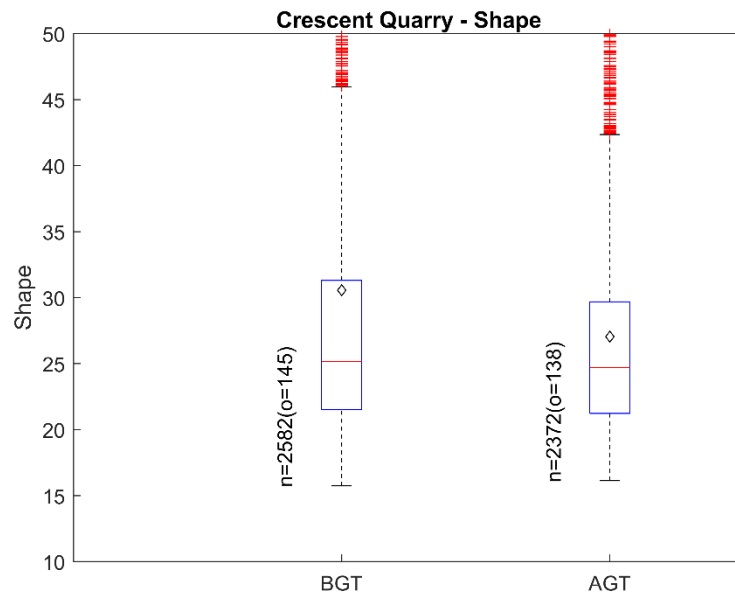


Figure 69. Comparison of shape factor for BGT and AGT specimens from Crescent Quarry

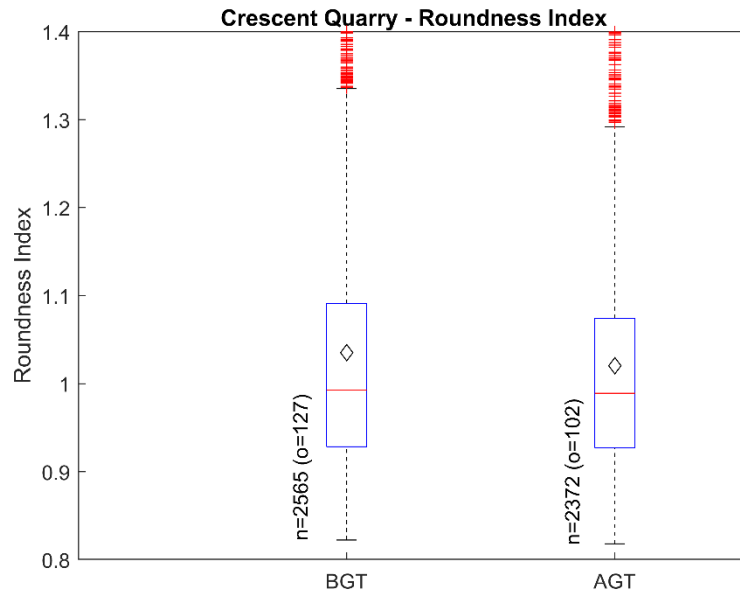


Figure 70. Comparison of roundness index for BGT and AGT specimens from Crescent Quarry

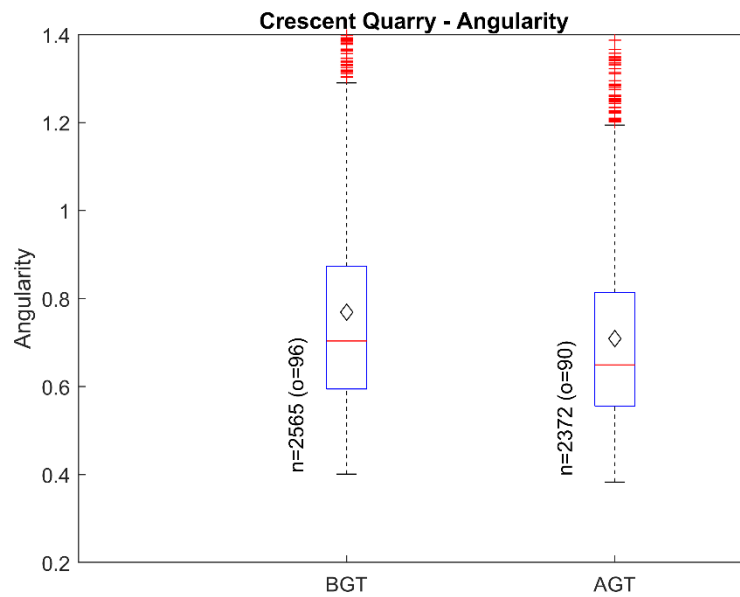
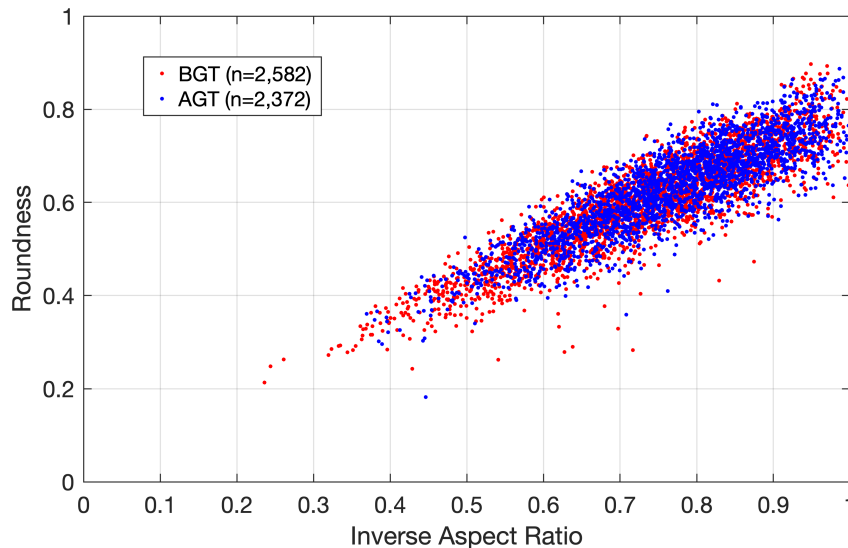


Figure 71. Comparison of angularity for BGT and AGT specimens from Crescent Quarry

Table 21. Statistical results of morphological parameters of Crescent Quarry specimens

Parameters	Sample Type (BGT/AGT)	Max. Value	Min. Value	Mean	Mode	Median	Std. Dev.	Skew-ness	Kurt-osis	Out-liers
Roundness	BGT	0.897	0.213	0.599	0.56	0.608	0.111	-0.305	2.806	16
	AGT	0.887	0.182	0.629	0.689	0.638	0.1	-0.346	2.897	11
	% increase			5.0%		4.9%				
Sphericity	BGT	0.807	0.001	0.510	0.547	0.517	0.113	-0.31	3.148	13
	AGT	0.796	0.162	0.537	0.554	0.543	0.106	-0.311	2.875	15
	% increase			5.3%		5.0%				
Form Factor (FF)	BGT	0.798	0.01	0.488	0.454	0.500	0.128	-0.477	2.99	13
	AGT	0.779	0.101	0.501	0.601	0.509	0.119	-0.382	2.711	9
	% increase			2.7%		1.8%				
Shape Factor (SF)	BGT	1204	15.74	30.57	21.71	25.16	48.76	18.94	395.8	145
	AGT	123.8	16.14	27.04	19.01	24.70	9.09	2.9	18.21	138
	% increase			-11.5%		-1.8%				
Roundness Index (RI)	BGT	5.075	0.822	1.035	0.993	0.992	0.189	8.712	167.7	127
	AGT	2.171	0.818	1.02	0.869	0.989	0.133	1.863	9.182	102
	% increase			-1.4%		-0.3%				
Angularity	BGT	4.387	0.401	0.769	0.637	0.704	0.261	3.209	32.54	96
	AGT	2.431	0.383	0.709	0.637	0.65	0.211	1.481	6.733	90
	% increase			-7.8%		-7.7%				

The roundness is plotted against inverse aspect ratio in Figure 72, from which a slight increase in roundness and inverse aspect ratio after gyratory testing is apparent.

**Figure 72. Roundness versus inverse of aspect ratio for BGT and AGT specimens from Crescent Quarry**

4.1.4.3 Gyratory Compaction Test Results for Crescent Quarry

The dry unit weight, shear resistance, and void ratio during the gyratory compaction test are plotted in Figure 73 and Figure 74 with respect to the compaction energy and number of gyrations. The corresponding changes in compaction energy and dry unit weight for both test stages are shown in Table 22. A decrease in void ratio of 63.1% and increase in dry unit weight of 35.5% occurred through both stages of the test. The point of maximum curvature for the dry unit weight occurred at a dry density of 124.58 pcf.

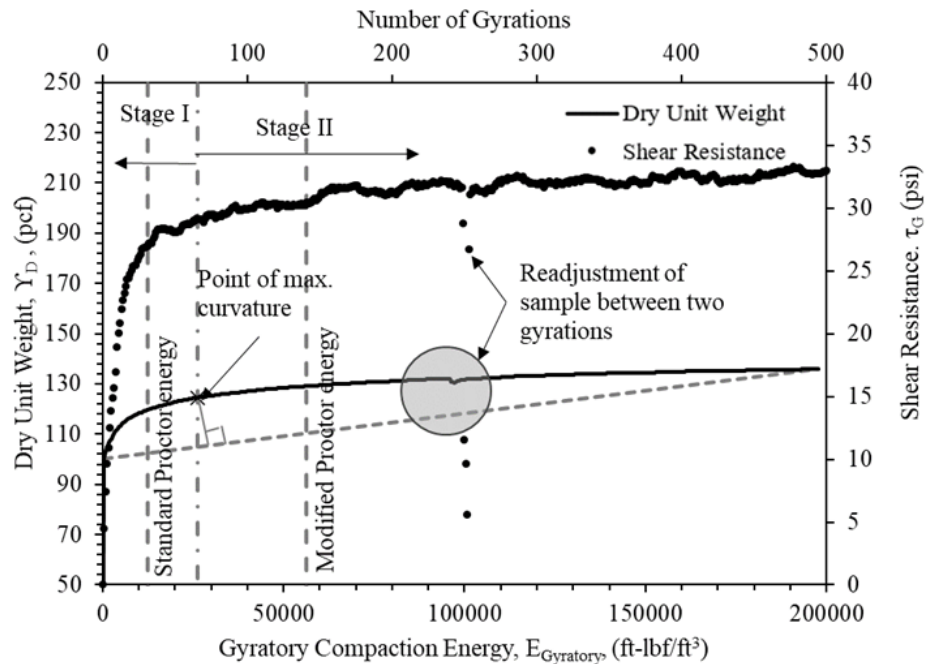


Figure 73. Relationships between dry unit weight, gyratory compaction energy, shear resistance, and number of gyrations for coarse aggregates from Crescent Quarry

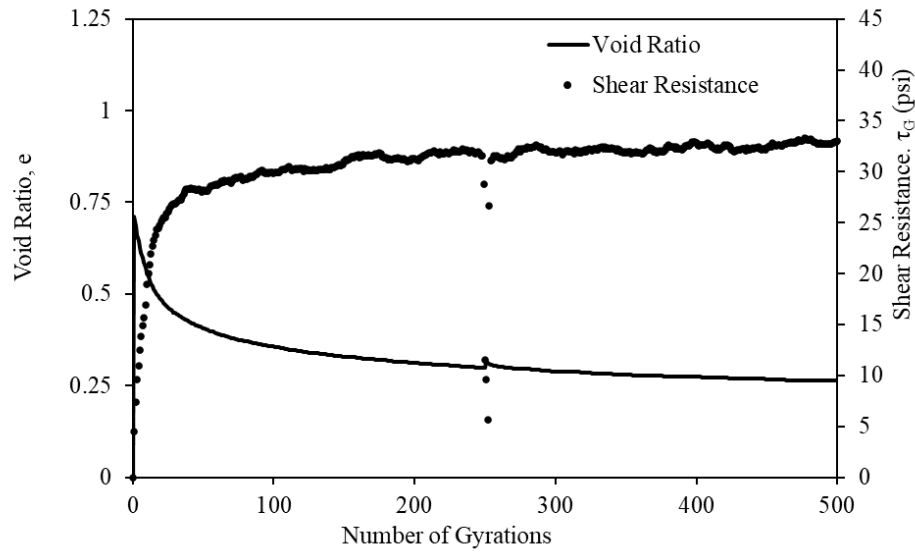


Figure 74. Changes in shear resistance and void ratio of coarse aggregate sample from Crescent Quarry during gyratory compaction test

Table 22. Gyratory compaction energy and dry unit weights for Stages I and II of gyratory compaction tests

Stage	Energy, E (ft-lbf/ft ³)			Dry Unit Weight, γ_d (pcf)		
	Initial E_i	Final E_f	Change ΔE	Initial γ_{di}	Final γ_{df}	Change $\Delta \gamma_d$
Stage I	334.17	26,138.13	25,803.96	100.26	124.58	24.32
Stage II	26,138.13	197,703.45	171,565.33	124.58	135.85	11.27

4.1.4.4 Triaxial Test Results for Crescent Quarry

Triaxial tests were performed on Crescent Quarry specimens with confining pressures of 3.7, 10.2 and 15.4 psi for the BGT specimens and 5.3, 10.3 and 15.4 psi for the AGT specimens. The Mohr-Coulomb plots of the results are shown in Figure 75 and Figure 76. The resulting cohesion and friction angle values of the BGT specimens were 2.54 psi and 37.9°, and those of the AGT specimens were 3.42 psi and 37.3°. The cohesion therefore increased by 34.6% after gyratory compaction while the friction angle decreased by 1.6%.

Mohr Circle Plot of CD Triaxial Tests of Crescent Quarry - BGT

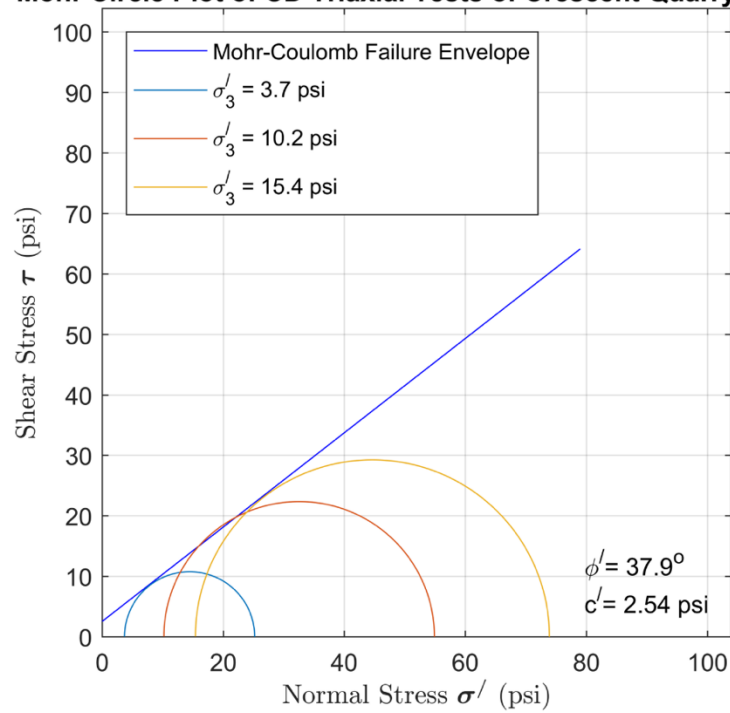


Figure 75. Mohr-Coulomb plot of samples from Crescent Quarry – before gyratory testing

Mohr Circle Plot of CD Triaxial Tests of Crescent Quarry - AGT

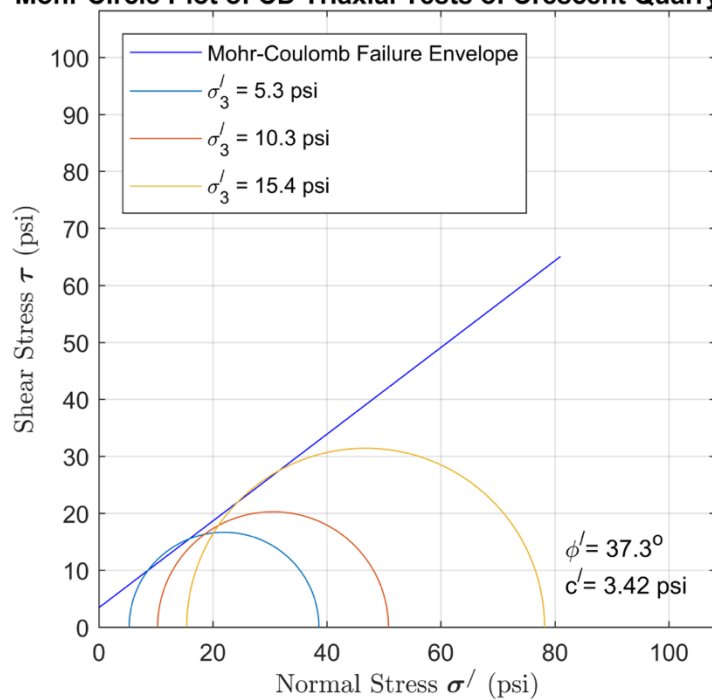


Figure 76. Mohr-Coulomb plot of samples from Crescent Quarry – after gyratory testing

4.1.4.5 Geological Tests for Crescent Quarry

The Crescent Quarry clean samples comprised six distinct rock types. These rock types were analyzed using thin sections, the results of which are presented in Table 23 for the BGT specimens and Table 24 for the AGT specimens. The grain densities of the six rock types ranged from 2.71 to 2.89 g/cm³ for the BGT specimens, and from 2.74 to 2.87 g/cm³ for the AGT specimens. The abundance of these rock types varied from 10% to 25% for BGT specimens and from 5% to 37% for AGT specimens. Specifically, RT1 (porous, calcite-cemented dolostone) decreased in abundance from 25% BGT to 17% AGT while the grain density was unchanged at 2.85 g/cm³. RT2 (dolomitic skeletal lime packstone) increased in abundance from 16% BGT to 37% AGT while the grain density increased from 2.71 to 2.74 g/cm³. RT3 (nonporous, fine grained, skeletal grainstone) decreased slightly from 12% BGT to 11% AGT, while the grain density increased from 2.73 to 2.79 g/cm³. RT4 (porous, coarse grained skeletal ooid grainstone) increased from 11% BGT to 22% AGT while the grain density remained at 2.74 g/cm³. RT5 (nonporous, coarse grained skeletal ooid grainstone; grain density 2.79 g/cm³) decreased completely from 11% BGT to 0% AGT. RT6 (skeletal dolo packstone) decreased from 10% BGT to 5% AGT while the grain density decreased from 2.89 to 2.87 g/cm³. Therefore, the muddiest lithology of RT2 and the coarse grained grainstone of RT4 gained in abundance while the dolomitic lithologies of RT1, RT5, and RT6 as well as the fine grained grainstone of RT3 decreased in abundance.

Thin sections were analyzed for the specimens, producing several interesting findings. First, magnified views of RT1 for the AGT specimen revealed cracks that formed both parallel and nonparallel to the edges, as well as healed fractures (Figure 77). Second, cracks following the grain boundaries as well as cracks cross-cutting the grains were observed for RT6 BGT and RT2 AGT (Figure 78). Finally, porous rims were observed to form in the AGT samples of RT5, as shown in the magnified view in Figure 79.

Camsizer tests were performed on Crescent Quarry BGT and AGT specimens for RT1, RT3, RT4 and RT6. The results, shown in Figure 80, indicate that RT1 and RT2 had bimodal particle size distributions that shifted to smaller particle sizes after gyratory compaction. Conversely, the distributions for RT3 and RT 4 shifted to larger sizes after gyratory compaction.

Table 23. Geological parameters of Crescent Quarry samples before gyratory compaction

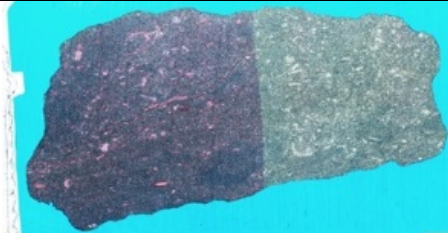
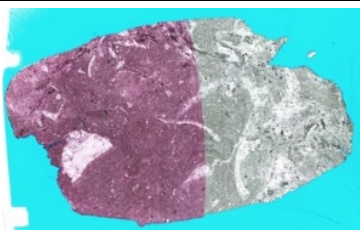
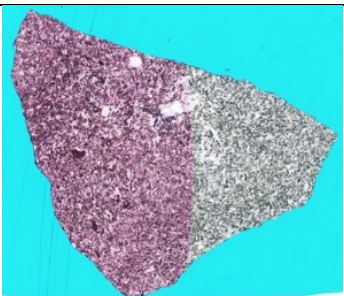
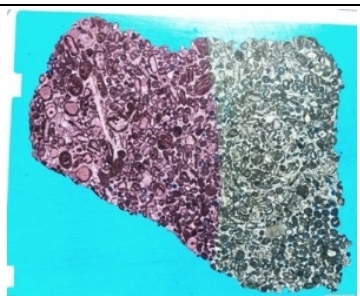
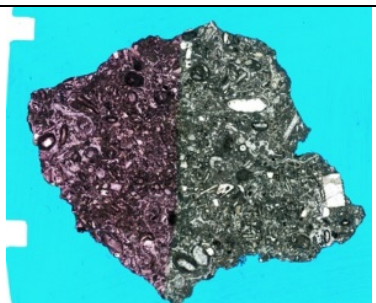
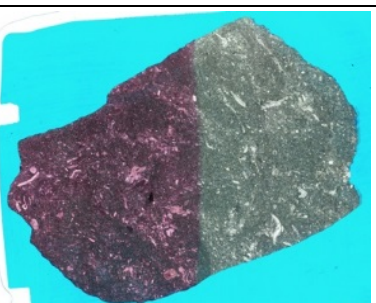
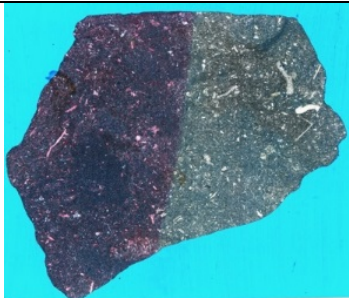
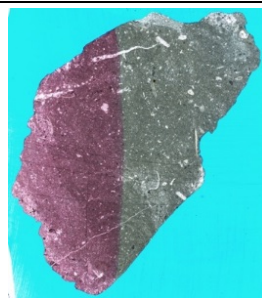
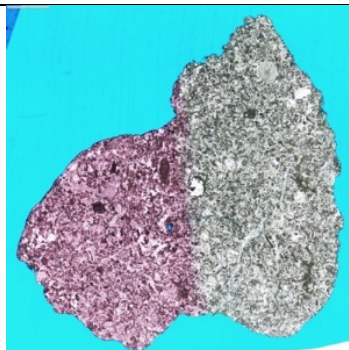
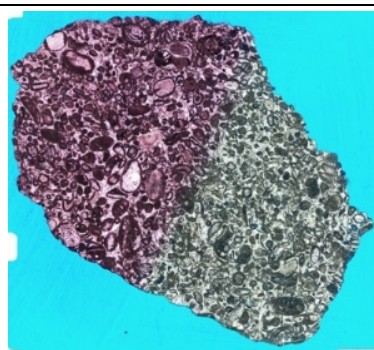

Geological Parameters	Rock Types	
	Rock Type 1	Rock Type 2
Grain Density	2.85	2.71
Abundance	25%	16%
Images of the Thin Sections		
	Rock Type 3	Rock Type 4
	Grain Density	2.72
Abundance	12 %	11%
Images of the Thin Sections		
	Rock Type 5	Rock Type 6
	Grain Density	2.79
Abundance	11%	10%
		

Table 24. Geological parameters of Crescent Quarry samples after gyratory compaction

Geological Parameters	Rock Types		
	Rock Type 1	Rock Type 2	
	Grain Density	2.85	2.74
Abundance	17 %	37%	
Images of the Thin Sections			
	Rock Type 3	Rock Type 4	
	Grain Density	2.79	2.74
	Abundance	11 %	22%
Images of the Thin Sections			
	Rock Type 5	Rock Type 6	
	Grain Density	NA	2.87
	Abundance	NA	5%
Images of the Thin Sections			

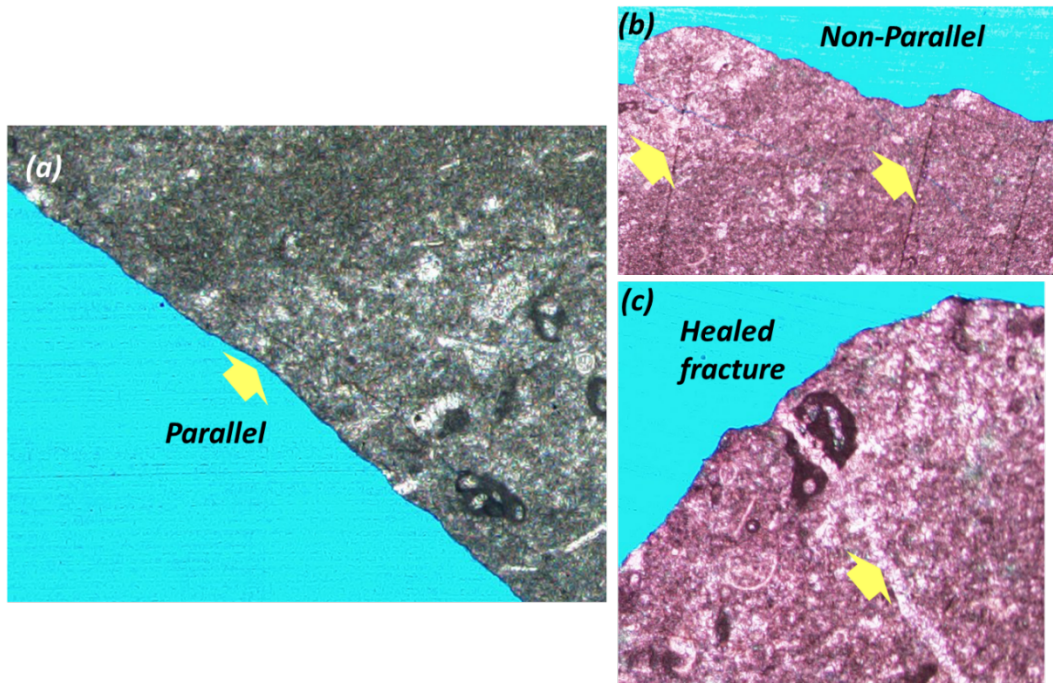


Figure 77. Magnified view of Rock Type 1 for Crescent Quarry AGT specimen: (a) cracks parallel to edge, (b) cracks nonparallel to edge, (c) healed fracture

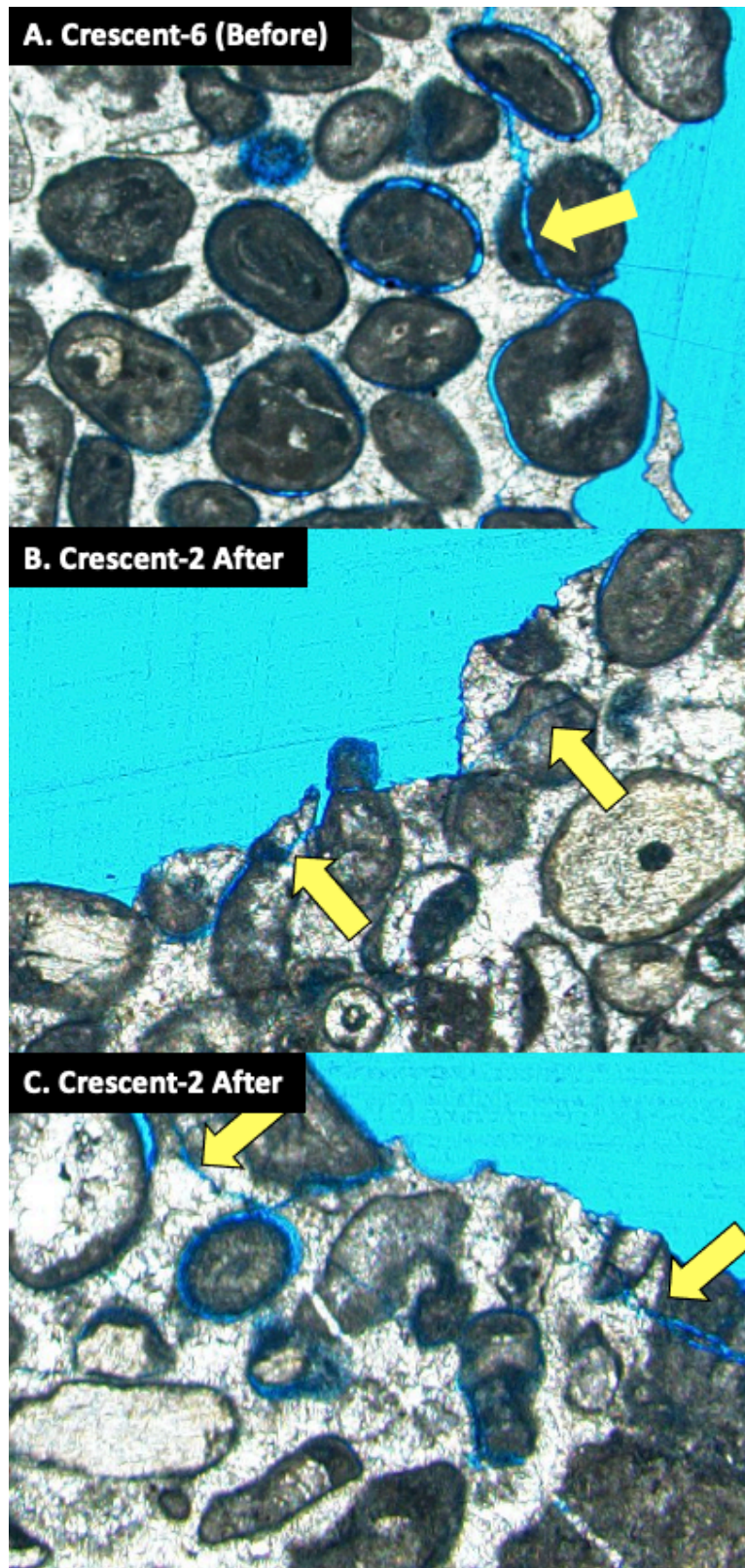


Figure 78. Grain-boundary hugging fractures visible in Crescent Rock Type 6 BGT and Rock Type 2 AGT

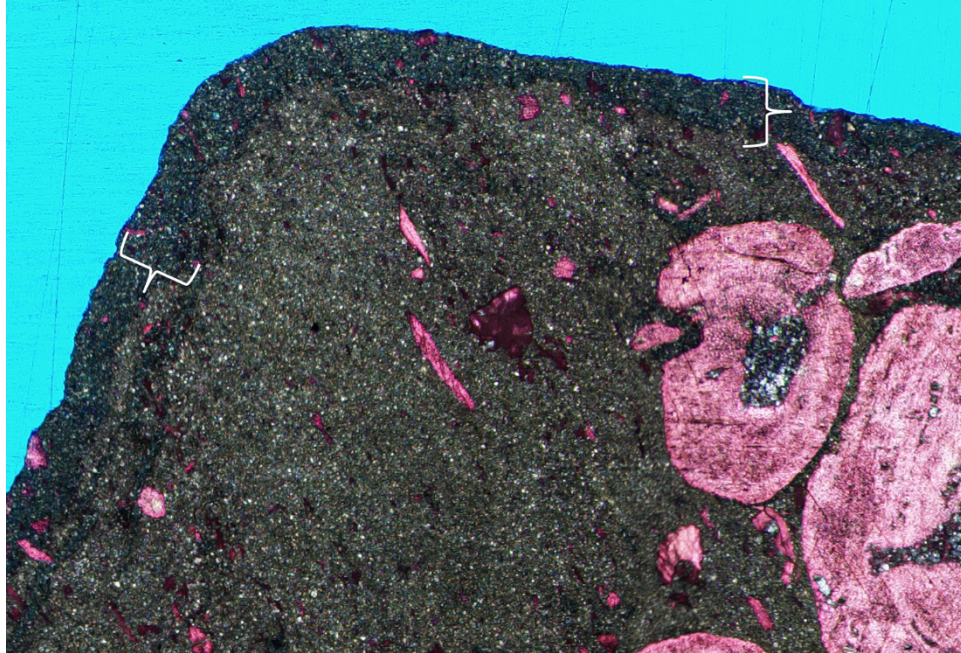


Figure 79. Magnified view of Rock Type 5 for Crescent Quarry AGT specimen showing porous rims

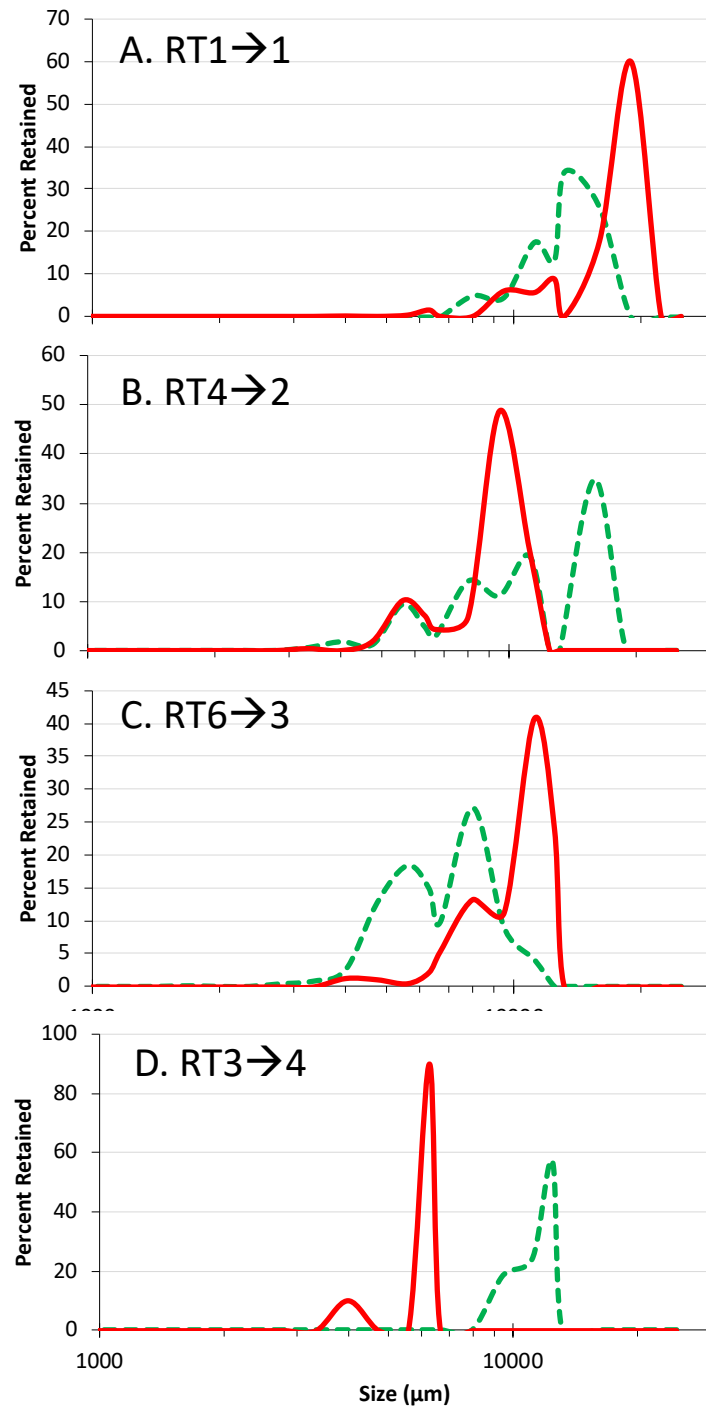


Figure 80. Camsizer data for four rock types from Crescent Quarry BGT (red lines) and AGT (green lines). Arrows indicate resulting changes in relative abundance AGT.

4.1.5 Pedersen Quarry Aggregates

4.1.5.1 PSD Comparison and Evaluation of Breakage Parameters for Pederson Quarry

The mechanical degradation of Pedersen Quarry Class A samples during gyratory compaction, as represented by Hardin's total breakage from the PSD curves, was very slight and determined to be 0.04 from laboratory sieve and hydrometer analysis (Figure 81) and 0.06 via 2D image analyses (Figure 82). The corresponding breakage parameters detailed in Table 25 show that the gravel fraction decreased by 5.2 % during the gyratory test, while the sand fraction increased by 5.2 % and the fines fraction was unchanged. These results indicate breakdown of the gravel sized particles into sand sized particles with no breakdown of sand into fines for this material.

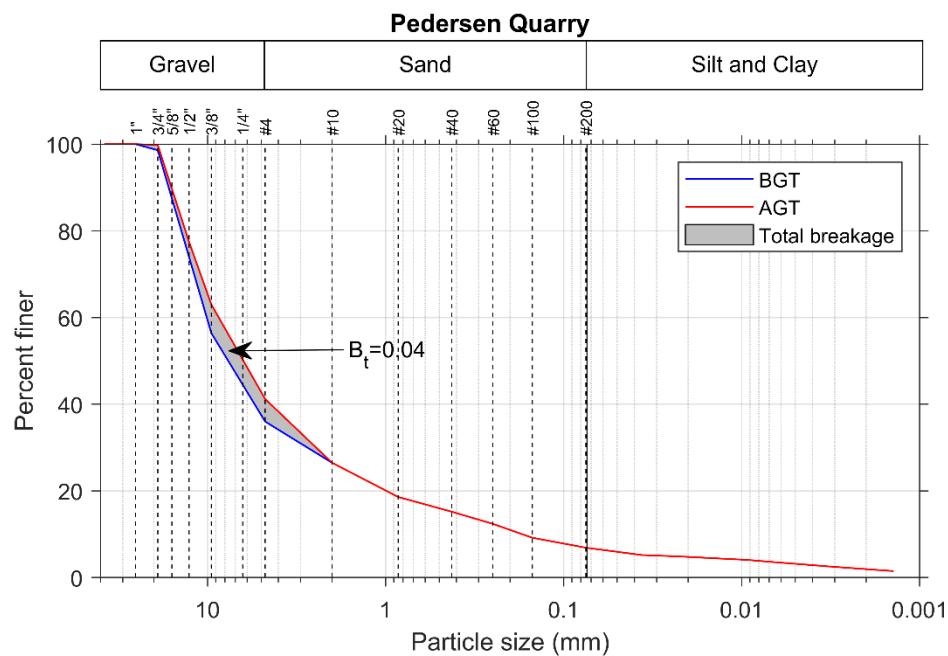


Figure 81. Particle size distributions from sieve and hydrometer analysis and evaluation of breakage of coarse fraction for samples from Pedersen Quarry

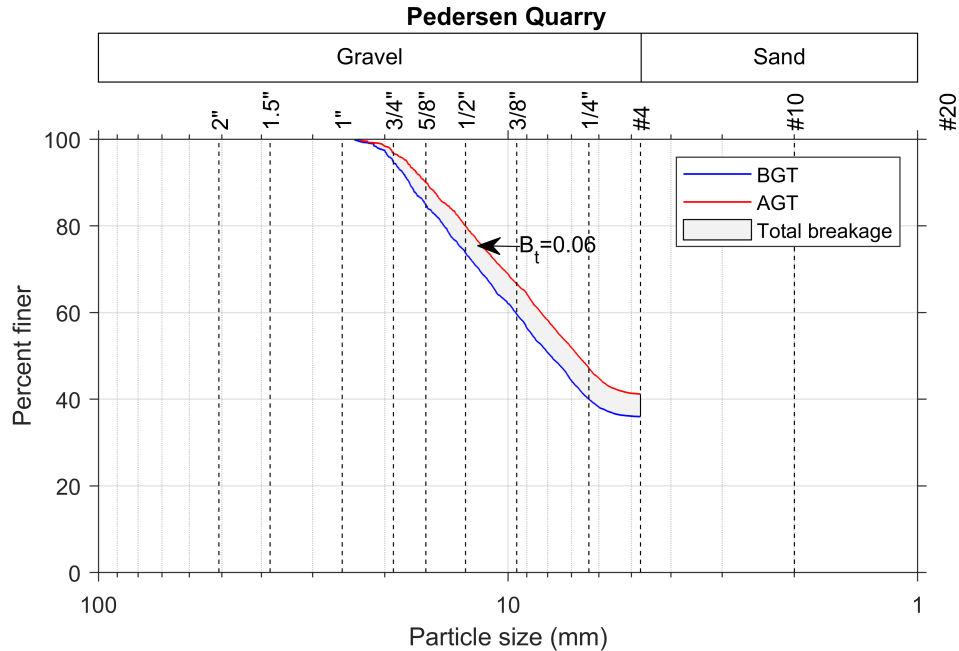


Figure 82. Particle size distributions from 2D image analysis and evaluation of breakage of coarse aggregate samples from Pedersen Quarry

Table 25. Breakage parameters determined from laboratory sieve and 2D image analyses, and corresponding percentages of gravel, sand, and fines for Pedersen Quarry samples

Analysis Type	Hardin's Breakage Parameters			% Gravel		% Sand		% Fines	
	Total Breakage, B_t	Breakage Potential, B_p	Relative Breakage, B_r	BGT	AGT	BGT	AGT	BGT	AGT
Lab Sieve Analyses	0.0388	1.6630	0.0233	64.0	58.8	29.1	34.3	6.9	6.9
				% Reduction (red.) or % Increase (inc.)					
				5.2 % red.		5.2 % inc.		0 % inc.	
2D Image Analyses	0.0591	0.4961	0.1190	NA*		NA*		NA*	

* Not Available: Only gravel sized particles retained on #4 (4.75 mm) sieve were scanned.

4.1.5.2 2D Image Analyses and Comparison of Morphological Parameters for Pederson Quarry

The calculated morphological parameters for the Pedersen Quarry BGT and AGT specimens are presented in Figure 83 through Figure 88, and the statistical outputs of these morphological parameters along with their changes during gyratory compaction are presented in Table 26. As can be seen in the figures, the total number of gravel-sized particles decreased from 2,758 to 2,463 due to particle breakage during gyratory compaction, and the number of outliers was typically between 0.4% and 10%. As shown in Table 26, the median values of roundness, sphericity, and form factor increased by 1.1%, 2.4%, and 0.3%, respectively, as the particles became more rounded and spherical under gyratory compaction. Conversely, corresponding

decreases of 0.4% in shape factor and roundness index along with a decrease of 5.7% in angularity were observed for the same specimens.

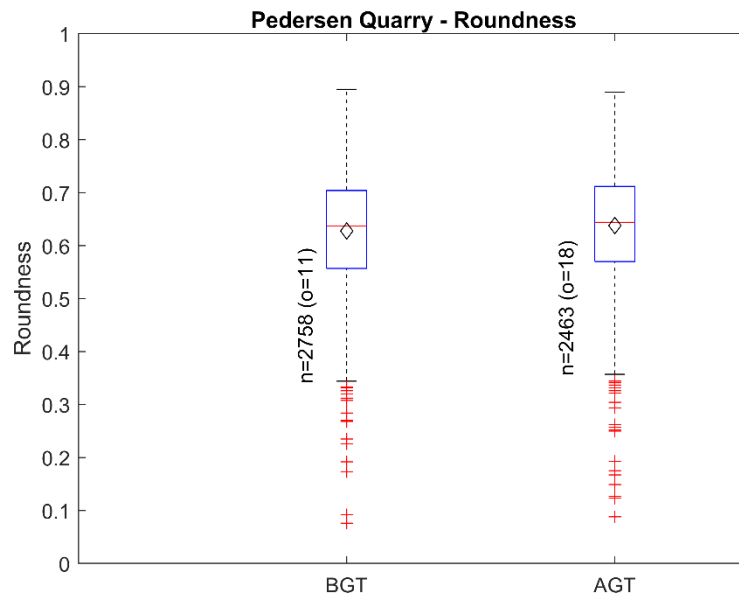


Figure 83. Comparison of roundness for BGT and AGT specimens from Pedersen Quarry

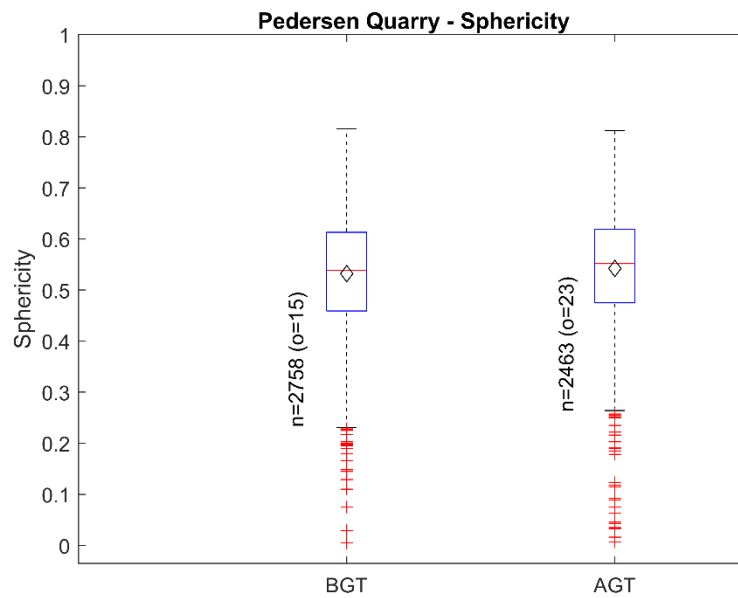


Figure 84. Comparison of sphericity for BGT and AGT specimens from Pedersen Quarry

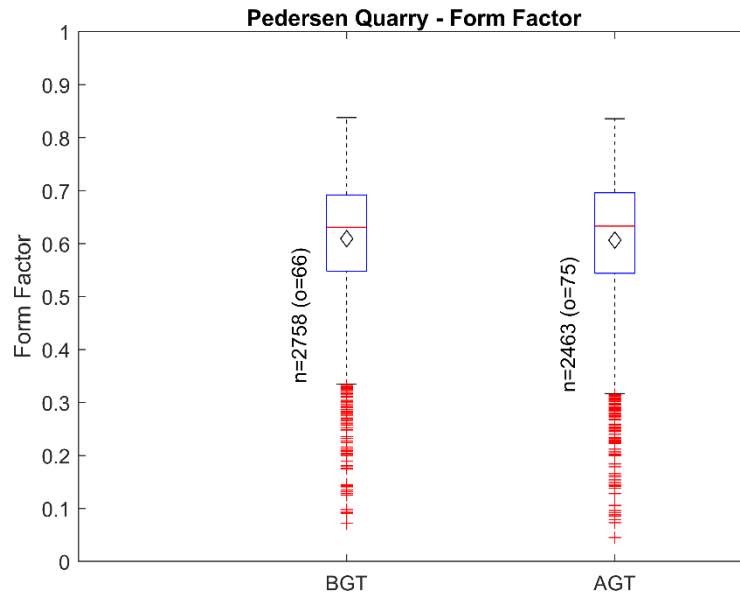


Figure 85. Comparison of form factor for BGT and AGT specimens from Pedersen Quarry

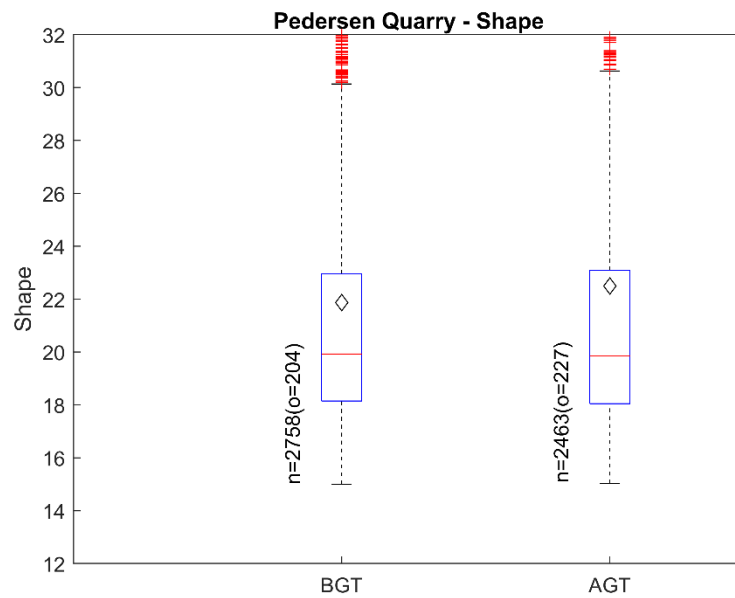


Figure 86. Comparison of shape factor for BGT and AGT specimens from Pedersen Quarry

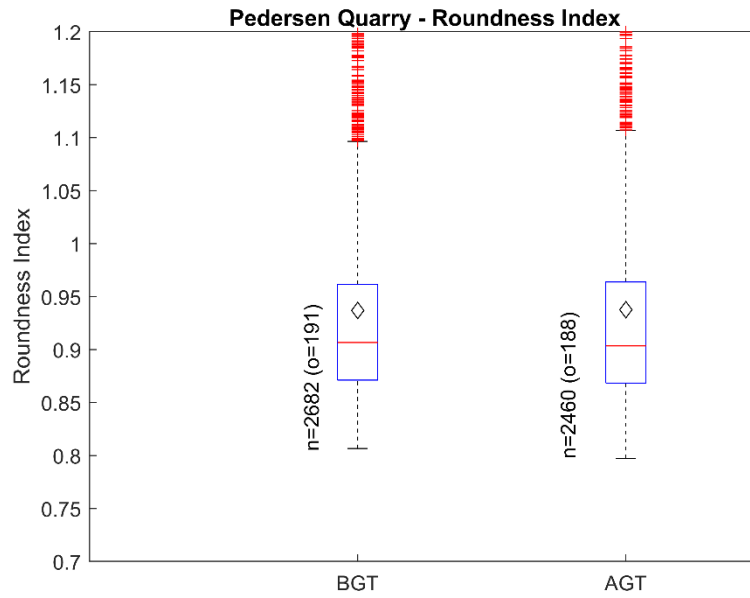


Figure 87. Comparison of roundness index for BGT and AGT specimens from Pedersen Quarry

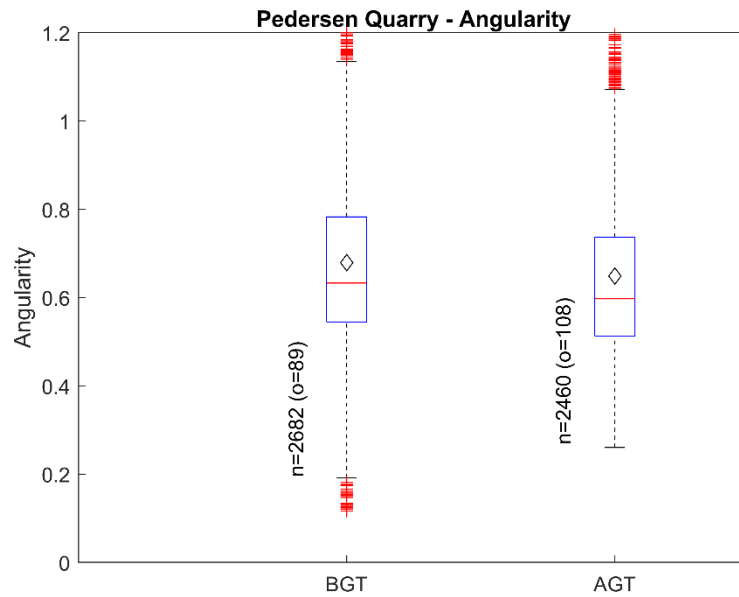


Figure 88. Comparison of angularity for BGT and AGT specimens from Pedersen Quarry

Table 26. Statistical results of morphological parameters of Pedersen Quarry samples

Parameter	Sample Type (BGT/AGT)	Max.	Min.	Mean	Mode	Median	Std. Dev.	Skew-ness	Kurt-osis	Out-liers
Roundness	BGT	0.895	0.076	0.628	0.664	0.637	0.107	-0.444	3.287	11
	AGT	0.890	0.088	0.638	0.711	0.644	0.104	-0.644	4.309	18
	% increase			1.6%		1.1%				
Sphericity	BGT	0.816	0.005	0.532	0.560	0.539	0.111	-0.411	3.327	15
	AGT	0.812	0.007	0.542	0.582	0.552	0.111	-0.699	4.373	23
	% increase			1.9%		2.4%				
Form Factor (FF)	BGT	0.838	0.072	0.609	0.631	0.631	0.115	-1.092	4.619	66
	AGT	0.836	0.045	0.607	0.629	0.633	0.126	-1.17	4.587	75
	% increase			-0.3%		0.3%				
Shape Factor (SF)	BGT	175.7	15	21.87	17.62	19.93	8.25	7.79	99.94	204
	AGT	276.4	15.03	22.50	18.94	19.85	11.41	9.51	147.6	227
	% increase			2.9%		-0.4%				
Roundness Index (RI)	BGT	2.048	0.807	0.937	0.818	0.907	0.112	3.468	22.74	191
	AGT	2.169	0.797	0.938	0.881	0.903	0.119	3.509	23.06	188
	% increase			0.1%		-0.4%				
Angularity	BGT	2	0.117	0.679	0.556	0.633	0.196	1.138	6.23	89
	AGT	2.025	0.26	0.649	0.453	0.597	0.188	1.583	6.842	108
	% increase			-4.4%		-5.7%				

The roundness is plotted against inverse aspect ratio in Figure 89, in which the changes after gyratory testing are only slightly apparent.

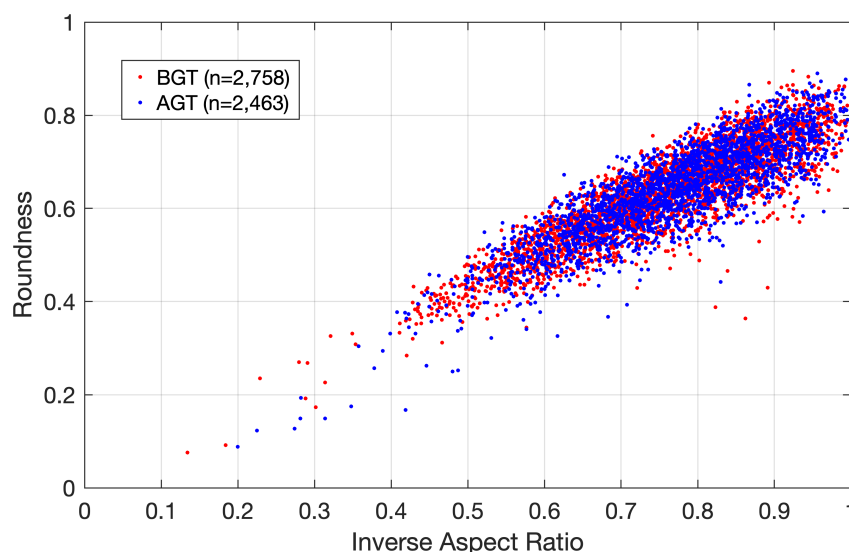


Figure 89. Roundness versus inverse of aspect ratio for BGT and AGT specimens from Pedersen Quarry

4.1.5.3 Gyrotory Compaction Test Results for Pederson Quarry

The void ratio and dry unit weight calculated from the specimen height during the gyrotory compaction test for the Pedersen Quarry specimen are plotted in Figure 90 and Figure 91 with respect to the number of gyrations and compaction energy. An overall 61% decrease in void ratio and 35% increase in dry unit weight were observed during the test. The calculated shear resistance is also shown in these plots. The point of maximum curvature for the plot of dry unit weight versus gyrotory compaction energy in Figure 90 occurs at a dry unit weight of 122.8 pcf, which is above Standard Proctor energy but below Modified Proctor energy. The corresponding changes in compaction energy and dry unit weight during Stages I and II are presented in Table 8.

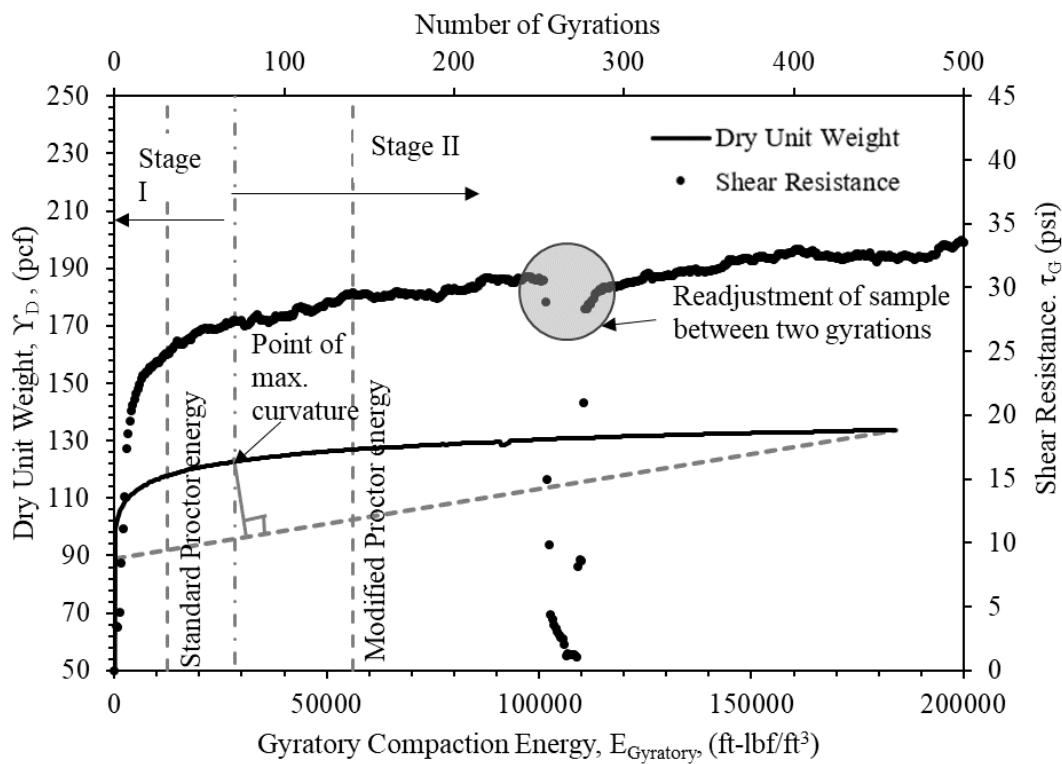


Figure 90. Relationships between dry unit weight, gyrotory compaction energy, shear resistance, and number of gyrations for coarse aggregates from Pedersen Quarry

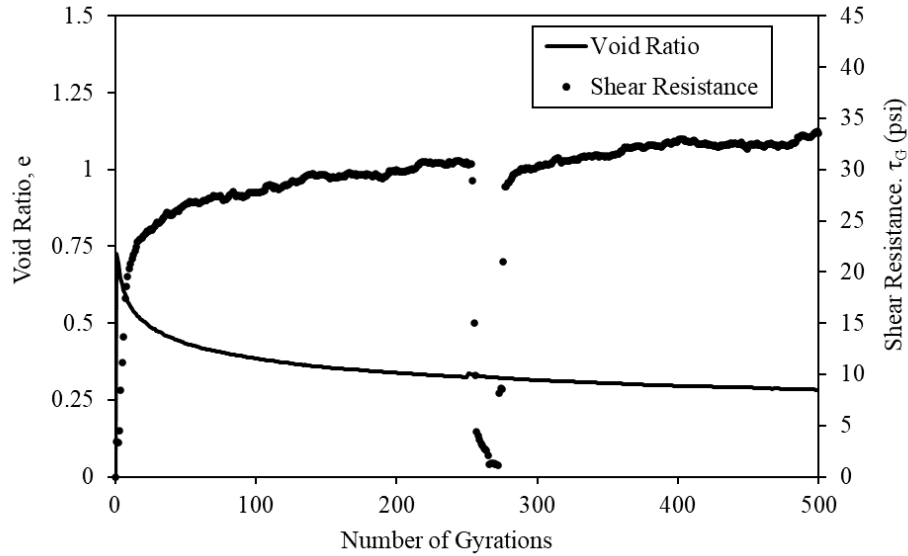


Figure 91. Changes in shear resistance and void ratio of coarse aggregates from Pedersen Quarry during gyratory compaction test

Table 27. Gyratory compaction energy and dry unit weights for Stages I and II of gyratory compaction test for Pedersen Quarry

Stage	Energy, E (ft-lbf/ft ³)			Dry Unit Weight, γ_d (pcf)		
	Initial	Final	Change	Initial	Final	Change
	E_i	E_f	ΔE	γ_{di}	γ_{df}	$\Delta \gamma_d$
I	270.1	28,301.6	28,031.6	99.44	122.80	23.36
II	28,301.6	184,218.0	155,916.4	122.80	133.75	10.95

4.1.5.4 Triaxial Test Results for Pedersen Quarry

Triaxial tests were performed on Pedersen Quarry specimens with confining pressures of 5.4, 9.9 and 15.6 psi applied to the BGT specimens, and 5.3, 10.4 and 15.4 psi applied to the AGT specimens. The Mohr-Coulomb plots of the results are shown in Figure 92 and Figure 93. The resulting cohesion and friction angle values of the BGT samples were 3.95 psi and 39.1°, while those of the AGT specimens were 2.24 psi and 41.5°. Therefore, the cohesion decreased by 43.3% while the friction angle increased by 6.1% due to gyratory compaction.

Mohr Circle Plot of CD Triaxial Tests of Pedersen Quarry - BGT

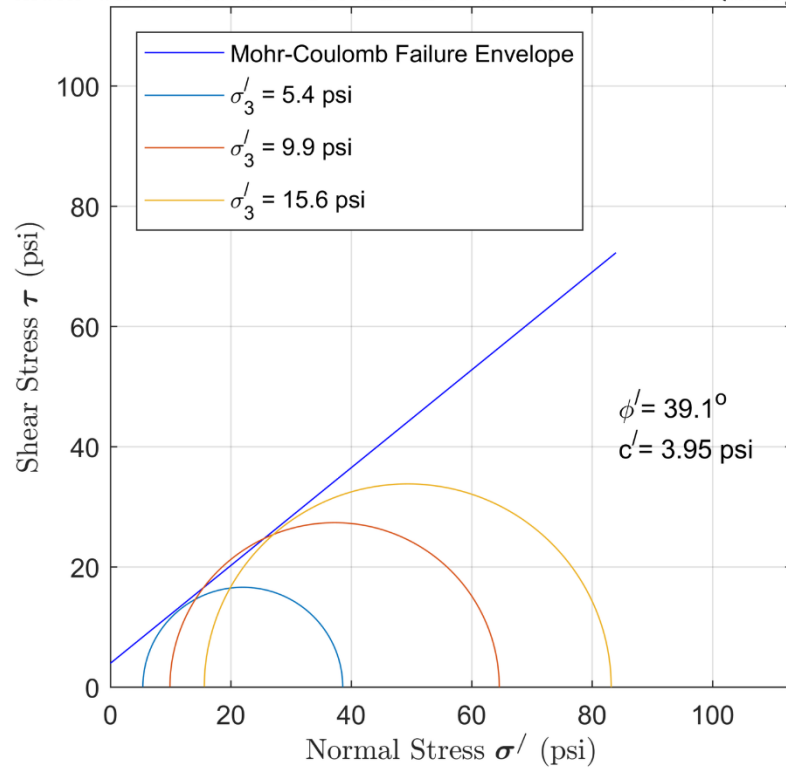


Figure 92. Mohr-Coulomb plot of samples from Pedersen Quarry – before gyratory testing

Mohr Circle Plot of CD Triaxial Tests of Pedersen Quarry - AGT

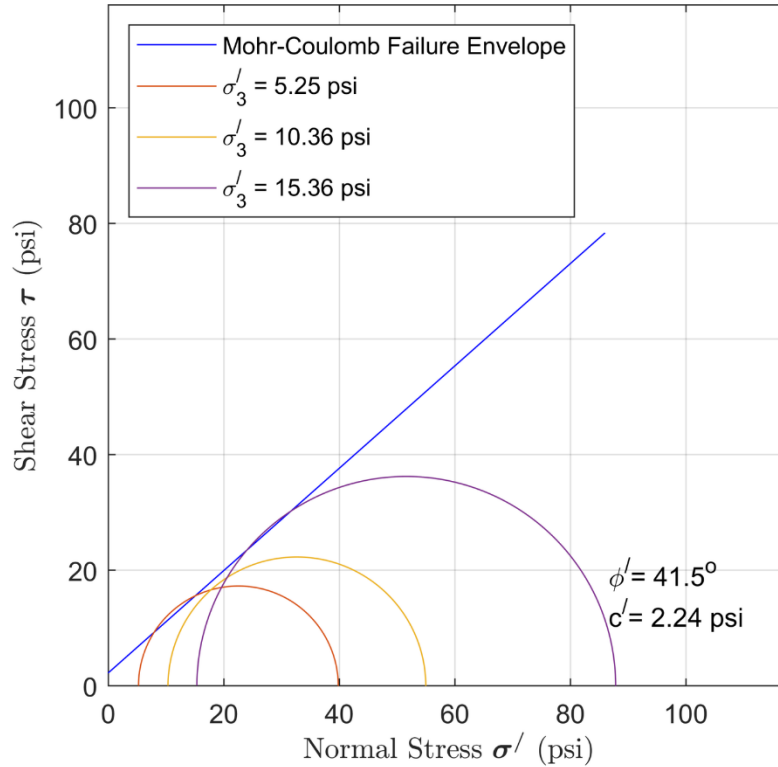


Figure 93. Mohr-Coulomb plot of samples from Pedersen Quarry – after gyratory testing

4.1.5.5 Geological Tests for Pederson Quarry

The Pedersen Quarry Class A samples comprised four distinct rock types. These rock types were analyzed using thin sections, the results of which are presented in Table 28 for the BGT sample and Table 29 for the AGT sample. The grain densities of the four rock types were similar, ranging from 2.72 to 2.73 g/cm³ for the BGT sample, and from 2.71 to 2.73 g/cm³ for the AGT samples. However, the abundance of these samples varied significantly, from a minimum of 8% to a maximum of 45% for BGT samples and from 4% to 50% for AGT samples. Specifically, RT1 (nonporous, fine grained ooid grainstone) increased in abundance from 45% BGT to 50% AGT, while the grain density decreased slightly from 2.73 to 2.72 g/cm³. RT2 (nonporous, fine grained ooid grainstone) decreased significantly from 30% BGT to 3% AGT, while its grain density remained constant at 2.72 g/cm³. RT3 (nonporous, skeletal packstone) also decreased from 14% BGT to 4% AGT with a fixed grain density of 2.73 g/cm³. RT4 (nonporous, skeletal packstone) increased significantly from 8% BGT to 42% AGT, while its grain density decreased slightly from 2.72 to 2.71 g/cm³. These data suggest that the more uniform lithology (ooid grainstone) was less resistant to degradation than more mixed lithologies (skeletal packstones) as long as they are all nonporous.

Camsizer measurements were performed for RT1 and RT4 from Pedersen Quarry, both of which showed shifts to smaller particle sizes (Figure 94). The shift for RT1 was minor, manifesting as a slight decrease in abundance of the largest particles and a slight increase for the smallest

particles. The shift for RT 4 was more pronounced, with the highest abundance grain size decreasing by a factor of 2 (from 20 mm to 10 mm).

Figure 95 provides macroscopic and microscopic views of RT2 for the BGT and AGT samples. These views confirm that the porous lithologies degraded more significantly during gyratory compaction testing, as substantiated by the abundance of RT2 decreasing from 30% to 3% and the abundance of RT3 (not shown) decreasing from 14% to 4%. Conversely, Rock Types 1 and 4 experienced much less degradation as evidenced by the abundance of RT1 increasing from 45% to 50% while that of RT4 increased from 8% to 42%.

Table 28. Geological parameters of Pedersen Quarry samples before gyratory test (BGT)

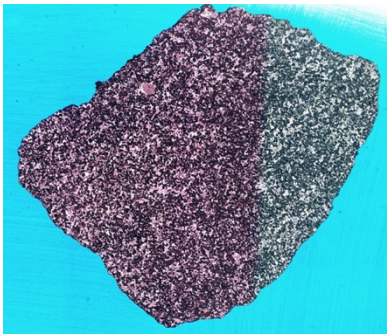
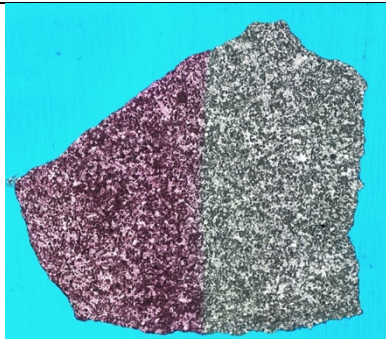
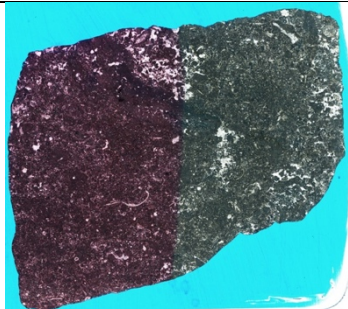
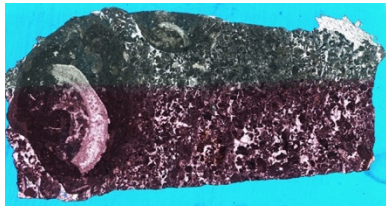
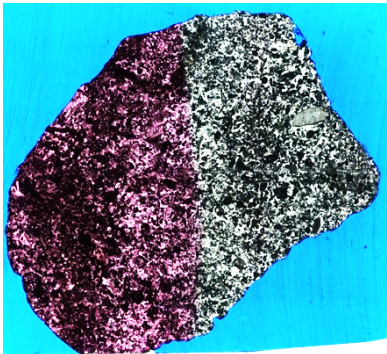

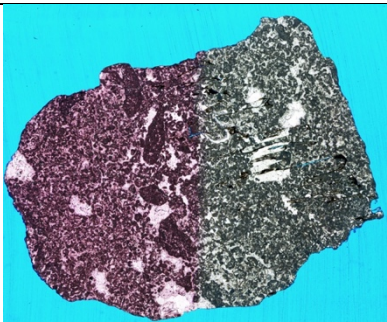
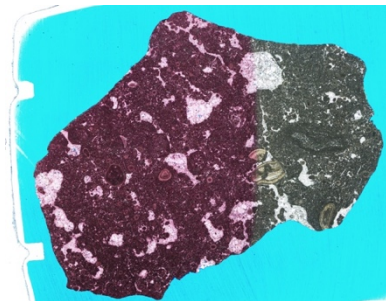
Geological Parameters	Rock Types	
	Rock Type 1	Rock Type 2
Grain Density	2.73	2.72
Abundance	45%	30%
Thin Section Images		
Geological Parameters	Rock Type 3	Rock Type 4
Grain Density	2.73	2.72
Abundance	14%	8%
Thin Section Images		

Table 29. Geological parameters of Pedersen Quarry samples after gyratory test (AGT)

Geological Parameters	Rock Types	
	Rock Type 1	Rock Type 2
Grain Density	2.72	2.72
Abundance	50%	3%
Thin Section Images		
Geological Parameters	Rock Type 3	Rock Type 4
Grain Density	2.73	2.71
Abundance	4%	42%
Thin Section Images		

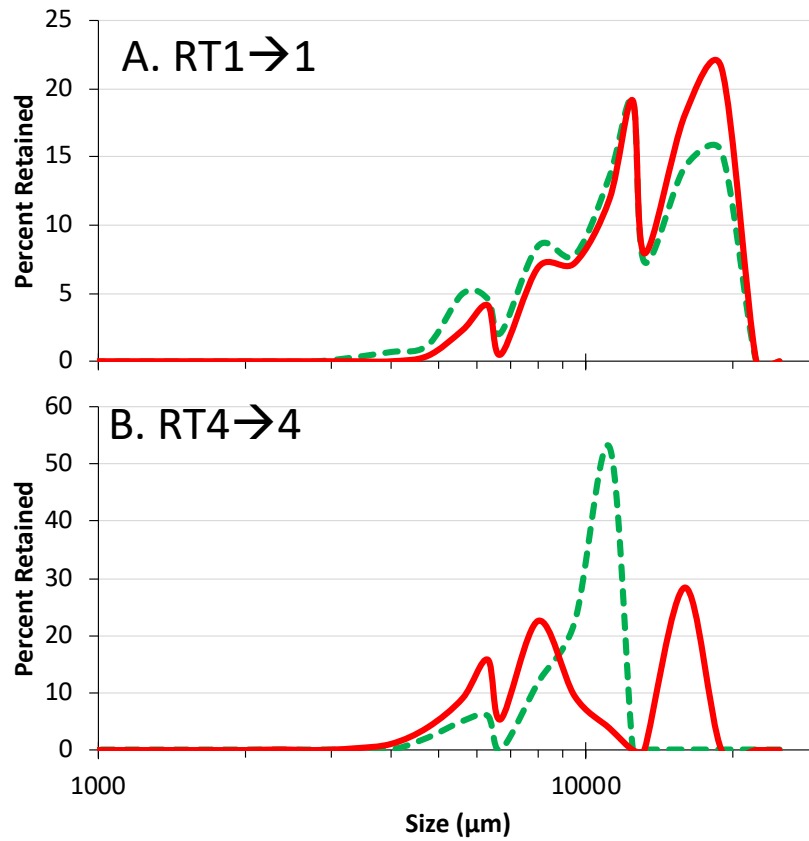


Figure 94. Camsizer data for two rock types from Pedersen Quarry BGT (red lines) and AGT (green lines). Arrows indicate resulting changes in relative abundance AGT.

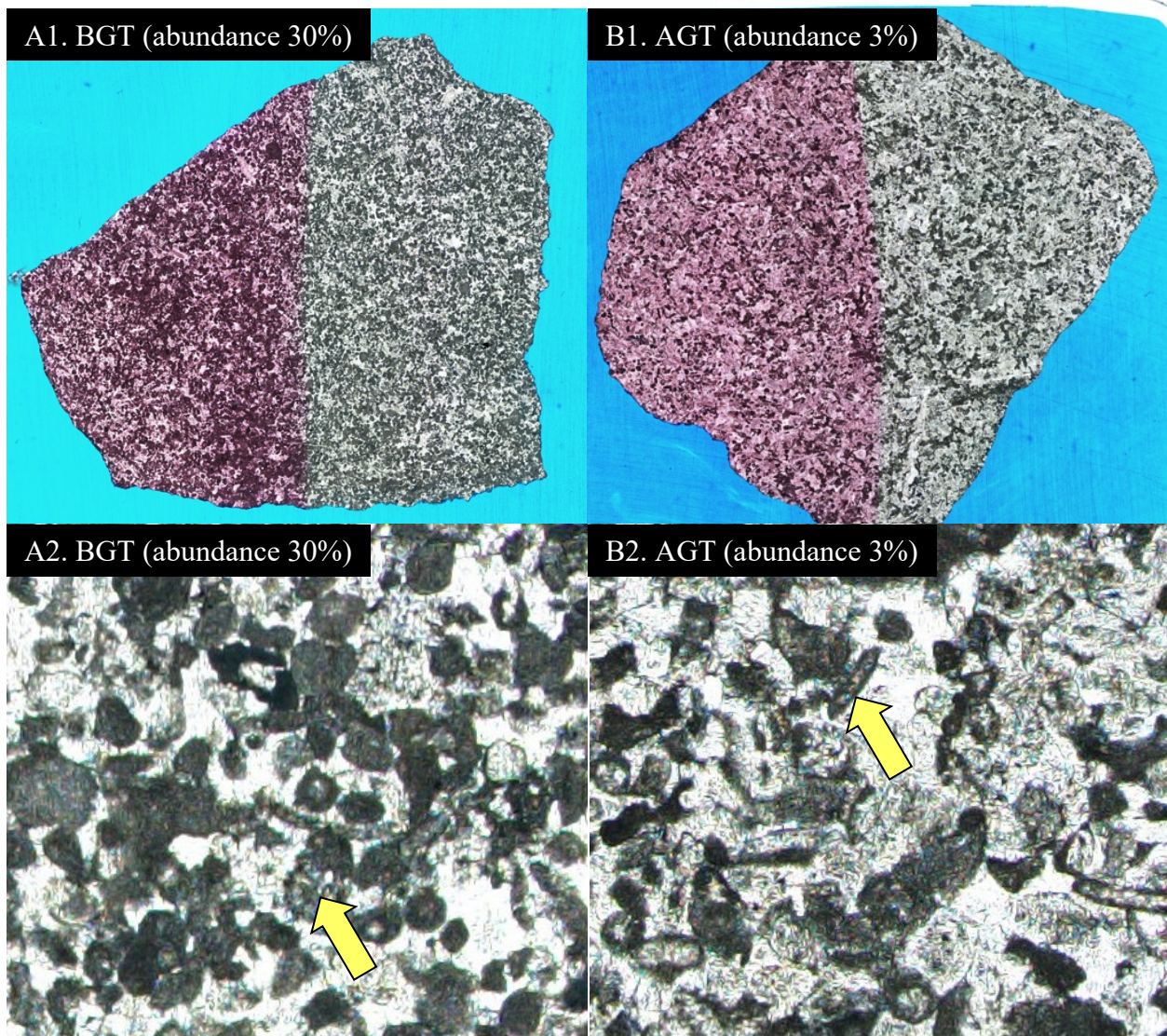


Figure 1. Macroscopic and microscopic views of thin sections of Pedersen Rock Type 2 BGT and AGT. Pore space is barely visible in macroscopic views (A1 and B1) but is more apparent at microscopic level (A2 and B2).

1.1.1 Photomicrographs of Additional Quarry Samples

Two specific microscopic features of pore systems were obvious in photomicrographs of coarse aggregate particles: pores and fractures. More porous rock types seemed to preferentially degrade whether they exhibited macroscopically visible pores as previously shown in Figure 48, or microscopic pores as shown in Figure 95. Photomicrographs were taken of additional quarry samples beyond those tested by gyratory compaction and triaxial tests. The results from these samples are included in this section to provide further data and observations on the relationships between coarse aggregate geology and deterioration. The complete collections of thin section photomicrographs are presented in [Appendix A](#) for the quarry samples and [Appendix B](#) for the roadway test section samples.

In two clay-rich rock types (Crescent RT5 and Moore RT4), porous rims were observed (Figure 96). In Crescent RT5, the rims were only present in the sample after gyratory compaction, while in the Moore RT4 sample they were present both before and after gyratory compaction.

The occurrence of interparticle (or intergranular) pore space was rare in coarse aggregates examined in this study (Figure 97A). It was found in only one source, that of Alden Quarry. Most similar lithologies (lime grainstones) had their pore space completely occluded by calcite cement, whereas pore occlusion in the Alden sample varied from nonexistent to complete over short length scales (Figure 97B).

Perhaps the most abundant pore type was microporosity (Figure 98). This pore type is characterized by a “blue hazy” appearance in thin sections due to the micron-sized crystals of calcite being intermixed with micron-sized pores filled with blue-dyed epoxy. Microporosity was present in grainy rocks (Figure 98A-D), muddy rocks (Figure 98E), and in chert (Figure 98F).

Separate vug pores were also identified in numerous coarse aggregate lithologies (Figure 99). These are characterized as large pores either unconnected to other pores or only connected through a microporous matrix. These were found within fossils (Figure 99A-B), within dolomite (Figure 99C), where grains had dissolved away (Figure 99D-E), and in stylolites (Figure 99F).

Intercrystalline pores, those between mineral crystals and not sedimentary grains, were found only in dolostone lithologies (Figure 100). Pore space was commonly open and well connected except where occluded by dolomite cement (Figure 100D) or rarely, calcite cement (Figure 100E). While most nonsedimentary particles were nonporous, one example of porous granite was observed (Figure 100F).

Hairline fractures (cracks) were observed paralleling edges of coarse aggregate particles of several rock types before and after compaction (Figure 101). In numerous other cases, fractures were observed perpendicular to particle edges both BGT and AGT (Figure 102). In one sample (Crescent RT1 AGT), both parallel and perpendicular fractures were observed in addition to healed fractures in the same particle (Figure 103). In other samples from Atlantic and Booneville, multiple parallel fractures were observed at an angle of approximately 30° to the particle edge (Figure 104). In one sample from Crescent, a fracture was observed hugging or cross-cutting sedimentary grains (ooids) (Figure 105).

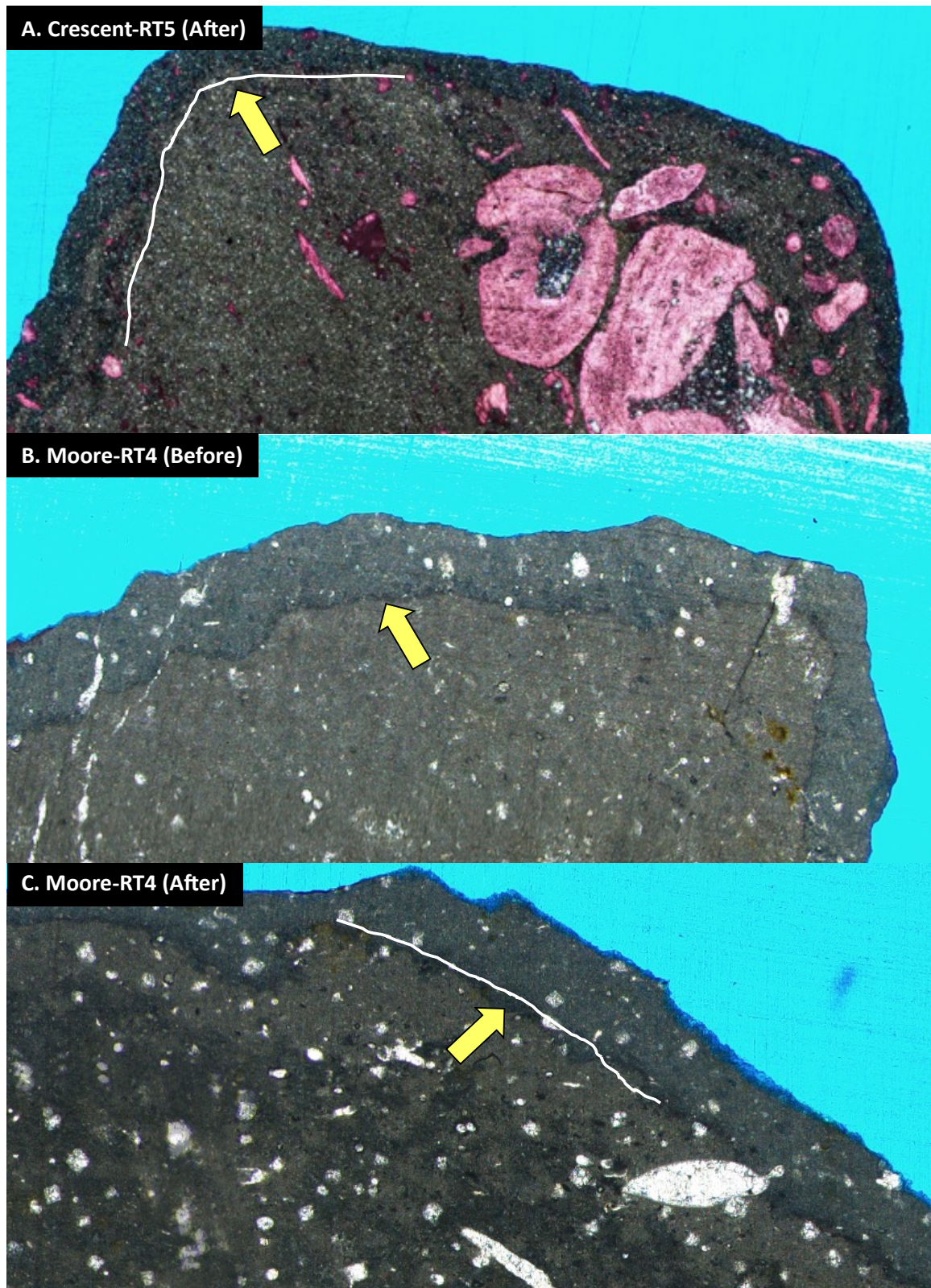


Figure 96. Porous rim visible in (A) Crescent Rock Type 5 AGT, (B) Moore Rock Type 4 BGT, and (C) Moore Rock Type 4 AGT

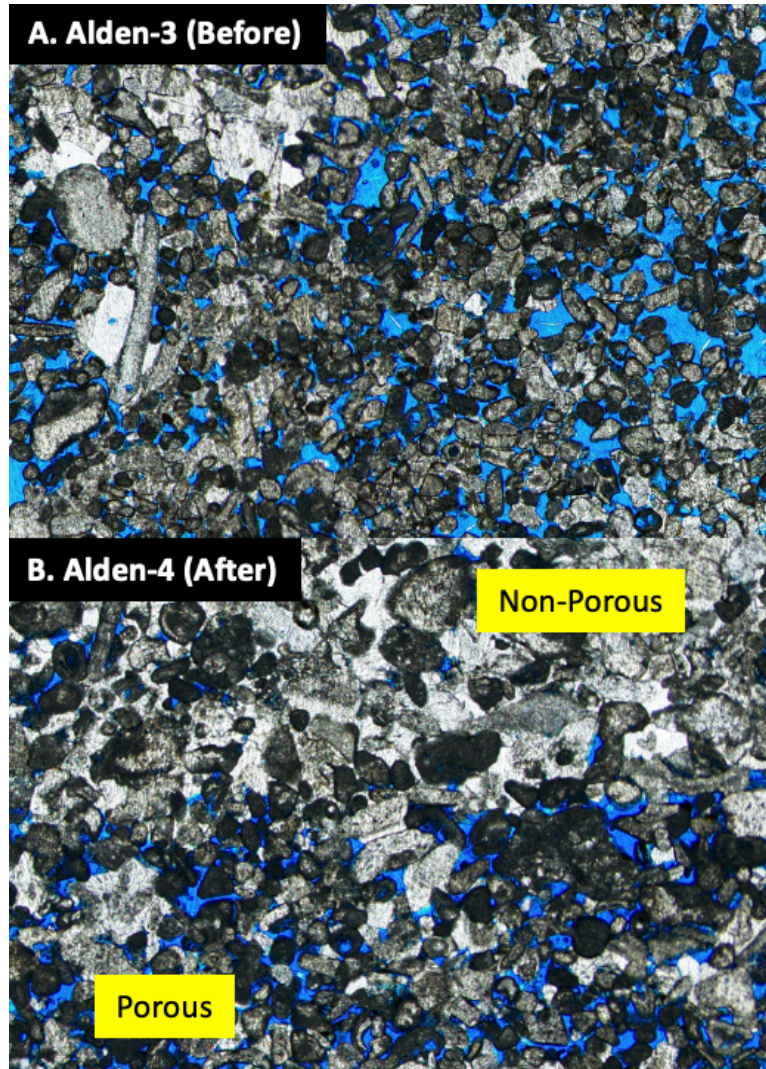


Figure 97. Examples of intergranular pore space (highlighted by blue-dyed epoxy) manifesting as open, connected pore space between sedimentary grains for Alden BGT and AGT samples

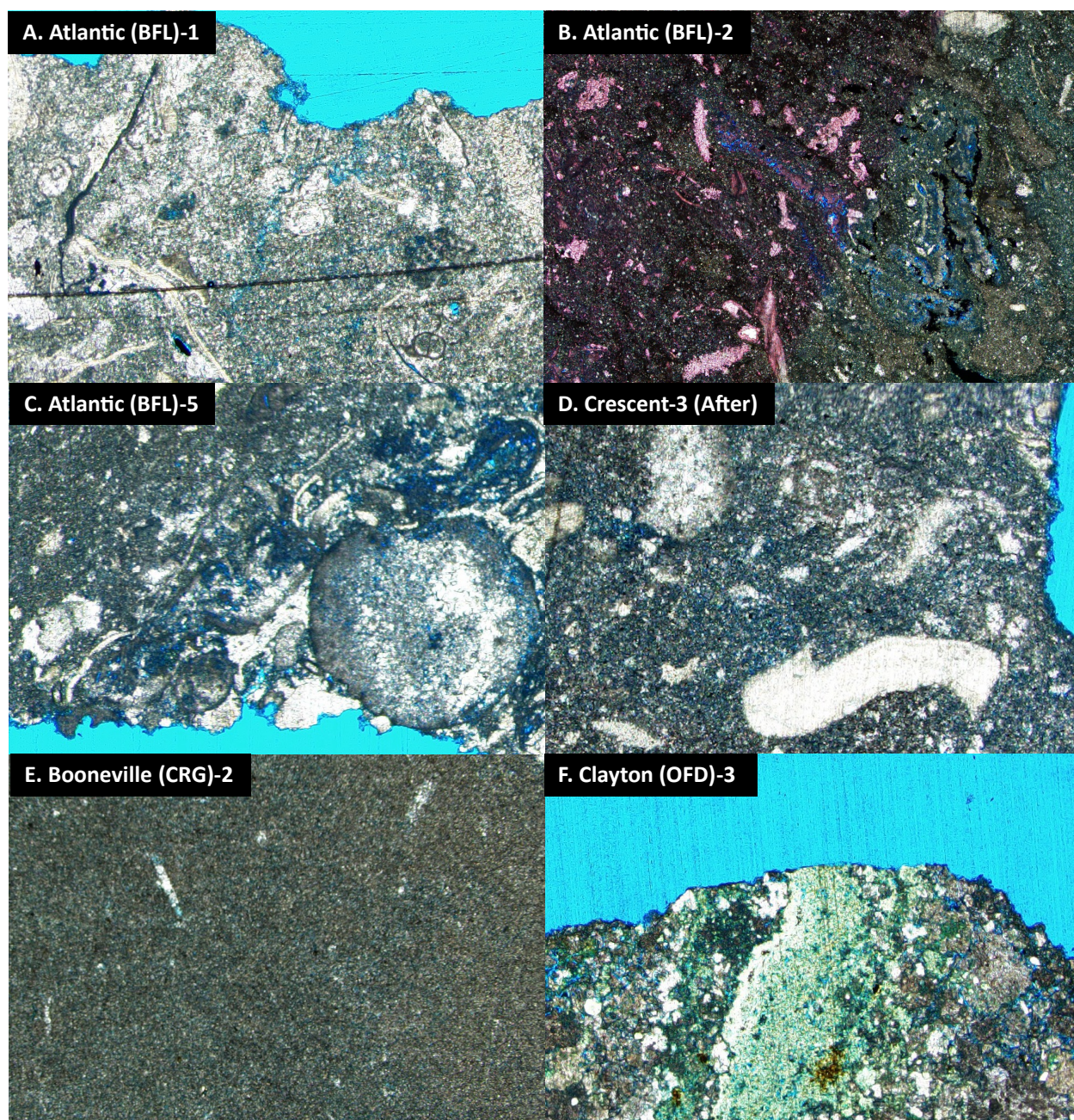


Figure 98. Examples of microporosity (highlighted by blue-dyed epoxy) manifesting as a hazy matrix between grains

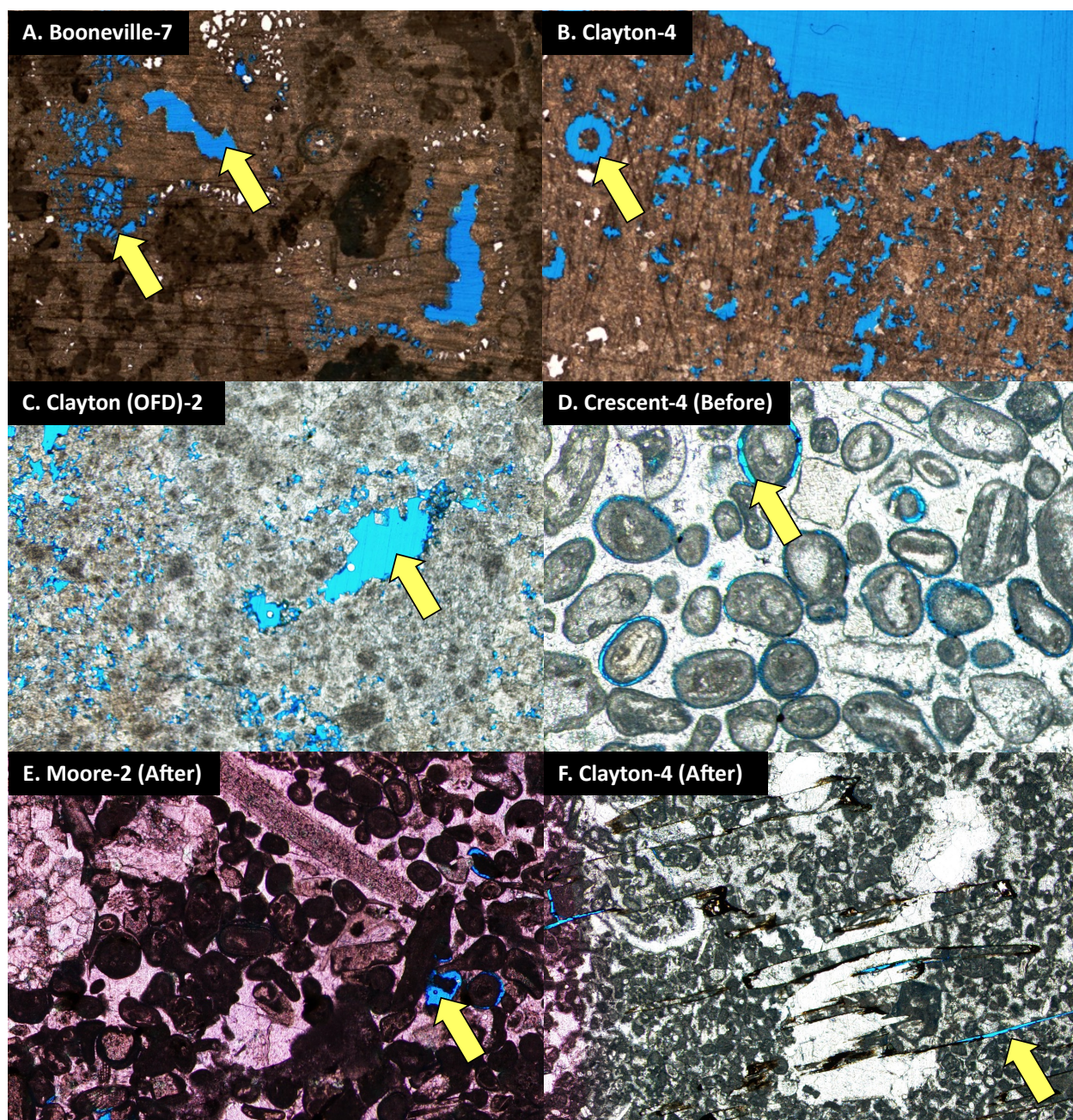


Figure 99. Examples of separate vuggy pore space (highlighted by blue-dyed epoxy) manifesting as pore spaces between sedimentary grains either completely disconnected from other pores or only connected through a microporous matrix

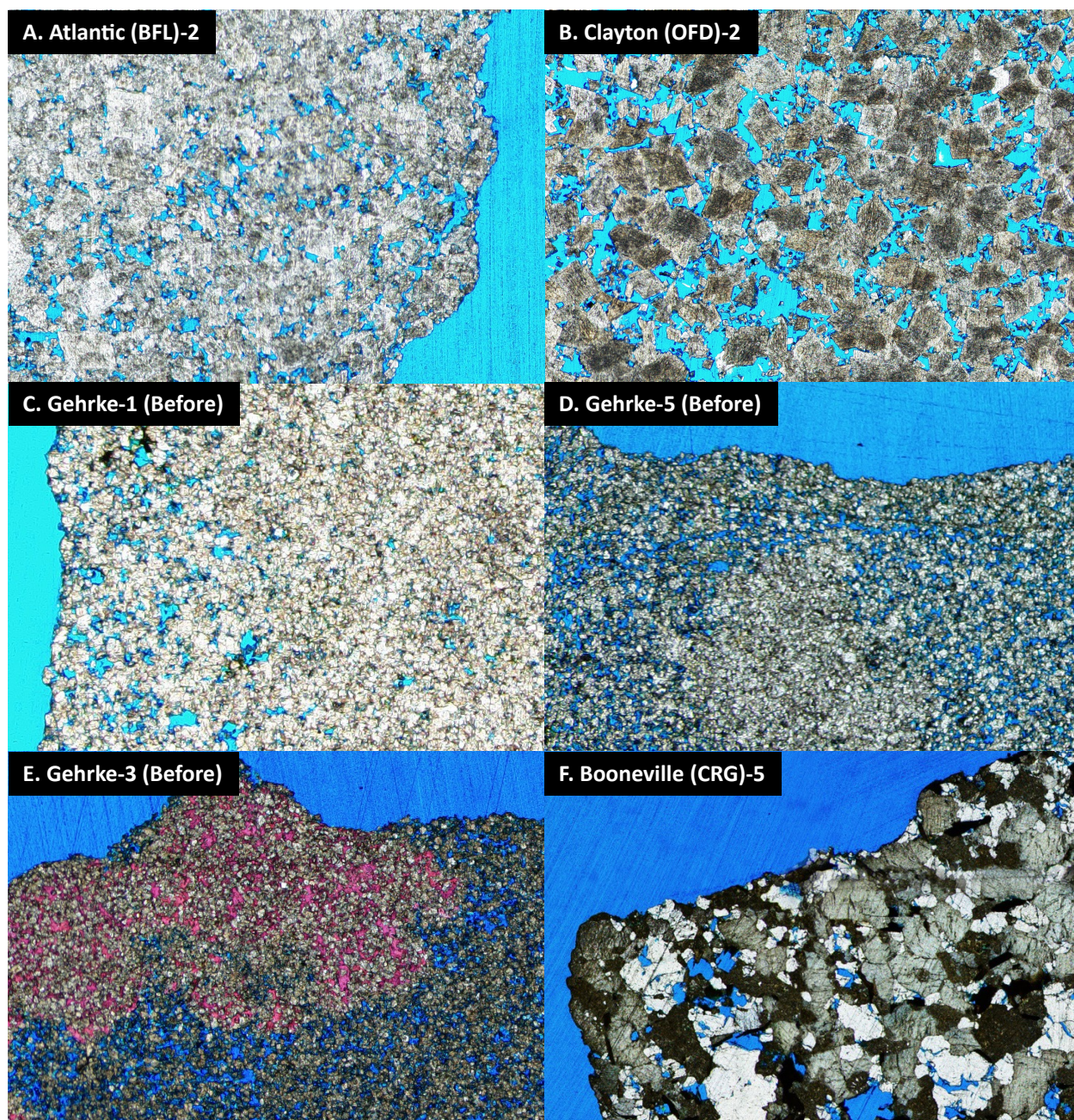


Figure 100. Examples of intercrystalline pore space

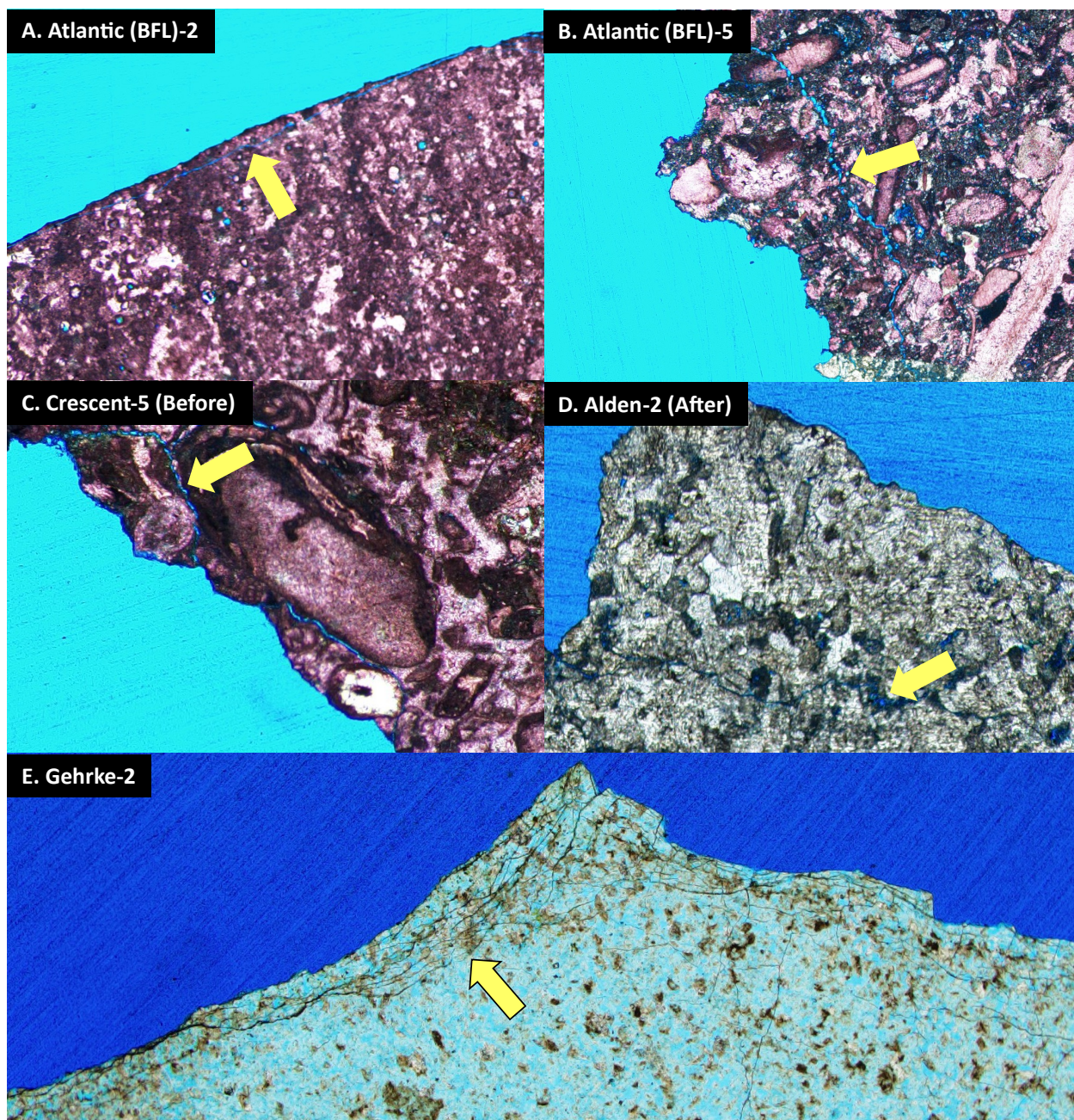


Figure 101. Hairline fractures parallel to particle edges visible in various rock types before and after compaction

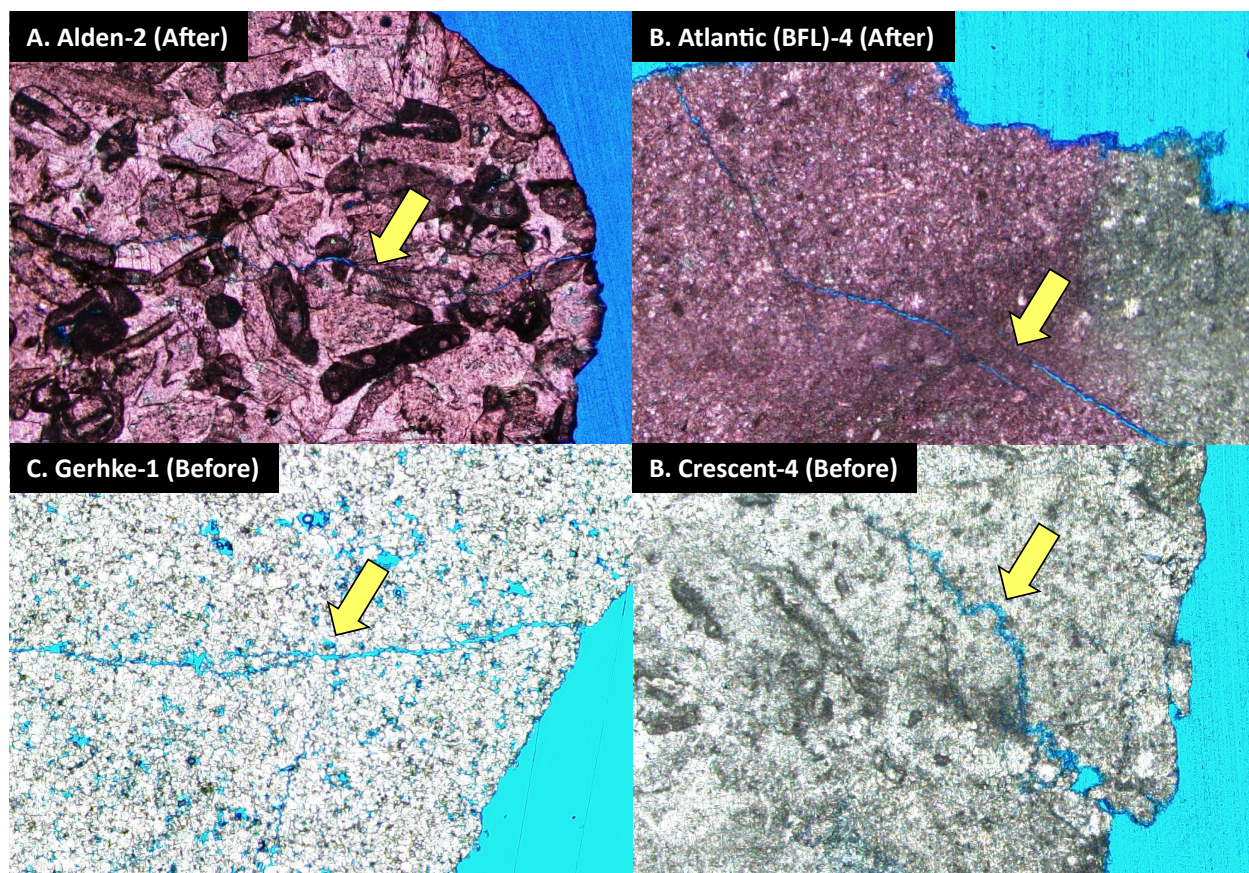


Figure 102. Hairline fractures perpendicular to particle edges visible in numerous rock types before and after gyratory compaction

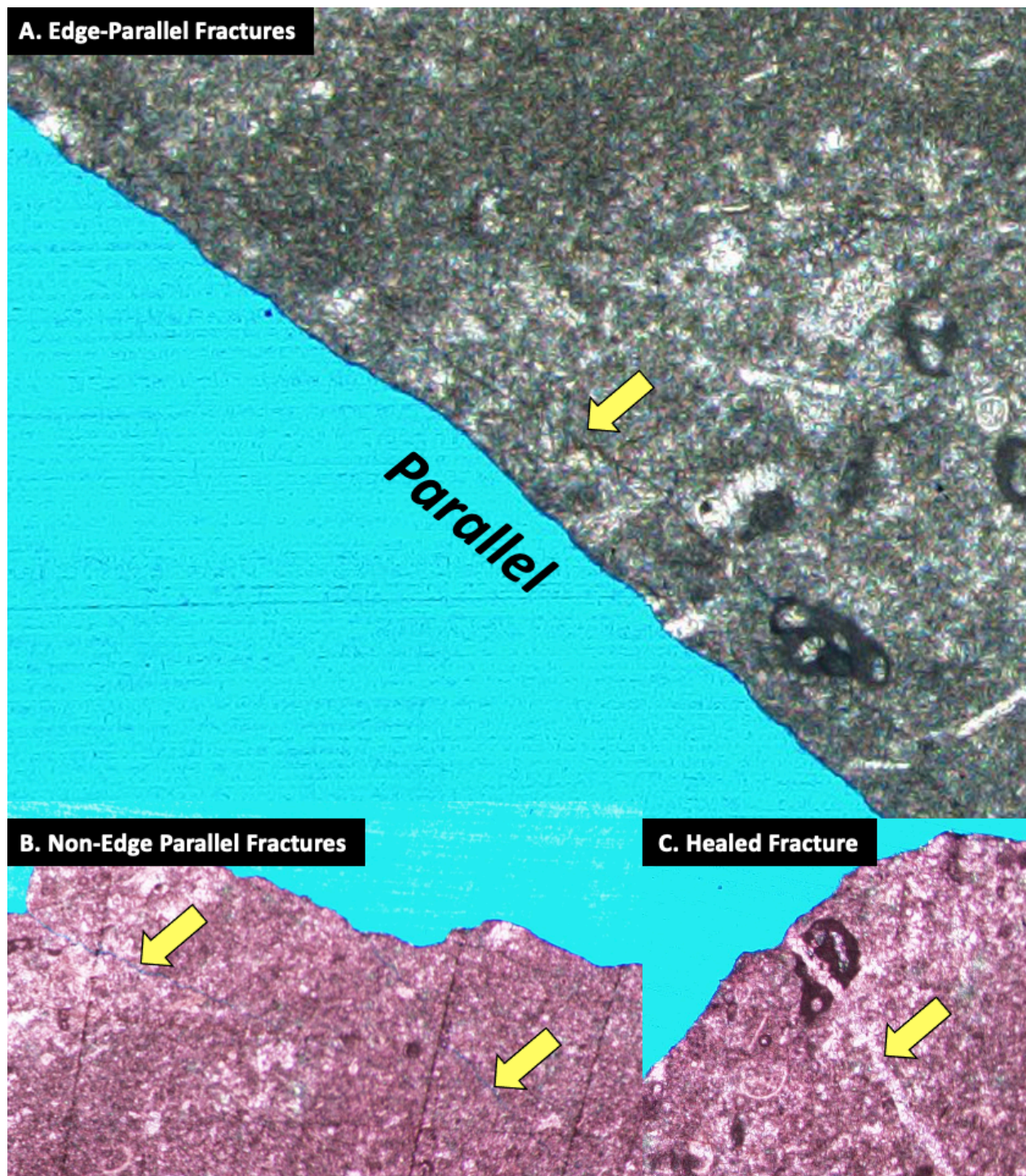


Figure 103. Hairline fractures parallel (A) and nonparallel (B) to particle edges in Crescent Rock Type 1 after gyratory compaction. Evidence of healed fractures from before quarrying (C) were also visible.

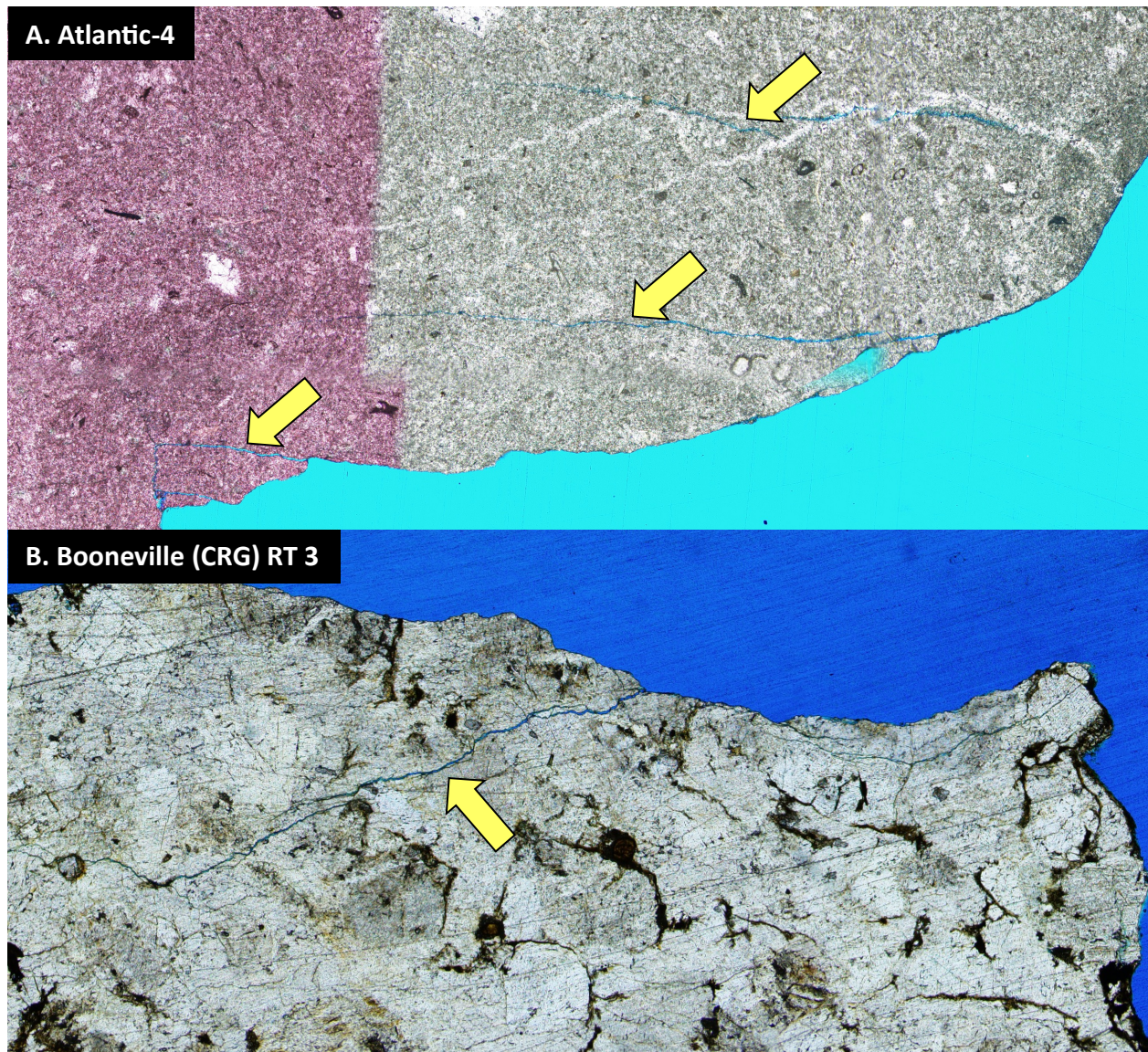


Figure 104. Multiple hairline fractures extending oblique from particle edge in Atlantic (BFL) RT4 and Booneville (CRG) RT3

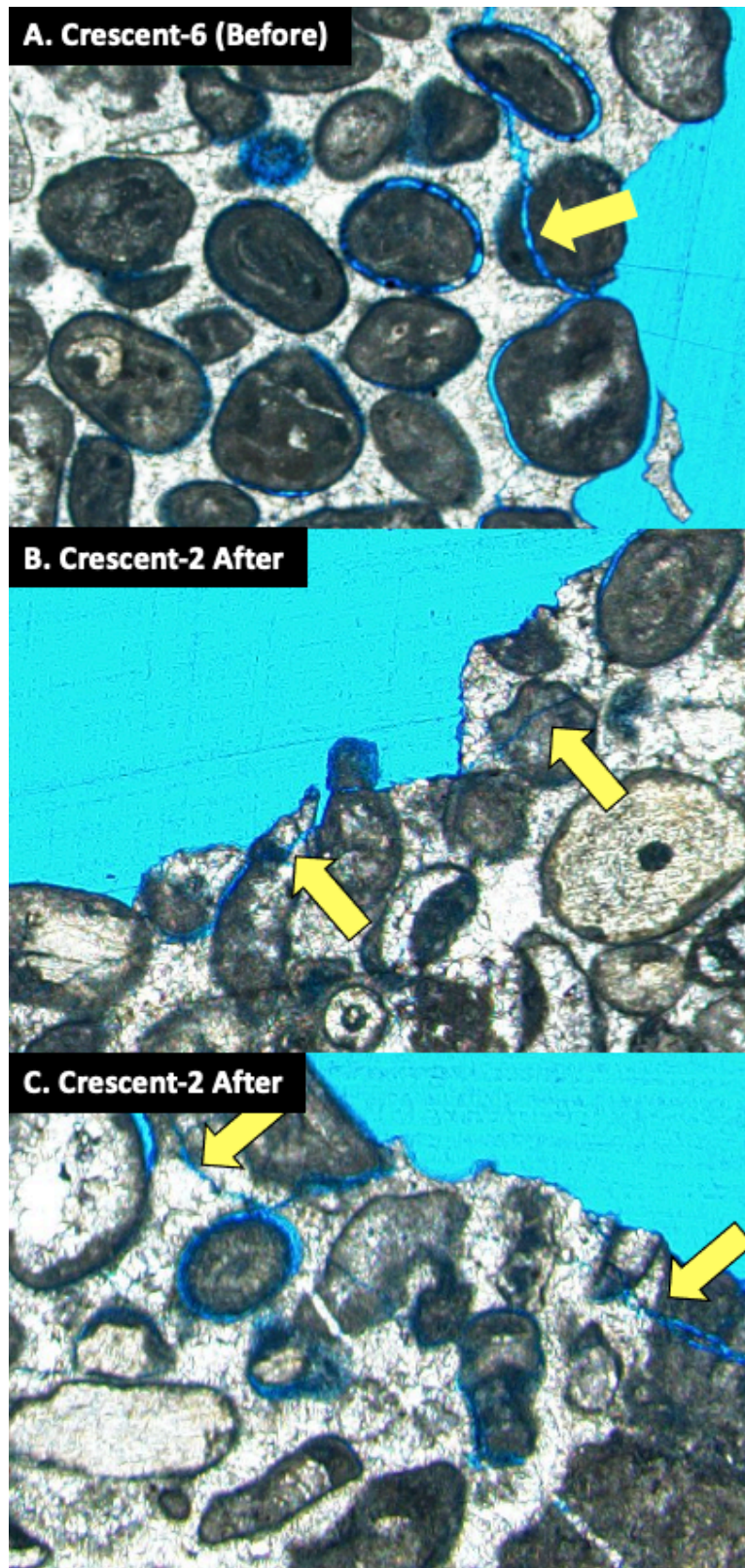


Figure 105. Grain-boundary hugging fractures visible in Crescent RT6 (BGT) and Crescent RT2 (AGT)

4.2 Coarse Aggregate Samples Collected from Test Sections of IHRB Project TR-704

4.2.1 *Bethany Falls Limestone (BFL) Class A Aggregates*

As part of the previous long-term IHRB Project TR-704, a 500 ft long and 4 in. thick test section was constructed at the project site on County Road J22 / Popcorn Road in Decatur County, Iowa utilizing Bethany Falls Limestone (BFL) Class A aggregates. The section was constructed in September 2016, after which maintenance was conducted in May 2017 and again in May 2018. The maintenance procedures consisted of placing new Class A material on top of the existing surface using dump trucks, then blade-mixing the new and existing surface materials together using a motor grader. Samples of the in-service surfacing materials from this section were collected over a period of two years during different phases: first in September 2016 after construction, then in April 2017 (following the first freeze-thaw season), then one month later in May 2017 (immediately after the first maintenance period), followed by June 2017, February 2018, April 2018 (after the second freeze-thaw season), May 2018 (after the second maintenance period) and finally April 2019 (after the third freeze-thaw season).

4.2.1.1 PSD Comparison and Evaluation of Breakage Parameters for BFL Class A Aggregates

To evaluate the mechanical degradation and material loss over time for the BFL test section, the data from the TR-704 project's final report was retrieved or otherwise digitized, and all available surplus BFL samples that were left over after completion of the TR-704 project were retrieved from storage for additional testing in the present project. During IHRB Project TR-704, samples were collected at five different points distributed over a given test section, then combined and mixed to obtain a representative sample for sieve analysis. For the surplus samples that could be located in the present study, new PSD curves were measured using laboratory sieve analyses and 2D image analyses. If surplus BFL materials could not be found for a given sampling date, then the PSD curves published in the TR-704 final report were digitized and analyzed instead. The mechanical degradation represented by Hardin's breakage parameters were then evaluated using the measured or digitized PSD curves for each test section.

Throughout this study, breakage of surface course materials from field test sections was calculated only for those time intervals in which the available records indicate no new maintenance aggregates were spread. The samples from the field test sections are thus assumed to represent the same material undergoing continual degradation over time. The validity of this assumption depends on the researchers' consistency in obtaining samples from similar locations each time, for example under a wheel path where the greatest degradation occurs as opposed to a shoulder where the least degradation occurs. The validity also depends on the accuracy of the maintenance records, because breakage can only be calculated for samples taken on two dates between which no new maintenance aggregates were spread. When records indicated that new maintenance aggregates were added, the breakage calculations were reset using the new reference date and the new PSD as the starting curve.

Specifically, the prior sieve analysis data from the TR-704 project was analyzed to calculate breakage for the samples collected in April 2017 relative to those collected just after construction

in September 2016 (Figure 106), for samples collected in June 2017 relative to those collected right after the first maintenance in May 2017 (Figure 107), and for samples collected in April 2019 relative to those collected after the second round of maintenance in May 2018 (Figure 108). These figures reveal that a large degree of breakage occurred within the first month of spreading the fresh aggregates in 2017 ($B_i=0.34$ in Figure 107), which was expected. Conversely, only a small amount of breakage was observed in the 12 months following the addition of fresh maintenance aggregates in May 2018 through April 2019 ($B_i=0.01$ in Figure 108), which was unexpected.

For the surplus samples retrieved from storage, breakage parameters were evaluated by 2D image analyses of particles individually arranged on the glass bed of a high-resolution document scanner as detailed in Section 3.2.2. Due to the time consuming nature of such tests, only the gravel-sized fraction of the specimens were scanned, requiring dozens of separate scans per sample. Therefore, the breakage parameters calculated from the PSDs based on image analysis apply only to the gravel (plus No. 4) fraction and are not directly numerically comparable to those calculated for the gravel and sand (plus No. 200) fractions from sieve analyses. In the PSD plots, the total breakage is therefore shown by the shaded gray area enclosed between the two PSD curves for grain sizes larger than 0.075 mm for sieve analyses, and for grain sizes larger than 4.75 mm (#4 sieve) for 2D image analyses.

PSD curves and breakage parameters were analyzed from 2D scans of the samples collected in June 2017 (Figure 109), February 2018 (Figure 110), and April 2018 (Figure 111) relative to those collected right after the first maintenance in May 2017, and also for the samples collected in April 2019 (Figure 112) relative to those collected after the second maintenance in May 2018. Additional details on the gradations and breakage parameters based on sieve analyses are presented in Table 30, while those calculated by 2D image analyses are presented in Table 31. These tables convey the total breakage values for timespans in which no new aggregates were placed, the breakage potential and relative breakage, and the percentages and changes of gravel, sand, and fines. The gravel, sand, and fines percentages for the samples collected over time are also displayed in a bar chart in Figure 113. Although the breakage parameters calculated by sieve analysis and 2D image analysis correspond to different size ranges, they both indicate much greater breakage for the May 2017–June 2017 timespan than for May 2018–April 2019. The data are also presented graphically in Figure 114 and Figure 115, which contain bar charts of the total breakage by sieve analyses and 2D image analyses, respectively.

In general, the gravel fraction is expected to decrease continually with time as the gravel-sized particles break down into sand- and fines-sized particles. The sand fraction may increase or decrease depending on the rates at which gravel degrades into sand and sand degrades into fines. The fines fraction should theoretically increase over time as both the gravel- and sand-sized particles degrade, but may decrease if the rate at which fines are lost to dust and erosion is high enough.

For the September 2016–April 2017 timespan, Table 30 and Figure 113 illustrate that the gravel fraction decreased significantly by 14.6% while the sand and fines fractions increased by 9.6% and 5.0%, respectively. Similarly, for the May 2017–June 2017 timespan, the gravel fraction

decreased significantly by 21.6% while the sand and fines fractions increased by 14.6% and 7.0%, respectively. However, for the May 2018–April 2019 timespan there was only a small 0.8% decrease in the gravel fraction accompanied by similarly small 0.8% and 0.1% increases in the sand and fines fractions. The data therefore indicates a decreasing trend in the gravel fraction and increasing trends for the sand and fines fractions for the samples collected after the first and second maintenance periods in May 2017 and May 2018, but relatively little change for subsequent samples.

The data in Table 30 and Figure 114 also show that the total breakage evaluated from sieve analyses produced valid positive values for the samples collected in April 2017, in June 2017 one month after the first maintenance period, and in April 2019 after the third freeze-thaw period. Similarly, Table 31 and Figure 114 illustrate that the total breakage evaluated from image analyses also exhibit positive values for all the time spans starting after the first maintenance period in June 2017. However, in both cases the total breakage decreases with time after June 2017, which is opposite the expected trend assuming no new materials were placed.

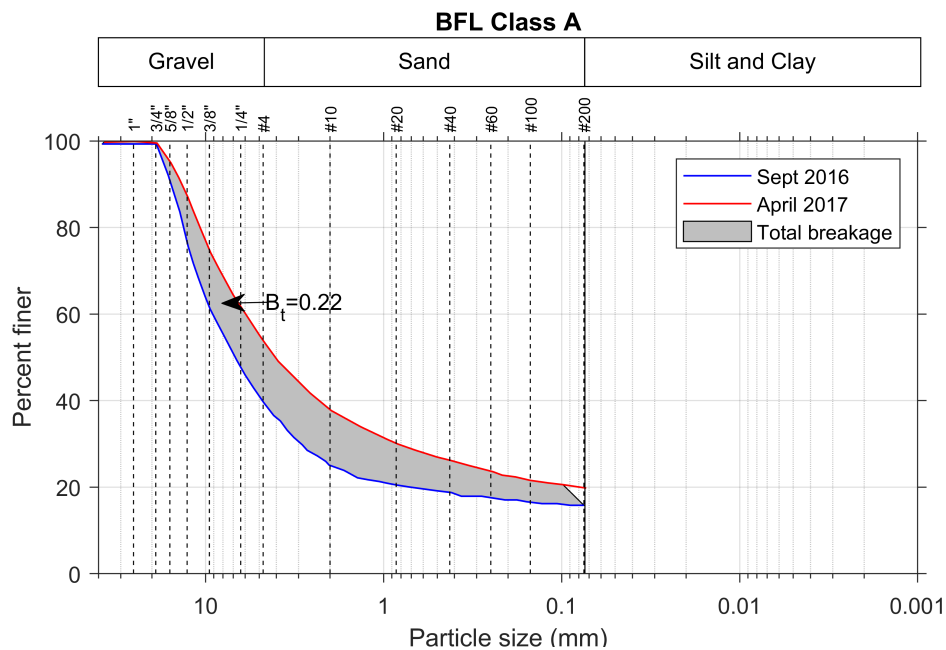


Figure 106. Particle size distributions of coarse fraction from sieve analysis and evaluation of total breakage between September 2016 and April 2017 for BFL Class A test section

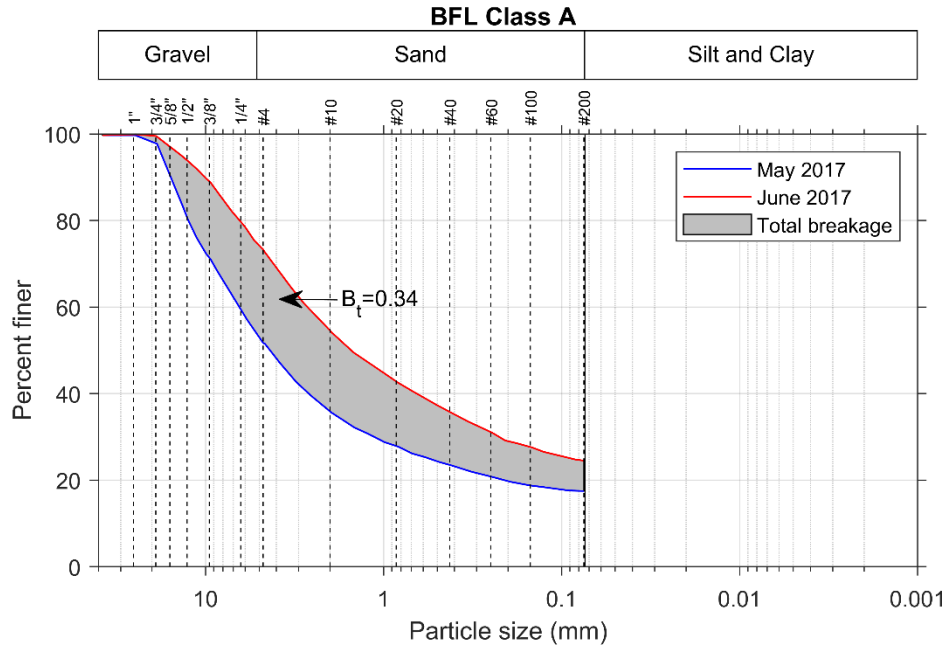


Figure 107. Particle size distributions of coarse fraction from sieve analysis and evaluation of total breakage between May 2017 and June 2017 for BFL Class A test section

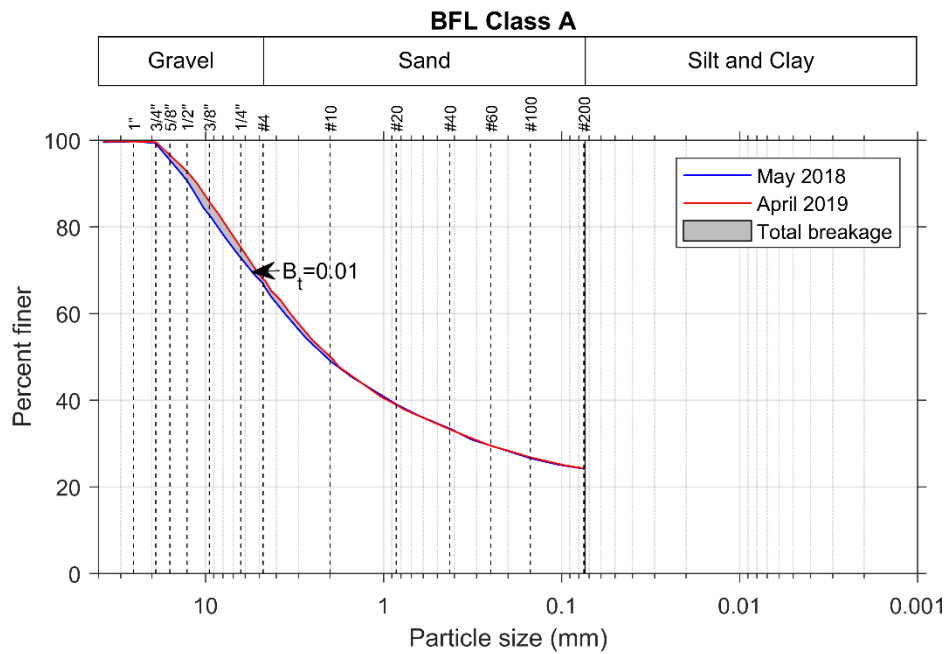


Figure 108. Particle size distributions of coarse fraction from sieve analysis and evaluation of total breakage between May 2018 and April 2019 for BFL Class A test section

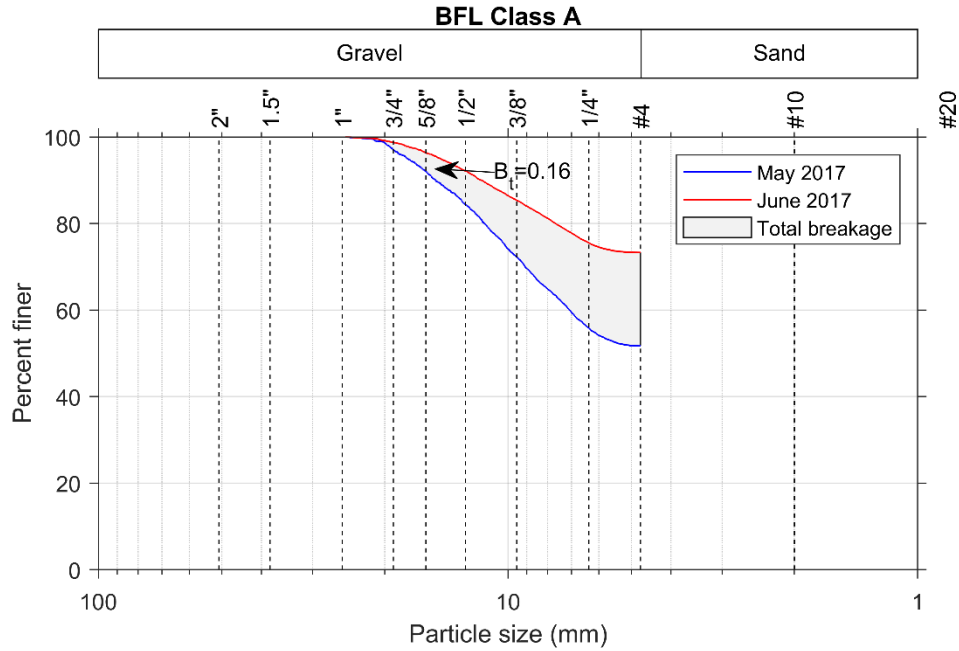


Figure 109. Particle size distributions of gravel fraction from 2D image analysis and evaluation of total breakage between May 2017 and June 2017 for BFL Class A test section

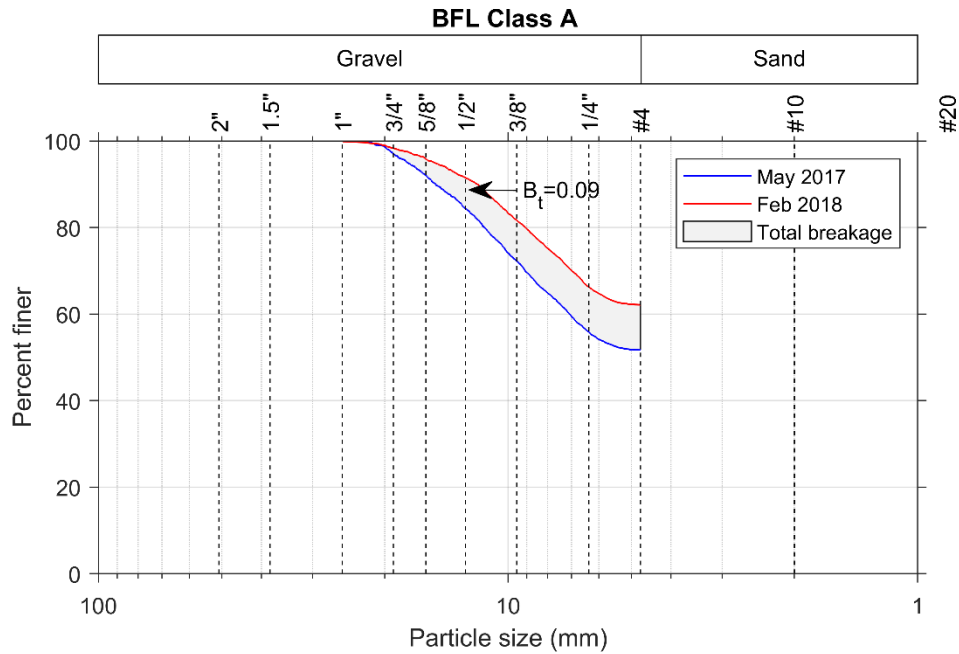


Figure 110. Particle size distributions of gravel fraction from 2D image analysis and evaluation of total breakage between May 2017 and February 2018 for BFL Class A test section

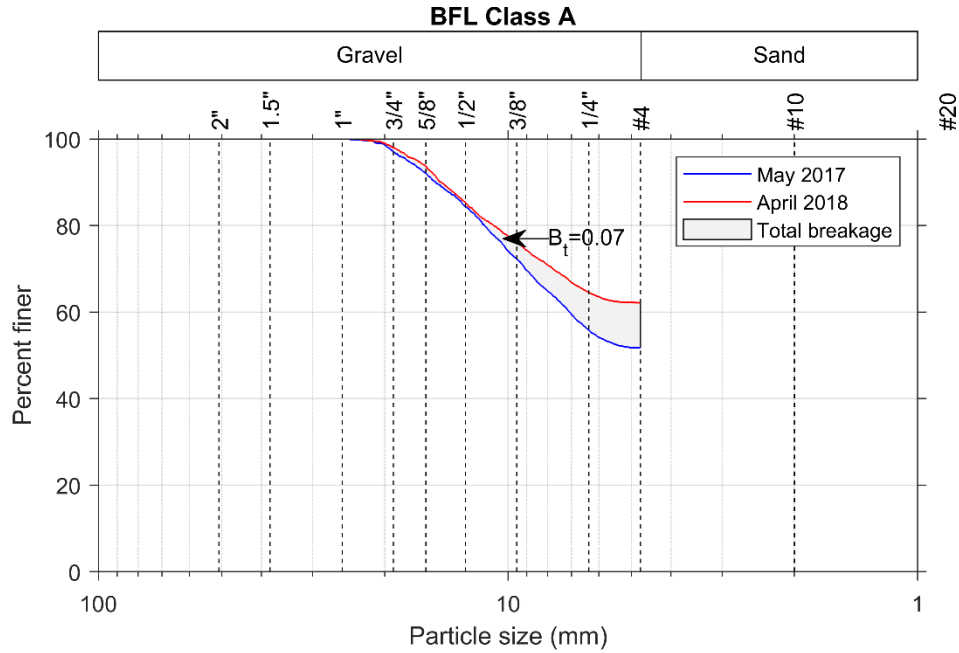


Figure 111. Particle size distributions of gravel fraction from 2D image analysis and evaluation of total breakage between May 2017 and April 2018 for BFL Class A test section

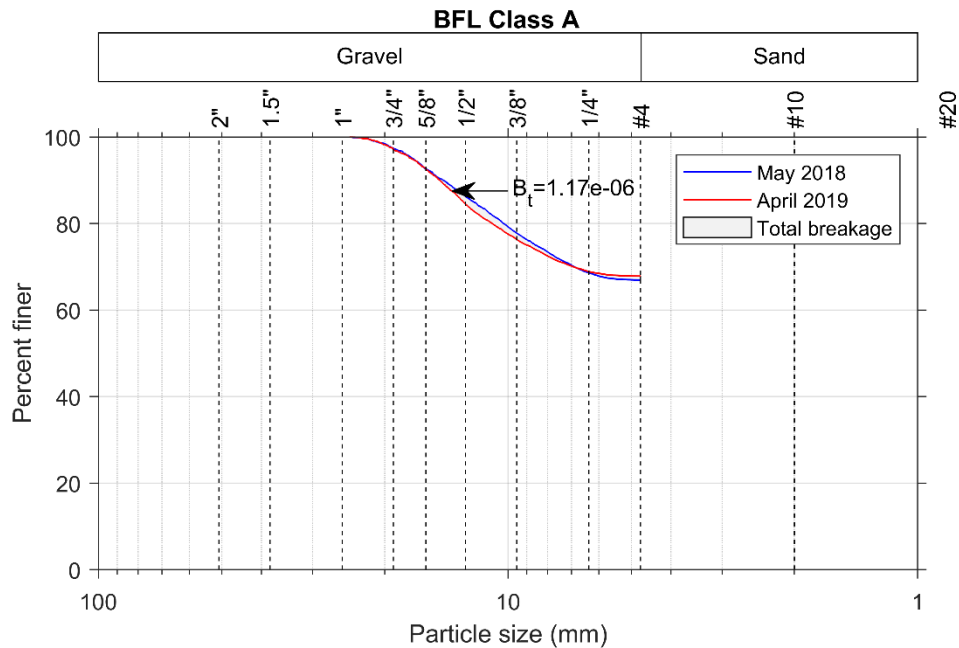


Figure 112. Particle size distributions of gravel fraction from 2D image analysis and evaluation of total breakage between May 2018 and April 2019 for BFL Class A test section

Table 30. Breakage parameters from sieve analysis and percent gravel, sand, and fines for BFL Class A samples collected over time

Sample Collection Date	Hardin's Breakage Parameters			% Gravel	% Gravel Red.**	% Sand	% Sand Inc. ††	% Fines	% Fines Inc.
	Total Breakage, B_t	Breakage Potential, B_p	Relative Breakage, B_r						
Sept 2016				61.0		24.1		15.0	
April 2017 ^a	0.2180	1.6106	0.1353	46.4	14.6	33.7	9.6	20.0	5.0
May 2017				48.3		34.2		17.5	
June 2017*	0.3436	1.4614	0.2351	26.7	21.6	48.8	14.6	24.5	7.0
April 2018*				37.9	10.4	40.1	5.9	22.0	4.5
May 2018*				33.0		42.8		24.2	
April 2019 [†]	0.0141	1.2004	0.0118	32.2	0.8	43.6	0.8	24.3	0.1

^a w.r.t. Sep 2016, * w.r.t. May 2017, [†] w.r.t. May 2018, ** Reduction, †† Increase

Table 31. Breakage parameters from 2D image analyses for BFL Class A samples collected over time

Sample Collection Date	Hardin's Breakage Parameters		
	Total Breakage, B_t	Breakage Potential, B_p	Relative Breakage, B_r
May 2017			
June 2017*	0.1634	0.3598	0.4543
Feb 2018*	0.0918	0.3598	0.2552
April 2018*	0.0701	0.3598	0.1949
May 2018			
April 2019 [†]	1.17E-06	0.2586	4.53E-06

* w.r.t. May 2017, [†] w.r.t. May 2018

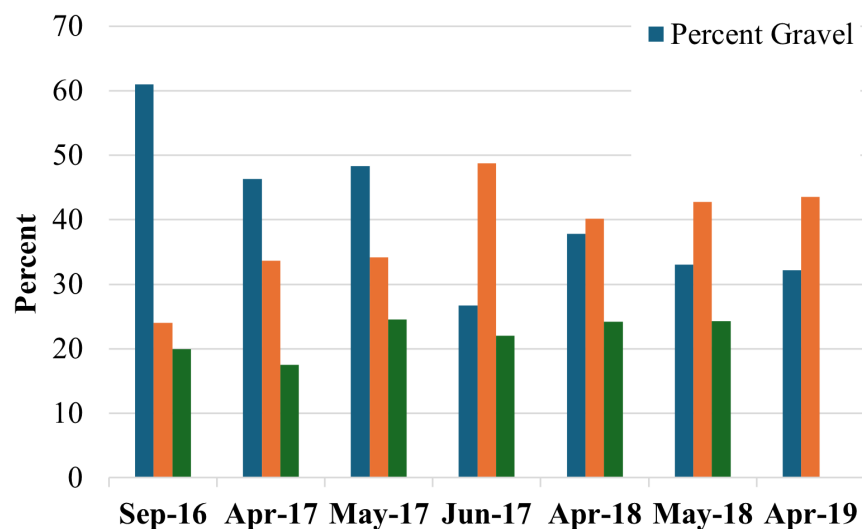


Figure 113. Percent gravel, sand, and fines for samples of BFL Class A collected over time

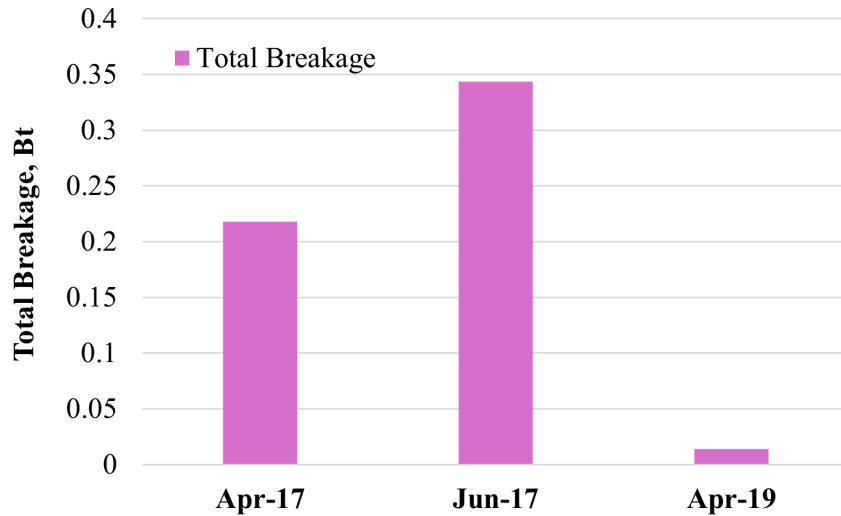


Figure 114. Total breakage of coarse fraction evaluated from sieve analyses of samples from BFL Class A section collected over time

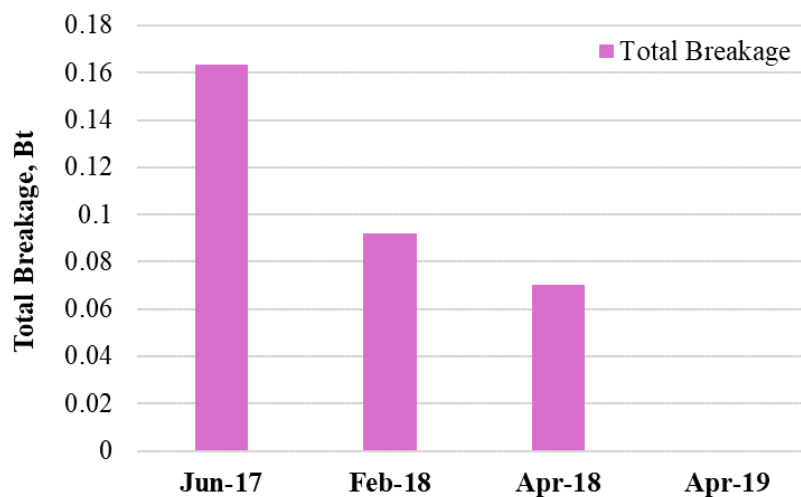


Figure 115. Total breakage of gravel fraction evaluated from 2D image analyses of samples from BFL Class A section collected over time

4.2.1.2 Comparison of Morphological Parameters from 2D Image Analyses for BFL Class A

In addition to quantifying breakage, the extensive image analyses were also used to determine changes in particle morphology over time. The specific morphological parameters evaluated are presented in Figure 116 through Figure 121. The parameters include roundness, sphericity, form factor, shape factor, roundness index, and angularity. The statistical output of these morphological parameters is summarized in Table 32. Relative to the samples collected after the first maintenance period of May 2017, the data reveal an increase in median particle sphericity of 0.2% by June 2017 and 1.1% by April 2018. This indicates that the particles generally became more spherical with time as their deterioration continued.

For the morphological parameters other than sphericity, Table 32 reveals that the samples collected in June 2017, February 2018 and April 2018 did not consistently exhibit morphological degradation relative to those collected after the first maintenance period in May 2017. However, the sample collected in April 2018 did show morphological degradation when compared to the February 2018 samples, via increases in median roundness, sphericity, and form factor of 1.5%, 2.1%, and 48.5%, respectively. These changes were accompanied by decreases in median shape factor, roundness index, and angularity values of 32.7%, 15.9%, and 9.8%, respectively. The samples collected after the second year's maintenance period in April 2019 showed clear morphological degradation, with increases in median roundness and form factor of 0.2% and 7.2% respectively, accompanied by decreases in median shape factor, roundness index, and angularity values by 6.7%, 2.5%, and 7.3%, respectively, compared to the samples from May 2018.

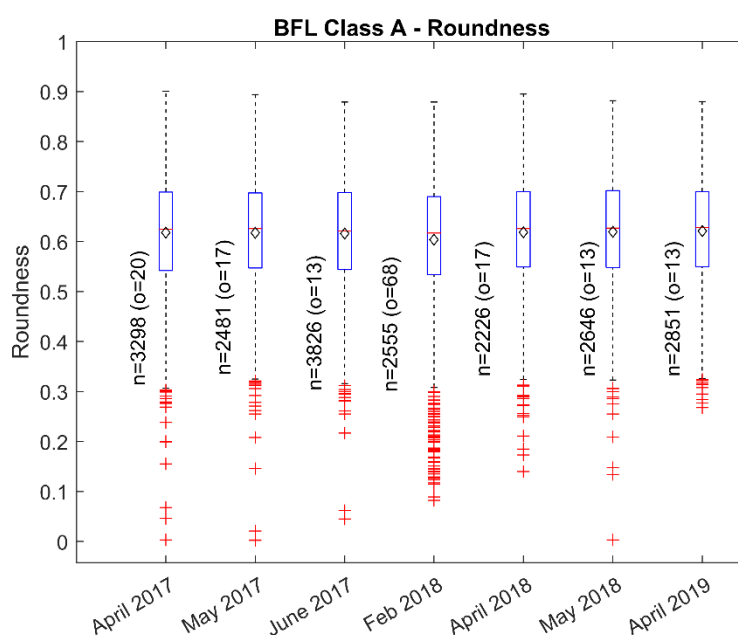


Figure 116. Comparison of roundness for BFL Class A samples collected over time

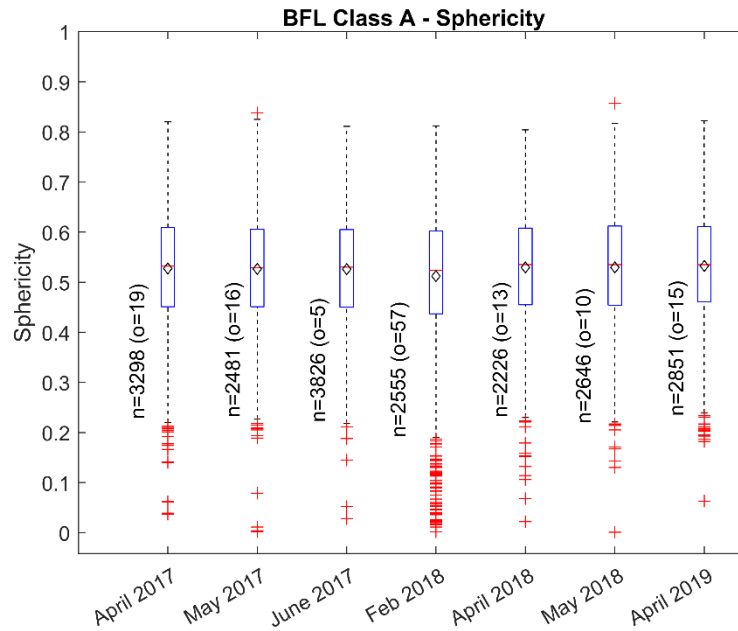


Figure 117. Comparison of sphericity for BFL Class A samples collected over time

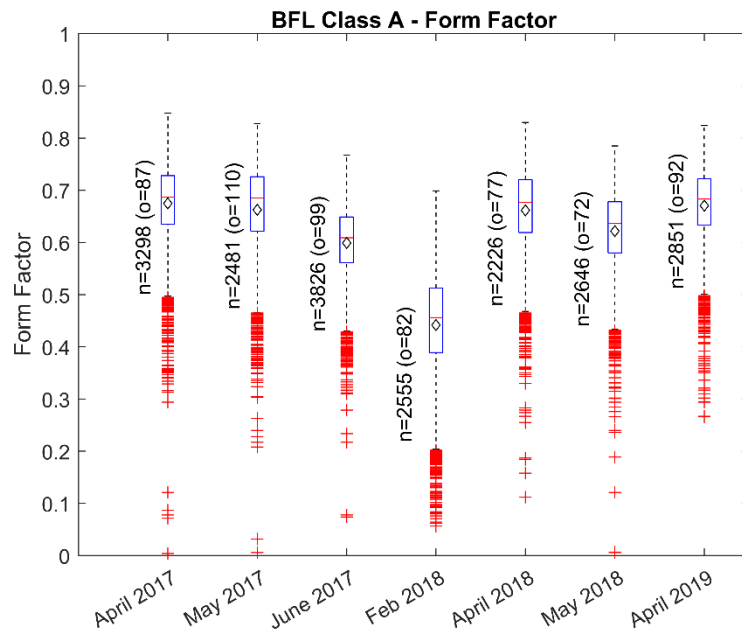


Figure 118. Comparison of form factor for BFL Class A samples collected over time

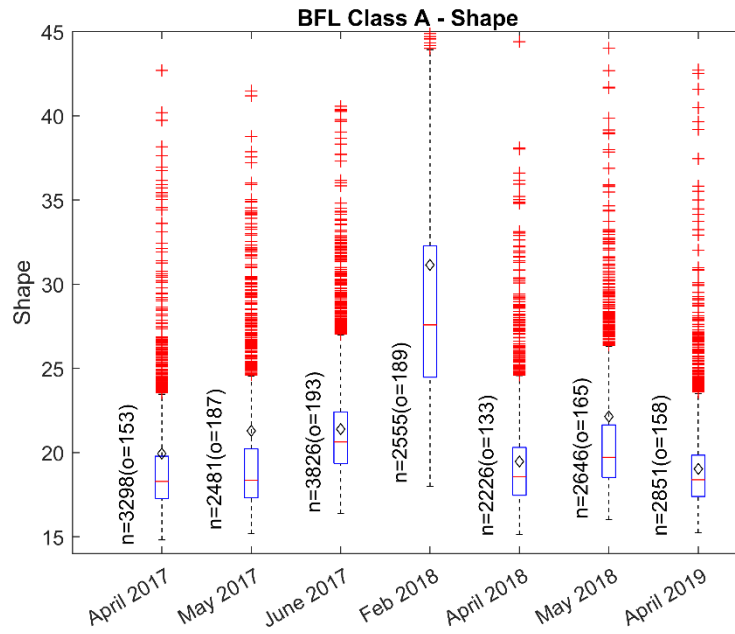


Figure 119. Comparison of shape factor for BFL Class A samples collected over time

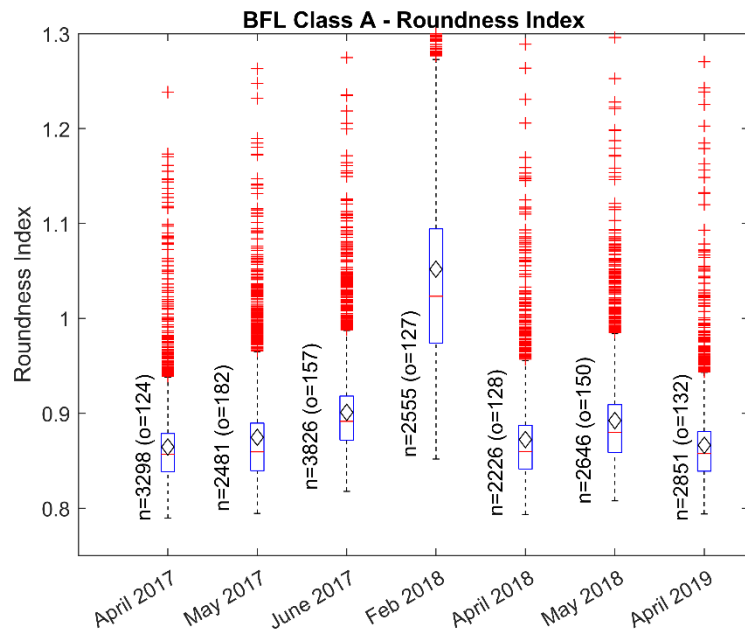


Figure 120. Comparison of roundness index for BFL Class A samples collected over time

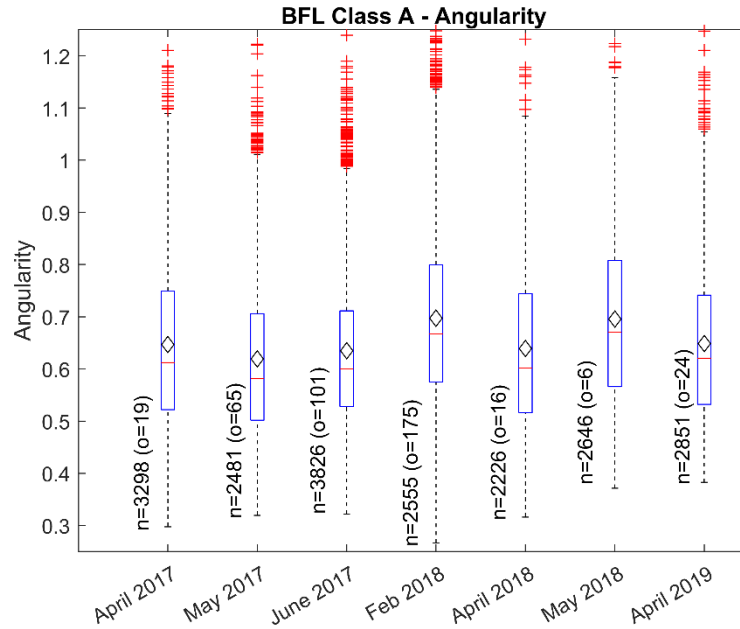


Figure 121. Comparison of angularity for BFL Class A samples collected over time

Table 32. Statistical results of morphological parameters of BFL Class A

Parameter	Sample Collection Date	Max. Value	Min. Value	Mean	Mode	Median	Std. Dev.	Skew-ness	Kurt-osis	Out-liers
Roundness	April 2017	0.901	0.003	0.618	0.602	0.625	0.113	-0.417	3.345	20
	May 2017	0.894	0.002	0.617	0.591	0.626	0.113	-0.492	3.734	17
	June 2017	0.879	0.045	0.616	0.626	0.621	0.109	-0.33	2.978	13
	% inc. *			-0.2%		-0.8%				
	Feb 2018	0.879	0.082	0.604	0.681	0.617	0.128	-0.883	4.42	68
	% inc. *			-2.1%		-1.4%				
	April 2018	0.895	0.14	0.618	0.668	0.626	0.112	-0.436	3.13	17
	% inc. *			0.2%		0.0%				
	% inc. **			2.3%		1.5%				
	May 2018	0.882	0.003	0.619	0.604	0.627	0.111	-0.481	3.511	13
	April 2019	0.88	0.268	0.621	0.606	0.628	0.108	-0.348	2.758	13
	% inc. †			0.3%		0.2%				

Parameter	Sample Collection Date	Max. Value	Min. Value	Mean	Mode	Median	Std. Dev.	Skew- ness	Kurt- osis	Out- liers
Sphericity	April 2017	0.82	0.037	0.528	0.529	0.532	0.114	-0.273	3.006	19
	May 2017	0.838	0.002	0.526	0.504	0.529	0.113	-0.304	3.29	16
	June 2017	0.811	0.028	0.526	0.511	0.530	0.11	-0.21	2.775	5
	% inc. *			0%		0.2%				
	Feb 2018	0.812	0.002	0.512	0.537	0.524	0.13	-0.803	4.322	57
	% inc. *			-2.7%		-1.0%				
	April 2018	0.804	0.022	0.529	0.508	0.535	0.113	-0.364	3.183	13
	% inc. *			0.6%		1.1%				
	% inc. **			3.3%		2.1%				
	May 2018	0.857	0.001	0.529	0.549	0.535	0.113	-0.314	2.988	10
	April 2019	0.822	0.063	0.532	0.534	0.535	0.109	-0.27	2.904	15
	% inc. †			0.6%		0.0%				
Form Factor (FF)	April 2017	0.848	0.004	0.675	0.71	0.687	0.079	-1.58	9.47	87
	May 2017	0.828	0.006	0.663	0.73	0.685	0.094	-1.493	6.992	110
	June 2017	0.767	0.074	0.599	0.64	0.609	0.072	-1.071	5.592	99
	% inc. *			-9.7%		-11.1%				
	Feb 2018	0.699	0.057	0.442	0.437	0.456	0.101	-0.895	4.029	82
	% inc. *			-33.3%		-33.4%				
	April 2018	0.83	0.112	0.661	0.708	0.677	0.085	-1.419	6.642	77
	% inc. *			-0.3%		-1.2%				
	% inc. **			49.6%		48.5%				
	May 2018	0.785	0.006	0.622	0.625	0.637	0.083	-1.339	6.869	72
	April 2019	0.824	0.266	0.671	0.683	0.683	0.076	-1.191	5.485	92
	% inc. †			7.9%		7.2%				
Shape Factor (SF)	April 2017	2971	14.81	19.93	17.02	18.29	51.67	56.54	3229	153
	May 2017	2249	15.18	21.29	17.19	18.35	61.05	34.42	1205	187
	June 2017	168.8	16.38	21.39	19.96	20.63	4.5	17.9	550.8	193
	% inc. *			0.5%		12.4%				
	Feb 2018	220.2	17.98	31.14	22.12	27.58	14.61	5.67	49.5	189
	% inc. *			46.3%		50.3%				
	April 2018	111.9	15.14	19.46	18.06	18.56	4.2	8.78	146.3	133
	% inc. *			-8.6%		1.1%				
	% inc. **			-37.5%		-32.7%				
	May 2018	2228	16.02	22.15	18.03	19.72	54.95	36.75	1375	165
	April 2019	47.2	15.25	19.03	17.28	18.39	2.76	3.3	22.9	158
	% inc. †			-14.1%		-6.7%				

Parameter	Sample Collection Date	Max. Value	Min. Value	Mean	Mode	Median	Std. Dev.	Skew-ness	Kurt-osis	Out-liers
Roundness Index (RI)	April 2017	1.483	0.79	0.865	0.828	0.857	0.044	3.645	30.59	124
	May 2017	1.444	0.795	0.875	0.828	0.859	0.058	2.768	15.92	182
	June 2017	1.31	0.818	0.901	0.869	0.891	0.046	2.209	12.28	157
	% inc. *			3.0%		3.7%				
	Feb 2018	2.143	0.852	1.052	0.993	1.023	0.12	2.35	13.14	127
	% inc. *			20.2%		19.1%				
	April 2018	1.452	0.793	0.872	0.815	0.86	0.053	3.203	21.47	128
	% inc. *			-0.3%		0.1%				
	% inc. **			-17.1%		-15.9%				
	May 2018	1.328	0.808	0.892	0.869	0.88	0.053	2.386	12.34	150
	April 2019	1.27	0.794	0.866	0.828	0.858	0.044	2.882	18.11	132
	% inc. †			-2.9%		-2.5%				
Angularity	April 2017	1.387	0.298	0.647	0.637	0.612	0.158	0.742	2.952	19
	May 2017	1.6	0.319	0.619	0.514	0.581	0.156	1.188	4.888	65
	June 2017	1.263	0.218	0.635	0.469	0.6	0.144	1	3.721	101
	% inc. *			2.6%		3.3%				
	Feb 2018	1.752	0.064	0.697	0.116	0.667	0.209	0.423	5.69	175
	% inc. *			12.6%		14.8%				
	April 2018	1.411	0.316	0.639	0.437	0.602	0.155	0.814	3.186	16
	% inc. *			3.2%		3.6%				
	% inc. **			-8.3%		-9.8%				
	May 2018	1.298	0.371	0.696	0.472	0.67	0.162	0.546	2.662	6
	April 2019	1.38	0.383	0.649	0.441	0.621	0.152	0.822	3.363	24
	% inc. †			-6.8%		-7.3%				

* w.r.t. May 2017, ** w.r.t. Feb 2018, †w.r.t. May 2018

For the samples collected after the first maintenance period in May 2017, the reduction in gravel fraction with accompanying increases in sand and fines fractions observed in the June 2017 and April 2018 samples (Table 30), along with positive values of Hardin's total breakage by 2D image analyses seen in the samples from June 2017, February 2018, and April 2018 (Table 31) also show degradation of the aggregate materials with time.

For the samples collected after the second maintenance period in May 2018, the reduced gravel fraction and increased sand and fines fractions observed in the May 2018–April 2019 timeframe indicate the breakdown of gravel into sand and finer particles (Table 30). Also, a positive value of Hardin's total breakage is seen in the samples collected in April 2019, as shown by both 2D image analyses and sieve analyses as previously discussed. Additionally, changes in the morphological parameters for the samples collected in April 2019 compared to May 2018 (Table 32) show an increase in median roundness and form factor, and a decrease in median shape factor, roundness index, and angularity, indicating degradation of the samples by April 2019.

4.2.1.3 Geological Tests for BFL Class A and Clean Samples

Geological tests were conducted on the surplus material samples collected from the BFL Class A section in April, May, and June of 2017, as well as in April and May of 2018, and April 2019. These tests identified five distinct rock types for the BFL Class A materials, as well as their relative abundances which varied over time as the five rock types degraded at different rates. Figure 122 and Table 33 display the percentages of these rock types in the BFL Class A samples over time, while Table 33 also reports the percentage changes in the rock types over time. Relative to the first maintenance period in May 2017, the data reveal that Rock Type 1 decreased by 6.1% by June 2017 and increased by 2.0% by April 2018. Additional aggregates were then spread during the maintenance performed in May 2018, after which the abundance of Rock Type 1 decreased by 5.3% by April 2019.

Similarly, Rock Type 2 first appeared in the sample taken after the first maintenance operation in May 2017, then increased by 15.5% in June 2017 and by 1.3% in April 2018 compared to the first maintenance period in May 2017, and further increased by 4.9% in April 2019 compared to the second maintenance period in May 2018. Rock Type 3 decreased by 7.8% in June 2017 and increased by 2.0% in April 2018 relative to the first maintenance period in May 2017, and it didn't show a change by April 2019 relative to the second maintenance period in May 2018. Relative to the first maintenance period in May 2017, Rock Type 4 decreased by 0.9% as of June 2017 and by 7.3% as of April 2018. RT4 also decreased by 5.8% in April 2019 compared to the second maintenance period in May 2018. Rock Type 5 decreased by 0.7% in June 2017 and increased by 2.0% in April 2018 compared to the first maintenance period, however it showed a significant increase of 6.2% for the samples collected in April 2019 relative to the second maintenance period in May 2018. Hence, overall Rock Types 2 and 5 generally showed an increasing trend with time, while Rock Types 1 and 4 showed a decreasing trend with time.

Beyond the in-service test section's samples described up to this point, additional samples of Clean and Class A materials collected from the Atlantic Quarry at the start of the previous TR-704 project were retrieved from storage and tested (Figure 123). Both the Clean and Class A quarry samples had five rock types, which spanned from mud-rich lime packstones to lime wackestones. All were nonporous. A difference was evident in the abundance of the muddier rock types (RT2 and RT3), with a total abundance of 31% for RT2 and RT3 in the Clean sample, compared to only 10% for RT2 with an absence of RT3 in the Class A sample.

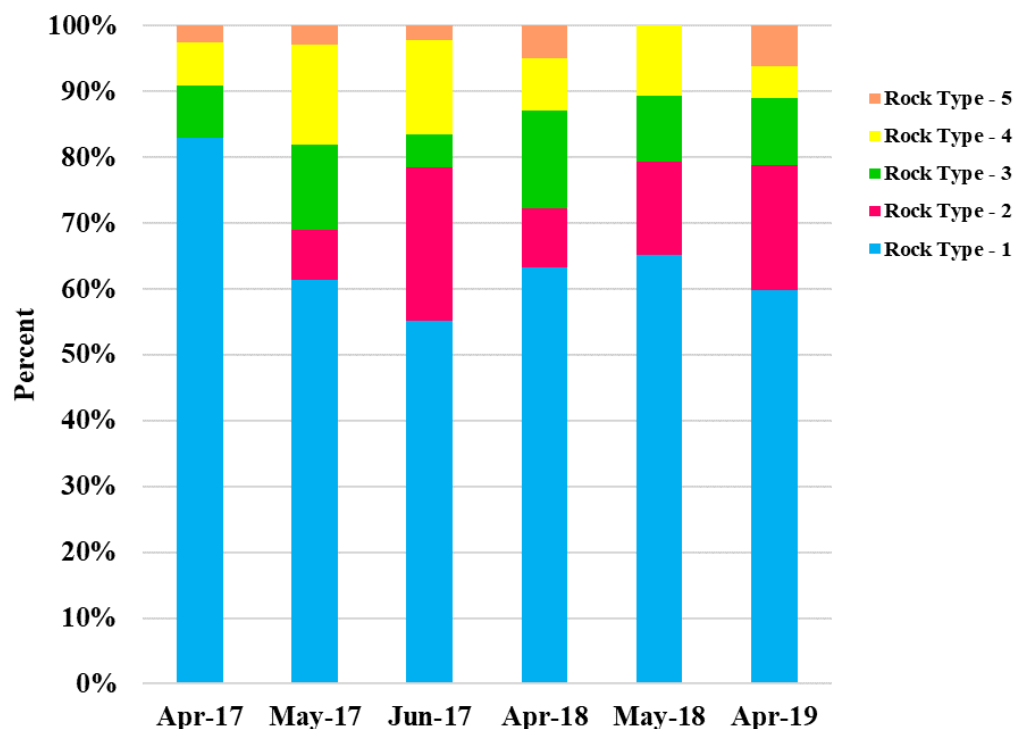


Figure 122. Percentages of rock types in BFL Class A samples collected over time

Table 33. Geological rock types and percent increase in rock types for the BFL Class A samples collected over time

Sample Collection Date	% Rock Type -1 (RT-1)	%Inc. ** in RT-1	% Rock Type -2 (RT-2)	%Inc. ** in RT-2	% Rock Type -3 (RT-3)	Inc. ** in RT-3	% Rock Type -4 (RT-4)	%Inc. ** in RT-4	% Rock Type -5 (RT-5)	%Inc. ** in RT-5
April 2017	83.0		0.0		7.9		6.6		2.5	
May 2017	61.3		7.7		12.9		15.2		2.9	
June 2017*	55.2	-6.1	23.2	15.5	5.1	-7.8	14.3	-0.9	2.2	-0.7
April 2018*	63.3	2.0	9.0	1.3	14.9	2.0	7.9	-7.3	4.9	2.0
May 2018	65.1		14.2		10.1		10.6		0.0	
April 2019†	59.8	-5.3	19.1	4.9	10.1	0.0	4.8	-5.8	6.2	6.2

* w.r.t. May 2017, †w.r.t. May 2018, ** Increase

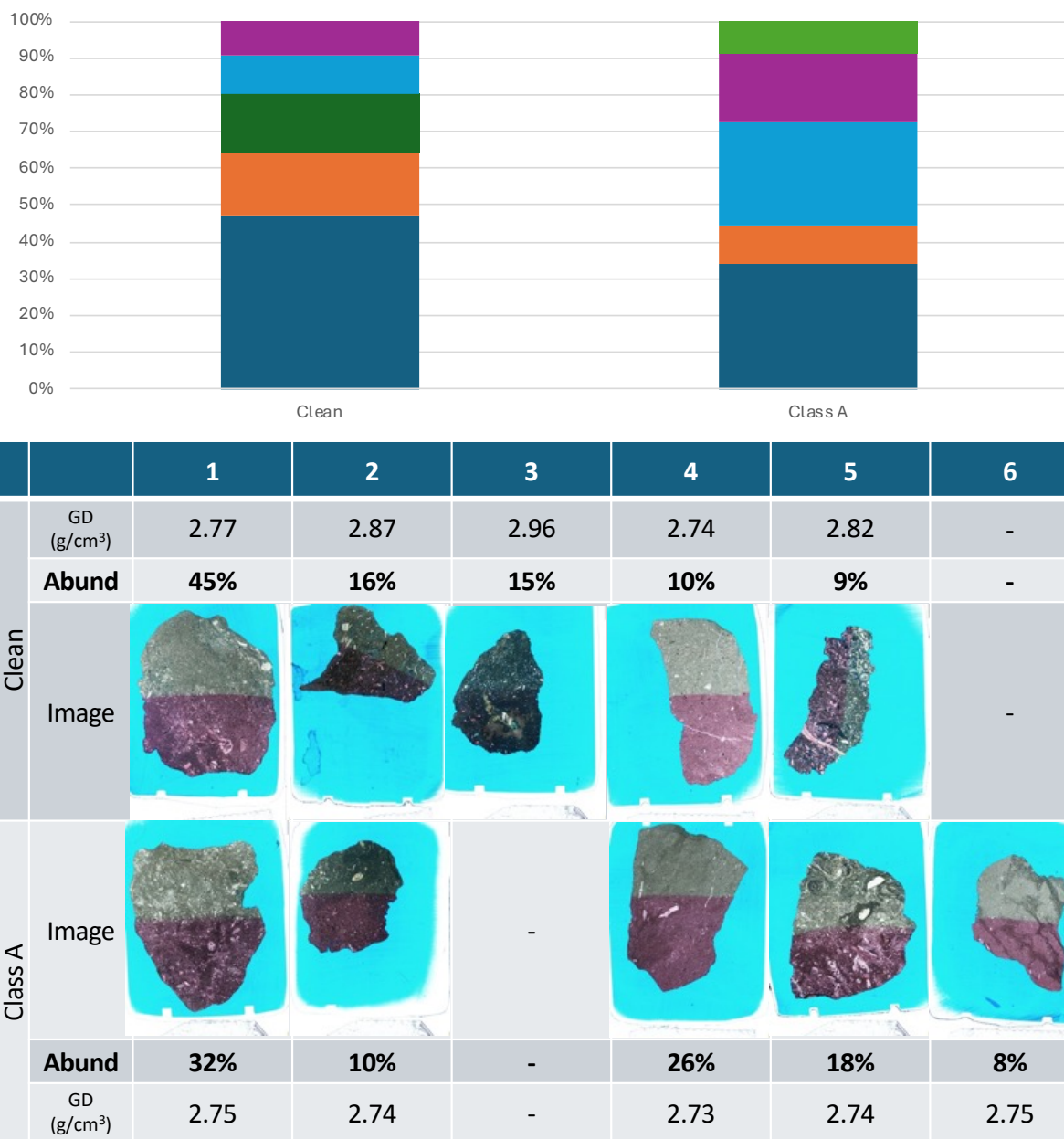


Figure 123. Rock types, grain densities, abundances, and thin section images for Clean versus Class A BFL quarry samples from TR-704 project

4.2.2 Lime Creek Formation (LCF) Class A Aggregates

A 500 ft long and 4 in. thick test section was constructed at the TR-704 project site utilizing Lime Creek Formation (LCF) Class A aggregates. The dates of construction, maintenance, and sample collection for the LCF test section were the same as those previously discussed for the BFL test section.

4.2.2.1 PSD Comparison and Evaluation of Breakage Parameters for LCF Class A Aggregates

To assess the mechanical degradation of the in-service LCF aggregates over time, breakage parameters were evaluated using data from sieve analyses and 2D image analyses for the LCF samples collected in April 2017 relative to those from after construction in September 2016, as well as samples from June 2017, February 2018 (breakage evaluated by 2D image analyses only) and April 2018 relative to those collected just after the first round of maintenance in May 2017. Finally, breakage parameters were evaluated for samples collected in April 2019 relative to those collected just after the second round of maintenance which included spreading new aggregates in May 2018. Results of the analyses are presented in Figure 124 through Figure 131 for the dates indicated in the figures. Summaries and further details on the corresponding breakage parameters are provided in Table 34 for results based on sieve analyses and Table 35 for results based on image analyses.

The percentages of gravel, sand, and fines over time for the sieve analysis samples are also presented as a bar chart in Figure 132, while corresponding bar charts of the total breakage are presented in Figure 133 for sieve analysis and Figure 134 for image analysis. In the periods following maintenance operations, the sieve analysis results in Table 34 and Figure 132 indicate a reduction in the gravel fraction by 1.0% for the May 2017–April 2018 timeframe, and by 9.3% for the May 2018–April 2019 timeframe. The corresponding sand fractions increased over time by 4.7% and 6.6%, respectively, while the fines fractions decreased by 3.7% and increased by 2.7%, respectively. This indicates breakage of gravel particles into sand and sand particles into fines, but in April 2018 the rate of fines loss from the test section was greater than the rate of sand breakage into fines. The sample collected in June 2017, just one month after maintenance, showed an increased gravel fraction—likely due to sampling error—that was equaled by reductions in the sand and fines fractions.

The breakage results based on sieve analyses presented in Table 34, Figure 132 and Figure 133 exhibit two invalid negative total breakage values, which results when a PSD curve migrates downwards instead of upwards over time. This could be due to sampling error because of the variability intrinsic to the five field samples that are intended to be representative of the entire test section on a given date, or could also result if a motor grader was used to blade coarser materials back over the degraded materials in the wheel paths at some point before sample collection. Theoretically, total breakage values for a series of dates all referenced back to a common starting date should continually increase over time, provided that the samples are actually representative of the same materials undergoing continual degradation (i.e., with no new material added during the time frame), but this was apparently not always the case for the field-collected samples. Valid positive breakage values were found for sieve analyses of the samples for the September 2016–April 2017 and May 2018–April 2019 time spans (see also Figure 124 and Figure 130). For the results based on 2D image analyses, Table 35 and Figure 134 show that the total breakage values were positive for all but the first time span from May 2017 to June 2017.

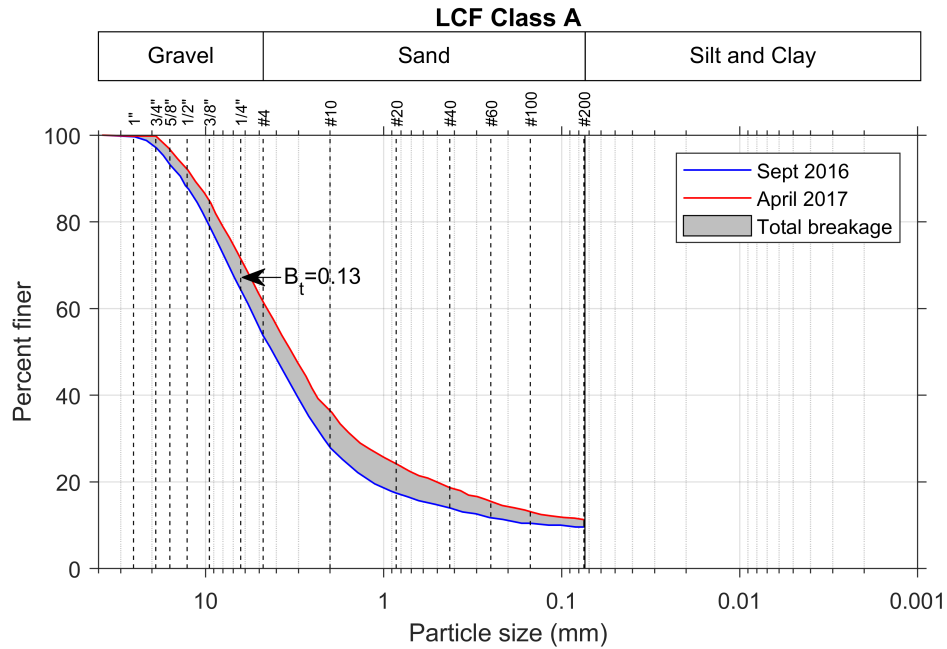


Figure 124. Particle size distributions of coarse fraction from sieve analysis and evaluation of total breakage between September 2016 and April 2017 for LCF Class A test section

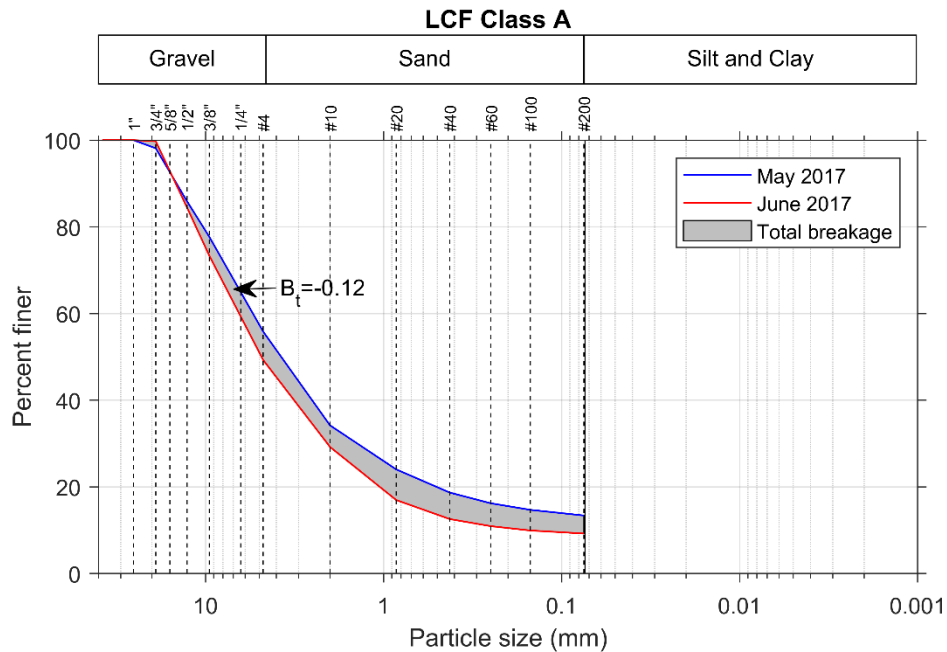


Figure 125. Particle size distributions of coarse fraction from sieve analysis and evaluation of total breakage between May 2017 and June 2017 for LCF Class A test section

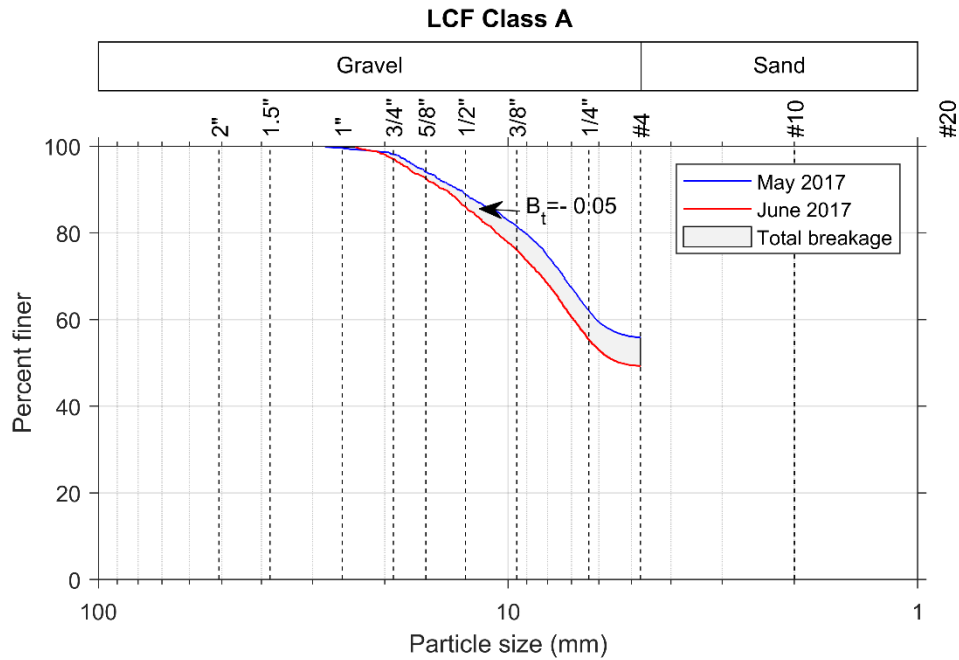


Figure 126. Particle size distributions of gravel fraction from 2D image analysis and evaluation of total breakage between May 2017 and June 2017 for LCF Class A test section

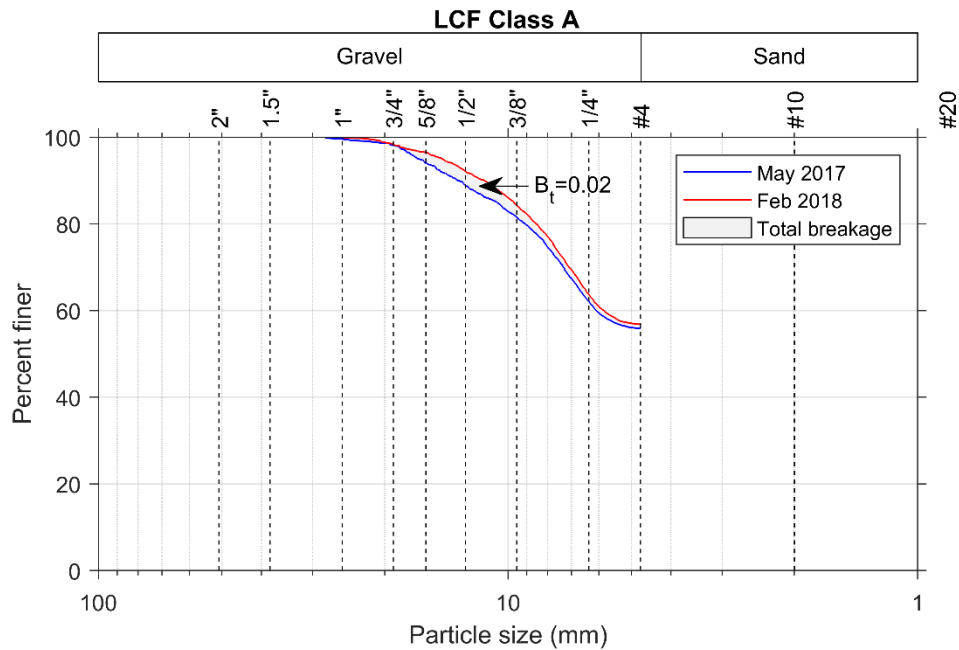


Figure 127. Particle size distributions of gravel fraction from 2D image analysis and evaluation of total breakage between May 2017 and February 2018 for LCF Class A test section

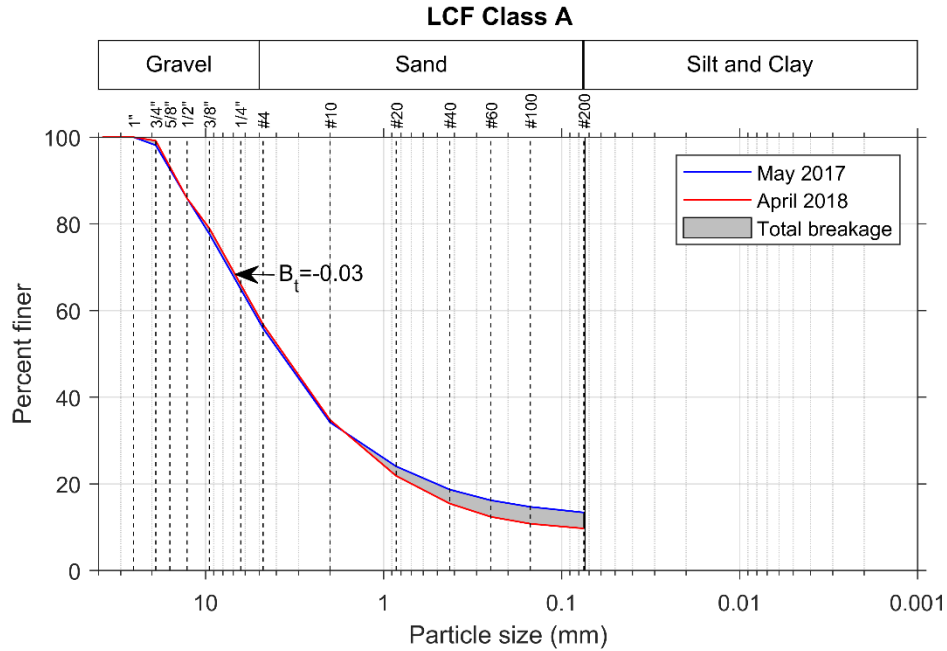


Figure 128. Particle size distributions of coarse fraction from sieve analysis and evaluation of total breakage between May 2017 and April 2018 for LCF Class A test section

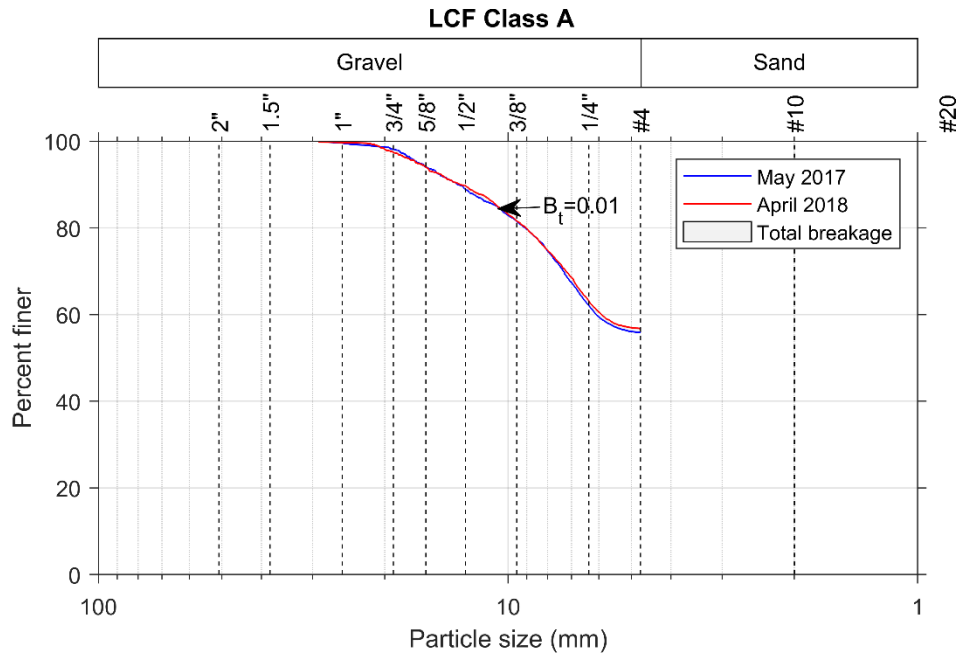


Figure 129. Particle size distributions of gravel fraction from 2D image analysis and evaluation of total breakage between May 2017 and April 2018 for LCF Class A test section

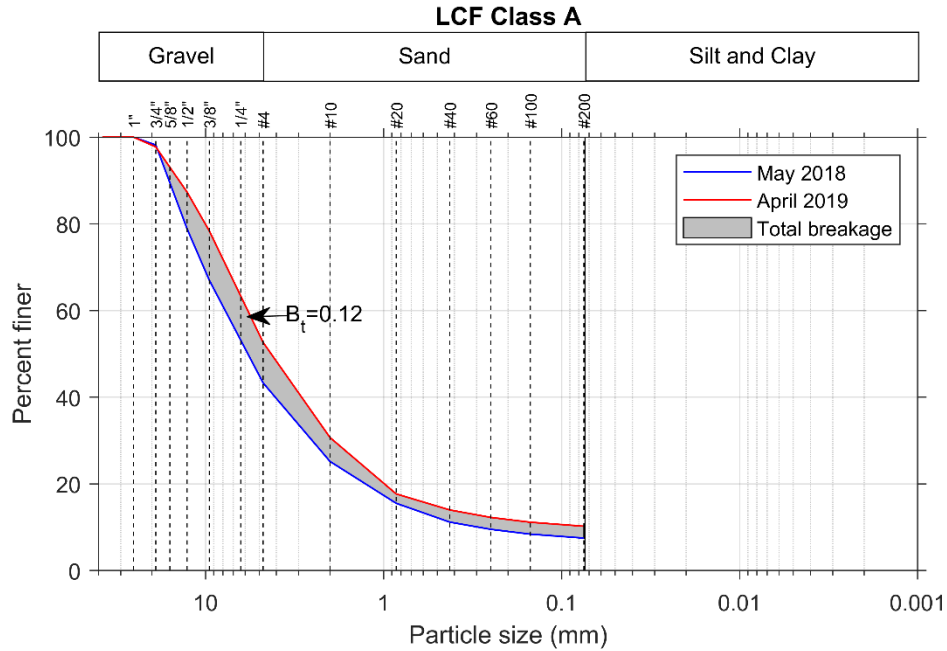


Figure 130. Particle size distributions of coarse fraction from sieve analysis and evaluation of total breakage between May 2018 and April 2019 for LCF Class A test section

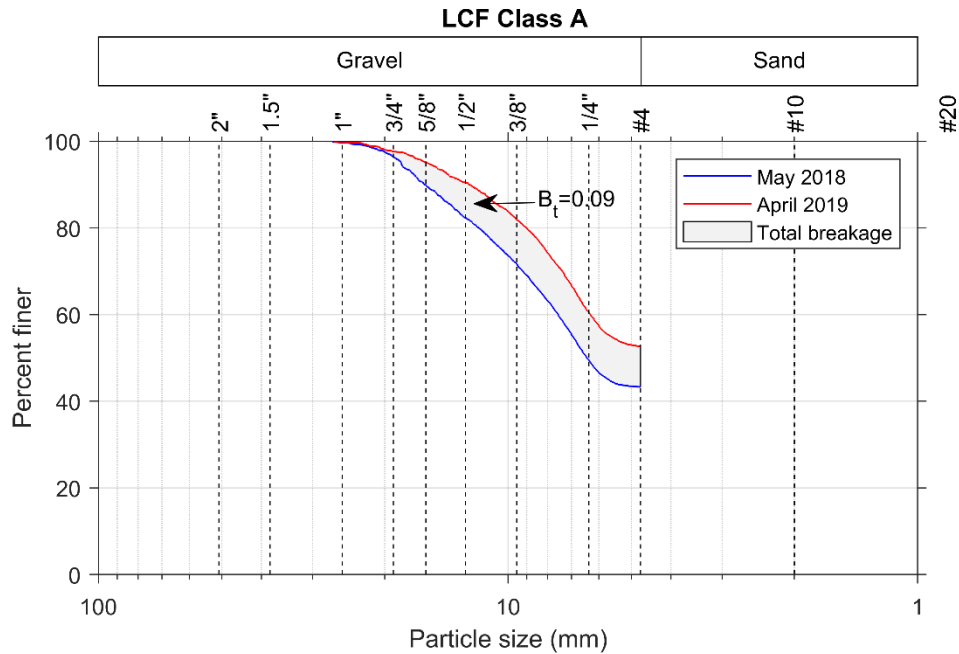


Figure 131. Particle size distributions of gravel fraction from 2D image analysis and evaluation of total breakage between May 2018 and April 2019 for LCF Class A test section

Table 34. Breakage parameters from sieve analysis and percent gravel, sand, and fines for LCF Class A samples collected over time

Sample Collection Date	Hardin's Breakage Parameters				% Gravel Red. **	% Sand	% Sand Inc. ††	% Fines	% Fines Inc.
	Total Breakage, B_t	Breakage Potential, B_p	Relative Breakage, B_r	% Gravel					
Sept 2016	-	-	-	46.4	-	44.2	-	9.4	-
April 2017 ^a	0.1312	1.5797	0.0831	39.2	7.2	49.5	5.3	11.2	1.8
May 2017	-	-	-	44.2	-	42.4	-	13.4	-
June 2017*	-0.1208	1.4866	-0.0812	50.7	-6.5	40.0	-2.4	9.3	-4.1
April 2018*	-0.0309	1.4866	-0.0208	43.2	1.0	47.1	4.7	9.7	-3.7
May 2018	-	-	-	56.7	-	35.8	-	7.5	-
April 2019 [†]	0.1211	1.6875	0.0718	47.4	9.3	42.4	6.6	10.2	2.7

* w.r.t. May 2017, [†]w.r.t. May 2018, ** Reduction, ††Increase

Table 35. Breakage parameters from 2D-image analyses and percent gravel, sand, and fines for LCF Class A samples collected over time

Sample Collection Date	Hardin's Breakage Parameters*		
	Total Breakage, B_t	Breakage Potential, B_p	Relative Breakage, B_r
May 2017	-	-	-
June 2017*	-0.0547	0.3077	-0.1777
Feb 2018*	0.0167	0.3077	0.0541
April 2018*	0.0062	0.3077	0.0201
May 2018	-	-	-
April 2019 [†]	0.0917	0.4136	0.2218

* w.r.t. May 2017, [†]w.r.t. May 2018

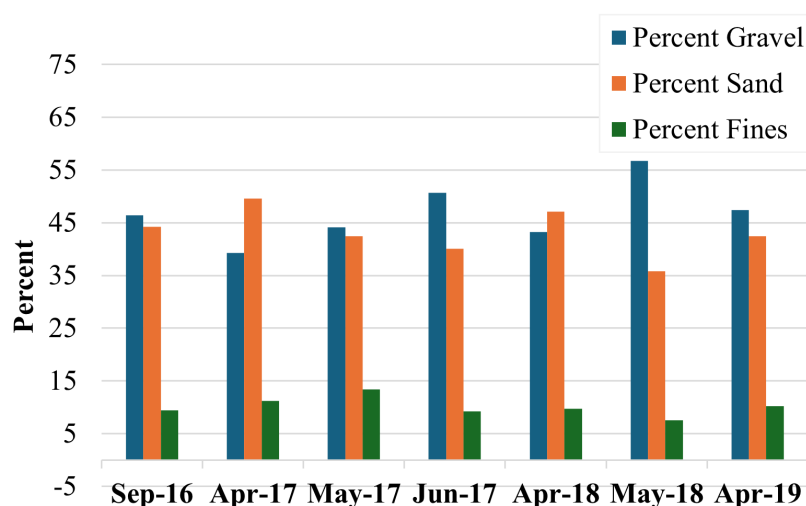


Figure 132. Percent gravel, sand, and fines for sieve analysis of samples from LCF Class A section collected over time

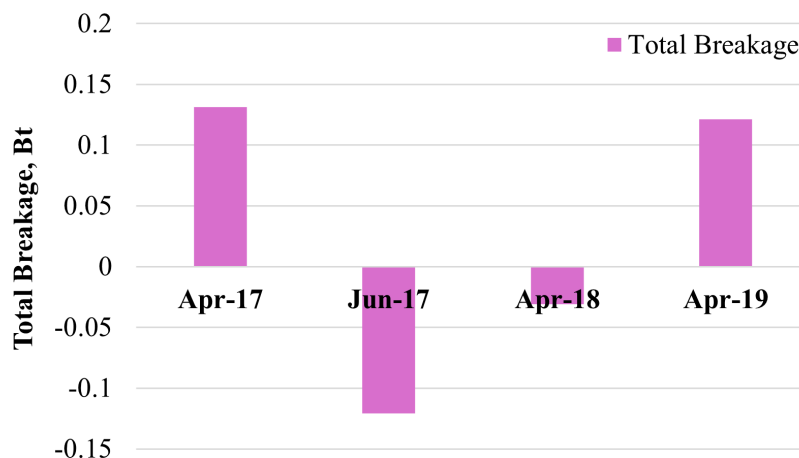


Figure 133. Hardin’s total breakage evaluated from sieve analyses of samples from LCF Class A section collected over time

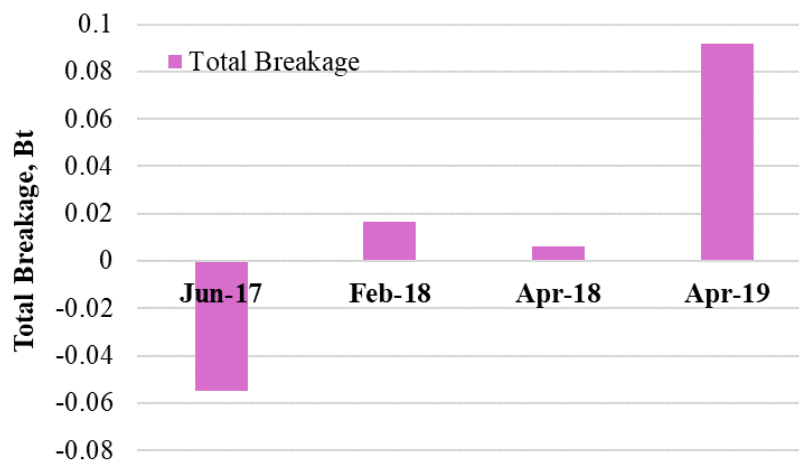


Figure 134. Hardin’s total breakage evaluated from 2D image analyses of samples from LCF Class A section collected over time

4.2.2.2 Comparison of Morphological Parameters from 2D Image Analyses for LCF Class A

The change in morphological parameters over time for the in-service LCF Class A aggregates are presented graphically in the form of boxplots in Figure 135 through Figure 139. The statistical details for these morphological parameters are presented in Table 36. The results quantify particle degradation after the maintenance operations of May 2017 through increases in median roundness of 0.5%, 0.6%, and 0.5% for the samples collected in June 2017, February 2018 and April 2018, respectively, along with an increase of 0.8% for the May 2018–April 2019 time span after the second round maintenance aggregates were placed. For the same time spans, particle degradation was also indicated by corresponding increases in median sphericity of 0.9%, 0.4%, 0.2% and 0.2% in Table 36. For the final May 2018–April 2019 time span, the data also show an

increase in median form factor of 1.0% accompanied by decreases in median shape factor by 1.0%, roundness index by 0.1%, and angularity by 4.1%. These changes quantify the mechanical degradation of the LCF samples collected on the several dates following the first maintenance period of May 2017 and after the second maintenance period of May 2018. However, for the samples collected in June 2017, February 2018 and April 2018 relative to May 2017, the data also indicated a decrease in form factor accompanied by increases in shape factor and angularity.

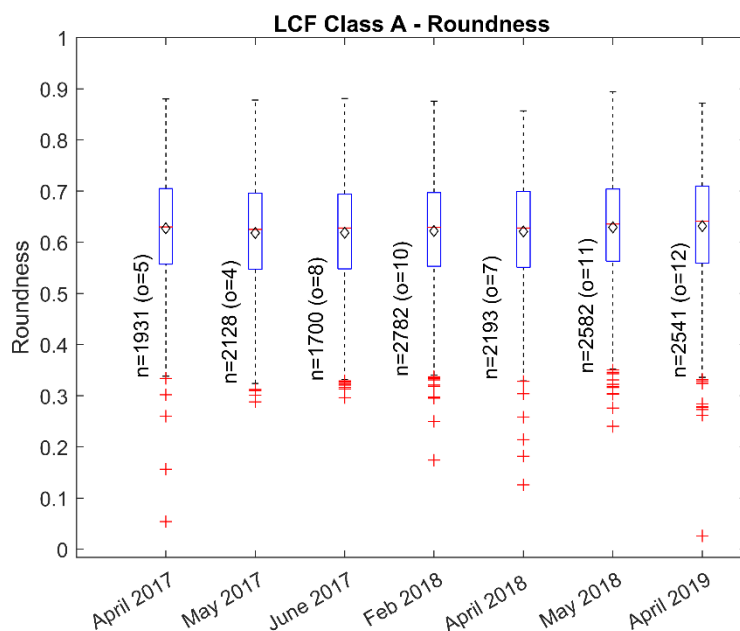


Figure 135. Comparison of roundness for LCF Class A samples collected over time

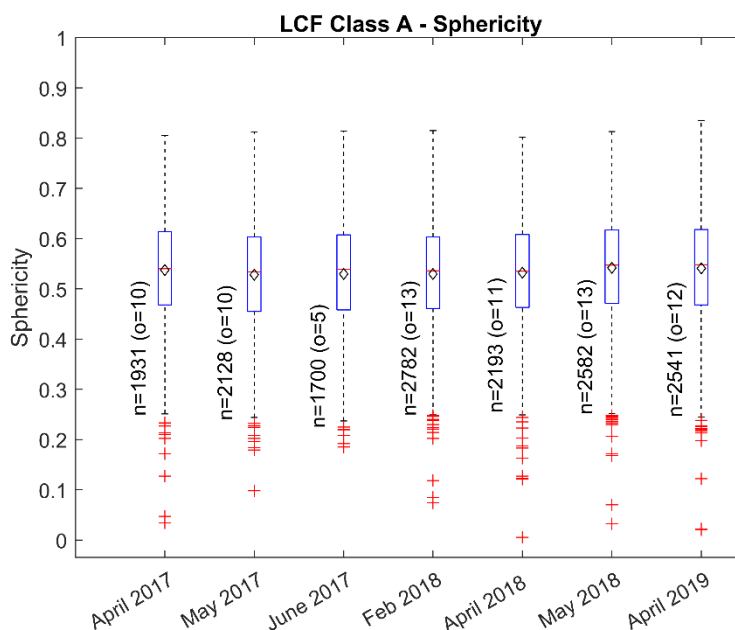


Figure 136. Comparison of sphericity for LCF Class A samples collected over time

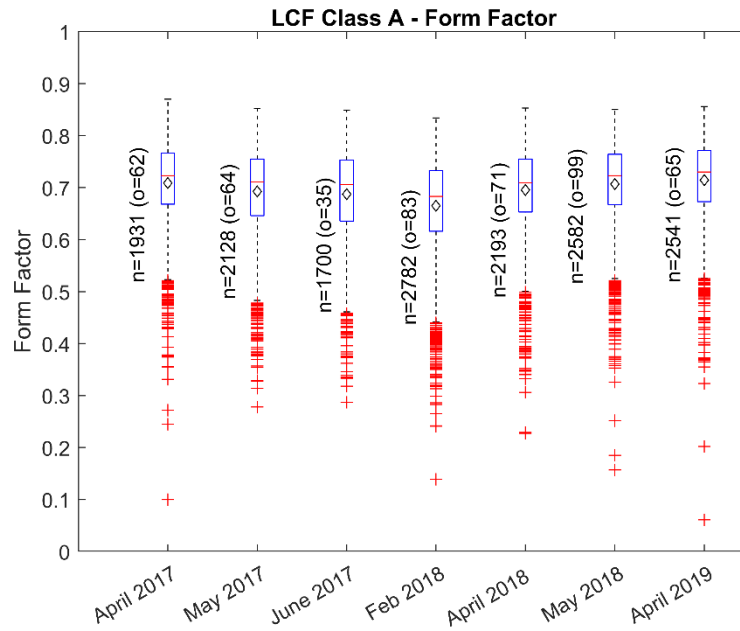


Figure 137. Comparison of form factor for LCF Class A samples collected over time

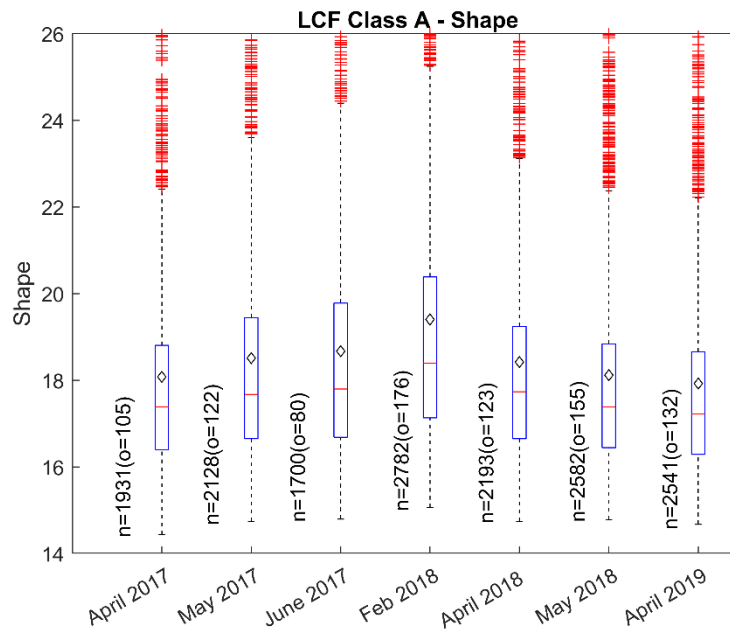


Figure 138. Comparison of shape factor for LCF Class A samples collected over time

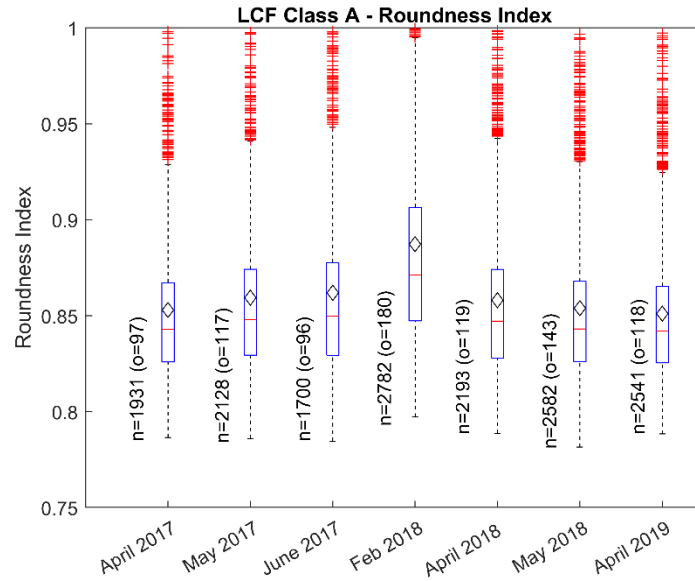


Figure 139. Comparison of roundness index for LCF Class A samples collected over time

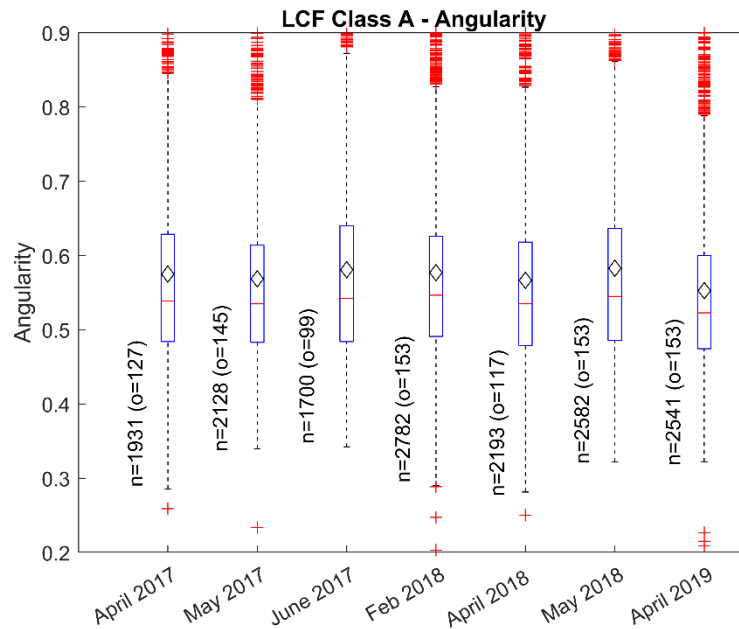


Figure 140. Comparison of angularity for LCF Class A samples collected over time

Table 36. Statistical results of morphological parameters of LCF Class A

Parameters	Sample Collection Date	Max. Value	Min. Value	Mean	Mode	Median	Std. Dev.	Skew- ness	Kurt- osis	Out- liers
Roundness	April 2017	0.880	0.054	0.627	0.651	0.630	0.104	-0.333	3.140	5
	May 2017	0.878	0.288	0.618	0.665	0.625	0.105	-0.295	2.668	4
	June 2017	0.881	0.296	0.619	0.599	0.628	0.105	-0.333	2.761	8
	% inc. *			0.1%		0.5%				
	Feb 2018	0.876	0.174	0.622	0.642	0.629	0.102	-0.321	2.841	10
	% inc. *			0.6%		0.6%				
	April 2018	0.857	0.126	0.621	0.590	0.628	0.105	-0.337	2.964	7
	% inc. *			0.4%		0.5%				
	May 2018	0.894	0.24	0.629	0.657	0.636	0.101	-0.332	2.865	11
	April 2019	0.872	0.026	0.631	0.650	0.641	0.105	-0.411	3.103	12
	% inc. †			0.3%		0.8%				
Sphericity	April 2017	0.805	0.034	0.538	0.464	0.54	0.106	-0.331	3.235	10
	May 2017	0.812	0.098	0.528	0.517	0.534	0.105	-0.243	2.893	10
	June 2017	0.814	0.185	0.53	0.484	0.539	0.106	-0.299	2.742	5
	% inc. *			0.3%		0.9%				
	Feb 2018	0.815	0.074	0.53	0.486	0.536	0.105	-0.292	2.939	13
	% inc. *			0.3%		0.4%				
	April 2018	0.802	0.005	0.532	0.558	0.535	0.105	-0.262	3.187	11
	% inc. *			0.8%		0.2%				
	May 2018	0.813	0.032	0.542	0.548	0.547	0.106	-0.348	3.113	13
	April 2019	0.835	0.021	0.541	0.569	0.548	0.108	-0.341	3.066	12
	% inc. †			-0.2%		0.2%				
Form Factor	April 2017	0.870	0.100	0.709	0.790	0.723	0.083	-1.346	6.526	62
	May 2017	0.852	0.278	0.692	0.731	0.711	0.087	-1.120	4.538	64
	June 2017	0.849	0.287	0.687	0.756	0.706	0.090	-1.013	4.123	35
	% inc. *			-0.8%		-0.7%				
	Feb 2018	0.834	0.139	0.665	0.713	0.683	0.095	-1.077	4.472	83
	% inc. *			-3.9%		-3.9%				
	April 2018	0.853	0.227	0.695	0.749	0.709	0.085	-1.236	5.453	71
	% inc. *			0.4%		-0.3%				
	May 2018	0.850	0.157	0.707	0.700	0.723	0.083	-1.366	6.085	99
	April 2019	0.856	0.061	0.715	0.756	0.73	0.080	-1.382	6.884	65
	% inc. †			1.1%		1.0%				

Parameters	Sample Collection Date	Max. Value	Min. Value	Mean	Mode	Median	Std. Dev.	Skew-ness	Kurt-osis	Out-liers
Shape Factor	April 2017	125.7	14.44	18.08	15.75	17.39	3.640	14.78	403.7	105
	May 2017	45.21	14.74	18.51	16.55	17.67	2.959	2.595	13.77	122
	June 2017	43.78	14.79	18.67	15.86	17.80	3.069	2.469	12.92	80
	% inc. *			0.9%		0.7%				
	Feb 2018	90.67	15.06	19.40	18.16	18.40	3.862	4.506	53.53	176
	% inc. *			4.8%		4.1%				
	April 2018	55.46	14.74	18.42	15.84	17.73	3.025	3.764	30.35	123
	% inc. *			-0.5%		0.4%				
	May 2018	80.11	14.78	18.12	16.09	17.39	3.092	6.627	99.52	155
	April 2019	206.6	14.67	17.92	16.31	17.22	4.533	29.14	1187	132
	% inc. †			-1.1%		-1.0%				
Roundness Index (RI)	April 2017	1.366	0.787	0.853	0.828	0.843	0.044	3.059	22.18	97
	May 2017	1.218	0.786	0.859	0.828	0.848	0.048	2.303	11.22	117
	June 2017	1.259	0.785	0.862	0.828	0.85	0.05	2.303	11.45	96
	% inc. *			0.3%		0.2%				
	Feb 2018	1.483	0.797	0.887	0.828	0.871	0.063	2.451	12.88	180
	% inc. *			3.3%		2.8%				
	April 2018	1.213	0.789	0.858	0.828	0.847	0.047	2.377	12.01	119
	% inc. *			-0.2%		-0.1%				
	May 2018	1.322	0.782	0.854	0.828	0.843	0.046	2.905	18.62	143
	April 2019	1.198	0.788	0.851	0.838	0.842	0.04	2.366	12.92	118
	% inc. †			-0.3%		-0.1%				
Angularity	April 2017	1.184	0.259	0.575	0.451	0.539	0.132	1.412	5.013	127
	May 2017	1.206	0.234	0.568	0.463	0.535	0.129	1.538	5.661	145
	June 2017	1.157	0.342	0.581	0.434	0.542	0.135	1.284	4.475	99
	% inc. *			2.2%		1.4%				
	Feb 2018	1.204	0.166	0.577	0.511	0.546	0.129	1.465	6.123	153
	% inc. *			1.5%		2.2%				
	April 2018	1.279	0.25	0.566	0.421	0.535	0.13	1.632	6.663	117
	% inc. *			-0.3%		0.0%				
	May 2018	1.343	0.322	0.583	0.449	0.545	0.139	1.484	5.603	153
	April 2019	1.175	0.209	0.552	0.637	0.523	0.119	1.53	6.132	153
	% inc. †			-5.2%		-4.1%				

* w.r.t. May 2017, †w.r.t. May 2018

Considering altogether the above discussed changes in gradation, breakage, and morphological parameters for the samples collected after the first maintenance period in May 2017, the reduction in gravel fraction and increase in sand fraction observed in April 2018 relative to May 2017 quantify the breakdown of gravel-sized particles into sand-sized particles. Additionally, the positive values of Hardin's total breakage for samples collected in February 2018 and April 2018, as shown by 2D image analyses, indicate ongoing breakage of surface gravel since May 2017, with higher breakage observed in the February 2018 samples. Furthermore, the increase in median sphericity and roundness in the samples collected in June 2017, February 2018, and April 2018 suggests some particle degradation in these samples after the first maintenance period.

Similarly, for the samples collected after the second maintenance period in May 2018, the reduced gravel fraction and increased sand and fines fractions observed by April 2019 quantify the breakdown of gravel into sand and finer particles. The positive total breakage values for April 2019 according to both 2D image analyses and sieve analyses further quantify the deterioration of the gravel fractions. Finally, the morphological parameters over the May 2018–April 2019 timeframe exhibited overall increases in median sphericity, roundness, and form factor, accompanied by overall decreases in median shape factor, roundness index, and angularity, indicating degradation of the samples.

4.2.2.3 Geological Tests for LCF Class A and Clean Samples

Geological tests were conducted on the previously described LCF Class A samples collected from the test section in April, May, and June of 2017, April and May of 2018, and April of 2019. The geological tests identified three primary rock types in the LCF Class A materials: buff micrite (RT1), buff birdseye (RT2), and dark stylolitic (RT3), the percentages of which over time are shown in Figure 141 and detailed in Table 37. The data reveal that following the first maintenance period in May 2017, buff micrite increased by 7% as of June 2017 and by 12% as of April 2018. However, it decreased by 26% in April 2019 relative to the second maintenance period in May 2018. Similarly, buff birdseye decreased by 3% as of June 2017 and by 13% as of April 2018 compared to the first maintenance period in May 2017, and further decreased by 30% as of April 2019 relative to the second maintenance period in May 2018. The dark stylolitic type didn't show a clear trend for the samples relative to the first maintenance period, however it showed a decrease of 3% for the samples collected in April 2019 relative to the second maintenance period in May 2018.

Additional geological tests were also conducted on virgin LCF Clean and Class A materials sampled from the quarry during the TR-704 project. Four rock types were found (Figure 142), and the most significant differences were in RT2, RT3 and RT4. Specifically, RT2 (nonporous laminated lime mudstone), had an abundance of 35% in the Clean material but only 5% in the Class A material, whereas RT 3 had an abundance of 11% in Clean and 5% in Class A, and RT4 had an abundance of 5% in Clean and 41% in Class A.

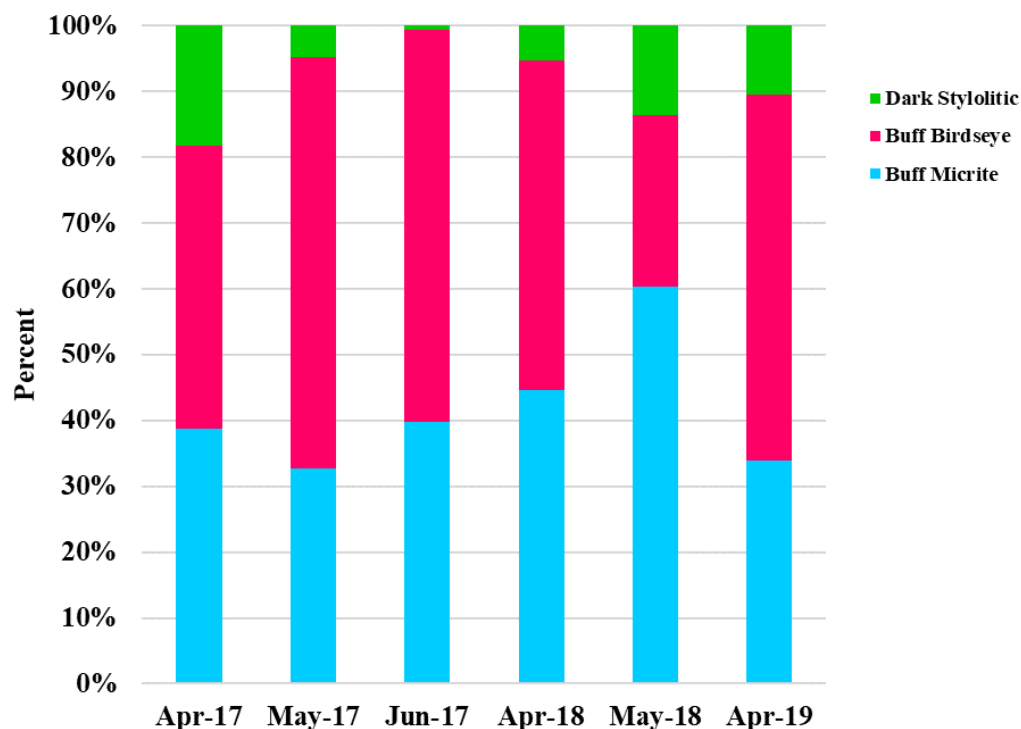
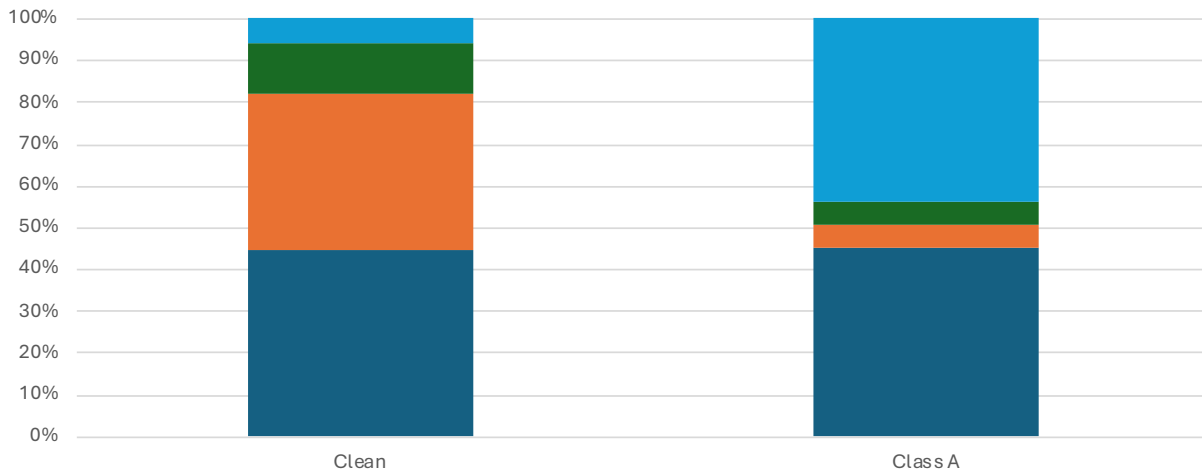


Figure 141. Percentages of rock types in LCF Class A samples collected over time

Table 37. Geological rock types and percent increase in rock types for the LCF Class A samples collected over time

Sample Collection Date	% Buff Micrite (BM)	%Inc. in BM	% Buff Birdseye (BB)	% Inc. in BB	% Dark Stylolitic (DS)	% Inc. in DS
April 2017	39		43		18	
May 2017	33		63		5	
June 2017*	40	7	60	-3	1	-4
April 2018*	45	12	50	-13	5	1
May 2018	60		26		14	
April 2019 [†]	34	-26	56	30	10	-3

*w.r.t. May 2017, [†]w.r.t. May 2018



		1	2	3	4
Clean	GD (g/cm ³)	2.71	2.72	2.75	2.78
	Abund	42%	35%	11%	5%
	Image				
Class A	Image				
	Abund	42%	5%	5%	41%
	GD (g/cm ³)	2.72	2.71	2.73	2.71

Figure 142. Rock types, grain densities, abundances, and thin section images for Clean versus Class A LCF quarry samples from TR-704 project

4.2.3 Oneota Formation Dolomite (OFD) Class A Aggregates

A 300 ft long and 4 in. thick test section using Oneota Formation Dolomite (OFD) Class A aggregates was also constructed in the TR-704 project. The dates of construction, maintenance, and sample collection for the OFD test section were the same as those previously discussed for the BFL and LCF test sections.

4.2.3.1 PSD Comparison and Evaluation of Breakage Parameters for OFD Class A Aggregates

To assess the mechanical degradation of the in-service OFD aggregates over time, breakage was evaluated using sieve analyses for samples collected in April 2017 relative to those collected after construction in September 2016, samples collected in June 2017 and April 2018 relative to the first round of maintenance in May 2017, and samples collected in April 2019 relative to the second round of maintenance in May 2018. Breakage was also analyzed by 2D image analysis for available samples from February and April 2018 relative to June 2017. Results of the analyses are presented in Figure 143 through Figure 148 for the dates indicated in the figures. Summaries and further details on the corresponding breakage parameters are provided in Table 38 for sieve analyses and Table 39 for 2D image analyses. The percentages of gravel, sand, and fines for the sieve analysis samples collected over time in Table 38 are also presented in a bar chart Figure 149, while Figure 150 and Figure 151 contain bar charts of total breakage from sieve and image analyses, respectively.

The results based on sieve analyses shown in Table 38 and Figure 150 exhibit invalid negative total breakage values for some of the sampling dates. Potential causes of negative breakage values were previously discussed in Section 4.2.2. However, the negative breakage values in Table 38 are essentially zero because there was practically no difference between the PSD curves. These negative OFD breakage values are most likely due to the error inherent in sampling and sieve analysis, and can be considered to lie within the margin of measurement error for the PSD curves. For the results based on 2D image analyses, Table 39 and Figure 151 show that the total breakage values were positive for all dates, and the breakage values were also very small because the PSD curves were nearly identical. The bar charts in Figure 149 confirm that the gravel, sand, and fines fractions changed very little over the duration of the project for the OFD section, meaning that this material had very little deterioration over the life of the project.

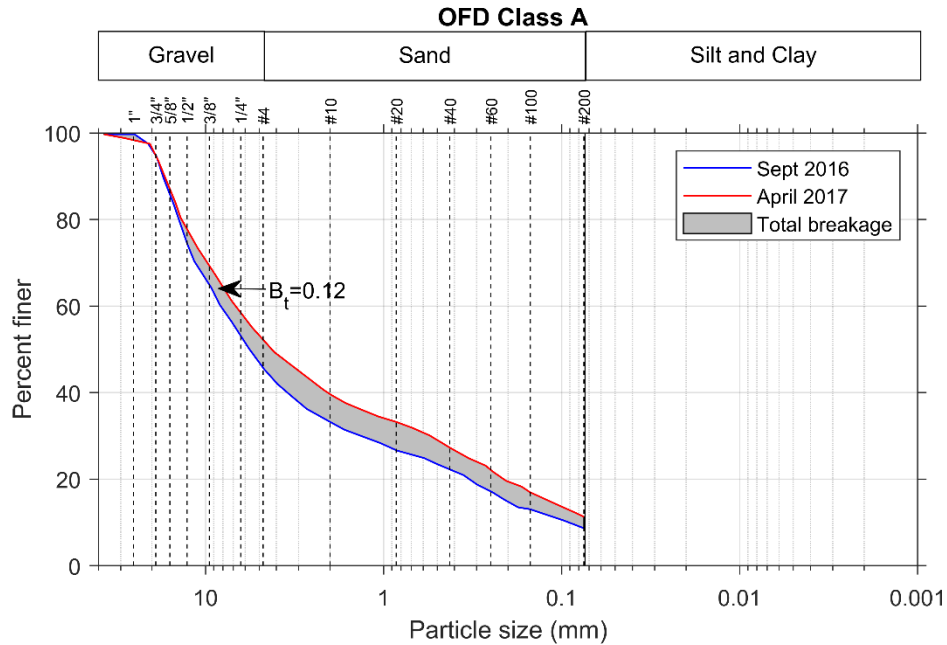


Figure 143. Particle size distributions of coarse fraction from sieve analysis and evaluation of total breakage between September 2016 and April 2017 for OFD Class A test section

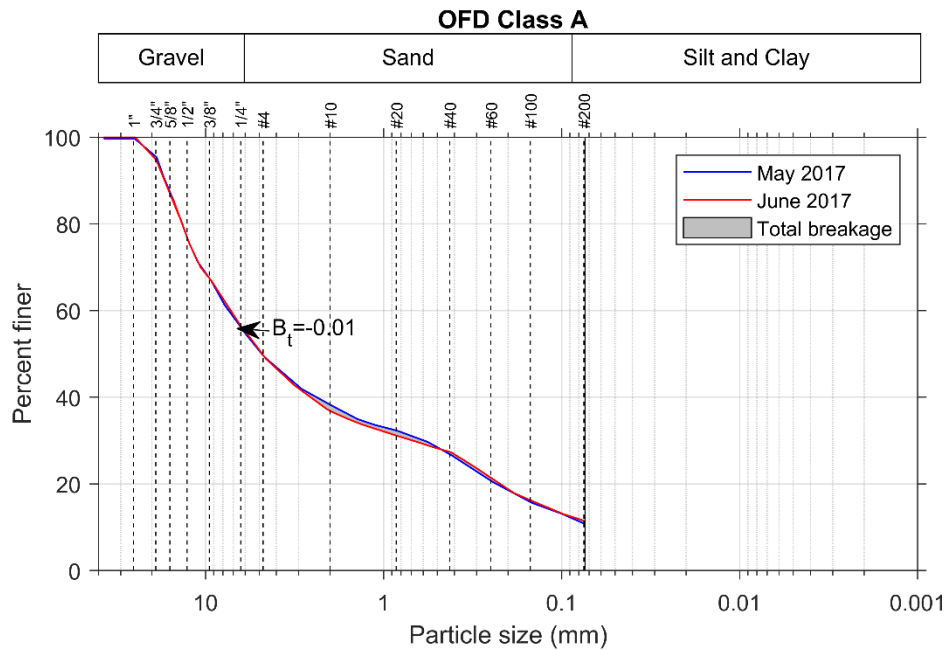


Figure 144. Particle size distributions of coarse fraction from sieve analysis and evaluation of total breakage between May 2017 and June 2017 for OFD Class A test section

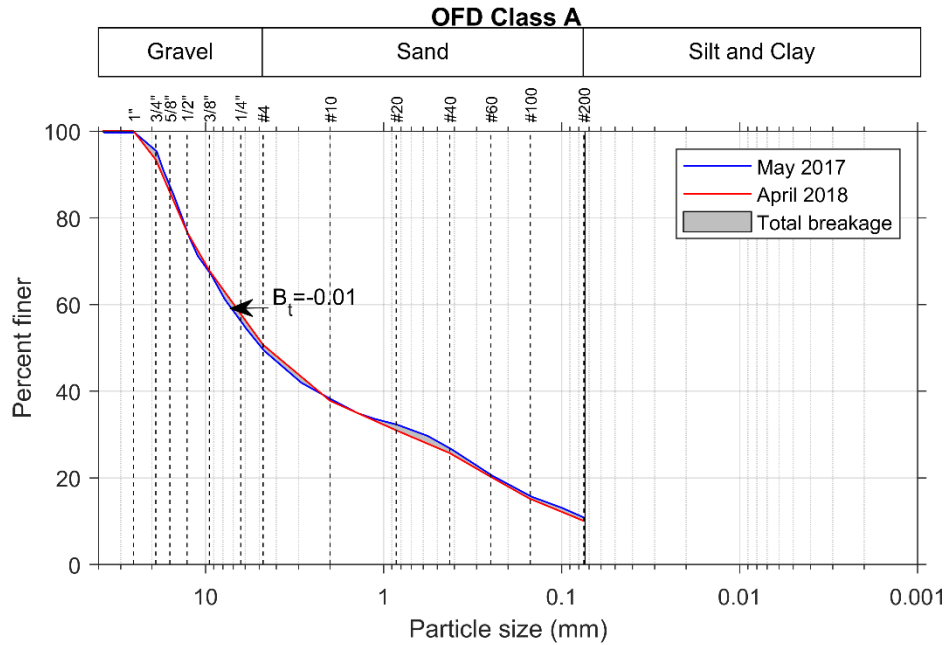


Figure 145. Particle size distributions of coarse fraction from sieve analysis and evaluation of total breakage between May 2017 and April 2018 for OFD Class A test section

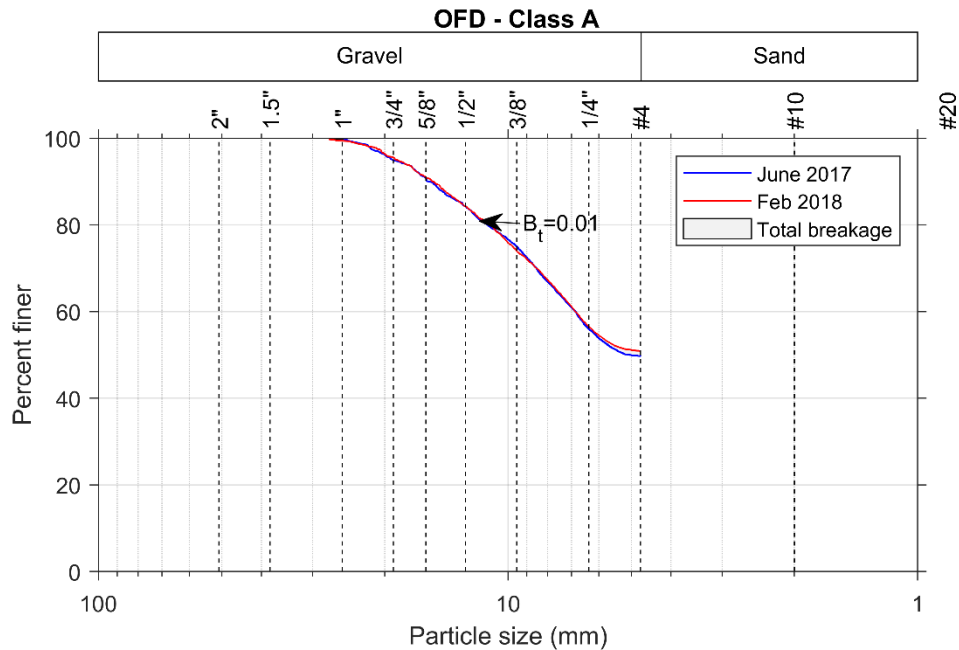


Figure 146. Particle size distributions of gravel fraction from 2D image analysis and evaluation of total breakage between June 2017 and February 2018 for OFD Class A test section

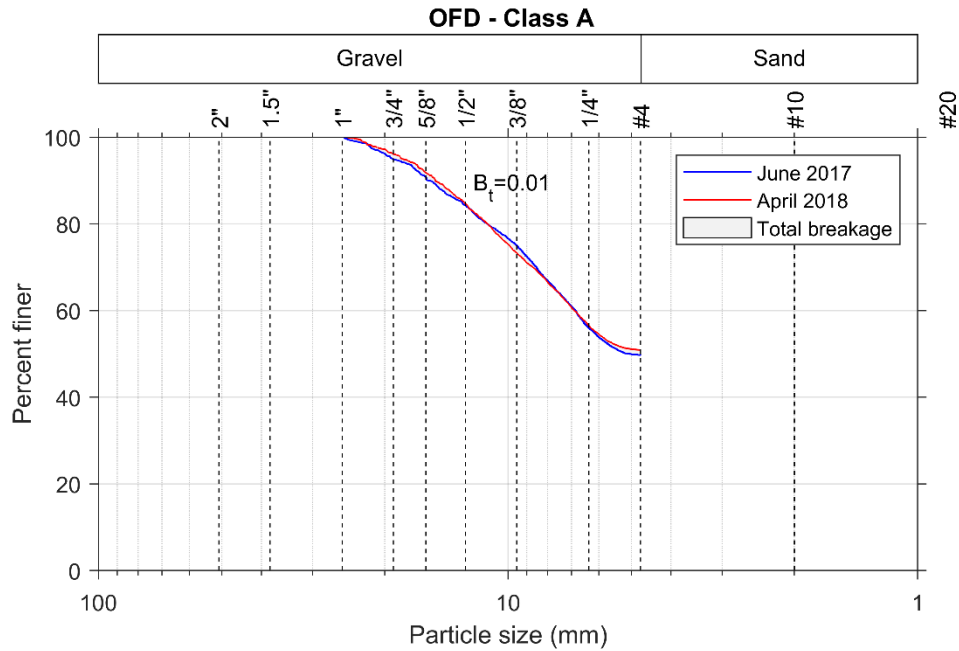


Figure 147. Particle size distributions of gravel fraction from 2D image analysis and evaluation of total breakage between June 2017 and April 2018 for OFD Class A test section

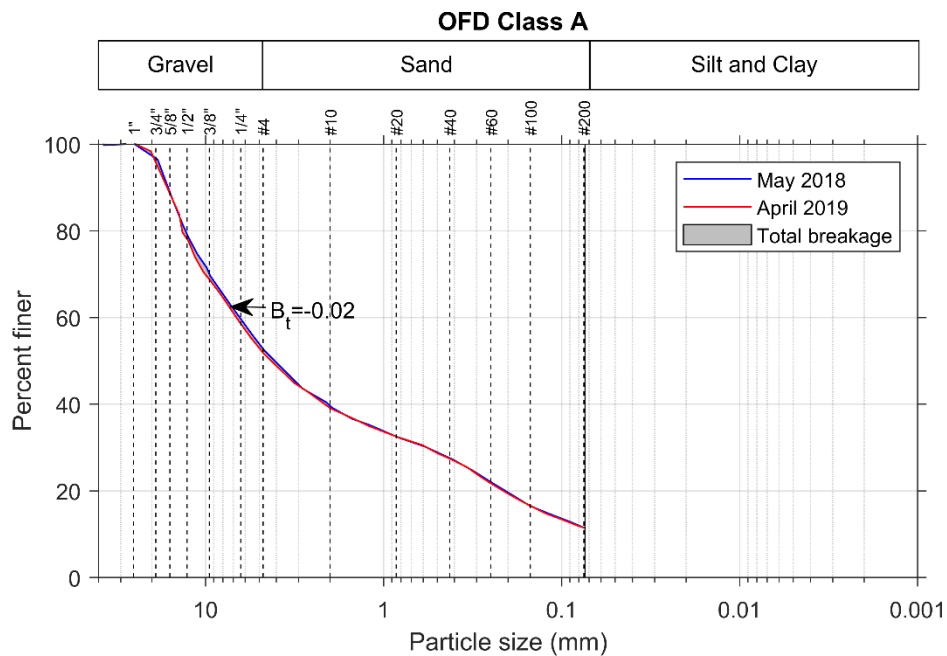


Figure 148. Particle size distributions of coarse fraction from sieve analysis and evaluation of total breakage between May 2018 and April 2019 for OFD Class A test section

Table 38. Breakage parameters from sieve analysis and percent gravel, sand, and fines for OFD Class A samples collected over time

Sample Collection Date	Hardin's Breakage Parameters			% Gravel	% Gravel Red. **	% Sand	% Sand Inc. ††	% Fines	% Fines Inc.
	Total Breakage, B_t	Breakage Potential, B_p	Relative Breakage, B_r						
Sept 2016	-	-	-	53.9	-	36.9	-	9.2	-
April 2017 ^a	0.1208	1.5626	0.0773	47.6	6.3	40.7	3.8	11.7	2.5
May 2017	-	-	-	50.3	-	38.5	-	11.2	-
June 2017*	-0.0107	1.4706	-0.0073	50.3	0.0	38.5	0.0	11.2	0.0
April 2018*	-0.0149	1.4706	-0.0101	49.1	1.2	40.8	2.3	10.1	-1.1
May 2018	-	-	-	46.8	-	41.9	-	11.3	-
April 2019 [†]	-0.0184	1.4350	-0.0128	48.0	-1.2	40.5	-1.4	11.5	0.2

^aw.r.t. Sept 2016, *w.r.t. May 2017, [†]w.r.t. May 2018, **Reduction, ††Increase

Table 39. Breakage parameters from 2D-image analyses and percent gravel, sand, and fines for OFD Class A samples collected over time

Sample Collection Date	Hardin's Breakage Parameters		
	Total Breakage, B_t	Breakage Potential, B_p	Relative Breakage, B_r
June 2017	-	-	-
Feb 2018*	0.0073	0.3675	0.0198
April 2018*	0.0063	0.3675	0.0172

*w.r.t. June 2017

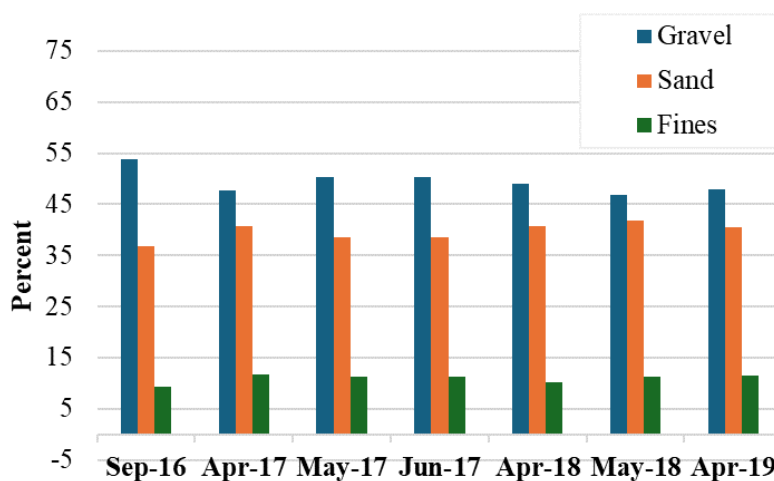


Figure 149. Percent gravel, sand, and fines for samples of OFD Class A collected over time

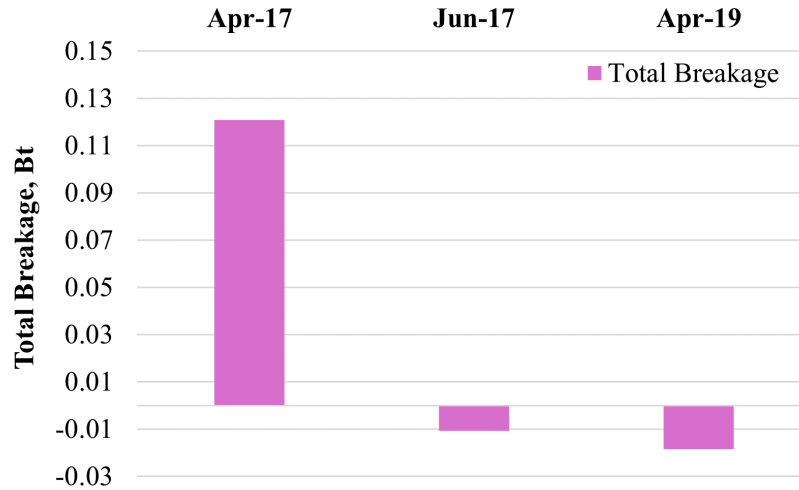


Figure 150. Hardin's total breakage evaluated from sieve analyses of samples from OFD Class A section collected over time

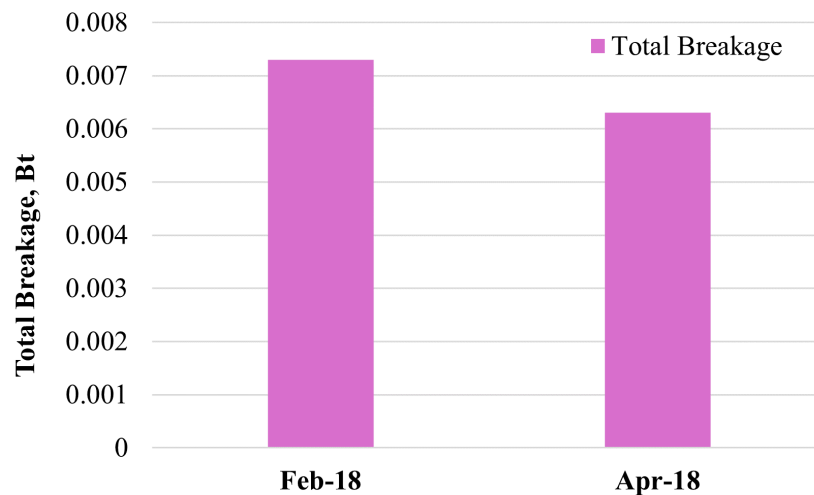


Figure 151. Hardin's total breakage evaluated from 2D image analyses of samples from OFD Class A section collected over time

4.2.3.2 Comparison of Morphological Parameters from 2D Image Analyses for OFD Class A

The changes in morphological parameters over time for the in-service OFD Class A aggregates are presented graphically in the form of boxplots in Figure 152 through Figure 156. The statistical details for these morphological parameters are presented in Table 40. The percent changes in median values of roundness, sphericity, and form factor were all negative (except for one small increase in form factor of 0.3%), indicating that the OFD aggregates tended to become less rounded and more angular and rougher over time upon fracturing and deteriorating. This conclusion is supported by the fact that the corresponding shape factor, roundness index, and angularity values all increased.

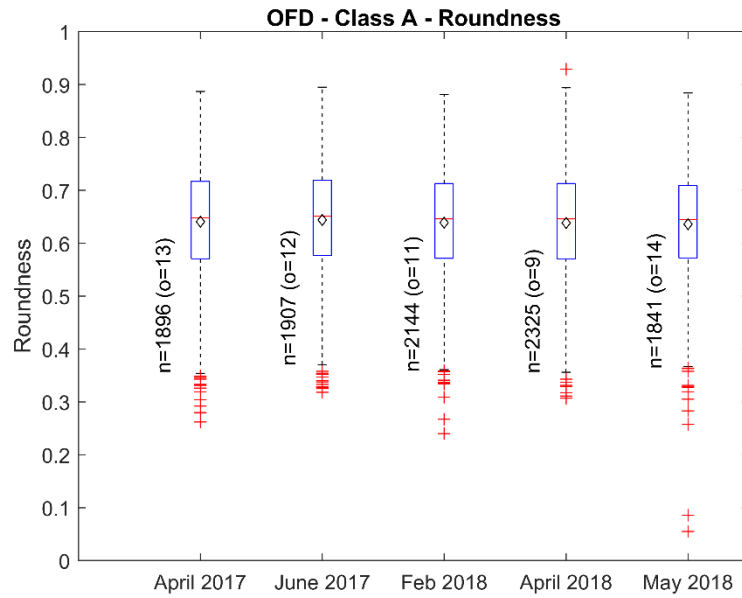


Figure 152. Comparison of roundness for OFD Class A samples collected over time

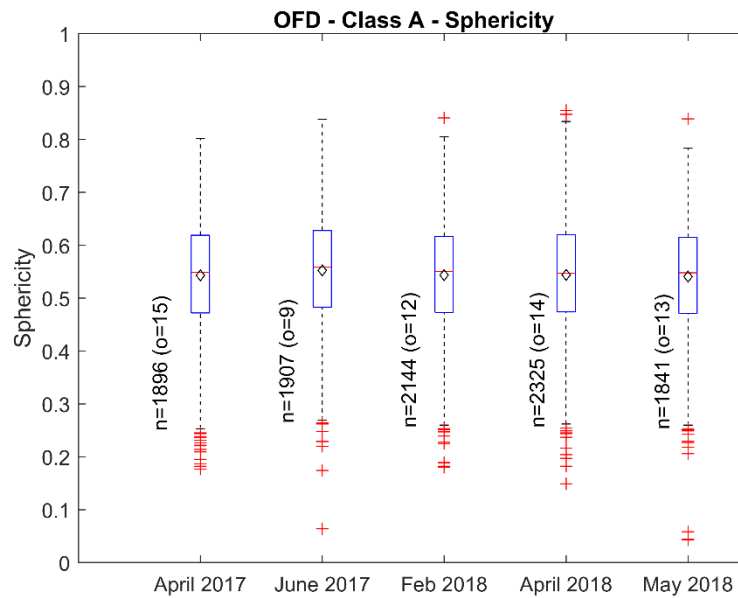


Figure 153. Comparison of sphericity for OFD Class A samples collected over time

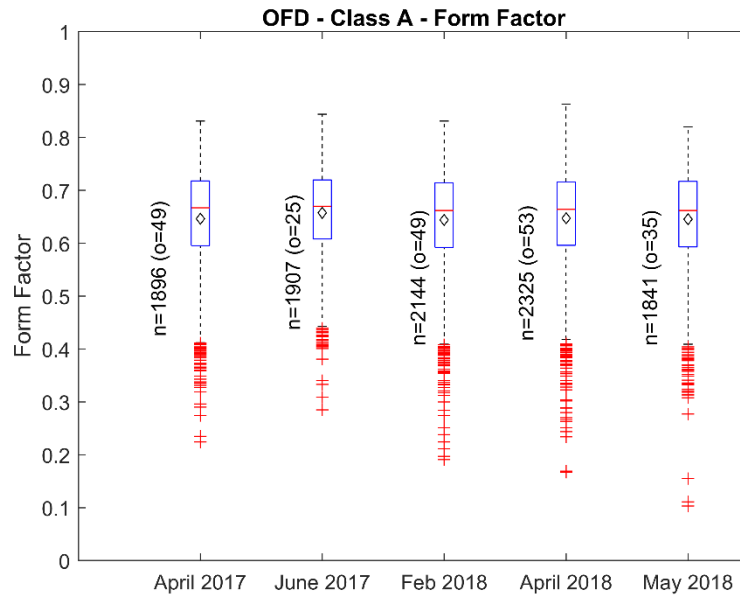


Figure 154. Comparison of form factor for OFD Class A samples collected over time

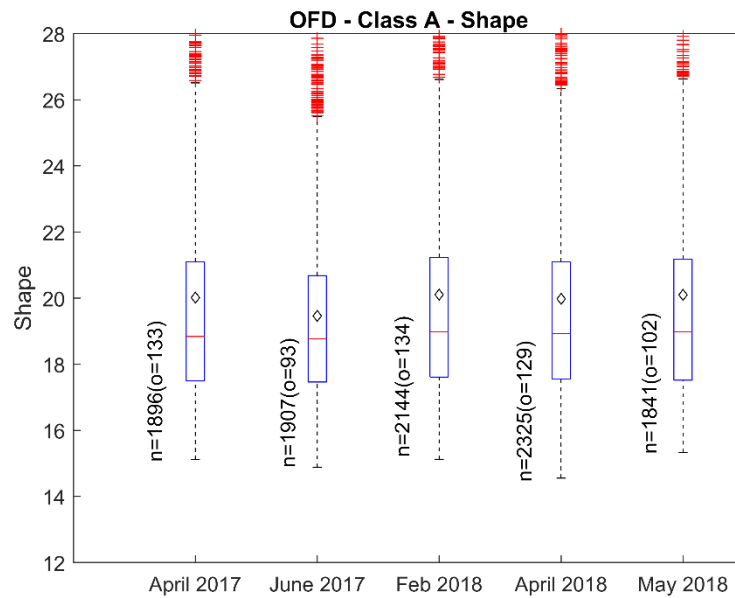


Figure 155. Comparison of shape factor for OFD Class A samples collected over time

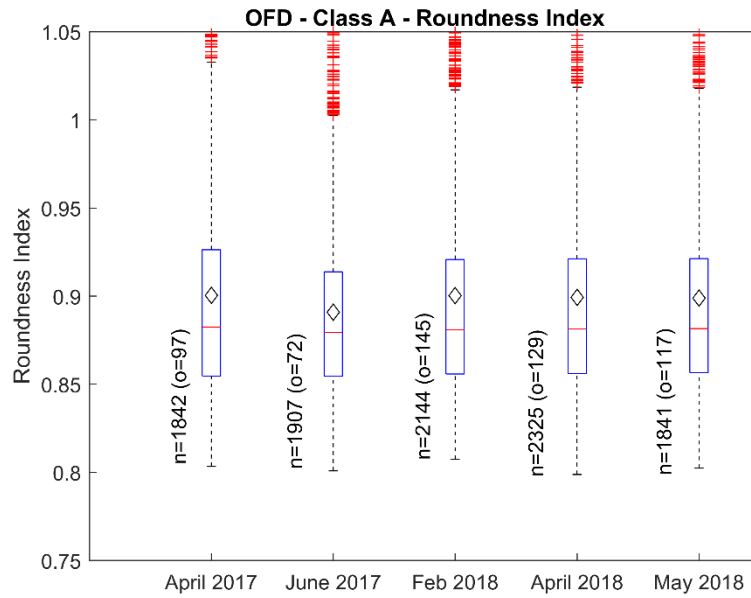


Figure 156. Comparison of roundness index for OFD Class A samples collected over time

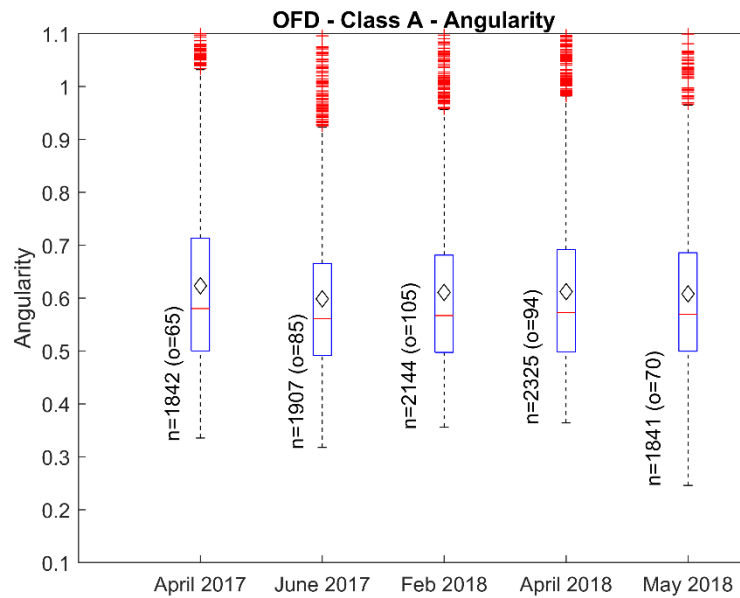


Figure 157. Comparison of angularity for OFD Class A samples collected over time

Table 40. Statistical results of morphological parameters for OFD Class A samples collected over time

Parameters	Sample Collection Date	Max. Value	Min. Value	Mean	Mode	Median	Std. Dev.	Skew- ness	Kurt- osis	Out- liers
Roundness	April 2017	0.887	0.262	0.641	0.572	0.648	0.103	-0.407	3.008	13
	June 2017	0.895	0.318	0.644	0.674	0.651	0.101	-0.328	2.768	12
	Feb 2018	0.881	0.24	0.639	0.598	0.646	0.099	-0.344	2.866	11
	% inc. *			-0.8%		-0.8%				
	April 2018	0.929	0.307	0.638	0.732	0.646	0.1	-0.298	2.766	9
	% inc. *			-0.9%		-0.8%				
	% inc. †			-0.2%		0.0%				
Sphericity	May 2018	0.884	0.055	0.636	0.667	0.645	0.102	-0.583	3.779	14
	April 2017	0.802	0.177	0.543	0.582	0.549	0.107	-0.292	2.929	15
	June 2017	0.838	0.064	0.552	0.617	0.559	0.104	-0.297	3.044	9
	Feb 2018	0.841	0.18	0.543	0.565	0.551	0.104	-0.265	2.909	12
	% inc. *			-1.6%		-1.4%				
	April 2018	0.855	0.149	0.544	0.602	0.547	0.104	-0.236	2.955	14
	% inc. *			-1.4%		-2.1%				
Form Factor	% inc. †			0.2%		-0.7%				
	May 2018	0.839	0.043	0.541	0.554	0.548	0.106	-0.38	3.38	13
	April 2017	0.831	0.224	0.646	0.694	0.667	0.098	-0.899	3.62	49
	June 2017	0.844	0.285	0.658	0.67	0.670	0.083	-0.716	3.417	25
	Feb 2018	0.831	0.191	0.644	0.69	0.662	0.096	-1.04	4.311	49
	% inc. *			-2.1%		-1.2%				
	April 2018	0.863	0.167	0.647	0.71	0.664	0.095	-1.019	4.503	53
Shape Factor	% inc. *			-1.7%		-0.9%				
	% inc. †			0.5%		0.3%				
	May 2018	0.82	0.103	0.645	0.719	0.662	0.096	-1.028	4.646	35
	April 2017	55.98	15.11	20.01	17.04	18.84	3.92	2.47	13.65	133
	June 2017	44.06	14.89	19.46	17.53	18.77	2.90	1.91	9.88	93
	Feb 2018	65.83	15.12	20.10	17.52	18.98	4.19	3.62	27.05	134
	% inc. *			3.3%		1.1%				
Shape Factor	April 2018	75.19	14.55	19.98	17.17	18.92	4.14	4.24	38.86	129
	% inc. *			2.7%		0.8%				
	% inc. †			-0.6%		-0.3%				
	May 2018	122.04	15.33	20.09	19.1	18.98	5.04	9.62	168.33	102

Parameters	Sample Collection Date	Max. Value	Min. Value	Mean	Mode	Median	Std. Dev.	Skew-ness	Kurt-osis	Out-liers
Roundness Index (RI)	April 2017	1.385	0.803	0.900	0.856	0.883	0.066	1.815	7.883	97
	June 2017	1.286	0.801	0.891	0.814	0.879	0.052	1.606	7.499	72
	Feb 2018	1.572	0.807	0.900	0.869	0.881	0.071	2.717	16.03	145
	% inc. *			1.0%		0.2%				
	April 2018	1.611	0.799	0.899	0.869	0.881	0.069	2.904	18.742	129
	% inc. *			0.9%		0.2%				
	% inc. †			-0.1%		0.0%				
	May 2018	1.56	0.802	0.899	0.836	0.882	0.065	2.335	13.255	117
Angularity	April 2017	1.366	0.335	0.623	0.449	0.58	0.165	1.077	3.75	65
	June 2017	1.267	0.318	0.598	0.456	0.561	0.149	1.279	4.646	85
	Feb 2018	1.742	0.356	0.611	0.427	0.567	0.159	1.497	6.253	105
	% inc. *			2.2%		1.1%				
	April 2018	1.401	0.364	0.612	0.416	0.572	0.156	1.162	4.149	94
	% inc. *			2.3%		2.0%				
	% inc. †			0.2%		0.9%				
	May 2018	1.364	0.246	0.608	0.399	0.569	0.152	1.17	4.429	70

*w.r.t. June 2017, †w.r.t. Feb 2018

Considering altogether the above discussed changes in gradation, breakage, and morphological parameters, the greatest amount of breakage occurred after construction during the September 2016–April 2017 timeframe. For these same sampling dates, the corresponding slight reduction in gravel fraction and increase in sand fraction by April 2017 quantify the breakdown of gravel-sized particles into sand-sized particles. Additionally, the positive values of total breakage based on image analysis for samples collected in February 2018 and April 2018 indicate ongoing breakage of surface gravel since June 2017, with higher breakage observed in the February 2018 samples. Furthermore, the increase in median form factor, and decrease in median shape factor and mean roundness index in the samples collected in April 2018 compared to February 2018 suggests much less particle degradation in these samples after the first maintenance period.

4.2.3.3 Geological Tests for OFD Class A

Geological tests were conducted on the available surplus samples of OFD Class A, which were collected from the test section in April 2017, April 2018, and May 2018. The tests identified five rock types, the percentages of which over time are shown in Figure 158 and Table 41. The percentage changes in the rock types over time are not calculated in Table 41 because these surplus samples were from different periods for which no samples were available from the corresponding reference construction or maintenance dates.

Virgin quarry samples of OFD Clean and OFD Class A collected in project TR-704 were also located and tested, and the properties and thin sections of the rock types found are reported in Figure 159. As shown in the figure, two rock types were found in the Clean sample whereas four rock types were found in the Class A sample. RT1 (porous dolostone) had an abundance of 79% and grain density of 2.88 g/cm³ in the Clean sample, compared to 53% and 2.83 g/cm³ in the Class A sample. RT2 (highly porous dolostone) had an abundance of 15% and grain density of

2.88 g/cm³ in the Clean material, compared to 5% and 2.85 g/cm³ for the Class A material. The Class A sample also contained RT3 (moderately porous dolostone) with 27% abundance and 2.86 g/cm³ grain density, and RT4 (cherty microporous dolostone) with 8% abundance and 2.65 g/cm³ grain density.

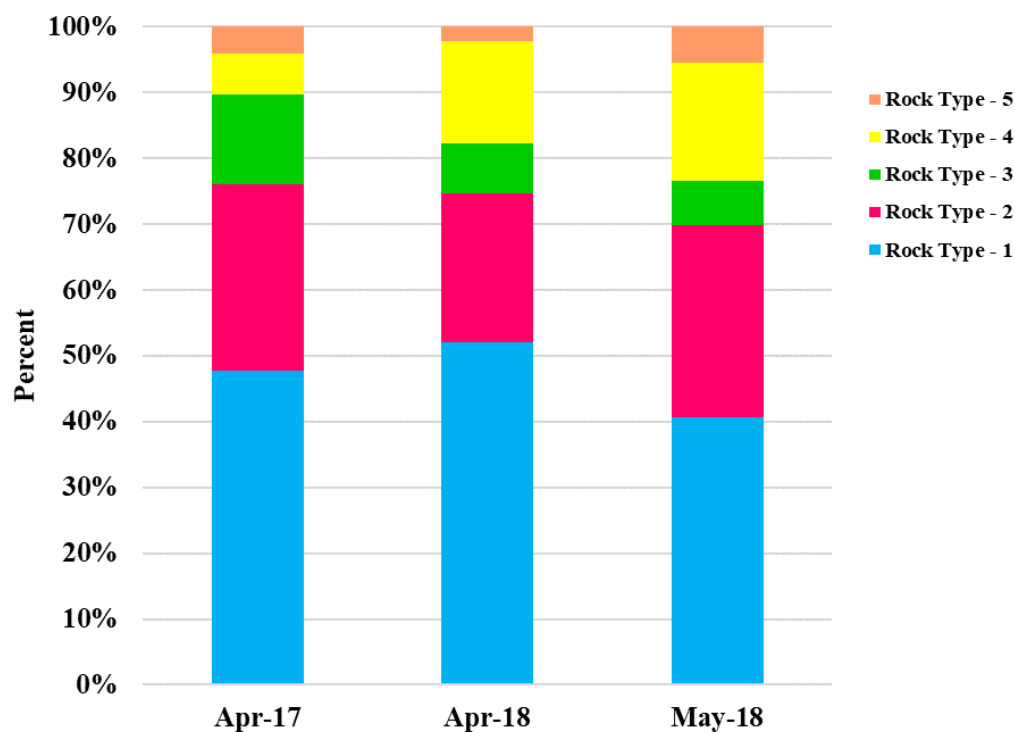
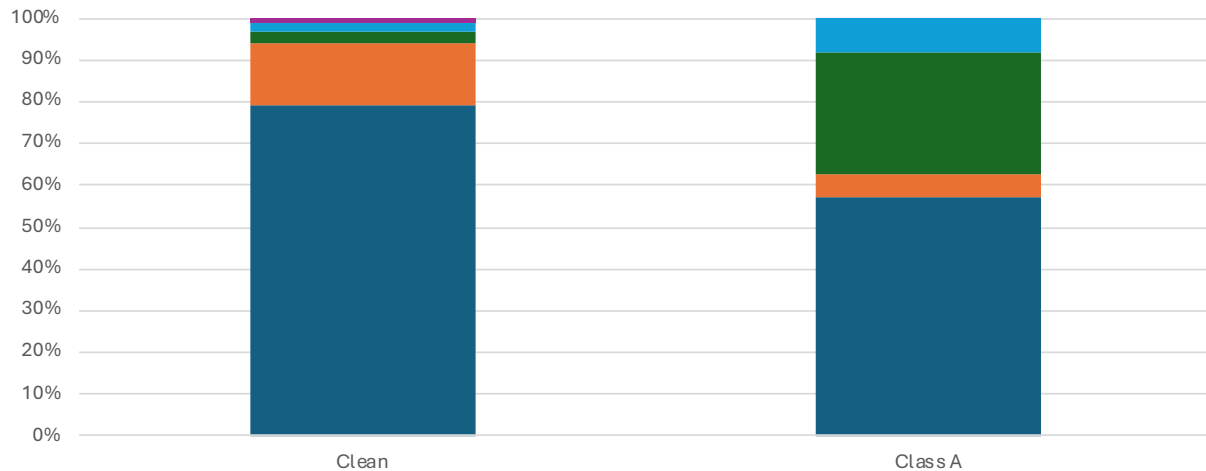


Figure 158. Percentages of rock types in OFD Class A samples collected over time

Table 41. Geological rock types and their percentages for OFD Class A samples collected over time

Sample Collection Date	% Rock Type 1	% Rock Type 2	% Rock Type 3	% Rock Type 4	% Rock Type 5
April 2017	47.7	28.4	13.6	6.2	4.1
April 2018*	52	22.6	7.6	15.6	2.2
May 2018	40.7	29.2	6.6	18	5.5




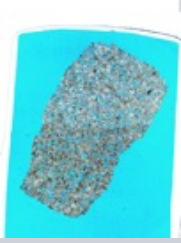




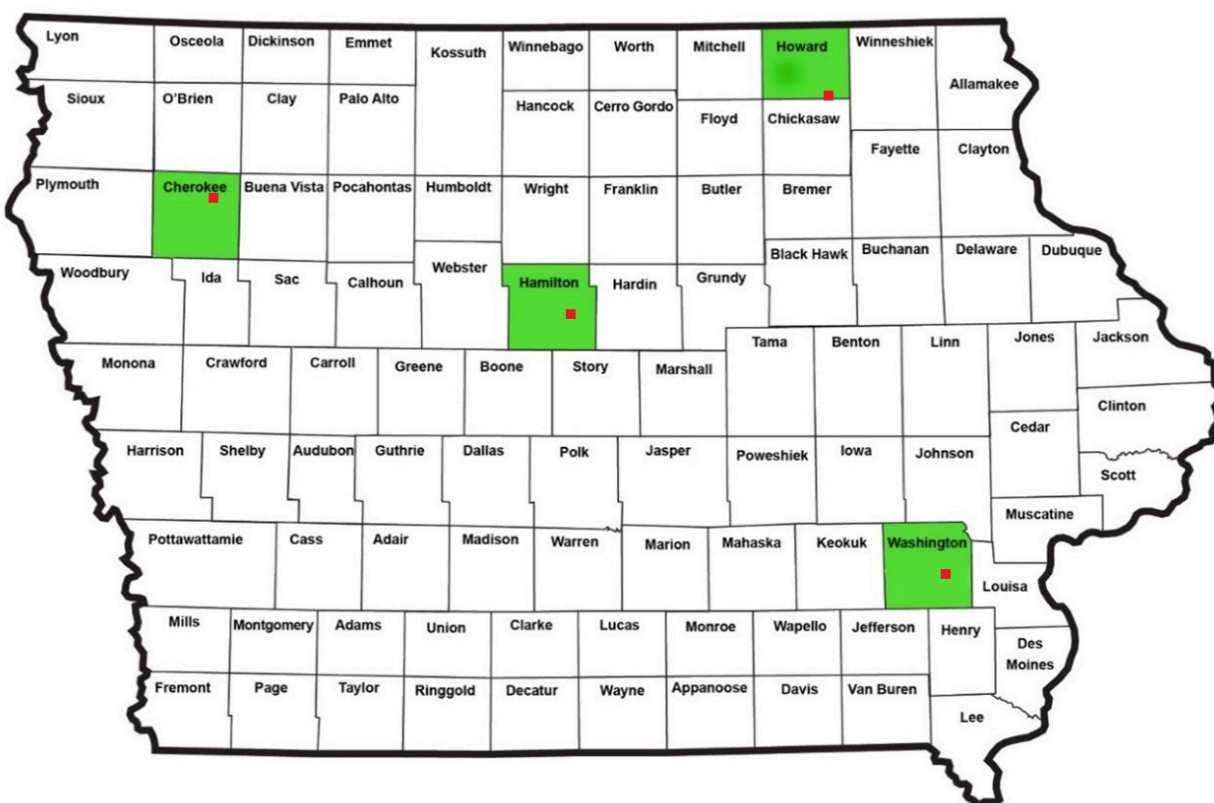
		1	2	3	4
Clean	GD (g/cm ³)	2.88	2.88		
	Abund	79%	15%		
	Image				
Class A	Image				
	Abund	53%	5%	27%	8%
	GD (g/cm ³)	2.83	2.85	2.86	2.65

Figure 159. Rock types, grain densities, abundances, and thin section images for Clean versus Class A OFD quarry samples from TR-704 project

4.3 Coarse Aggregate Samples Collected from Test Sections of IHRB Project TR-721

To further understand the deterioration of aggregates sourced from various quarries and used in granular road surfaces, data from the previous long-term IHRB Project TR-721 was analyzed, and surplus samples that could be located were retrieved from storage and tested. In the project, 31 test sections were built in four separate Iowa counties. The purpose was to investigate the effectiveness of different chemical and mechanical stabilization methods on reducing freeze-thaw and moisture related damage for granular-surfaced roads. The study was designed to cover

a range of different aggregate sources, subgrade soil types, and weather conditions across the state. The locations of the test sites, shown in Figure 160, were as follows: (1) Vail Avenue between 300th St and 310th St in Hamilton County, (2) Old 21 Road between 480th St and 490th St in Cherokee County, (3) 100th St between Pine Ave and Quail Ave in Howard County, and (4) 260th St between Palm Ave and Quince Ave in Washington County. The test sections in each county included one Control section, one Optimized Gradation with Clay Slurry (OGCS) section, and one Aggregate Columns section. Additionally, multiple mechanically stabilized sections were constructed in Howard and Cherokee Counties, and multiple chemically stabilized sections were constructed in Hamilton and Washington Counties.



Xue et al. 2022

Figure 160. Locations of test sections for TR-721 project in Hamilton, Cherokee, Howard, and Washington Counties

The Control sections in all four counties were representative of the typical road surfacing materials and local maintenance practices used, with no modifications made. To achieve a consistent aggregate surface thickness of 4 in., maintenance aggregates were uniformly spread on the surface of each Control section and bladed to a crown of 4 degrees during construction. For the present project, surplus aggregate samples collected over time from the Control, Aggregate Columns, and OGCS sections were tested, and PSD data from the TR-721 report was analyzed for these sections. The study aimed to construct test sections in areas with high traffic volumes and similar truck counts. The annual average daily traffic (AADT) levels for the test section

roads in all four counties are listed in Table 42, indicating that the four counties experienced comparable levels of daily traffic activity.

Table 42. Traffic counts and overall lengths of TR-721 test sites

County	Test Site	Length (ft)	AADT	AADT Year	Trucks
Hamilton	Vail Avenue between 300th and 310th Streets	5,210	70	2011	High
Cherokee	Old 21 Road between 480th and 490th Streets	3,233	100*	2011	Moderate
Howard	100th Street between Pine and Quail Avenues	5,333	110	2013	High
Washington	260th Street between Palm and Quince Avenue	3,936	90	2010	High

*160 vpd for aggregate columns section in Cherokee County

Source: Xue et al. 2022

4.3.1 Howard County – Control Section

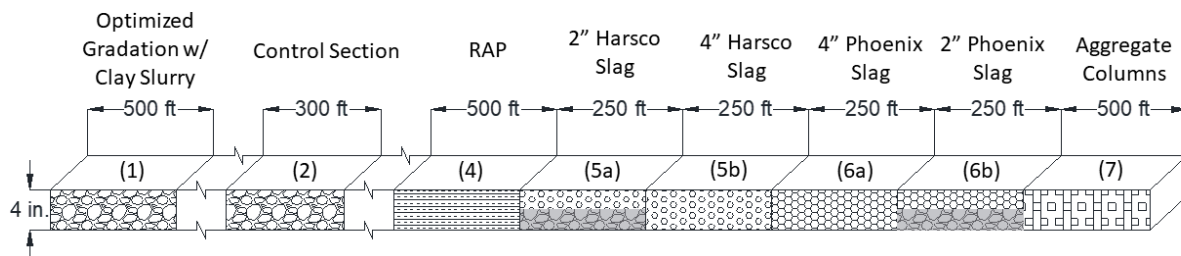
Seven types of mechanically stabilized test sections and a control section were constructed in Howard County as part of IHRB Project TR-721. A satellite image of the location and a schematic diagram illustrating the layout of the test sections are shown in Figure 161 and Figure 162, respectively. The 300 ft long Control section was constructed to evaluate the performance of the test sections against the county’s typical construction and maintenance practices. To construct the Control section in fall 2018, maintenance aggregates were spread over the existing road surfacing material so that the initial thickness started at 4 in. Around 40 tons of additional maintenance aggregates were spread over the section in fall 2019. Throughout the project duration, granular surface materials were collected from the Control section over a period of two years, specifically during the construction phase in fall 2018 and again in spring 2019, fall 2019, and spring 2020.

Howard County: 100th St between Pine Ave. and Quail Ave. <https://goo.gl/maps/AfArYpCrzBH2>



Figure 161. Satellite image of Howard County mechanically stabilized test sections

Howard County:



Xue et al. 2022

Figure 162. Layouts of mechanically stabilized test sections in Howard County

4.3.1.1 Comparison of Breakage Parameters for Howard County Control Section

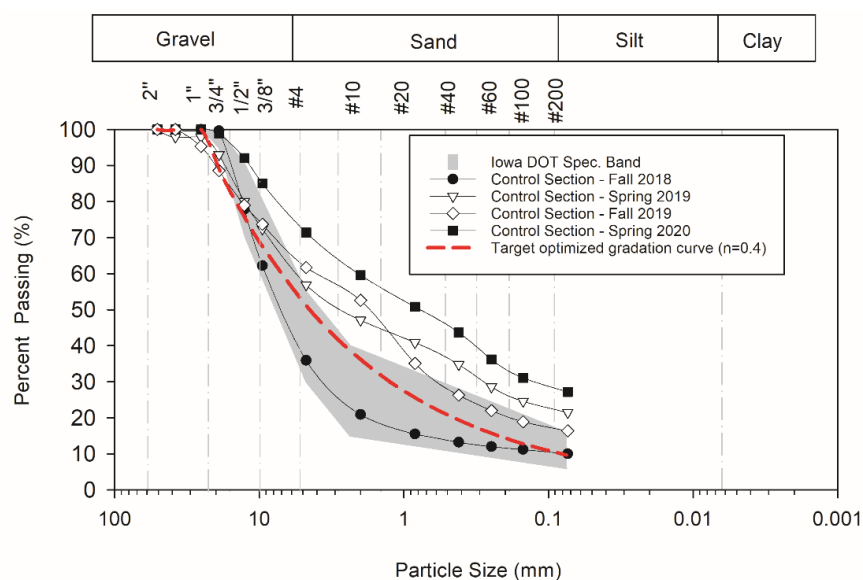
In the TR-721 project, PSD analyses were performed on the collected materials through laboratory sieve and hydrometer tests to determine mechanical degradation and material loss over time. The PSD curves from these tests for Howard County samples are shown in Figure 163. The PSD curves of the spring 2019 and spring 2020 samples shifted upwards significantly with respect to their starting curves from fall 2018 and fall 2019, in both cases ending up far above both the target optimized gradation curve and the Iowa DOT Class A/B specification band, indicating significant breakage of the gravel road surface material with time.

The PSD curves were digitized in the present study to analyze the mechanical degradation for the Control section samples collected in spring 2019 relative to those collected during construction in fall 2018. For spring 2020, the breakage parameters were evaluated relative to those collected in fall 2019 after spreading of the new surface material. The digitized PSD curves and resulting total breakage values are shown in Figure 164 and Figure 165 for the samples collected in spring 2019 and spring 2020, respectively. The corresponding Hardin's total breakage, breakage potential, and relative breakage are also detailed in Table 43 along with the percentages of gravel, sand, and fines for the samples collected over time. Figure 166 presents a bar chart of the cumulative total breakage for these two time intervals, showing that the total breakage was significant after placing fresh aggregate each year, and was greater in the first year than in the second year.

The percentages of gravel, sand, and fines for the samples collected over time are also presented in a bar chart Figure 167. The data in Table 43 and Figure 167 indicate a 21% reduction in the gravel fraction, 9.5% increase in the sand fraction, and 11.5% increase in the fines fraction during the Fall 2018–Spring 2019 period. Similarly, after placing new maintenance aggregates there was a 23.3% reduction in the gravel fraction, 12.5% increase in sand fraction, and 10.8% increase in fines fraction during the Fall 2019–Spring 2020 period.

4.3.1.2 Visual Surveys for Howard County Control Section

Visual surveys of the Control section's surface conditions are shown in Figure 168. In both years, the test sections were in good condition after spreading of new aggregates in fall but suffered significant distress and material breakdown by the following spring. The surface also exhibited considerable rutting, potholes and frost boils in both spring sampling periods.



Xue et al. 2022

Figure 163. Particle size distribution curves of Howard County Control Section for samples collected over time

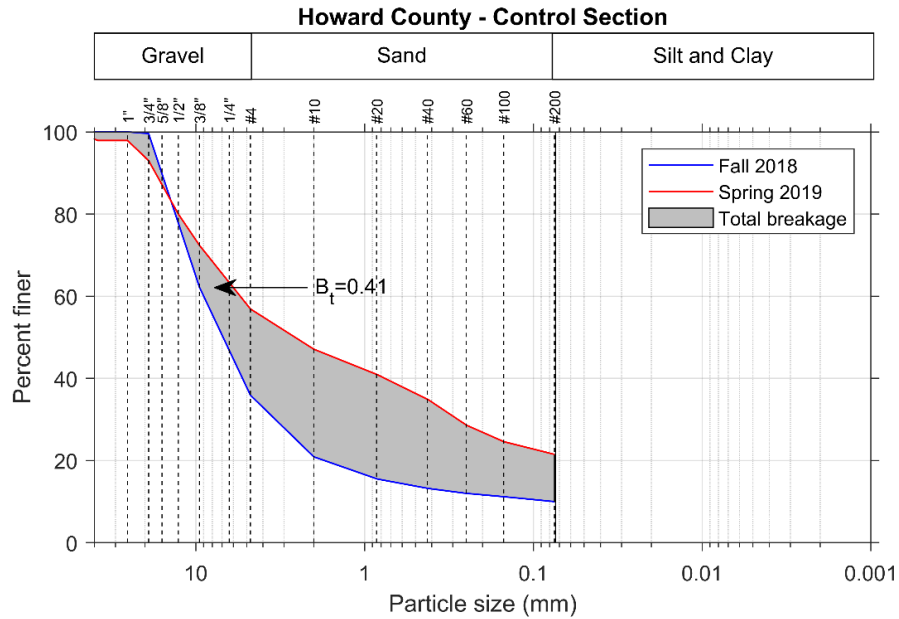


Figure 164. Particle size distributions and total breakage of coarse fraction for Howard County Control section between fall 2018 and spring 2019

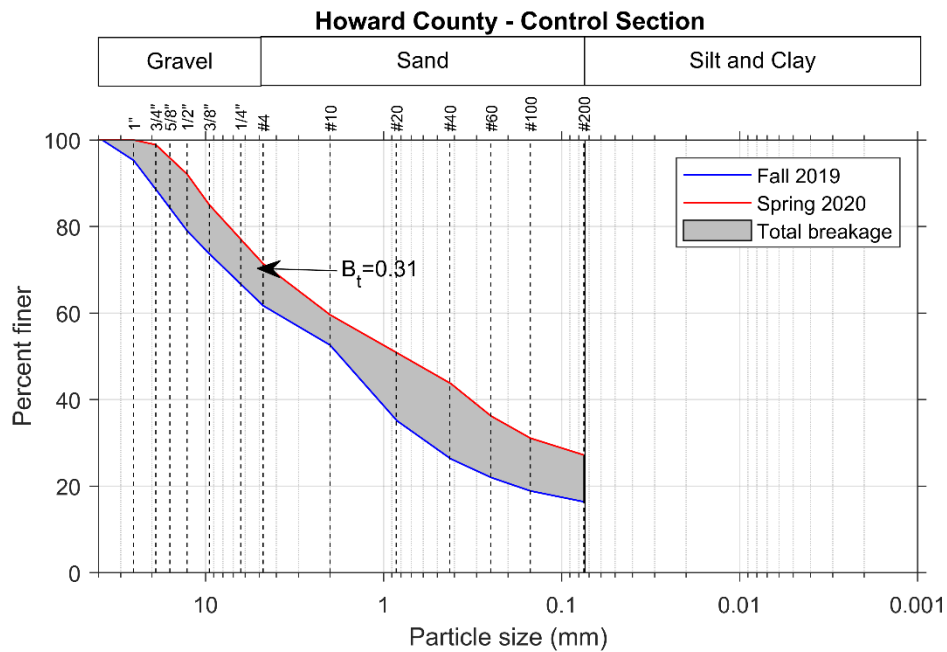


Figure 165. Particle size distributions and total breakage of coarse fraction for Howard County Control section between fall 2019 and spring 2020

Table 43. Breakage parameters from laboratory sieve analyses and percent gravel, sand, and fines for the samples of Howard County Control section

Sample Collection Date	Hardin's Breakage Parameters			% Gravel	% Gravel Red. [†]	% Sand	% Sand Inc. [†]	% Fines	% Fines Inc. [†]
	Total Breakage, B _t	Breakage Potential, B _p	Relative Breakage, B _r						
Fall 2018	-	-	-	64.1	-	25.9	-	10.0	-
Spring 2019*	0.4117	1.7139	0.2402	43.1	21.0	35.4	9.5	21.5	11.5
Fall 2019	-	1.7452	-	38.3	-	45.3	-	16.4	-
Spring 2020**	0.3052	1.3510	0.2259	15.0	23.3	57.8	12.5	27.2	10.8

* w.r.t. Fall 2018; ** w.r.t. Fall 2019; [†]Red. = Reduction; Inc. = Increase

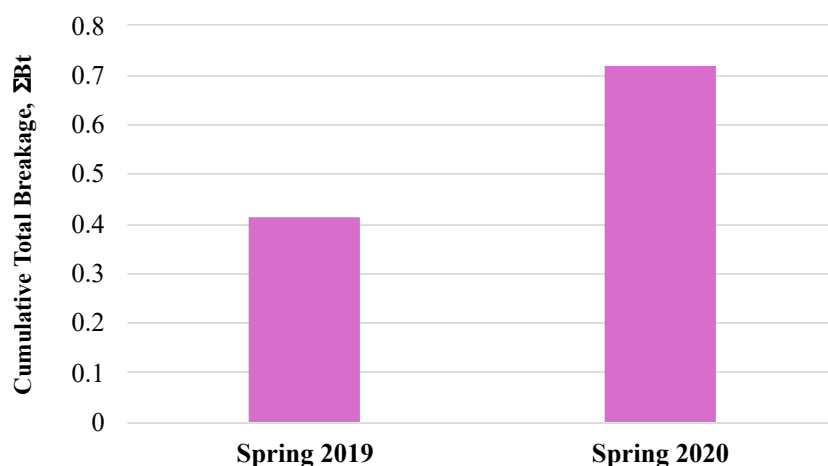


Figure 166. Cumulative total breakage of samples from Howard County Control section collected over time

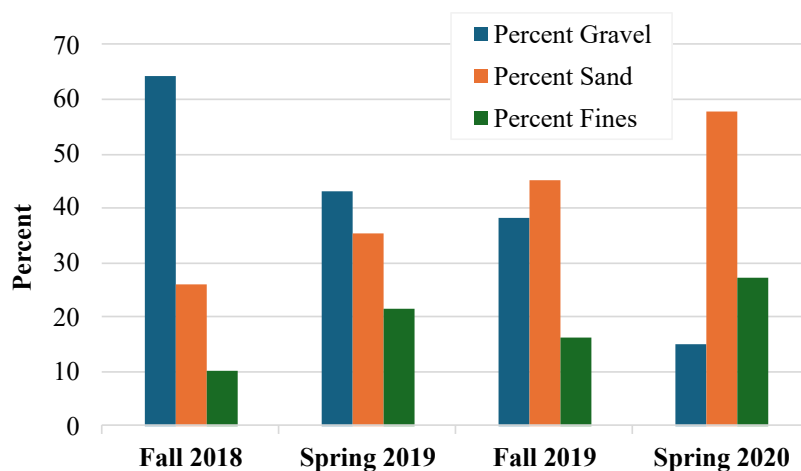


Figure 167. Gravel, sand and fines fractions of samples from Howard County Control section collected over time

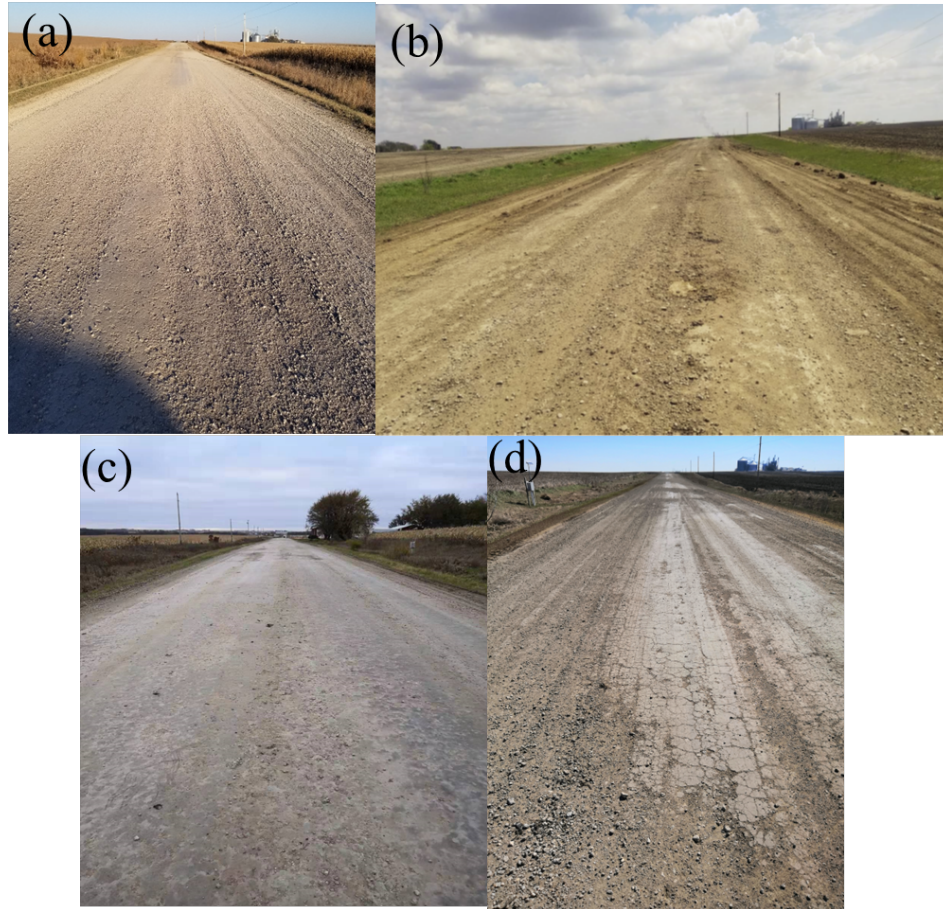


Figure 168. Visual surveys of Howard County Control section over time: (a) fall 2018 (b) spring 2019, (c) fall 2019, (d) spring 2020

4.3.2 Howard County – Optimized Gradation with Clay Slurry Test Section

As part of the completed IHRB Project TR-721, a 500 ft long stabilized test section was constructed in Howard County in August 2018 using the Optimized Gradation with Clay Slurry method developed in the project (Li et al. 2018). The OGCS method involves placing an optimized blend of aggregates to achieve tight particle packing as determined using the Gradation Optimization spreadsheet tool developed in IHRB Project TR-685, along with spraying a clay slurry that is then mixed into the surface course to add plasticity and bind the aggregate particles. Samples of the in-service OGCS surface course materials were collected from this field test section over a period of two years during different phases of the TR-721 project: first in fall 2018 during construction, then in spring 2019, fall 2019, and spring 2020.

4.3.2.1 Comparison of Breakage Parameters for Howard County OGCS Section

To evaluate the OGCS surface material's mechanical degradation and material loss over time, the PSD curves measured in the prior project were analyzed (Figure 169). Hardin's breakage parameters were then evaluated for the collected samples relative to those collected during

construction in fall 2018. This degradation is presented in Figure 170, Figure 171 and Figure 172 for the samples collected in spring 2019, fall 2019, and spring 2020, respectively. Details of the corresponding breakage parameters including total breakage, breakage potential, and relative breakage are presented in Table 44 along with the percentages of gravel, sand, and fines for the OGCS samples collected over time. The total breakage relative to fall 2018 is also presented in Figure 173, showing the expected trend of increasing total breakage with time.

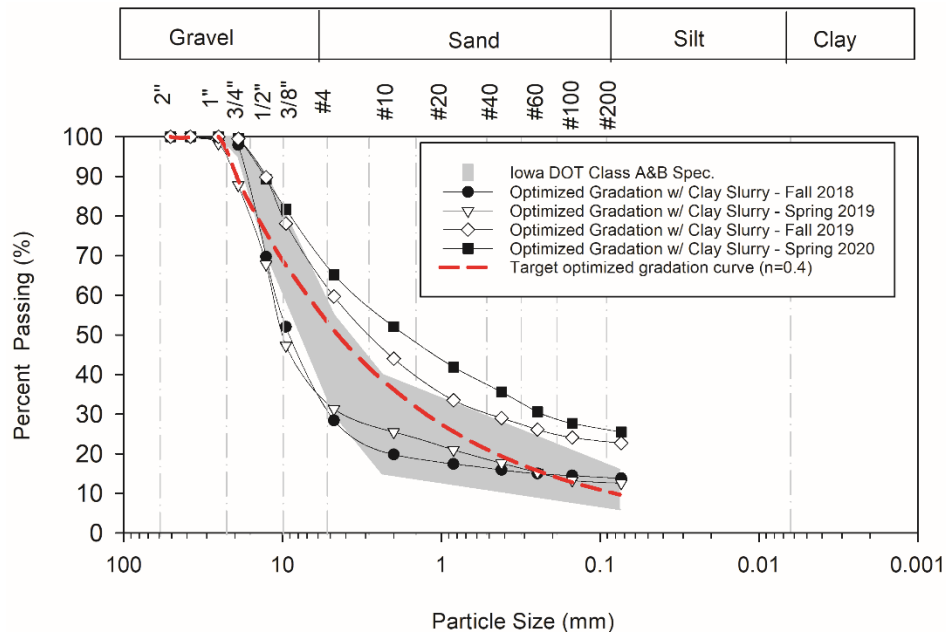
The breakage of 0.013 in the OGCS section as of spring 2019 (the first spring thaw following construction) was much lower than the corresponding value of 0.4117 for the nearby Control section reported in Table 43 and Figure 166. Additionally, the Control section required spreading of new maintenance aggregates by fall 2019 which then experienced another significant total breakage of 0.3052 by spring 2020, whereas the OGCS section didn't require maintenance aggregates. The OGCS breakage values are therefore cumulative as they are all referenced to the same post-construction PSD of fall 2018, whereas the Control section's spring 2020 breakage calculation had to be "reset" by referencing it to fall 2019 after spreading the maintenance aggregates. Therefore, summing the Control section's total breakage for spring 2019 and spring 2020 (because new aggregates were placed) gives a cumulative total breakage of 0.7169, compared to a cumulative total breakage of 0.5644 by spring 2020 for the OGCS section. The OGCS section therefore significantly reduced the amount of gravel breakage and eliminated the need for maintenance aggregates compared to the Control section, thereby demonstrating the performance benefit gained by OGCS stabilization.

The percentages of gravel, sand, and fines for the samples collected over time are also presented in a bar chart in Figure 174. The chart and the data in Table 44 demonstrate a continual reduction in the gravel-sized fraction over time, starting from 71.6% at the time of construction and decreasing to 34.8% by spring 2020. As the gravel-sized particles continually break down to smaller sizes, the corresponding sand fraction increases over time, going from 14.6% during construction to 39.7% by spring 2020, while the fines fraction starts at 13.8% during construction before decreasing slightly to 12.6% by spring 2019, then continually increases to 25.5% by spring 2020. Consistent with the material in the test section continually breaking down to smaller sizes, the PSD curves in Figure 169 shifted upwards with time. However as shown in Xue et al. (2022), compared to the Control section the OGCS curves stayed much closer to the target optimized gradation curve and the Iowa DOT Class A and B specification band, indicating less breakdown of the gravel road surface material with time. By spring 2020, the OGCS section still had a 34.8% gravel fraction and a sand fraction of 39.7% (Table 44 and Figure 174), whereas the Control section fared worse with only 15% gravel and a much higher sand fraction of 57.8% (Table 43 and Figure 167).

4.3.2.2 Visual Surveys for Howard County OGCS Section

Photos from visual surveys of the Howard County OGCS section taken over time are shown in Figure 175. The visual surveys confirmed that the OGCS test section had less breakage over time compared to the control section, as the clay slurry hardened into a smooth and tight surface that bound the aggregates and resembled pavement in dry conditions. Over time, the photos show that the finer material comprising the smooth surface was gradually worn away and lost, releasing

some of the bound aggregates and allowing them to break down. As detailed in Xue et al. (2022), the performance of the OGCS test section in terms of surface distresses including rutting, potholes, washboarding, and raveling was much better than the adjacent Control section and surrounding roads, despite a very wet spring with flooding and saturation that made many roads in the area nearly impassable.



Xue et al. 2022

Figure 169. Particle size distribution of coarse fraction of Howard County OGCS test section over time

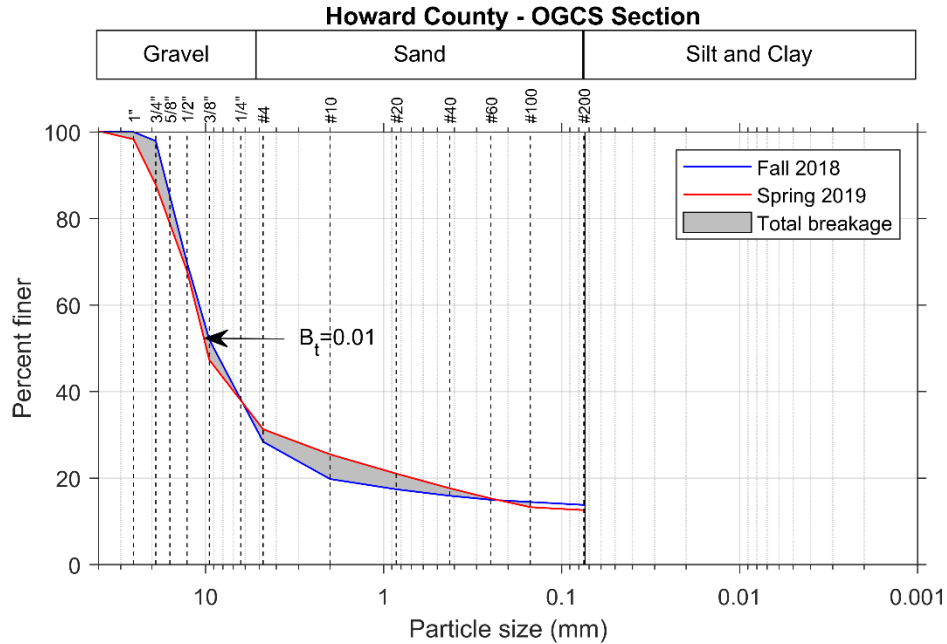


Figure 170. Particle size distributions of coarse fraction from sieve analyses and evaluation of total breakage between fall 2018 and spring 2019 for OGCS test section

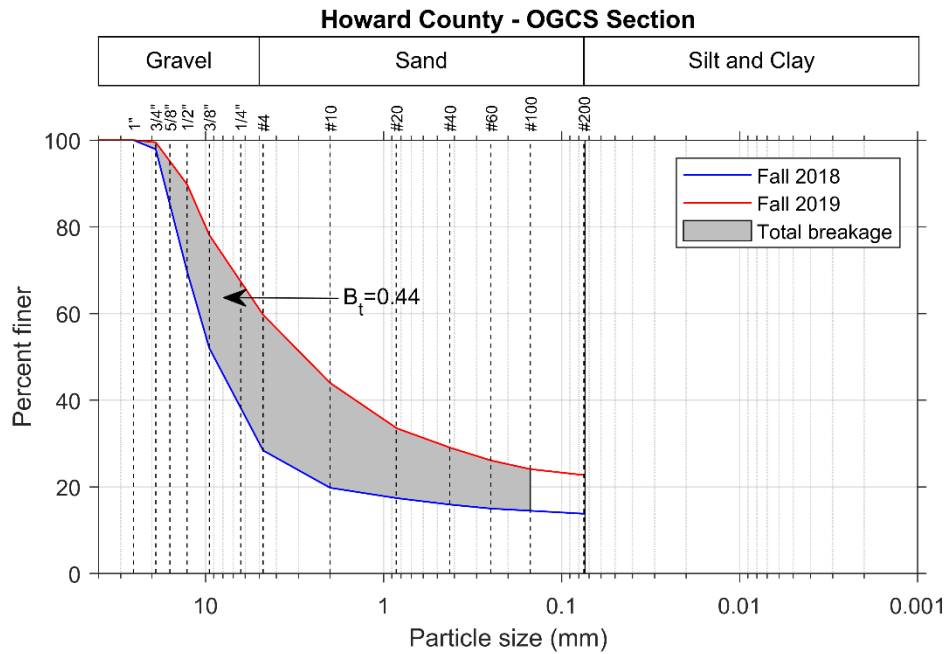


Figure 171. Particle size distributions of coarse fraction from sieve analyses and evaluation of total breakage between fall 2018 and fall 2019 for OGCS test section

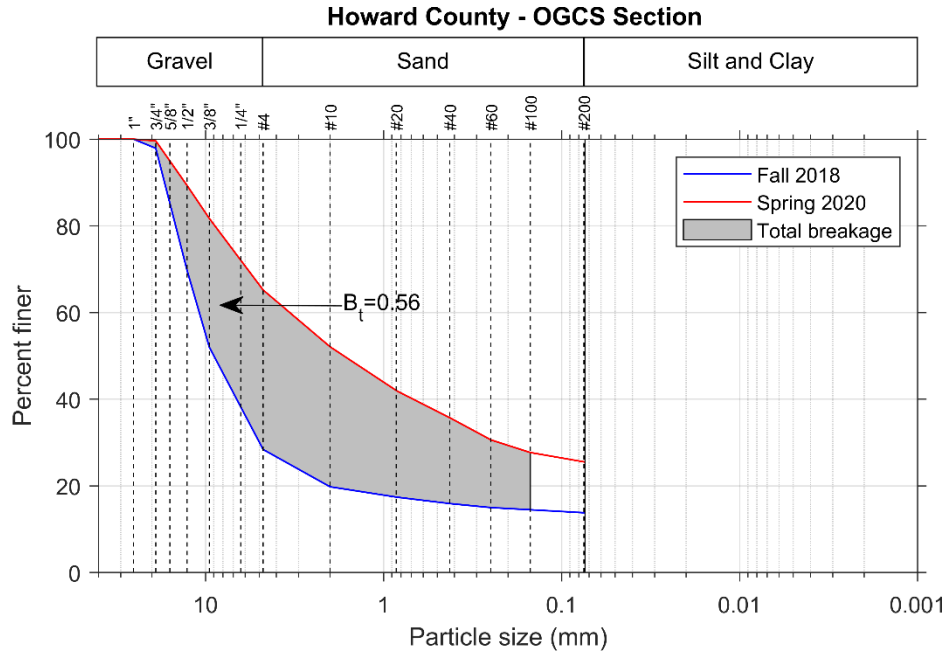


Figure 172. Particle size distributions of coarse fraction from sieve analyses and evaluation of total breakage between fall 2018 and spring 2020 for OGCS test section

Table 44. Breakage parameters from sieve analyses and percent gravel, sand, and fines for Howard County OGCS samples collected over time

Sample Collection Date	Hardin's Breakage Parameters*			% Gravel	% Gravel Red.**	% Sand	% Sand Inc.††	% Fines	% Fines Inc.††
	Total Breakage, B_t	Breakage Potential, B_p	Relative Breakage, B_r						
Fall 2018	-	-	-	71.6	-	14.6	-	13.8	-
Spring 2019	0.013	1.7452	0.0074	68.7	2.9	18.7	4.1	12.6	-1.2
Fall 2019	0.4385	1.7452	0.2512	40.3	31.3	37.0	22.4	22.7	8.9
Spring 2020	0.5644	1.7452	0.3224	34.8	36.8	39.7	25.1	25.5	11.7

*w.r.t. Fall 2018, **Reduction, ††Increase

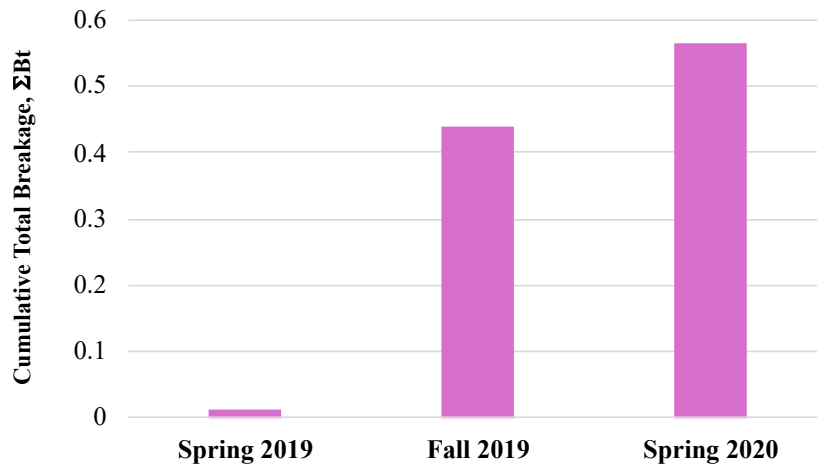


Figure 173. Cumulative total breakage for Howard County OGCS samples collected over time

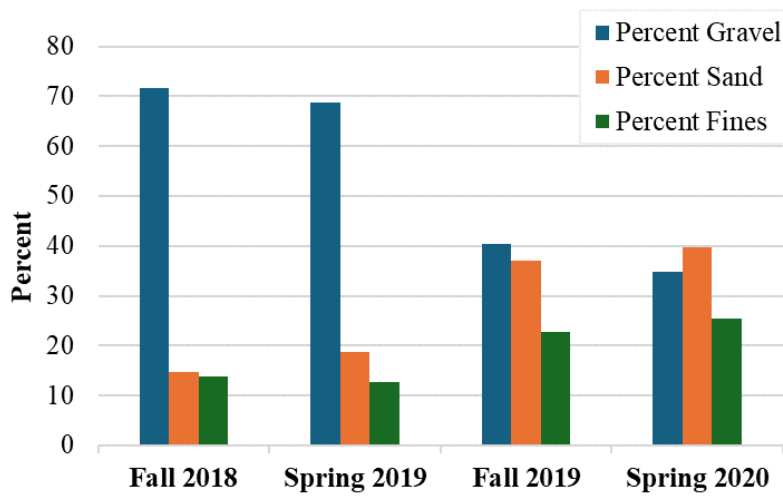


Figure 174. Percent gravel, sand, and fines for Howard County OGCS samples collected over time

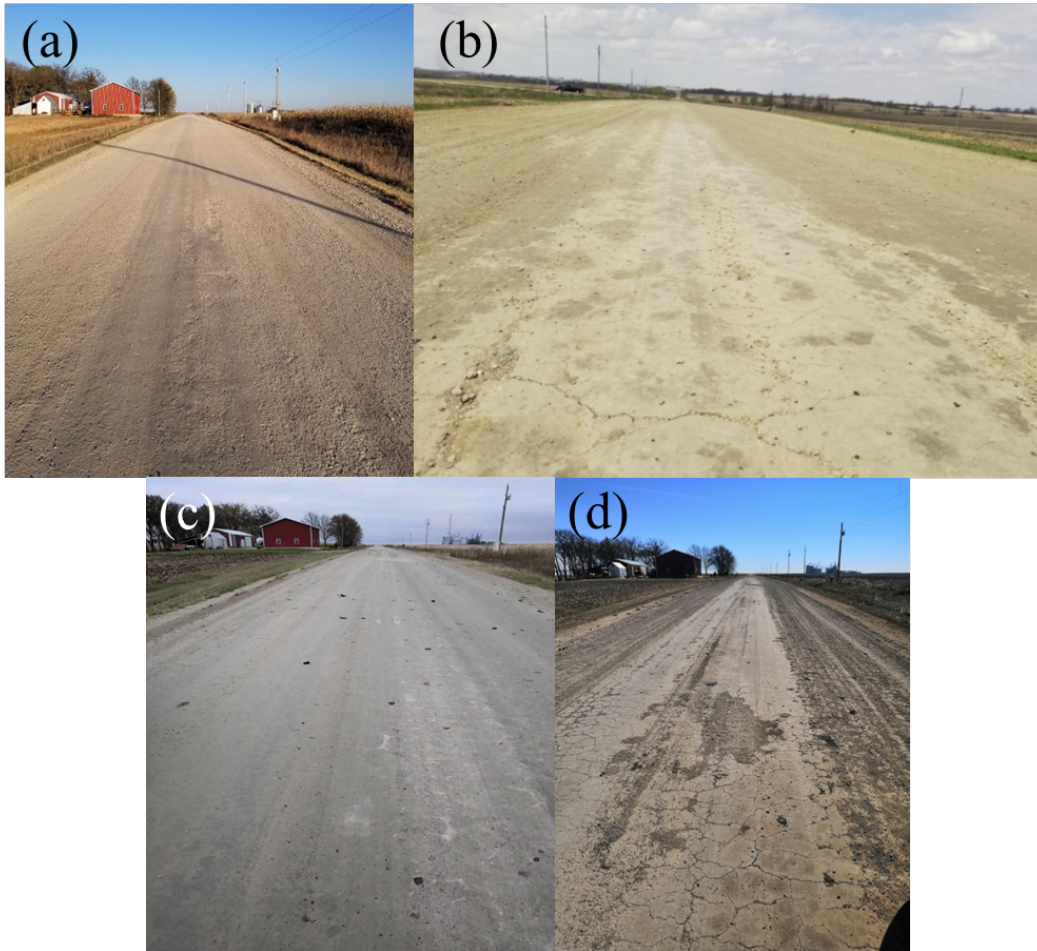


Figure 175. Visual surveys of Howard County OGCS section over time: (a) fall 2018, (b) spring 2019, (c) fall 2019, (d) spring 2020

4.3.3 Howard County – Aggregate Columns Section

A 500 ft long Aggregate Columns test section was constructed in Howard County in August 2018 as part of IHRB Project TR-721. To construct the columns, 12 in. diameter by 7 ft deep holes were augured in the 10 ft grid pattern shown in Figure 176 and backfilled with 1 in. clean aggregate, then the road surface was covered with Class A/B road rock. Samples of the granular surface materials were collected from the road surface over a period of two years, specifically during the construction phase in fall 2018, then again in spring 2019, fall 2019, and spring 2020. No additional aggregates were placed on the section prior to fall 2019. However, 15 tons of maintenance aggregates were added to the surface sometime after the sample collection in fall 2019. Particle size distribution analyses were performed on the collected samples through laboratory sieve and hydrometer tests in IHRB Project TR-721. The PSD curves from these tests are shown in Figure 177.

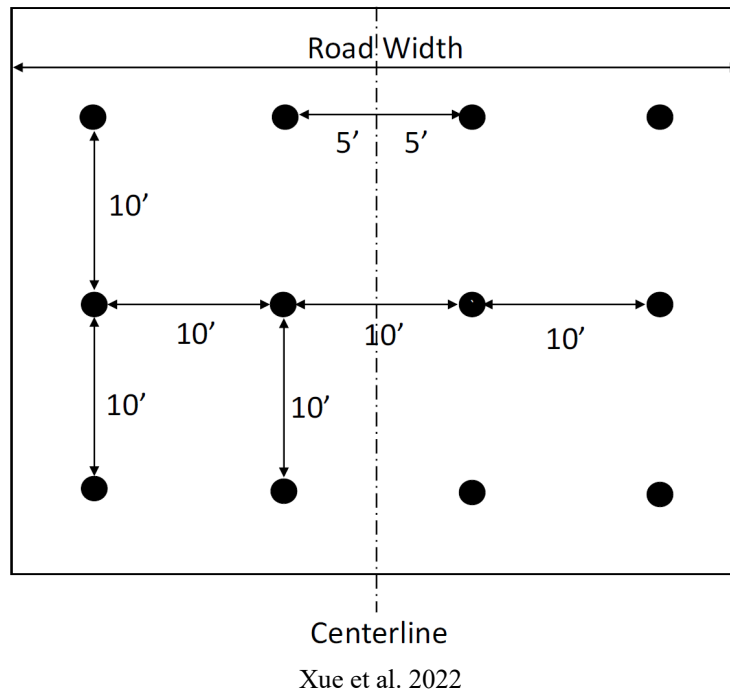


Figure 176. Column layout pattern for Howard County Aggregate Columns section, road width = 40 ft

4.3.3.1 Comparison of Breakage Parameters for Howard County Aggregate Columns Section

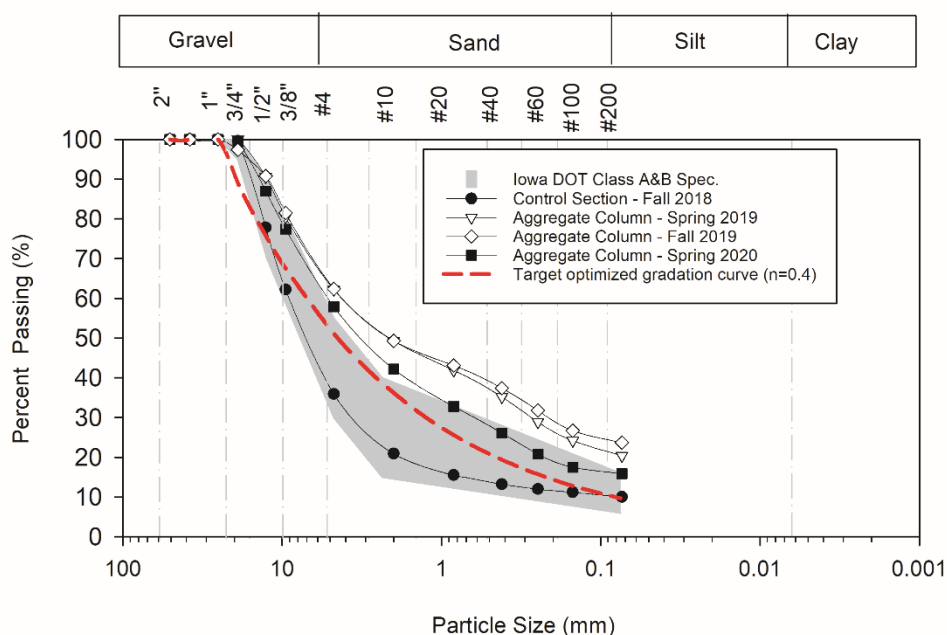
In the present study, the PSD curves of Figure 177 were digitized to analyze the mechanical degradation represented by Hardin's breakage parameters. The breakage was evaluated for the samples collected in spring 2019 and fall 2019 relative to those collected during construction in fall 2018. Breakage could not be calculated for the samples collected in spring 2020 because no new samples were collected after the maintenance aggregates were added in fall 2019. The total breakage relative to fall 2018 is presented in Figure 178 and Figure 179 for the samples collected in spring 2019 and fall 2019. The total breakage, breakage potential, and relative breakage along with the percentages of gravel, sand, and fines for the samples collected from the Howard County Aggregate Columns section over time are detailed in Table 45. The cumulative total breakage for the samples from spring 2019 and fall 2019 relative to fall 2018 are also shown in a bar chart in Figure 180. The bar chart illustrates that a significant total breakage of $B_t=0.4905$ occurred between fall 2019 and spring 2019, but increased only slightly to $B_t=0.5177$ between spring and fall of 2019.

The percentages of gravel, sand, and fines for the samples collected over time are also presented in a bar chart Figure 181. From the time of construction up through spring 2019, the data in Table 45 and Figure 181 indicate a significant 26.3% reduction in the gravel fraction along with increases in the sand and fines fractions of 15.9% and 10.4%, respectively. Measuring from construction through fall 2019, the total reduction in gravel content increased only slightly further to 26.5%, while the increases in sand and fines fractions changed to 12.8% and 13.7%, respectively. As is evident in Figure 177, the PSD curves for spring 2019 and fall 2019 had

shifted upwards with respect to the fall 2018 sample, ending up above the Iowa DOT Class A/B specification band and indicating breakdown of the gravel road surface material with time. However, the sample collected in spring 2020 reflected the increased gravel fraction and decreased sand and fines fractions gained by spreading the maintenance aggregate in late fall 2019, lowering the PSD curve almost entirely back within the Class A/B specification band.

4.3.3.2 Visual Surveys for Howard County Aggregate Columns Section

Photos from visual surveys of the Howard County Aggregate Columns section taken over time are shown in Figure 182. The visual surveys confirm that the decrease in gravel fraction and increase in fines fraction were most significant between construction in fall 2018 and the following spring 2019, then they changed very little through fall 2019, and finally the gravel fraction increase provided by the maintenance aggregates was still visually evident by spring 2020.



Xue et al. 2022

Figure 177. Particle size distributions of Howard County Aggregate Columns surface materials for samples collected over time

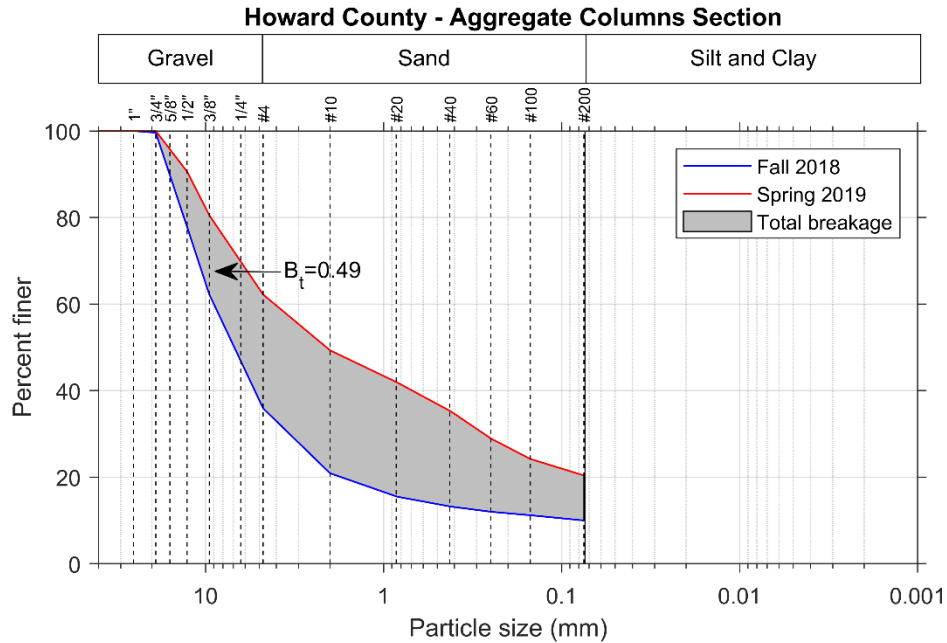


Figure 178. Particle size distributions and evaluation of total breakage of coarse aggregate for Howard County Aggregate Columns section from fall 2018 to spring 2019

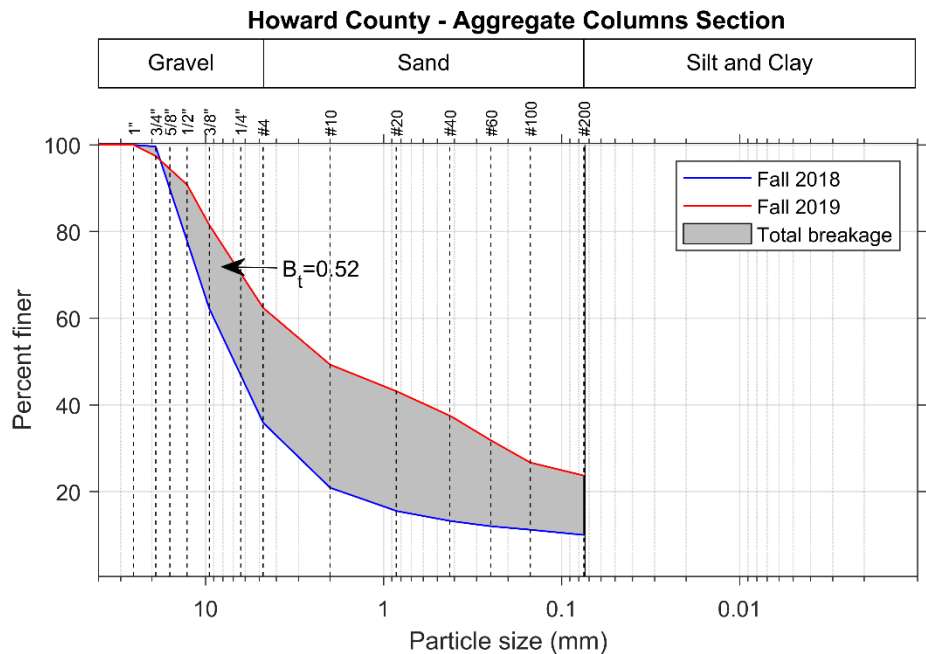


Figure 179. Particle size distributions and evaluation of total breakage of coarse aggregate for Howard County Aggregate Columns section from fall 2018 to fall 2019

Table 45. Breakage parameters from laboratory sieve analyses and percent gravel, sand, and fines for samples of Howard County Aggregate Columns section

Sample Collection Date	Hardin's Breakage Parameters			% Gravel	% Gravel Red. [†]	% Sand	% Sand Inc. [†]	% Fines	% Fines Inc. [†]
	Total Breakage, B _t	Breakage Potential, B _p	Relative Breakage, B _r						
Fall 2018	-	-	-	64.1	-	25.9	-	10.0	-
Spring 2019*	0.4905	1.7139	0.2862	37.8	26.3	41.8	15.9	20.4	10.4
Fall 2019*	0.5177	1.7139	0.3020	37.6	26.5	38.7	12.8	23.7	13.7
Spring 2020**	-	-	-	42.1	-	42.0	-	15.9	-

*w.r.t. Fall 2018; ** No initial PSD for determining breakage; [†]Red. = Reduction; Inc. = Increase

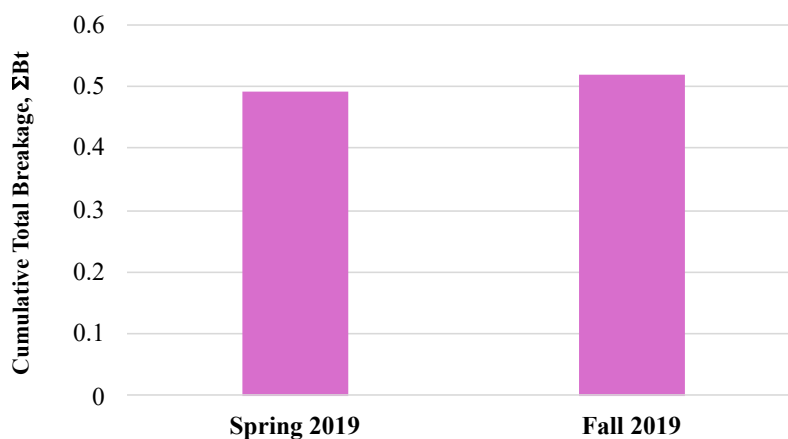


Figure 180. Cumulative total breakage of surface course of Howard County Aggregate Columns section over time

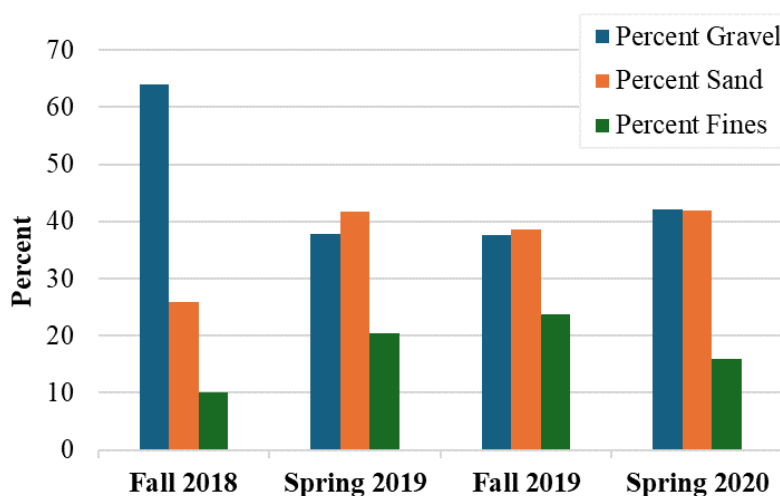
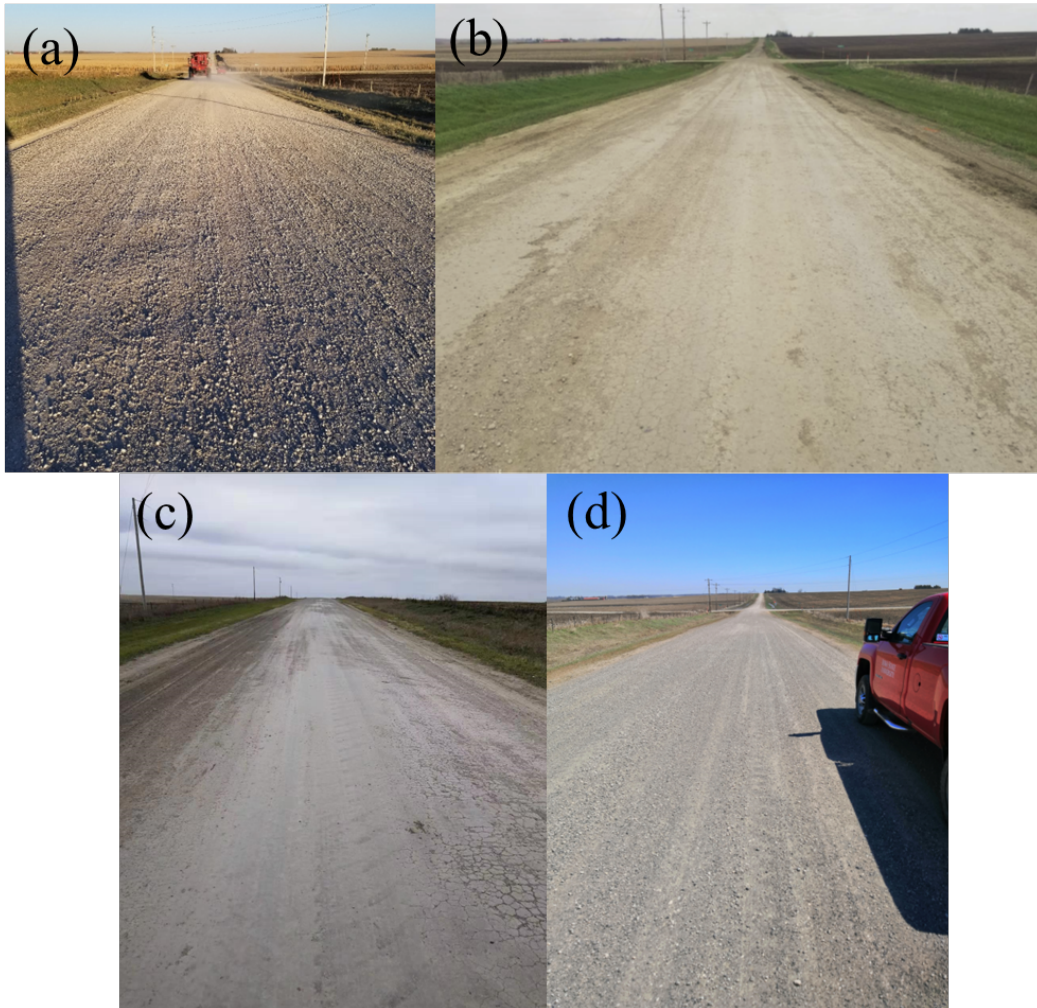


Figure 181. Percent gravel, sand, and fines fraction of the samples from Howard County Aggregate Columns section collected over time



Xue et al. 2022

**Figure 182. Visual surveys of Howard County Aggregate Columns section over time:
(a) fall 2018, (b) spring 2019, (c) fall 2019, (d) spring 2020**

4.3.4 *Comparison of Gravel Deterioration for Howard County Test Sections*

4.3.4.1 Comparison of Breakage Parameters for Howard County Sections

As detailed in previous sections of this report, Hardin's breakage parameters were evaluated for samples collected over time from the Control, OGCS, and Aggregate Columns test sections in Howard County. Comparisons of the cumulative total breakage and cumulative relative breakage for these test sections are shown in Figure 183 and Figure 184. As previously described, no maintenance aggregates were required for the OGCS test section. For the Control and Aggregate Columns sections, however, maintenance was carried out in fall 2019 at which time new aggregates were spread. From the PSD curves, it was apparent that addition of the maintenance aggregates in fall 2019 took place before field sampling of the Control section, but after field sampling of the Aggregate Columns section. Therefore, breakage could not be determined for the

Spring 2019–Fall 2019 timeframe for the Control section, nor for the Fall 2019–Spring 2020 timeframe for the Aggregate Columns section. The breakage parameters were thus evaluated for the Fall 2018–Spring 2019 and Fall 2019–Spring 2020 timeframes for the Control section, and the Fall 2018–Spring 2019 and Fall 2018–Fall 2019 timeframes for the Aggregate Columns section. To track the cumulative amount of total breakage occurring in test sections for which new maintenance aggregates were placed, the total breakage before placing the new aggregates was added to the subsequent total breakage of the new material.

The comparison of results shows that the OGCS section had the lowest total and relative breakage for the spring 2019 samples, whereas the Aggregate Columns section had the highest values. However, both total and relative breakage for the OGCS section exhibited a significant increase by fall 2019. By spring 2020, however, the OGCS section had lower cumulative total and relative breakage than the Control section, whereas breakage could not be determined for the Aggregate Columns section as previously explained.

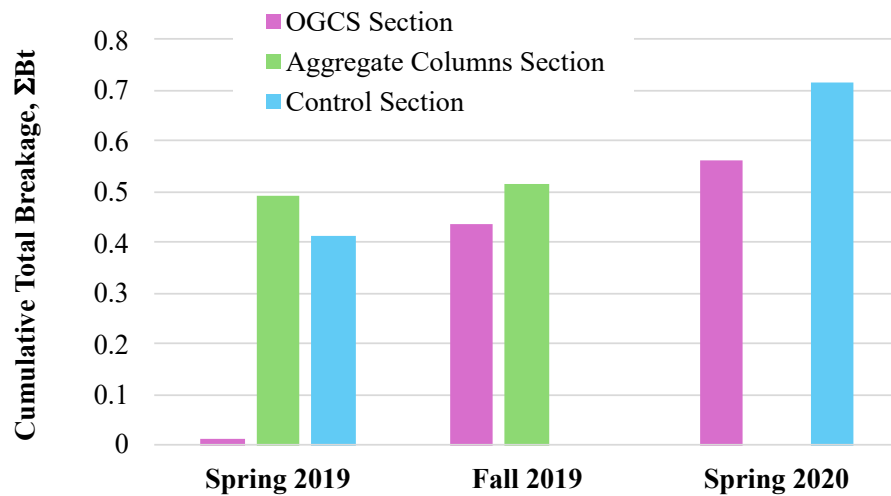


Figure 183. Comparison of cumulative total breakage of samples from Howard County OGCS section, Aggregate Columns section, and Control section collected over time

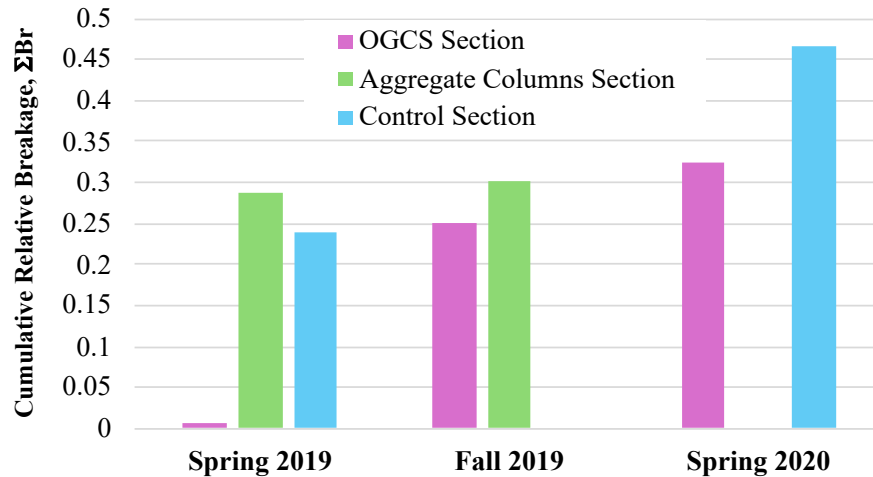


Figure 184. Comparison of cumulative relative breakage of samples from Howard County OGCS section, Aggregate Columns section, and Control section collected over time

4.3.4.2 Comparison of Changes in Gravel, Sand and Fines Fractions for Howard County Sections

The gravel fractions evaluated for samples collected across the different time intervals for the three Howard County test sections are compared in Figure 185. The plot illustrates that the gravel fraction continually decreased for all sections, except for the Aggregate Columns section where the gravel fraction increased in spring 2020 due to spreading of the new maintenance aggregates after sampling in fall 2019. The corresponding percent decreases in gravel fraction for the timeframes over which breakage was calculated are shown in Figure 186. For spring 2019, the OGCS section had the smallest percent change in gravel fraction while the Aggregate Columns section had the largest change. Over the following two years, however, the OGCS section had a greater percent decrease in gravel than the other two sections. Again, since maintenance aggregate was spread on the Control section, one could sum the percent decreases in gravel for the Control section in a cumulative sense.

The corresponding sand fractions over time are plotted in Figure 187 and their percent changes are plotted in Figure 188. All sections exhibited an increasing trend in sand fraction over time, with the Control section having the highest value. However, by spring 2020 the percent change in sand fraction was greatest for the OCGS section.

Finally, Figure 189 and Figure 190 show comparisons of the fines fractions and their percent increases over time. All sections exhibited a generally increasing trend in fines fraction by roughly 10% over time, except for the Aggregate Columns section in spring 2020 for which the fines fraction decreased due to the spreading of new aggregate.

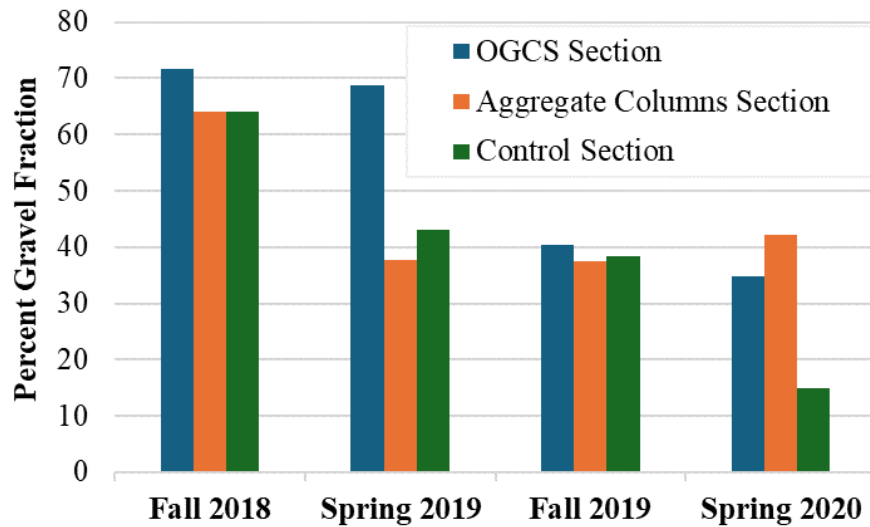


Figure 185. Comparison of gravel fraction for samples from Howard County OGCS section, Aggregate Columns section, and Control section collected over time

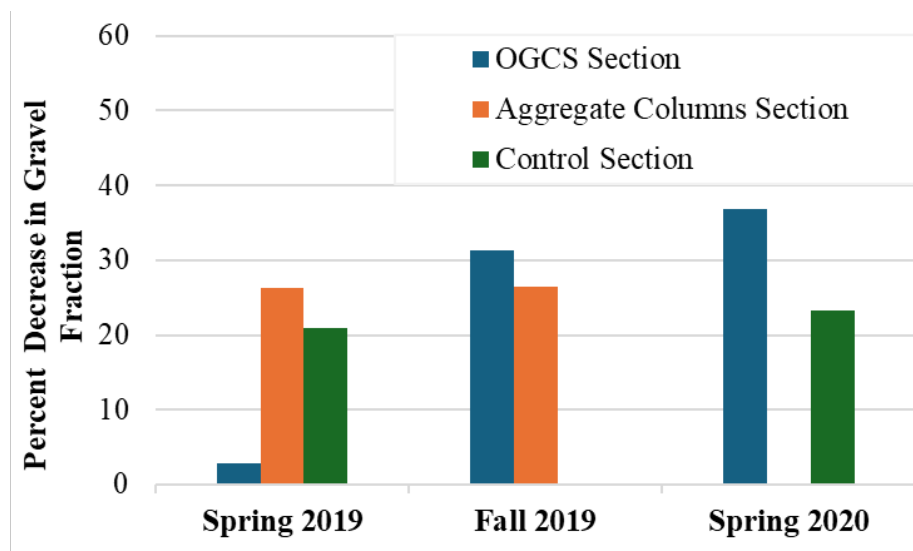


Figure 186. Comparison of percent decrease in gravel fraction of samples from Howard County OGCS section, Aggregate Columns section, and Control section collected over time

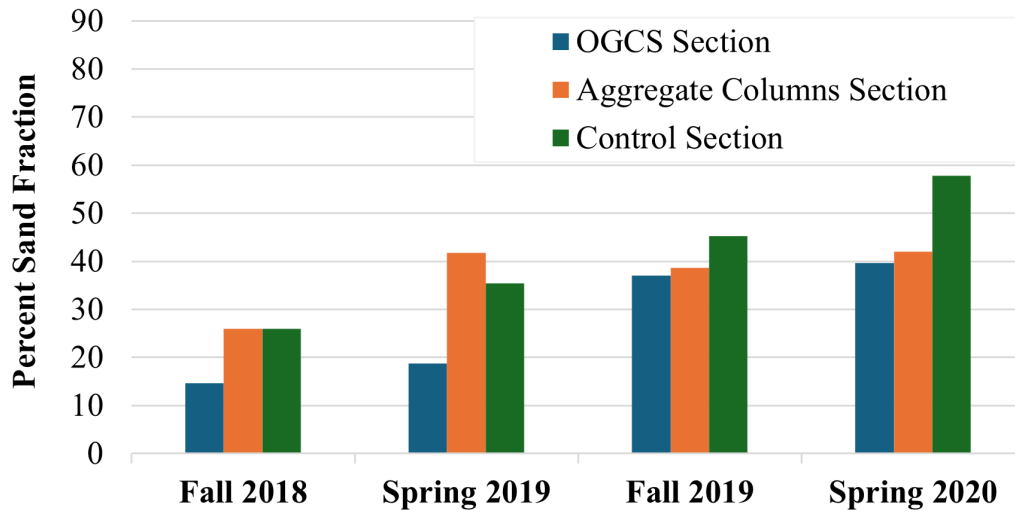


Figure 187. Comparison of sand fraction for samples from Howard County OGCS section, Aggregate Columns section, and Control section collected over time

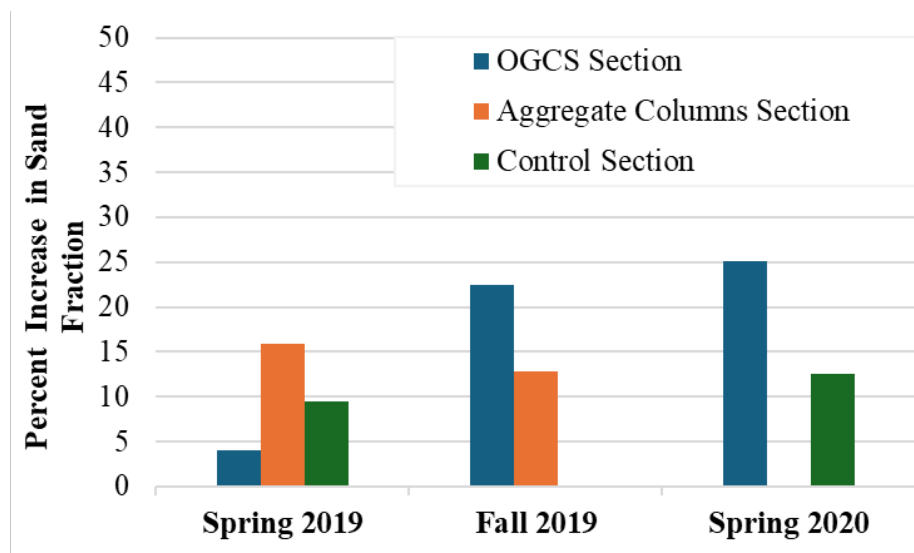


Figure 188. Comparison of percent increase in sand fraction for samples from Howard County OGCS section, Aggregate Columns section, and Control section collected over time

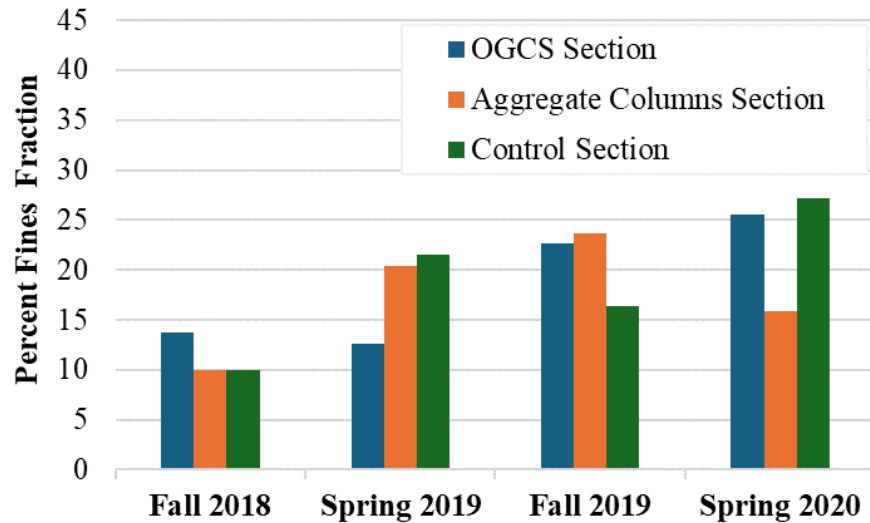


Figure 189. Comparison of fines fraction for samples from Howard County OGCS section, Aggregate Columns section, and Control section collected over time

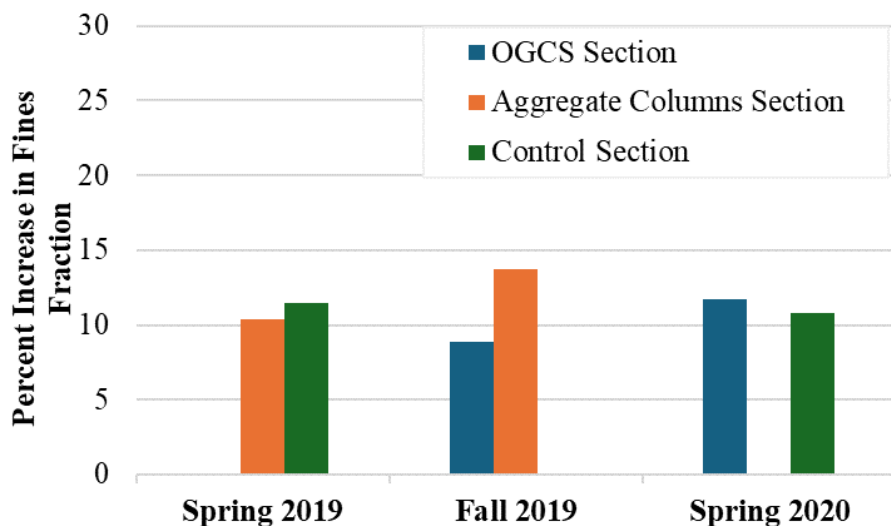


Figure 190. Comparison of percent increase in fines fraction for samples from Howard County OGCS section, Aggregate Columns section, and Control section collected over time

Considering the breakage parameters, percent decrease in gravel fraction, and percent increase in the sand and fines fractions of the three test sections, by the first year after construction (in spring 2019), the OGCS had the lowest values of all these parameters whereas the Aggregate Columns section had the highest values. By the last two sampling periods the OGCS and Aggregate Columns sections had lower cumulative breakage than the Control section (where data was available), and the OGCS section was the only one that didn't require maintenance aggregates. These findings suggest that OGCS stabilization was by far the most effective in minimizing gravel breakage in the first year during which time the Aggregate Columns and

Control sections offered similar performance, and the OGCS section had the least breakage after two years.

4.3.5 Hamilton County – Control Section

In IHRB Project TR-721, three types of chemically stabilized test sections were constructed along with two mechanically stabilized test sections and a control section in Hamilton County on Vail Avenue between 300th Street and 310th Street. A satellite image of the location and a schematic diagram illustrating the layout of the test sections are shown in Figure 191 and Figure 192, respectively. The cement-treated test Sections 2 and 3 shown in Figure 191 were not actually constructed because a contractor could not be found to incorporate the portland cement. The 500 ft long control section was constructed to evaluate the performance of the test sections against the current construction and maintenance practices for gravel roads in Hamilton County. To construct the Control section, fresh aggregates were spread over the existing road surfacing material to an initial thickness of 4 in. in fall 2018.

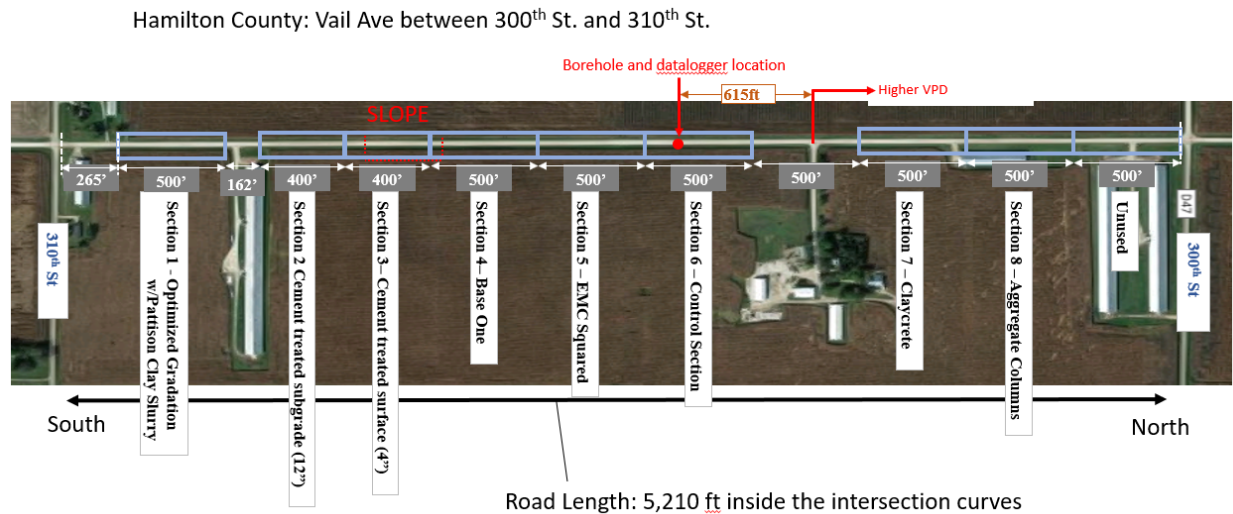
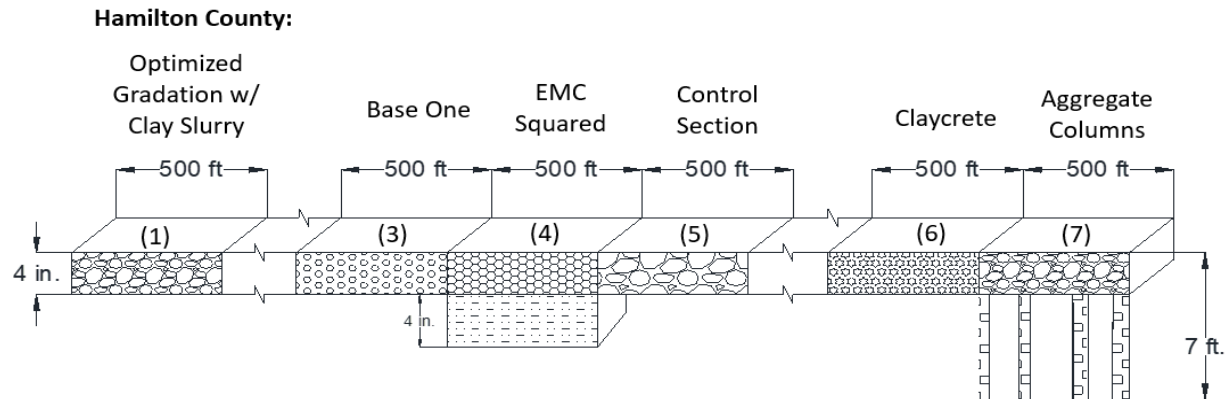


Figure 191. Satellite image of Hamilton County chemically and mechanically stabilized test sections



Xue et al. 2022

Figure 192. Layouts of chemically and mechanically stabilized test sections in Hamilton County

Samples of the surface aggregates were collected from the Hamilton County Control section over a period of two years, specifically during the construction phase in fall 2018 and during spring 2019, fall 2019, and spring 2020. According to the Hamilton Secondary Roads personnel, no new aggregates were spread on the test sections during these intervals. Therefore, the breakage can be determined between the representative samples from any pair of these dates, and the cumulative breakage can be determined for all sample dates with respect to fall 2018. Particle size distribution curves were determined for these collected materials through laboratory sieve and hydrometer tests in the previous project. The resulting PSD curves from these tests for Hamilton County samples are shown in Figure 193.

The PSD curves in Figure 193 were digitized to determine the mechanical degradation represented by Hardin's breakage parameters relative to the PSD after construction in fall 2018. This degradation is shown in Figure 194, Figure 195 and Figure 196 for the samples collected in spring 2019, fall 2019 and fall 2020, respectively. Table 46 summarizes the corresponding breakage parameters along with the percentages of gravel, sand, and fines for the samples collected over time. The cumulative total breakage is shown in a bar chart in Figure 197 and exhibits a continual increase in total breakage over time as expected.

The percentages of gravel, sand, and fines for the samples collected over time are also presented as a bar chart in Figure 198. The data in Table 46 and Figure 198 indicate a significant reduction in the gravel fraction, from 67.9% after construction in fall 2018 falling to 31.1% at the next sampling date in spring 2019, after which the gravel content remained fairly constant hovering around 30%. In contrast, the sand fraction increased from 25.2% after construction in fall 2018 to 60.3% by fall 2019, before falling to 47.3% by spring 2020. The fines fraction increased over time as well, starting at 6.9% after construction and ending at 19.3% by spring 2020. A slight increase in the gravel fraction and a decrease in sand fraction is noted between fall 2019 and spring 2020. This might be due to sampling error arising from nonuniform distribution of aggregate materials in the test section. The overall increasing trends in total breakage as well as sand and fines percentages, and decreasing trend in gravel percentage indicate that the gravel fraction in the road surface broke down significantly due to traffic loading and weather

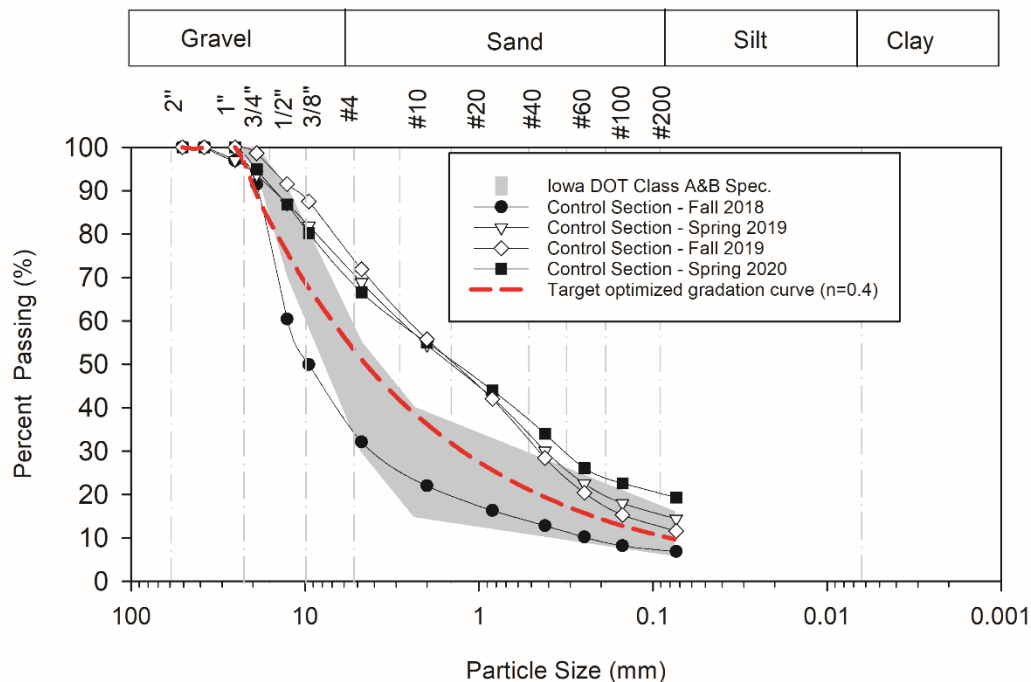
conditions. As seen in Figure 193, the PSD curves migrated up a great distance between fall 2018 and spring 2019, then changed comparatively little over time except for the fine sand range and fines contents.

4.3.5.1 2D Image Analyses and Comparison of Morphological Parameters for Hamilton County Control Section

The 2D image analyses were also performed for surplus samples from spring 2019 and fall 2019. The morphological parameters evaluated are presented in Figure 199 through Figure 204, and the statistical output of these morphological parameters is presented in Table 47. The data shows increases in median values of roundness, sphericity, and form factor by 1.9%, 2.8%, and 3.2%, respectively. The corresponding median values of shape factor, roundness index, and angularity decreased by 3.1%, 0.6%, and 4.3%. These changes in morphological parameter values quantify the degradation and evolving geometry of the gravel fraction of the Hamilton County Control section over this roughly six-month timespan.

4.3.5.2 Visual Surveys for Hamilton County Control Section

Photos from visual surveys of the Hamilton County Control section taken over time are shown in Figure 205. The visual surveys confirmed that the gravel fraction of the surfacing materials decreased over time while the sand and fines fractions increased.



Xue et al. 2022

Figure 193. Particle size distribution curves of Hamilton County Control Section for samples collected over time

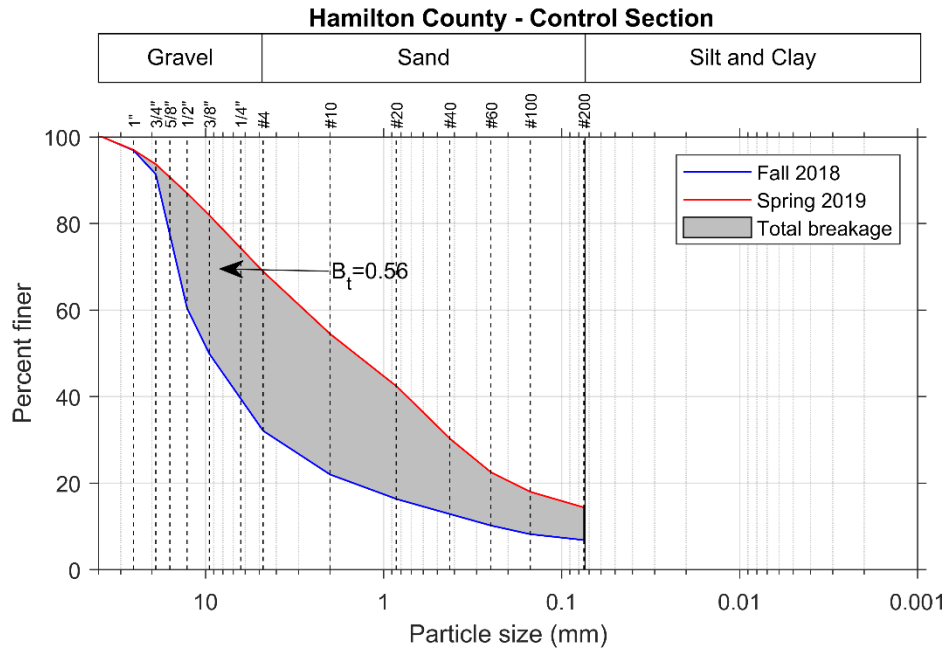


Figure 194. Particle size distributions and evaluation of total breakage of coarse fraction for Hamilton County Control section between fall 2018 and spring 2019

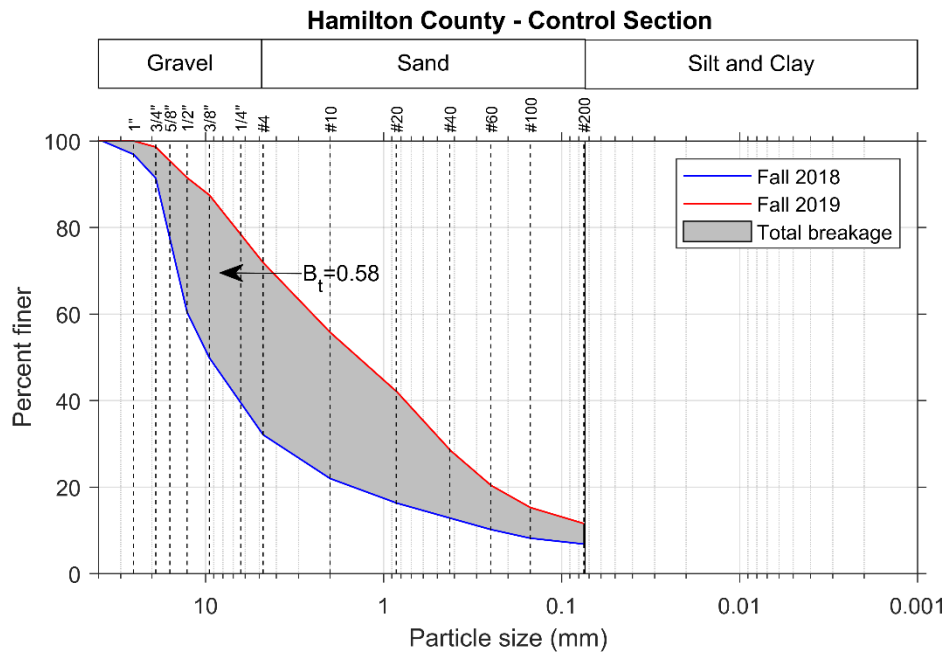


Figure 195. Particle size distributions and evaluation of total breakage of coarse fraction for Hamilton County Control section between fall 2018 and fall 2019

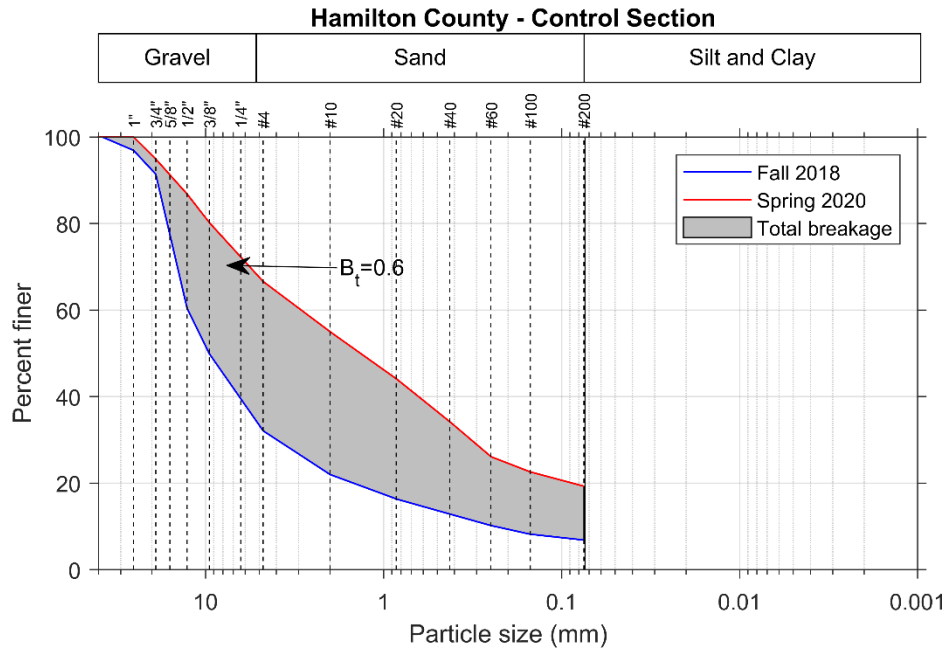


Figure 196. Particle size distributions and evaluation of total breakage of coarse fraction for Hamilton County Control section between fall 2018 and spring 2020

Table 46. Breakage parameters from laboratory sieve analyses and percent gravel, sand, and fines for samples of Hamilton County Control section

Sample Collection Date	Hardin's Breakage Parameters*			% Gravel	% Gravel Red.*	% Sand	% Sand Inc.*	% Fines	% Fines Inc.*
	Total Breakage, B_t	Breakage Potential, B_p	Relative Breakage, B_r						
Fall 2018	-	-	-	67.9	-	25.2	-	6.9	-
Spring 2019	0.5577	1.8072	0.3086	31.1	36.8	54.5	29.3	14.4	7.5
Fall 2019	0.5817	1.8072	0.3219	28.1	39.8	60.3	35.1	11.6	4.7
Spring 2020	0.5979	1.8072	0.3308	33.4	34.5	47.3	22.1	19.3	12.4

*w.r.t. Fall 2018; Red. = Reduction; Inc. = Increase

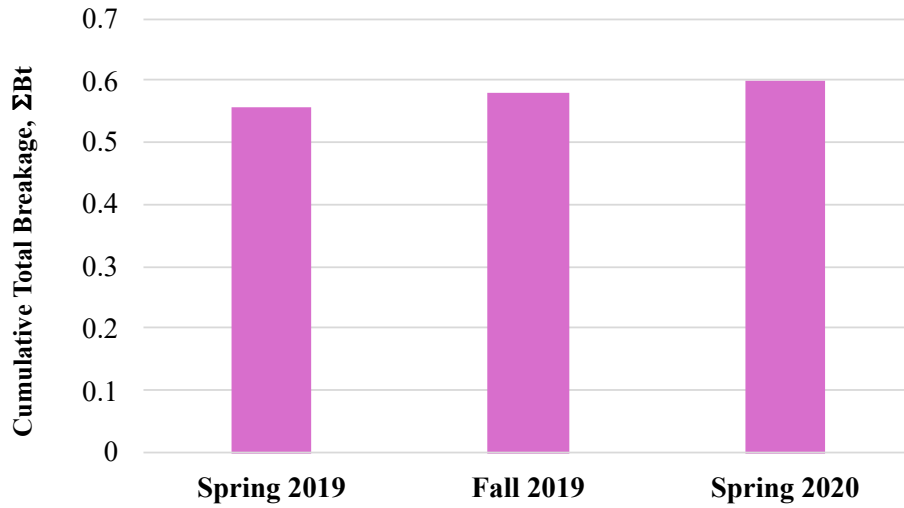


Figure 197. Cumulative total breakage of samples from Hamilton County Control section collected over time

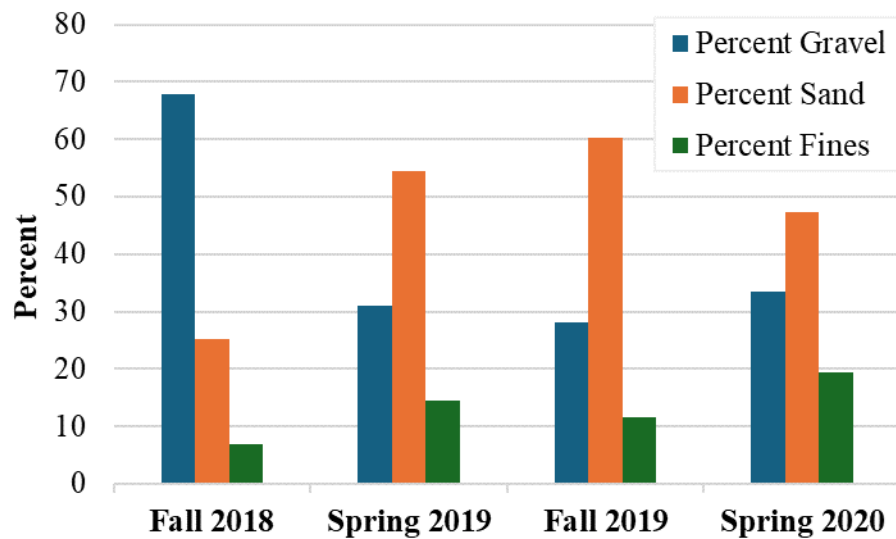


Figure 198. Gravel, sand and fines fractions of samples from Hamilton County Control section collected over time

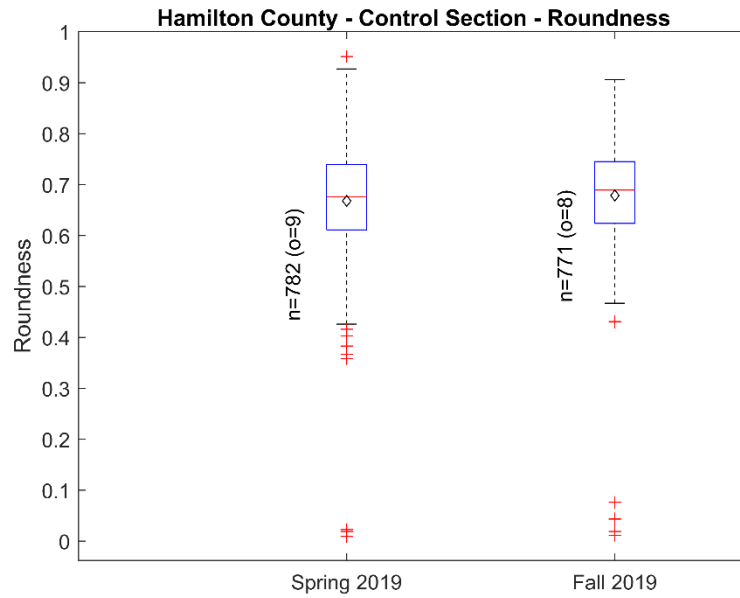


Figure 199. Comparison of roundness for Hamilton County Control section samples from spring 2019 and fall 2019

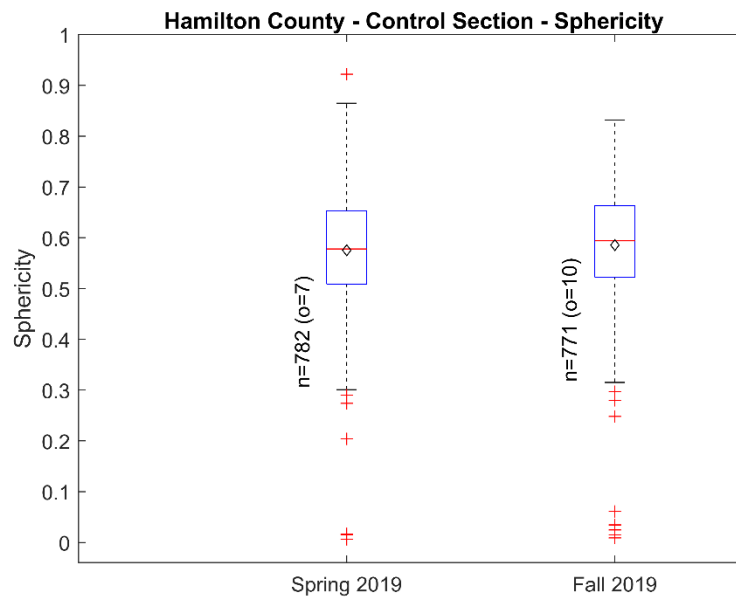


Figure 200. Comparison of sphericity for Hamilton County Control section samples from spring 2019 and fall 2019

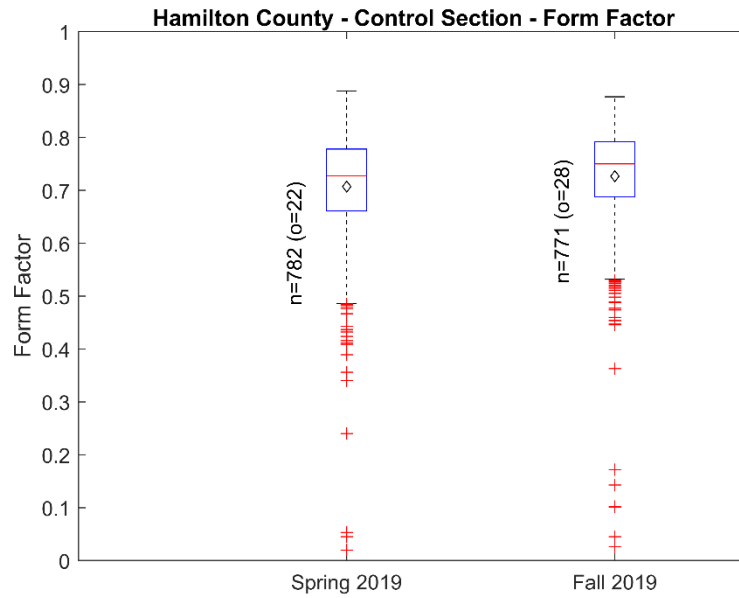


Figure 201. Comparison of form factor for Hamilton County Control section samples from spring 2019 and fall 2019

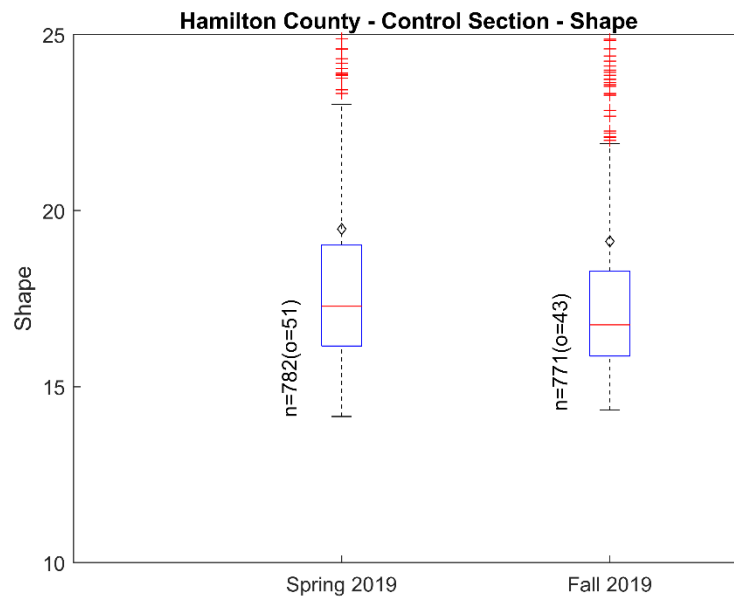


Figure 202. Comparison of shape factor for Hamilton County Control section samples from spring 2019 and fall 2019

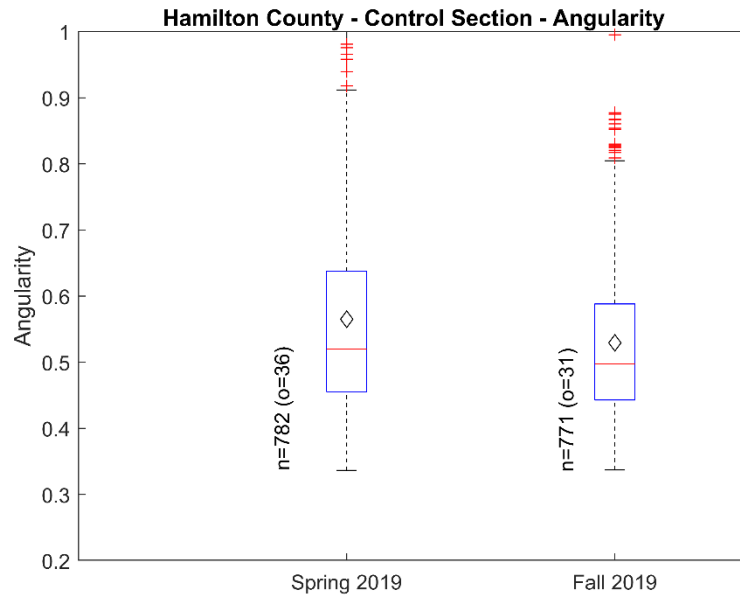


Figure 203. Comparison of angularity for Hamilton County Control section samples from spring 2019 and fall 2019

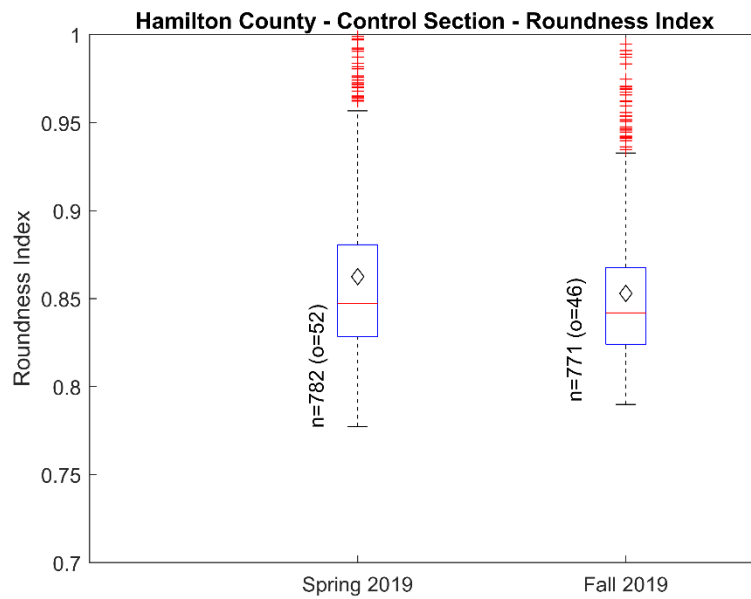
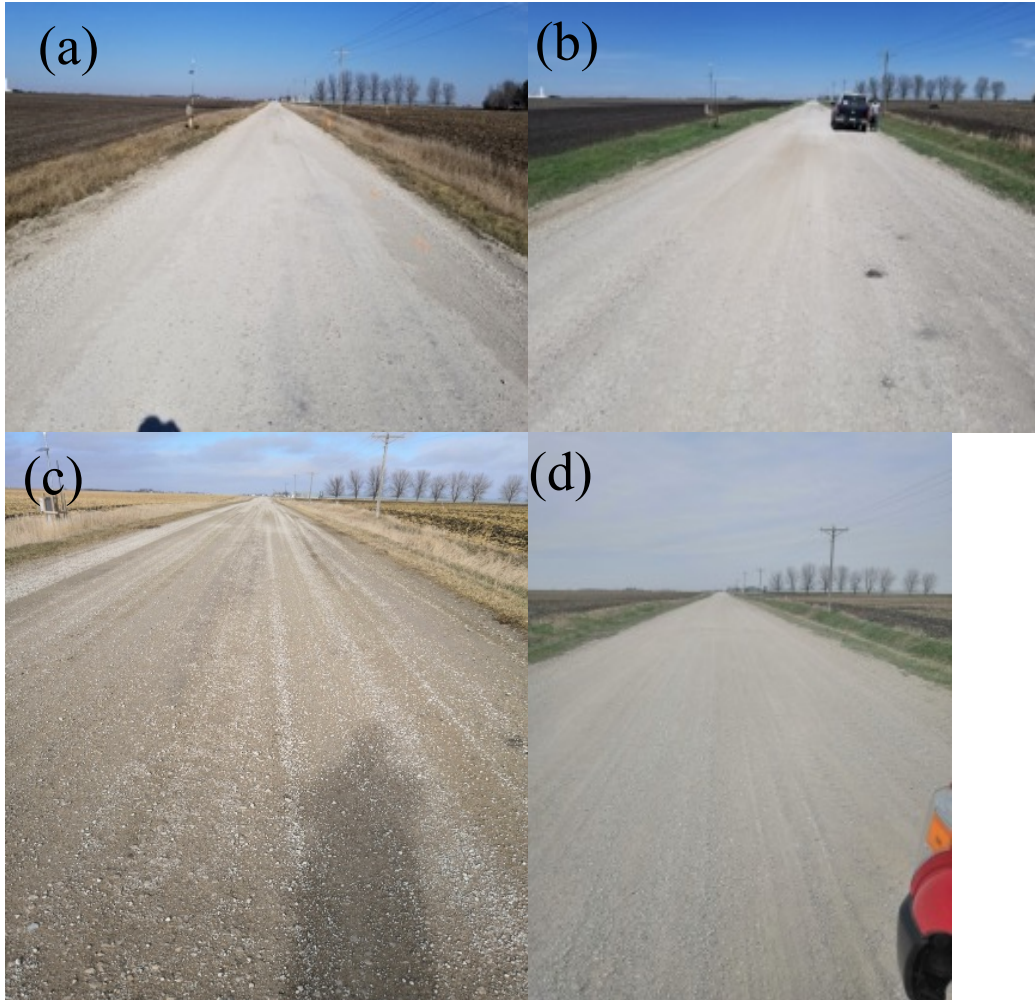


Figure 204. Comparison of roundness index for Hamilton County Control section samples from spring 2019 and fall 2019

Table 47. Statistical results of morphological parameters of Hamilton County Control section for spring 2019 and fall 2019 samples

Parameter	Sample Collection Date	Max.	Min.	Mean	Mode	Median	Std. Dev.	Skew-ness	Kurt-osis	Out-liers
Roundness	Spring 2019	0.951	0.009	0.668	0.676	0.676	0.105	-1.078	7.718	9
	Fall 2019	0.906	0.011	0.678	0.725	0.689	0.103	-1.93	13.09	8
	% increase			1.6%		1.9%				
Sphericity	Spring 2019	0.922	0.006	0.575	0.576	0.578	0.11	-0.688	4.979	7
	Fall 2019	0.832	0.009	0.586	0.681	0.594	0.109	-1.316	7.899	10
	% increase			1.8%		2.8%				
Form Factor (FF)	Spring 2019	0.888	0.02	0.707	0.791	0.727	0.101	-1.866	10.35	22
	Fall 2019	0.877	0.026	0.727	0.765	0.75	0.101	-2.771	16.60	28
	% increase			2.8%		3.2%				
Shape Factor (SF)	Spring 2019	618	14.2	19.5	15.2	17.3	24.9	20.2	451.8	51
	Fall 2019	485.8	14.3	19.1	15.3	16.8	22.5	15.9	288.3	43
	% increase			-1.8%		-3.1%				
Roundness Index (RI)	Spring 2019	1.248	0.777	0.863	0.817	0.847	0.054	2.354	11.65	52
	Fall 2019	1.203	0.79	0.853	0.828	0.842	0.043	2.087	10.65	46
	% increase			-1.1%		-0.6%				
Angularity	Spring 2019	1.629	0.336	0.565	0.417	0.52	0.158	1.811	8.064	36
	Fall 2019	1.228	0.337	0.529	0.437	0.498	0.118	1.359	5.731	31
	% increase			-6.4%		-4.3%				



Xue et al. 2022

Figure 205. Visual surveys of Hamilton County Control section over time: (a) fall 2018, (b) spring 2019, (c) fall 2019, (d) spring 2020

4.3.6 Hamilton County – Optimized Gradation with Clay Slurry Section

The 500 ft long OGCS test section was constructed in Hamilton County in September 2018. Details of the OGCS stabilization method are presented in Section 4.3.2 of this report. Samples of surface materials were collected from the Hamilton County OGCS section over two years of IHRB Project TR-721 during different phases: first in fall 2018 during construction, then again in spring 2019, fall 2019, and spring 2020. The PSD curves from the TR-721 report for this test section are shown in Figure 206. The curves show very little change between fall 2018 and spring 2019 except for a slight decrease in the fine sand range and fines content, followed by a general upward migration over time as the material gradually broke down to a finer gradation. As of fall 2019, the PSD curve was still within the Iowa DOT Class A/B specification band, but by spring 2020 it had migrated above the band in the gravel and coarse sand ranges. In contrast, the PSD of the nearby Control section was already far above the specification band by spring 2019

and remained there through spring 2020, ending with a fines content of approximately 20% (see Figure 193).

4.3.6.1 Comparison of Breakage Parameters for Hamilton County OGCS Section

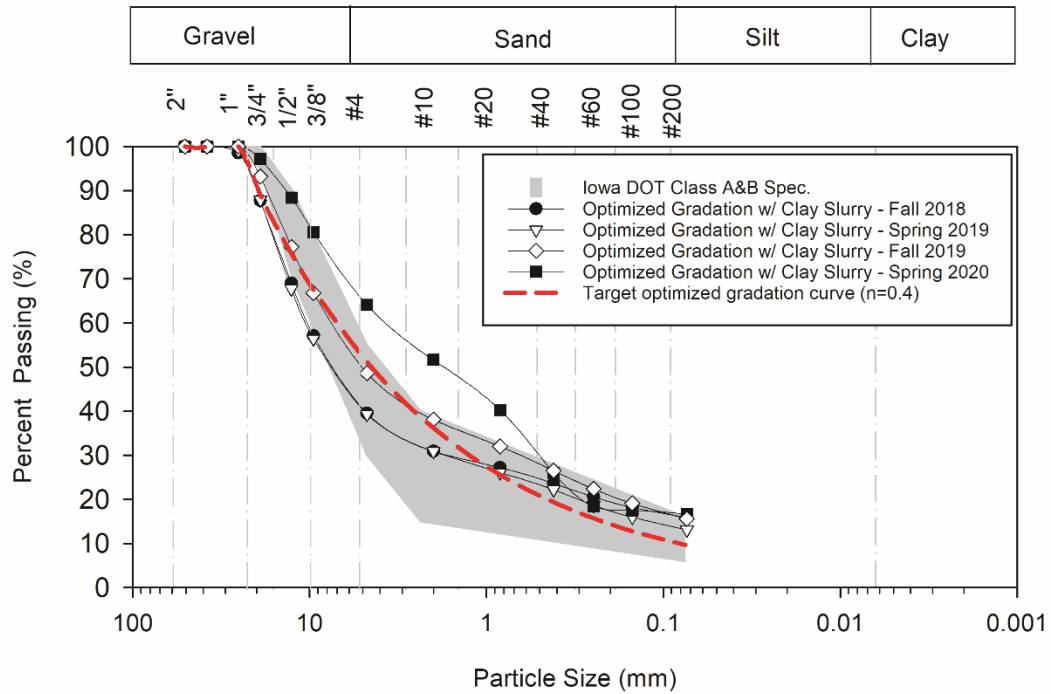
The mechanical degradation relative to fall 2018 is quantified by total breakage based on laboratory sieve analyses in Figure 207, Figure 208, and Figure 209 for the samples collected in spring 2019, fall 2019, and spring 2020, respectively. The corresponding breakage parameters and percentages of gravel, sand, and fines over time are detailed in Table 48. The cumulative total breakage is shown graphically in Figure 210, starting with a small negative value due to experimental error but increasing consistently with time as expected. The percentages of gravel, sand, and fines for the samples collected over time are also presented as a bar chart in Figure 211. The gravel fraction exhibited an overall decreasing trend with time, starting at 60.5% in fall 2018 and ending up at 35.9% by spring 2020. In contrast, the sand fraction increased over time, starting at 23.6% and ending at 47.4%, whereas the fines fraction increased from 15.9% to 16.7%.

4.3.6.2 2D Image Analyses and Comparison of Morphological Parameters for Hamilton County OGCS Section

The 2D image analyses were also performed for surplus samples, which only existed for fall 2018, spring 2019, and spring 2020. The resulting particle size distribution curves for the gravel fraction and corresponding total breakage values are shown in Figure 212 and Figure 213, while the other breakage parameters are also detailed in Table 49. The PSD curves of the gravel fraction from image analysis gave total breakage values of approximately 0.03 for both spring 2019 and spring 2020 relative to fall 2018. The morphological parameters from 2D image analyses are presented graphically in Figure 214 through Figure 219, while the complete statistical output is presented in Table 50. The statistical data indicate increases in median roundness, sphericity, and form factor of 1.4%, 0.7%, and 1.2%, respectively for spring 2019 samples, and larger increases of 3.4%, 2.5%, and 2.0%, respectively for spring 2020 samples. Consistent with these changes are corresponding decreases in median values of shape factor, roundness index, and angularity of 1.2%, 0.1%, and 3.8% respectively for spring 2019 and 1.8%, 0.5%, and 10.4% for spring 2020. The continuous increasing trends in roundness, sphericity, and form factor along with the continuous decreasing trends in shape factor, roundness index, and angularity quantify the continual degradation of the gravel sized particles from fall 2018 through spring 2020 for this test section.

4.3.6.3 Visual Surveys for Hamilton County OGCS Section

Visual surveys of the Hamilton County OGCS section over the duration of the TR-721 project are shown in Figure 220. As seen in the photos, the increase in cohesion offered by the clay fines in the slurry resulted in improved binding of the aggregates, reducing their loss and slowing their degradation relative to the control section.



Xue et al. 2022

Figure 206. Particle size distribution curves of Hamilton County OGCS Section for samples collected over time County

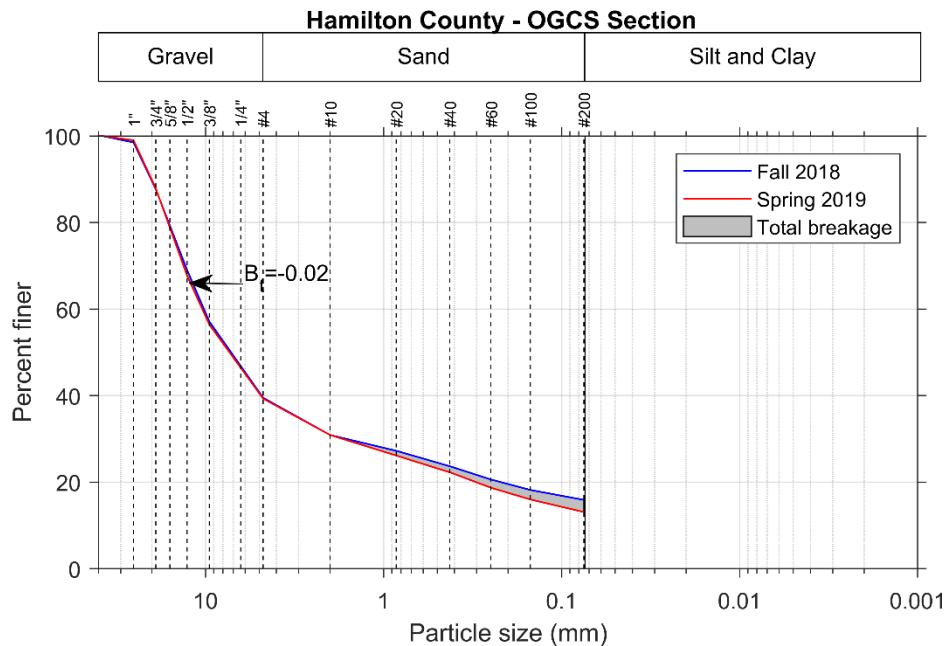


Figure 207. Particle size distributions and evaluation of total breakage of coarse fraction for Hamilton County OGCS section between fall 2018 and spring 2019

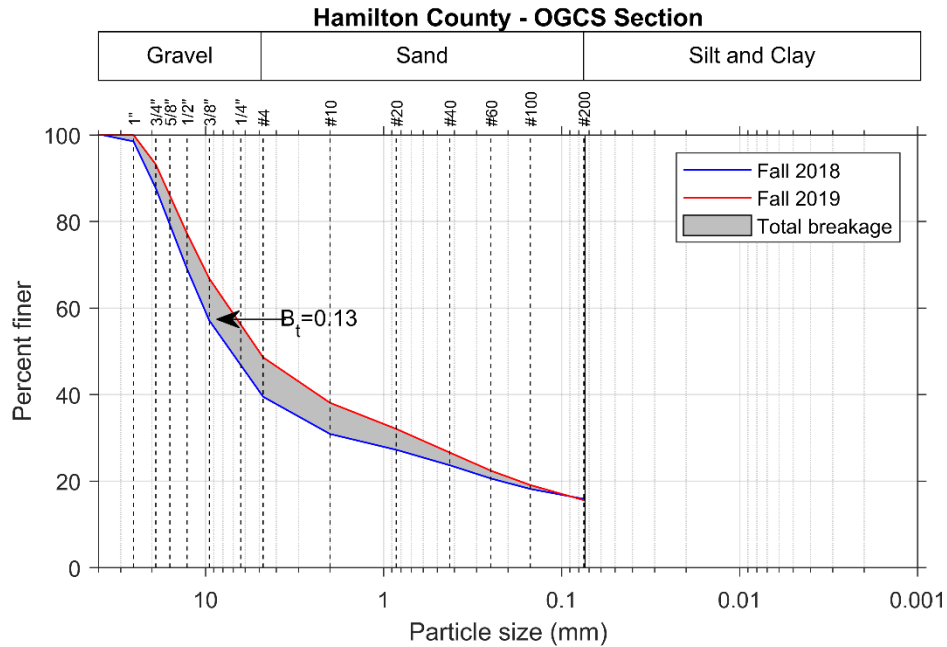


Figure 208. Particle size distributions and evaluation of total breakage of coarse fraction for Hamilton County OGCS section between fall 2018 and fall 2019

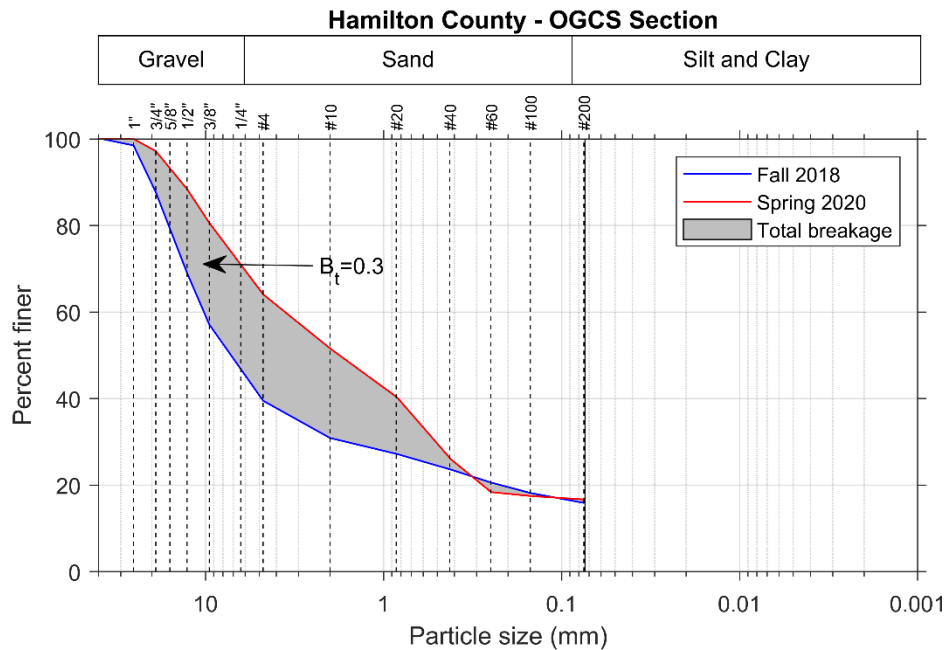


Figure 209. Particle size distributions and evaluation of total breakage of coarse fraction for Hamilton County OGCS section between fall 2018 and spring 2020

Table 48. Breakage parameters of coarse fraction by laboratory sieve analyses and percent gravel, sand, and fines for samples of Hamilton County OGCS section

Sample Collection Date	Hardin's Breakage Parameters*				%		%		%
	Total Breakage, B _t	Breakage Potential, B _p	Relative Breakage, B _r	% Gravel	Gravel Red.*	% Sand	Sand Inc.*	% Fines	Fines Inc.*
Fall 2018	-	-	-	60.5	-	23.6	-	15.9	-
Spring 2019	-0.0249	1.5946	-0.0156	60.7	-0.2	26.2	2.6	13.1	-2.8
Fall 2019	0.1314	1.5946	0.0824	51.4	9.1	33.0	9.4	15.6	-0.3
Spring 2020	0.3025	1.5946	0.1897	35.9	24.6	47.4	23.8	16.7	0.8

*w.r.t. Fall 2018; Red. = Reduction; Inc. = Increase

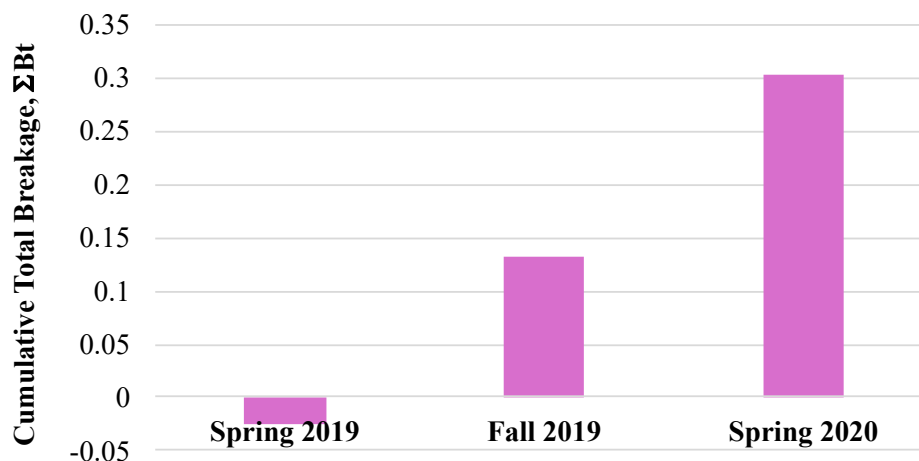


Figure 210. Cumulative total breakage of coarse fraction for Hamilton County OGCS section samples collected over time

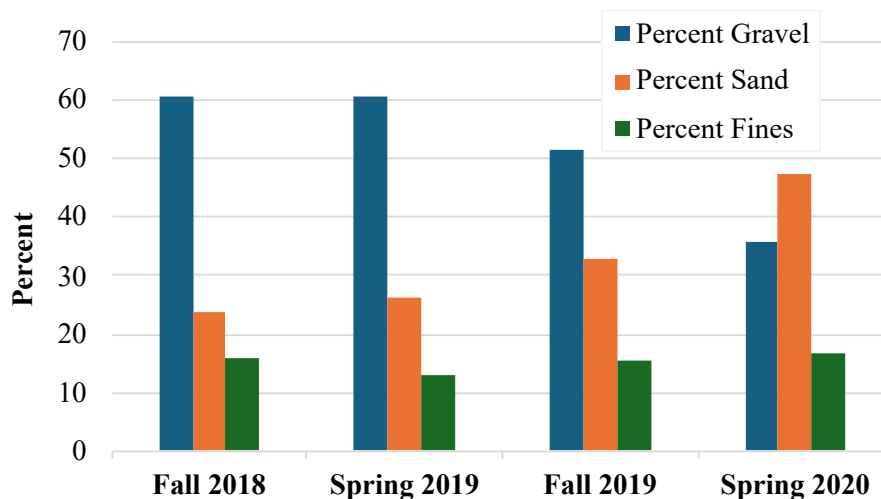


Figure 211. Gravel, sand and fines fractions of the samples from Hamilton County OGCS section collected over time

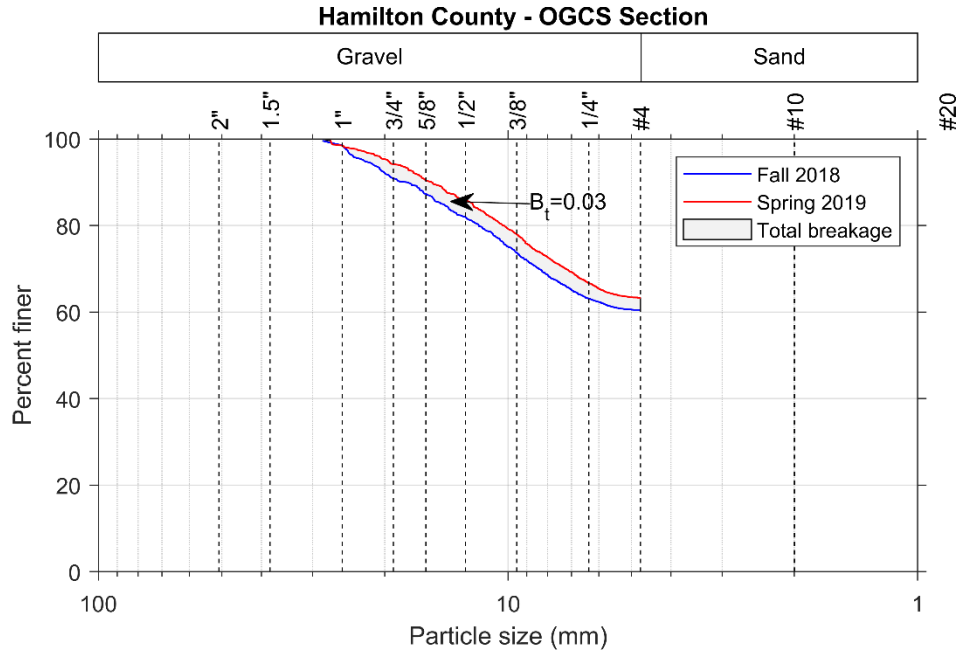


Figure 212. Particle size distributions by 2D image analysis and evaluation of total breakage of gravel fraction for Hamilton County OGCS section between fall 2018 and spring 2019

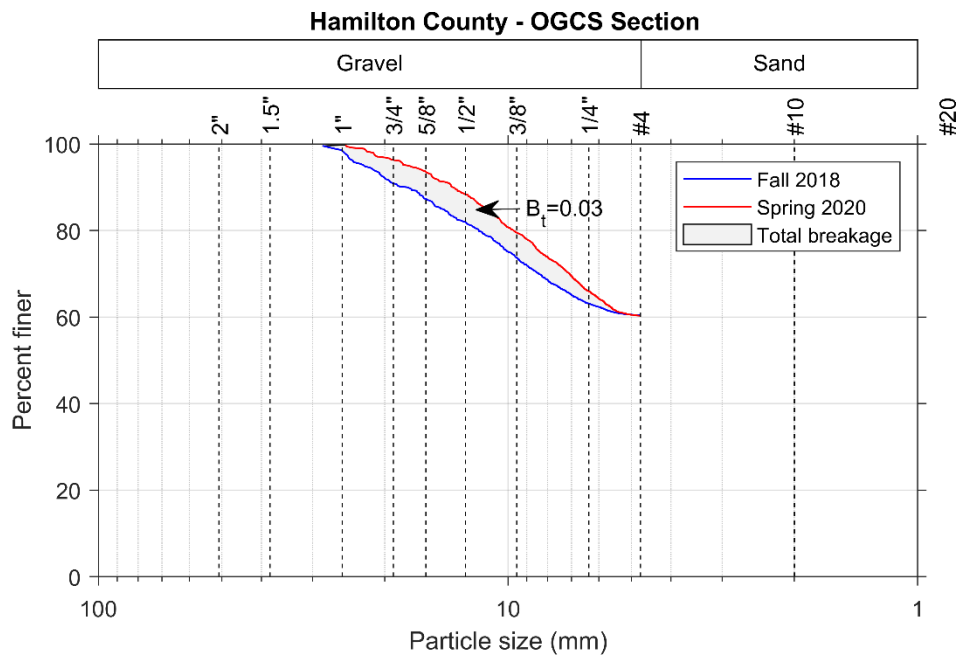


Figure 213. Particle size distributions by 2D image analysis and evaluation of total breakage of gravel fraction for Hamilton County OGCS section between fall 2018 and spring 2020

Table 49. Breakage parameters from 2D image analyses for the samples from Hamilton County OGCS section

Sample Collection Date	Hardin's Breakage Parameters*		
	Total Breakage, B_t	Breakage Potential, B_p	Relative Breakage, B_r
Spring 2019	0.0345	0.3172	0.1088
Spring 2020	0.0300	0.3172	0.0946

*w.r.t. Fall 2018; Red. = Reduction; Inc. = Increase

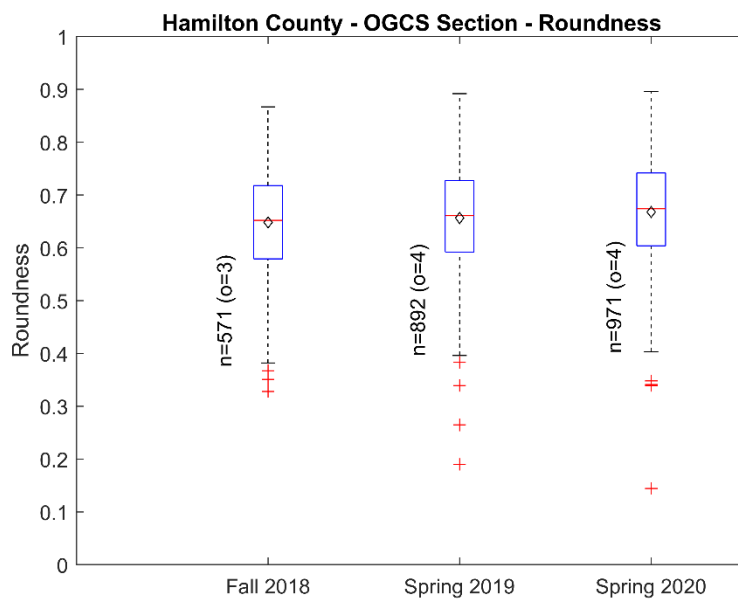


Figure 214. Comparison of roundness for Hamilton County OGCS section samples from fall 2018, spring 2019 and spring 2020

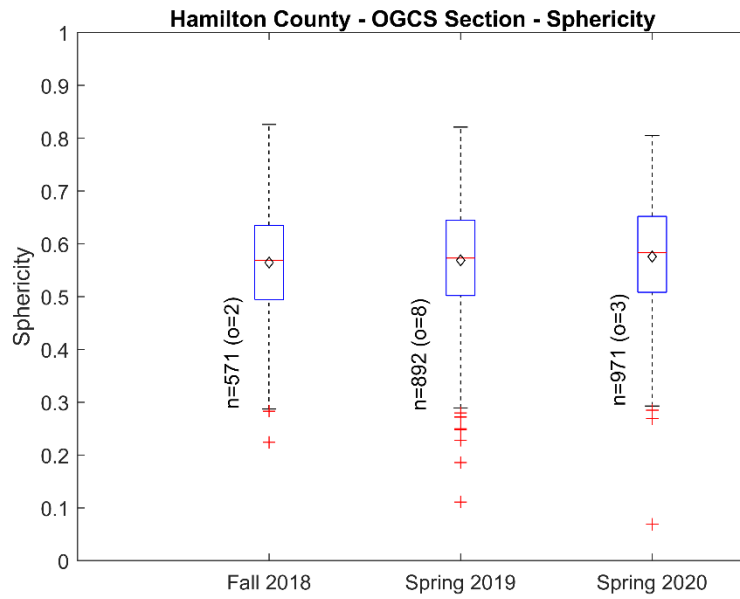


Figure 215. Comparison of sphericity for Hamilton County OGCS section samples from fall 2018, spring 2019 and spring 2020

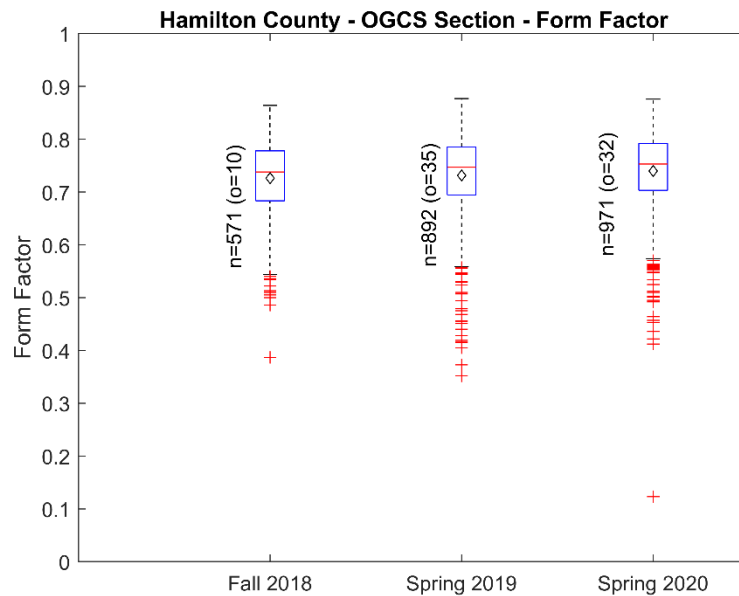


Figure 216. Comparison of form factor for Hamilton County OGCS section samples from fall 2018, spring 2019 and spring 2020

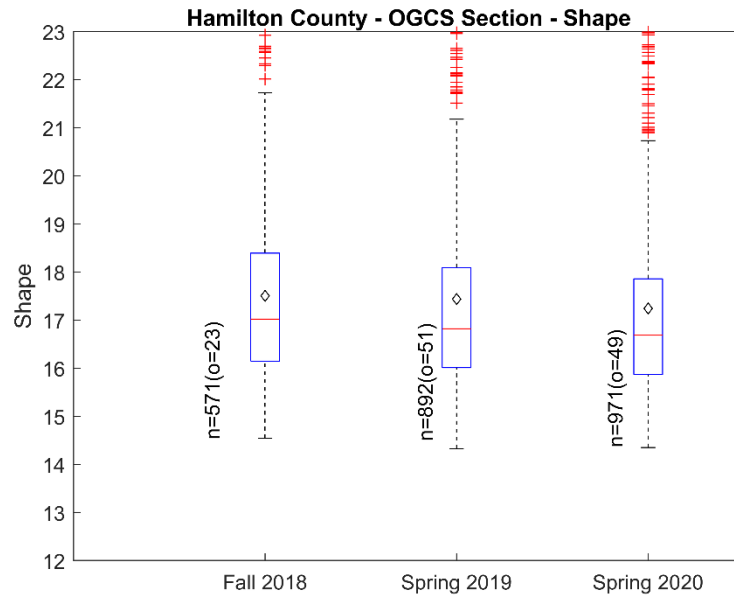


Figure 217. Comparison of shape factor for Hamilton County OGCS section samples from fall 2018, spring 2019 and spring 2020

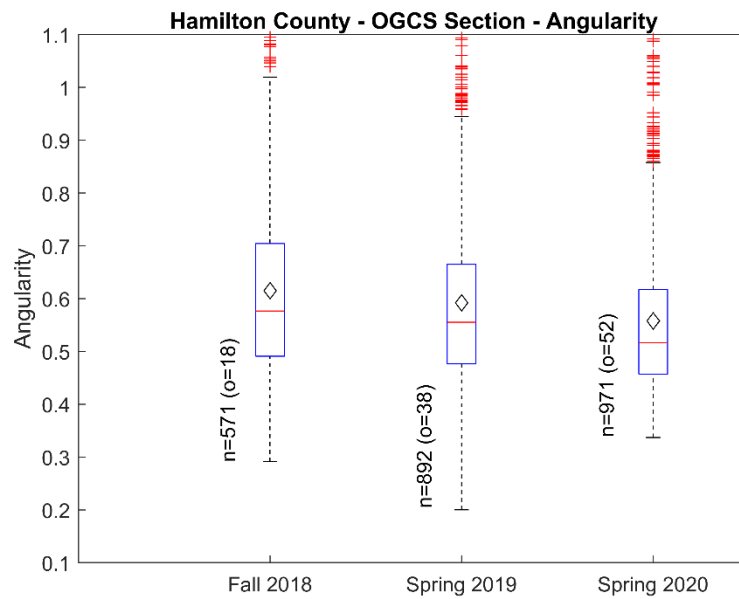


Figure 218. Comparison of angularity for Hamilton County OGCS section samples from fall 2018, spring 2019 and spring 2020

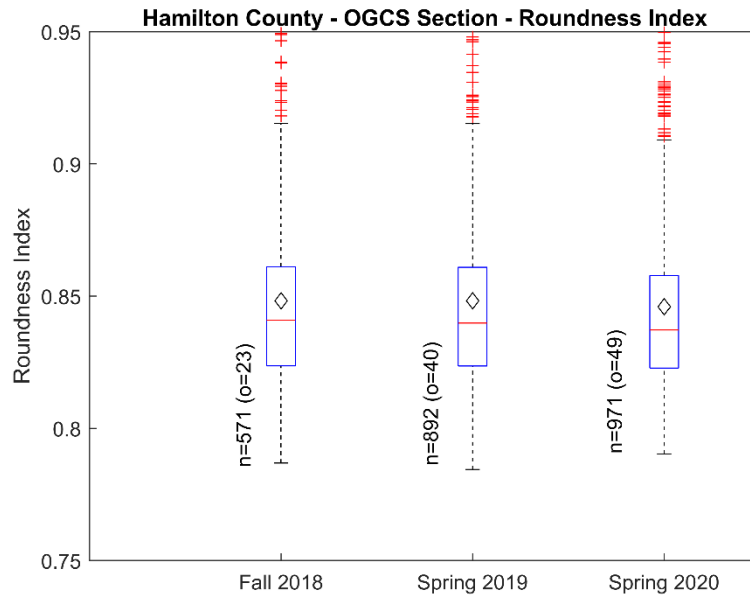


Figure 219. Comparison of roundness index for Hamilton County OGCS section samples from fall 2018, spring 2019 and spring 2020

Table 50. Statistical results of morphological parameters for Hamilton County OGCS section samples from fall 2018, spring 2019 and spring 2020

Parameter	Sample Collection	Max.	Min.	Mean	Mode	Median	Std. Dev.	Skew-ness	Kurt-osis	Out-liers
	Date									
Roundness	Fall 2018	0.867	0.328	0.648	0.694	0.652	0.098	-0.296	2.865	3
	Spring 2019	0.892	0.190	0.657	0.704	0.661	0.099	-0.38	3.299	4
	% increase*			1.4%		1.4%				
	Spring 2020	0.896	0.144	0.668	0.635	0.674	0.098	-0.45	3.442	4
	% increase*			3.1%		3.4%				
Sphericity	Fall 2018	0.826	0.224	0.565	0.540	0.569	0.101	-0.185	2.813	2
	Spring 2019	0.821	0.111	0.569	0.598	0.573	0.105	-0.353	3.189	8
	% increase*			0.7%		0.7%				
	Spring 2020	0.805	0.069	0.576	0.562	0.583	0.103	-0.411	3.255	3
	% increase*			1.9%		2.5%				
Form Factor (FF)	Fall 2018	0.864	0.387	0.726	0.722	0.738	0.073	-0.892	3.829	10
	Spring 2019	0.877	0.352	0.731	0.771	0.747	0.079	-1.335	5.615	35
	% increase*			0.7%		1.2%				
	Spring 2020	0.876	0.123	0.74	0.758	0.753	0.074	-1.602	9.201	32
	% increase*			1.9%		2.0%				
Shape Factor (SF)	Fall 2018	32.4	14.5	17.5	15.5	17.0	2.0	1.9	9.3	23
	Spring 2019	35.7	14.3	17.4	17.1	16.8	2.4	2.8	14.8	51
	% increase*			-0.6%		-1.2%				
	Spring 2020	102.4	14.4	17.2	15.4	16.7	3.4	17.1	424.7	49
	% increase*			-1.7%		-1.8%				
Roundness Index (RI)	Fall 2018	1.041	0.787	0.848	0.844	0.841	0.035	1.552	6.606	23
	Spring 2019	1.144	0.784	0.848	0.820	0.840	0.039	2.455	13.26	40
	% increase*			0.0%		-0.1%				
	Spring 2020	1.212	0.790	0.846	0.828	0.837	0.039	2.763	17.23	49
	% increase*			-0.2%		-0.5%				
Angularity	Fall 2018	1.201	0.291	0.615	0.544	0.577	0.169	1.083	3.831	18
	Spring 2019	1.172	0.200	0.592	0.404	0.555	0.158	1.146	4.125	38
	% increase*			-3.7%		-3.8%				
	Spring 2020	1.191	0.337	0.558	0.637	0.517	0.141	1.398	5.019	52
	% increase*			-9.3%		-10.4%				

*w.r.t. Fall 2018

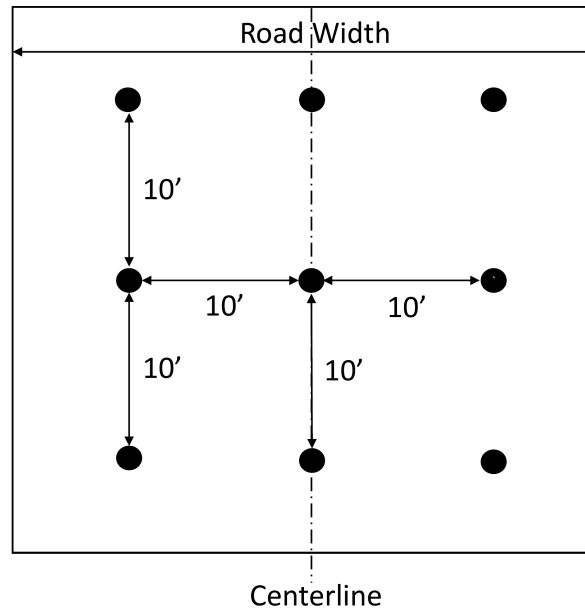


Xue et al. 2022

Figure 220. Visual surveys of Hamilton County OGCS section over time: (a) fall 2018, (b) spring 2019, (c) fall 2019, (d) spring 2020

4.3.7 Hamilton County – Aggregate Columns Section

A 500 ft long Aggregate Columns test section was constructed in Hamilton County in September 2018 as part of IHRB Project TR-721. The columns consisted of 12 in. diameter by 7 ft deep augered holes drilled in a 10 ft grid as shown in Figure 221 and backfilled with 1 in. clean aggregate and the road surface was covered with Class A/B road rock. Samples of the surface aggregates were collected from the test section over a period of two years, specifically during the construction phase in fall 2018 and during spring 2019, fall 2019, and spring 2020. Particle size distribution analyses were performed on these collected materials by sieve and hydrometer tests in IHRB Project TR-721 to determine the gradation change over time (Figure 222). The PSD curves were digitized in the present study to analyze the mechanical degradation and material loss over time.



Xue et al. 2022

Figure 221. Column layout pattern for Hamilton County Aggregate Columns section, road width = 28 ft

4.3.7.1 Comparison of Breakage Parameters for Hamilton County Aggregate Columns Section

The mechanical degradation in the form of breakage parameters was evaluated for the samples relative to those collected during construction in fall 2018. This degradation is presented in Figure 223, Figure 224 and Figure 225 for the samples collected in spring 2019, fall 2019 and fall 2020, respectively. Table 51 summarizes the resulting breakage parameters along with the percentages of gravel, sand, and fines for the samples collected from the Hamilton County Aggregate Columns section over time. Figure 226 presents a bar chart of the cumulative total breakage for samples from spring 2019, fall 2019, and spring 2020, showing a general increase in total breakage over time as expected. However, the total breakage of the spring 2020 sample is slightly lower than that of the fall 2019 sample, which could be due to the sample collection methodology or spatial variability, as previously discussed.

The percentages of gravel, sand, and fines for the samples collected over time are also presented as a bar chart in Figure 227. The data in Table 51 and Figure 227 indicate a significant reduction in the gravel fraction, from 67.9% at the time of construction in fall 2018 to 31.4% in spring 2020, with a general decreasing trend in the gravel fraction except for a slight increase between fall 2019 and spring 2020. This increase may have been caused by sampling error arising from nonuniform distribution of aggregate materials in the test section. In contrast, the sand fractions increased over time, from 25.4% at the start of construction in fall 2018 to 44.3% in spring 2020, while the fines fraction increased from 6.9% to 24.3%. The increasing trend in total breakage, increasing sand and fines percentages, and decreasing trend in gravel percentage indicate that the gravel in the road surface was breaking down significantly into sand and fines size fractions due to traffic loading and weather conditions. Additionally, the PSD curves migrated upwards with

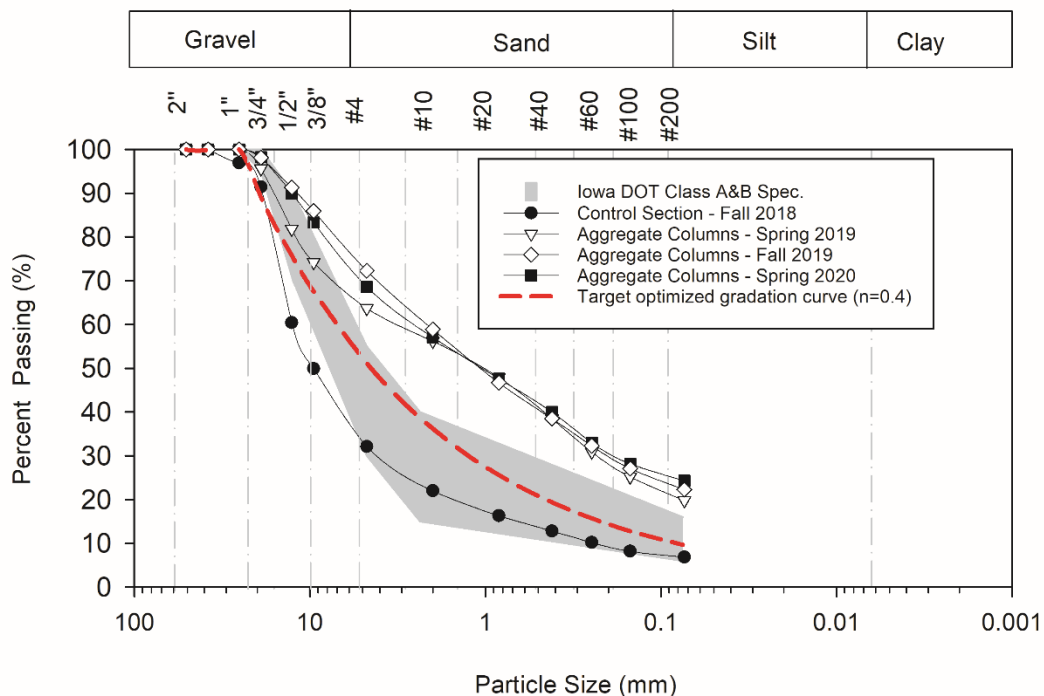
time, ending well above the Iowa DOT Class A/B specification band and indicating the increase in sands and fines with time.

4.3.7.2 2D Image Analyses and Comparison of Morphological Parameters for Hamilton County Aggregate Columns Section

The 2D image analyses were also performed for two available samples, which were collected in spring and fall 2019. The resulting morphological parameters are presented in Figure 228 through Figure 233. The statistical output of these morphological parameters is presented in Table 52, showing increases in median values of roundness, sphericity, and form factor by 1.0%, 2.6%, and 4.1%, respectively. Conversely, the median values of shape, angularity, and roundness decreased by 4.1%, 9.7%, and 1.3%, respectively. These changes quantify the degradation and evolving geometry of the gravel sized particles over the six month period.

4.3.7.3 Visual Surveys for Hamilton County Aggregate Columns Section

Photos from visual surveys of the Hamilton County Aggregate Columns section taken over time are shown in Figure 234. The visual surveys confirm that the gravel fraction of the surfacing materials decreased over time while the sand and fines fractions increased.



Xue et al. 2022

Figure 222. Particle size distributions of Hamilton County Aggregate Columns surface materials for samples collected over time

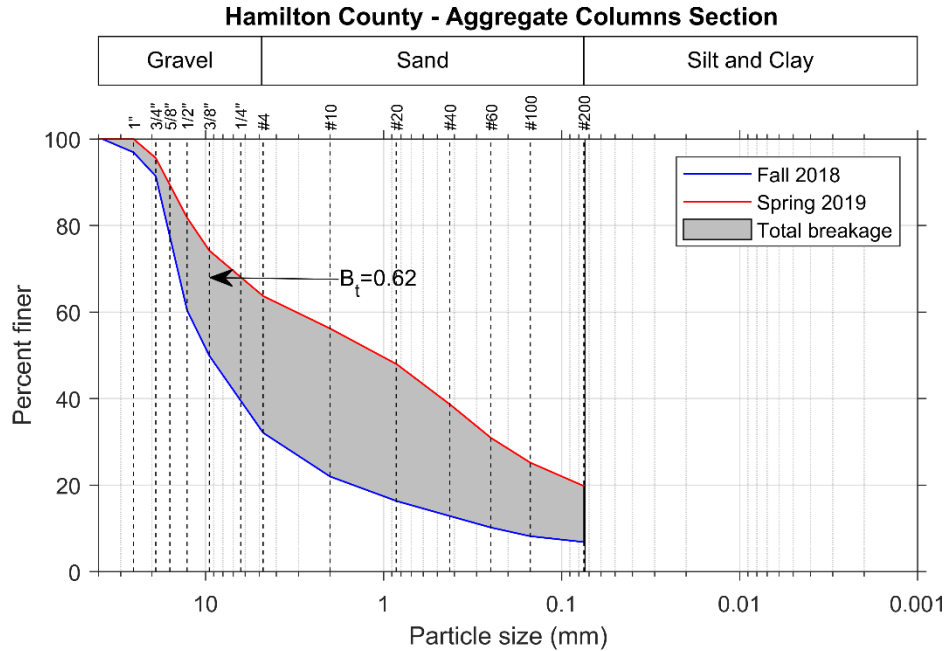


Figure 223. Particle size distributions and evaluation of total breakage of coarse aggregate for Hamilton County Aggregate Columns section from fall 2018 to spring 2019

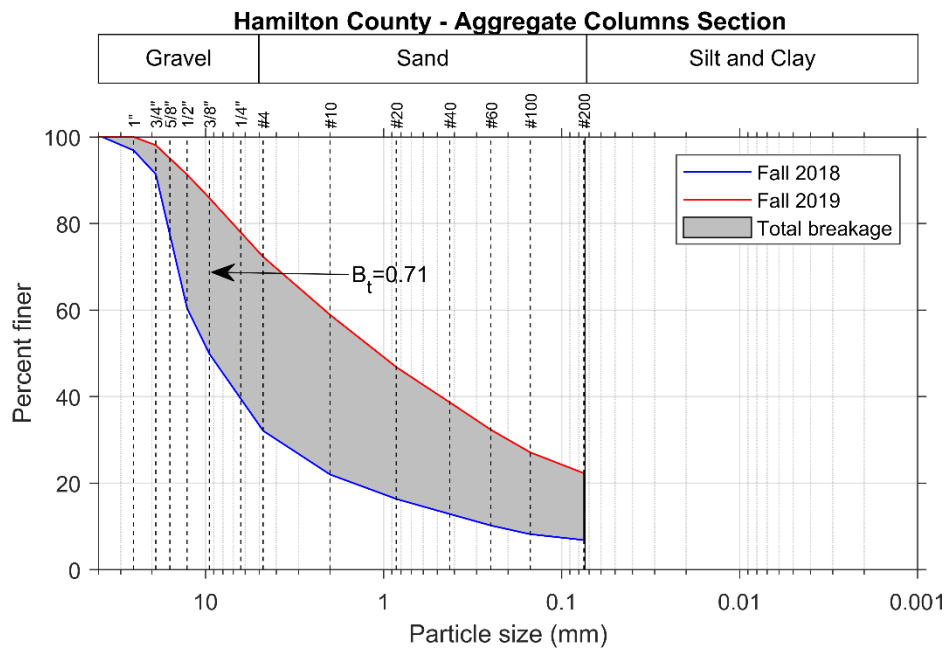


Figure 224. Particle size distributions and evaluation of total breakage of coarse aggregate for Hamilton County Aggregate Columns section from fall 2018 to fall 2019

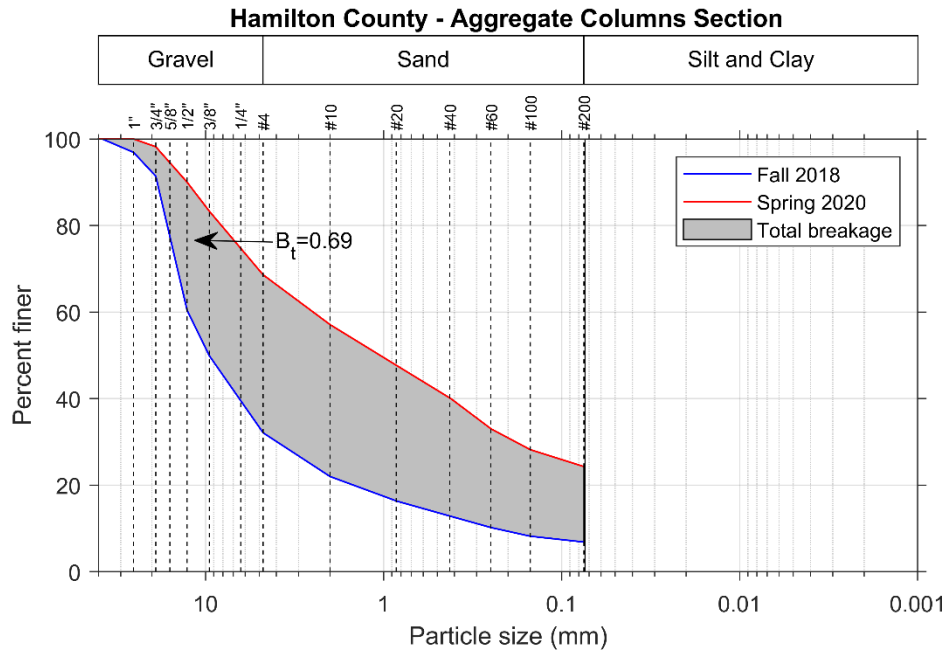


Figure 225. Particle size distributions and evaluation of total breakage of coarse aggregate for Hamilton County Aggregate Columns section from fall 2018 to spring 2020

Table 51. Breakage parameters from laboratory sieve analyses and percent gravel, sand, and fines for samples of Hamilton County Aggregate Columns section

Sample Collection Date	Hardin's Breakage Parameters*			% Gravel	% Gravel Red.*	% Sand	% Sand Inc.*	% Fines	% Fines Inc.*
	Total Breakage, B_t	Breakage Potential, B_p	Relative Breakage, B_r						
Fall 2018	-	-	-	67.9	-	25.2	-	6.9	-
Spring 2019	0.6167	1.8072	0.3412	36.3	31.6	43.9	18.7	19.8	12.9
Fall 2019	0.7069	1.8072	0.3912	27.7	40.2	50.0	24.8	22.3	15.4
Spring 2020	0.6948	1.8072	0.3845	31.4	36.5	44.3	19.1	24.3	17.4

*w.r.t. Fall 2018; Red. = Reduction; Inc. = Increase

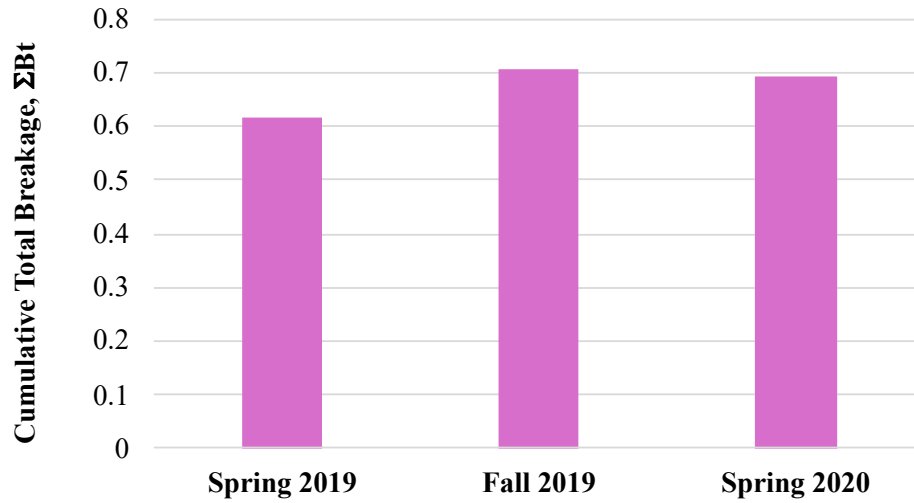


Figure 226. Cumulative total breakage of surface course of Hamilton County Aggregate Columns section over time

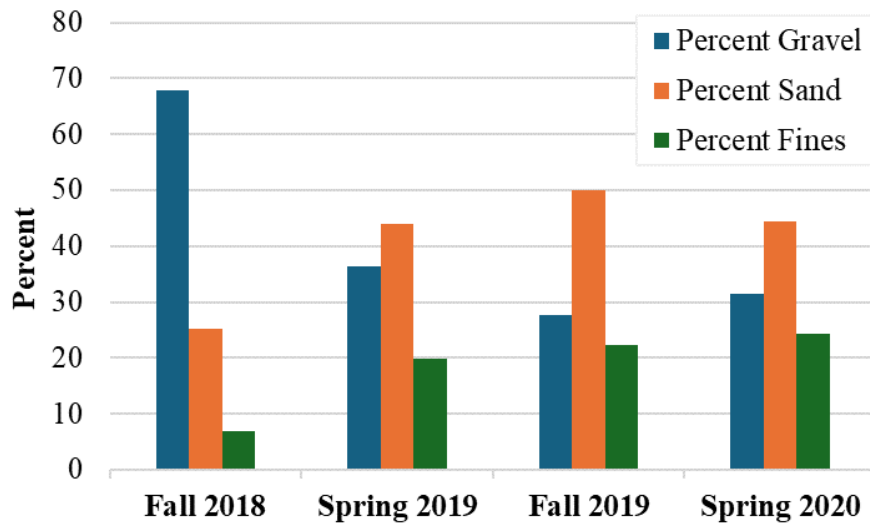


Figure 227. Gravel, sand and fines fractions of surface course of Hamilton County Aggregate Columns section over time

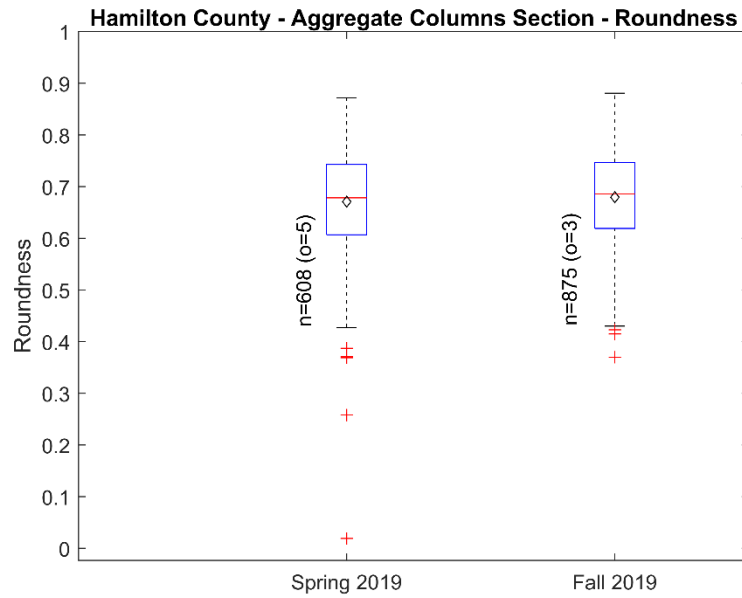


Figure 228. Comparison of roundness for Hamilton County Aggregate Columns section samples from spring 2019 and fall 2019

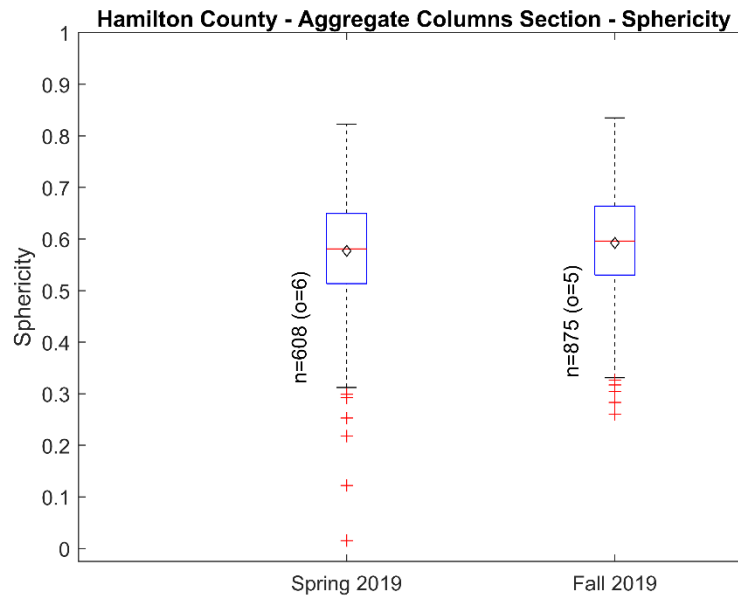


Figure 229. Comparison of sphericity for Hamilton County Aggregate Columns section samples from spring 2019 and fall 2019

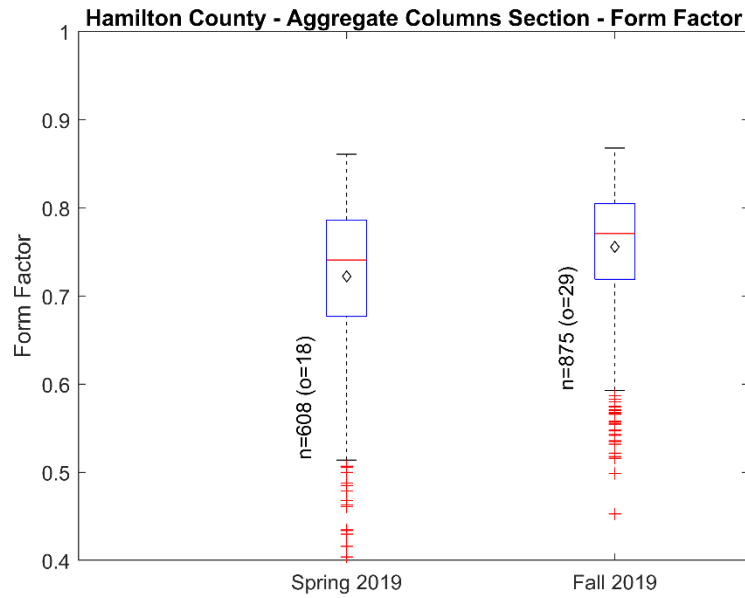


Figure 230. Comparison of form factor for Hamilton County Aggregate Columns section samples from spring 2019 and fall 2019

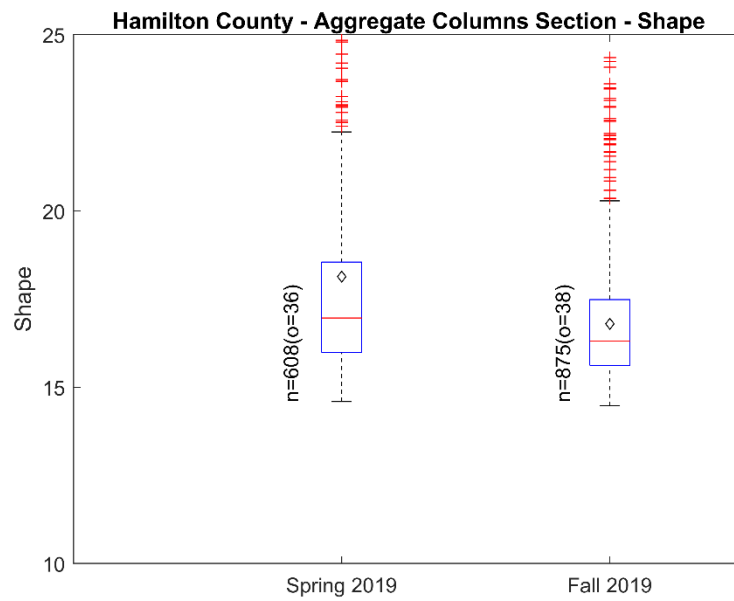


Figure 231. Comparison of shape factor for Hamilton County Aggregate Columns section samples from spring 2019 and fall 2019

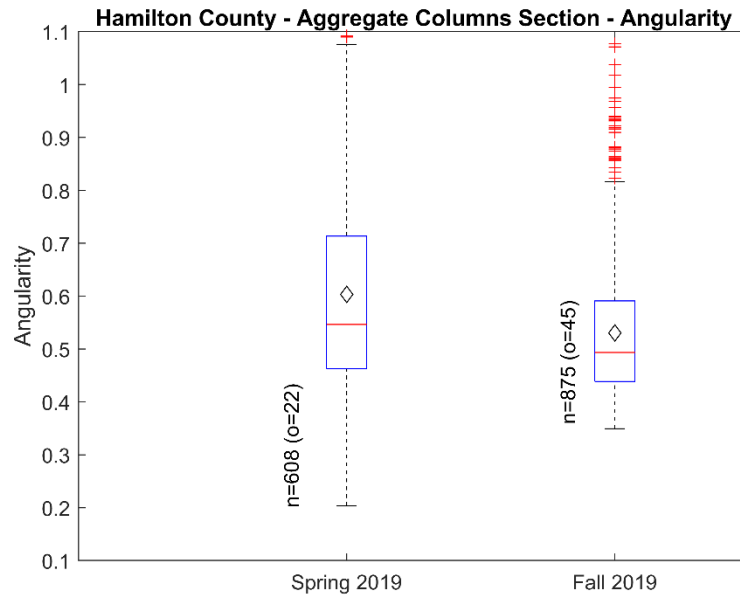


Figure 232. Comparison of angularity for Hamilton County Aggregate Columns section samples from spring 2019 and fall 2019

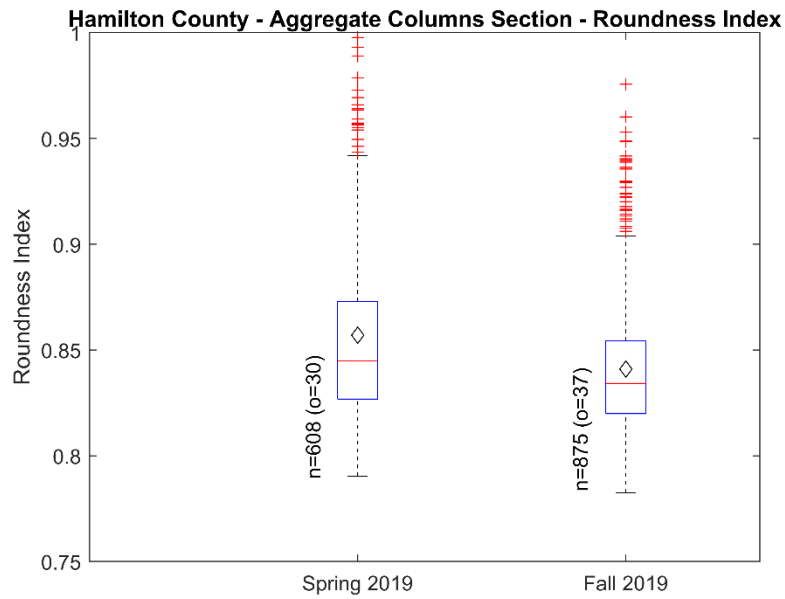
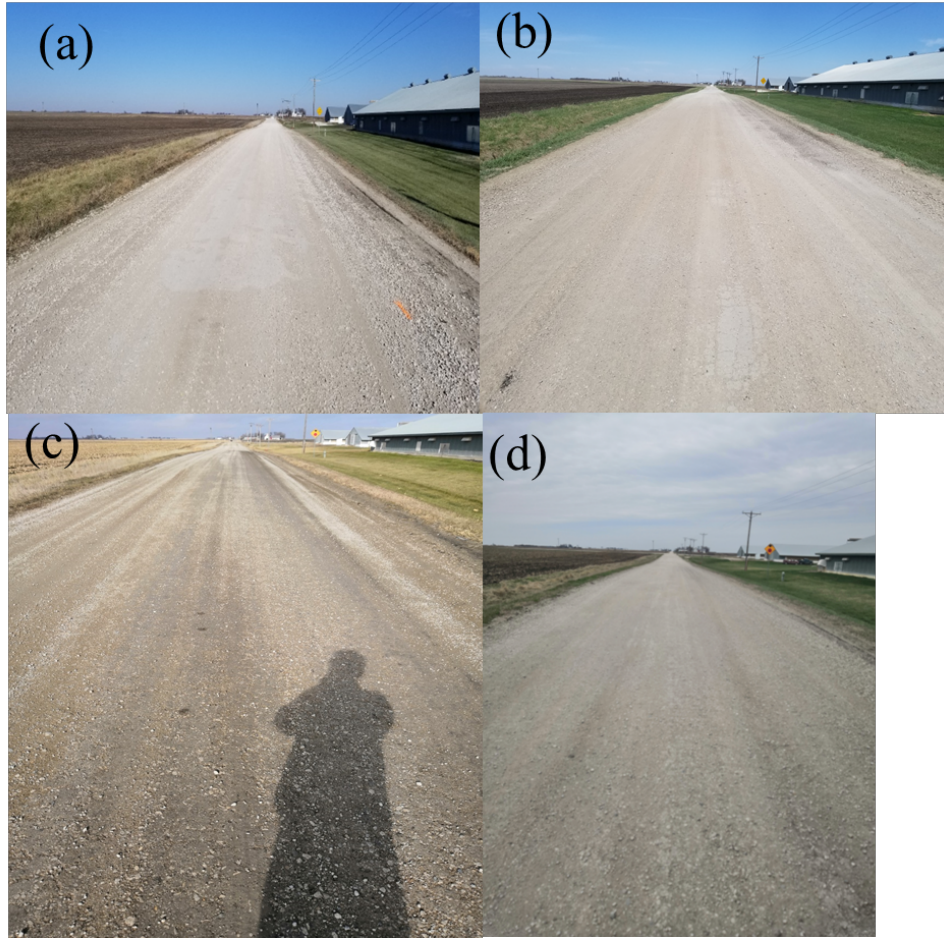


Figure 233. Comparison of roundness index for Hamilton County Aggregate Columns section samples from spring 2019 and fall 2019

Table 52. Statistical results of morphological parameters of Hamilton County Aggregate Columns section, spring 2019 and fall 2019 samples

Parameter	Sample Collection Date	Max.	Min.	Mean	Mode	Median	Std. Dev.	Skew-ness	Kurt-osis	Out-liers
Roundness	Spring 2019	0.872	0.019	0.671	0.683	0.679	0.097	-0.835	6.14	5
	Fall 2019	0.881	0.37	0.679	0.704	0.686	0.092	-0.365	2.811	3
	% increase			1.2%		1.0%				
Sphericity	Spring 2019	0.823	0.015	0.577	0.545	0.581	0.106	-0.575	4.434	6
	Fall 2019	0.835	0.26	0.592	0.571	0.596	0.098	-0.273	2.828	5
	% increase			2.6%		2.6%				
Form Factor (FF)	Spring 2019	0.861	0.044	0.722	0.721	0.741	0.092	-1.732	9.142	18
	Fall 2019	0.868	0.361	0.756	0.793	0.771	0.07	-1.37	5.917	29
	% increase			4.7%		4.1%				
Shape Factor (SF)	Spring 2019	283.6	14.6	18.1	15.5	17	11.1	22.3	530.4	36
	Fall 2019	34.9	14.5	16.8	15.6	16.3	1.9	3	19.9	38
	% increase			-7.2%		-4.1%				
Roundness Index (RI)	Spring 2019	1.298	0.203	0.603	0.203	0.546	0.188	0.983	3.299	22
	Fall 2019	1.077	0.349	0.530	0.375	0.493	0.125	1.404	5.09	45
	% increase			-12.1%		-9.7%				
Angularity	Spring 2019	1.305	0.79	0.857	0.819	0.845	0.049	2.749	17.84	30
	Fall 2019	1.188	0.783	0.841	0.828	0.834	0.033	3.104	25.98	37
	% increase			-1.9%		-1.3%				



Xue et al. 2022

Figure 234. Visual surveys of Hamilton County Aggregate Columns section over time: (a) fall 2018, (b) spring 2019, (c) fall 2019, (d) spring 2020

4.3.8 Comparison of Gravel Deterioration for Hamilton County Test Sections

4.3.8.1 Comparison of Breakage Parameters for Hamilton County Sections

The cumulative total breakage for the three Hamilton County test sections is compared in Figure 235 and the cumulative relative breakage is compared in Figure 236, both evaluated relative to the initial samples collected in fall 2018. The results reveal that the OGCS section experienced the lowest total breakage and relative breakage over time. On the other hand, the Aggregate Columns section consistently had the highest breakage values, followed by the Control section.

These results provide new insights into the relative performance of the OGCS and Aggregate Columns stabilization methods examined in IHRB Project TR-721. Specifically, the results demonstrate that the OGCS method remained effective in slowing the breakage of aggregates for at least two years, whereas the surface course of the Aggregate Columns section showed practically no additional breakage over the last year. However, as explained in the TR-721

report, the Aggregate Columns method aims to improve the supporting subgrade to minimize moisture related surface damage such as rutting and potholes, and does not include any stabilization of the surface course materials which are the same as those in the Control section.

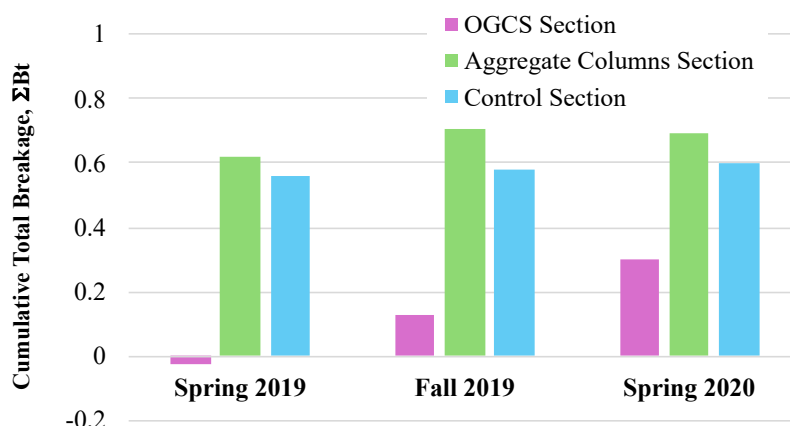


Figure 235. Comparison of cumulative total breakage of samples from Hamilton County OGCS section, Aggregate Columns section, and Control section collected over time

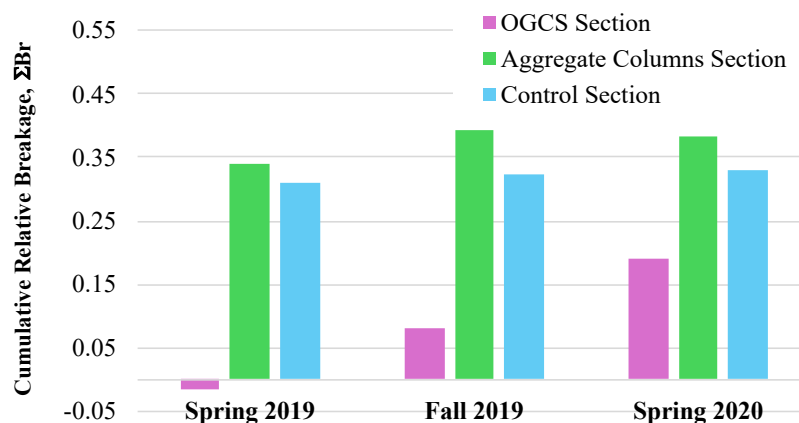


Figure 236. Comparison of cumulative relative breakage of samples from Hamilton County OGCS section, Aggregate Columns section, and Control section collected over time

4.3.8.2 Comparison of Change in Gravel, Sand and Fines Fractions for Hamilton County Sections

The gravel, sand, and fines fractions evaluated in previous sections of this report for the three Hamilton County test sections are compared in Figure 237 and Figure 238 for the gravel fraction, Figure 239 and Figure 240 for the sand fraction, and Figure 241 and Figure 242 for the fines fraction. The results show that the OGCS section performed the best as it experienced the smallest decrease in gravel percentage, the smallest increase in sand percentage through fall 2019, and nearly zero change in the fines percentage over the entire period of study. Conversely, the Control section and Aggregate Columns sections exhibited greater decreases in their gravel fraction and greater overall increases in their sand and fines fractions over time.

Considering the rates of breakage, decreases in gravel fraction, and increases in sand and fines fractions altogether, the OGCS section had the smallest total and relative breakage and the smallest decrease in gravel fraction over time, as well as the smallest increases in sand and fines fractions over time. On other hand, the Aggregate Columns section showed the greatest total and relative breakage over time, followed by the Control section. The Control section also showed the greatest decrease in gravel fraction for spring 2019, whereas the Aggregate Columns section showed the greatest decrease in gravel fraction for fall 2019 and spring 2020. These findings signify that OGCS stabilization was most effective in minimizing the breakage and loss of gravel, with the Aggregate Columns and Control sections offering similar effectiveness and inferior performance compared to the OGCS section.

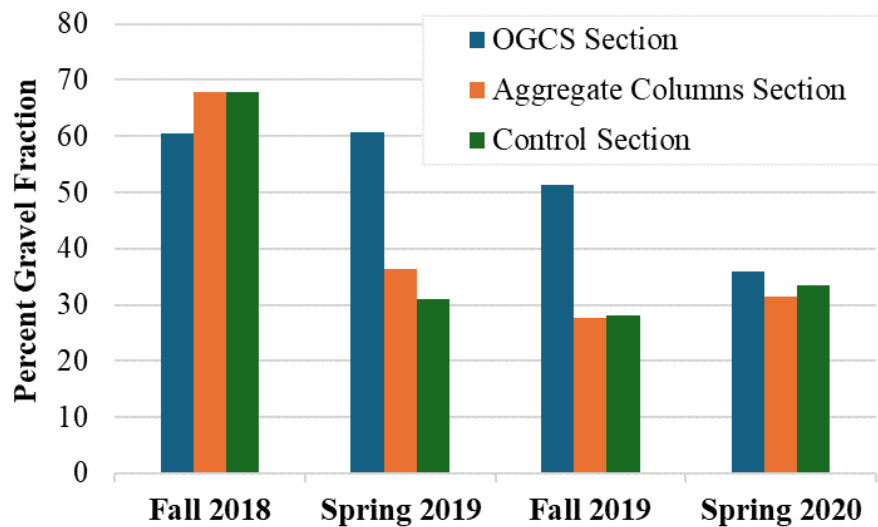


Figure 237. Comparison of gravel fraction for samples from Hamilton County OGCS section, Aggregate Columns section, and Control section collected over time

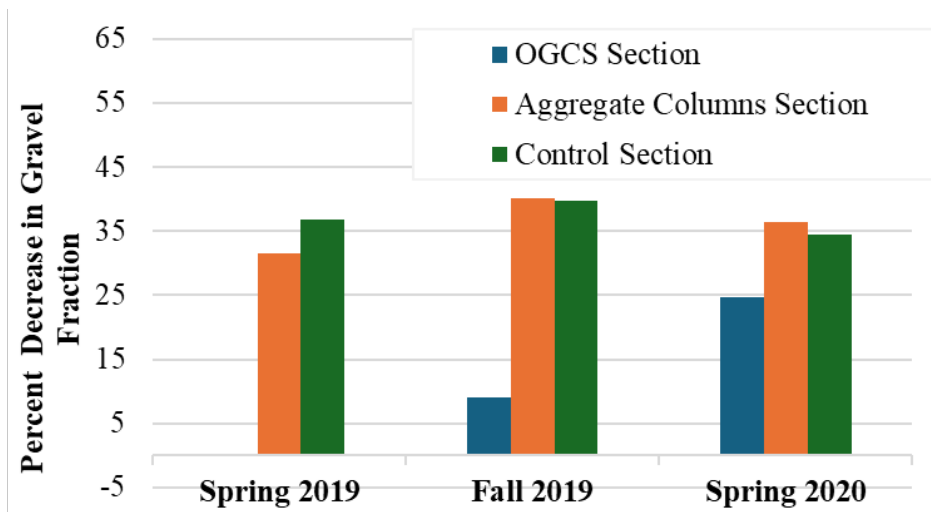


Figure 238. Comparison of percent decrease in gravel fraction relative to 2018 for samples from Hamilton County OGCS section, Aggregate Columns section, and Control section collected over time

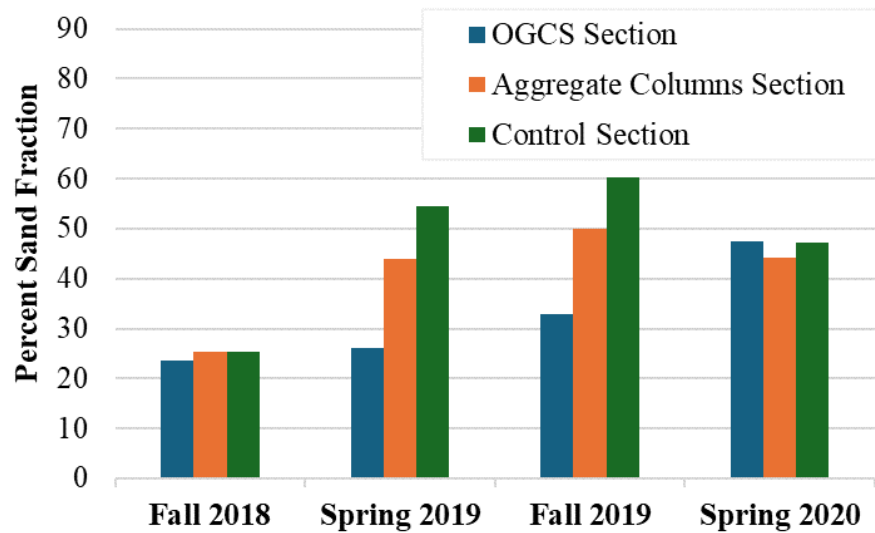


Figure 239. Comparison of sand fraction for samples from Hamilton County OGCS section, Aggregate Columns section, and Control section collected over time

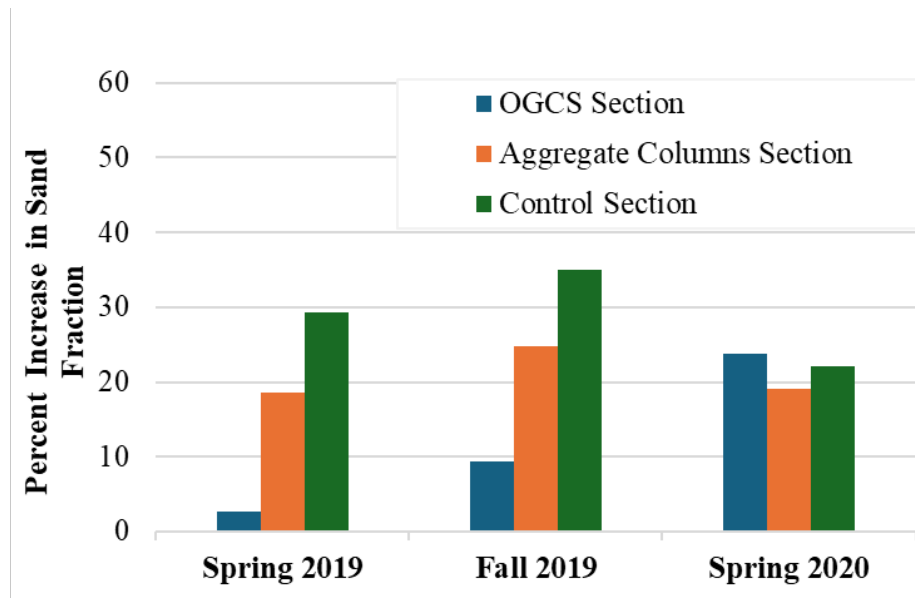


Figure 240. Comparison of percent increase in sand fraction relative to 2018 for samples from Hamilton County OGCS section, Aggregate Columns section, and Control section collected over time

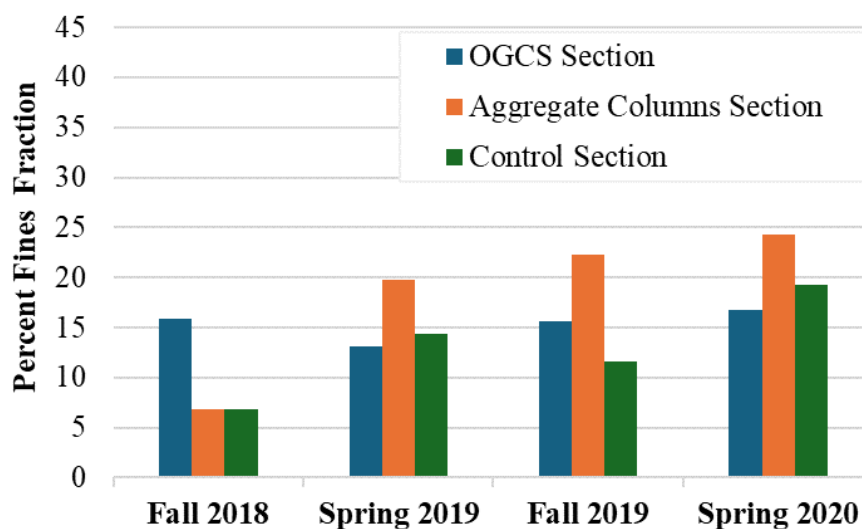


Figure 241. Comparison of fines fraction for samples from Hamilton County OGCS section, Aggregate Columns section, and Control section collected over time

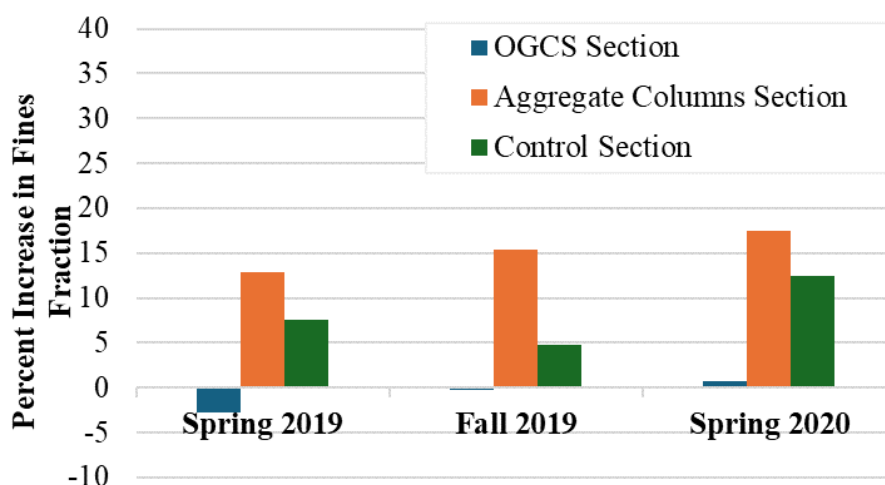


Figure 242. Comparison of percent increase in fines fraction relative to 2018 for samples from Hamilton County OGCS section, Aggregate Columns section, and Control section collected over time

4.3.9 Washington County – Control Section

In IHRB Project TR-721, five types of chemically stabilized test sections were constructed along with two mechanically stabilized test sections and a control section in Washington County on 260th Street between Palm and Quince Avenues. A satellite image of the location and a schematic diagram illustrating the layout of the test sections are shown in Figure 243 and Figure 244, respectively. The 300 ft long control section was constructed to evaluate the performance of the test sections against the current construction and maintenance practices for gravel roads in

Washington County. To construct the control section, fresh aggregates were spread over the existing road surfacing material to an initial thickness of 4 in. in fall 2018.

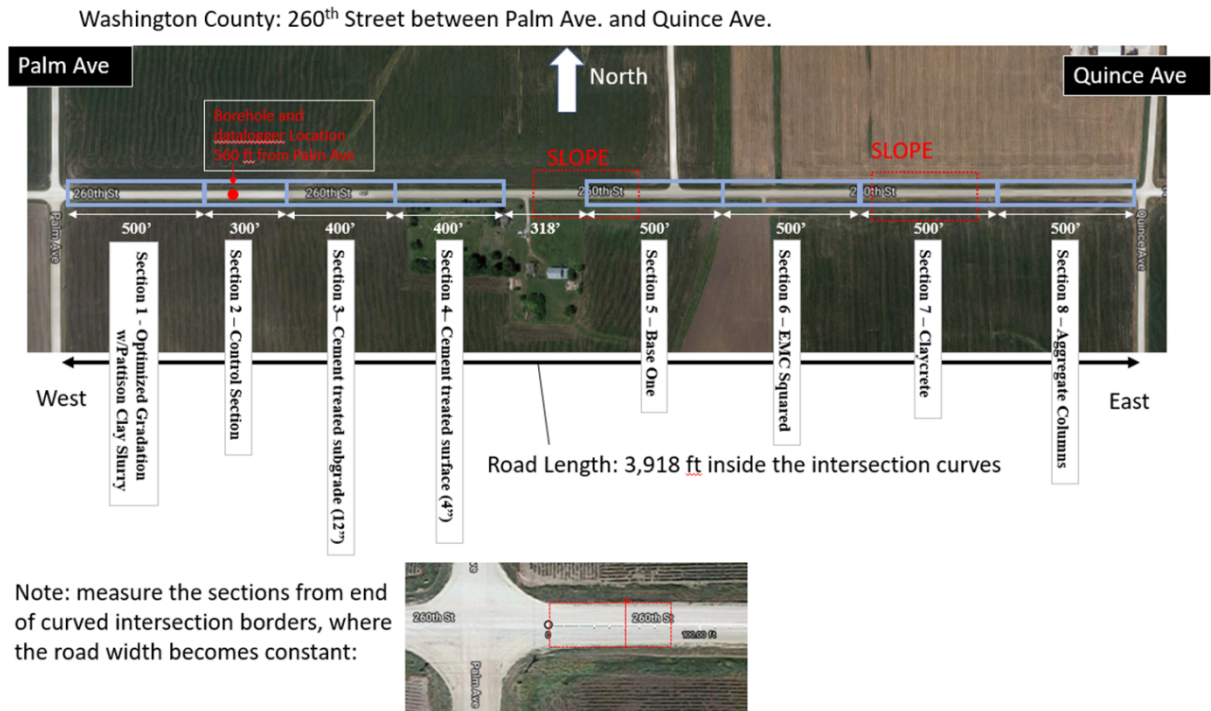


Figure 243. Satellite image of Washington County chemically and mechanically stabilized test sections

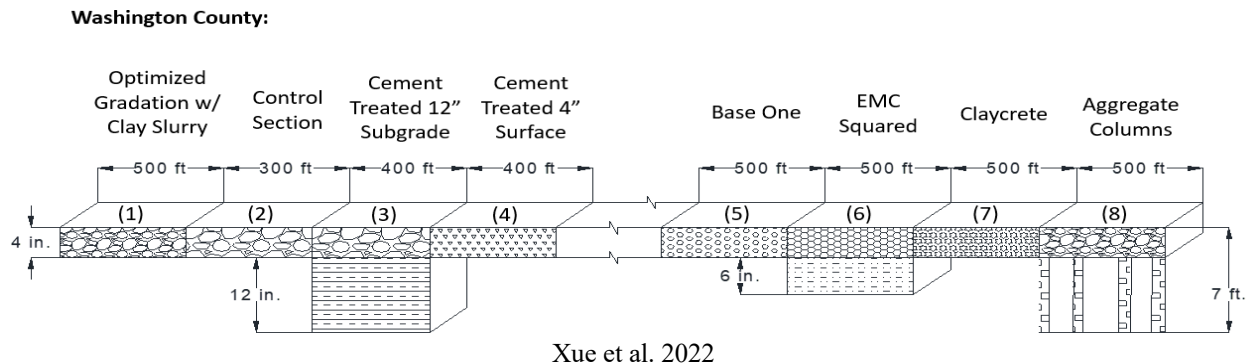


Figure 244. Layouts of chemically and mechanically stabilized test sections in Washington County

4.3.9.1 Comparison of Breakage Parameters for Washington County Control Section

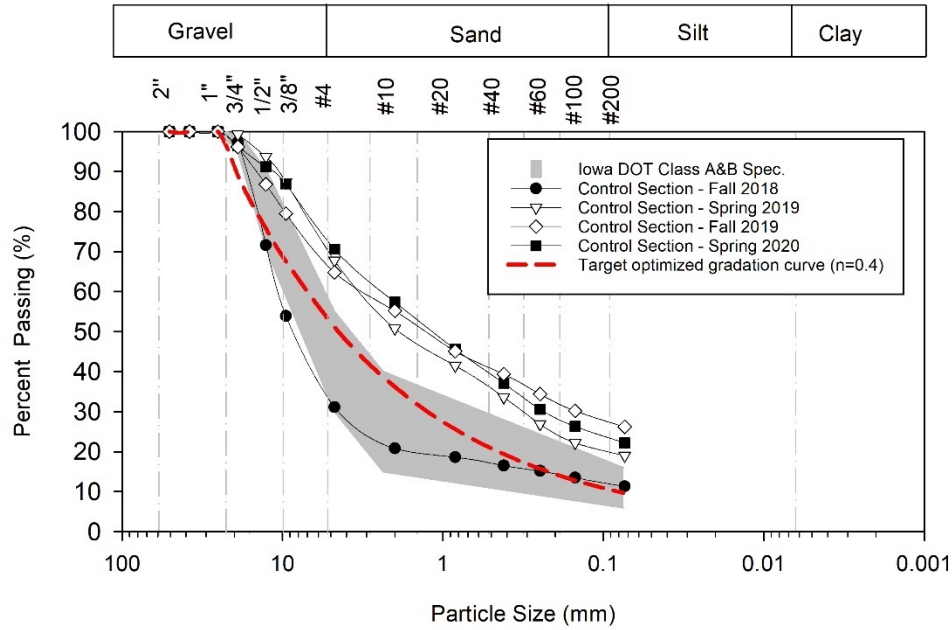
Samples of the surface aggregates were collected from the control section in Washington County over a period of two years during IHRB Project TR-721, specifically during the construction phase in fall 2018 and during spring 2019, fall 2019, and spring 2020. According to the Washington Secondary Roads personnel, no new aggregates were spread on the test sections

during these intervals. Therefore, the breakage can be determined between the representative samples from any pair of these dates. The PSD curves for these samples are shown in Figure 245, and the corresponding breakage evaluations relative to construction in fall 2018 are presented in Figure 246, Figure 247, and Figure 248 for the samples collected in spring 2019, fall 2019, and fall 2020, respectively. Table 53 summarizes the breakage parameters along with the percentages of gravel, sand, and fines determined from the PSD curves, and the cumulative total breakage is shown graphically in Figure 249. The cumulative total breakage increases continually over time as expected.

The percentages of gravel, sand, and fines for the samples collected over time are also presented as a bar chart in Figure 250. The data indicate a significant reduction in the gravel fraction, decreasing from 68.9% at the time of construction in fall 2018, to 29.4% by spring 2020. A slight increase in the gravel fraction is noted between spring and fall 2019 which may be caused by sampling error arising from nonuniform distribution of aggregate materials in the test section, or could result from a loss of sand and fines due to runoff and dust in the intervening summer months. In contrast, the combined sand and fines fractions increased over time, from 31.1% at the start of construction in fall 2018 to 70.6% in spring 2020. The increasing trend in total breakage, increasing sand and fines percentages, and decreasing trend in gravel percentage suggest that the gravel in the road surface was breaking down significantly due to traffic loading and weather conditions, with the gravel breaking down into sand and fines size fractions, and the sand also breaking down into fines. This is evident by the PSD moving upwards with time, ending up well above the Iowa DOT Class A/B specification band in Figure 245.

4.3.9.2 Visual Surveys for Washington County Control Section

Photos from visual surveys of the Washington County Control section taken over time are shown in Figure 251. The visual surveys confirmed that the gravel fraction of the surfacing materials decreased over time while the sand and fines fractions increased. The degradation and loss of aggregates caused by traffic loading and runoff, combined with the weakened and saturated subgrade conditions during spring thaw, contributed to the observed surface distresses including rutting, potholes, washboarding, and raveling.



Xue et al. 2022

Figure 245. Particle size distribution curves of Washington County Control section for samples collected over time

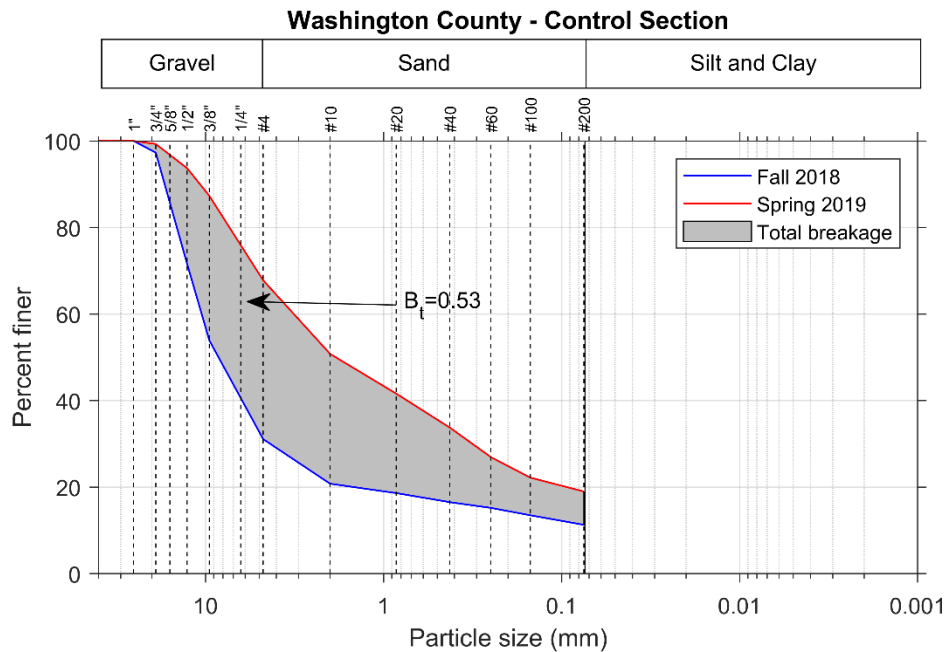


Figure 246. Particle size distributions and evaluation of total breakage of coarse aggregate samples of Washington County Control section between fall 2018 and spring 2019

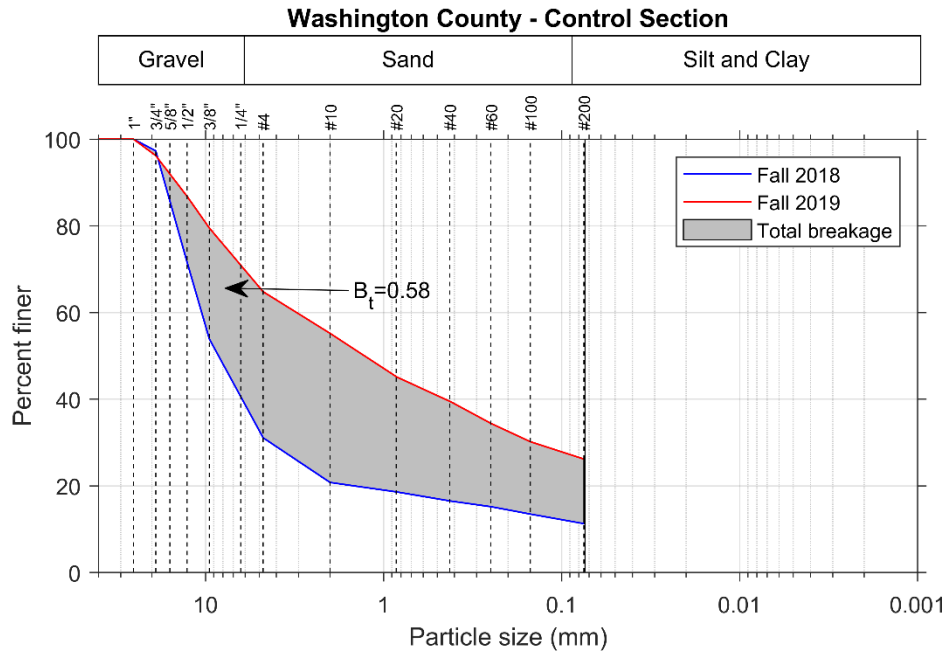


Figure 247. Particle size distributions and evaluation of total breakage of coarse aggregate samples of Washington County Control section between fall 2018 and fall 2019

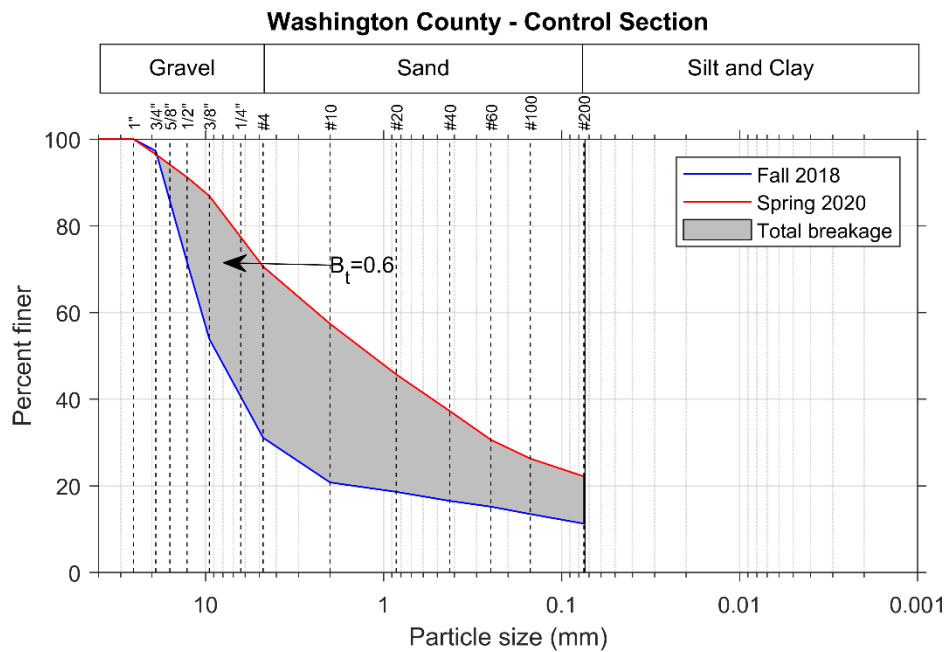


Figure 248. Particle size distributions and evaluation of total breakage of coarse aggregate samples of Washington County Control section between fall 2018 and spring 2020

Table 53. Breakage parameters from laboratory sieve analyses and percent gravel, sand, and fines for samples of Washington County Control section

Sample Collection Date	Hardin's Breakage Parameters*			%	% Gravel Red.*	%	% Sand Inc.*	%	% Fines Inc.*
	Total Breakage, B _t	Breakage Potential, B _p	Relative Breakage, B _r						
Fall 2018	-	-	-	68.9	-	19.8	-	11.3	-
Spring 2019	0.5285	1.7267	0.3061	32.2	36.7	48.8	29.0	19	7.7
Fall 2019	0.5796	1.7267	0.3357	35.2	33.7	38.6	18.8	26.2	14.9
Spring 2020	0.6011	1.7267	0.3481	29.4	39.5	48.4	28.6	22.2	10.9

*w.r.t. Fall 2018; Red. = Reduction; Inc. = Increase

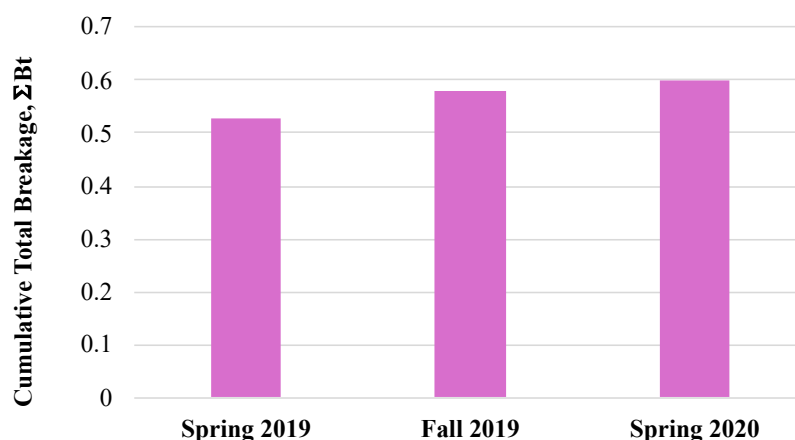


Figure 249. Cumulative total breakage of samples from Washington County Control section over time

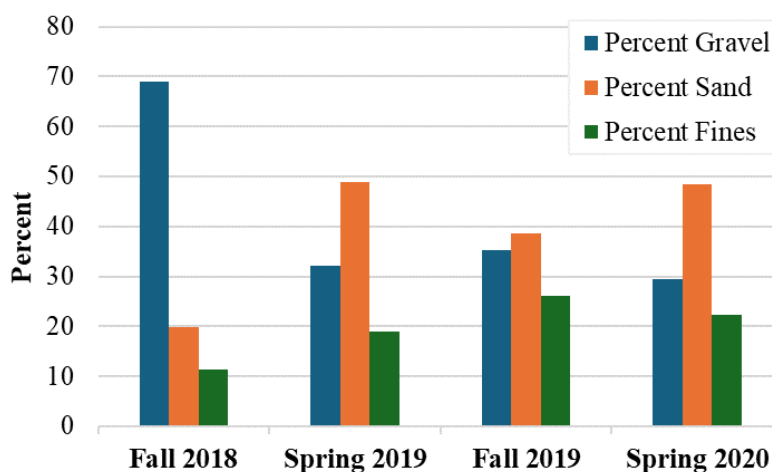
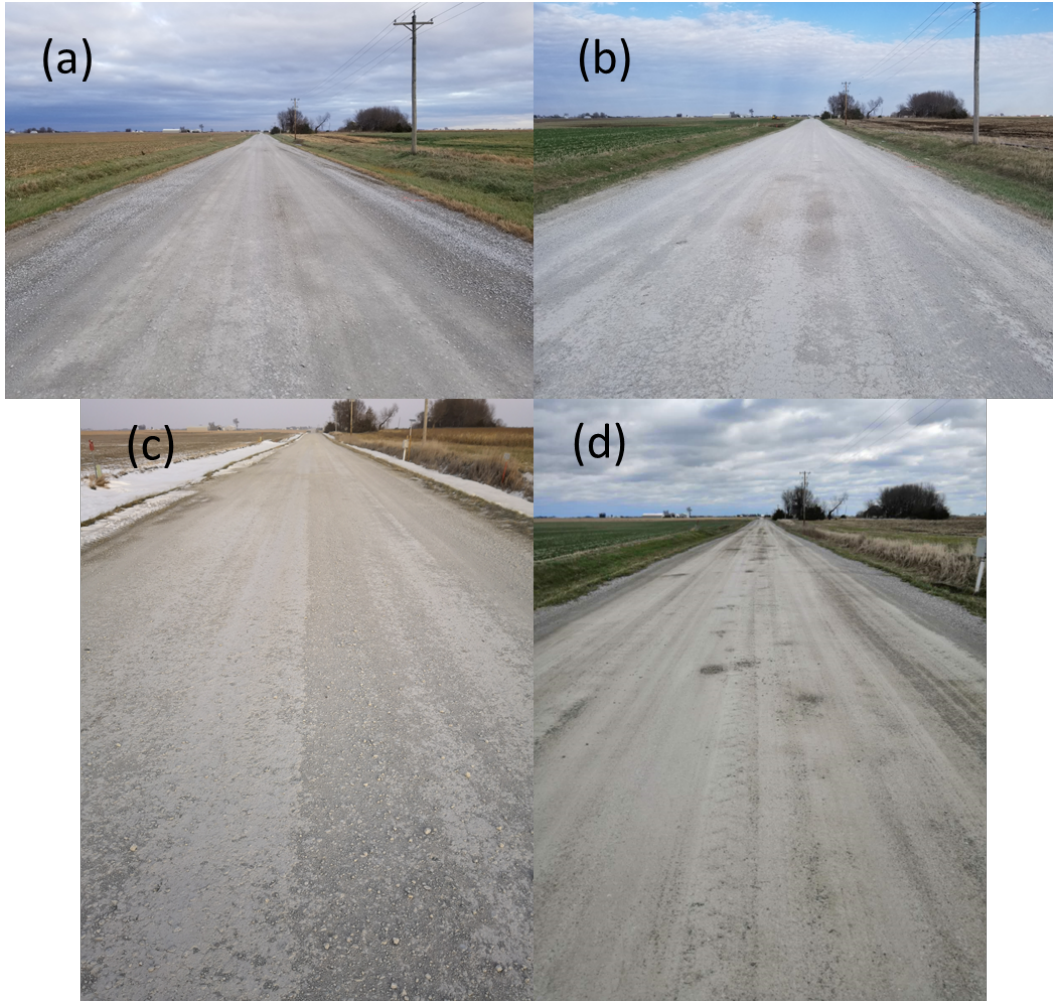


Figure 250. Gravel, sand and fines fractions of samples from Washington County Control section over time



Xue et al. 2022

Figure 251. Visual surveys of Washington County Control section over time: (a) fall 2018, (b) spring 2019, (c) fall 2019, (d) spring 2020

4.3.10 Washington County – Optimized Gradation with Clay Slurry Section

The 500 ft long OGCS test section was constructed in Washington County in August 2018. Samples of surface materials were collected from the Washington County OGCS section over two years of IHRB Project TR-721 during different phases: first in fall 2018 during construction, then again in spring 2019, fall 2019, and spring 2020. The PSD curves from the TR-721 report for this test section are shown in Figure 252. The curves show a slight upward migration over time as the material gradually broke down to a finer gradation, but the amount of migration was much less than that of the nearby Control section shown in Figure 245.

4.3.10.1 Comparison of Breakage Parameters for Washington County OGCS Section

The mechanical degradation relative to fall 2018 is quantified by Hardin's total breakage in Figure 253, Figure 254, and Figure 255 for the samples collected in spring 2019, fall 2019, and

fall 2020, respectively. The corresponding breakage parameters and percentages of gravel, sand, and fines over time are detailed in Table 54. The percentages are also presented in a bar chart in Figure 256, while cumulative total breakage is shown graphically in Figure 257. If the samples are assumed to be representative of the test section and no new materials were added, then the total breakage is expected to continually increase over time. As shown in Figure 257, the breakage did increase as expected between fall 2019 and spring 2019, however it decreased between spring 2019 and spring 2020. This might be a result of statistical variation, or the field samples not being taken in consistent locations in the wheel path, because a sample nearer the shoulder typically has a greater amount of unbroken gravel. Nevertheless, compared to the Control section, the OGCS section had a consistently low value of total breakage that varied over a smaller range.

According to the data in Table 54 and Figure 256, the gravel fraction exhibited an overall decreasing trend with time, starting at 55.4% after construction and ending up at 44.0% by spring 2020. In contrast, the combined sand and fines fraction increased over time, starting at 44.6% and ending at 56.0%. The changes in the gravel, sand, and fines fractions over time were much lower in the OGCS section than the Control section. These reduced changes together with the lower total breakage indicate less deterioration of the gravel materials and therefore improved performance of the OGCS test section compared to the Control section.

4.3.10.2 2D Image Analyses and Comparison of Morphological Parameters for Washington County OGCS Section

The 2D image analyses were also performed for the existing surplus samples from fall 2018 and fall 2019. The evaluation of the total breakage from the PSD curves of the gravel fraction is shown in Figure 258 and summarized in Table 55, and the morphological parameters are presented statistically in Figure 259 through Figure 264. The complete statistical results of these morphological parameters are presented in Table 56, revealing increases in median roundness, sphericity, and form factor of 3.4%, 3.1%, and 1.4%, respectively. Consistent with these results, corresponding decreases of 1.3% for shape factor and 3.8% for angularity were observed.

4.3.10.3 Visual Surveys for Washington County OGCS Section

Visual surveys of the Washington County OGCS section over the duration of the TR-721 project are shown in Figure 265. The survey photos show that the surface of the OGCS test section held up well for the duration of the project, with only minor potholes starting to form by spring 2020. The increase in cohesion offered by the clay fines in the slurry resulted in improved binding of the aggregates, reducing their loss and slowing their degradation compared to the other test sections.

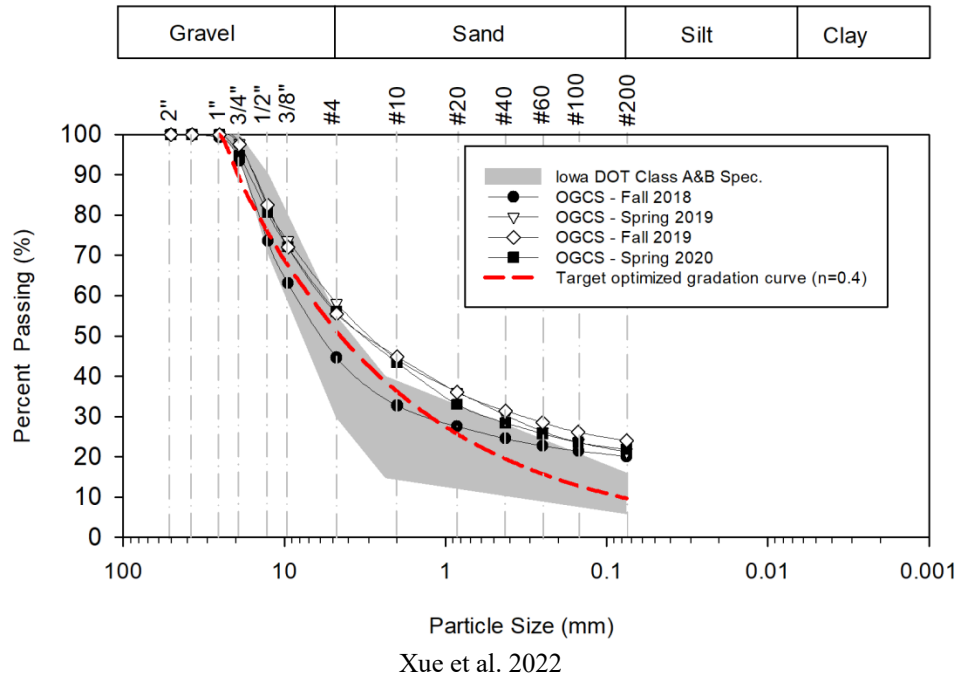


Figure 252. Particle size distribution curves of Washington County OGCS section for samples collected over time

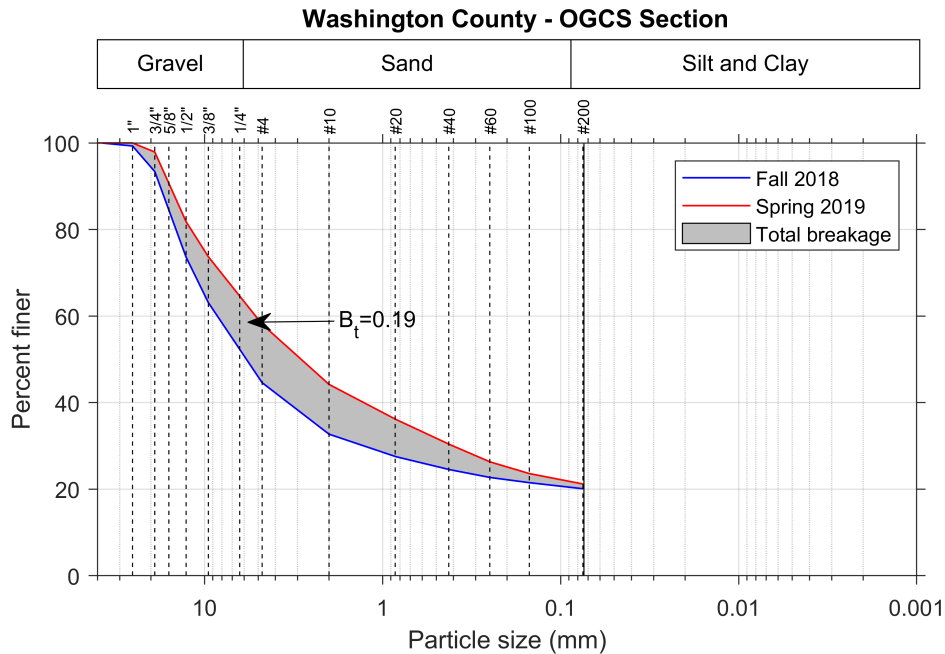


Figure 253. Particle size distributions and evaluation of total breakage of coarse aggregate samples of Washington County OGCS section between fall 2018 and spring 2019

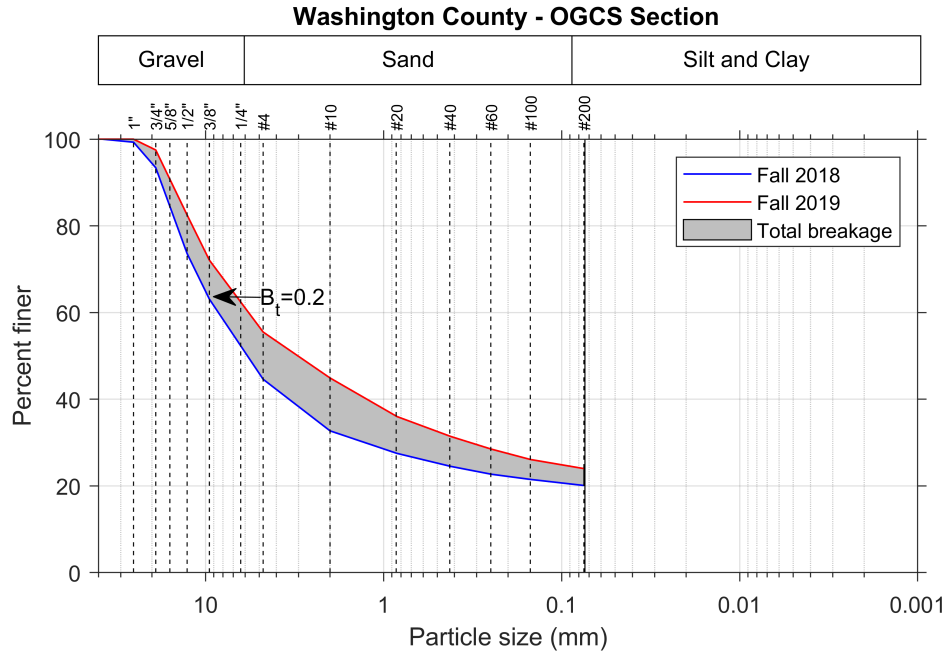


Figure 254. Particle size distributions and evaluation of total breakage of coarse aggregate samples of Washington County OGCS section between fall 2018 and fall 2019

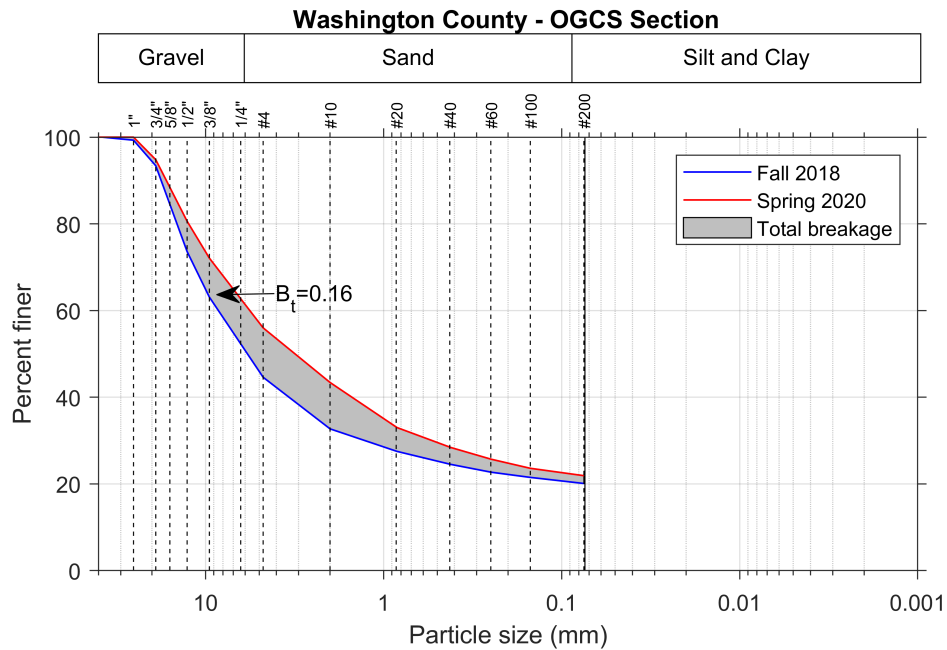


Figure 255. Particle size distributions and evaluation of total breakage of coarse aggregate samples of Washington County OGCS section between fall 2018 and spring 2020

Table 54. Breakage parameters for coarse fraction from laboratory sieve analyses and percent gravel, sand, and fines for samples of Washington County OGCS section

Sample Collection Date	Hardin's Breakage Parameters*				% Gravel Red.*	% Sand	% Sand Inc.*	% Fines	% Fines Inc.*
	Total Breakage, B _t	Breakage Potential, B _p	Relative Breakage, B _r	% Gravel					
Fall 2018	-	-	-	55.4	-	24.5	-	20.1	-
Spring 2019	0.1915	1.5178	0.1262	41.9	10.9	36.9	12.4	21.2	1.1
Fall 2019	0.2008	1.5178	0.1323	44.5	11.4	31.5	7.0	24.0	3.9
Spring 2020	0.1557	1.5178	0.1026	44.0	55.4	34.1	9.6	21.9	1.8

*w.r.t. Fall 2018; Red. = Reduction; Inc. = Increase

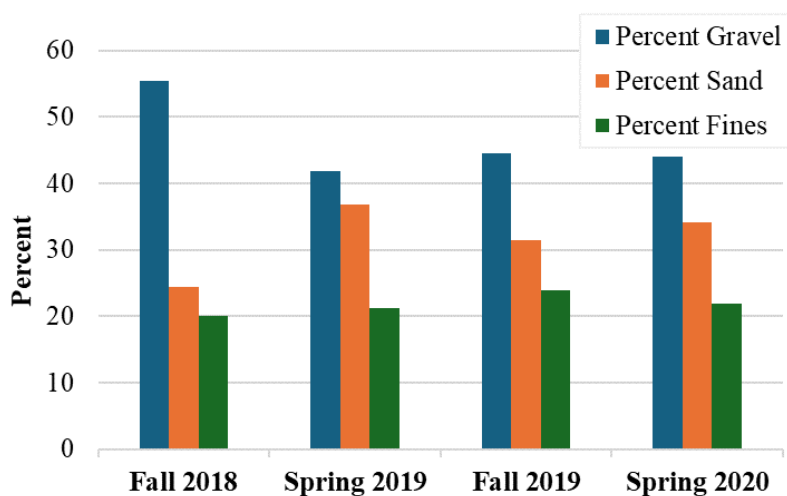


Figure 256. Gravel, sand and fines fractions of samples from Washington County OGCS section collected over time

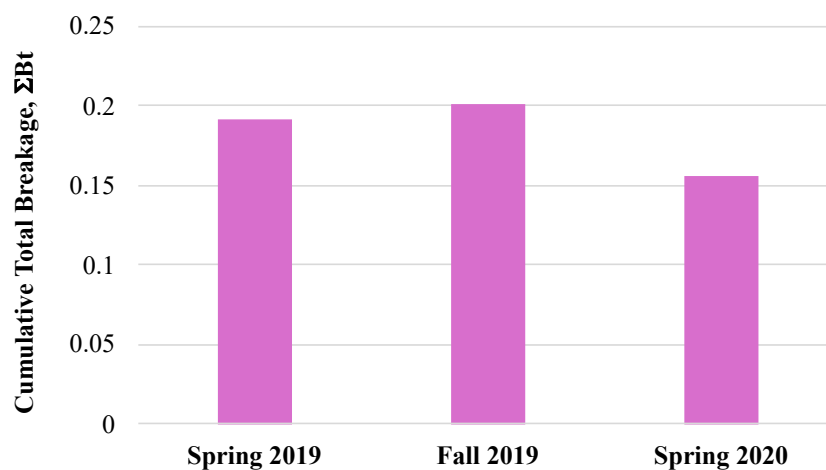


Figure 257. Cumulative total breakage of samples from Washington County OGCS section collected over time

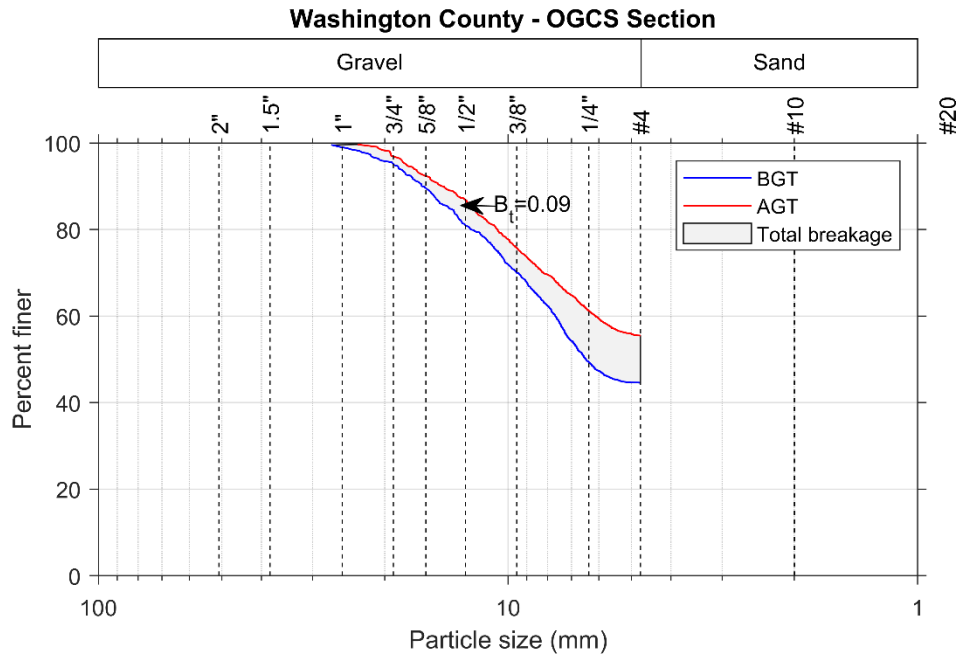


Figure 258. Particle size distributions from 2D image analysis and evaluation of total breakage of gravel fraction for Washington County OGCS section between fall 2018 and fall 2019

Table 55. Breakage parameters for gravel fraction from 2D image analyses for samples of Washington County OGCS section

Sample Collection Date	Hardin's Breakage Parameters*		
	Total Breakage, B_t	Breakage Potential, B_p	Relative Breakage, B_r
Fall 2018	-	-	-
Spring 2019	0.0129	0.7389	0.0174

*w.r.t. Fall 2018

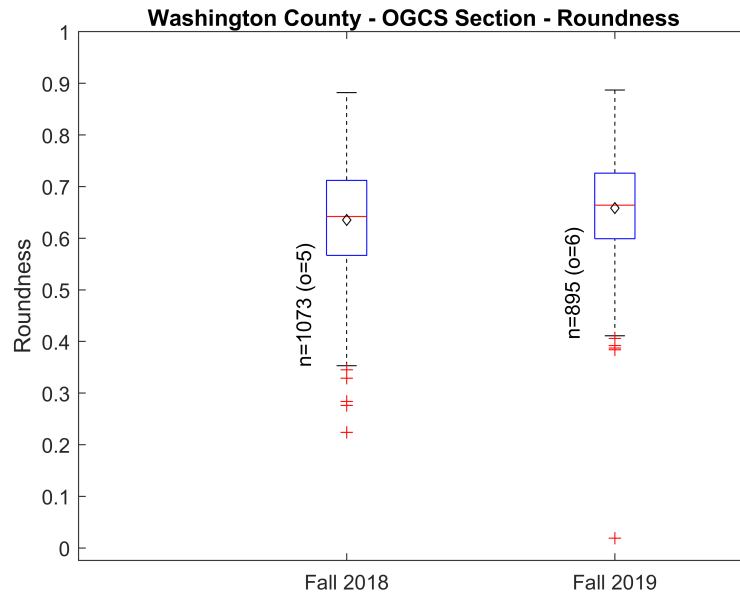


Figure 259. Comparison of roundness for Washington County OGCS samples from fall 2018 and fall 2019

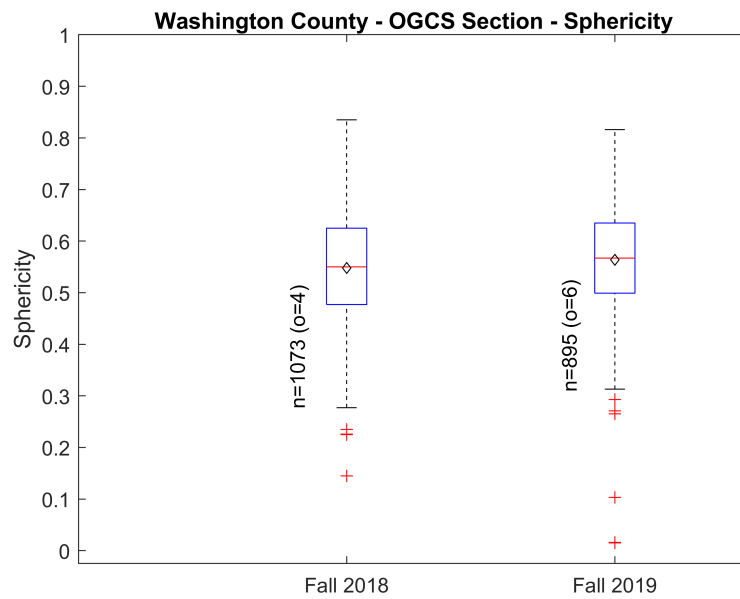


Figure 260. Comparison of sphericity for Washington County OGCS samples from fall 2018 and fall 2019

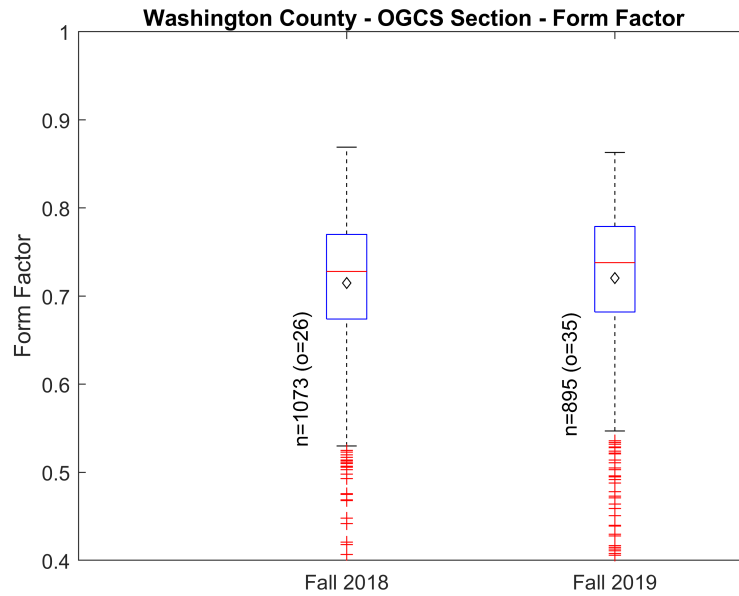


Figure 261. Comparison of form factor for Washington County OGCS samples from fall 2018 and fall 2019

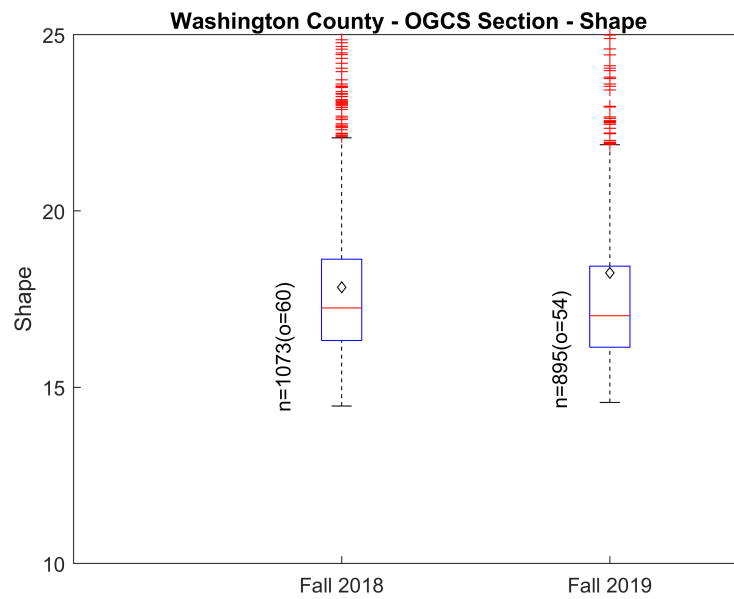


Figure 262. Comparison of shape factor for Washington County OGCS samples from fall 2018 and fall 2019

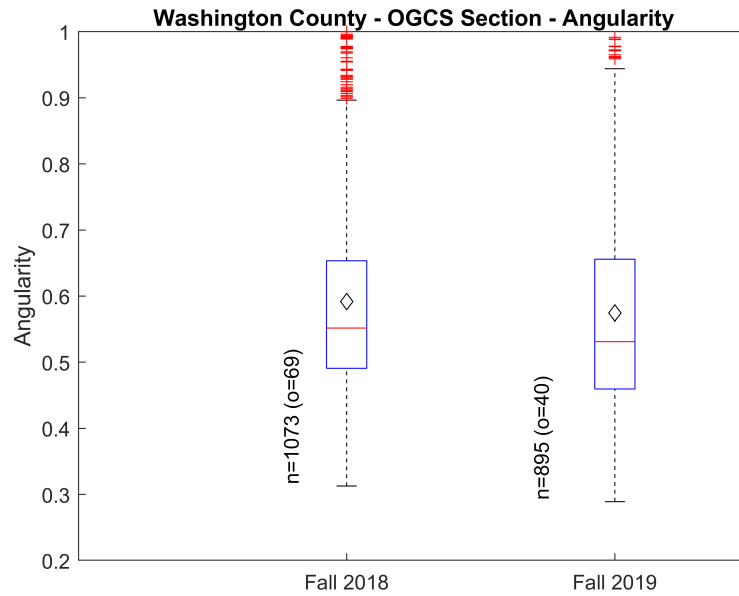


Figure 263. Comparison of angularity for Washington County OGCS samples from fall 2018 and fall 2019

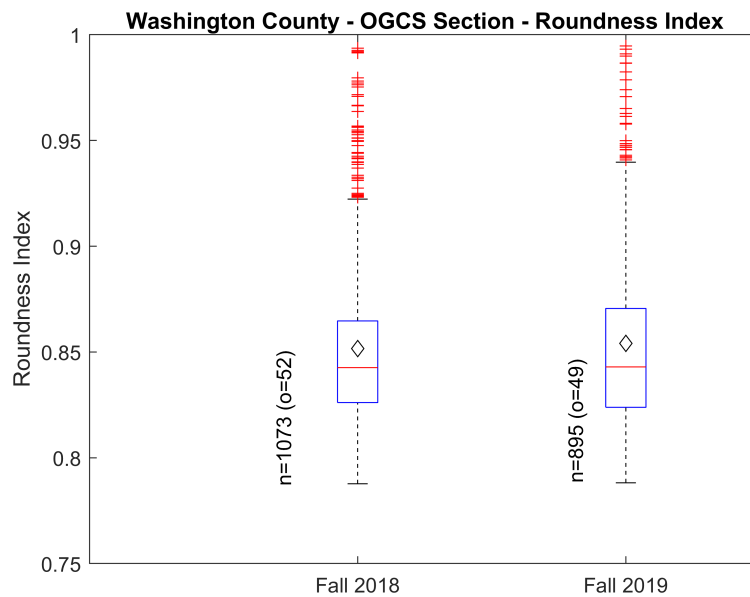
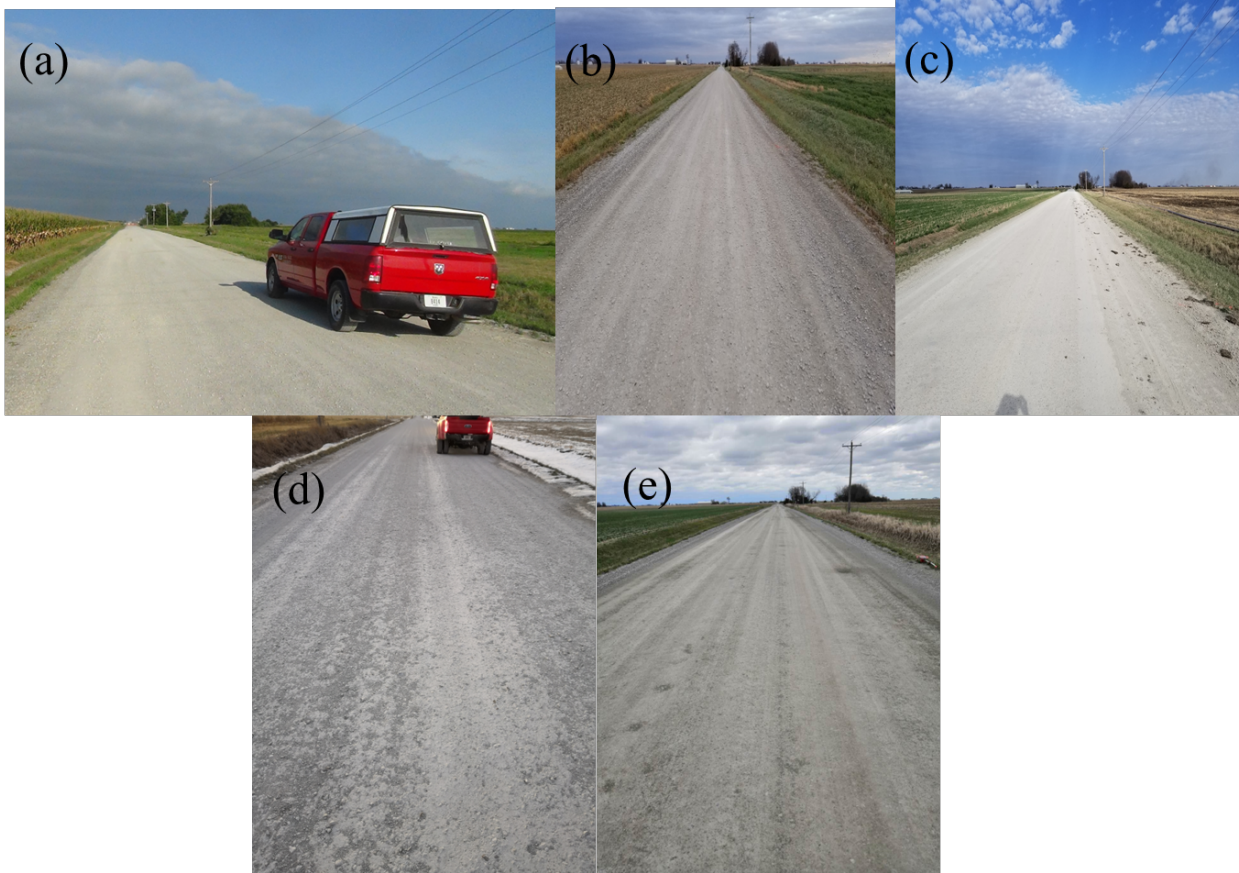


Figure 264. Comparison of roundness index for Washington County OGCS samples from fall 2018 and fall 2019

Table 56. Statistical results of morphological parameters of Washington County OGCS section for fall 2018 and fall 2019 samples

Parameters	Sample Collection Date	Max. Value	Min. Value	Mean	Mode	Median	Std. Dev.	Skew- ness	Kurt- osis	Out- liers
Roundness	Fall 2018	0.882	0.224	0.636	0.567	0.642	0.103	-0.328	2.915	5
	Fall 2019	0.887	0.019	0.658	0.661	0.664	0.094	-0.915	6.949	6
	% increase			3.5%		3.4%				
Sphericity	Fall 2018	0.835	0.145	0.548	0.550	0.550	0.105	-0.187	2.805	4
	Fall 2019	0.816	0.015	0.564	0.532	0.567	0.101	-0.578	4.614	6
	% increase			2.9%		3.1%				
Form Factor (FF)	Fall 2018	0.869	0.290	0.715	0.753	0.728	0.078	-1.126	5.026	26
	Fall 2019	0.863	0.045	0.721	0.789	0.738	0.086	-2.047	12.06	35
	% increase			0.8%		1.4%				
Shape Factor (SF)	Fall 2018	43.41	14.47	17.84	16.27	17.25	2.433	2.984	20.72	60
	Fall 2019	279.1	14.57	18.25	15.24	17.03	12.39	19.87	411.5	54
	% increase			2.3%		-1.3%				
Roundness Index (RI)	Fall 2018	1.269	0.788	0.852	0.828	0.843	0.046	2.551	17.26	52
	Fall 2019	1.137	0.788	0.854	0.807	0.843	0.046	2.126	9.424	49
	% increase			0.2%		0.0%				
Angularity	Fall 2018	1.224	0.313	0.592	0.463	0.552	0.145	1.234	4.305	69
	Fall 2019	1.227	0.289	0.575	0.457	0.531	0.149	1.186	4.224	40
	% increase			-2.9%		-3.8%				



Xue et al. 2022

Figure 265. Visual surveys of Washington County OGCS section over time: (a) fall 2018, (b) spring 2019, (c) fall 2019, (d) spring 2020

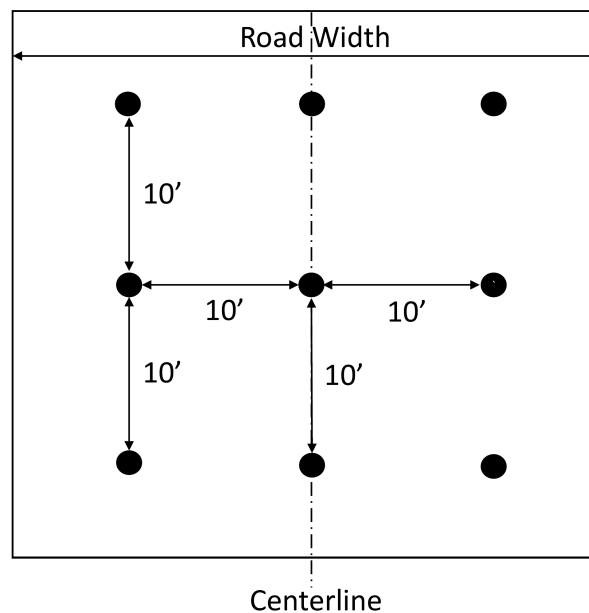
4.3.11 Washington County – Aggregate Columns Section

As part of IHRB Project TR-721, a 500 ft long Aggregate Columns test section was constructed in Washington County, consisting of a pattern of 12 in. diameter by 7 ft deep augered holes backfilled with 1 in. clean aggregate then covered with a surface course of Class A aggregate (Figure 266). Samples of the gravel surface course materials were collected from the test section over a period of two years, specifically during the construction phase in fall 2018 as well as spring 2019, fall 2019, and spring 2020. The PSD curves from sieve analyses performed over the duration of the TR-721 project are shown in Figure 267, showing an upwards migration of the curves indicating a finer gradation with time.

4.3.11.1 Comparison of Breakage Parameters for Washington County Aggregate Columns Section

The mechanical degradation was evaluated for the samples collected over time relative to those collected during construction in fall 2018. Because no surplus samples existed for this section, the PSD curves from the TR-721 final report shown in Figure 267 were digitized and used to

calculate the breakage parameters. The results are presented in Figure 268, Figure 269 and Figure 270 for the samples collected in spring 2019, fall 2019, and spring 2020, respectively. Table 57 lists the corresponding breakage parameters along with the percentages of gravel, sand, and fines for the samples. The latter percentages are also presented in a bar chart in Figure 271, showing a reduction in gravel content over time accompanied by a continual increase in fines, while the sand content initially increases in the first year then decreases over the following two years. Figure 272 presents the cumulative total breakage of the coarse fraction over time in the form of a bar chart, showing an increasing trend in total breakage over time as expected.



Xue et al. 2022

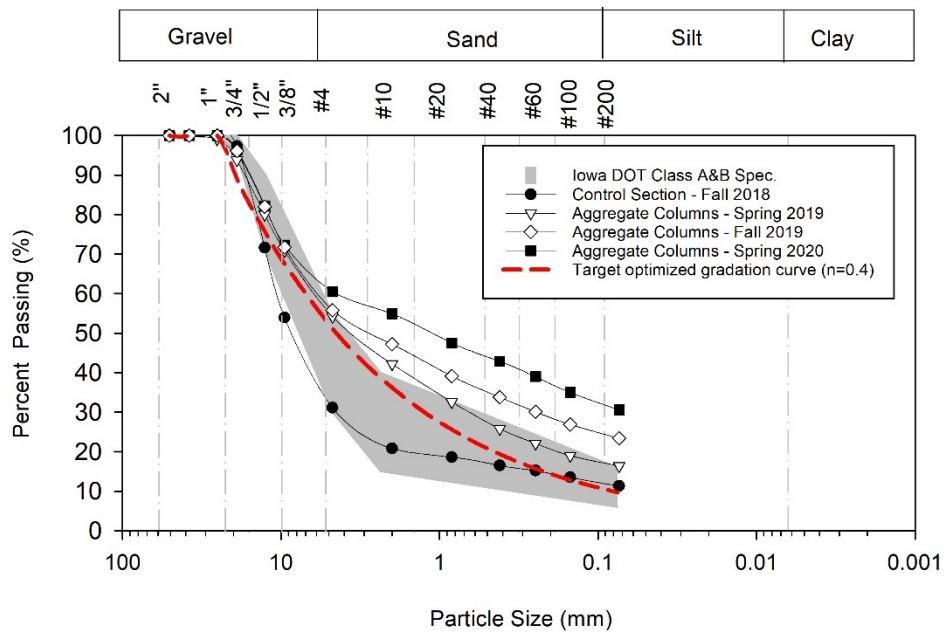
Figure 266. Column layout pattern for Washington County Aggregate Columns section, road width = 31 ft

The data in Table 57 and Figure 271 indicate a significant reduction in the gravel fraction from 68.9% at the time of construction in fall 2018 to 39.5% by the end of the study in spring 2020. In contrast, the combined sand and fines fraction increased over time, from 31.1% in fall 2018 to 60.5% in spring 2020. The increasing trends in Hardin's total breakage and combined sand and fines fractions, along with the decreasing trend in gravel fraction, quantify the rate at which the gravel in the road surface was breaking down due to traffic loading and weather conditions. Additionally, similar to the Washington County Control section, the PSD curves moved upwards with time and ended up well above the Iowa DOT Class A/B specification band, indicating an increase in sand and fines contents with time.

4.3.11.2 Visual Surveys for Washington County Aggregate Columns Section

Visual surveys of the test section surface conditions taken each year are shown in Figure 273. In general, the Aggregate Columns section held up well relative to the control section during the

study, with the exception of spring 2020 where surface distresses in the form of minor potholes were found.



Xue et al. 2022

Figure 267. Particle size distributions of Washington County Aggregate Columns surface materials for samples collected over time

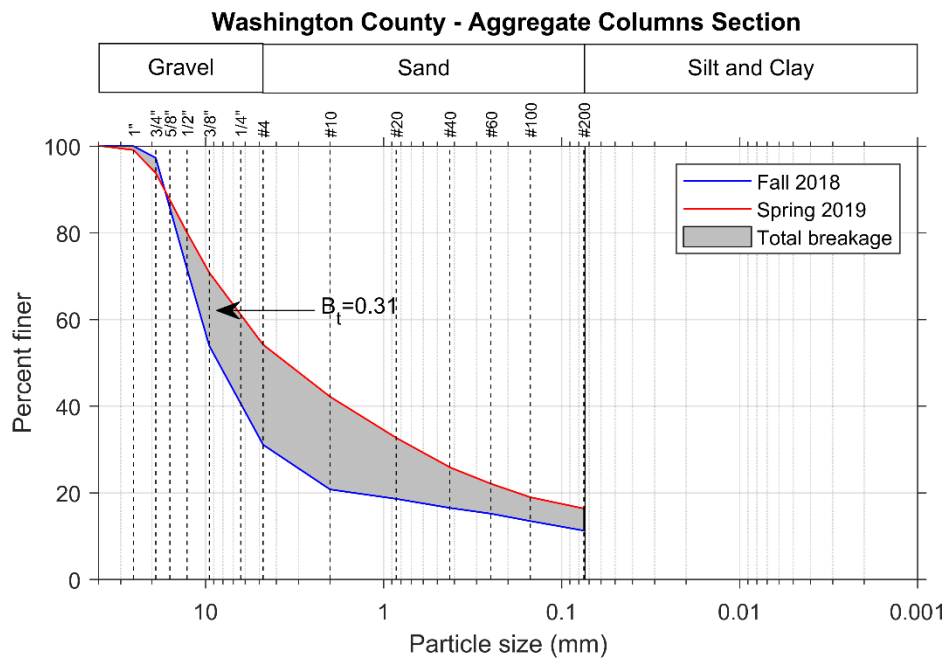


Figure 268. Particle size distributions and evaluation of total breakage of coarse aggregate for Washington County Aggregate Columns section from fall 2018 to spring 2019

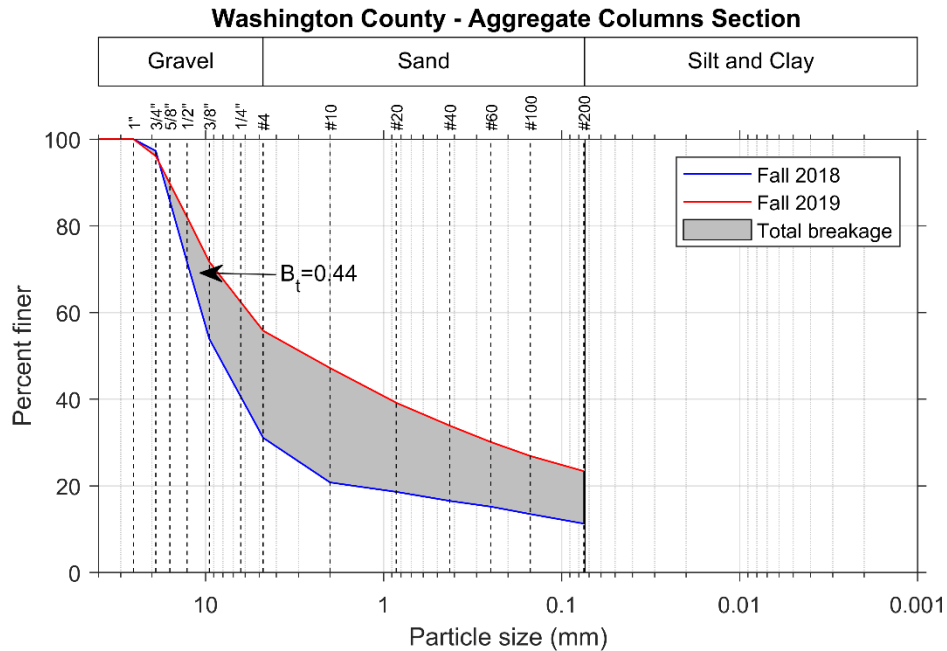


Figure 269. Particle size distributions and evaluation of total breakage of coarse aggregate for Washington County Aggregate Columns section from fall 2018 to fall 2019

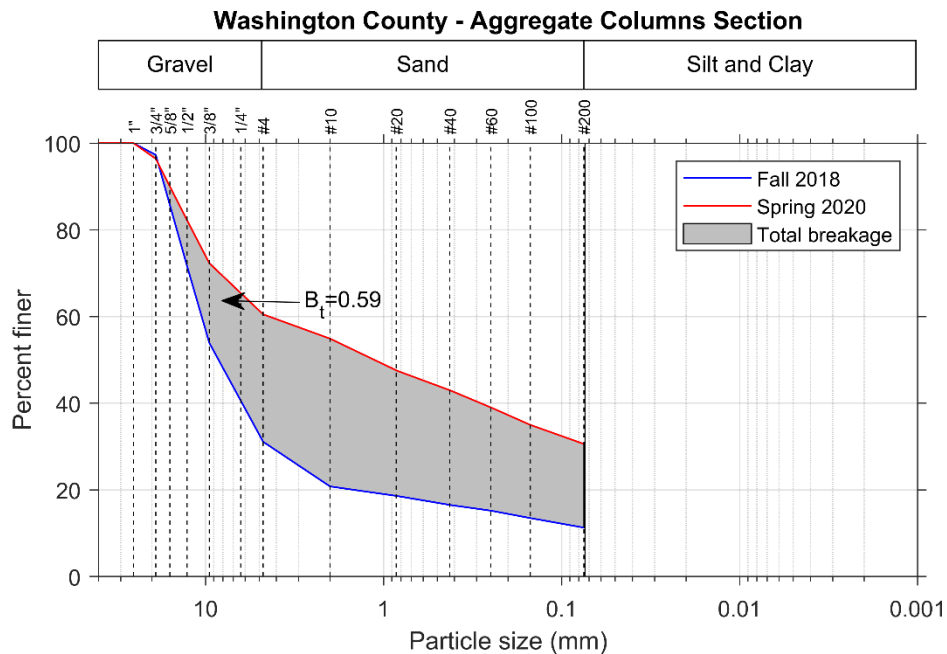


Figure 270. Particle size distributions and evaluation of total breakage of coarse aggregate for Washington County Aggregate Columns section from fall 2018 to spring 2020

Table 57. Breakage parameters from laboratory sieve analyses and percent gravel, sand, and fines for samples of Washington County Aggregate Columns section

Sample Collection Date	Hardin's Breakage Parameters*			% Gravel	% Gravel Red.*	% Sand	% Sand Inc.*	% Fines	% Fines Inc.*
	Total Breakage, B_t	Breakage Potential, B_p	Relative Breakage, B_r						
Fall 2018	-	-	-	68.9	-	19.8	-	11.3	-
Spring 2019	0.3107	1.7267	0.1799	45.8	23.1	37.8	18.0	16.4	5.1
Fall 2019	0.4372	1.7267	0.2532	44.2	24.7	32.4	12.6	23.4	12.1
Spring 2020	0.5889	1.7267	0.3411	39.5	29.4	29.9	10.1	30.6	19.3

*w.r.t. Fall 2018; Red. = Reduction; Inc. = Increase

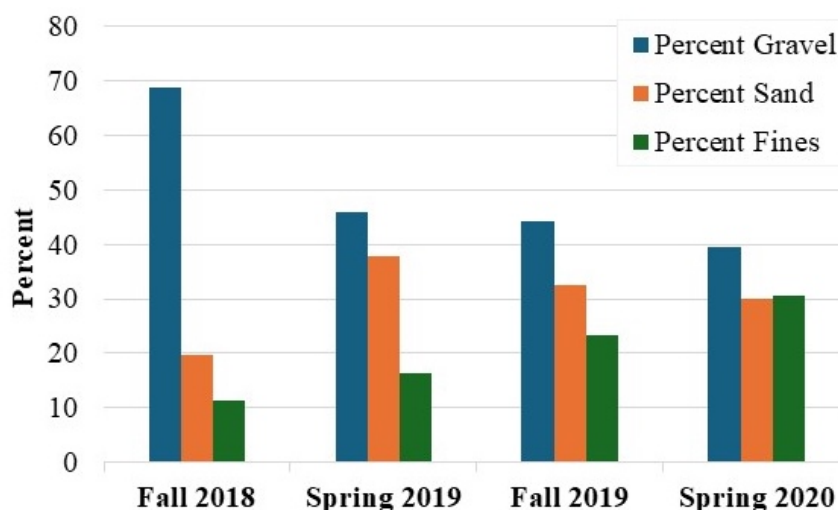


Figure 271. Percent gravel, sand, and fines of surface course of Washington County Aggregate Columns section over time

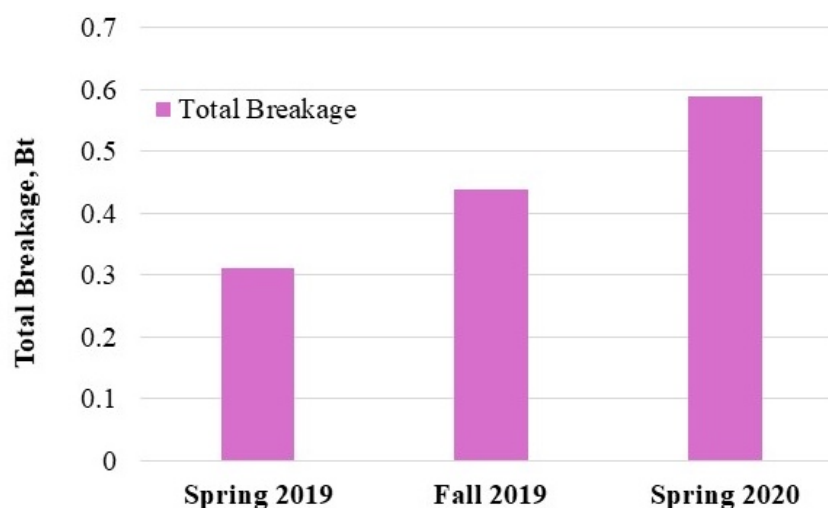
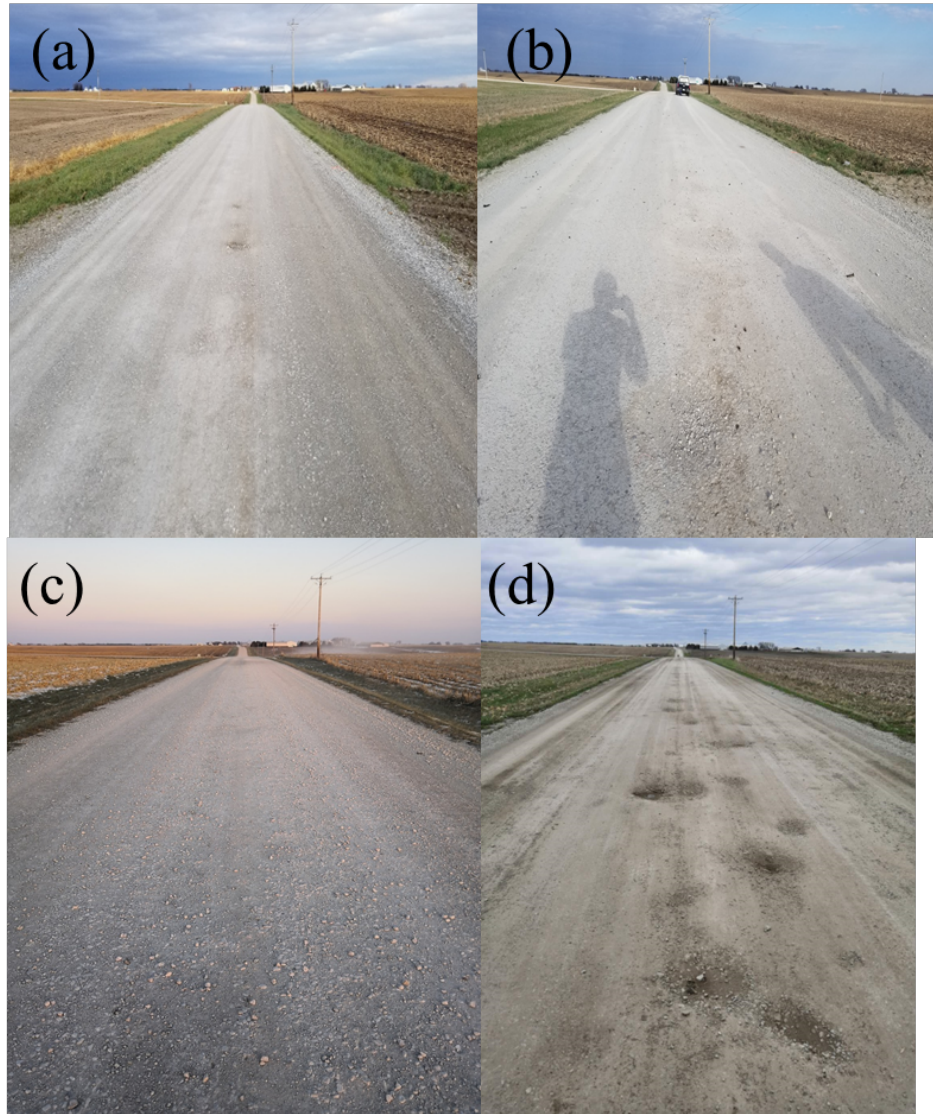


Figure 272. Cumulative total breakage of surface course of Washington County Aggregate Columns section over time



Xue et al. 2022

Figure 273. Visual surveys of Washington County Aggregate Columns section over time: (a) fall 2018, (b) spring 2019, (c) fall 2019, (d) spring 2020

4.3.12 Comparison of Gravel Deterioration for Washington County Test Sections

4.3.12.1 Comparison of Breakage Parameters for Washington County Sections

As detailed in previous sections of this report, Hardin's breakage parameters were evaluated for the Control, OGCS, and Aggregate Columns test sections in Washington County for samples collected in fall 2018 as well as spring 2019, fall 2019, and spring 2020. The cumulative total breakage parameters for these test sections are compared in Figure 274 and the cumulative relative breakage parameters are compared in Figure 275, both evaluated relative to the initial samples collected in fall 2018. The results reveal that the OGCS section experienced the lowest total and relative breakage over time. Furthermore, after the initial increase, the breakage

remained relatively constant over time in the OGCS test section. On the other hand, both total and relative breakage exhibited a progressive increase over time for the Control and Aggregate Columns sections. The Control section consistently had the highest breakage values followed by the Aggregate Columns section which had noticeably less breakage in spring and fall of 2019, but eventually approached that of the Control section by fall 2020.

The new insights beyond those of the previous project are that the OGCS method remained effective in slowing the breakage of aggregates for at least two years (similar to Washington County), whereas the surface course of the Aggregate Columns section showed the lowest increase in total breakage in the last year. However, as previously noted, the Aggregate Columns method aims to improve the supporting subgrade to minimize moisture related surface damage such as rutting and potholes. The method does not include any stabilization of the surface course materials, which are the same as those in the Control section.

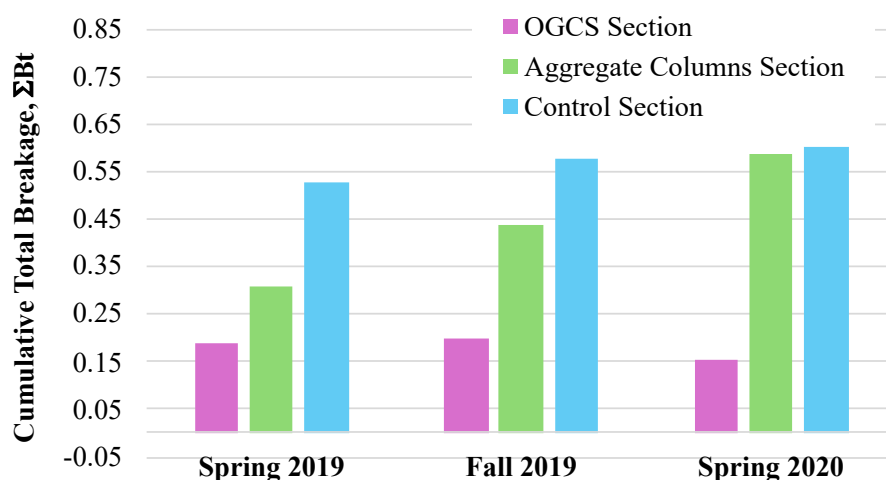


Figure 274. Comparison of Hardin’s total breakage of samples from Washington County OGCS section, Aggregate Columns section, and Control section collected over time

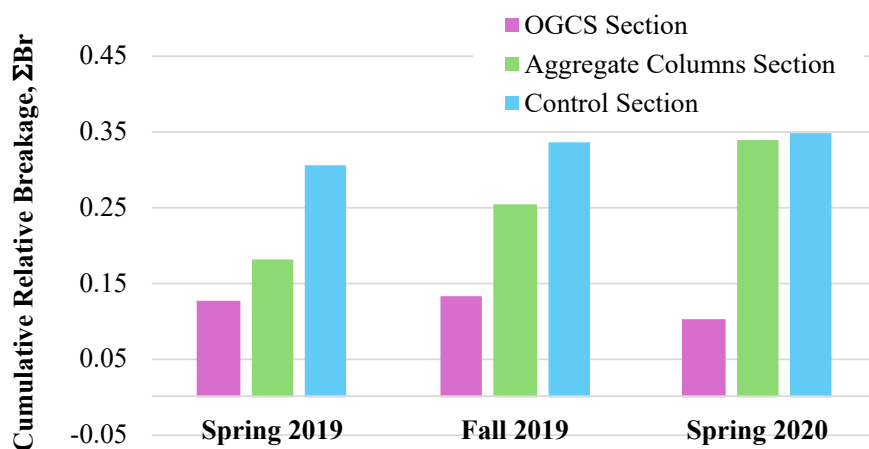


Figure 275. Comparison of Hardin’s relative breakage of samples from Washington County OGCS section, Aggregate Columns section, and Control section collected over time

4.3.12.2 Comparison of Change in Gravel, Sand and Fines Fractions for Washington County Sections

The gravel, sand, and fines fractions evaluated in previous sections of this report for the three Washington County test sections are compared in Figure 276 and Figure 277 for the gravel fraction, Figure 278 and Figure 279 for the sand fraction, and Figure 280 and Figure 281 for the fines fraction. The findings show that the OGCS section fared the best as it experienced the smallest decrease in gravel percentage and smallest increase in sand and fines percentages over time. Conversely, the Control section exhibited the worst performance via the greatest decrease in gravel fraction over time, followed by the Aggregate Columns section. Similarly, the Control section showed the greatest increase in sand fraction over time, followed by the Aggregate Columns section. However, the Aggregate Columns section showed a greater increase in fines fraction over time compared to the Control section.

Considering the rates of breakage, decreases in gravel fraction, and increases in sand and fines fractions altogether, the OGCS section had the smallest total and relative breakage and the smallest decrease in gravel fraction over time, as well as the smallest increase in sand and fines fraction over time. The Control section showed the greatest total and relative breakage over time, followed by the Aggregate Columns section. The Control section also showed the greatest decrease in gravel fraction over time and the greatest increase in sand fraction over time. These findings suggest that OGCS stabilization was most effective in minimizing gravel breakage, with the Aggregate Columns section offering intermediate effectiveness, and the Control section displaying the highest breakage rates.

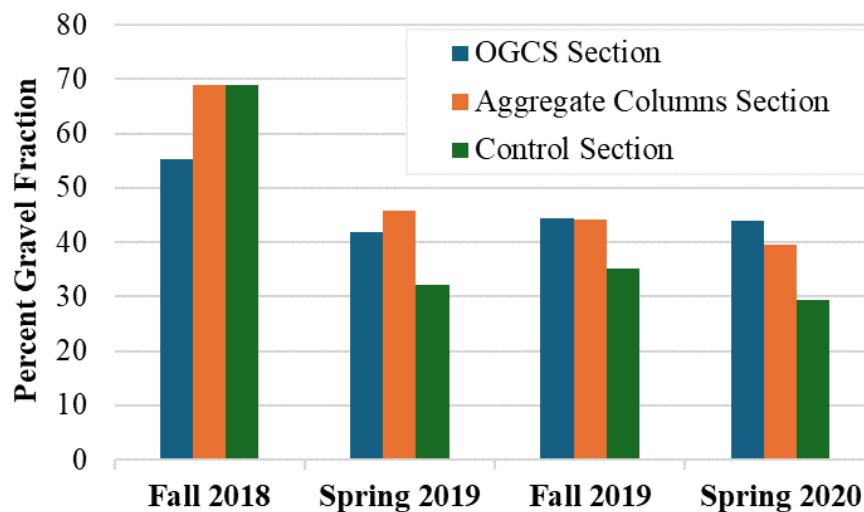


Figure 276. Comparison of gravel fraction for samples from Washington County OGCS section, Aggregate Columns section, and Control section collected over time

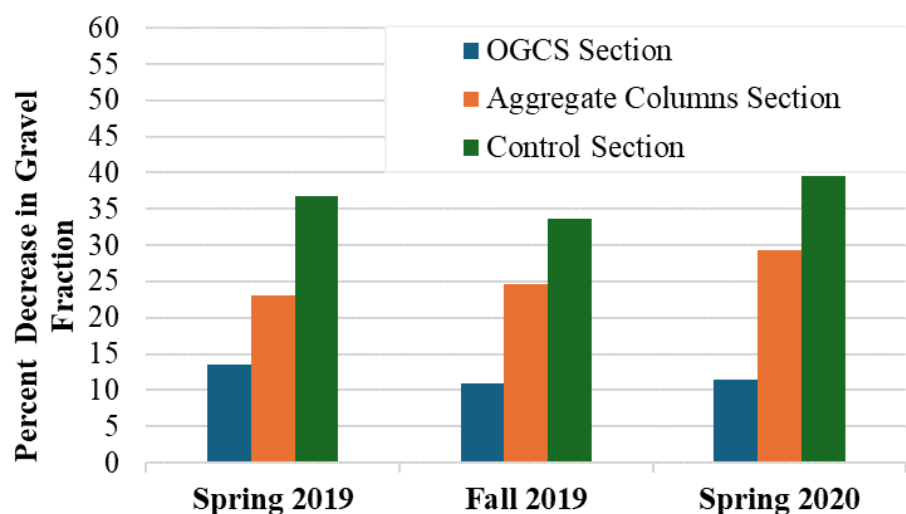


Figure 277. Comparison of percent decrease in gravel fraction relative to 2018 for samples from Washington County OGCS section, Aggregate Columns section, and Control section collected over time

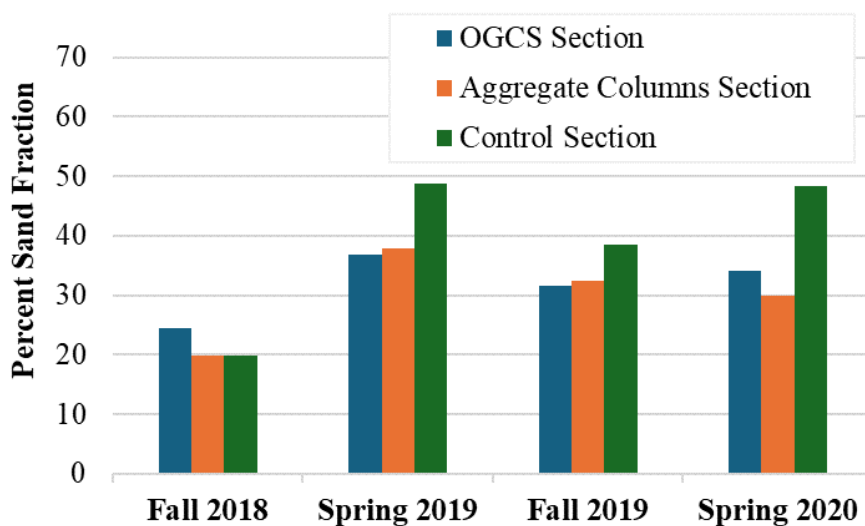


Figure 278. Comparison of sand fraction for samples from Washington County OGCS section, Aggregate Columns section, and Control section collected over time

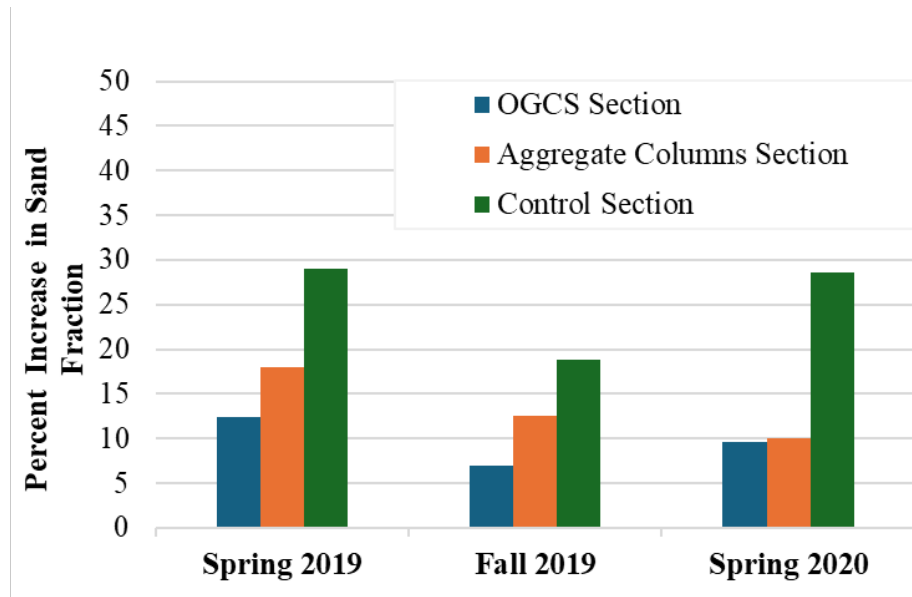


Figure 279. Comparison of percent increase in sand fraction relative to 2018 for samples from Washington County OGCS section, Aggregate Columns section, and Control section collected over time

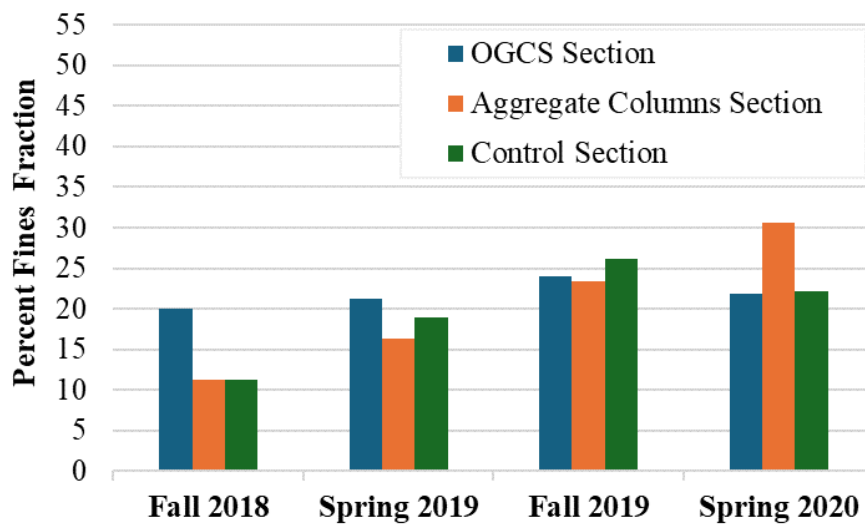


Figure 280. Comparison of fines fraction for samples from Washington County OGCS section, Aggregate Columns section, and Control section collected over time

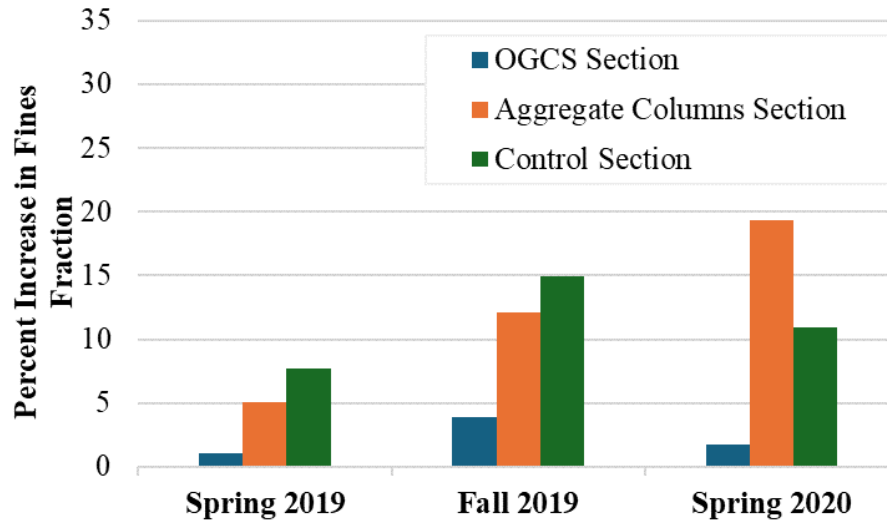
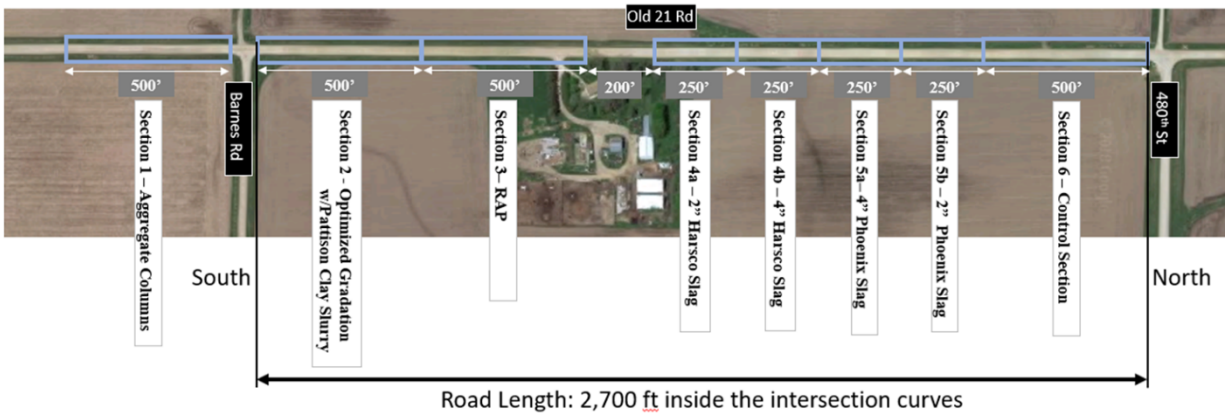


Figure 281. Comparison of percent increase in fines fraction relative to 2018 for samples from Washington County OGCS section, Aggregate Columns section, and Control section collected over time

4.3.13 Cherokee County – Control Section

In IHRB Project TR-721, seven types of mechanically stabilized test sections were constructed along with a control section in Cherokee County on Old 21 Road between 480th Street and 490th Street. A satellite image of the location and a schematic diagram illustrating the layout of the test sections are shown in Figure 282 and Figure 283, respectively. The 500 ft long control section was constructed to evaluate the performance of the test sections against the current construction and maintenance practices for gravel roads in Cherokee County. To construct the Control section, fresh aggregates were spread over the existing road surfacing material to an initial thickness of 4 in. in fall 2018.

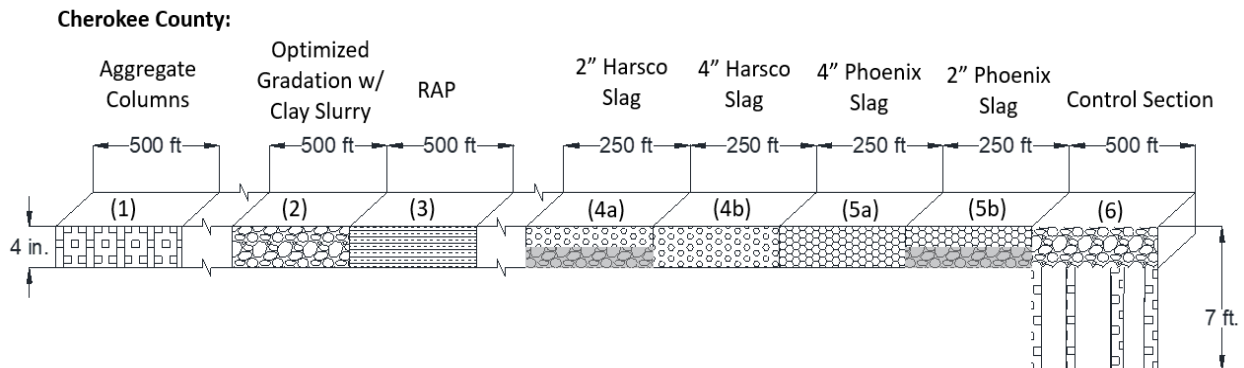
Cherokee County: Old 21 Rd between 480th St. and 490th St.



Note: measure the sections from end of curved intersection borders, where the road width becomes constant:



Figure 282. Satellite image of Cherokee County mechanically stabilized test sections



Xue et al. 2022

Figure 283. Layout of mechanically stabilized test sections in Cherokee County

4.3.13.1 Comparison of Breakage Parameters for Cherokee County Control Section

Samples of the surface aggregates were collected from the Cherokee County Control section over a period of two years, specifically during the construction phase in fall 2018 and during spring 2019, fall 2019, and spring 2020. According to the Cherokee Secondary Roads personnel, no new aggregates were spread on the Control section during these intervals except for spring 2020. Therefore, breakage is expected to be positive between the representative samples from any pair of these dates except for spring 2020. The PSD curves measured in IHRB Project TR-721 for this section are shown in Figure 284.

By digitizing the PSD curves shown in Figure 284, the mechanical degradation represented by Hardin's breakage parameters was evaluated for the Control section samples relative to those collected during construction in fall 2018. This degradation is presented in Figure 285, Figure 286, and Figure 287 for the samples collected in spring 2019, fall 2019, and fall 2020, respectively. Table 58 summarizes the breakage parameters along with the percentages of gravel, sand, and fines for the samples collected over time. The cumulative total breakage between samples from fall 2018 and those from spring 2019, fall 2019, and spring 2020 is presented in a bar chart in Figure 288, showing an increase in total breakage over time prior to 2020 as expected. Spreading of new aggregates in spring 2020 resulted in a coarser gradation and therefore a smaller calculated apparent breakage value compared to fall 2019. However, the breakage value for fall 2019 is already a cumulative value because no new aggregate had been spread to that point. Therefore, the fall 2019 total (and cumulative) breakage value of 0.2896 in Table 58 was added to the spring 2020 breakage value of 0.1790 to calculate the cumulative breakage of 0.4686 up to that time, as plotted in Figure 288.

The percentages of gravel, sand, and fines for the samples collected over time are also presented as a bar chart in Figure 289. The data in Table 58 and Figure 289 indicate a significant reduction in the gravel fraction, decreasing from 52.8% at the time of construction in fall 2018 to 38.2% by fall 2019. In contrast, the sand fraction increased from 34.6% to 40.9% over the same time period, while the fines fraction increased from 12.6% to 20.9%. A slight increase in gravel fraction is noted between spring 2019 and fall 2019 despite no new material being placed. This might be caused by sampling error arising from nonuniform distribution of aggregate materials in the test section, or could also happen if the maintainer raked coarser gravel from the shoulders back into the roadway in between sampling dates.

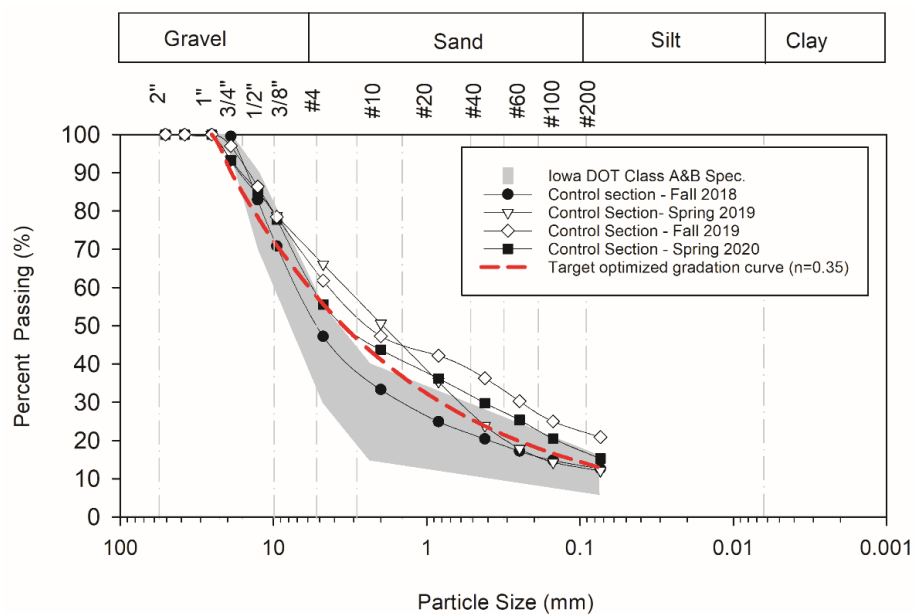
For the fall 2018 through fall 2019 timeframe before new aggregate was spread, the overall increasing trend in total breakage, increasing sand and fines percentages, and decreasing trend in gravel percentage suggest that the gravel in the road surface was breaking down significantly due to traffic loading and weather conditions, with the gravel breaking down into sand and fines size fractions, and the sand also breaking down into fines. The PSD curves in Figure 284 moved upwards through spring 2019 and fall 2019, ending up well above the Iowa DOT Class A/B specification band as a result of the decrease in gravel and increases in sands and fines with time.

4.3.13.2 2D Image Analyses and Comparison of Morphological Parameters for Cherokee County Control Section

The 2D image analyses were also performed for surplus samples collected in spring 2019 and fall 2019 for the Cherokee County Control section. The morphological parameters evaluated are presented in statistical boxplots in Figure 290 through Figure 294, and the statistical output of these morphological parameters is presented in Table 59. The results show a slight decrease of 0.3% in median roundness, but the expected trends of increases in median sphericity and form factor by 4.1% and 6.6%. Consistent with these trends, the median values of shape factor, roundness index, and angularity all decreased by 1.3%, 0.6%, and 6.2%, quantifying the degradation and evolving geometry of the surface aggregates over time.

4.3.13.3 Visual Surveys for Cherokee County Control Section

Photos from visual surveys of the Cherokee County Control section taken over time are shown in Figure 296. The visual surveys confirmed that the gravel fraction of the surfacing materials decreased over time from fall 2018 to fall 2019 while the sand and fines fractions increased. The section also exhibited significant rutting and frost boils in spring 2019.



Xue et al. 2022

Figure 284. Particle size distribution curves of Cherokee County Control Section for samples collected over time

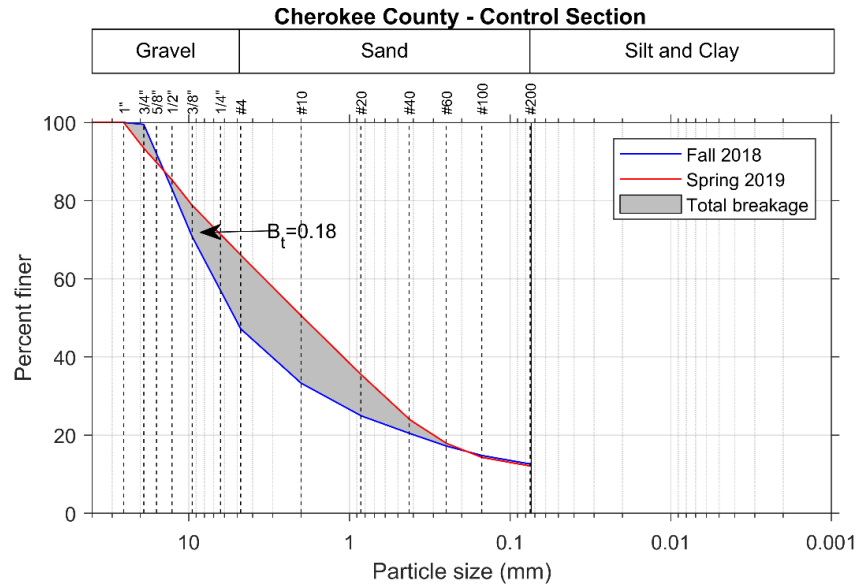


Figure 285. Particle size distributions and evaluation of total breakage of coarse fraction for Cherokee County Control section between fall 2018 and spring 2019

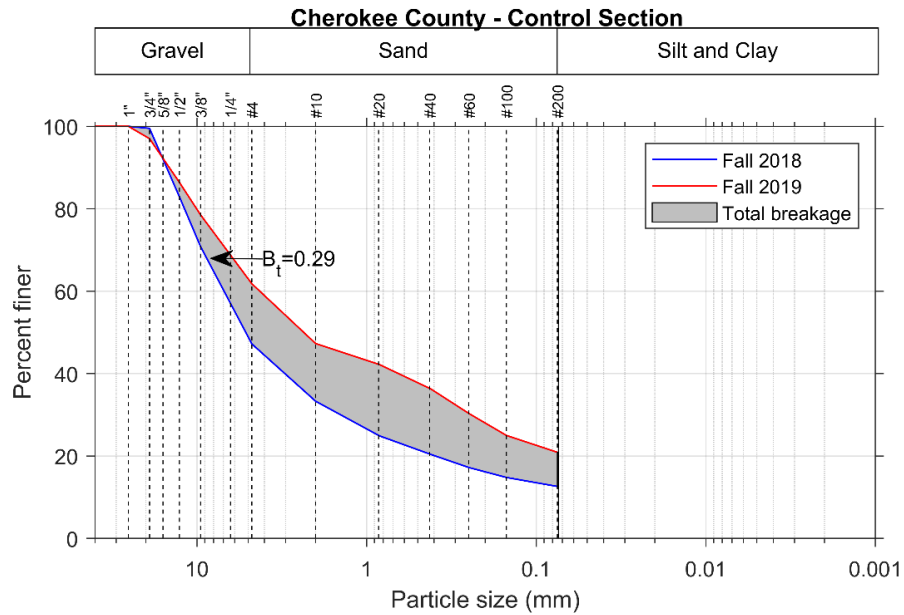


Figure 286. Particle size distributions and evaluation of total breakage of coarse fraction for Cherokee County Control section between fall 2018 and fall 2019

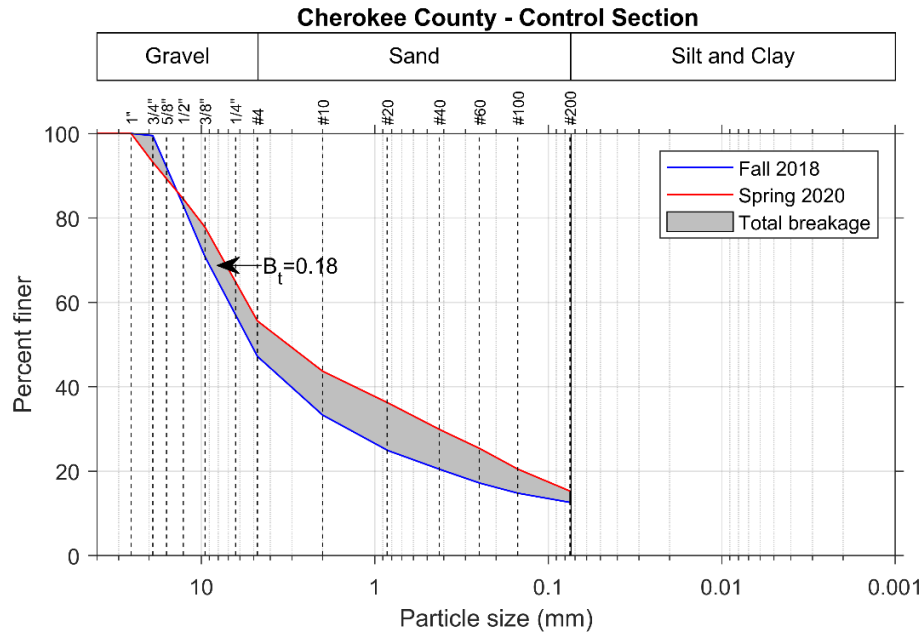


Figure 287. Particle size distributions and evaluation of apparent total breakage of coarse fraction for Cherokee County Control section between fall 2018 and after new aggregate was spread in spring 2020

Table 58. Breakage parameters from laboratory sieve analyses and percent gravel, sand, and fines for samples of Cherokee County Control section

Sample Collection Date	Hardin's Breakage Parameters*			% Gravel	% Gravel Red.*	% Sand	% Sand Inc.*	% Fines	% Fines Inc.*
	Total Breakage, B_t	Breakage Potential, B_p	Relative Breakage, B_r						
Fall 2018	-	-	-	52.8	-	34.6	-	12.6	-
Spring 2019	0.1850	1.5271	0.1211	33.9	18.9	54.0	19.4	12.1	-0.5
Fall 2019	0.2896	1.5271	0.1896	38.2	14.6	40.9	6.3	20.9	8.3
Spring 2020 [†]	0.1790	1.5271	0.1152	44.4	8.4	40.3	5.7	15.3	2.7

*w.r.t. Fall 2018; Red. = Reduction; Inc. = Increase; [†]After new aggregate spread

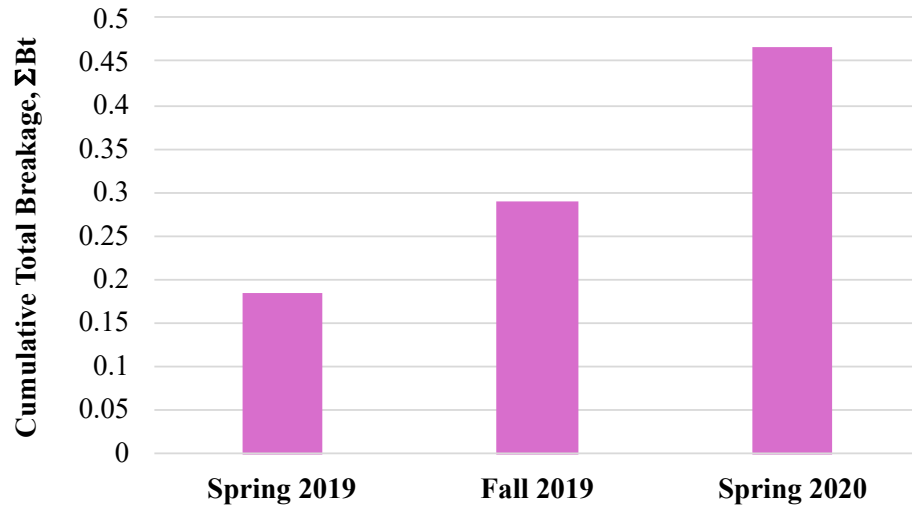


Figure 288. Cumulative total breakage of samples from Cherokee County Control section collected over time

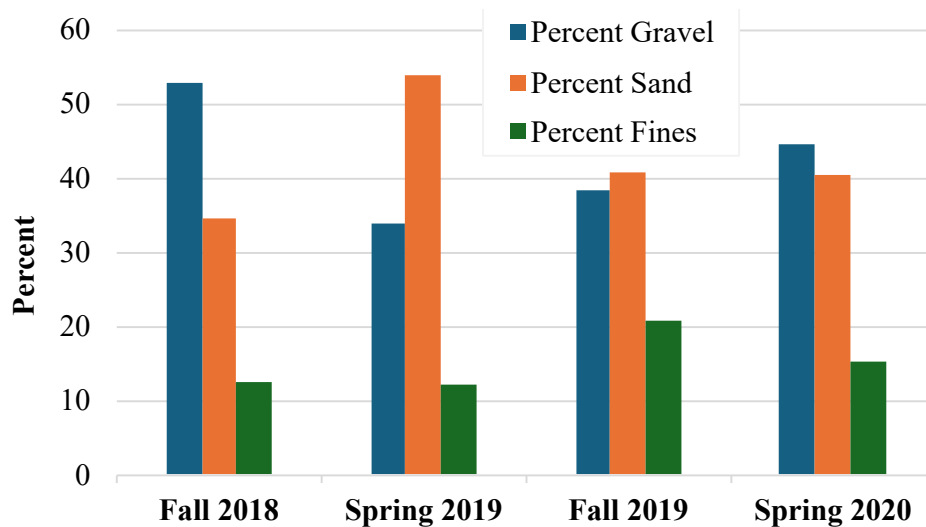


Figure 289. Gravel, sand and fines fractions of samples from Cherokee County Control section collected over time

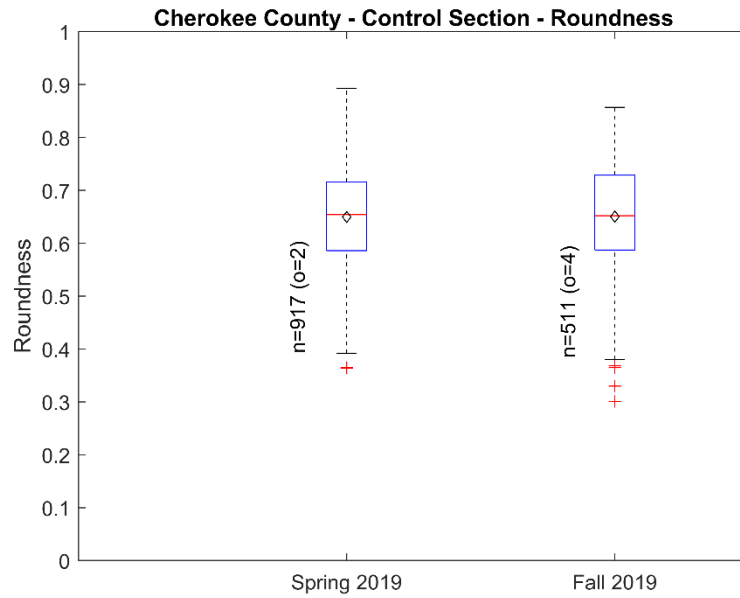


Figure 290. Comparison of roundness for Cherokee County Control section samples from spring 2019 and fall 2019

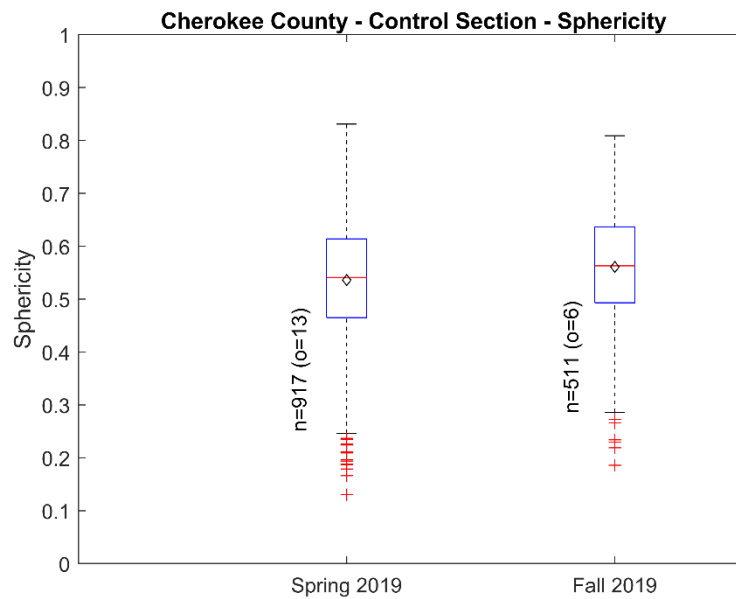


Figure 291. Comparison of sphericity for Cherokee County Control section samples from spring 2019 and fall 2019

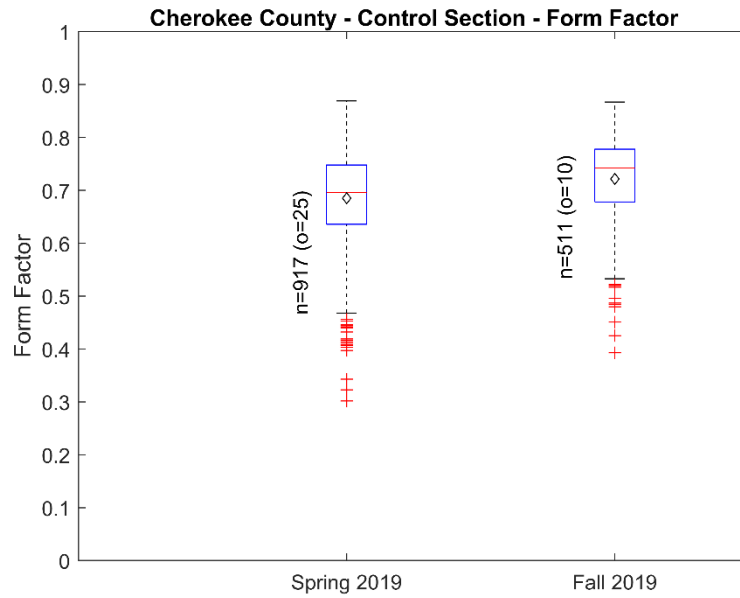


Figure 292. Comparison of form factor for Cherokee County Control section samples from spring 2019 and fall 2019

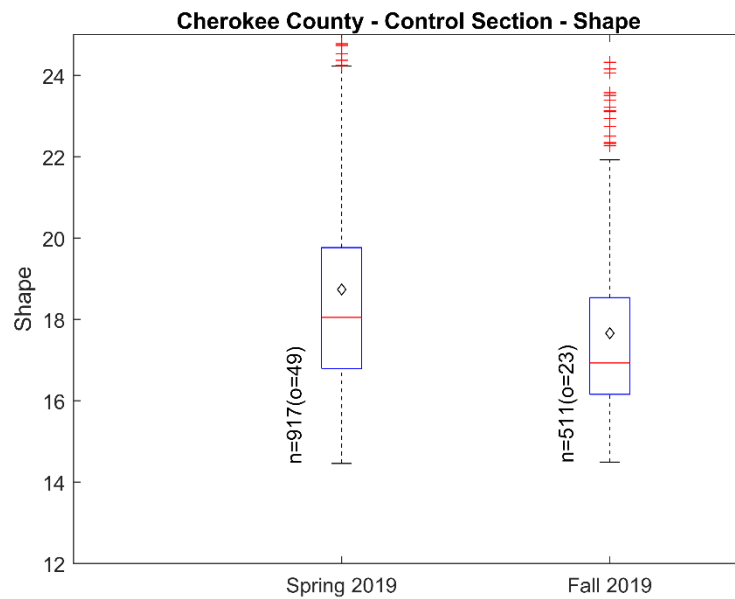


Figure 293. Comparison of shape factor for Cherokee County Control section samples from spring 2019 and fall 2019

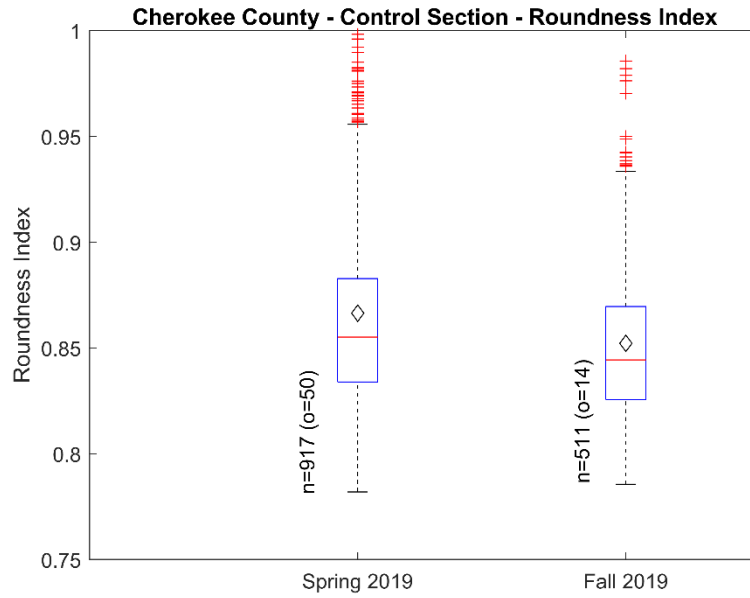


Figure 294. Comparison of roundness index for Cherokee County Control section samples from spring 2019 and fall 2019

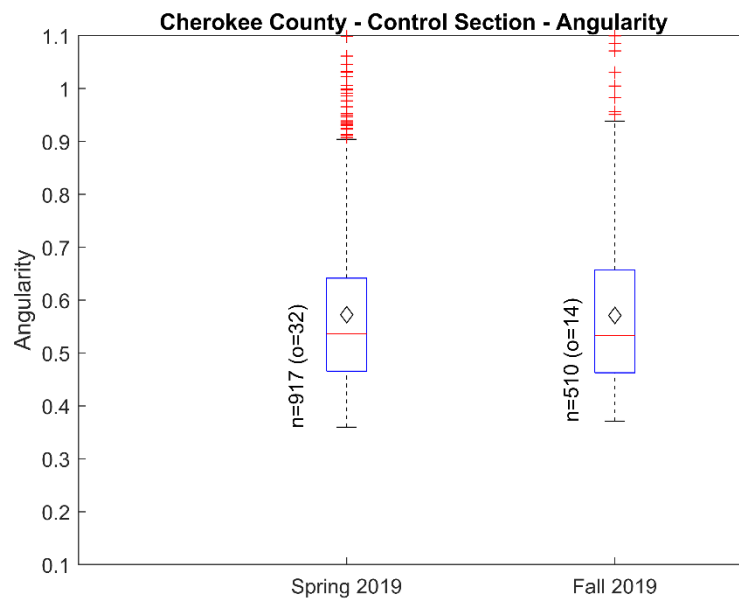


Figure 295. Comparison of angularity for Cherokee County Control section samples from spring 2019 and fall 2019

Table 59. Statistical results of morphological parameters of Cherokee County Control section for spring 2019 and fall 2019 samples

Parameter	Sample Collection Date	Max.	Min.	Mean	Mode	Median	Std. Dev.	Skew- ness	Kurt- osis	Out- liers
Roundness	Spring 2019	0.893	0.364	0.65	0.618	0.654	0.096	-0.243	2.768	2
	Fall 2019	0.857	0.301	0.651	0.585	0.652	0.101	-0.46	2.982	4
	% increase			0.1%		-0.3%				
Sphericity	Spring 2019	0.831	0.13	0.536	0.524	0.541	0.114	-0.404	3.275	13
	Fall 2019	0.809	0.186	0.561	0.555	0.563	0.107	-0.429	3.102	6
	% increase			4.7%		4.1%				
Form Factor (FF)	Spring 2019	0.869	0.302	0.685	0.651	0.696	0.091	-0.898	4.054	25
	Fall 2019	0.867	0.393	0.721	0.783	0.742	0.079	-0.963	3.828	10
	% increase			5.3%		6.6%				
Shape Factor (SF)	Spring 2019	41.6	14.46	18.74	16.71	18.05	3.087	2.313	11.569	49
	Fall 2019	32	14.49	17.66	15.14	16.93	2.262	1.911	8.722	23
	% increase			-1.7%		-1.3%				
Roundness Index (RI)	Spring 2019	1.253	0.782	0.867	0.825	0.855	0.049	2.078	10.55	50
	Fall 2019	1.055	0.786	0.852	0.842	0.844	0.039	1.515	6.813	14
	% increase			-0.3%		-0.6%				
Angularity	Spring 2019	1.172	0.36	0.573	0.386	0.536	0.144	1.201	4.237	32
	Fall 2019	1.345	0.371	0.571	0.48	0.533	0.145	1.328	5.459	14
	% increase			-5.8%		-6.2%				



Xue et al. 2022

Figure 296. Visual surveys of Cherokee County Control section over time: (a) fall 2018, (b) spring 2019, (c) fall 2019, (d) spring 2020

4.3.14 Cherokee County Optimized Gradation with Clay Slurry Section

4.3.14.1 Comparison of Breakage Parameters for Cherokee County OGCS Section

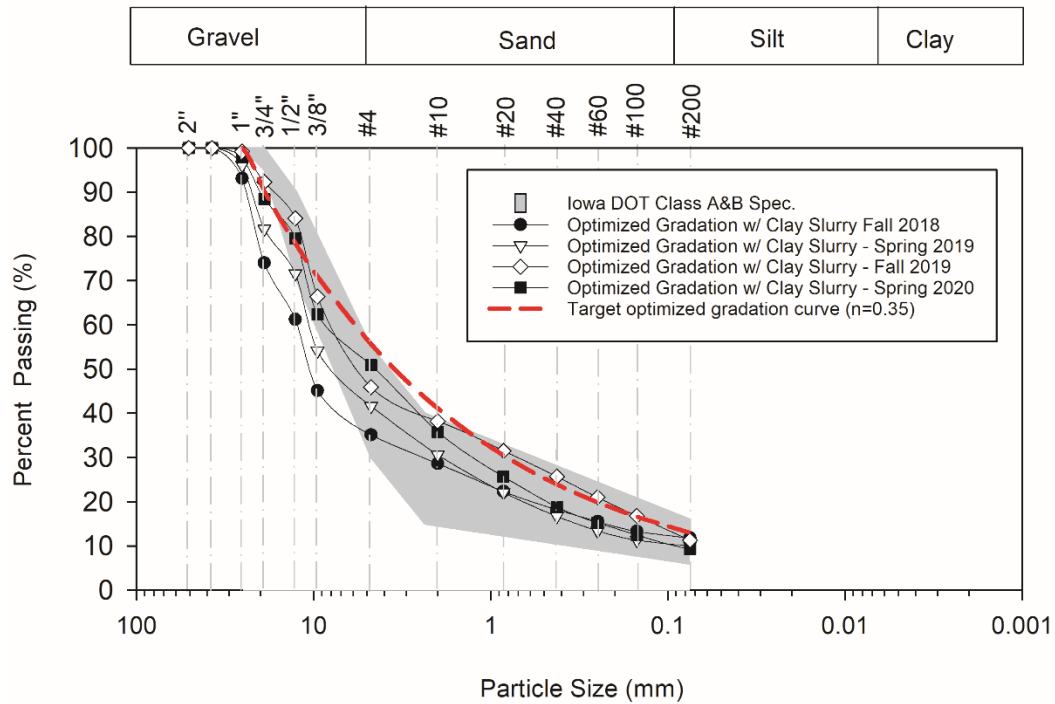
The 500 ft long OGCS test section was constructed in Cherokee County in September 2018. Details of the OGCS stabilization method are presented in Section 4.3.2 of this report. Samples of surface materials were collected from the Cherokee County OGCS section over two years of IHRB Project TR-721 during different phases: first in fall 2018 during construction, then again in spring 2019, fall 2019, and spring 2020. According to the Cherokee County Engineer's office, no maintenance aggregates were spread on the section during the project. The PSD curves from

the TR-721 report for this test section are shown in Figure 297. The curves show a general upward migration over time as the material gradually broke down to a finer gradation, ending with a fines content of 9.3%. As of spring 2020, the PSD curve was still within the Iowa DOT Class A/B specification band. In contrast, the PSD of the nearby Control section was already far above the specification band by spring 2019 and spring 2020, ending with a fines content of approximately 15.3% (Figure 284).

The PSD curves in Figure 297 were digitized to determine the mechanical degradation relative to fall 2018 as quantified by Hardin's total breakage. The results are shown in Figure 298, Figure 299, and Figure 300 for the samples collected in spring 2019, fall 2019, and spring 2020, respectively. The corresponding breakage parameters and percentages of gravel, sand, and fines over time are detailed in Table 60. The percentages are also presented in a bar chart in Figure 301, while the cumulative total breakage is shown graphically in Figure 302. The gravel fraction shown in Table 60 and Figure 301 exhibited an overall decreasing trend with time, starting at 64.9% in fall 2018 and ending up at 49.1% by spring 2020. In contrast, the sand fraction increased over time, starting at 23.3% and ending at 41.6%. The fines content exhibited small decreases throughout the project duration, but stayed relatively constant at around 10%, indicating that the cohesive strength of the clay slurry provided good binding over the entire project duration and did not wash or blow away significantly. The cumulative total breakage in Figure 302 exhibited an increasing trend for spring 2019 and fall 2019 as expected, but then decreased by spring 2020 counter to expectation. This could be attributable to sampling error, but it is also possible that similar to the nearby Control section, new aggregate was spread on this section but not reported after the change in leadership in Cherokee County during the project.

4.3.14.2 Visual Surveys for Cherokee County OGCS Section

Visual surveys of the Cherokee County OGCS section over the duration of the TR-721 project are shown in Figure 303. The photos confirm that the increase in cohesion offered by the clay fines in the slurry resulted in improved binding of the aggregates, reducing their loss and slowing their degradation relative to the control section. Some slight rutting and potholes were observed in spring 2019 for this section.



Xue et al. 2022

Figure 297. Particle size distribution curves of Cherokee County OGCS Section for samples collected over time

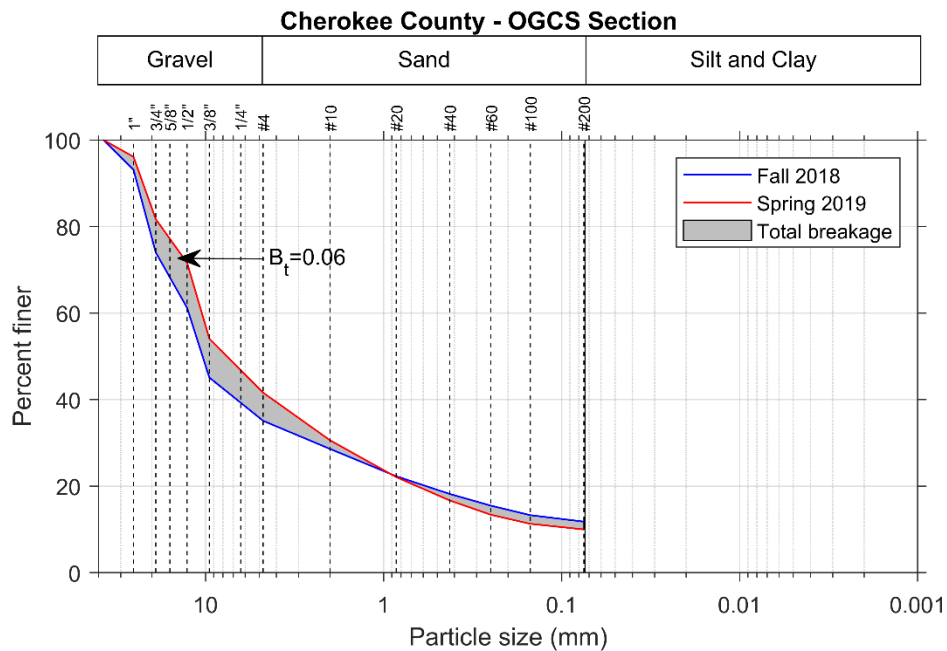


Figure 298. Particle size distributions and evaluation of total breakage of coarse fraction for Cherokee County OGCS section between fall 2018 and spring 2019

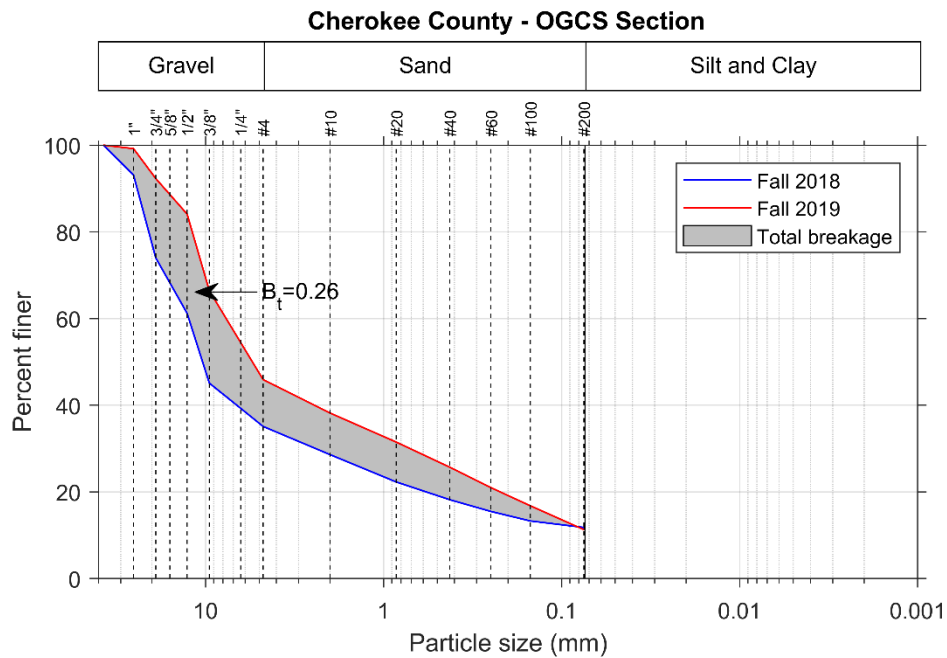


Figure 299. Particle size distributions and evaluation of total breakage of coarse fraction for Cherokee County OGCS section between fall 2018 and fall 2019

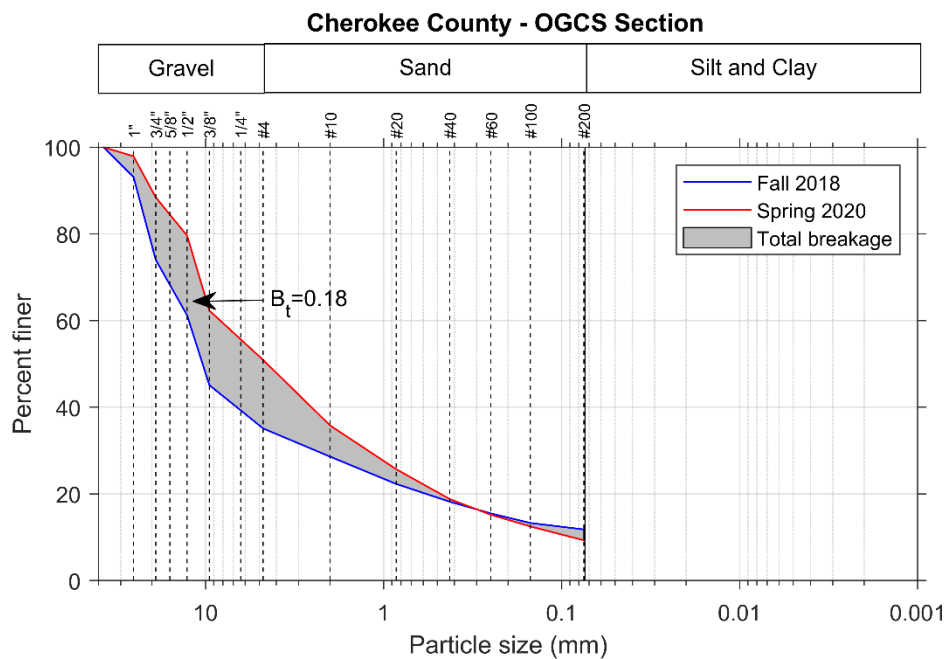


Figure 300. Particle size distributions and evaluation of total breakage of coarse fraction for Cherokee County OGCS section between fall 2018 and spring 2020

Table 60. Breakage parameters of coarse fraction by laboratory sieve analyses and percent gravel, sand, and fines for samples of Cherokee County OGCS section

Sample Collection Date	Hardin's Breakage Parameters*			% Gravel	% Gravel Red.*	% Sand	% Sand Inc.*	% Fines	% Fines Inc.*
	Total Breakage, B _t	Breakage Potential, B _p	Relative Breakage, B _r						
Fall 2018	-	-	-	64.9	-	23.3	-	11.8	-
Spring 2019	0.0629	1.7460	0.0360	58.4	6.5	31.6	8.3	10.0	-1.8
Fall 2019	0.2606	1.7460	0.1493	54.1	10.8	34.6	11.3	11.3	-0.5
Spring 2020	0.1800	1.7460	0.1031	49.1	15.8	41.6	18.3	9.3	-2.5

*w.r.t. Fall 2018; Red. = Reduction; Inc. = Increase

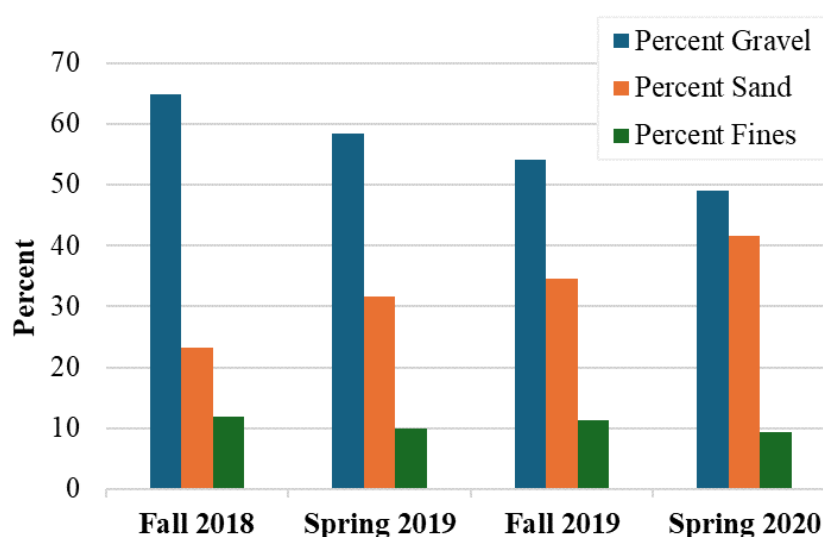


Figure 301. Gravel, sand and fines fractions of samples from Cherokee County OGCS section collected over time

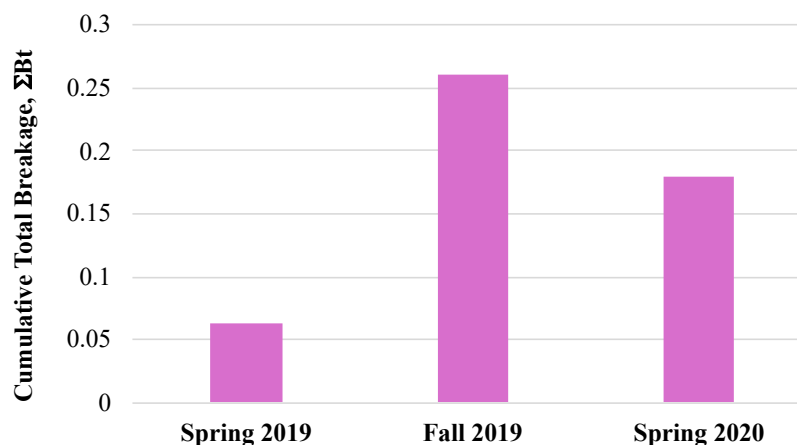
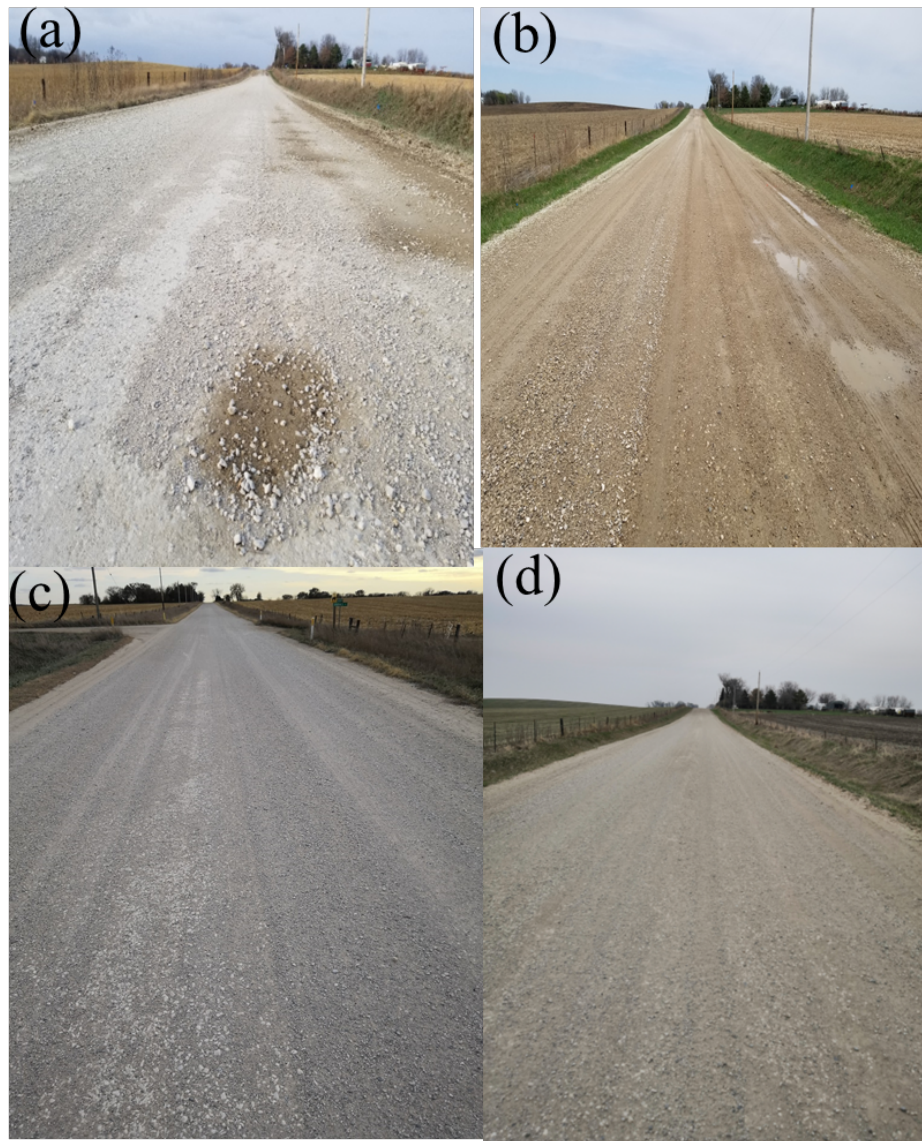


Figure 302. Total breakage of coarse fraction for Cherokee County OGCS section samples collected over time



Xue et al. 2022

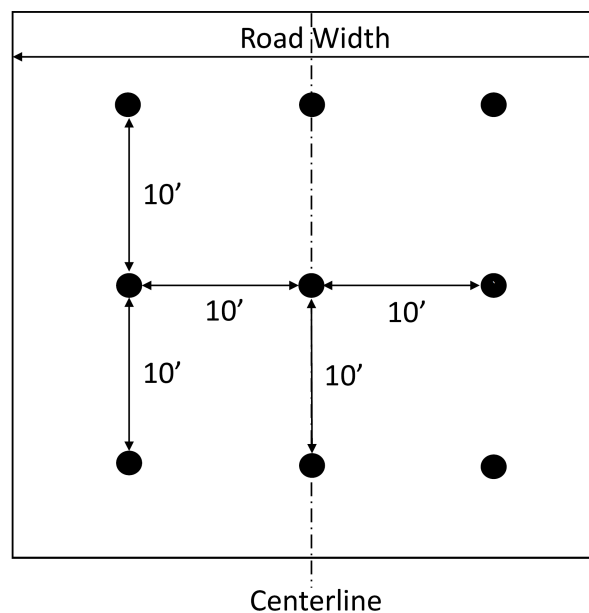
Figure 303. Visual surveys of Cherokee County OGCS section over time: (a) fall 2018, (b) spring 2019, (c) fall 2019, (d) spring 2020

4.3.15 Cherokee County Aggregate Columns Section

4.3.15.1 Comparison of Breakage Parameters for Cherokee County Aggregate Columns Section

A 500 ft long Aggregate Columns test section was constructed in Cherokee County in September 2018 as part of IHRB Project TR-721. The columns consisted of 12 in. diameter by 7 ft deep augered holes drilled in a 10 ft grid as shown in Figure 304 and backfilled with 1 in. clean aggregate. Samples of the surface aggregates were collected from the test section over a period of two years, specifically during the construction phase in fall 2018 and during spring 2019, fall

2019, and spring 2020. Particle size distribution analyses were performed on these collected materials by sieve and hydrometer tests in IHRB Project TR-721 to determine the gradation change over time (Figure 305). The PSD curves were digitized in the present study to analyze the mechanical degradation and material loss over time.



Xue et al. 2022

Figure 304. Column layout pattern for Cherokee County Aggregate Columns section, road width = 26 ft

The mechanical degradation represented by Hardin's breakage parameters was evaluated for the collected samples relative to those collected during construction in fall 2018. This degradation is presented in Figure 306, Figure 307, and Figure 308 for the samples collected in spring 2019, fall 2019, and fall 2020, respectively. The corresponding breakage parameters and percentages of gravel, sand, and fines over time are detailed in Table 61. The percentages are also presented in a bar chart in Figure 309, while total breakage is shown graphically in Figure 310. As shown in Figure 310, the cumulative total breakage increased as expected between fall 2019 and spring 2020, however it first decreased significantly between spring 2019 and fall 2019. This decrease could potentially be a result of statistical variation, field samples not being taken in consistent locations in the wheel path, raking of coarse gravel back in from the shoulders, or unreported maintenance aggregates.

According to Table 61 and Figure 309, the gravel fraction exhibited an overall decreasing trend with time as expected, starting at 52.8% and ending up at 44.7% by spring 2020. Accordingly, the sand fraction increased from 34.6% to 39.9%, while the fines fraction increased from 12.6% to 15.4%.

4.3.15.2 2D Image Analyses and Comparison of Morphological Parameters for Cherokee County Aggregate Columns Section

The 2D image analyses were also performed for surplus samples that could be located for fall 2018 and fall 2019. The resulting particle size distributions of the gravel fraction are shown in Figure 311, and the morphological parameters are presented in Figure 312 through Figure 316. The statistical output of these morphological parameters is presented in Table 63, indicating particle degradation through increases in median roundness, sphericity, and form factor of 1.9%, 1.4%, and 0.4%, respectively, along with decreases of 0.4% for shape factor and 4.0% for angularity.

4.3.15.3 Visual Surveys for Cherokee County Aggregate Columns Section

Visual surveys of the Cherokee County aggregate columns section over the duration of the TR-721 project are shown in Figure 318. Overall, the photos agree with the observations from sieve and image analyses in that a modest change in gravel content was accompanied by a relatively small increase in fines content.

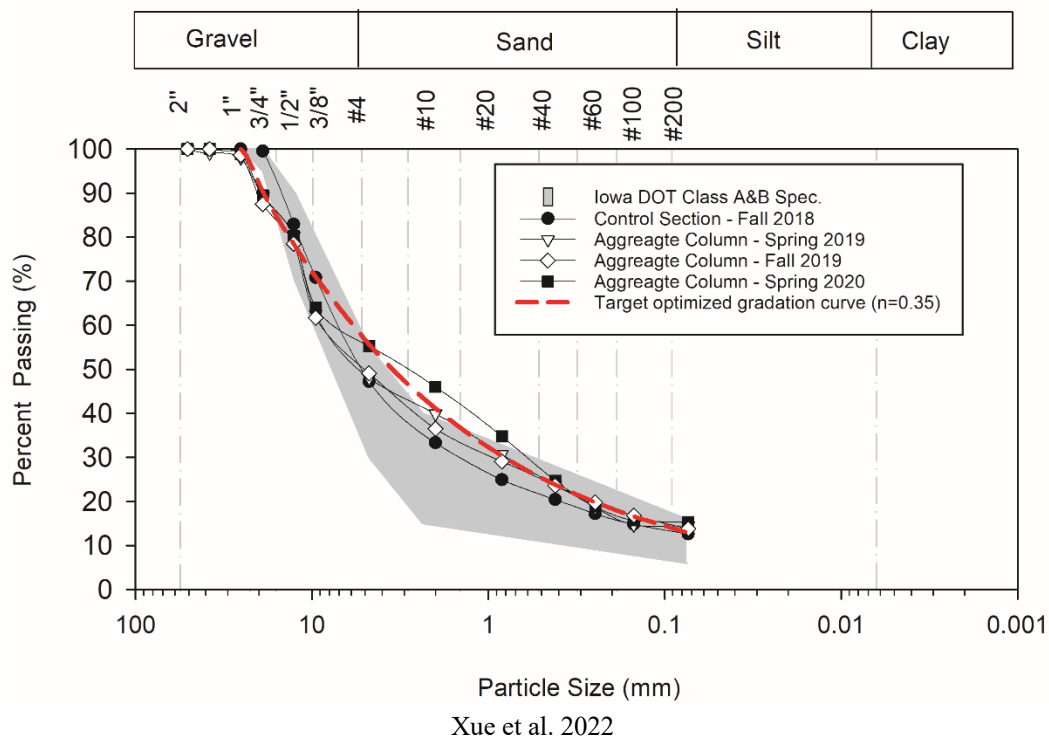


Figure 305. Particle size distributions of Cherokee County Aggregate Columns surface materials for samples collected over time

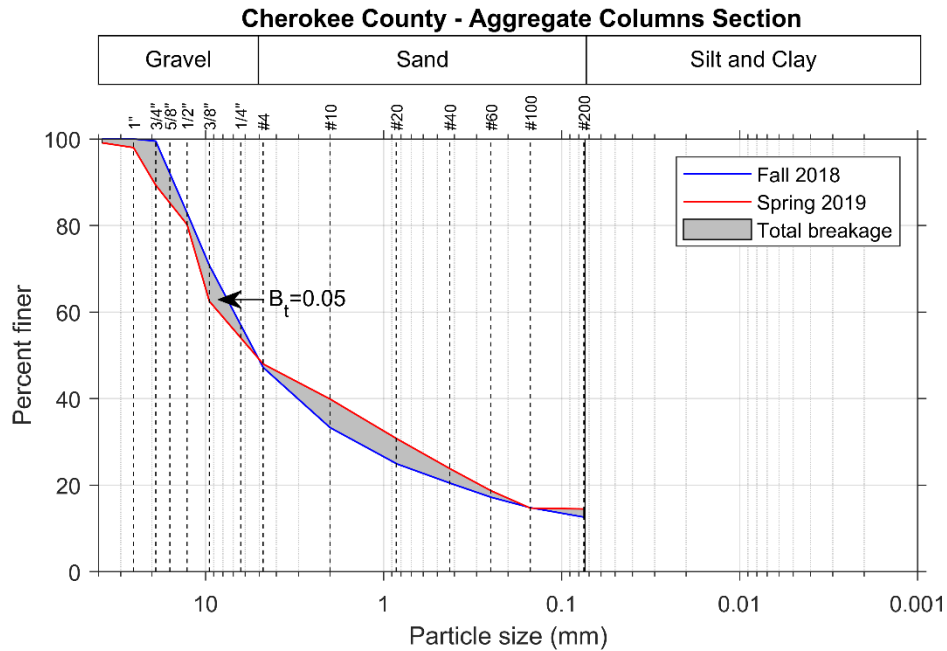


Figure 306. Particle size distributions and evaluation of total breakage of coarse aggregate for Cherokee County Aggregate Columns section from fall 2018 to spring 2019

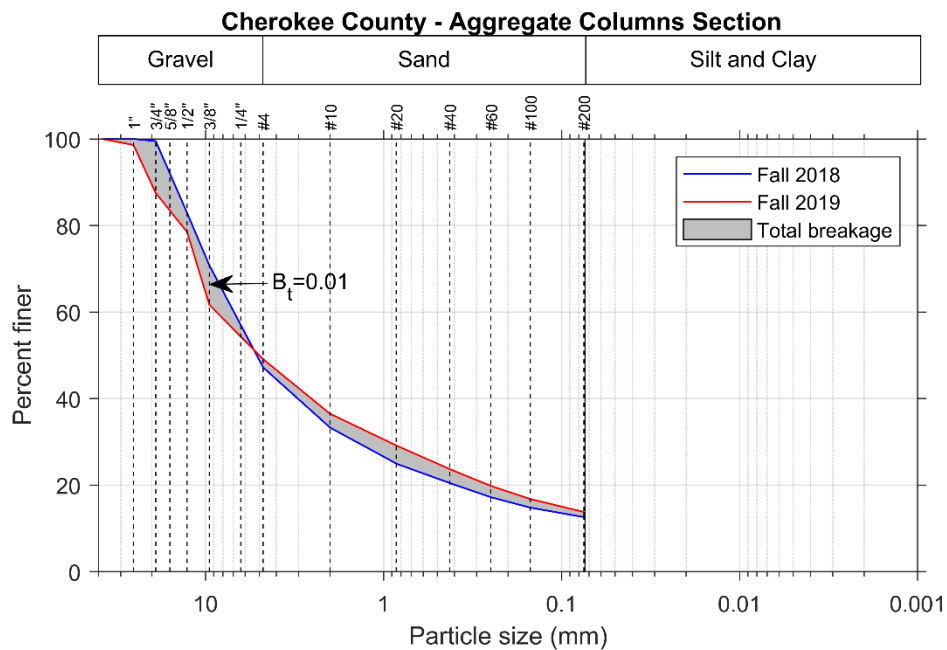


Figure 307. Particle size distributions and evaluation of total breakage of coarse aggregate for Cherokee County Aggregate Columns section from fall 2018 to fall 2019

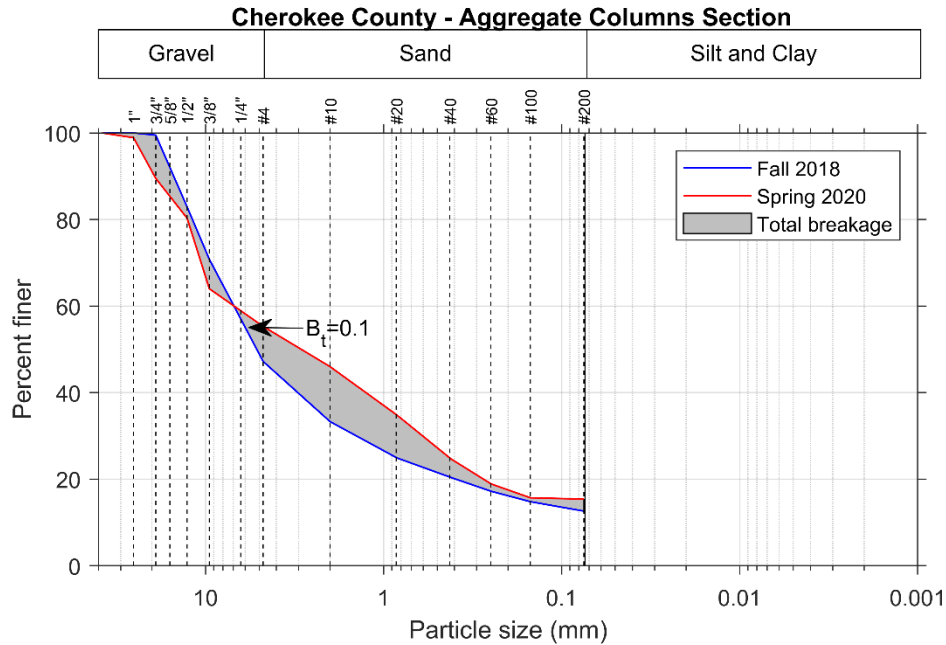


Figure 308. Particle size distributions and evaluation of total breakage of coarse aggregate for Cherokee County Aggregate Columns section from fall 2018 to spring 2020

Table 61. Breakage parameters from laboratory sieve analyses and percent gravel, sand, and fines for samples of Cherokee County Aggregate Columns section

Sample Collection Date	Hardin's Breakage Parameters*			% Gravel	% Gravel Red.*	% Sand	% Sand Inc.*	% Fines	% Fines Inc.*
	Total Breakage, B_t	Breakage Potential, B_p	Relative Breakage, B_r						
Fall 2018	-	-	-	52.8	-	34.6	-	12.6	-
Spring 2019	0.0454	1.5271	0.0297	52.0	0.8	33.5	-1.1	14.5	1.9
Fall 2019	0.0078	1.5271	0.0051	50.9	1.9	35.3	0.7	13.8	1.2
Spring 2020	0.0955	1.5271	0.0625	44.7	8.1	39.9	5.3	15.4	2.8

*w.r.t. Fall 2018; Red. = Reduction; Inc. = Increase

Table 62. Breakage parameters for gravel fraction from 2D image analyses for samples of Cherokee County Aggregate Columns section

Sample Collection Date	Hardin's Breakage Parameters*		
	Total Breakage, B_t	Breakage Potential, B_p	Relative Breakage, B_r
Fall 2018	-	-	-
Fall 2019	0.0285	0.3586	0.0795

*w.r.t. Fall 2018

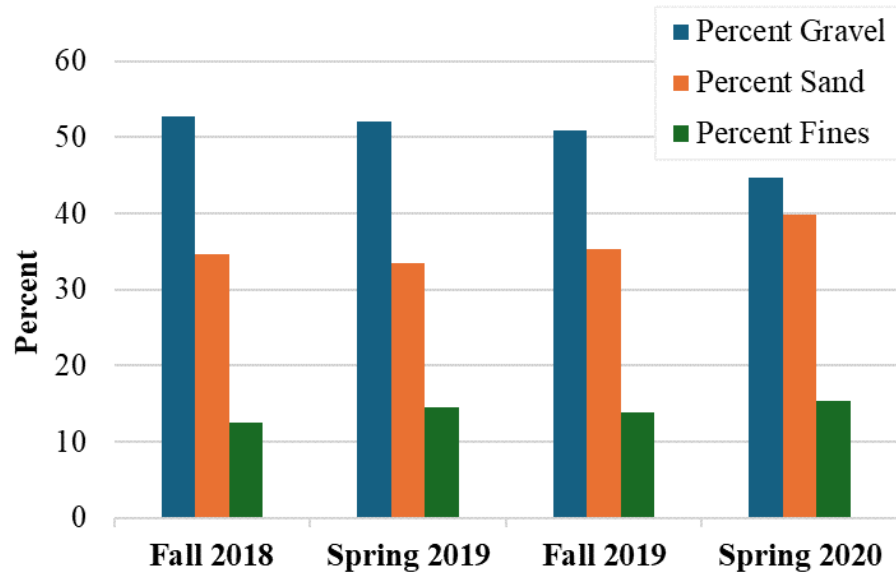


Figure 309. Gravel, sand and fines fractions of surface course of Cherokee County Aggregate Columns section over time

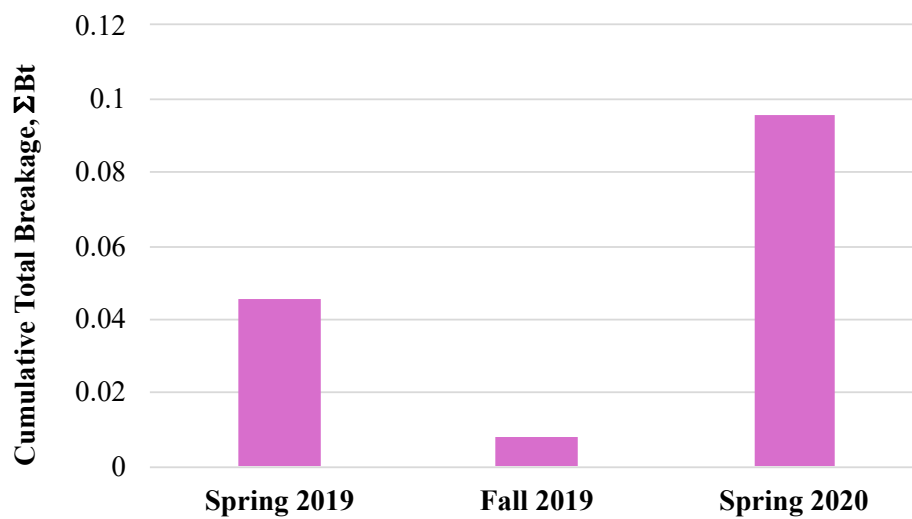


Figure 310. Cumulative total breakage of surface course of Cherokee County Aggregate Columns section over time

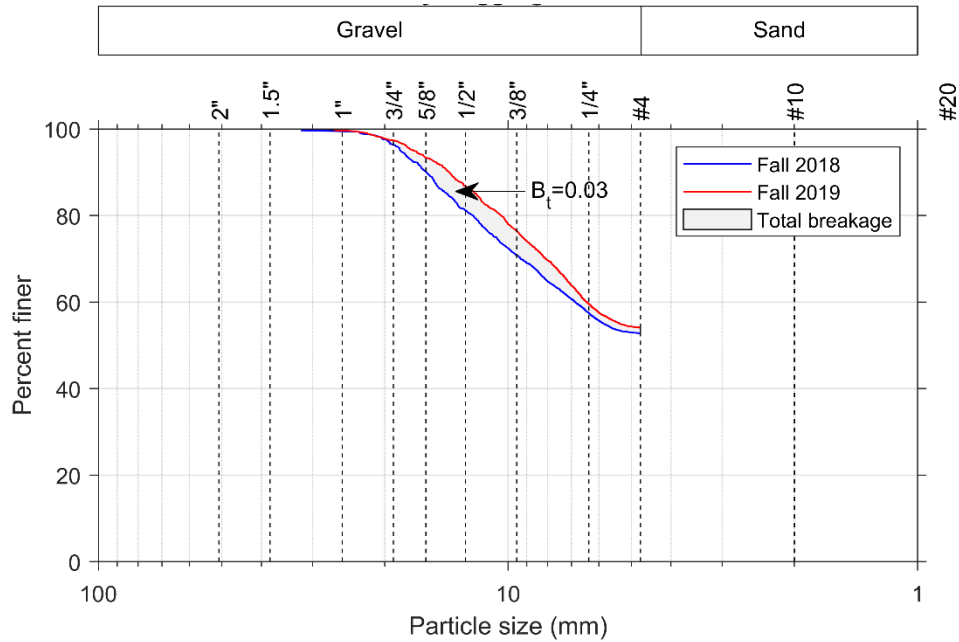


Figure 311. Particle size distributions from 2D image analysis and evaluation of total breakage of gravel fraction for Cherokee County Aggregate Columns section between fall 2018 and fall 2019

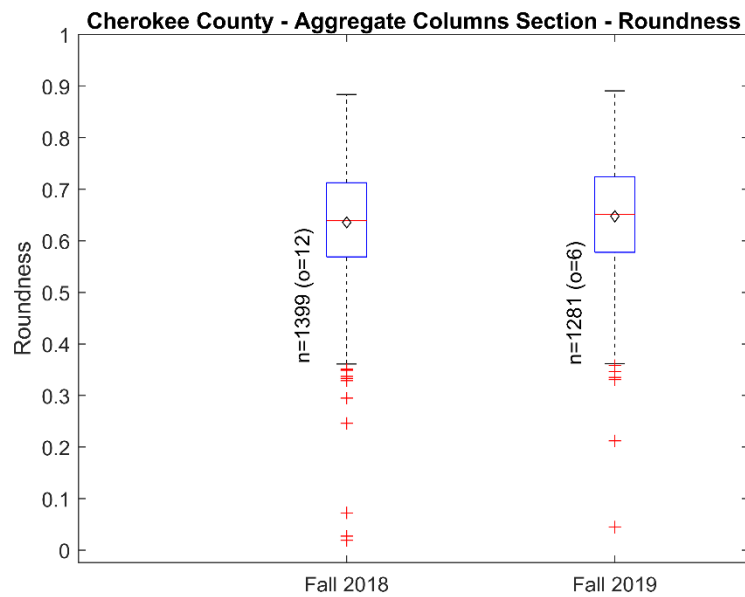


Figure 312. Comparison of roundness for Cherokee County Aggregate Columns section samples from fall 2018 and fall 2019

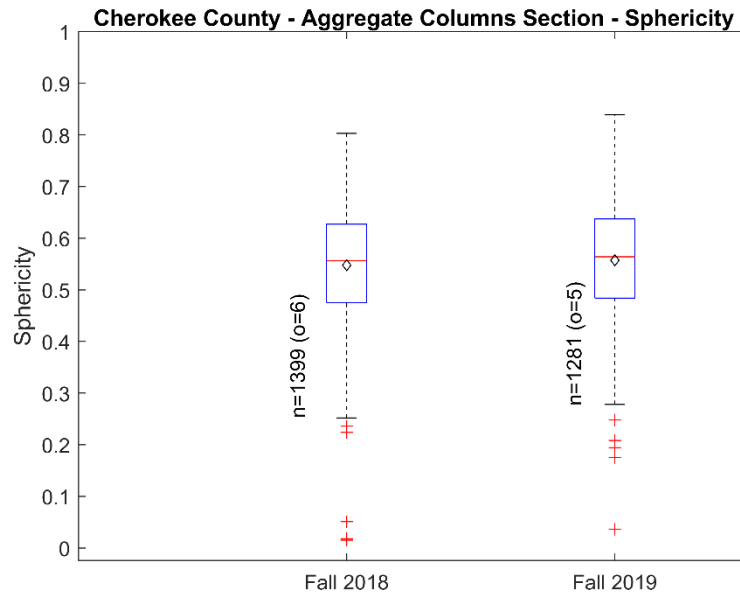


Figure 313. Comparison of sphericity for Cherokee County Aggregate Columns section samples from fall 2018 and fall 2019

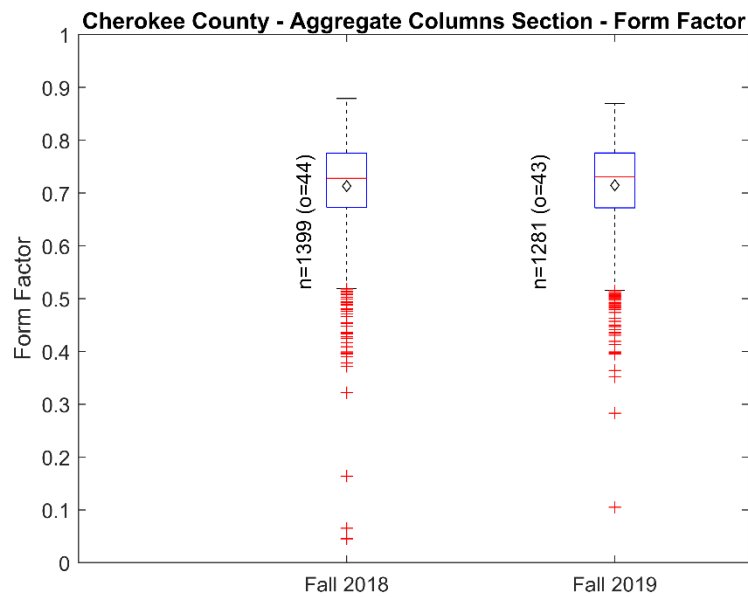


Figure 314. Comparison of form factor for Cherokee County Aggregate section samples from fall 2018 and fall 2019

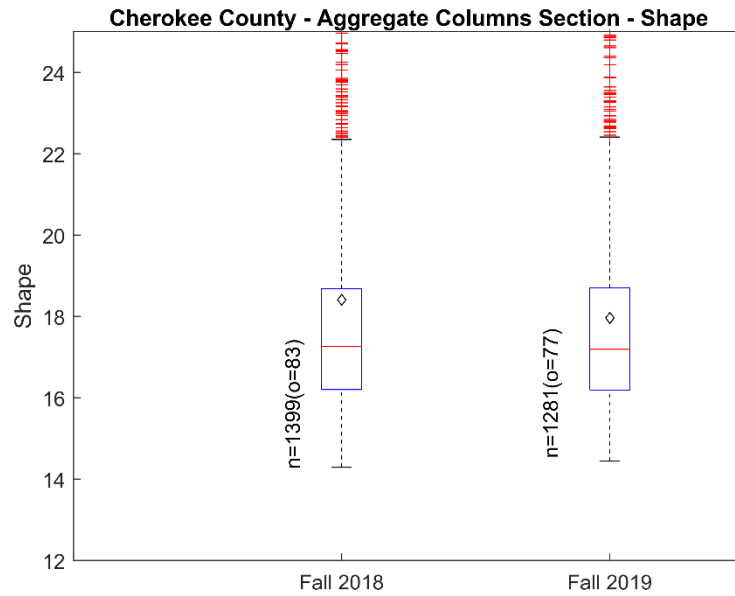


Figure 315. Comparison of shape factor for Cherokee County Aggregate Columns samples from fall 2018 and fall 2019

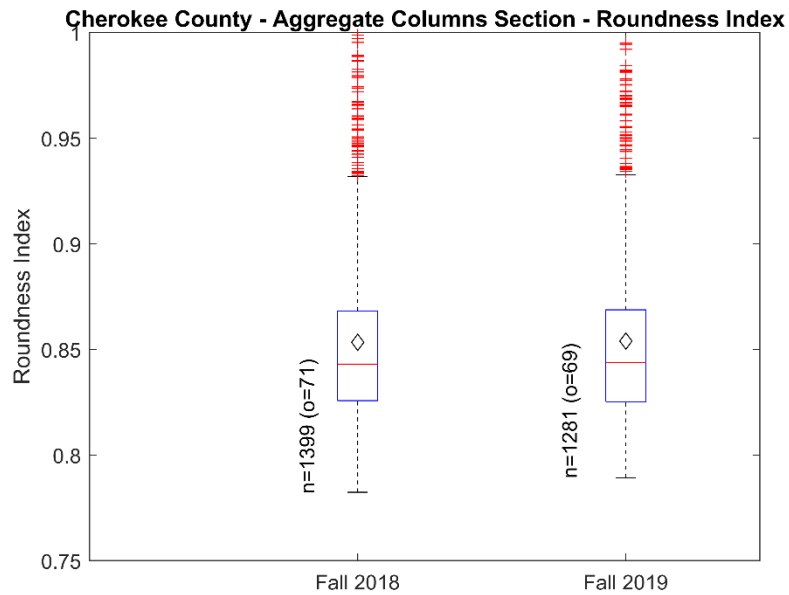


Figure 316. Comparison of roundness index for Cherokee County Aggregate Columns samples from fall 2018 and fall 2019

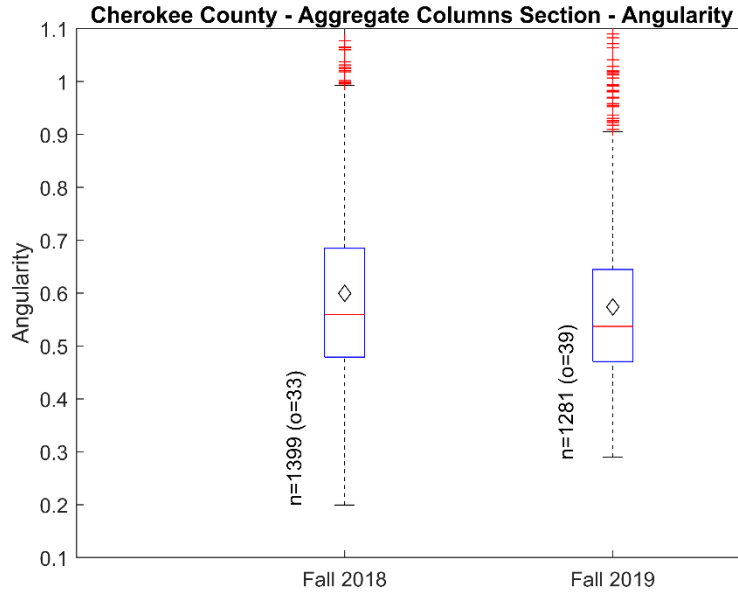
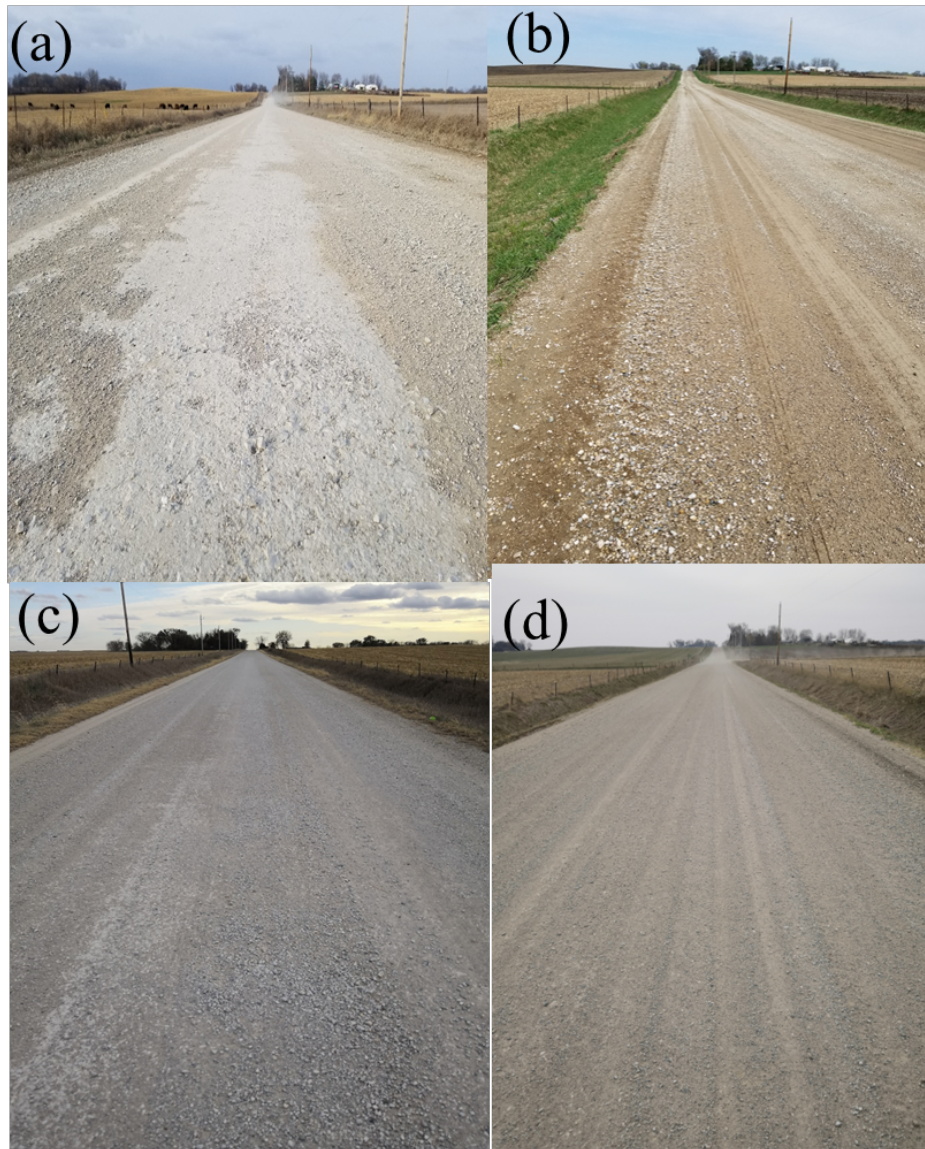


Figure 317. Comparison of angularity for Cherokee County Aggregate Columns samples from fall 2018 and fall 2019

Table 63. Statistical results of morphological parameters of Cherokee County Aggregate Columns section for fall 2018 and fall 2019 samples

Parameter	Sample Collection Date	Max.	Min.	Mean	Mode	Median	Std. Dev.	Skew-ness	Kurt-osis	Out-liers
Roundness	Fall 2018	0.884	0.019	0.636	0.632	0.639	0.109	-0.735	5.147	12
	Fall 2019	0.891	0.045	0.648	0.645	0.651	0.103	-0.387	3.586	6
	% increase			1.8%		1.9%				
Sphericity	Fall 2018	0.803	0.015	0.548	0.541	0.556	0.11	-0.51	3.809	6
	Fall 2019	0.839	0.036	0.557	0.575	0.564	0.108	-0.341	3.115	5
	% increase			1.7%		1.4%				
Form Factor (FF)	Fall 2018	0.879	0.045	0.713	0.728	0.728	0.09	-1.829	10.506	44
	Fall 2019	0.87	0.105	0.714	0.733	0.731	0.087	-1.311	6.23	43
	% increase			0.2%		0.4%				
Shape Factor (SF)	Fall 2018	276.6	14.3	18.4	17	17.3	11.2	20	435.6	83
	Fall 2019	119.3	14.4	18	15.8	17.2	3.9	14.6	359.6	77
	% increase			-2.4%		-0.4%				
Roundness Index (RI)	Fall 2018	1.189	0.782	0.853	0.829	0.843	0.044	2.302	11.57	71
	Fall 2019	1.248	0.789	0.854	0.828	0.844	0.045	2.454	13.81	69
	% increase			0.1%		0.1%				
Angularity	Fall 2018	1.221	0.199	0.6	0.407	0.559	0.158	0.993	3.643	33
	Fall 2019	1.173	0.29	0.574	0.39	0.537	0.142	1.161	4.269	39
	% increase			-4.3%		-4.0%				



Xue et al. 2022

**Figure 318. Visual surveys of Cherokee County Aggregate Columns section over time:
(a) fall 2018, (b) spring 2019, (c) fall 2019, (d) spring 2020**

4.3.16 Comparison of Gravel Deterioration for Cherokee County Test Sections

4.3.16.1 Comparison of Breakage Parameters for Cherokee County Sections

As detailed in previous sections of this report, Hardin's breakage parameters were evaluated for the Control, OGCS, and Aggregate Columns test sections in Cherokee County for samples collected after construction in fall 2018 as well as in spring 2019, fall 2019, and spring 2020. The cumulative total and relative breakage parameters for these test sections are compared in Figure 319 and Figure 320, respectively. Both are evaluated relative to the initial samples collected in

fall 2018. The results reveal that the aggregate columns section experienced the lowest total breakage and relative breakage over time. On the other hand, the control section consistently had the highest cumulative breakage values, followed by the OGCS section. As previously noted, however, due to the change in Cherokee County Engineer position during the TR-721 project there was some uncertainty and information loss as to whether maintenance aggregates were spread on these sections. The new insights beyond those of the previous project are that both the OGCS and Aggregate Columns methods remained somewhat effective in slowing the breakage of aggregates for at least two years, with the breakage being much lower for the Aggregate Columns section in this particular county. However, as previously discussed in Sections 4.3.2, 4.3.6, and 4.3.10 for Howard, Hamilton, and Washington Counties, the OGCS section exhibited the least breakage in those counties.

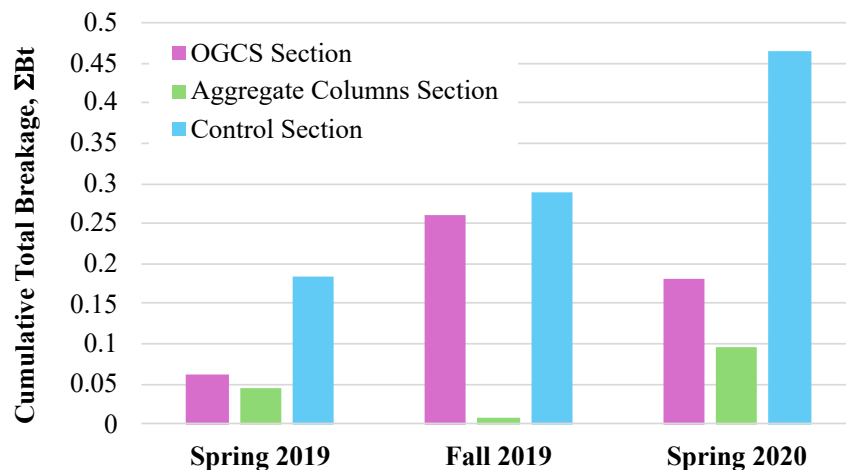


Figure 319. Comparison of cumulative total breakage of samples from Cherokee County OGCS section, Aggregate Columns section, and Control section collected over time

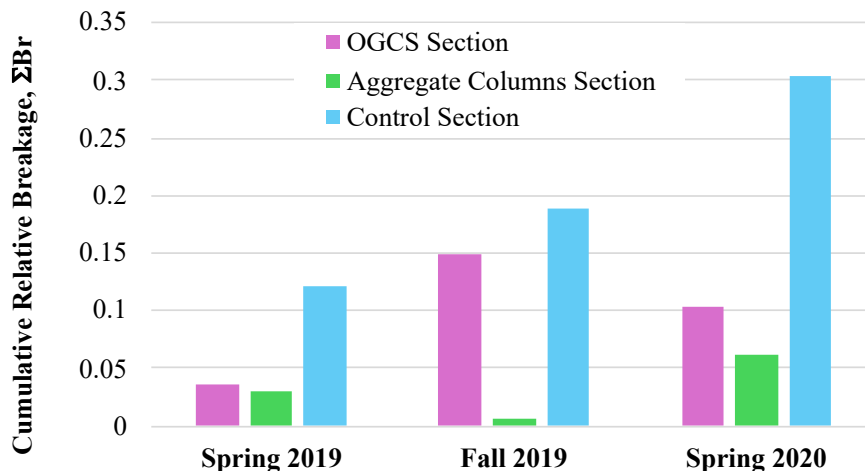


Figure 320. Comparison of cumulative relative breakage of samples from Cherokee County OGCS section, Aggregate Columns section, and Control section collected over time

4.3.16.2 Comparison of Change in Gravel, Sand and Fines Fractions for Cherokee County Sections

The gravel, sand, and fines fractions evaluated in previous sections of this report for the three Cherokee County test sections are compared in Figure 321 and Figure 322 for the gravel fraction, Figure 323 and Figure 324 for the sand fraction, and Figure 325 and Figure 326 for the fines fraction. The results show that the Aggregate Columns section performed the best, as it experienced the smallest overall decrease in gravel fraction and the smallest increase in sand fraction over the entire period of study, followed by the OGCS section. Conversely, the Control section generally exhibited a greater overall decrease in gravel fraction and increase in sand fraction up through Fall 2019 before maintenance aggregates were placed. Regarding fines content, the Control section had the greatest percent increase in fines fraction over time, followed by the Aggregate Columns section. The fines content in the OGCS section actually decreased slightly over the project duration.

Considering the rates of breakage, decreases in gravel fraction, and increases in sand and fines fractions through Fall 2019 in Cherokee County, the Aggregate Columns section had the smallest total and relative breakage and the smallest decrease in gravel fraction over time, as well as the smallest increases in sand fractions. On other hand, the Control section showed the greatest total and relative breakage, followed by the Aggregate Columns section. These findings suggest that Aggregate Columns section was most effective in minimizing gravel breakage, followed by the OGCS section offering intermediate effectiveness and the Control section offering the least effectiveness.

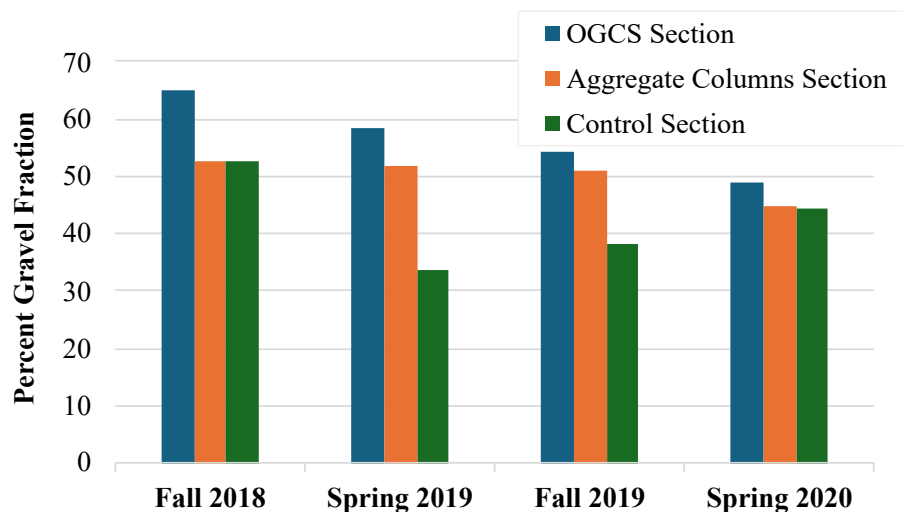


Figure 321. Comparison of gravel fraction for samples from Cherokee County OGCS section, Aggregate Columns section, and Control section collected over time

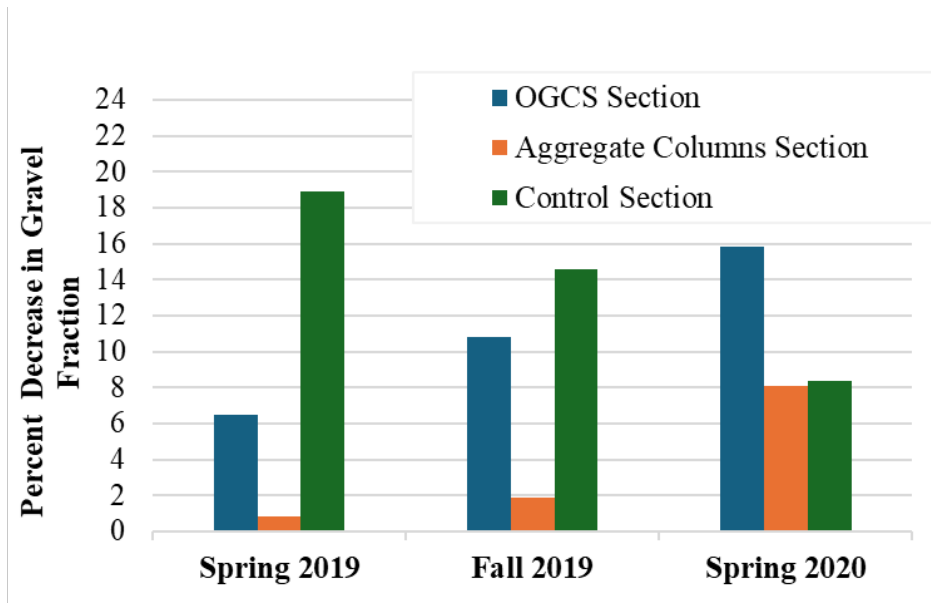


Figure 322. Comparison of percent decrease in gravel fraction relative to 2018 for samples from Cherokee County OGCS section, Aggregate Columns section, and Control section collected over time

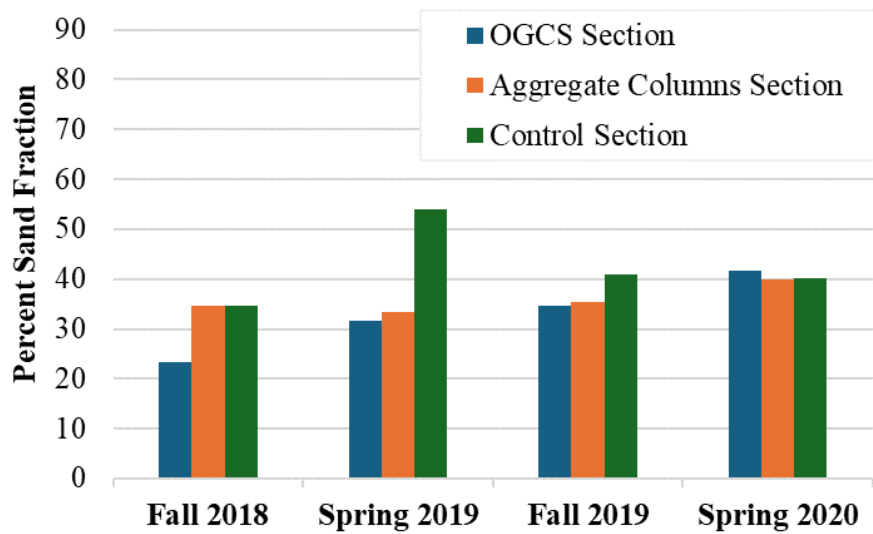


Figure 323. Comparison of sand fraction for samples from Cherokee County OGCS section, Aggregate Columns section, and Control section collected over time

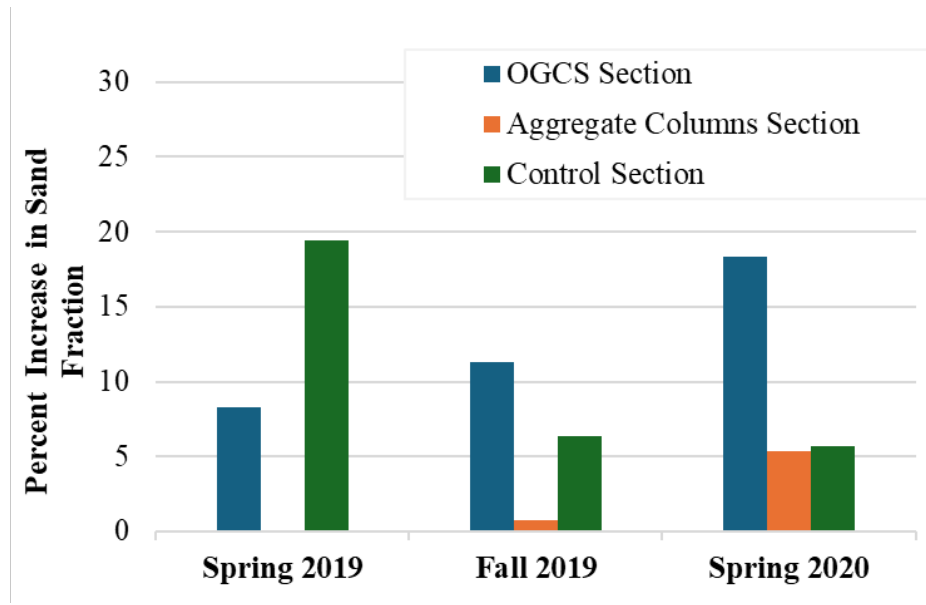


Figure 324. Comparison of percent increase in sand fraction relative to 2018 for samples from Cherokee County OGCS section, Aggregate Columns section, and Control section collected over time

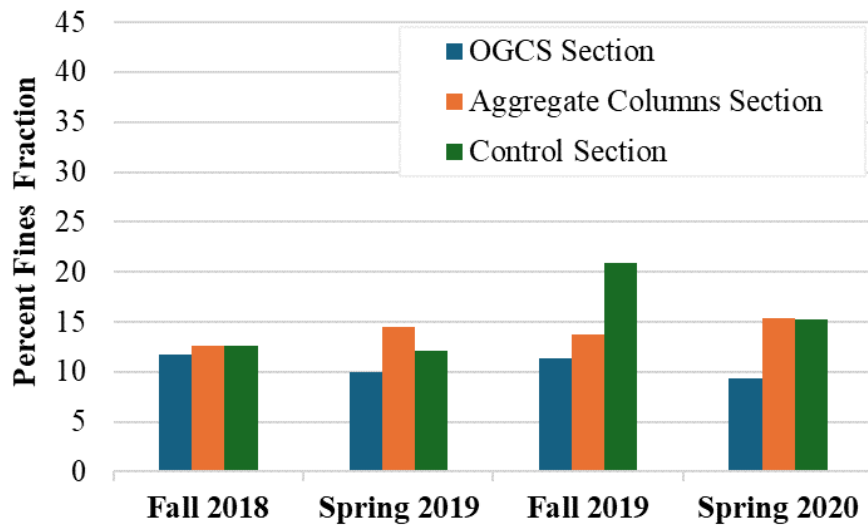


Figure 325. Comparison of fines fraction for samples from Cherokee County OGCS section, Aggregate Columns section, and Control section collected over time

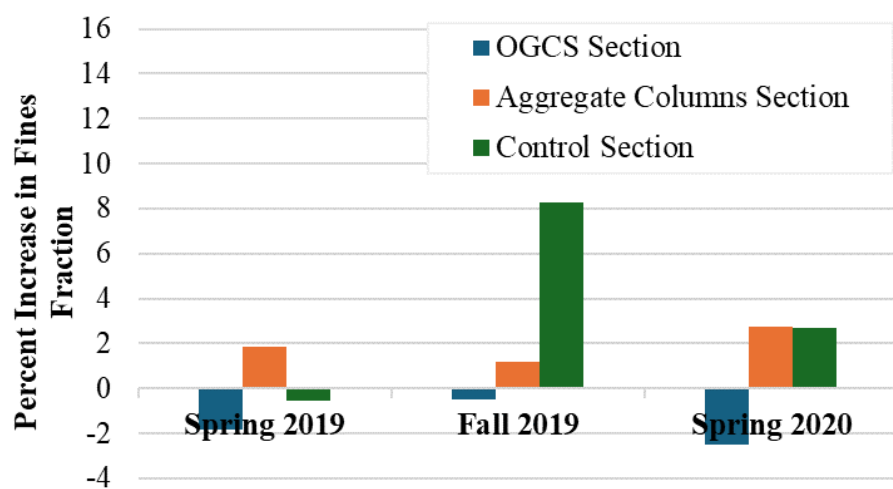


Figure 326. Comparison of percent increase in fines fraction relative to 2018 for samples from Cherokee County OGCS section, Aggregate Columns section, and Control section collected over time

CHAPTER 5. CONCLUSIONS AND RECOMMENDATIONS

5.1 Comparison of Breakage and Morphological Parameters for Different Aggregate Sources

To aid in assessing the relative performance of the various aggregate types examined in this study, Table 64 provides a summary of the total breakage and percent change in the six key morphological parameters. In the following three subsections, results are compared and discussed first for the quarry specimens subjected to laboratory gyratory compaction tests, then the samples from field test sections subjected to traffic loading, and finally the triaxial test results for quarry specimens.

5.1.1 *Comparison of Quarried Aggregate Samples Subjected to Laboratory Gyratory Compaction Tests*

The first five rows of Table 64 contain results for the quarry samples, for which the total breakage values were determined using PSD curves from sieve analyses performed before and after gyratory compaction tests. The corresponding changes in morphological parameters for the quarry samples in the first five rows were determined by 2D image analyses of the same specimens before and after the gyratory tests. These results therefore quantify the performance of the different quarry materials obtained in highly repeatable laboratory tests having the same number of gyrations, loading eccentricity, and applied vertical pressure, with the exact same specimens examined before and after gyratory compaction. For the morphological parameters, particle degradation is generally associated with increases in roundness, sphericity, and form factor, and decreases in shape factor, roundness index, and angularity.

The quarry sample results in Table 64 reveal that the Gehrke Quarry Class A aggregates had the highest total breakage of 0.4461, closely followed by the Alden Quarry Clean aggregates with a breakage of 0.3938. The other three materials had much lower breakage values of 0.0720 for Moore Quarry Class A, 0.0563 for Crescent Quarry Class A, and 0.0388 for Pedersen Quarry Class A. Despite Gehrke having the greatest total breakage, its particles experienced the smallest increase in roundness (tied with Pedersen at 1.1%), and the second lowest increase in sphericity of 3.7% (surpassing only Pedersen at 2.4%). The greatest increases in roundness and sphericity were observed for Alden at 8.4% and 7.9%, respectively, followed by Moore (5.6% and 5.3%) and Crescent (4.9% and 5.0%). Gehrke had the highest increase in form factor of 44.7%, followed by Moore at 20.1%, while the other three quarry materials had small increases of less than a few percent.

For the shape factor and roundness index, Gehrke had the greatest decreases of -30.9% and -14.4%, respectively, followed by Alden (-28.7% and -13.3%) and Moore (-16.8% and -7.0%). For Crescent and Pederson, the decreases in shape factor and roundness index were below a few percent. The decreases in angularity were greatest for Alden and Moore at -24.0% and -22.0%, respectively, and smallest for Crescent and Pedersen at -7.7% and -5.7%, respectively. In contrast to the other quarry materials which all decreased in angularity, the Gehrke Clean aggregate exhibited an increase in angularity of 42.3%, meaning the Gehrke particles were more

angular after breaking while those of the other quarries were less angular. This is consistent with Gehrke having among the smallest increase in roundness compared to the other quarries.

Overall, the Pedersen, Crescent, and Moore aggregates were strongest in terms of having the lowest total breakage during gyratory compaction testing, with the Pedersen aggregates exhibiting the smallest changes in morphology. The Alden and Gehrke aggregates had the highest breakage values and some of the largest changes in morphology during gyratory compaction tests.

Table 64. Comparative summary of total breakage and changes in median morphological parameters for all materials

Materials	Timing of Sample Collection	Total Breakage**	% Change in Median of Morphological Parameters					
			Roundness	Sphericity	Form Factor	Shape Factor	Roundness Index	Angularity
Moore Quarry (Class A)	07/2019	0.0720	5.6%	5.3%	20.1%	-16.8%	-7.0%	-22.0%
Alden Quarry (Clean)	08/2019	0.3938	8.4%	7.9%	0.3%	-28.7%	-13.3%	-24.0%
Gehrke Quarry (Clean)	08/2019	0.4461	1.1%	3.7%	44.7%	-30.9%	-14.4%	42.3%
Crescent Quarry (Class A)	07/2019	0.0563	4.9%	5.0%	1.8%	-1.8%	-0.3%	-7.7%
Pedersen Quarry (Class A)	08/2019	0.0388	1.1%	2.4%	0.3%	-0.4%	-0.4%	-5.7%
TR-704 Section-BFL Class A	04/2017 ^a	0.2180	-	-	-	-	-	-
	06/2017 [*]	0.3436	-0.8%	0.2%	-11.1%	12.4%	3.7%	3.3%
	02/2018 [*]	-	-1.4%	-1.0%	-33.4%	50.3%	19.1%	14.8%
	04/2018 [*]	-	0.0%	1.1%	-1.2%	1.1%	0.1%	3.6%
	04/2018 ^{*†}	-	1.5%	2.1%	48.5%	-32.7%	-15.9%	-9.8%
	04/2019 [†]	0.0141	0.2%	0.0%	7.2%	-6.7%	-2.5%	-7.3%
TR-704 Section- LCF Class A	04/2017 ^a	0.1312	-	-	-	-	-	-
	06/2017 [*]	-0.1208	0.5%	0.9%	-0.7%	0.7%	0.2%	1.4%
	02/2018 [*]	-	0.6%	0.4%	-3.9%	4.1%	2.8%	2.2%
	04/2018 [*]	-0.0309	0.5%	0.2%	-0.3%	0.4%	-0.1%	0.0%
	04/2019 [†]	0.1211	0.8%	0.2%	1.0%	-1.0%	-0.1%	-4.1%
TR-704 Section-OFD Class A	04/2017 ^a	0.1208	-	-	-	-	-	-
	06/2017 [*]	-0.0107	-	-	-	-	-	-
	02/2018 ^{††}	-	-0.8%	-1.4%	-1.2%	1.1%	0.2%	1.1%
	04/2018 [*]	-0.0149	-0.8%	-2.1%	-0.9%	0.8%	0.2%	2.0%
	04/2018 ^{*†}	-	0.0%	-0.7%	0.3%	-0.3%	0.0%	0.9%
	04/2019 [†]	-0.0184	-	-	-	-	-	-
TR-721 – Howard County Control Section	Spring 2019 [×]	0.4117	-	-	-	-	-	-
	Spring 2020 ^{×†}	0.3052	-	-	-	-	-	-
TR-721 – Howard County OGCS Section	Spring 2019 [×]	0.0130	-	-	-	-	-	-
	Fall 2019 [×]	0.4384	-	-	-	-	-	-
	Spring 2020 [×]	0.5644	-	-	-	-	-	-
TR-721 – Howard County Aggregate Columns Section	Spring 2019 [×]	0.4905	-	-	-	-	-	-
	Fall 2019 [×]	0.5177	-	-	-	-	-	-

Materials	Timing of Sample Collection	Total Breakage**	% Change in Median of Morphological Parameters					
			Roundness	Sphericity	Form Factor	Shape Factor	Roundness Index	Angularity
TR-721 – Hamilton County Control Section	Spring 2019 ^x	0.5577	-	-	-	-	-	-
	Fall 2019 ^x	0.5817	1.9% ^{xx}	2.8% ^{xx}	3.2% ^{xx}	-3.1% ^{xx}	-0.6% ^{xx}	-4.3% ^{xx}
	Spring 2020 ^x	0.5979	-	-	-	-	-	-
TR-721 – Hamilton County OGCS Section	Spring 2019 ^x	-0.0249	1.4%	0.7%	1.2%	-1.2%	-0.1%	-3.8%
	Fall 2019 ^x	0.1314	-	-	-	-	-	-
	Spring 2020 ^x	0.3025	3.4%	2.5%	2.0%	-1.8%	-0.5%	-10.4%
TR-721 – Hamilton County Aggregate Columns Section	Spring 2019 ^x	0.6167	-	-	-	-	-	-
	Fall 2019 ^x	0.7069	1.0% ^{xx}	2.6% ^{xx}	4.1% ^{xx}	-4.1% ^{xx}	-9.7% ^{xx}	-1.3% ^{xx}
	Spring 2020 ^x	0.6948	-	-	-	-	-	-
TR-721 – Washington County Control Section	Spring 2019 ^x	0.5285	-	-	-	-	-	-
	Fall 2019 ^x	0.5796	-	-	-	-	-	-
	Spring 2020 ^x	0.6011	-	-	-	-	-	-
TR-721 – Washington County OGCS Section	Spring 2019 ^x	0.1915	-	-	-	-	-	-
	Fall 2019 ^x	0.2008	3.4%	3.1%	1.4%	-1.3%	0.0%	-3.8%
	Spring 2020 ^x	0.1557	-	-	-	-	-	-
TR-721 – Washington County Aggregate Columns Section	Spring 2019 ^x	0.3107	-	-	-	-	-	-
	Fall 2019 ^x	0.4372	-	-	-	-	-	-
	Spring 2020 ^x	0.5889	-	-	-	-	-	-
TR-721 – Cherokee County Control Section	Spring 2019 ^x	0.1850	-	-	-	-	-	-
	Fall 2019 ^x	0.2896	-0.3% ^{xx}	4.1% ^{xx}	6.6% ^{xx}	-1.3% ^{xx}	-0.6% ^{xx}	-6.2% ^{xx}
	Spring 2020 ^x	0.1790	-	-	-	-	-	-
TR-721 – Cherokee County OGCS Section	Spring 2019 ^x	0.0629	-	-	-	-	-	-
	Fall 2019 ^x	0.2606	-	-	-	-	-	-
	Spring 2020 ^x	0.1800	-	-	-	-	-	-
TR-721 – Cherokee County Aggregate Columns Section	Spring 2019 ^x	0.0454	-	-	-	-	-	-
	Fall 2019 ^x	0.0078	1.9%	1.4%	0.4%	-0.4%	0.1%	-4.0%
	Spring 2020 ^x	0.0955	-	-	-	-	-	-

** From sieve analyses before versus after gyratory compaction tests for quarry samples, from sieve analysis of field samples over time for test sections

^aw.r.t. Sep 2016, ^{*}w.r.t. May 2017, [†]w.r.t. May 2018, ^{**†}w.r.t. Feb 2018, ^{††}w.r.t. June 2017, ^xw.r.t. Fall 2018, ^{x†}w.r.t. Fall 2019, ^{xx}w.r.t. Spring 2019

5.1.2 Comparison of Aggregates from Field Test Sections Subjected to Traffic Loading

For the TR field test sections shown in Table 64, the values in the Total Breakage column quantify the changes in the coarse fraction determined using the PSD curves measured in the previous TR-704 and TR-721 projects. For the present study, new 2D image analyses of particle morphology were also performed for the dates for which surplus samples were left over from these projects. As previously discussed, the test specimens for a given field section and date were obtained by blending samples taken at several different points within the test section, which may introduce more spatial sampling error and variations in traffic loading compared to the quarry specimens which were subjected to the more repeatable gyratory compaction tests in the lab. Therefore, it is more difficult to make direct comparisons of aggregate performance among the field test sections. However, some general conclusions can be drawn from the data.

First, the highest rates of breakage in field test sections were typically observed within the first few months after placing new aggregates for construction or maintenance and tended to decrease thereafter. Theoretically, for the same finite volume of aggregates subject to continual traffic loading with no new materials placed, the total breakage should continually increase as the PSD migrates upward towards a finer gradation with time. However, each time new maintenance aggregates were placed the overall gradation of the test section was altered, so the breakage calculation had to start over to reference the latest date of material placement.

Second, the majority of the total breakage values for the field test sections in Table 64 exhibited valid positive values, while a few cases had small negative values which were likely due to sampling or experimental error, or an unreported addition of maintenance aggregates. Because the various test sections received different amounts and timing of maintenance aggregates, it is most consistent to compare the total breakage values for the first several months immediately following construction. For the TR-704 test sections, this corresponds to the samples from April 2017 referenced to the end of construction in September 2016. For the TR-721 test sections, this corresponds to the samples from Spring 2019 referenced to the end of construction in Fall 2018.

For the TR-704 test sections sampled in April 2017, the data of Table 64 reveal that the BFL aggregates had the highest total breakage value of 0.2180 while the OFD aggregates had the lowest value of 0.1208, and the LCF aggregates were only slightly higher at 0.1312. Although no surplus samples from April 2017 existed for image analysis among these three test sections, several samples were found for the other test dates. The resulting morphological parameters for the BFL and LCF sections showed increases in roundness, sphericity, and form factor for some of the dates, whereas those for the OFD section showed small decreases in these same parameters. The corresponding values of shape factor, roundness index, and angularity for LCF and BFL were found to decrease for only the last two sampling dates, whereas OFD again exhibited very little change. Overall, the BFL materials yielded the greatest changes in morphological parameters over time, whereas LCF exhibited slight changes and OFD exhibited the smallest changes. These results are consistent with BFL being the weakest in terms of breakage values, and OFD (closely followed by LCF) being the strongest. It should be noted that the Crescent Quarry samples of the previous section were also from the Bethany Falls Ledge. As detailed in the previous section, they were among the strongest of the quarry samples, but the

BFL samples from the field test sections were the weakest. Further study is required to determine the reason for this contradictory behavior for these two materials from the same ledge.

For the Howard County TR-721 test sections sampled in Spring 2019 compared to the post-construction conditions of Fall 2018, the Control and Aggregate Columns sections had relatively high total breakage values of 0.4117 and 0.4905, respectively, while the OGCS section had a very low breakage of 0.0130 likely due to the binding action of the added clay fines helping to keep the gravel particles in place. No surplus samples from the Howard County test sections were available for image analysis.

The Hamilton County TR-721 test sections showed similar results to Howard County for the first Spring 2019 samples, but with the Control and Aggregate Columns sections exhibiting even higher breakage values of 0.5577 and 0.6167, while the OGCS section had a very low negative breakage of -0.0249 which is practically zero considering experimental and sampling error. Image analysis was performed on Hamilton County samples from Fall 2019 that could be located for the Control and Aggregate Columns sections, and from Spring 2019 and Spring 2020 for the OGCS section. The results all showed gravel degradation through increases in roundness, sphericity, and form factor ranging from 0.7% to 4.1%, and decreases in shape factor, roundness index, and angularity ranging from 0.1% to 10.4%. Unfortunately, the dates of the available surplus OGCS samples did not coincide with the dates of the other two test sections. However, apart from a 10.4% decrease in angularity in Spring 2020, the percent changes in the other five morphological parameters for OGCS were smaller than those of the Control and Aggregate Columns sections.

The Washington County sections exhibited similar behavior to Howard and Hamilton Counties, with higher breakage values for the Control (0.5285) and Aggregate Columns (0.3107) sections and the lowest breakage for the OGCS (0.1915) section, although the OGCS breakage was significantly higher than in the other two counties. Only one surplus sample was located for image analysis, belonging to the OGCS section from Fall 2019. The results showed increases on the order of a few percent in roundness, sphericity, and form factor, along with a 1.3% decrease in shape factor, no change in roundness index, and a 3.8% decrease in angularity.

Finally, the Cherokee County sections exhibited different behavior than the other three counties in Spring 2019. First, although the breakage was highest for the Control section, it was a modest 0.1850. The OGCS breakage was relatively small at 0.0629 as expected, but the Aggregate Columns section had the lowest breakage at 0.0454, which was unexpected. Surplus samples were only available for the Control and Aggregate Columns sections, both collected in Fall 2019. Although the changes in morphological parameters were referenced to different dates, the Control section showed a small 0.3% decrease in roundness while the Aggregate Columns section showed a small 0.1% increase in roundness index, both of which are opposite the expected directions of change. The remaining parameters all showed the expected directions of change, with the Control section exhibiting greater increases in sphericity and form factor and greater decreases in shape factor and angularity than the Aggregate Columns section.

5.1.3 Comparison of Triaxial Test Results for All Quarries

The triaxial test results from all five quarries are compared in Table 65. Before gyratory compaction testing, the initial friction angles ranged from 37.5° to 43.9° and the initial cohesion values ranged from 1.33 psi to 4.52 psi. The Moore Quarry aggregates had the lowest initial friction angle but the greatest initial cohesion. Conversely, the Alden Quarry aggregates had the highest initial friction angle but the smallest initial cohesion. These trends held true after degradation of the aggregates by gyratory compaction testing, as the Moore Quarry aggregates ended up with the lowest friction angle the greatest cohesion, whereas the Alden Quarry aggregates again had the highest friction angle and lowest cohesion after the GC tests. Gyratory compaction testing caused the cohesion values to increase for the Moore, Gehrke, and Crescent aggregates, and to decrease for the Alden and Pedersen aggregates. The greatest percent decrease in cohesion was exhibited by the Alden Quarry aggregates which lost 86.4% of their initial cohesion, while the greatest percent increase was exhibited by the Gehrke aggregates which gained 66.5% over their initial cohesion.

Table 65. Summary of triaxial test results for the quarry samples

Quarry	Drained Friction Angle, ϕ' (degrees)	Drained Cohesion, c' (psi)
Moore - BGT	37.5	4.52
Moore - AGT	32.5	6.14
% change	13.3% dec.	35.8% inc.
Alden - BGT	43.9	1.33
Alden - AGT	43.4	0.181
% change	1.1% dec.	86.4% dec.
Gehrke - BGT	41.2	1.64
Gehrke - AGT	37.8	2.73
% change	8.3% dec.	66.5% inc.
Crescent - BGT	37.9	2.54
Crescent - AGT	37.3	3.42
% change	1.6% dec.	34.6% inc.
Pedersen - BGT	39.1	3.95
Pedersen - AGT	41.5	2.24
% change	6.1% inc.	43.3% dec.

The friction angles for Moore, Alden, Gehrke, and Crescent Quarries all decreased by 13.3%, 1.1%, 8.3%, and 1.6%, respectively, whereas the friction angle for Pedersen increased by 6.1%. A decrease in friction angle could result from particles becoming more rounded and less angular during gyratory compaction, but the gradation and particle packing will also affect the BGT and AGT friction values. Conversely, an increase in friction angle as exhibited by the Pedersen aggregates could indicate that particles became less rounded and more angular when breaking in the gyratory compaction test, and/or the PSD became more well-graded with tighter particle packing. However, the mean morphological parameters of the gravel fraction from 2D image analysis of the Pedersen materials did not exhibit this type of behavior, as they showed slight increases of 1.6% in roundness and 1.9% in sphericity, along with a 4.5% decrease in angularity.

On the other hand, the Moore, Alden, and Crescent Quarry materials all showed much greater increases in roundness and decreases in angularity than the Pedersen Quarry materials. As a result, the friction angles of the Moore, Alden, and Crescent materials are expected to decrease more than those of Pedersen. This is largely the case for the data of Table 65, with the exception of the Gehrke aggregates. Although the Gehrke aggregates had a large decrease in friction angle, which is consistent with them having the smallest increase of 1.3% in mean roundness, they were the only material to actually exhibit an increase in mean angularity (by 42.3%). The large increase in angularity of the gravel fraction was perhaps overshadowed by the change in gradation for the Gehrke aggregates, leading to an overall decrease in friction angle.

5.2 Conclusions from Geological Tests on Quarry and Field Samples

For the geological tests, the following four hypotheses were examined in this study using the petrography, pycnometry, mercury porosimetry, and grain size analysis tests:

1. The coarse aggregates are composed of multiple rock types.
2. The Clean and Class A coarse aggregates have different relative abundances of rock types.
3. Relative abundances of rock types change over time in granular-surfaced roads.
4. Relative abundances of rock types change during laboratory-performed gyratory compaction tests.

For the first hypothesis, seven different sources were sorted by rock type and the results supported the hypothesis in that each was composed of at least four different rock types.

For the second hypothesis, three samples had examples from each of these aggregate types: Atlantic (BFL), Ames Mine (LCF), and Clayton (OFD) from the TR-704 project. In each case, the Class A samples showed a significant difference in the relative abundance of rock types compared to the Clean samples.

For the third hypothesis, changes over time in the relative abundance of rock types from field test sections (BFL, LCF, and OFD) were examined. In general, the less durable rock types such as those with higher clay contents or greater porosities experienced a greater reduction in abundance over time.

Regarding the fourth hypothesis, all four of the aggregate types were tested before and after gyratory tests. All four types showed changes in the relative abundances of lithologies.

5.3 Recommendations for Implementation and Further Research

Recommendations for implementation and further research are proposed herein based on the findings garnered from the geotechnical and geological tests performed on the numerous samples from quarries and field test sections.

- To implement the results of this study, county engineers can select from the material types that produced the least breakage in quarry samples and field test sections, as evaluated in this chapter by breakage determined from both gyratory compaction tests and field PSD curves over time.
- Among the field test sections from project TR-704, in the present study the technical advisory committee (TAC) instructed the research team to focus only on the three constructed with a single material type (BFL, LCF, and OFD). However, four other test sections were also constructed in that project, each with a blend of BFL Class A with one of four different Clean material types. The PSD curves from that project could also be re-analyzed to understand the performance of the blended test sections in terms of Hardin's breakage parameters. Additionally, if surplus samples from those test sections can also be located in storage, then new gyratory compaction tests, 2D image analyses (using the Iowa DOT's Camsizer for improved efficiency), and geological tests can be performed to help quantify the field performance and coarse aggregate deterioration for granular-surfaced roads constructed with such material blends.
- Similarly, project TR-721 also contained several other chemically and mechanically stabilized test sections not covered in this study (the TAC advised to include only the natural aggregate materials without chemical stabilization to maintain a reasonable scope in this study). The existing data from the TR-721 project report could also be analyzed to assess the breakage parameters for such test sections, and surplus samples can be tested if they can be found in storage.
- The body of knowledge from the present study could also be expanded upon by sampling a wider variety of quarry materials and field test section samples from around the state, using the methods described herein.
- The methods of this study could also be expanded to include other types of recycled or synthetic aggregates, or those stabilized with chemical or mechanical methods, to assess the differences in breakage and morphology over time.
- To enhance the usefulness of the 2D image analyses performed in the present study, the image data can be further mined to investigate a wider range of morphological parameters beyond the six focused on in this study.
- To improve the understanding of particle breakage and abrasion at the microscopic scale for both gyratory compaction in the laboratory and traffic loading in the field, scanning electron microscope (SEM) imaging could be performed on the remaining samples. In future studies, SEM imaging can be added to the experimental plans.
- Another possible research direction is to construct and monitor new test sections using the materials that had the best performance and lowest deterioration in this study.

REFERENCES

- AASHTO. (2001). *AASHTO Provisional Standards, Interim Edition*. American Association of State Highway and Transportation Officials, Washington DC.
- Alshibli, K. A., Druckrey, A. M., Al-Raoush, R. I., Weiskittel, T., and Lavrik, N. V. (2015, May). Quantifying morphology of sands using 3D imaging. *Journal of Materials in Civil Engineering*, 27(10), 04014275. doi:10.1061/(asce)mt.1943-5533.0001246.
- Arasan, S., Akbulut, S., and Hasiloglu, A. S. (2011). The relationship between the fractal dimension and shape properties of particles. *KSCE Journal of Civil Engineering*, 15(7), 1219–1225. doi:DOI 10.1007/s12205-011-1310-x.
- Aschenbrenner, B. C. (1956). A new method of expressing particle sphericity. *Journal of Sedimentary Research*, 26, 15–31.
- Baker, D., and Johnson, G. D. (2000). *Evaluation of Aggregate Sections at Mn/ROAD*. No. MN/RC-2000-29. Minnesota. Department of Transportation, St. Paul, MN.
- Barrett, P. J. (1980). The shape of rock particles, a critical review. *Sedimentology*, 27, 291–303.
- Baumel, C. P., Miller, S. B., Pautsch, G. R. and Hamlett, C. A. (1989). *The Local Rural Road System: Alternative Investment Strategies*. Center for Agricultural and Rural Development (CARD) Publications 89-tr6. Iowa State University, Ames, IA.
- Berthelot, C., and Carpentier, A. (2003). Gravel Loss Characterization and Innovative Preservation Treatments of Gravel Roads: Saskatchewan, Canada. *Transportation Research Record*, 1819(2), 180–184.
- Blott, S. J., and Pye, K. (2008). Particle shape: A review and new methods of characterization and classification. *Sedimentology*, 55(1), 31–63.
- Cerni, G., and Camilli, S. (2011). Comparative analysis of gyratory and proctor compaction processes of unbound granular materials. *Road Materials and Pavement Design*, 12(2), 397–421.
- Clayton, C. R., Abbireddy, C. O., and Schiebel, R. (2009). A method of estimating the form of coarse particulates. *Geotechnique*, 59, 493–501.
- Corey, A. T., Albertson, M. L., Fults, J. L., Rollins, R. L., Gardner, R. A., Klinger, B., and Bock, R. O. (1949). Influence of shape on the fall velocity of sand grains. Master's thesis. Colorado Agricultural and Mechanical College.
- Cox, E. P. (1927). Method of A method of assigning numerical and percentage values to the degree of roundness of sand grains. *Journal of Paleontology*, 1(3), 179–183.
- Dawson, M. R. (2021). *Evaluation of the Retsch Technology Camsizer P4 to Assess the Shape of Crushed Particles Proposed to be Added to Natural Sand Fine Aggregate Used in Portland Cement Concrete*. SP&R Project 20-SPR1-001. Federal Highway Administration, Washington, DC.
- Dubois, C., Deceuster, J., Kaufmann, O., and Rowberry, M. D. (2015). A new method to quantify carbonate rock weathering. *Mathematical Geosciences*, 47(8), 889–935.
- FHWA. (2015). *Gravel Roads Construction and Maintenance Guide*. Federal Highway Administration, Washington, DC.
<https://www.fhwa.dot.gov/construction/pubs/ots15002.pdf>.
- Hardin, B. O. (1985). Crushing of soil particles. *Journal of Geotechnical Engineering*, 111(10), 1177–1192.

- Hasiuk F., Ridzuan M. F. A., and Taylor, P. (2017). *Calibrating the Iowa Pore Index with Mercury Intrusion Porosimetry and Petrography*. InTrans Project 15-553. Institute for Transportation, Ames, IA.
- Hasiuk F. and Orso, J. (2019). *Calibrating the Iowa Pore Index with Mercury Intrusion Porosimetry and Petrography – Phase II*. InTrans Project 15-553. Institute for Transportation, Ames, IA.
- Hasiuk F. and Ishutov, S. (2019). *Petrographic and Petrophysical Analysis of Decades-Old Iowa Portland Cement Concretes*. InTrans Project 15-553. Institute for Transportation, Ames, IA.
- Huntington, G. and Ksaibati, K., (2011). Management of unsealed gravel roads: State of the practice in American counties. *Transportation Research Record*, 2232,1–9.
- Janoo, V. C. (1998). *Quantification of Shape, Angularity, and Surface Texture of Base Course Materials*. US Army Corps of Engineers, Cold Region Research and Engineering Laboratory.
- Johansson, J., and Vall, J. (2011). Friktionsjords kornform: Inverkan på geotekniska egenskaper, beskrivande storheter och bestämningsmetoder. Master's thesis. Luleå University of Technology, Luleå, Sweden.
- Krumbein, W. C. (1941). Measurement and geological significance of shape and roundness of sedimentary particles. *Journal of Sedimentary Research*, 11, 64–72.
- Krumbein, W. C., and Sloss, L. L. (1963). *Stratigraphy and Sedimentation* (2nd Ed.). San Francisco: W.H. Freeman.
- Landini, G. (2006, February 17). Quantitative analysis of the epithelial lining architecture in radicular cysts and odontogenic keratocysts. *Head and Face Medicine*, 2, 1–9. doi:10.1186/1746-160X-2-4.
- Landini, G., Randell, D. A., and Galton, A. P. (2012). Intelligent imaging using discrete mereotopology. *Proceedings of the Fourth ImageJ User and Developer Conference*, pp. 99–103. Luxembourg.
- Lee, K., Prezzi, M., and Kim, N. (2007). Subgrade design parameters from samples prepared with different compaction methods. *Journal of Transportation Engineering*, 133(2), 82–89.
- Li, C. (2013). Using the Iowa K test and the gyratory compaction test to improve the compaction forecasting expert database. Master's thesis. Iowa State University, Ames, IA.
- Li, C., Ashlock, J. C., White, D. J., and Vennapusa, P. (2015). *Low-Cost Rural Surface Alternatives: Demonstration Project*. Institute for Transportation, Iowa State University, Ames, IA. https://www.intrans.iastate.edu/wp-content/uploads/2018/03/low-cost_rural_surface_alternatives_demo_w_cvr.pdf.
- Li, C., Ashlock, J., White, D., and Vennapusa, P. (2018). *Feasibility of Granular Road and Shoulder Recycling*. Ames, IA: Institute for Transportation, Iowa State University. https://intrans.iastate.edu/app/uploads/2018/07/granular_rd_and-shoulder_recycling_feasibility_w_cvr.pdf.
- Li, C., Vennapusa, P., Ashlock, J. C., and White, D. J. (2017). Mechanistic-based comparisons for freeze-thaw performance of stabilized unpaved roads. *Cold Regions Science and Technology*, 141, 97–108.
- Maroof, M. A., Mahboubi, A., Noorzad, A., and Safi, Y. (2020, March). A new approach to particle shape classification of granular materials. *Transportation Geotechnics*, 22. doi: 10.1016/j.trgeo.2019.100296.

- Mitchell, J. K., and Soga, K. (2005). *Fundamentals of Soil Behavior* (Vol. 3). New York: John Wiley & Sons.
- Mokwa, R., Cuelho, E., and Browne, M. (2008). Laboratory testing of soil using the Superpave gyratory compactor. Transportation Research Board 87th Annual Meeting, January 13–17, Washington, DC.
- Myers, J. D., and Dubberke, W. (1980). *Iowa Pore Index Test*. Interim Report. Iowa Department of Transportation Office of Materials, Ames, IA.
- Paige-Green, P., and Visser, A. T. (1991). Comparison of the impact of various unpaved road performance models on management decisions. *Transportation Research Record*, 1291, 137–142.
- Patterson, W. (1991). Deterioration and maintenance of unpaved roads: Models of roughness and material loss. *Transportation Research Record*, 1291, 143–156.
- Pentland, A. (1927). A method of measuring the angularity of sands. *Proceedings and Transactions of the Royal Society of Canada*, 21(3), 43.
- Ping, W. V., Xing, G., Leonard, M., and Yang, Z. (2003). *Evaluation of Laboratory Compaction Techniques for Simulating Field Soil Compaction (Phase II)*. Florida Department of Transportation, Tallahassee, FL.
- Powers, M. C. (1953). A new roundness scale for the sedimentary. *Journal of Sedimentary Petrology*, 23, 117–119.
- Reyes, A. M., Dawson, M. R. (2010). Overview of economic geology as related to the Iowa DOT and Conklin and Klein Quarries in the geology of Klein and Conklin Quarries, Johnson County, Iowa. Eds. T. Marshall and C. Fields. *Geological Society of Iowa Guidebook*, 87, 9–14.
- Ridzuan, M. F., Hasiuk, F., and Taylor, P. (2017). *Calibrating the Iowa Pore Index with Mercury Intrusion Porosimetry and Petrography*. National Concrete Pavement Technology Center and Midwest Transportation Center, Iowa State University, Ames, IA.
- Riley, N. A. (1941, August). Projection Sphericity. *Journal of Sedimentary Petrology*, 11(2), 94–97.
- Smadi, A., Hough, J., Schulz, L. and Birst, S. (1999). North Dakota gravel road management: Alternative strategies. *Transportation Research Record*, 1652, 16–22.
- Sneed, E. D., and Folk, R. L. (1958). Pebbles in the lower Colorado River, Texas a study in particle morphogenesis. *The Journal of Geology*, 66, 114–150.
- Tickell, F. G. (1931). *The Examination of Fragmental Rocks*. Stanford: Stanford University Press.
- Uys, R. (2011). Evaluation of gravel loss deterioration models: Case study. *Transportation Research Record*, 2205, 86–94.
- van Dam, T. (2012). *Gravel Surfacing Guidelines for South Dakota*. SD2009-08. South Dakota Department of Transportation, Pierre, SD.
- van Zyl, G., Henderson, M., and Uys, R. (2007). Applicability of existing gravel-road deterioration models questioned. *Transportation Research Record*, 1989, 217–225.
- Wadell, H. (1932). Volume, shape, and roundness of rock particles. *The Journal of Geology*, 40, 443–451.
- Wadell, H. (1933, April-May). Sphericity and roundness of rock particles. 41(3), 310–331.
- Wadell, H. (1934). Shape determinations of large sedimental rock fragments. *The Pan-American Geologist*, 61, 187–220.

- Walker, D.M. (1991). Evaluation and rating of gravel roads. *Transportation Research Record*, 1291.
- Washburn, E. W. (1921). Note on a method of determining the distribution of pore sizes in a porous material. *Proceedings of the National Academy of Sciences of the United States of America*, 7(4), 115–116.
- Wentworth, C. K. (1922). The shapes of beach pebbles. *U.S. Geological Survey Bulletin*, 131C, 75–83.
- White, D. and Vennapusa, P. (2013). *Low-Cost Rural Surface Alternatives: Literature Review and Recommendations*. Institute for Transportation, Ames, IA.
- Xue, Z., Ashlock, J. C., Cetin, B., Wu, Y., and Ceylan, H. (2022). *Low-Cost Rural Surface Alternatives Phase III: Demonstration Project*. Ames, IA: Institute for Transportation, Iowa State University. <https://www.intrans.iastate.edu/wp-content/uploads/2022/05/low-cost-rural-surface-alternatives-phase-iii-demonstration-w-cvr.pdf>.
- Zavala, J. R. (2012). Particle shape quantities and influence on geotechnical properties: A review. Ph.D. dissertation. Luleå University of Technology.
- Zheng, J., and Hryciw, R. D. (2015). Traditional soil particle sphericity, roundness and surface roughness by computational geometry. *Géotechnique*, 65, 494–506.
- Zingg, T. (1935). Beitrage zur Schotteranalyse. Ph.D. thesis. Zurich, ETH.
- Zhang, J., White, D. J., and Vennapusa, P. (2017). Estimating mechanistic parameters for subgrade using gyratory compaction with pressure distribution analyzer. *Journal of Materials in Civil Engineering*, 29(11), 04017216.

APPENDIX A. THIN SECTION PHOTOMICROGRAPHS OF GRAVEL ROCK TYPES COLLECTED FROM QUARRIES

The content for Appendix A is available at https://www.intrans.iastate.edu/wp-content/uploads/2025/07/coarse_aggregate_deterioration_in_granular_surfaces_and_shoulders_Appendix_A.pdf.

APPENDIX B. THIN SECTION PHOTOMICROGRAPHS OF GRAVEL ROCK TYPES COLLECTED FROM ROADWAY TEST SECTIONS

The content for Appendix B is available at https://www.intrans.iastate.edu/wp-content/uploads/2025/07/coarse_aggregate_deterioration_in_granular_surfaces_and_shoulders_Appendix_B.pdf.

**THE INSTITUTE FOR TRANSPORTATION IS THE FOCAL POINT FOR TRANSPORTATION
AT IOWA STATE UNIVERSITY.**

InTrans centers and programs perform transportation research and provide technology transfer services for government agencies and private companies;

InTrans contributes to Iowa State University and the College of Engineering's educational programs for transportation students and provides K–12 outreach; and

InTrans conducts local, regional, and national transportation services and continuing education programs.



**IOWA STATE
UNIVERSITY**

Visit InTrans.iastate.edu for color pdfs of this and other research reports.